NON-IDEAL COMPRESSIBLE-FLUID DYNAMICS SIMULATION WITH SU2: NUMERICAL ASSESSMENT OF NOZZLE AND BLADE FLOWS FOR ORGANIC RANKINE CYCLE APPLICATIONS

G. Gori[1*], A. Guardone[1], S. Vitale[2], A. J. Head[2], M. Pini[2], P. Colonna[2]

[1] Politecnico di Milano, Department of Aerospace Science and Technologies,
Via La Masa 34, 20156 Milano, Italy
giulio.gori@polimi.it

[2] Delft University of Technology,
Kluyverweg 1, 2629 HS Delft
s.vitale@tudelft.nl

ABSTRACT

The growing interests towards Organic Rankine Cycle (ORC) turbo-machinery calls for reliable and well-established simulation and design tools, including Computational Fluid Dynamics (CFD) software, accounting for non-ideal thermodynamic behaviour in close proximity to the liquid-vapour saturation curve and critical point, as well as two-phase properties. SU2, an open-source CFD solver originally developed at Stanford University, Palacios et al. (2013, 2014), was recently extended to deal with non-ideal thermodynamics, including state-of-the-art multi-parameter equations of state implemented in the FluidProp library, Colonna and van der Stelt (2004), and it is now in the process of becoming a reliable simulation tool for academic and industrial research on ORC machinery. The investigation of SU2 performances in connection with the numerical simulation of steady nozzle and turbine flows of interest for ORC applications are provided. Numerical simulations refer to both inviscid and viscous flow, with diverse thermodynamic (ideal gas, Van der Waal gas, Peng- obinson Stryjek-Vera, Span-Wagner multi-parameter equation of state) and turbulence (Spalart-Allmaras, SST-k) models. Considered geometries include straight axis planar nozzle, and a typical ORC turbine blade passage.

1. INTRODUCTION

Nowadays applications involving non-ideal compressible flows can be found in numerous industrial problems and are spread over heterogeneous fields. During the last decade Organic Rankine Cycle turbo-machinery became of utmost importance for the future design of highly efficient energy production systems. In practical applications the ORC machinery make use of particular fluids that, under certain conditions of pressure and density, may show non-ideal thermodynamic behaviour. For these fluids the ideal gas law is proved to fail in describing accurately the thermodynamic behaviour when pressure and temperatures are close to the liquid-vapour saturation curve, in the region near the critical point. The rising of non-ideal compressible fluid phenomena thus calls for more complex equations of state, like for instance the Van der Waals or the Peng-Robinson Stryjek-Vera equation of state or the multi-parameter equation of state. These complex gas models are of utmost importance and can possibly provide a more accurate description of the thermodynamic behaviour that characterizes these fluids. Nowadays the community can only rely on a few computational tools capable of dealing with real fluid flows. One of these tools is *zFlow*, developed by S. Rebay and P. Colonna, a solver suitable for compressible inviscid dense gas flows where an hybrid Finite-volume/Finite-element discretization scheme is adopted, Colonna et al. (2002). Such code has been already proved to provide accurate predictions of the flow field inside ORC three-dimensional radial turbine. Today the academic community and the industry desire for a more reliable and well-maintained investiga-

tion tool, to prove the accuracy of the state-of-the-art equation of state and to foster the design of new, more efficient, power production systems. This tool should serve as a framework from which users can start developing their own real-gas models, including new numerical algorithms and customized features, without worrying about the maintenance of the overall structure. The Stanford University Unstructured (SU2) software suite recently became a promising candidate for this role. SU2 is a popular open-source platform for solving multi-physics PDE problems and PDE-constrained optimization problems on general, unstructured meshes. The core of SU2 is a Reynolds-averaged Navier-Stokes (RANS) solver dedicated to the simulation of compressible, turbulent flows. The capabilities of this solver are various and their number is growing quickly as developers from the international team contribute to improve the code, providing new features and extending its capabilities. A joint research team composed by researchers from Delft University of Technology, from the Politecnico di Milano, and from the Stanford University recently undertook a collaborative effort to bring the SU2 at the cutting-edge for non-ideal compressible fluid-dynamics (NICFD) simulation, Vitale et al. (2015),, extending SU2 capabilities to a wider range of pertinence with the inclusion of the Van der Waals and the Peng-Robinson Stryjek-Vera equation of state. The early work has been lately extended with the inclusion of the FluidProp, Colonna and van der Stelt (2004), thermodynamic library which opens the path to the exploitation of the state-of-the-art multi-parameter equation of state. The SU2 suite already included a library for thermo-physical properties of reacting non-equilibrium flows, such as those involving combustion, though a computational framework for NICFD simulation was completely missing. In compliance with the open-source philosophy of the project all the modifications are made available to the community, thus contributing to promote a worldwide access to state-of-the-art analysis tool for NICFD. The actual characteristics of dense vapours, supercritical flows and compressible two-phase flows, in close proximity to the saturation curve near the critical point, entail that the thermodynamic behaviour of the fluid differs considerably from that described by the perfect gas law and, under particular conditions, they may even exhibit non-classical gas-dynamic phenomena. The nature of this particular phenomena is related to the value of the fundamental derivative of gas-dynamics Γ. A non-monotonic Mach number trend along expansion is typical for values of Γ enclosed between 0 and 1, while negative values may bring to the occurrence of inverse gas-dynamics phenomena such as rarefaction shock waves, splitting waves or even composite waves. Heavy complex molecule in the vapour region are expected to show inverse gas-dynamics behaviour, Colonna et al. (2007), and recently two-phase rarefaction shock waves have been recognized as physically realizable close to the critical point of simple compounds, Nannan et al. (2014).

The paper is organized as follows: the first part recalls a brief description of the governing equations for an arbitrarily complex fluid at equilibrium condition and a short review of the numerical method implemented in the SU2 suite. In the second part we present some exemplary results involving simple geometries such as straight axis planar nozzles and a typical ORC turbine blade passage.

2. NUMERICAL MODEL

This section outlines the most distinguishing features of the SU2 solver for non-ideal compressible fluid flows. We first remember that, differently from past attempts and commercial alternatives, the modular and open-source infrastructure of the SU2 suite is largely suitable to build upon the existing flow model new knowledge and methods for fundamental and applied studies for non-ideal fluid flows. Currently, SU2 solves the equilibrium compressible RANS equations, Landau and Lifshitz (1993), by levering on a general formulation enabling the use of arbitrary thermo-physical models. The system of PDE equations including the inviscid and

viscous terms is written as

$$\partial_t U + \nabla \cdot \vec{F}^c - \nabla \cdot \vec{F}^v = Q \quad \text{in } \Omega,\, t > 0 \tag{1}$$

Equation (1) describes how mass, momentum and energy evolve in a control domain. $\vec{U}$ symbolizes the vector of conservative variables, i.e. $\vec{U} = (\rho, \rho v_1, \rho v_2, \rho v_3, \rho E)^T$, where ρ is the fluid density, E is the total energy per unit mass, and $\vec{v} = (v_1, v_2, v_3) \in \mathbb{R}^3$ is the flow velocity in a Cartesian coordinate system. The imposition of the boundary conditions follows the approach proposed in Guardone et al. (2011) to automatically detect inflow/outflow boundaries for hyperbolic systems. Notably the convective and viscous fluxes are given by

$$\vec{F}_i^c = \begin{pmatrix} \rho v_i \\ \rho v_i v_1 + P\delta_{i1} \\ \rho v_i v_2 + P\delta_{i2} \\ \rho v_i v_3 + P\delta_{i3} \\ \rho v_i H \end{pmatrix}, \quad \vec{F}_i^v = \begin{pmatrix} \cdot \\ \tau_{i1} \\ \tau_{i2} \\ \tau_{i3} \\ v_j \tau_{ij} + k_{\text{tot}} \partial_i T \end{pmatrix}, \quad i = 1, \ldots, 3 \tag{2}$$

P is the static pressure, T is the temperature, H is the total enthalpy, δ_{ij} is the Kronecker delta function, and the viscous stresses can be compactly written as $\tau_{ij} = \mu_{tot}\left(\partial_j v_i + \partial_i v_j - \frac{2}{3}\delta_{ij}\nabla \cdot \vec{v}\right)$. The total viscosity and the total thermal conductivity result from a molecular, μ_{mol},k_{mol} and a turbulent, μ_{tur}, k_{tur} contribution. Convective fluxes are properly reconstructed by means of the generalized Roe's approximate Riemann solver (ARS) proposed in Montagne and Vinokur (1990). Second-order accuracy is resolved using a Monotone Upstream-centered Schemes for Conservation Laws (MUSCL) approach, van Leer (1979), with gradient limitation. On the other hand, viscous fluxes are evaluated by averaging the flow variables, flow derivatives, and transport properties at two neighbouring cells whereas the *Thin Shear-Layer* approximation, Blazek (2005), is employed for gradient calculation.

For pure fluids and mixture of given composition in a stable equilibrium state the thermodynamic state can be retrieved by using ρ and internal energy e as follows

$$\rho = U_1, \quad e = \frac{U_5}{U_1} - \frac{(U_2 + U_3 + U_4)^2}{2U_1^2} = E - \frac{\|v\|^2}{2}. \tag{3}$$

The required thermo-physical quantities are conveniently expressed as a function of the ρ, e, i.e. $P = P(\rho, e) = P(U), T = T(\rho, e) = T(U), \mu_{\text{mol}} = \mu_{\text{mol}}(\rho, T(\rho, e)) = \mu_{\text{mol}}(U), k_{\text{mol}} = k_{\text{mol}}(\rho, T(\rho, e)) = k_{\text{mol}}(U)$. The SU2 embeds polytropic models (Van der Waals and Peng-Robinson) for rough and quick estimate of non-ideal flows properties. The other properties characterizing the fluid such as the specific heat capacity C_p and all the transport quantities can be conveniently expressed as

$$\begin{aligned} \mu_{\text{mol}} &= \mu_{\text{mol}}(\rho, T) = \mu_{\text{mol}}(\rho, T(\rho, e)) = \mu_{\text{mol}}(U), \\ k_{\text{mol}} &= k_{\text{mol}}(\rho, T) = k_{\text{mol}}(\rho, T(\rho, e)) = k_{\text{mol}}(U), \\ C_p &= C_p(P, T) = C_p(P(\rho, e), T(\rho, e)) = C_p(U). \end{aligned} \tag{4}$$

For more accurate predictions the SU2 embedded thermo-physical library was recently extended with the inclusion of the FluidProp software, Colonna and van der Stelt (2004), a general purpose thermo-physical database originally accomplished at Delft University of Technology. FluidProp contains several thermo-physical models and provides easy access to the quantities necessary for SU2 simulation, with possibility of handling look-up table interpolations Pini et al. (2014) to fasten the calculation. This opens the path to a wide variety of new capabilities: the properties of fluids –such as viscosity and thermal conductivity– whose thermodynamic state is characterized by a value of pressure and temperature close to the liquid-vapour saturation curve in the region near the critical point, can now be computed with a higher level of accuracy.

The aforementioned non-ideal fluid models now available for SU2 make it possible to represents non-ideal and non-classical phenomena such as rarefaction shock waves or compression fans. Beyond the embedded thermodynamic models, the high flexibility of SU2 and the re-usable thermodynamic infrastructure allows for the future implementation of novel fluid model.

This more general approach calls then for a reformulation of the equations involved by the numerical method. Indeed the ideal gas assumption does apply no more and a general formulation can be obtained from the spectral decomposition of the Roe's averaged state Jacobian. By means of the Roe averaging procedure (5), it follows that a supplemental condition arises (6), namely:

$$\left(\vec{F}_{\mathrm{i}}^{c} - \vec{F}_{j}^{c}\right) = \bar{A}\left(U_{\mathrm{i}} - U\mathrm{j}\right), \quad \bar{A} = A(\bar{U}) \tag{5}$$

$$\bar{\chi}(\rho_{\mathrm{i}} - \rho_{\mathrm{j}}) + \bar{\kappa}(\rho_{\mathrm{i}} e_{\mathrm{i}} - \rho_{\mathrm{i}} e_{\mathrm{j}}) = (P_{\mathrm{i}} - P_{\mathrm{j}}), \tag{6}$$

where $\bar{\chi}$ and $\bar{\kappa}$ are the average of these two thermodynamics quantities defined in eq. (7) and (8).

$$\chi = \left(\frac{\partial P}{\partial \rho}\right)_{\rho e} = \left(\frac{\partial P}{\partial \rho}\right)_{e} - \frac{e}{\rho}\left(\frac{\partial P}{\partial e}\right)_{\rho} \tag{7}$$

$$\kappa = \left(\frac{\partial P}{\partial \rho e}\right)_{\rho} = \frac{1}{\rho}\left(\frac{\partial P}{\partial e}\right)_{\rho} \tag{8}$$

For a PIG fluid this last condition is automatically satisfied as χ equals to zero and κ is constantly equal to $\gamma - 1$. On the other hand, using a NICF model only one relation (6) is provided for the two unknowns $\bar{\chi}$ and $\bar{\kappa}$. Therefore, the Roe-average state remains uniquely defined if and only if a proper closure condition is given.

3. RESULTS

In this section we present some exemplary test case in order to show the reliability of the SU2 suite and to highlight some typical application which may take advantages from the SU2 extended thermo-dynamic library. The considered test cases include simple geometries such as straight axis two-dimensional planar nozzles and a typical ORC turbine blade passage.

3.1 2-D TROVA nozzle

The TROVA (Test Rig for Organic Vapors) experimental facility was built at Laboratorio di Fluidodinamica delle Macchine (LFM) of Politecnico di Milano, Spinelli et al. (2012), and Guardone and Dossena (2012), in collaboration with Turboden s.r.l. and within the frame of the project Solar. In this section we show the flow field predicted by SU2 for a MDM fluid at operating condition listed in table 1: MDM properties, such as thermal conductivity or viscosity, are assumed to be constant through the nozzle. Values are given for the fluid at the inlet conditions and were computed using FluidProp. Results for three different fluid model, namely the polytropic ideal gas law, the polytropic Van der Waals and the polytropic Peng-Robinson Stryjek-Vera from the embedded SU2 thermo-dynamic library, are compared to show how a different level of accuracy in the description of the fluid behaviour may bring to different results. The domain represents a planar two-dimensional straight axis nozzle discharging into a reservoir: the computational grid is an hybrid mesh, hexahedrons were used to describe the boundary-layer region while tetrahedrons to discretize the core region and the reservoir. With reference to Fig 1: a no-slip condition is applied along nozzle wall and on the vertical wall in $x \approx 0.18$, symmetry condition is imposed at the centreline and at the upper boundary of the reservoir. Inlet and outlet conditions are resumed in table 1. The grid in the boundary layer region is extremely refined: this is due to the fact that properties needed for the computation of the first cell height–such as kinematic viscosity–are difficult to determine accurately for the

Fluid	MDM
Gas Constant	35.152 $(J/K/kg)$
Specific heat ratio	1.0125
Critical temperature	564.1 $^{\circ}K$
Critical pressure	1415000 Pa
Acentric factor	0.529
Total inlet temperature	526.35 $^{\circ}K$
Total inlet pressure	400000 Pa
Static outlet pressure	1000 Pa
Molecular viscosity	1.376E-5 $Pa \times s$
Thermal conductivity	0.04728 $W/m/K$
Turbulence model	SST-kω and SA
Spatial scheme	Upwind generalized Roe 1^{nd} order

Table 1: Test conditions for the 2D TROVA nozzle simulation.

involved fluid. Indeed the first cell height for this test case is $\approx 1e^{-7}[m]$–flow involving air in standard condition requires $\approx 1e^{-5}[m]$–. The nozzle is studied when the discharge occurs in off-design conditions, namely when the coefficient of expansion is 5.58 (design conditions correspond indeed to 10), in this test case the nozzle is then operating in an under-expanded regime. The predicted flow-field is shown in figure 1: the upper half of the picture refers to a grid composed by $\approx 75k$ elements while Mach contours in the lower half is related to a $\approx 180k$ cells mesh. This result was obtained using the ideal gas law to describe the fluid thermodynamic behaviour and the SST-$k\omega$ for modelling turbulence. At the discharge section a Prandtl-meyer expansion occurs: the flow is turned outwards and redirected towards the reservoir wall, where a symmetry boundary condition holds. The supersonic flow hence hits the boundary fostering the rise of a compression shock-wave: a system of reflected shock-wave then propagates through the reservoir. Figure 1 shows how a more refined discretization of the reservoir is needed in order to represent the wave reflecting system with a higher level of resolution. This was expected since a numerical scheme of the first order is highly dissipative and hence strongly dependent on the grid spacing: shock-wave in the coarser mesh is indeed smeared out moving along the nozzle axis. Mach and pressure trends along the centreline for the three different equation of state, computed using the SST-$k\omega$ turbulence model, are reported in figure 2 and 3.

3.2 2-D ORCHID nozzle

The ORCHID (Organic Rankine Cycle Hybrid Integrated Device) is an experimental facility being constructed at the Aerospace Propulsion and Power (APP) Lab. of the Delft University of Technology. It will be used to perform gas dynamic studies of non-ideal expansions and performance comparisons of high-speed ORC turbomachinery. The facility has been set up in collaboration with Robert Bosch GmbH (Solar ORC turbogenerator for zero-energy buildings) and by Dana-Spicer Corp (Mini-ORC turbogenerator for combined cycle powertrains). In this section we show a flow field simulated by SU2 for the linear siloxane hexamethyldisiloxane (MM); namely one of the working fluids considered in the design of the ORCHID with simulation parameters and set values specified in Table 2. RANS equations are solved with the slip condition at the walls and symmetry along the mid-plane. The FEQ Helmholtz equation of state implemented in the FluidProp thermo-dynamic library is used to model the fluid behaviour, the result is compared to the output from the integral balance equations for an adiabatic flow and a steady oblique shock wave. The test case is presented in Figure 4; a two-dimensional converging-diverging nozzle generated with a MoC code, Guardone and Dossena (2012), with a model placed 18 mm from the throat with a flow turning angle $\theta = 20^{\circ}$ along the centreline. Figure 5 depicts the terminology used, with β corresponding to the oblique shock wave angle and V to the velocity before and after the shock. The shock wave resulting from the CFD computation is 45.0 $^{\circ}$ and is reflected off the nozzle profile wall, subsequently

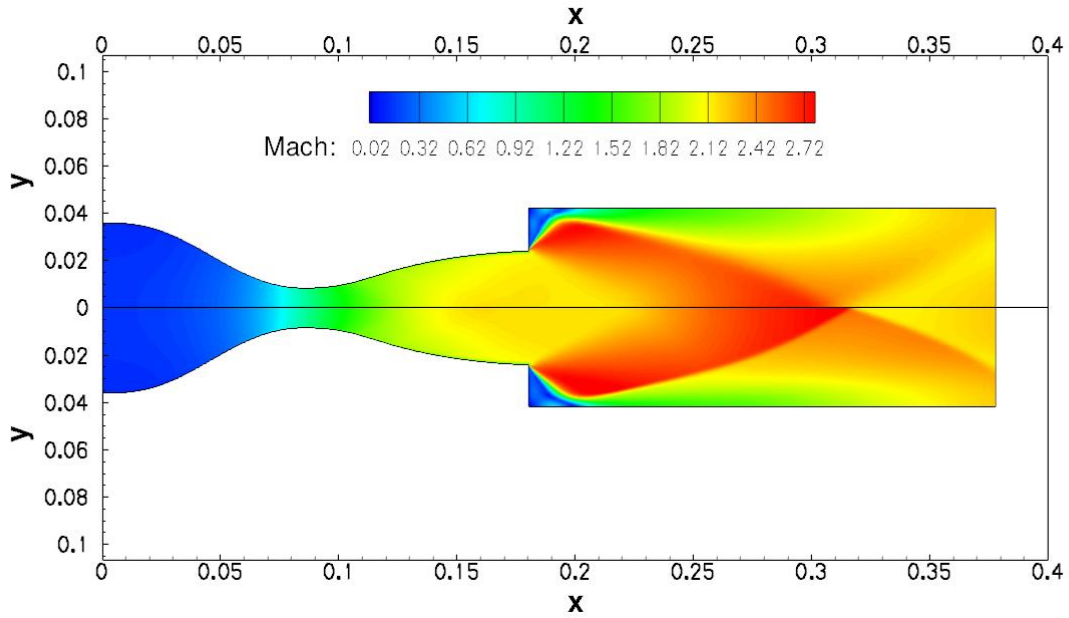

Figure 1: Mach contour in TROVA nozzle using polytropic ideal gas equation of state and SST-$k\omega$ turbulence model for two different level of mesh refinement: respectively $\approx 74k$ elements (upper side) and $\approx 180k$ elements (lower side). Axis refers to dimensional length [m].

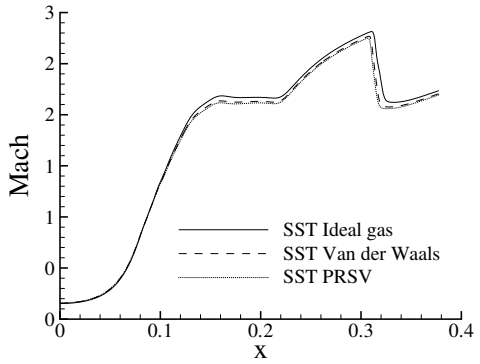

Figure 2: Comparison of Mach number trends along the centreline.

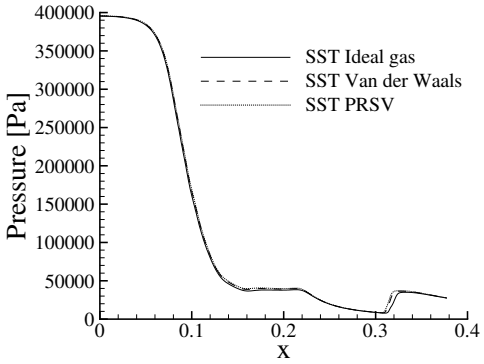

Figure 3: Comparison of pressure trends along the centreline.

Fluid	MM
Thermodynamic model	FEQ Helmholtz
Critical temperature	518.75 K
Critical pressure	19.39 bar
Total inlet temperature	525.15 K
Total inlet pressure	18.4 bar
Spatial scheme	Upwind generalized Roe 2nd order
Turbulence model	SST-kω
Inlet turbulence intensity	0.001
Reynolds Number Throat	1.642E6
Spatial scheme	Upwind generalized Roe 2nd order

Table 2: Main parameters of the 2D ORCHID supersonic nozzle simulation.

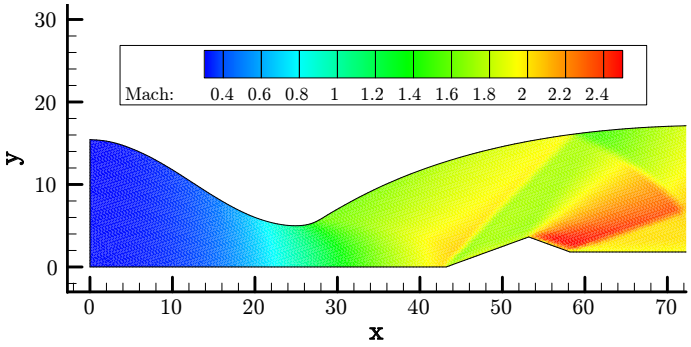

Figure 4: Mach contours of the 2D nozzle.

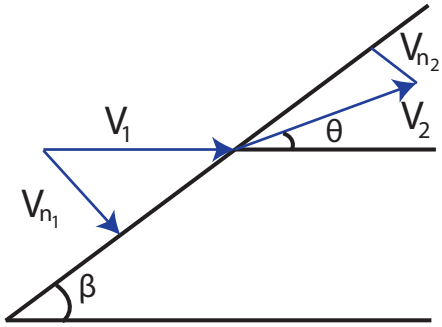

Figure 5: Oblique Shock Wave Angles and Vectors.

cutting the expansion fan that is generated from the back of the model. It is well known that the conditions across the surfaces of discontinuities are governed by the integral conservation equations. The jump conditions across a steady shock-wave for the continuity, momentum and energy equations cannot be solved with a simple closed-form expression as is the case for an ideal gas. The Rankine-Hugoniot relations are rendered obsolete and thus, for a non-ideal gas which uses more complicated equations of state, an iterative calculation procedure is employed to obtain the thermodynamic change across a shock wave and is given by Grossman (2000). It is now possible to determine the relationship between the M_1-β-θ variables and when providing inputs such as θ, V_1, P_1 and ρ_1, properties after the shock may be calculated. This allows calculation of relevant data such as shock strength, angle and the location along the mid-plane where detachment occurs, while maintaining relatively fast computational times. The resulting β is 44.3° and represents a 1.5 % deviation in the solution compared to the results in Figure 4 above.

3.3 Supersonic ORC turbine stator

In this test-case the capabilities of the new NICFD solver are tested in predicting the flow feature of a supersonic ORC turbine cascade. The calculations are performed using the inviscid solver, the SA and the SST-$k\omega$ turbulence models. Table 3 summarizes the main inputs for the solver.

Figure 6 plots the Mach contour of the simulation using the SST-$k\omega$, and, as can be noticed, the flow field is characterized by intense shocks and expansion fan interactions at the outlet. It is important to predict these phenomena with high accuracy because they generally represent the main source of fluid-dynamic losses for these particular applications. As can be seen indeed from Fig. 7 no distinctions can be appreciated in the pressure distribution trends plotted for the three different simulations. Figure 8 confirms the predominance of supersonic effect on the flow solutions, and a very low discrepancy can be appreciated on the flow Mach number trend at the outlet section.

4. CONCLUSIONS

In this paper SU2 CFD suite was considered as a possible candidate for representing a reliable investigation tool for the study and for the design of Organic-Rankine Cycle turbo-machinery. SU2 simulating capabilities were recently extended to real gas flows by the inclusion of an embedded collection of fluid models, which comprehend three different equation of state–polytropic ideal gas, polytropic Van der Waals and polytropic Peng-Robinson Stryjek-Vera–for the description of fluid behaviour and also by the inclusion of the FluidProp thermo-physical library.

Fluid	MDM
Specific heat ratio	1.0214
Total inlet temperature	545.17 $^{\circ}K$
Total inlet pressure	800000 Pa
Static outlet pressure	10000 Pa
Molecular viscosity	1.0461E-5 $Pa \times s$
Thermal conductivity	0.028085 $W/m/K$
Turbulence model	SST-kω and SA
Inlet turbulence intensity	0.05
Spatial scheme	Upwind generalized Roe 2nd order

Table 3: Test conditions for the 2D supersonic stator.

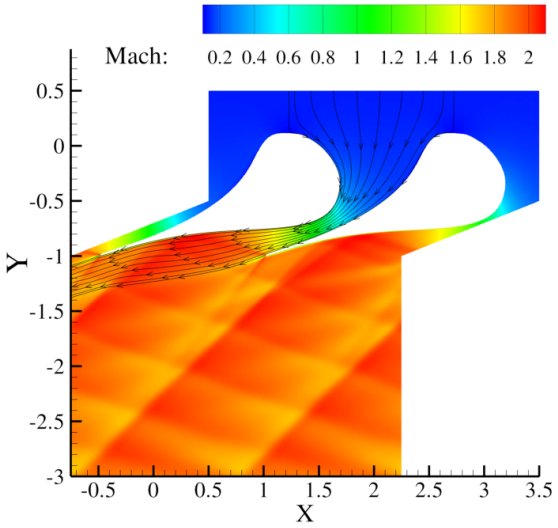

Figure 6: Mach flow field of the 2D supersonic stator fusing the SST-$k\omega$ turbulence model. Units on the axis are scaled due to industrial secrecy.

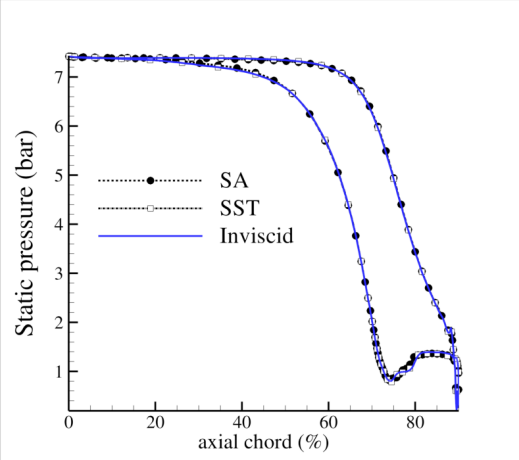

Figure 7: Pressure distribution around the blade profile for the inviscid case and with SA and SST turbulence models.

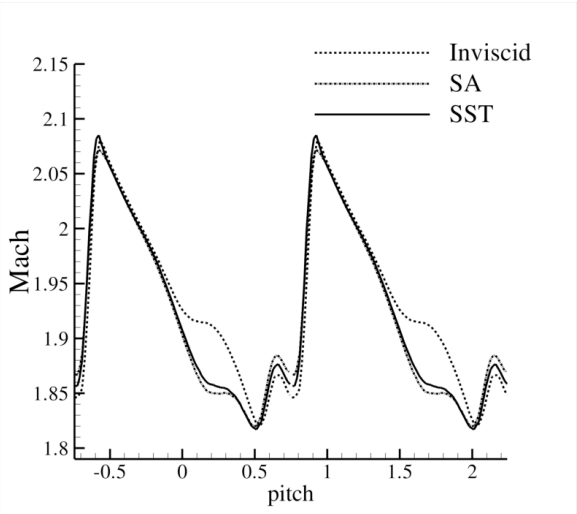

Figure 8: Mach trend at the outlet for the inviscid case and with SA and SST turbulence models.

Within the aim of SU2 it is possible to manage non-ideal compressible flows that may exhibit

non-classical gas-dynamic phenomena. This include fluid flows that slightly depart from an ideal behaviour but also fluid flows that give birth to rarefaction shock-waves and compression fans. The open-source trait opens the path to a wide range of possibilities: the integration of new software packages devoted to real gas applications is easily achievable within the SU2 framework. In this paper we showed that SU2 is already capable of tackling problems that engineers or researchers may face in typical ORC applications: simulation involving geometries of utmost importance such as nozzles and a typical ORC turbine blade passage were carried out. Different equation of state were used to describe the thermodynamic behaviour of fluids characterized by a highly complex molecular structure and using both first and second order numerical schemes.

REFERENCES

Blazek, J. (2005). *Computational Fluid Dynamics: Principles and Applications*. Elsevier, Oxford.

Colonna, P., Guardone, A., and Nannan, N. R. (2007). Siloxanes: a new class of candidate Bethe-Zeldovich-Thompson fluids. *Physics of Fluids*, 19.

Colonna, P., Rebay, S., and Silva, P. (2002). Computer simulations of dense gas flows using complex equations of state for pure fluids and mixtures and state of the art numerical schemes. Technical report.

Colonna, P. and van der Stelt, T. P. (2004). FluidProp: a program for the estimation of thermo physical properties of fluids. software.

Grossman, B. (2000). Fundamental concepts of real gasdynamics. Technical report, Virginia Polytechnic Institute and State University.

Guardone, A., Isola, D., and Quaranta, G. (2011). Arbitrary Lagrangian Eulerian formulation for two-dimensional flows using dynamic meshes with edge swapping. *Journal of Computational Physics*, 230(20):7706–7722.

Guardone, A. Spinelli, A. and Dossena, V. (2012). Influence of molecular complexity on nozzle design for an organic vapor wind tunnel. *J. of Eng. For Gas Turb. And Power*.

Landau, L. and Lifshitz, E. (1993). *Fluid Mechanics (2nd Edition)*. Pergamon Press.

Montagne, J. and Vinokur, M. (1990). Generalized flux-vector splitting and Roe average for an equilibrium real gas. *Journal of Computational Physics*, 89(2):276–300.

Nannan, N., Guardone, A., and Colonna, P. (2014). Critical point anomalies include expansion shock waves. *Physics of Fluids*, 26:021701–7.

Palacios, F. et al. (2013). Stanford university unstructured (su2): An open-source integrated computational environment for multi-physics simulation and design. *AIAA Paper 2013-0287*.

Palacios, F. et al. (2014). Stanford university unstructured (su2): Open-source analysis and design technology for turbulent flows. *AIAA Paper 2014-0243*.

Pini, M., Spinelli, A., Persico, G., and Rebay, S. (2014). Consistent Look-up Table Interpolation Method for Real-Gas Flow Simulations. *submitted to Computers & Fluids*.

Spinelli, A. et al. (2012). Design, simulation, and construction of a test rig for organic vapors. *J. of Eng. For Gas Turb. And Power*.

van Leer, B. (1979). Towards the ultimate conservative difference scheme V. a second-order sequel to Godunov's method. *Journal of Computational Physics*, 32(1):101–136.

Vitale, S. et al. (2015). Extension of the SU2 Open Source CFD code to the simulation of turbulent flows of fluids modelled with complex thermophysical laws. *AIAA (accepted for pubblication)*.

ACKNOWLEDGEMENT

The research is partially funded by the European Research Council under Grant ERC Consolidator 2013, project NSHOCK 617603.

FLUID DYNAMIC DESIGN AND ANALYSIS OF A HIGHLY LOADED CENTRIFUGAL ROTOR FOR MINI ORC POWER SYSTEMS

Salvatore Vitale[1*], Matteo Pini[1], Antonio Ghidoni[2] and Piero Colonna[1]

[1] Delft University of Technology, Propulsion and Power,
Delft, The Netherlands
s.vitale@tudelft.nl

[2] Universita' degli studi di Brescia, Department of Mechanical and Industrial Engineering,
Brescia, Italy

* Corresponding Author

ABSTRACT

This article presents the fluid-dynamic design and analysis of a high-loaded centrifugal rotor for mini ORC applications. Recently a vast interest about mini ORC turbogenerators is growing up. These systems must be equipped with high-efficient turbines to maximize their overall efficiency. Recent works demonstrated that, among the various alternatives, the multi-stage centrifugal turbine may be extremely attractive for such applications. However, this turbine is characterized by a very high loaded first stage whose design has a key role for the success of the technology. In order to cope with these severe conditions we propose a design methodology specifically tailored for radial-outflow cascades. The method combines NURBS curves and flow passage area control to "physically" drive the construction of the profiles. As exemplary test case, we apply the new procedure to the design of the first rotor of a $10kW_e$ micro centrifugal turbine for heat recovery application. Finally, we assess the performance of the designed rotor by means of 2D and 3D turbulent simulations, providing an extensive comparison against preliminary estimates based on Traupel and Craig&Cox loss correlations. The results show that the design method is flexible and quick enough to minimize losses by few manual iterations. Furthermore, it turned out that both loss models fairly well estimate profile losses, even if Traupel seems to be more accurate than Craig&Cox model to predict secondary and tip clearance loss effects.

1. INTRODUCTION

Organic Rankine Cycles (ORC) power systems are, nowadays, a well-established technology for the conversion of thermal energy sources in the small-to-medium power range (from 100 kWe to few MWe), D'Amelio (1935); Tabor and Bronicki (1964); Angelino et al. (1984); Verneau (1987). Miniaturized (5-30 kWe) systems are particularly attractive for waste heat recovery onboard mobile applications, e.g. trucks or aircrafts, and for decentralized energy production in combination with solar heat sinks.

The realization of successful mini ORC (*m*ORC) power systems demands to desigh highly efficient (>75%) mini-turboexpanders, to be competitive with respect to existing alternatives like fuel-cells. As well documented, the use of organic media generally leads to unusual turbine configurations, Macchi (1985, 1977): few axial stages or a single centripetal stage, often characterized by supersonic flows and strong shocks. These phenomena are even worse in small blade passages, due to the interaction with tip and secondary vortex structures. The achievement of high-efficient mini-turbines implies a full redefinition of the design strategy of the expander, starting from the turbine concept, passing through dedicated preliminary design optimization, Pini et al. (2013); Casati et al. (2014), and eventually arriving at a complete new definition of the optimal blade profiles through advanced methodologies, Persico et al. (2013); Pini et al. (2014).

Recently, the multi-stage radial-outflow turbine (ROT) has been thoroughly studied for ORC power sys-

tems. This configuration naturally accommodates the high volumetric flow ratios typical of ORC fluids and allows for compact multi-stage arrangements, thus preventing high supersonic flows. Although in a previous work the authors already demonstrated with a preliminary investigation that ROT may allow for compact and efficient turbo-expanders for *m*ORCsystems, Casati et al. (2014), many challenges are still to be addressed for the success of this architecture. One of the open issue regards the design and performance evaluation of the first stage, which operates under very unfavorable flow conditions. Notably, this stage usually features a rotor characterized by high flow deflection, low aspect ratio and significant tip-to-blade height clearance, resulting in low fluid dynamic performance that may compromise the efficiency of the whole machine. Moreover, the rotor is subject to non-inertial effects, i.e. centrifugal and Coriolis fictitious forces, and to a high increase of the flow passage in the radial direction that pose additional concerns during the blade design process.

Consequently, demonstrating that the first rotor can be designed with acceptable efficiency is crucial to quantify the actual gain offered by the ROT concept for *m*ORCwith respect to axial and radial-inflow competitors. For this reason the objective of this work is to perform a trustworthy fluid dynamic design of the first rotor of a 5-stages small centrifugal turbine preliminary which was designed following the methodology provided in Casati et al. (2014). The study is supported by detailed 2D and 3D CFD analysis and complemented by a comparison between the computed and predicted (by means of the widely used empirical correlations Craig and Cox (1971); Traupel (1977)) loss coefficients.

The blade profile definition is carried out by a novel methodology for the aerodynamic design of centrifugal blades based on NURBS curves and flow passage area detection. The algorithm is implemented in a new CAD Turbine Blade Modeler (TBM) exploiting the Python API of the open-source (LGPL License) Software FreeCAD Falck and Collette (2012). The TBM is in turn automatically linked with two in house mesh generators (named UMG2 and UMG3, respectively) to create high quality 2D and 3D grids. The flow calculations are carried out by resorting to the SU2 solver, recently extended by the authors to deal with arbitrary thermo-physical models Vitale et al. (2015).

The paper is organized as follows: Section 2 illustrates the procedure devised for the design of centrifugal cascades, Section 3 extensively describes the design of the first rotor of a *m*ORC for heat recovery applications, while section 4 analyses the performance of the considered cascade with blade-to-blade and 3D simulations.

2. METHODOLOGY

This section briefly recalls the tools adopted in this work and reports extensively the methodology devised for the design of centrifugal blades.

2.1 Numerical Methods

The CFD solution is obtained by coupling the in-house mesh generation software UMG2 and UMG3, Ghidoni et al. (2006), to the SU2 suite. SU2 discretizes and solves the fluid governing equations using the finite volume approach on unstructured grids. The code has been recently extended by the authors to treat non-ideal compressible fluid flows that commonly occur in ORC turbines. An exhaustive description of the solver characteristics alongside the numerical validation process can be found in Vitale et al. (2015).

2.2 Centrifugal Blade Construction

In the centrifugal architecture the peripheral speed does not change along the blade span allowing to resort to untwisted blades. For this reason, the construction of a centrifugal blade reduces to the definition of a 2D blade profile simply lofted to construct the 3D geometry.

Figure 1 illustrates the construction of the centrifugal camber-line using NURBS curve. The camber-line is completely defined by the inlet blade angle β_{in}, the outlet blade angle β_{out}, the stagger angle γ, the radial chord c_{rad} and the *LE* position. As a matter of fact the *TE* position is uniquely defined by the *LE*,

γ and c_{rad}, and an additional third point P_{int} resulting from the intersection of the inlet and and outlet lines. These two lines follow the direction of β_{in} and β_{out}, respectively, which are defined in the radial reference of framework.

Using three *CPs* the camber-line assumes a quadratic shape, and changing the weight value of the intersecting control points the ensemble of the quadratic curves can be represented as an arc of parabola (w_{int} = 1.0), hyperbole (w_{int} > 1.0), ellipse or circle (w_{int} < 1.0) Piegl and Tiller (1997).

The approach used for the construction of the pressure and suction side is based partially on the work of Vestraete (2010) for the construction of 2D axial turbine blade. The *SS* and *PS* are NURBS curves themselves whose shape is specified by distributing the *CPs* according to a thickness law as a function of the camber-line length. Figure 2 shows an example of *TD* for the suction side, and, on top, the corresponding distribution of the *CPs* on the *SS* along the blade camber-line. It is worth to note that by properly tuning the *TD* law any desired blade loading trend can be met.

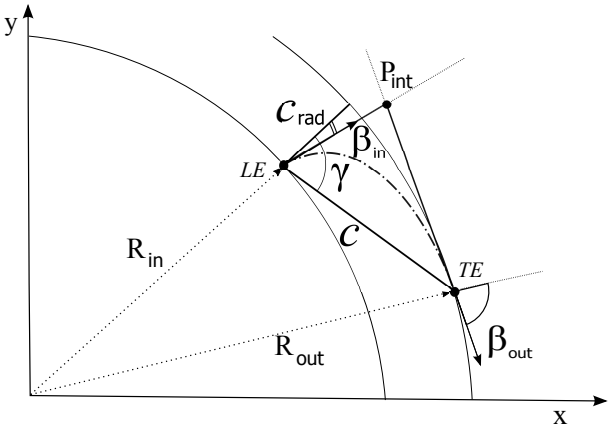

Figure 1: Camber-line construction for a centrifugal turbine using NURBS curve.

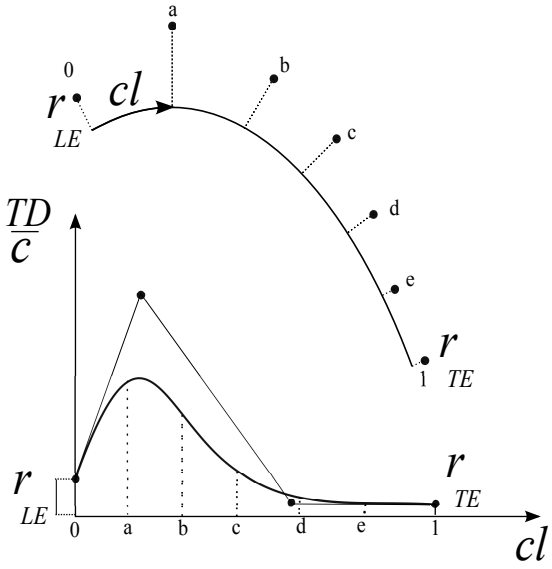

Figure 2: 2D centrifugal profile construction using NURBS curve.

3. 2D DESIGN OF A CENTRIFUGAL ROTOR FOR MINI-ORC APPLICATIONS

This section presents the design of a high loaded centrifugal rotor by using the TBM and the NICFD solver in an iterative manner to attain a convenient blade shape.

3.1 Design of the Rotor Blade

We here consider the first rotor of the 5-stage small-scale transonic ROT as exemplary test case. The total-total efficiency of the machine was predicted by the Traupel's loss model to be approximately 80%. The main data for the blade geometry construction and the boundary conditions for the CFD simulation are provided in Table 1 and 2, respectively. Figure 3 shows the trends of the main parameters influencing the performance of the turbine cascades: blade deflection, aspect ratio and the tip clearance. The first rotor (blade row n°2 in Fig.3) is characterized by the most severe conditions: extremely high flow deflection, low aspect ratio and high tip clearance to blade height ratio. Additionally, Fig. 4 reports the relative increase of the passage area and peripheral speed of each blade row for the same turbine. Due to the high increase of the peripheral speed along the stream-wise direction, the first rotor is furthermore subject to a significant rise of the (relative) fluid mechanical energy from the inlet to the outlet. As a consequence, higher Mach numbers are expected to occur at the rotor outlet compared to stationary cascades of similar geometry, working under the equivalent expansion ratio. On the other hand, if not properly handled, the radial evolution of the machine may lead to unexpected converging-diverging passage areas even

adopting purely converging blades with sudden flow supersonic excursions and generation of strong shocks.

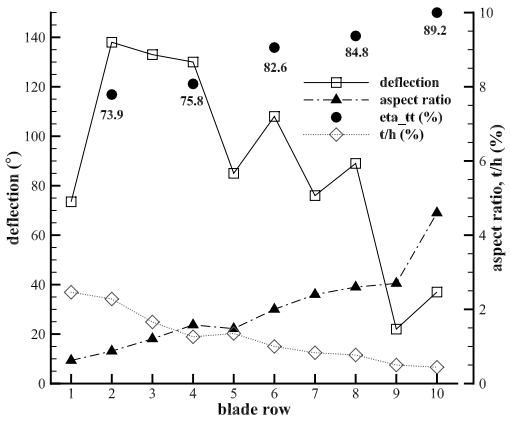

Figure 3: Flow deflection, aspect ratio, tip clearance for each blade row and total total efficiency for each stage of the 5-stage mini centrifugal turbine.

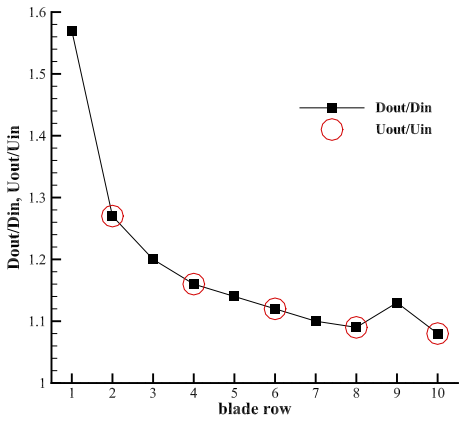

Figure 4: Rate of increase of the diameter for each blade row and of the peripheral speed for each rotor blade of the 5-stage mini centrifugal turbine.

The design of centrifugal profiles cannot follow any standard design rule established for axial cascades, as already pointed out in Persico et al. (2015), where the analysis was restricted to slender profiles for low deflection radial cascades and suggested rather simple design criteria, i.e. elliptic mean-arc and thickness distribution taken from existing profiles, that are almost useless in presence of high-loaded blades with relevant radial area evolution. Hence, we adopt the more general approach explained in the previous section to achieve a suitable blade profile for such unconventional configuration.
As anticipated the degrees of freedom for the 2D profile are the stagger angle γ and the thickness distribution for the pressure (TD_{PS}) and suction side (TD_{SS}). R_{in}, c_{rad}, β_{out}, N°_{blades}, TE_{th} are the inputs for the TBM, while the prescribed blade throat width o_{out} is achieved by selecting the appropriate TD_{PS}, TD_{SS}, and γ.

R_{in}	1.88 cm
c_{rad}	0.5 cm
β_{in}	66.0 °
β_{out}	-74.1 °
N°_{blades}	38 [-]
o_{out}	0.1 cm
te_{th}	100 μm

Table 1: Geometrical parameters for the desing of the rotor blade.

Fluid	D4
$T_{t,in}$	305.79 °*C*
$P_{t,in}$	3.66 *bar*
$P_{s,out}$	1.655 *bar*
$\beta_{flow,in}$	66.0 °
N	19000.0 rpm

Table 2: Main input data for the CFD simulation.

Figure 5 shows the designed rotor cascade. As highlighted in the top picture of Fig. 6, the radial evolution of the cascade dictates an unusual non-monotonic trend of the flow passage area (PA). The inlet semi-bladed region is characterized by a throat located where the flow encounters the *SS* at the *LE*. Then the PA increases until the flow reaches the *PS*. If not conveniently controlled this trend may generate undesired supersonic flow bubbles with high risk of flow separation on the *SS*. Consequently strong adverse pressure gradients may establish on both pressure and suction sides with the increasing of the boundary layer. Also in the semi-bladed outlet region the PA increases, triggering the onset of strong shock waves on the suction side.

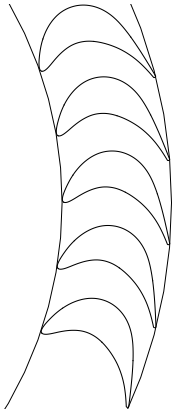

Figure 5: Centrifugal rotor 2D profile.

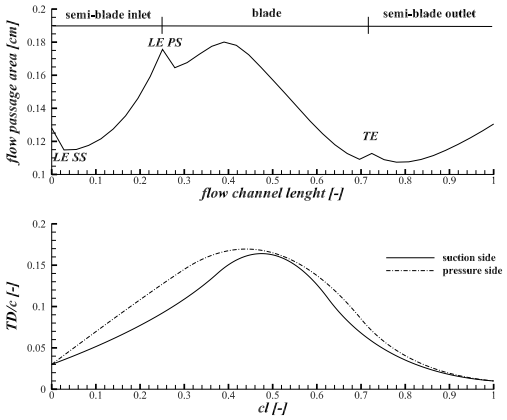

Figure 6: Flow passage area distribution and TD_{SS} and TD_{PS} of the 2D centrifugal rotor.

The optimal rotor configuration should mitigate all these loss mechanisms. The final blade shape was derived by iteratively changing the TD_{SS}, the TD_{PS} and the γ. Each blade profile was tested by means of 2D viscous simulations using the SST turbulence model and few design adaptations were necessary to minimize the fluid-dynamic losses. The bottom picture of Fig. 6 displays the final TD_{SS} and TD_{PS} laws used to construct the final profile. A value of 22.5 was set for the stagger angle. It can be observed that the *LE* thickness is thin, especially on the *SS*, in order to avoid the creation of a throat in the semi-bladed inlet region; in the middle part the profile is rather thick so as to better guide the flow and prevent separations; the *TE* is conversely set to the smallest value, compatible with manufacturing limits, in order to reduce wake and mixing losses. Figure 7 shows the relative Mach contour of the designed centrifugal rotor; it can be appreciated that no shocks appear upstream of the blade and no flow separations occur on both suction and pressure sides. As expected, shock waves are clearly visible downstream of the blade as a result of the flow over-expansion on the rear suction side.

A further improvement of the rotor performance can be certainly achieved by means of shape optimization algorithms. However, as demonstrated, a thorough understanding of the physical problem can already aid the initial design of the cascade without the need of expensive optimization procedures. Furthermore, the present algorithm can greatly help to drive the automated design algorithms in the early steps.

4. NUMERICAL VERIFICATION OF THE CENTRIFUGAL ROTOR

In this section we illustrate the fluid-dynamic performance of the designed high loaded centrifugal rotor by means of blade-to-blade and fully 3D simulations.

4.1 2D CFD analysis

The blade-to-blade performance of the final rotor configuration are now discussed in detail. The siloxane D4 is modeled as a polytropic Peng-Robinson gas. Table 3 summarizes the main results of the 2D simulation. The profile losses are estimated by resorting to the mixed-out average at inlet section and at a section placed 5% of the radial chord downstream of the trailing-edge. At nominal conditions the corresponding kinetic energy loss coefficient is nearly 3.9%, while values predicted by the Traupel's and Cox's model are about 3.2% and 5%, respectively. Considering that these correlations were developed for axial cascades, we can conclude that, at least at a preliminary level, they provide a reasonable measure of the 2D performance of the cascade and can be used in the design phase of *m*ORC.

$\dot{m}_l$	1.64 $kg/s/m$
M_{out}	1.05 [-]
$\beta_{out,flow}$	74.49 °
ζ_{is}	3.9 [-]

Table 3: Main results of the blade to blade simulations

When assembling the full row we considered the number of blades as a fixed input from the preliminary design phase. However, as well known in turbomachinery theory, the solidity largely affects the overall fluid-dynamic performance of the cascade. In case of radial *m*ORCthe direct application of the solidity correlations for axial turbines is somewhat questionable and therefore accurate numerical predictions may be necessary to determine the optimal value. Figure 8 presents a study of the optimal number of blades to minimize the profile losses. All the profiles have the same TD_{SS} and TD_{PS}, yet a different stagger angle in order to keep constant the gauging angle $\left(\frac{o}{s}\right)$. The minimum profile losses arises for 38 blades, surprisingly in accordance with the number of blades estimated by the Zweifel criterion, Zweifel (1945), and used in the preliminary design phase. Figure 9 shows that in all cases two successive shock waves occur on the suction side though of different intensity. The first shock, that is weaker for the row with 32 blades, is generated by the interaction of the suction flow with the expansion fan impinging on the suction side. It is interesting to note that increasing the number of blades the flow experiences larger acceleration on the suction side, leading to a stronger fishtail shock wave. All these phenomena are amplified by the diverging shape of the streamtube along the radial direction, which emphasizes the flow accelerations and arrests. An opposite trend manifests just upstream of the trailing-edge. The reduction of blade loading induces lower velocities and adverse pressure gradients, resulting in a much weaker second shock for the case with 45 blades. The profile losses are greatly influenced by the combination of these two shocks and the final optimum solidity is reached with 38 blades, which may represent the trade-off between the two opposite situations.

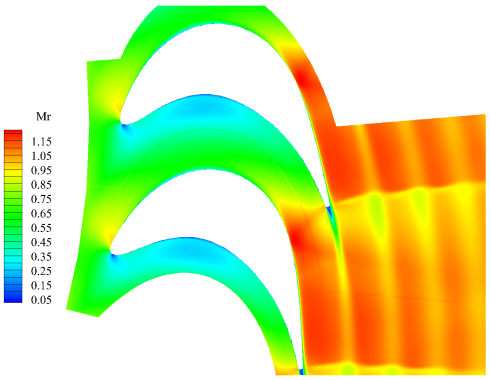

Figure 7: Mach contour of the designed centrifugal rotor.

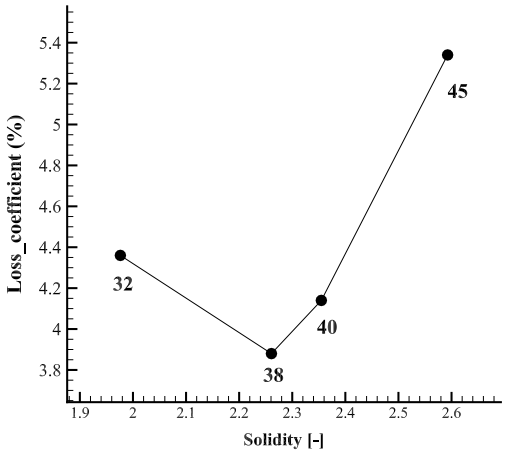

Figure 8: CFD blade to blade results of the solidity optimization for the centrifugal rotor.

Besides the major role on the fluid dynamic losses, the solidity parameter influences the flow slip and, eventually, the work extraction from the radial cascade. Figure 10 shows the angular difference between the rotor simulated as a rotating cascade and as a stationary cascade (provided consistent relative boundary conditions) for different number of blades. In order to avoid any post expansion and post compression effect, that can modify the outlet flow angle, the boundary conditions for the static case are chosen to obtain the same averaged flow Mach number at the outlet. The results are qualitatively in

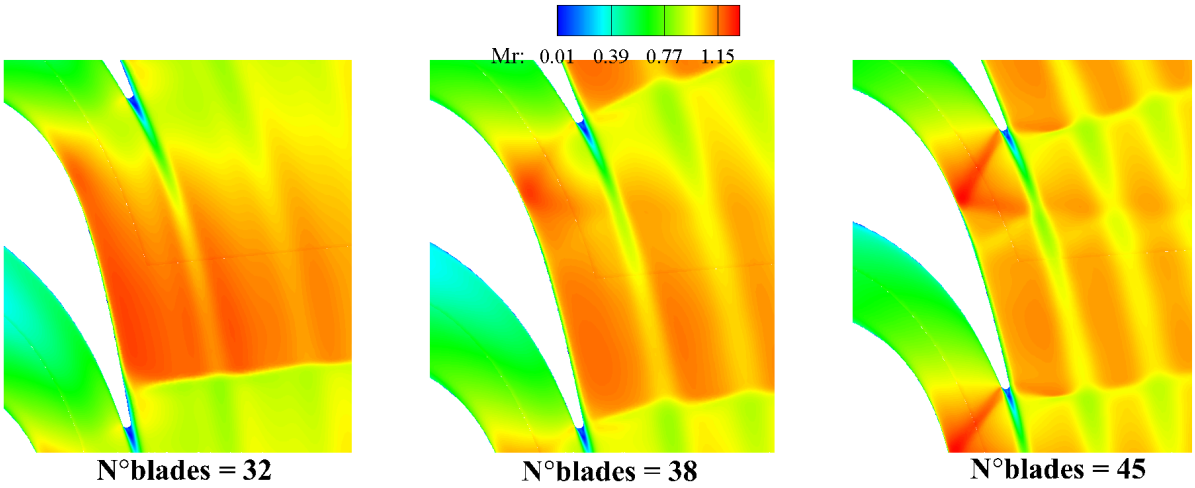

Figure 9: Rotor profile and its blade channel curve.

agreement with the general theory of circulation, which admits, for purely radial cascades, the presence of a counter-rotating vortex acting on the blade to blade plane ($\nabla W = -2\omega$). The net effect is the appearance of a fictitious force deflecting the flow (slip effect) in the tangential direction, namely in the opposite direction to the verse of rotation of the turbine. As expected, the slip vanishes for a high number of blades, as occurs in the first rotor of *m*ORCturbines.

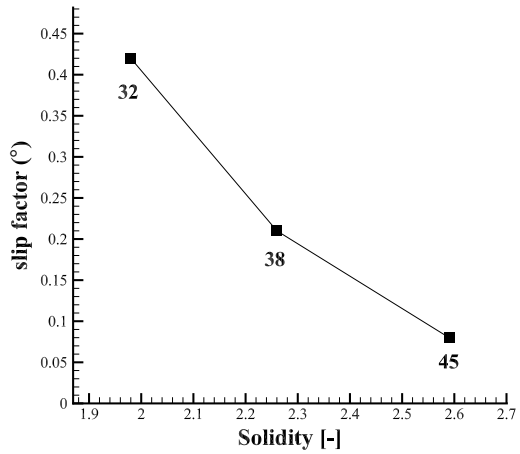

Figure 10: Slip factor for 3 centrifugal cascade with 32, 38 and 45 blades.

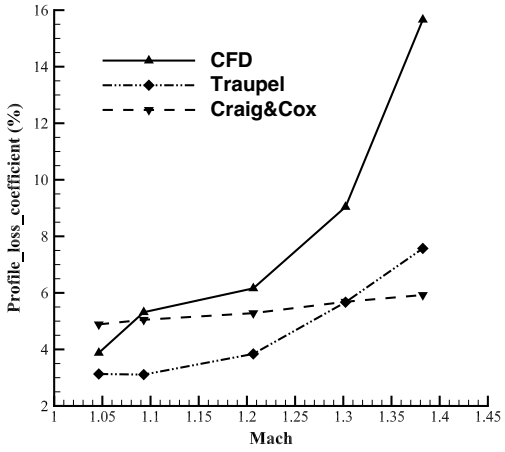

Figure 11: Comparison of the profile losses estimation.

Another key aspect of the radial cascades is their behaviour at off-design conditions. This is particularly relevant for small-scale turbines, as their functioning is intimately connected to the energy demand of the load. The blade to blade analysis of the 38 blade cascade is herein extended at moderate partial loads, until reaching an outlet Mach number of 1.4. To aid the reader we remember that Mach 1.4 is the traditional design limit in axial configurations to retain purely converging blades. The objective of the study is twofold: to assess the reliability of the correlations, and to gain knowledge about the characteristic of converging centrifugal blades for weakly supersonic flows. The outcomes are illustrated in Fig.11. As well visible, the results show that up to Mach 1.2 the predictions of the loss models are fairly in accordance with CFD results. While the C& C correlation displays a smaller deviation and fails to capture the correct slope of the loss curve, the Traupel's correlation provides a more reliable trend, even if it underestimates the losses for the whole range of operating conditions. This suggests that using such

correlations for weakly and fully supersonic flows in *m*ORCturbines may result in the over-prediction of the expander total-to-total efficiency. Likewise some general recommendations can be drawn on the basis of the CFD predictions. The exponential-like growth of the rotor losses above Mach 1.2 indicates that radial-outward converging blades optimized for transonic regimes may suffer of severe drawbacks already at moderate off-design conditions, strengthening the idea that robust fluid-dynamic design of mini-ROT can be truly achieved by fully multi-stage robust optimization procedures.

4.2 3D CFD analysis

This section briefly describes the 3D CFD analysis of the rotor cascade. As previously mentioned the 3D profile is generated simply lofting the 2D profile. The blade height (*blh*= 0.43 cm) is calculated by using the linear mass flow computed with the blade to blade analysis and the expected mass flow ($\dot{m}$ = 0.266 kg/s) of the turbine (*blh* = $\frac{\dot{m}}{\dot{m}_l}$).

Three 3D configurations have been considered to investigate the different loss mechanisms occurring in the 3D blade passage: a geometry i) with slip end-walls to determine the profile losses, ii) with no slip end-walls to estimate secondary flows, and iii) with a tip clearance *tcl* = 100μm and *tcl* = 200μm to examine the tip loss mechanism.

The calculations were performed using the same boundary conditions specified for the 2D case and unstructured meshes of about 3 million elements. Convergence was approximately reached after 10000 iterations (10 hours on 20 cores, Intel®Xeon(R) CPU E5-2687W 3.10GHz).

Table 4 shows the breakdown of the loss sources. As expected the tip clearance losses highly penalize the performance of small-scale ORC cascades. As a matter of fact, as depicted in Fig. 13, even with *tcl* over *blh* around $\frac{1}{40}$, the tip clearance vortex covers about 25 % of the flow passage area. Such vortex structure causes a considerable distortion of the flow angle at tip, see Fig. 12, which eventually leads to a lower averaged outlet flow angle and, hence, a significant reduction of work extraction. Indeed a even worse situation would occur by doubling the *tcl* to 200 μm. Finally, Table 5 compares the fluid dynamics losses estimated by the CFD and empirical correlations. The C & C model fails in predicting the secondary and tip losses whereas the Traupel, though with some overestimation, better captures the trends.

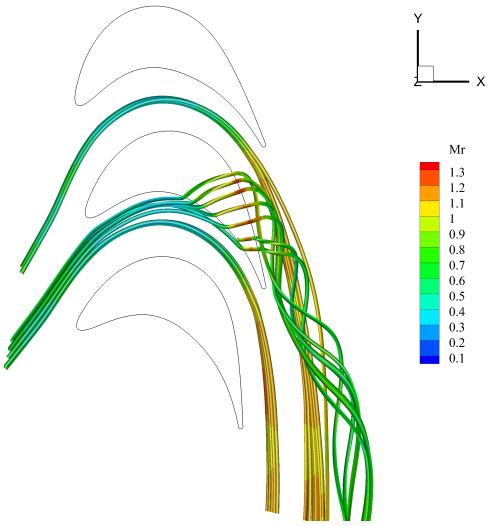

Figure 12: 3D stream lines of the flow solution with tip clearance 100 μm top view.

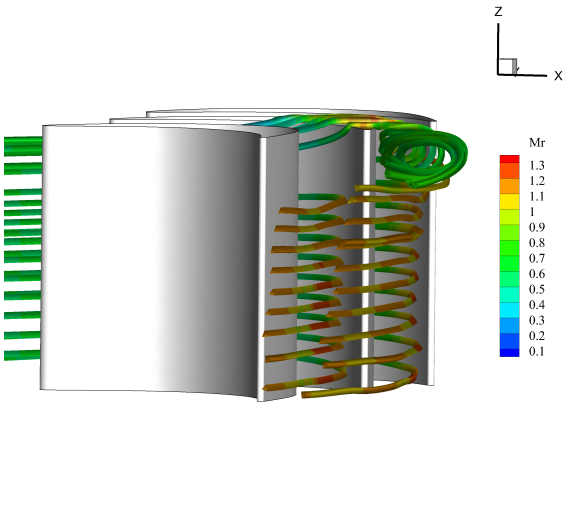

Figure 13: 3D stream lines of the flow solution with tip clearance 100 μm downstream view.

5. CONCLUSIONS

This work illustrated the application of a novel blade design methodology to the development of a high loaded centrifugal blade for mini-ORC turbines. The use of a physical-based approach allows to obtain a

case	$\zeta_{is,tot}$	$\beta_{flow,out}$	ew
Blade to blade	3.9	74.5	6.84
3D no tip	7.3	74.4	6.66
3D 100 μm tip	17.0	72.24	6.20
3D 200 μm tip	24.8	70.5	6.05

Table 4: Main results of the simulations.

tool	$\zeta_{is,p}$	$\zeta_{is,s}$	$\zeta_{is,tcl,100}$	$\zeta_{is,tcl,200}$
CFD	3.9	3.4	9.7	17.5
C & C	4.9	11.7	3.8	8.3
Traupel	3.2	5.9	14.1	22.7

Table 5: Comparison between the CFD results and the loss models.

blade design, comparable with the performance predicted at a preliminary design level. However, CFD results show that, due to the complexity of the fluid-dynamic phenomena involved (shock wakes and vortex interactions), there is indeed room to further improve the actual efficiency of the blade by resorting to advanced shape optimization methods. Finally the loss models used for the preliminary design of the turbine were assessed against CFD predictions. For the specific application here considered the Traupel's model outperforms the Craig & Cox model, which fails in reproducing secondary and tip phenomena. Hence, the use of the Traupel's model at a preliminary design level may lead to a more reliable design for such unconventional turbines.

NOMENCLATURE

NICFD	Not Ideal Compressible Fluid-Dynamics	
ROT	Radial-Outflow Turbine	
TBM	Turbine Blade Modeler	
β	blade and flow angles	(°)
γ	stagger angle	(°)
LE	leading-edge	
TE	leading-edge	
P	pressure	(bar)
T	temperature	(C°)
N	rotational speed	(rpm)
blh	blade height	(rpm)
c	blade chord	(m)
cl	camber-line length	(m)
o	throat width	(m)
tcl	tip-clearance	(m)
$\dot{m}$	mass flow	(kg/s)
M	flow Mach number	$(-)$
ζ_{is}	kinetic energy loss coefficient	$(\%)$
ew	eulerian work	(kJ/kg)
TD	thickness distribution	
SS	suction side	
PS	pressure side	
CPs	control points	
w	weight of the NURBS	

Subscript

is	isentropic
int	intersected
l	linear
th	thickness

REFERENCES

Angelino, G., Gaia, M., and Macchi, E. (1984). A review of Italian activity in the field of Organic Rankine Cycles. In *VDI Berichte - Proceedings of the International VDI Seminar*, volume 539, pages 465--482, Düsseldorf. VDI Verlag.

Casati, E., Vitale, S., Pini, M., Persico, G., and Colonna, P. (2014). Centrifugal Turbines for Mini-Organic Rankine Cycle Power Systems. *ASME Journal of Engineering for Gas Turbines and Power*, 136(122607):1--11.

Craig, H. and Cox, H. (1971). Performance estimation of axial flow turbines. *Proceedings Institution of Mechanical Engineers*, 185-32/71:407--424.

D'Amelio, L. (1935). *Impiego di vapori ad alto peso molecolare in piccole turbine e utilizzazione del calore solare per energia motrice*. Industria Napoletana Arti Grafiche.

Falck, D. and Collette, B. (2012). *FreeCAD [How-to]*. Packt Publishing.

Ghidoni, A., Pelizzari, E., Rebay, S., and Selmin, V. (2006). 3d anisotropic unstructured grid generation. *International journal for numerical methods in fluids*, 51(9□10):1097--1115.

Macchi, E. (1977). *Lecture series 100 on Closed-Cycle gas turbines*, chapter Design criteria for turbines operating with fluids having a low speed of sound. Von Karman Institute for Fluid Dynamics.

Macchi, E. (1985). Design limits: basic parameter selection and optimization methods in turbomachinery design. volume 97 Av 2, pages 805--828, Izmir, Turk. Martinus Nijhoff Publ., Dordrecht, The Netherlands.

Persico, G., Pini, M., Dossena, V., and Gaetani, P. (2013). Aerodynamic Design and Analysis of Centrifugal Turbine Cascades. In *ASME Turbo Expo 2013*, number GT2013-95770.

Persico, G., Pini, M., Dossena, V., and Gaetani, P. (2015). Aerodynamics of Centrifugal Turbine Cascades. *Journal of Engineering for*, 19.

Piegl, L. and Tiller, W. (1997). *The NURBS Book (2Nd Ed.)*. Springer-Verlag New York, Inc., New York, NY, USA.

Pini, M., Persico, G., Casati, E., and Dossena, V. (2013). Preliminary design of a centrifugal turbine for organic Rankine cycle applications. *Journal of Engineering for Gas Turbines and Power-Transactions of the ASME*, 135:042312--1--9.

Pini, M., Persico, G., Pasquale, D., and Rebay, S. (2014). Adjoint method for shape optimization in real-gas flow applications. *Journal of Engineering for Gas Turbines and Power*, 137(3):032604--032604.

Tabor, H. and Bronicki, L. (1964). Establishing criteria for fluids for small vapor turbines. In *SAE National Transportation, Powerplant, and Fuels and Lubricants Meeting*, number 640823.

Traupel, W. (1977). *Thermische Turbomaschinen*. Springer-Verlag, Berlin.

Verneau, A. (1987). *Lecture series 1987-07*, chapter Small high pressure ratio turbines. Supersonic turbines for organic Rankine cycles from 3 to 1300 kW. Von Karman Institute for Fluid Dynamics.

Vestraete, T. (2010). CADO: a Computer Aided Design and Optimization Tool for Turbomachinery Applications. 2nd International Conference on Engineering Optimization.

Vitale, S., Gori, G., Pini, M., Guardone, A., Palacios, F., Economon, T., Alonso, J., and Colonna, P. (2015). Extension of the SU2 Open Source CFD code to the simulation of turbulent flows of fluids modelled with complex thermophysical laws. In *AIAA 22th Computational Fluid-Dynamics Conference*, number CFD-16, 2148971, Dallas.

Zweifel, O. (1945). The spacing of turbo-machine blading especially with large angular deflection. *Brown Boveri Review*.

ACKNOWLEDGEMENT

Salvatore Vitale would like to acknowledge the FPP master student Roel de Koning, for his collaboration on the development of the TBM, and the support of the STW and Dana Spicer on the CC-PowerTrain project.

AUTOMATIC DESIGN OF ORC TURBINE PROFILES USING EVOLUTIONARY ALGORITHMS

Pablo Rodriguez-Fernandez, Giacomo Persico

Laboratorio di Fluidodinamica delle Macchine,
Politecnico di Milano,
Via Lambruschini 4, I-20156 Milano, Italy
e-mail: giacomo.persico@polimi.it
Web page: http://www.lfm.polimi.it

ABSTRACT

In this paper, an automated design tool for Organic Rankine Cycle (ORC) turbines is presented. Supersonic flows and real-gas effects featuring ORC turbines complicate significantly their aerodynamic design, which may benefit significantly from the application of systematic optimization methods. This study proposes a complete method to perform shape optimization of ORC turbine blades, constructed as a combination of a generalized geometrical parametrization technique, a high-fidelity Computational Fluid Dynamic (CFD) solver (including real gas and turbulence models) and an evolutionary algorithm. As a result, a non-intrusive tool, with no need for gradients definition, is developed. The high computational burden typical of evolutionary methods is here tackled by the use of a surrogate-based optimization strategy, for which a Gaussian model is applied. Application to ORC turbines has been proved to be successful, resulting in a comprehensive method for a very wide range of applications. In particular, the present optimization scheme has been applied to the re-design of the supersonic nozzle of an axial-flow turbine. In this design exercise very strong shocks are generated in the rear blade suction side and shock-boundary layer interaction mechanisms occur. Optimization aiming at a more uniform flow at the blade outlet section is shown to minimize the shock losses, resulting in a significant improvement in the nozzle efficiency. The optimal configuration determined with the present design tool is also successfully validated against the outcome of a previous optimization performed with a gradient-based method, demonstrating the reliability and the potential of the design methodology here proposed.

1. INTRODUCTION

Thanks to the progressive increase of computational capability, optimization techniques based on high-fidelity flow models play a key role in the present-day design process of turbomachinery. The turbomachinery design process offers optimization challenges at different fidelity levels, from the zero-dimensional stage-by-stage definition (Pini et al. (2013)), to the axisymmetric design (Larocca (2008); Pasquale et al. (2014)), up to the detailed blade shape definition (Verstraete et al. (2010); Pini et al. (2014)).

In the last decades several CFD-based shape optimization procedures were specifically developed in Aerodynamics, such as inverse design methods (Demeulenaere et al. (1997)), adjoint-based gradient methods (Peter and Dwight (2010)), or evolutionary algorithms (Coello (2000)). These latter techniques allow to explore a wider range of feasible solutions, identifying the best individual, and also allow to handle multi-objective optimization problems (Pierret et al. (2006)).

In this paper, a novel optimization package is presented, based on evolutionary algorithms, specifically oriented to the design of turbomachinery blades. Thanks to the high-fidelity flow model, which includes turbulence models and a generalized thermodynamic treatment of the working fluid, the method is particularly attractive for ORC turbines, that feature severe supersonic flows and strong real-gas effects. Several optimization algorithms are tested and the application of the design tool to a highly complex

ORC turbine indicates that dramatic performance improvement is achievable by systematic application of the proposed optimization method.

The paper is structured as follows: in Section 2, the methodology behind the shape optimization tool is described in detail; in Section 3, the different optimization strategies applied and the environment in which they are implemented are discussed. Section 4 finally reports the results of the application to a supersonic ORC turbine nozzle, considering the effectiveness of optimization as well as its implications on the cascade aerodynamics.

2. METHODOLOGY

The optimization strategy here presented is constructed by combining four main blocks, namely a geometry parameterization code, a high-fidelity CFD solver, a library of evolutionary algorithms, and a meta-model interpolation tool. All these items are discussed in detail in the present Section. In particular, Subsection 2.1 describes how B-Spline curves are used to generate the blade geometry; in Subsection 2.2, the CFD model employed for the present high-fidelity calculations is summarized; in Subsection 2.3, genetic algorithms and evolutionary strategies are presented; finally, in Subsection 2.4 the surrogate model used in this study is defined.

2.1 Geometry Parameterization

A key feature of shape-optimization problems in aerodynamics is the technique used to reconstruct the shape of profiles by employing a minimum number of variables. In this work, B-Spline curves are used to parameterize the blade geometry, as the shape can be easily described by a certain number of so-called control points. Thanks to this and other features, B-Spline curves are presently recognized as a powerful tool in both application and theory for aerodynamic designs (Farin (2002)).

A B-Spline can be defined as a piecewise curve with components of degree n that provide local support and whose smoothness and continuity can be adjusted. Thus, a B-Spline curve can be described as a weighted sum of basis functions as follows:

$$x(u) = \sum_{j=0}^{L} d_j N_j^n(u) \tag{1}$$

where $\{d_j\}$, with $j = 0, \ldots, L$, are the control points, and $N_j^n(u)$ are the corresponding n-degree B-Spline bases. These can be defined recursively in the form:

$$\begin{aligned} N_j^k(u) &= \frac{u - u_{j-1}}{u_{j+k-1} - u_{j-1}} N_j^{k-1}(u) + \frac{u_{j+k} - u}{u_{j+k} - u_j} N_{j+1}^{k-1}(u) \\ N_j^0(u) &= \begin{cases} 0 & \text{if} \quad u_{j-1} \le u < u_i, \\ 1 & \text{otherwise} \end{cases} \end{aligned} \tag{2}$$

where $\{u_j\}$, with $j = 0, \ldots, K$, is the knot sequence and u is a parameter. Notice that $K = L + n - 1$.

At this point, a first algorithm can be developed to generate a B-Spline curve from a given set of control points, as it is depicted in Figure 1.

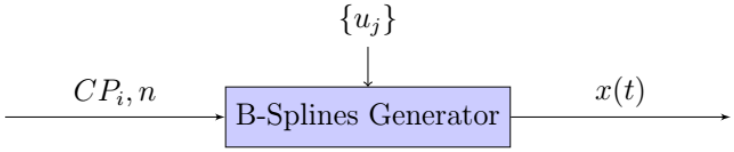

Figure 1: Geometry generation algorithm. CP_i and n are the control points and the degree of the curve, respectively; $\{u_j\}$ is the knot sequence. As output, the B-Spline curve $x(t)$ is generated.

The optimization tool described in this study is able to build an approximate representation of the shape of the blade using a B-Spline curve, defined and manipulated by the position of the control points. In order to generate this curve, the baseline geometry needs to be interpolated. In this work, a least squares interpolation method is used.

It is assumed that $P+1$ data points p_i are given, with $i = 0, \ldots, P$, and we seek to find the approximated B-Spline curve $x(u)$ of degree n and $K+1$ knots u_k, with $k = 0, \ldots, K$. This B-Spline curve will be defined by $L+1$ control points d_j, with $j = 0, \ldots, L$, such that $L = K - n + 1$. The error of the approximation for a given point can be expressed as $\|p_i - p(w_i)\|$, where w_i, with $i = 0, \ldots, P$, are the data parameters of the problem. Therefore, the objective is to minimize the total approximation error:

$$f(x) = \sum_{i=0}^{P} \|p_i - x(w_i)\| \tag{3}$$

If we rewrite Equation (3) using Equation (1) and perform a least squares minimization process, a final expression for the $L+1$ normal equations is derived:

$$\sum_{j=0}^{L} d_j \sum_{i=0}^{P} N_j^n(w_i) N_k^n(w_i) = \sum_{i=0}^{P} p_i N_k^n(w_i); \tag{4}$$

This equation leads to a linear system $A \cdot x = B$ that is solved, in this work, by using Cholesky Decomposition. At this point, a new algorithm can be defined, to find the control points that best represent a given geometry, as it is depicted in Figure 2.

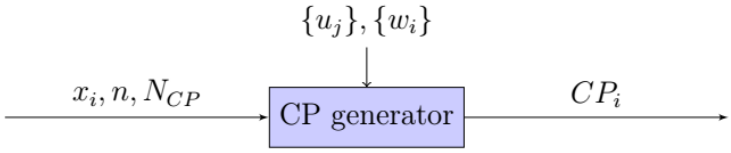

Figure 2: Interpolation algorithm. x_i, n and N_{CP} are the data points, the degree of the B-Spline curve and the desired number of control points, respectively. $\{u_j\}$ and $\{w_j\}$ are the knot sequence and the data parameters. As output, the control points CP_i of the B-Spline are generated.

The sequence of data parameters $\{w_i\}$ is built using a centripetal parameterization. With regard to the knot sequence, it can control the shape of the final interpolated B-Spline. It divides the curve into segments, defined on a knot span. In this work, the knot sequence is used to regulate the position of the control points that serve as design variables of the optimization problem. In this way, one can identify areas prone to optimization and thus assign a different number of control points for each region during the interpolation process.

In this study, both pressure and suction sides of the blade are generated with a unique B-Spline curve. However, the trailing edge will be considered separately, as it is best represented by a circular arc. As a result, the B-Spline curve is constrained to pass through the first and last data points to create a closed curve along with the circular-shaped trailing edge. Continuity and regularity are ensured by imposing same derivative. Additionally, no weights for the control points are used during the interpolation.

2.2 CFD Codes

The present optimization strategy makes use of high-fidelity numerical simulations of the selected blade configurations, performed applying a fully-turbulent and real-gas CFD model based on the ANSYS-CFX solver. As only blade-to-blade effects are of interest, quasi-3D simulations are carried out, using 2D profiles generated with the geometry parameterization algorithm and considering a straight stream-tube around midspan. The effects of turbulence are introduced by resorting to the $\kappa - \omega$ SST model,

providing a proper clustering of the cells in the near-wall region so to ensure y^+ below unity along the blade. The real-gas thermodynamic behavior of the working fluid is treated by means of a Look-up-Table (LuT) interpolation method; the LuT was constructed in primitive variables (P, T) by resorting to the Span-Wagner equations of state implemented in the FluidProp database (Colonna et al. (2008)). Total conditions, flow angles, and turbulence quantities are assigned at the inlet, and static pressure is given at the outlet. The onset of spurious pressure wave reflections from the downstream boundary is avoided by placing the outflow boundary three axial chords away from the trailing edge. High resolution numerical schemes are used for advective and diffusive fluxes.

2.3 Genetic Algorithms

The interest in single and multi-objective optimization has grown dramatically in the last decades, thanks to the progressive increase of computational power. In engineering, this has led to the development of several methods which apply the concepts of optimization to support the design of components. Thus, design-oriented optimization can be pursued by applying inverse design methods, gradient-based methods, or heuristic methods. For aerodynamic design purposes, the application of heuristic methods is particularly attractive, as it can be performed by using direct calculation models (such as CFD).

Within the class of heuristic methods, Evolutionary Algorithms (EAs) have become very interesting in a wide range of applications, due to many advantages that make them outperform other optimization methods. Among them, Genetic Algorithms (GAs) have the possibility of dealing with oscillating or smooth-less objective functions; they also allow to introduce constraints in a relatively easy way, and to treat multi-objective optimization as well. Furthermore, genetic algorithms are global optimization methods and, hence, are best suited for optimization problems with multiple local optima, for which gradient methods are too computationally expensive or not readily available. In many optimization problems, GAs quickly identify promising regions of the design space where the global optimum might be located. The interested reader is invited to consult Reeves and Rowe (2002) for a complete description of different GA approaches.

However, the flexibility and simplification provided by GAs are achieved through a massive application of the direct computational model of interest, and thousands of evaluations are usually needed to identify the optimum. Shape-optimization problems in aerodynamics require the application of CFD models, which are expensive tools requiring at least some minutes of calculation to achieve convergence (a reliable optimization requires, in general, fully turbulent flow models and an appropriate grid resolution). As a consequence the direct application of CFD-based genetic optimization is usually not feasible for aerodynamic design purposes. To tackle this unacceptable computational cost, surrogate models can be used. Surrogate models, also known as meta-models or response surfaces, are analytical functions that relate the design variables with performance (i.e., the objective function) in an approximate way. A mathematical representation is selected for the objective function with no relation with the physical phenomena of the real problem (namely, with the CFD model). As it will be discussed later, the mathematical model is trained along the process, resulting in a dramatic reduction of computational burden, as the genetic algorithm is applied directly to the meta-model.

2.4 Surrogate Models

An extensive theory about surrogate models has been developed and many schemes are currently available (the interested reader is referred to Simpson et al. (2001) for a review of available techniques). In this study, the Kriging model is used as the mathematical approximate objective function or non-linear constraint. The Kriging technique is based on a set of interpolation methods, sometimes called Gaussian Processes, originally developed for geostatistic problems and nowadays widely used in many engineering fields. The mathematical model of Kriging can be understood as the linear combination of a trend function and the implementation of a stochastic process. The most common form of a Kriging model is as follows:

$$\tilde{f}(x) = g(x)^T\beta + r(x)^T R^{-1}(f - G\beta) \tag{5}$$

where x is the point to be evaluated; $g(x)^T\beta$ is the trend function evaluated at x, whose coefficients are estimated using a least squares approach; $r(x)$ is the correlation vector with the data points; R is the correlation matrix for all of the data points; f is the response values vector; and $G\beta$ is a vector that contains the trend function evaluated at all data points. The terms in the correlation vector ($r(x)$) and correlation matrix (R) are computed using a Maximum Likelihood Estimation (MLE) procedure.

The implementation of this meta-model in the evolutionary optimization strategy is described in Section 3.

3. IMPLEMENTATION

In this study the optimization problem has been assembled in the object-oriented framework Dakota (Adams et al. (2013)). Dakota provides optimization algorithms, i.e. single-objective and multi-objective genetic algorithms, as well as surrogate models and optimization strategies.

To perform the optimization using genetic algorithms, the JEGA library is used. JEGA (Java Engine for Genetic Algorithms) is a framework that provides a flexible and extensible optimization environment for computational models. Different optimization approaches have been considered and tested to investigate the performance and eventually improve the automatic design tool developed in this research. The initial database is built using Latin Hypercube sampling technique. Usually the size of the population is taken as 2 to 4 times the number of design variables. For example in the present case, a population of 50 individuals is chosen, in line with the 16 design variables used. The probability of crossover and mutation are 80% and 20%, respectively. Elitism is used as selection technique.

To determine the Kriging parameters, the Surfpack library is employed. In this case, it uses a global search method called *DiRect* algorithm (dividing rectangles), a derivative-free global optimization method that balances search in promising and unexplored regions. The trend function is built using a reduced quadratic expression. When working with non-linear constraints, a Kriging model is also built as a mathematical expression for each of them.

Regarding optimization strategies, local and global schemes are tested. In **surrogate-based local optimization** (SBLO), also called Trust Region technique, the optimization algorithm operates directly on a surrogate model that is built using an initial database composed by a certain number of individuals. However, the surrogate model has a limited reliability (especially at the beginning of the process), and hence the fidelity of the approximation is assessed by comparing with the high-fidelity expensive tool (by running the CFD solver). The main feature of the local optimization is the use of a trust region approach, which defines the extent of the approximation. SBLO method needs to generate and update the data fit in each trust region, performing high-fidelity evaluations over a design of experiments. Although a local approach, each sampling in the trust region can be performed globally, which allows to extract relevant global design trends. The comparison between the surrogate and the high-fidelity evaluations, formulated as a trust region ratio, is used to define the step acceptance and trust region size and position of the next iteration.

On the other hand, in a **surrogate-based global optimization** (SBGO), the algorithm is not supported by a trust-region approach. It starts from an initial sample of points and the optimizer operates on that surrogate, by updating its parameters after a new optimum is found and added to the sample. This approach should be used carefully, as there is no guarantee of convergence. It should be used either when there exists the need of using an initial database or when the surrogate needs, somehow, to be updated globally. The surrogate becomes more accurate as the iterations progress. In the present study, both global and local schemes are compared and tested.

4. RESULTS

An exercise of shape-optimization is discussed in the following to demonstrate the capabilities of the design tool presented in this paper. To show the flexibility and the wide range of application of the technique, a particularly severe test-case is considered, namely a converging-diverging supersonic nozzle for an axial-flow ORC turbine operating with MDM. The original blade geometry, shown in Figure 3 and called Baseline in the following, was designed by means of the method of characteristics (MOC) for the diverging part and features a highly smooth leading edge to reduce the sensitivity to incidence variations. The optimization process aims at maximizing the performance of the cascade operating with an expansion ratio of 8 starting from a superheated condition ($P_{T,in} = 8bar$, $T_{T,in} = 272C$) close to the saturation line. As a result, supersonic flows are induced (in fact, the cascade-exit Mach number exceeds 2) and strong real-gas effects occur in the expansion, justifying the use of a LuT approach for the thermodynamic modeling of the fluid.

The blade geometry has been first interpolated and parametrized using the method described in Subsection 2.1. Once the right number of control points is established, their relative position can be adjusted by modifying the knot sequence. In this work, 30 control points have been found to be sufficient to provide an accurate interpolation. From the complete set, the vertical positions (y-coordinate) of 16 control points define the set of design variables for the optimization problem (see Figure 3). The leading edge and the front part (roughly up to the throat) are kept fixed during the optimization process and a larger number of control points is chosen in these regions. The trailing edge width is kept constant so to guarantee the structural resistance of the blade, and therefore only one control point is needed to determine the location of the trailing edge.

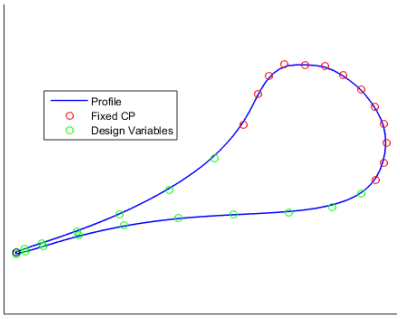

Figure 3: Baseline profile shape and control points distribution. Green circles indicate design variables, while red ones are kept fixed during optimization. The black circle indicates de control point that moves accordingly to keep the trailing edge width constant.

High-fidelity calculations were performed on structured grids composed by 400,000 hexahedral elements. The reliability of the numerical model used in this context was previously assessed against experiments performed by the authors themselves on a research turbine stage installed at Politecnico di Milano (Persico et al. (2012)). The CFD model was shown to accurately predict the fully three-dimensional and unsteady flow physics of the whole turbine stage, and provided estimates of stage efficiency within 1% of the experimental datum, i.e. comparable to the uncertainty of the measurement technique.

In the following, several optimization tests are discussed, with the aim of investigating the impact of different approaches on both the computational cost and the fitness of the design outcome. Different surrogate strategies are considered, also in comparison to gradient-based optimization techniques; it is shown how the proposed automatic design tool provides, in addition to the specific optimized geometry, some intuitive design guidelines for supersonic ORC turbines.

4.1 Impact of the optimization strategy

At first, the comparison between the Global (training) and Local (trust regions) optimization strategies is performed. For both cases the same objective function is used, defined as the standard deviation of the azimuthal pressure distribution evaluated half axial chord downstream the blade trailing edge. The minimization of this quantity in a supersonic cascade is expected to reduce the shock strength, thus increasing the cascade performance.

For the construction of the Kriging surrogate model, a minimum sample size of 5 times the number of design variables is commonly considered. In this study, 16 design variables are set to optimize the geometry, and hence a database of 80 individuals is, in all cases, considered. In the global approach,

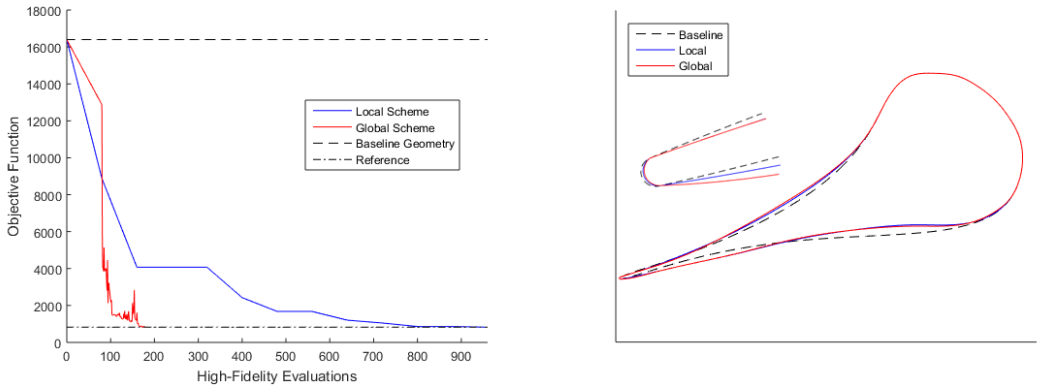

Figure 4: Left: convergence history of global and local strategies for surrogate-based optimization. Right: optimized geometry using global and local strategies for surrogate-based optimization.

this means that the code builds the initial Kriging model over this initial sample. After a complete GA-optimization applied only to the mathematical model, the result is assessed via the high-fidelity tool and added to the population (updating the Kriging parameters in each iteration). On the other hand, the local approach builds a new Kriging model after each GA-optimization. These different features are clearly visible in the left frame of Figure 4, where the paths towards optimization are compared for the two methods; in particular, it is observed how the local scheme advances only each 80 high-fidelity evaluations, while the global method advances continuously after the initial 80 iterations. As a result the local approach shows a much slower trend, even though the local and global schemes obtain a very similar minimization of the objective function, significantly reduced with respect to the baseline configuration. For this reason, in the following only the global scheme will be used.

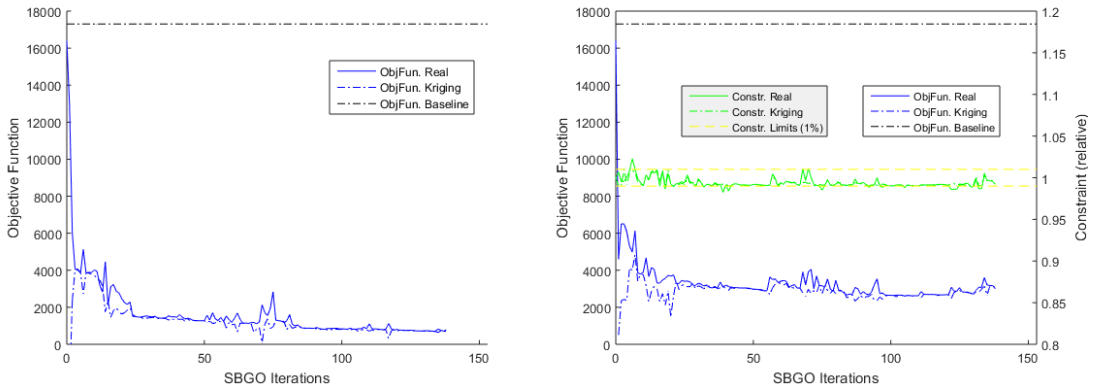

Figure 5: Convergence history of Kriging model for (left) non-constrained, and (right) constrained optimization, using a global strategy for surrogate-based optimization.

When performing evolutionary optimization using surrogate strategies, the convergence of the approximate model to the actual response surface of the problem needs to be verified. The left frame of Figure 5 shows that the surrogate model quickly matches the high-fidelity tendency, except for some spikes of progressively reduced amplitude as the algorithm converges to the optimum. This allows to conclude that the training procedure chosen for the Kriging model is appropriate for the present design problem. The smooth convergence trends observed so far have been achieved without the application of explicit constraints to the optimization. However from the engineering perspective it is interesting to investigate how the optimization proceeds when a relevant quantity is constrained; for example, when looking to

the turbine cascade performance, the flow rate is usually a fixed parameter whose variation needs to be limited in a narrow range. The right-hand side of Figure 5 shows the results a non-linear constrained optimization, by forcing the flow rate to stay within ±1% with respect to the baseline value. A specific Kriging model is built for the constraint. It is observed how, after a significant reduction of the objective function in the initial phase, the constraint prevents the optimization from progressing further, resulting in a lower fitness of the outcome. It is also very interesting to note that the flow rate of the optimized cascade achieved via non-constrained global optimization is, in fact, within the limits. This is probably because the front part of the blade up to the throat is kept fixed and hence the flow rate is somehow imposed indirectly in the present chocked flow configuration. This seems to be a more effective procedure when dealing with supersonic cascades.

4.2 Aerodynamic analysis

The flow configuration established in the cascade optimized via the non-constrained global strategy is now discussed, in comparison to the baseline configuration and to another optimized case. This latter configuration was obtained by applying an adjoint-based gradient method developed by Pini et al. (2014); it was performed using the same objective function used here and was based on an inviscid flow solver; the result here reported is, however, the high-fidelity calculation of that optimized configuration.

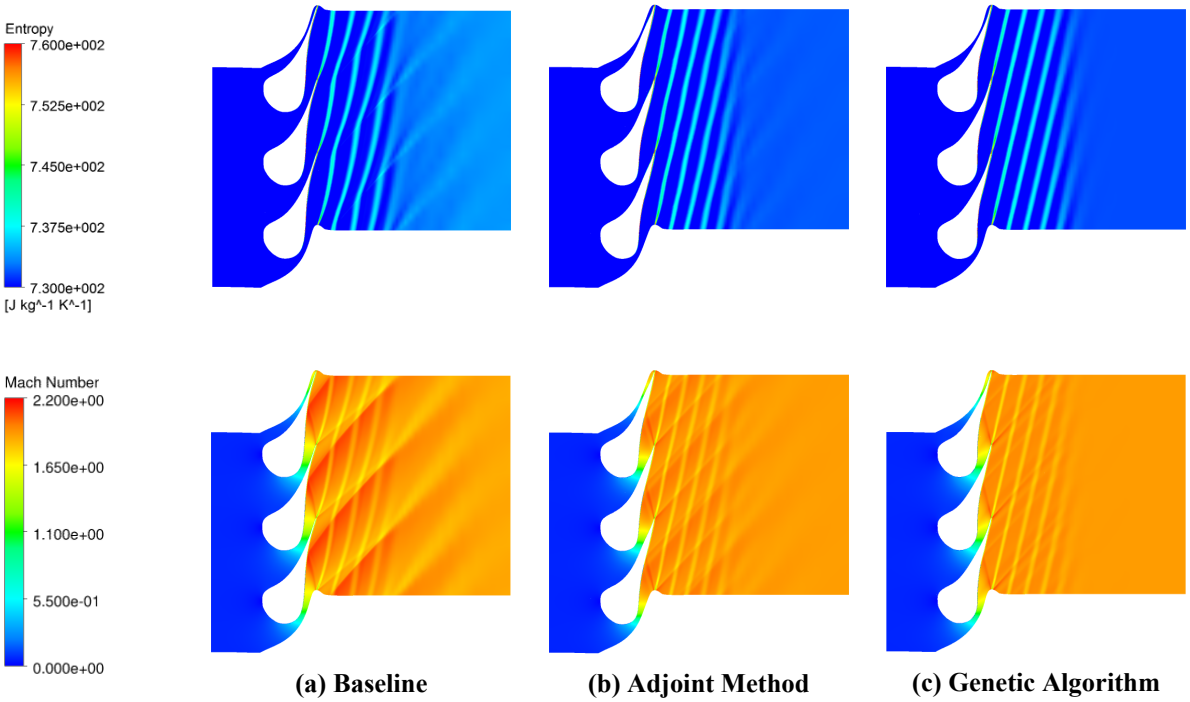

Figure 6: Comparison of the Mach number (bottom) and Entropy (top) distributions for (a) Baseline, (b) Adjoint method (Pini et al. (2014)), and (c) present study using the global strategy.

The entropy and Mach number field on the blade-to-blade surface are reported for the three cases in Figure 6. The effect of the optimization is clearly visible by comparing the optimized and baseline configurations; in particular the minimization of the pressure oscillations downstream of the cascade leads to a dramatic reduction of the main shock strength. Hence, the severe pressure gradient observed in the baseline case is highly weakened and the weaving path of the blade wakes is almost eliminated. As a result, the overall entropy generation is significantly reduced in the optimized cases. The two optimized blades exhibit very similar flow configurations, even though the two approaches make use of very different methods based on different flow models; this suggests that both the methods are converging towards the same optimum, which is probably the global optimum for the present problem. The evolutionary optimization leads, in fact, to a slightly more uniform flow, due to the slightly weaker fishtail shock system

at the blade trailing edge; such a shock system is not accurately captured by the inviscid flow model used in the adjoint-based optimization (due to the missing displacement thickness of the boundary layers), and this may explain the slight differences observed. However the outcome of the adjoint optimization still remains an excellent result considering its extremely limited computational cost (less than an hour on a standard PC) with respect to that of the present GA strategy (20 hours on a 15-processor cluster).

Figure 7 reports the pressure distribution on the three blades, in the form of isentropic Mach number, and explains the reason for the improved performance of the optimized configurations. Both optimal blades move ahead the acceleration of the flow on the suction side, just downstream of the sonic throat and still within the bladed channel; as a result the over-speed on the rear suction side is limited and hence the subsequent diffusion is eliminated. In this way the onset of the strong shock observed in the baseline configuration is prevented. Once again the two optimized configurations show very similar trends, with local differences especially close to the trailing edge.

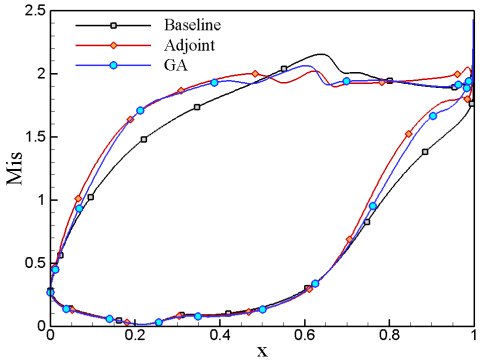

Figure 7: Isentropic Mach Number distribution over the blade for the Baseline configuration, the optimized blade using the Adjoint Method (Pini et al. (2014)) and using genetic algorithms.

To quantify the impact of the optimization on the cascade performance the Total Pressure Loss Coefficient is used, defined as the total pressure loss referred to the exit dynamic pressure ($Y = \frac{P_{T,in} - P_T}{P_{T,in} - P}$). The results, considering an outlet placed at 2 chords downstream the blade (where the flow can be considered mixed-out) are summarized in Table 1. It can be concluded that the more uniform flow achieved in the downstream region leads to a relevant decrease of the total pressure loss coefficient, which reduces from 15.0 to 9.3%.

	Baseline	Adjoint Method	GA
Y	0.15	0.11	0.093

Table 1: Total Pressure Loss Coefficient at two axial chords downstream the blade.

5. CONCLUSIONS

This paper has presented a novel package for the automatic design of ORC turbines based on an evolutionary strategy. Detailed descriptions of all the steps of the optimization scheme have been provided, namely the geometry parametrization, the high-fidelity flow solver and the genetic algorithm.

The blade shape is parametrized via B-Splines, whose local control capability allowed a detailed shape reconstruction while preserving surface smoothness. The implementation of advanced high-fidelity flow models, of paramount importance for ORC turbines, is easily attained thanks to the non-intrusive character of the evolutionary optimization strategy here used. To tackle the computational burden typical of CFD-driven evolutionary strategies, the genetic algorithm is coupled to a surrogate model that reflects the influence of the design variables on the objective function. Several optimization strategies have been discussed to evaluate the convergence process and the associated computational cost.

Application to a supersonic ORC turbine nozzle has demonstrated that relevant performance improvements can be achieved by maximizing flow uniformity downstream the blade. A further comparison, for the same test case, against an alternative optimization approach has assessed the validity of the present design methodology. Results have also allowed to quantify the impact of the application of high-fidelity flow models within the optimization process. Future research will be addressed towards the applica-

tion of the present shape-optimization tool to the design of novel turbine blade configurations for ORC applications.

REFERENCES

Adams, B., Bauman, L., Bohnhoff, W., Dalbey, K., Ebeida, M., Eddy, J., Eldred, M., Hough, P., Hu, K., Jakeman, J., Swiler, L., and Vigil, D. (2013). Dakota, a multilevel parallel object-oriented framework for design optimization, parameter estimation, uncertainty quantification, and sensitivity analysis: Version 5.4 user's manual. *Sandia Technical Report SAND2010-2183*.

Coello, C. (2000). An updated survey of GA-based multiobjective optimization techniques. *ACM Computing Surveys*, 32(2):109–143.

Colonna, P., Nannan, N., and Guardone, A. (2008). Multiparameter equations of state for siloxanes: [(ch3)3-si-o1/2]2-[o-si-(ch3)2]i=1,...,3, and [o-si-(ch3)2]6. *Fluid Phase Equilibria*, 263(2):115 – 130.

Demeulenaere, A., Leonard, O., and Van Den Braembussche, R. (1997). A two-dimensional Navier-Stokes inverse solver for compressor and turbine blade design. *Journal of Power and Energy*, 211(4):299–307.

Farin, G. (2002). *Curves and Surfaces for CAGD: A Practical Guide*. Morgan Kaufmann Publishers Inc., San Francisco, CA, USA, 5th edition.

Larocca, F. (2008). Multiple objective optimization and inverse design of axial turbomachinery blade. *Journal of Propulsion and Power*, 24(5):1093–1099.

Pasquale, D., Persico, G., and Rebay, S. (2014). Optimization of Turbomachinery Flow Surfaces Applying a CFD-Based Troughflow Method. *Journal of Turbomachinery*, 136(3):031013 1–11.

Persico, G., Mora, A., Gaetani, P., and Savini, M. (2012). Unsteady aerodynamics of a low aspect ratio turbine stage: Modeling issues and flow physics. *Journal of Turbomachinery*, 134(6).

Peter, J. and Dwight, R. (2010). Numerical sensitivity analysis for aerodynamic optimization: A survey of approaches. *Computers & Fluids*, (39):373–391.

Pierret, S., Coelho, R., and Kato, H. (2006). Multidisciplinary and multiple operating points shape optimization of three-dimensional compressor blades. *Structural and Multidisciplinary Optimization*, 33(1):61–70.

Pini, M., Pasquale, D., Persico, G., and Rebay, S. (2014). Adjoint method for shape optimization in real-gas flow applications. *Journal of Engineering for Gas Turbines and Power*, 137:032604.

Pini, M., Persico, G., Casati, E., and Dossena, V. (2013). Preliminary design of a centrifugal turbine for ORC applications. *ASME Journal of Engineering for Gas Turbines and Power*, 135(042312).

Reeves, C. R. and Rowe, J. E. (2002). *Genetic Algorithms: Principles and Perspectives: A Guide to GA Theory*. Kluwer Academic Publishers, Norwell, MA, USA.

Simpson, T., Poplinski, J., Koch, P. N., and Allen, J. (2001). Metamodels for computer-based engineering design: Survey and recommendations. *Engineering with Computers*, 17(2):129–150.

Verstraete, T., Alsalihi, Z., and Van Den Braembussche, R. (2010). Multidisciplinary Optimization of a Radial Compressor for Microgas Turbine Applications. *Journal of Turbomachinery*, 132:031004.

SCREW EXPANDERS IN ORC APPLICATIONS, REVIEW AND A NEW PERSPECTIVE

Henrik Ohman[1]*, Per Lundqvist[2]

[1]KTH, Royal institute of Technology,
Department of Energy Technology,
Stockholm, Sweden
henrik@hohman.se

[2]KTH, Royal Institute of Technology,
Department of Energy Technology,
Stockholm, Sweden
per.lundqvist@energy.kth.se

* Corresponding Author

ABSTRACT

Performance of Organic Rankine Cycles is sensitive not only to the entry temperature ratio between heat source and heat sink but also to the temperature degradation of the heat source flow, caused by the heat transfer to the process in pre-heater, evaporator and super heater. In order to adopt the cycle to the great variety of heat sources a multitude of fluids are required. Alternatively fluid mixtures, trans-critical or supercritical fluid conditions can be used to match the process temperatures with the heat source. Screw expanders offer an alternative, new approach to the matching problem of ORC's as they allow for flexible multi-phase expansion. Hereby the vapour fraction at the expander entry can be used to partially match the temperatures of the process to a particular heat source. To provide a perspective on the use of such screw expanders in ORC-systems previous experimental and commercial experience have been reviewed and discussed.

Screw expanders are versatile machines used for the production of mechanical work in power ranges from 3kW to 1.5MW. As the functional characteristics differ significantly from dynamic expanders the explanatory models used to generalise results are different. Plenty of research has resulted in well generalized explanatory models for dynamic expander analysis. For screw expanders similar explanatory models exist mainly in commercially confidential environments. A few public sources disclose test data. In the few cases data has been investigated the analyses tend to rely on thermodynamic models suitable for dry gas expansion. Typically that leads to reasonable replication of test results but seldom to models suitable for detailed understanding of the process. In applications with 2-phase expansion the theories used to simulate functional characteristics is entirely insufficient. The main reason for the scarcity of work in this field is probably the empirical difficulties in obtaining good measuring data in multi-phase conditions.

This paper describes a review of multi-phase screw expander experiences and explains why a unique theory is required to model its characteristics. In the absence of such a unique theory a correlation based in empirical data is presented. This allow for estimations of screw expander efficiency in multi-phase conditions. Measured efficiency with dry expansion, or such efficiency simulated, can be used to estimate adiabatic efficiency with expansion entry vapor fractions ranging from 0 to 1 by using this correlation. Hence estimating expansion efficiency during multi-phase expansion is simplified, allowing for better optimisation of the ORC-systems. This way a new perspective of screw expander potential in ORC system integration can be presented.

1. INTRODUCTION

Historical background, experiences with screw expanders in ORC's, 2-phase expansion and the implications of using 2-phase expansion in ORC's are explained to create a perspective of the future potentials in combining the two.

Helical, rotating piston-type, fluid expansion machines have been around as long as their equivalent fluid compression machines. The ideas for developing such devices constitute natural progressions of the Archimedes Screw, known by the ancients. Heinrich Krigar patented a twin rotor helical liquid pump in 1878, with an alternative use as *presse*. The latter term would be similar to the modern term *blower,* i.e. a positive displacement fan with no internal compression. In the 1920's jet engine designer Alf Lysholm started the development of a series of twin screw compressors for the application of combustion chamber air compression in airborne jet engines and turbo-props, see Figure 1. Lysholm and Boestad (1935) describe a fully industrialized twin screw compressor, sold on five continents only two years later. After that an impressive evolution of designs and applications for twin screw compressor technology emerged. They have revolutionized technical systems architecture in combustion engines, refrigeration and air conditioning plants, industrial gas cleaning and pressurized air systems.

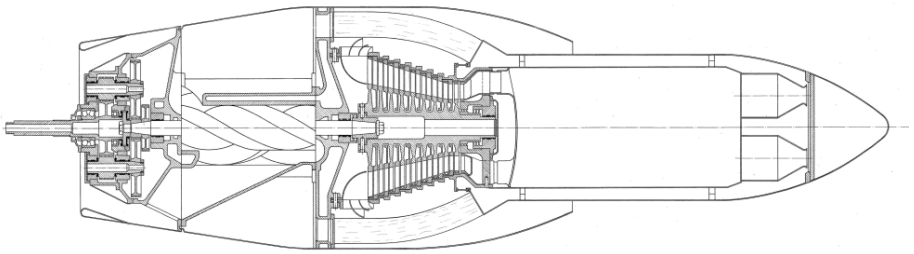

Figure 1. Early integration of twin screw machine in Gas Turbine aircraft engine.

The opportunity of reverse use, i.e. twin screw expanders, was obvious to anyone involved. However markets for supply of shaft power always tended to be smaller than for supply of compressed gases. Therefore commercial volumes, and consequently the variations of designs, are significantly less for screw expanders than its reversely operating sibling. From the same reasons scientific investigation of twin screw expanders is limited and many industrial records have been cleaned out.
One branch of screw expander applications is steam expansion with dry entry. Such applications were common before the advent of affordable, variable speed, electric drives and have seen a revival in modern small scale distributed power generation. Significant knowledge exists in industry and science and that branch will not be specifically addressed in this paper.

With modern developments towards local small scale power generation, as well as widespread availability of thermodynamic computational tools, development of various ORC systems has increased. The use of screw expanders in such applications is still in its infancy and requires more scientific study. Furthermore the screw expanders currently used tend to be limited to designs based on screw compressor design optimizations, leaving room for significant improvements of the machine design itself.
One of the perhaps most interesting possibilities to improve the technology of ORC's is implementing the unique characteristic of allowing efficient expansion of mixtures of gas and liquid from the beginning of the expansion process. Sample effects on ORC system efficiency and specific cost were demonstrated in Öhman and Lundqvist (2014). Using standard practice thermodynamic analysis tools economic optimization of cycle design, and cost allocation, becomes trivial provided that the efficiency of the mixed phase expansion process can be estimated.

Little information on 2-phase expansion efficiency of screw expanders is available. Part of the historic experience of using screw expanders is therefore presented below as well as state-of-the-art on performance prediction and its implications on ORC system optimization.

2. PRIOR FIELD EXPERIENCES WITH ORC'S

Very little of industrial knowledge prior to the digital revolution is traceable without having access to proprietary archives. Also such information is hard to come by as most companies involved has ceased to exist over time and their records scattered. Traces however can be found, often tracked in interviews with elderly engineers and scientists, or in technical periodicals.

One cannot write about twin screw machines without briefly mentioning the late engineering company ALÅ/SRM, 1908-2011. *Aktiebolaget Ljungströms Ångturbin, later renamed Svenska Rotor Maskiner AB*. As described in Timuska (2008) and Svenningson et al (2010) SRM dominated the systematic development of twin screw machines and by licensing the technology to most suppliers on the market the impact of their development cannot be overestimated. SRM's archives originally contained design calculations and performance data from worldwide screw expander power generation systems from 1932 to 2011. Unfortunately that archive is only partly available and could be expected to be partly shattered. The information in this paper is based on interviews with experienced engineers and available publications.

ORC's using screw expanders was well known in the 1960's. Minto (1967) describe an automotive version of an ORC and Behrendt (1970) cites Minto implementing it in 2 different full scale cars, one of them using a 112mm, A-profile screw expander and R114 as seen in Figure 2.

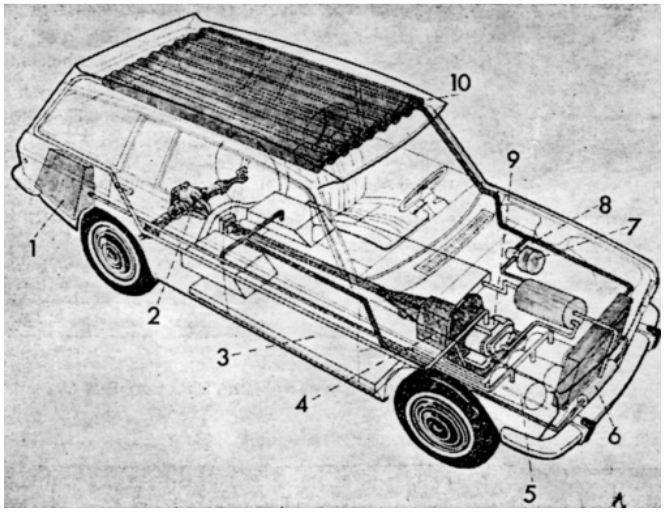

Figure 2. Schematic image of a Datsun station wagon equipped with a Minto ORC drive train.

Before Mintos automotive ORC, Linde created so called MK-systems integrating an ORC-system with an air conditioning system, also using R114. 5 sizes of such machines where developed in the 1960's, using integrated screw expander-screw compressor-liquid pump units as described by Öhman (1997). CIT-ALCATEL sold ORC-units for solar energy pumping stations in the 1970's, developed in the 1960's. They used a 112mm, A-profile, screw expander and R114, see Figure 3, similar to at least one of Mintos ORC-driven prototype vehicles. Thermofrost developed a 10kW waste heat driven ORC with a screw expander, followed by a similar 350kW ORC, with screw expanders reengineered from standard screw compressors of Japanese making. One of the latter was using waste heat form Korsnäs Pulp factory in mid-Sweden. A German supplier built a handful of ORC screw expanders for waste heat recovery purposes in the 1980's and 1990's as well as one 60kW, iso-butane ORC-expander in Biburg, Germany as of 2004.

Rumors of several sizes of field applications with ORC's using screw expanders from Japanese suppliers echoes from 1970's to 1990's though that information has not been verified. In 2003 ITRI installed a field pilot of a 50kW ORC in a waste heat recovery plant in Taiwan. They used a 113mm, semi-hermetic, screw expander using R141b.

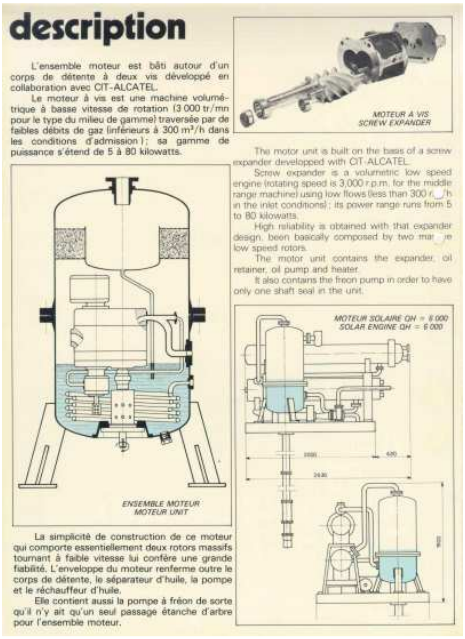

Figure 3. Detail of commercial leaflet on Solar driven ORC. *Mid 1970's, not dated*.

Between 2005 and 2012 a Swedish supplier commissioned 4 waste heat recovery ORC units with 254mm screw expanders; 350kW/R410a, 750kW/NH3 *described in Öhman and Lundqvist (2012)*, 650kW/R410a and 600kW/R236fa. The latter was installed for jacket cooling water waste heat recovery on a 14MW marine diesel in a commercial freight ship. Allegedly they are still in operation. During the same time period a UK supplier commissioned a significant number of 65kW ORC units using R245fa. *Data for those screw expanders are yet unavailable to the authors*. An Australian supplier commissioned a 450kW screw expander ORC for waste heat recovery on a gas turbine in 2014. Biederman and Brasz (2014) describe four parallel 1MW/R245fa geothermal ORC expanders in Lightning Dock, New Mexico. Reports are coming in on some recent Chinese pilot installations of screw expander ORC's. This list of experiences is not conclusive but indicates that significant amount of industrial experience is available though scarcely seen in scientific literature.

3. TWO PHASE EXPANDERS

A screw expander consists of two rotating, helical bodies creating "chambers" with certain characteristics between them. Each chamber starts from a volume of zero, is expanded to a maximal volume and thereafter compressed to a volume of zero. The typical cycle time for one chamber process is about 700 degrees rotation of the Male rotor. Figure 4 indicates that during the first part of volume expansion the chamber is in contact with a suction line, feeding fluid into the chamber at almost constant pressure. During the second part of chamber expansion the chamber is isolated, forcing the pressure to decline. After passing the apex of volume the chamber comes into contact with a discharge line, emptying the expanded fluid at almost constant pressure. Work is produced during the expansion by a combination of rotational speed and distribution of fluid forces onto the two rotors. The rotors can be separated by lubrication liquid or external synchronization gear wheels depending on type of design. Rotor combinations can be designed in multiple ways with two, three or more rotors interacting. Twin screw expanders are the most common and will be discussed further under the name *screw expanders*. Triple screw machines, with one Male rotor and two Gate rotors also called

single screw machines, and multiple screw design are mechanically complex and therefore less suitable in 2-phase expansion applications.

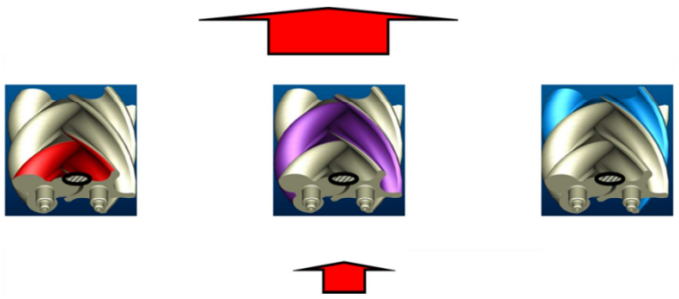

Figure 4. Schematic image of screw expander rotors indicated entry port and chamber volume development.

Screw expander rotors can be designed in multiple manners. The most common is two parallel rotors with constant diameter and constant helix. Olofsson (1989) showed a variant with non-constant helix rotors and non-parallel shaft centers. *Herring bone* arrangements, with minimal axial bearing forces as in Figure 5, were popular in the 1960's but disappeared from the market, most likely due to difficulties of manufacture.

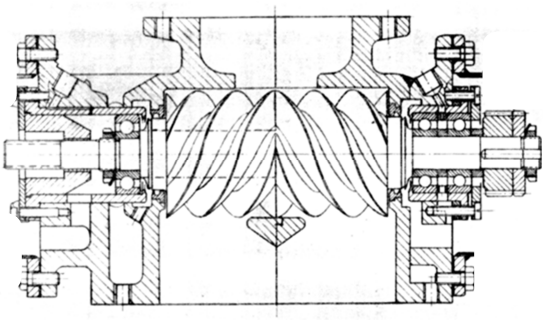

Figure 5. Example of a Herring bone type screw expander from the Japanese market.

Regardless of macro-design parameters, such as diameters, lengths, helix and shaft angles all screw expander rotors need a suitable profile. It is defined by micro-design parameters controlling the seals between chambers, port flow velocities, bending, vibrational stability and substrate erosion. Rotor profiles are typically defined as hypo-cycloids or epi-cycloids alternatively generating mating geometries with a predefined distribution of clearances to allow machining tolerances and material deflections.

During the 1950's and 1960's a series of design rules for screw compressors were issued by some of the manufactures. Also design rules for screw expanders were produced. They all have in common being based on three design handbooks from SRM, popularly called the *Compressor Bibles* and the *Expander Bible*. Such documents are of course currently replaced by computer models. Interestingly enough designs according to the *Expander Bible* are still competitive to most available designs on the market. The *Bibles* were distributed among screw compressor manufacturers but due to their age few can be expected to be still available. As determining the geometrical entities of screw expanders is known this paper focus on the significantly more difficult issue of predicting, and consequently optimizing, functional efficiency.

3.1 Experience from testing of 2-phase expansion in screw expanders

Wagenius (1958) show test data from a 40mm screw expander with a mixture of air and oil. Weiss et al (1975), Steidel et al (1977), Steidel et al (1981), McKay (1982) and Kauder and Kliem (2003) reported on 2-phase expansion with steam. Kliem (2005) tested improved filling solutions with 2-phase steam expansion. Schibbye (1959) reports test data from 3-phase expansion, gas/liquid/solid, of air and humidity. Sprankle (1973), Brasz (2003) and Öhman (2004) discuss the expansion of flashing liquid in screw expanders, also displaying some test data. Merigaux and Pocard (1978), Smith et al (1994) and Öhman and Lundqvist (2013) present data on 2-phase expansion of refrigerants.

The nature of 2-phase screw expander applications is such that pressure level, nominal power, temperatures, fluid and machine tip speed often differs, making comparison difficult. Furthermore the design of each screw expander is unique. Oil injected machines are to be compared to synchronized, sleeve bearing designs to anti friction bearing designs and stiff rotors to weak rotors. Also the built in volume ratio is not always optimal for the test conditions and seldom explicitly stated. Öhman and Lundqvist (2013) explain the logical complexity of simulating 2-phase expansion in a screw machine and yet, to date, there are no physics based models claiming to predict adiabatic efficiency of such expansion with any accuracy. In the same article a method according to Equation (1) is established using information on peak efficiency and efficiency at saturated gas conditions in order to determine adiabatic efficiency as a function of expansion entry vapor fraction.

$$\eta_{ad}\left(X_{entry}\right) = \eta_{ad,sat} + \psi_{2phase} \cdot \left(1 - X_{entry}\right) \cdot 10 \tag{1}$$

The correlation is defined by Equation (2), as of Öhman and Lundqvist (2013)

$$\psi_{2phase} = \frac{d\eta_{ad}}{dX_{entry}} = -0.15 \cdot \eta_{ad,peak} + 0.09 \tag{2}$$

Note that the sign of the first term is derived from table data and graph in the reference. There is an obvious typographic error regarding the sign in the equation in the reference.

In reality adiabatic efficiency of screw expanders is relatively insensitive to the degree of superheat at expansion entry why Equation (3) is more practical to use. *Note that the correlation only allows us to estimate the effect of variations in adiabatic efficiency. The magnitude needs to be determined by physical tests or simulations using dry expansion entry conditions.*

$$\eta_{ad}\left(X_{entry}\right) = \eta_{ad,peak} + \psi_{2phase} \cdot \left(1 - X_{entry}\right) \cdot 10 \tag{3}$$

As can be seen in Figure 6 the correlation predicts a linear relation between vapor fraction and adiabatic efficiency. *Seemingly too simple the sources support the conclusion of a linear realtion, see for example Figure 2-6, p. 2-27 in McKay (1982) or Figure 8, p. 1217 in Öhman and Lundqvist (2013).* Hereby cycle simulations can be performed as discussed in Chapter 4.

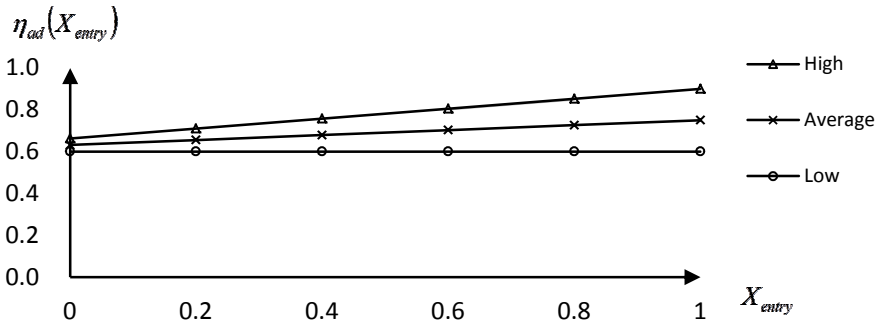

Figure 6. Adiabatic efficiency with 2-phase expansion entry vs. vapor fraction. Peak efficiencies *High (90%), Average (75%), Low (60%) as of Öhman and Lundqvist (2014)*

3.2 On the difficulty of modeling performance of a 2-phase screw expander

A 2-phase mixture of working fluid needs to be in equilibrium to be stable. Equations of state, used to determine the energy of a fluid, assume that such equilibrium exists, *quasi-static conditions*. The problem with a 2-phase screw expander is that no quasi-static conditions will exist. Therefore any modeling using conventional thermodynamic entities of the fluid will be susceptible to errors by definition.

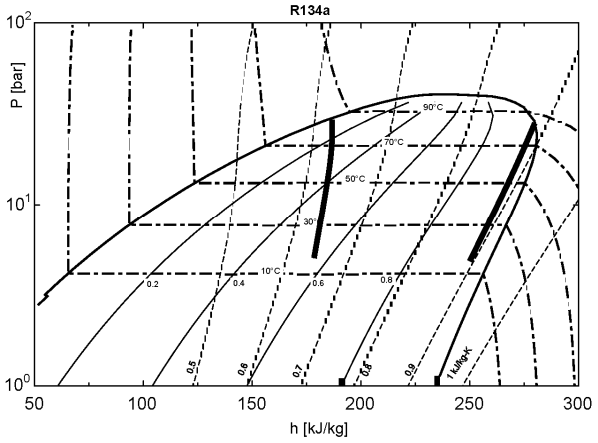

Figure 7. Schematic indication of non-reversible expansion of left side: saturated liquid, right side: saturated gas, R134a

One way to explain the process is to use the simplified Figure 7. The mixture can be schematically separated into; expansion of liquid, left side of the diagram and of gas, right side of the diagram.

Expansion of the pure liquid leads to immediate flashing of liquid, a process well handled in refrigeration condensate valve technology and conventional Trilateral Flash Cycles. The evaporated gas tends to counteract the pressure reduction in the chamber meaning that we need very detailed information on the flashing in order to predict chamber pressure. Flashing also absorbs heat from the liquid, a process also requiring detailed simulation in order to predict the consequential chamber pressure. Expansion of the saturated gas, as in a conventional ORC without superheat, would quasi-statically lead to an immediate condensation of some fluid. The condensation is however not immediate, something well known to engineers designing screw expanders for ice production. Instead the gas can exist in sub-cooled conditions for a remarkably long time. Theories for sub cooled gas behavior are established in steam turbine expansion thermodynamics. However, in screw expanders the two expansion processes co-exist in the same chamber with undefined thermal contact, interacting with each other. This disqualifies any existing theory for dynamic expansion.

Commonly used models, using this logic of Figure 7, assume local equilibrium to simulate fluid states. To the knowledge of the authors no evidence of accuracy suitable to explain details of the expansion process, nor to predict performance for practical use, has been published. Research on flashing of liquid is ongoing, see Polanco et al (2010), but the methodologies are not yet well adapted to flash expansion in volumetric machines.

Physically modeling the expansion seems complicated but not impossible. However, on top of the basic thermodynamics we need to add strong centrifugal effects within the chamber, leakage of hot/cold gas/liquid of non-quasi-static conditions as well as the existence of lubrication oil. Solubility of fluid in oil is a function of pressure and temperature. Further increasing complexity by using fluid mixtures limits the probability designing a theoretical model to predict performance.

With the perspective of the above the approach of Equations (1) and (3) seems as a better short term alternative to predict performance and thereby implementing the unique characteristics of 2-phase expansion in screw expanders.

4. A NEW PERSPECTIVE ON ORC CYCLE DESIGN

In optimizing ORC performance adaption of cycle temperature to that of the heat source has critical impact on the results. Of course a balanced approach is required due to the trade-off between high cycle efficiencies and high cost of heat exchanger area. Saleh et al (2007), Pierobon et al (2014) and many others have developed methodologies to choose an appropriate working fluid for any particular application. Woodland et al (2013) showed that the combination of mixed flow expansion and fluid blends can provide opportunities to improve ORC design. *The downside of choosing the appropriate working fluid/fluid blend for every application is obviously the lack of standardization and the difficulty of moving one ORC unit from one application to another, or shifting its operating conditions*.

Öhman and Lundqvist (2014) showed that when ORC's can be optimized on expansion entry vapor fraction then the sensitivity to choice of working fluid is significantly reduced. Thus an ORC unit, designed for variable vapor fraction, can more easily be adapted to various heat sources and achieve better industrial cost efficiency. In the comparison a marine diesel engine cooling water waste heat recovery application was investigated assuming 3 radically different working fluids, R717/R134a/R245fa. To estimate the effects of component efficiencies three grouped efficiency classes were used, see reference for details.

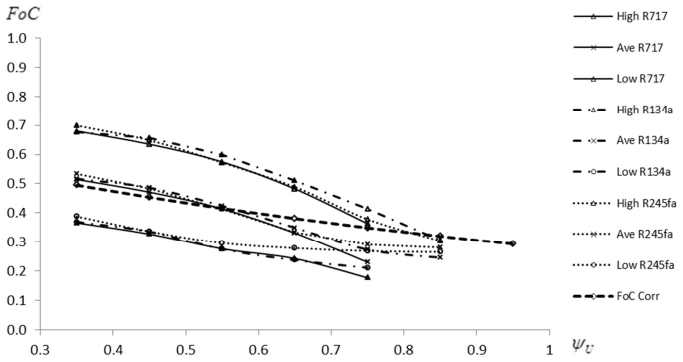

Figure 8. Fraction of Carnot vs. Utilization, both non-dimensional, in a marine diesel waste heat recovery ORC optimized on vapor fraction using R717, R134a and R245fa. *High, Ave and Low indicate grouped component efficiency class levels as of Öhman and Lundqvist (2014). FoC Corr is an estimation of current market product performance for the same conditions, same reference.*

As seen in Figure 8 the optimized thermal efficiency of the three different fluids was found very similar, with concern taken to different component efficiency classes. *If the ORC cycles would have been limited to saturated, or superheated, expansion entry conditions the outcome of the three different working fluids would have been significantly more different*. Another observation from the comparison was that there are specific cost minima with significant effects on plant architecture. Those specific cost minima are strongly dependent on the vapor fraction.

5. DISCUSSION

As far as is known by the Authors very few publications addressing variable vapor fraction ORC system optimization exists. The work in Öhman and Lundqvist (2014) only demonstrates the effects and the subject matter needs further investigations in order to establish limitations of opportunities. However, the work supports the assumption that by using screw expanders to allow variable vapor fraction expansion entry conditions opportunities exist to significantly increase cost efficiency of ORC systems compared to current practice.

An obvious weak point in the theoretical simulations is the correlation of adiabatic expansion efficiency explained in Chapter 3.1. The proposed correlation in Equation (2) is based on a limited

amount of test data with many unknown parameters. Further refinement of that correlation is however time consuming and costly. One could argue that a wiser use of such resources might be to focus more on simulation of the physical processes inside the chamber.
A reflection on the work is that there is an apparent need to rethink our assumptions on what an ORC is and reconsider our approaches to choice of working fluid. The Authors look forward to further improvements in the methodologies for design choice of working fluid in the perspective of the above. Equation (2) means that fundamentally new modeling tools are not immediately required.

6. CONCLUSIONS

This review shows that a multitude of experience of using twin screw expanders in ORC applications exists. However such experience seems to be mostly industrial and not well explained scientifically. The review also shows that multi-phase expansion in screw machines is a well proven technology. Also, in determining expansion efficiency, while having mixed flow at expansion entry, a correlation can be used. A final conclusion is that the above findings allows for a new perspective on optimization of ORC's to its heat sources and significantly affects opportunities to standardize choices of working fluid.

NOMENCLATURE

X_{entry}	Vapor fraction at expansion entry	(-)
η_{ad}	Adiabatic efficiency (isentropic and adiabatic)	(-)
$\eta_{ad,sat}$	Adiabatic efficiency, with saturated gas entry	(-)
$\eta_{ad,peak}$	Adiabatic efficiency, at peak efficiency entry condition	(-)
ψ_{2phase}	Correlation factor due to vapor fraction	(-)
FoC	Fraction of Carnot, ratio of real-to-reversible thermal efficiency	(-)
ψ_U	Utilization of available heat transport from source to sink	(-)

REFERENCES

Behrendt, E., 1970, Freon-Motor als Fahrzeugantrieb, *Automobil Revue*., vol. 6, no. 3, p. 32-33, (In German)

Biederman, T., Brasz, J., 2014, Geothermal ORC systems using large screw expanders, *22nd International Compressor engineering Conference at Purdue. July 14-17. 2014,* Nr. 1470, Purdue University, Purdue,

Brasz, J., 2000, Screw expressor testing on R134a chiller-efficiency, liquid carry over and chiller benefit, *Compressors and their systems,* ISSN:1356-1448, ISBN:1860584179, ImechE Conference Transactions., vol. 2,

Kauder, K., Kliem, B., 2003, *The operating conditions of 2-phase screw motors with internal evaporation,* ISSN:0945-1870, Dortmund University, Dortmund, vol. 11, p. 69-84, (In German),

Kliem, B., 2005, *Fundamentals of the two-phase screw-type engine*, Dortmund University, Dortmund , 140 p., (In German)

Lysholm, A., Boestad, G., 1935, Compressor apparatus, US Patent nr 2111560,

McKay, R., 1982, *Helical screw expander evaluation project final report,* DOE/ET/28329-1, Jet Propulsion Laboratory, US Department of Energy, (JPL-Pub-82-5),

Merigoux, J. M., Pocard, P., 1980, Solar power units with screw expanders, *Solar 3 (1980).*, 80/25169, p. 1293-1317,

Minto, W. L, 1967, Low entropy engine, US Patent nr 3479817,

Öhman, H., 1997, Refrigerant expanders for use in Organic Rankine Cycles (ORC), *SRM Technical Screw Compressor Conference 1997.*, SRM, p. 2-6,

Öhman, H., 2004, Test results of a screw type expander/compressor and the implication of phase separators on the refrigeration process, *International Refrigeration and Air Conditioning Conference at Purdue. July 12-15. 2004,* R025, Purdue University, Purdue,

Öhman, H., 2012, Implementation and evaluation of a low temperature waste heat recovery power cycle using NH3 in an Organic Rankine Cycle, *Energy*., vol. 48, p. 227-232

Öhman, H., Lundqvist, P., 2013, Experimental investigation of a Lysholm turbine operating with superheated, saturated and 2-phase inlet conditions, *Applied Thermal Engineering*., vol. 50, p. 1211-1218, (http://dx.doi.org/10.1016/j.applthermaleng.2012.08.035)

Öhman, H., Lundqvist, P., 2014, *Organic Rankine Cycles with variable vapor fraction expansion entry*, TRITA-REFR REPORT 14:2, KTH, Stockholm. Sweden, ISBN 978-91-7595-224-6,

Olofsson, H., 1989, Rotary positive displacement machine for compressible working fluid, US Patent nr 4863357,

Pierobon, L., Casati, E., Casella, F., Haglind, F., Colonna, P., 2014, Design methodology for flexible energy conversion systems accounting for dynamic performance, *Energy*., vol. 68, p. 667-679

Polanco, G., Holdo, A., E., Munday, G., 2010, General review of flashing jet studies, *Journal of Hazardous Materials*., vol. 173, p. 2-18,

Saleh, B., Koglbauer, G., Wendland, M., Fischer, J., 2007, Working fluids for low-temperature Rankine cycles, *Energy*., vol. 32, no. 7, p. 1210-1221, (doi:10.1016/j.energy.2006.07.001)

Schibbye, H., 1959, *Performance of gearless screw expander*, SRM Technical report 1045/M-25, SRM, Stockholm, (opcon.se/web/Reports_2.aspx, 06.12.2011),

Smith, I. K., Stocik, N., Aldis, C. A., 1994, Lysholm machines as two-phase expanders, *International Compressor Engineering Conference,* Paper 957, Purdue University, Purdue, (http://docs.lib.purdue.edu/icec/957),

Steidel, R., Weiss, H., Hower, J. E., 1977, *Performance characteristics of the Lysholm engine as tested for geothermal power applications in the Imperial valley*, Rept. UCRL-80151, Lawrence Livermore Laboratory, Livermore, California, USA,

Steidel, R., Pankow, D., Berger, R. E., 1981, Performance characteristics of the Lysholm engine as tested for geothermal applications, *16th Intersociety Energy Conversion Engineering Conference, IECEC*., vol. 2,

Svenningson, K., Sjölin, U., Öhman, H., 2010, *The screw compressor development at SRM*, SRM, Stockholm, www.opcon.se/web/History_4.aspx, 02.12.2015,

Timuska, K., 2008, *100 years of energy efficiency*, SRM, Stockholm, www.opcon.se/web/History_1.aspx, 02.20.2015,

Wagenius, B., 1958, SRM machines of helical body type, for compression and expansion; their operational characteristics, design and application in refrigeration technology, *Kylteknisk Tidskrift*., vol. 1, p. 1-7, (In Swedish),

Wiess, H., Steidel, R., Lundberg, A., 1975, *Performance characteristics of a Lysholm engine*, Rept. UCRL-51861, Lawrence Livermore Laboratory, Livermore, California, USA,

Woodland, B., J., Krishna, A., Groll, E., A., Brown, J., E., Horton, W., T., Garimella, S., V., 2013, Thermodynamic comparison of organic rankine cycles employing liquid-flooded expansion or a solution circuit, *Applied Thermal Engineering*., vol. 61, p. 859-865

DYNAMIC MODEL FOR THE PERFORMANCE PREDICTION OF A TWIN SCREW EXPANDER IN AN ORC

I. Papes*, J. Degroote, J. Vierendeels [1]

[1]Ghent University,Department of Flow, Heat and Combustion Mechanics, Ghent, Belgium

*iva.papes@ugent.be

ABSTRACT

The Organic Rankine Cycle (ORC) is well known and proven technology for waste heat recovery. The current generation of twin screw expanders used for low-grade heat recovery are in fact compressors working in the opposite sense. In this paper a mathematical model for calculating the performance of a twin screw expander is presented. The model is based on geometrical parameters which describe volume and leakage areas for every angular position. With these functions the entire design of a screw expander is determined. The differential equations used in the model are derived from the mass and energy conservation laws and are solved together with the appropriate Equation of State in the instantaneous control volumes. Since R245fa is selected as a working fluid, the Aungier Redlich-Kwong Equation of State has been used. The results of the mathematical model are compared to the 3D Computational Fluid Dynamics (CFD) calculations of the same twin screw expander using the same working fluid. To calculate the mass flow rates through the leakage paths formed inside the screw expander, flow coefficients are considered as constant and they are derived from 3D CFD calculations. The outcome of the mathematical model is the P-V indicator diagram which is compared to CFD results of the same twin screw expander. It is shown that the developed model accurately predicts the performance of the expander.

1. INTRODUCTION

With increasing concerns over energy pollution and consumption constraints the interest in waste heat recovery has grown in the past years. A large portion of waste heat is available at low temperatures (350K-400K) from industrial processes which can be converted into mechanical power. The most widely used technology for waste heat recovery is the Organic Rankine Cycle (ORC). Although ORC systems are now well developed, efforts have been increasingly directed towards higher efficiencies and power outputs. The key element for the power generation in ORC systems is the expander. The choice of the expander is crucial and it depends on the amount of available heat and operating conditions. For small scale ORC system studied in this paper, displacement machines are highly suitable (Lemort, 2013).

The first analytical procedure for the expander's performance prediction has been reported by (Margolis, 1978). More recently, the numerical and experimental study of an oil injected twin screw expander for both air and R113 has been presented in (Wang, 2010). A mathematical model was verified with an experimental study and flow coefficients used in the leakage models were derived from it.

The capability to analyse the performance of such complex screw machines by thermodynamic models which describe the behaviour of the fluid are often limited because of inability to get

proper experimental data. With Computational Fluid Dynamic (CFD) it is possible to analyse the flow within screw expanders and to get a better view on different phenomena that occur within such machines. In previous studies the authors presented a 3D CFD simulation of a twin screw expander using R245fa (also known as 1,1,1,3,3-Pentafluoropropane) as the working fluid (Papes, 2014). R245fa is characterized by a positive slope of the saturated vapor line in a T-s diagram which will prevent the formation of liquid droplets at the exit of the expander. The mesh motion is handled by an in-house code which generates a block-structured grid with the help of solutions of Laplace problems on an unstructured triangular grid (Vande Voorde, 2004).

The aim of this paper is to present a mathematical model of a twin screw expander and to validate it with CFD results. Moreover, the goal is to extract the coefficients used in the isentropic converging nozzle leakage model from the 3D CFD analysis. Several objective performance indicators such as mass flow rates, pressure-volume diagrams and power output are used to compare these two models.

2. GEOMETRY

The geometry of a twin screw expander used in this study is shown in Figure 1a. There are four male lobes and six female lobes with asymmetrical rotor profiles. The outer diameter of the male and female rotors is approximately $70mm$ with L/D ratio of 1.9.

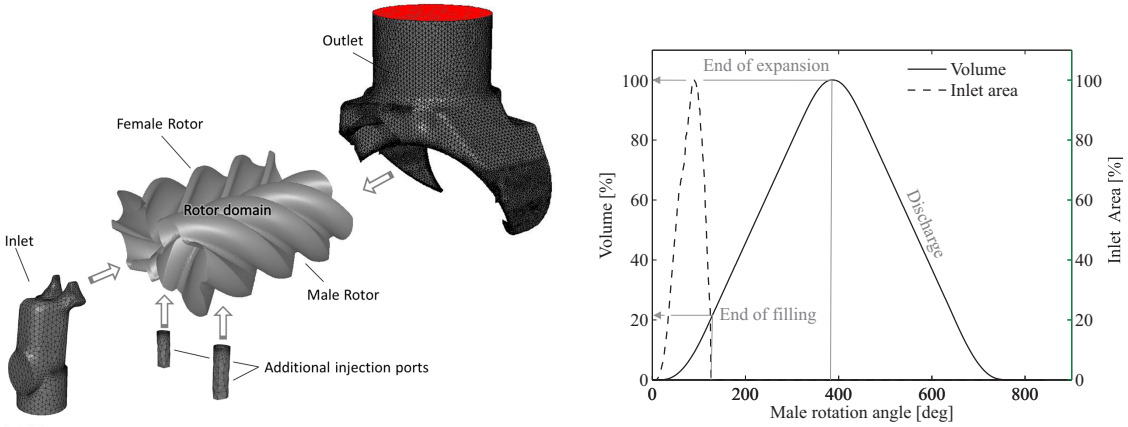

(a) Geometry **(b) Volume of the chamber**

Figure 1: Geometry of a twin screw expander with the analytical description of the geometrical parameters used in the mathematical model

The volume curve of the screw expander is shown in Figure 1b. The formation of a chamber starts at $\theta = 0°$ in Figure 1b. When $\theta = 7°$, the chamber is in connection with the inlet port. As the rotor rotate, the volume of the chamber increases with increasing inlet surface area, and the chamber is filled with the working fluid. When the inlet area starts to decrease, the volume of the chamber is still increasing. This can already cause the **pre-expansion** of the working fluid. The filling ends at $\theta = 126°$ after which the working fluid expands with increasing volume of the chamber. At $\theta = 387°$, the working chamber is connected to the outlet and the working fluid is discharged through the outlet port.

Within twin screw expanders, it is possible to identify four types of leakage paths. All four types of leakages in screw expanders are depicted in Figure 2 and are characterized by the length of the leakage path and the area of the clearance.

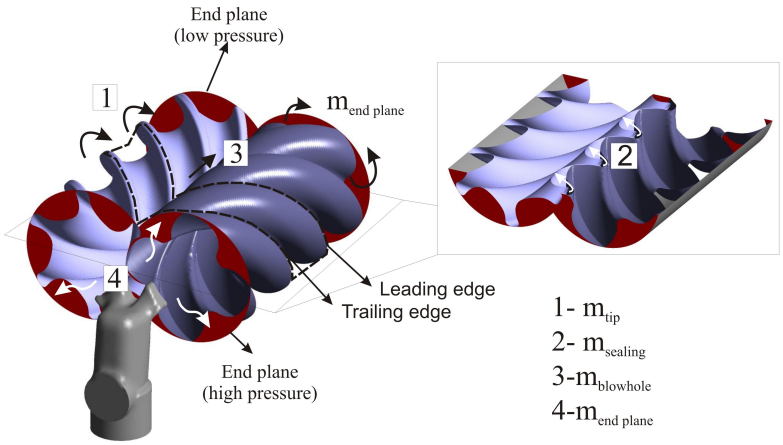

Figure 2: Different leakage types inside the twin screw expander

3. CFD ANALYSIS

The flow calculations inside a screw expander are performed by Ansys Fluent with the use of User Defined Functions (UDFs) to handle the grid movement and real gas model as presented in (Papes, 2014). The mathematical model consists of a set of momentum, energy and mass conservation equations, which are accompanied by the Aungier Redlich-Kwong (ARK) EoS and $k-\varepsilon$ turbulence model. The spatial discretization is second order upwind. Both CFD and mathematical model presented in this paper used the same geometry from Figure 1b. A result of the CFD analysis for pressure ratio of 6 is presented in Figure 3.

In order to calculate flow coefficients for different leakage paths, the mass flow rate through the corresponding leakage path was correlated with the pressure ratio between chambers that are forming that leakage path and its area according to equation of isentropic converging nozzle.

By analysing the results of CFD calculations, it was seen that pulsations in the inlet pipe play an important role in the pressure difference which influences the mass flow during the filling. These pulsations can be captured with 3D CFD calculations or with a one-dimensional model. In this study pulsations in the pipe before the inlet port are obtained from the CFD results and are used in the developed mathematical model. The results of pressure pulsations for different

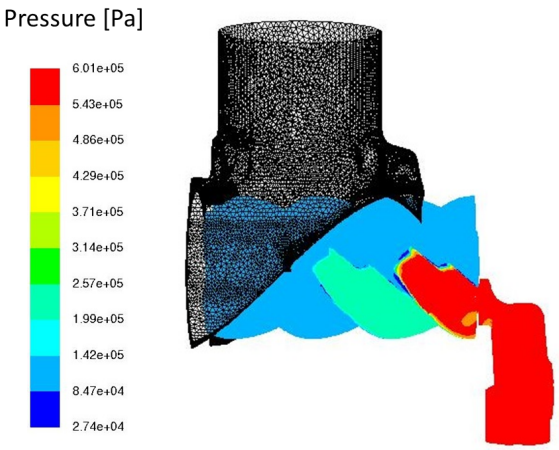

Figure 3: Pressure within twin screw expander (results of CFD analysis)

pressure ratios and rotational speeds were calculated through the reference plane as shown in Figure 4.

4. EQUATIONS GOVERNING SCREW EXPANDER PROCESS

The zero-dimensional mathematical model described in this paper employs the mass and energy conservation equations, accompanied by the geometrical model which describes the change in volume with the time or angular position, as well as change in the inlet and leakage path areas. Also in this model, the ARK EoS is used to describe real gas effects of R245fa.

When analysing the flow within the screw expander, the following assumptions have been made:

- The heat transfer between the working fluid and the rotor or between the casing and the ambient are not included in the model (they are also neglected in CFD simulations).
- Mechanical losses of the screw expander are not included in the model.
- Potential and kinetic energy of the working fluid are negligible.
- The flow through the leakage paths and inlet port is assumed to pass through an isentropic nozzle.
- Leakage flows through the end planes are not included in the model since they are not modelled. in the CFD calculations.
- The discharge process occurs at constant pressure.

The following equations were applied for each working chamber:

$$\frac{dm_{ch}}{dt} = \sum_i \dot{m}_i \tag{1}$$

$$\frac{dT}{dt} = \frac{-T\left(\frac{\partial \rho}{\partial T}\right)_v \left[\frac{dV}{dt} - v\frac{dm_{ch}}{dt}\right] - h\frac{dm_{ch}}{dt} + \sum_i \dot{m}_i h}{m_{ch} c_v} \tag{2}$$

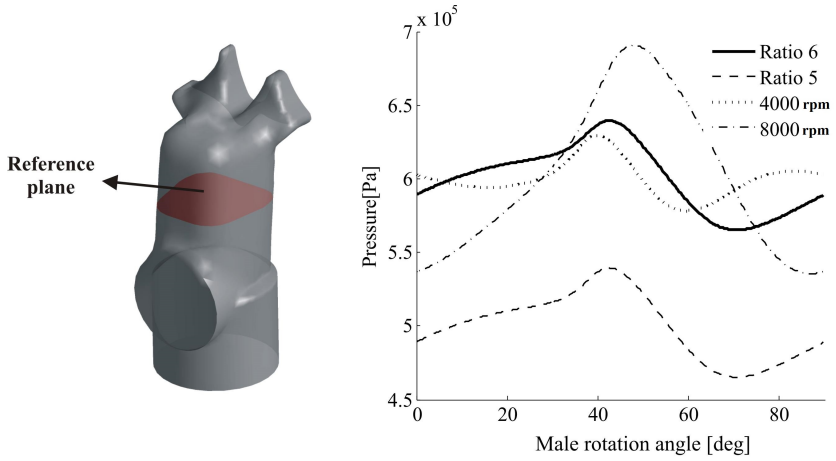

Figure 4: Pressure pulsations in the reference plane of the inlet port (results from CFD analysis)

This system of differential equations is solved by using the forward Euler method applied simultaneously on all chambers. Once the geometrical inputs (volume change and leakage areas) have been provided to the model, the pressure and the temperature are initialized with guess values. After that, for each iteration step, the mass flows going in or out of the chamber are calculated and the temperature in the next step is obtained. Since the mass, the volume and the temperature are then known, the pressure and the density can be updated.

The mass flow through the leakage paths and the inlet port is calculated using the isentropic nozzle model (Bell, 2011):

$$\dot{m}_{nozzle} = CA\sqrt{p_{up}\rho_{up}}\sqrt{\frac{2k}{k-1}\left(p_{ratio}^{2/k} - p_{ratio}^{(k+1)/k}\right)} \tag{3}$$

Where the function of pressure ratio is defined as:

$$p_{ratio} = \begin{cases} \left(1+\dfrac{k-1}{2}\right)^{k/(1-k)} & p_{down}/p_{up} \leq \left(1+\dfrac{(k-1)}{2}\right)^{k/(1-k)} \\ p_{down}/p_{up} & p_{down}/p_{up} > \left(1+\dfrac{(k-1)}{2}\right)^{k/(1-k)} \end{cases}$$

Flow coefficients C are constant in time and are obtained from CFD calculations. The indicated work of a twin screw expander can be expressed as the area of the P-V indicator:

$$W_{ind,cycle} = \int_{cycle} V dp \tag{4}$$

The power of the twin screw expander can be then calculated as:

$$P_{ind} = \frac{W_{ind,cycle} z n}{60} \tag{5}$$

with z the number of lobes and n the rotational speed.

5. RESULTS AND DISCUSSION

There are different parameters to be compared between the developed mathematical model and the CFD analysis. One is the P-V indicator diagram of the screw expander, which will show how the pressure in every moment is changing with the instantaneous volume. If the calculated P-V indicator diagram agrees with the results of CFD analysis, the overall performance will be well predicted. However, additional parameters like mass in the chamber or leakage flow through the clearance paths should be checked and compared.

In Table 1, comparison for power and mass flow rate between the developed model and the CFD analysis are presented. The comparison has been made for pressure ratios $\pi = 6, 5$ and 4 and for rotational speeds of $6000rpm$ (nominal speed), $4000rpm$ and $8000rpm$.

5.1 Evaluation with different pressure ratio

In Figure 5 the P-V indicator diagrams for pressure ratio of $\pi = 6, 5$ and 4 are shown. From Table 1 it can be seen that the difference in power outputs between CFD analysis and developed model is from $2 - 6\%$.

Pressure ratio	Speed	CFD		MODEL	
		Flow rate [kg/s]	Power [kW]	Flow rate [kg/s]	Power [kW]
6	6000	0.1469	4.72	0.1415	4.61
5	6000	0.1210	3.46	0.1160	3.30
4	6000	0.0955	2.18	0.0922	2.05
6	4000	0.1055	3.18	0.1028	3.23
6	8000	0.1618	5.11	0.1619	5.30

Table 1: Results for mass flow rates and power outputs for the developed model and the CFD analysis

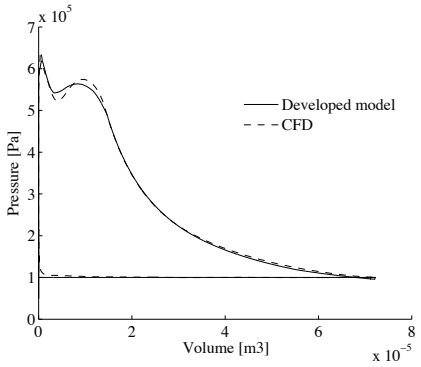

(a) Pressure ratio 6

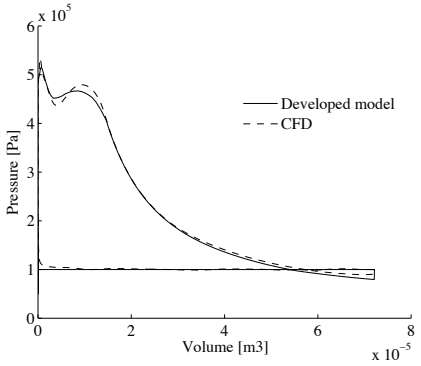

(b) Pressure ratio 5

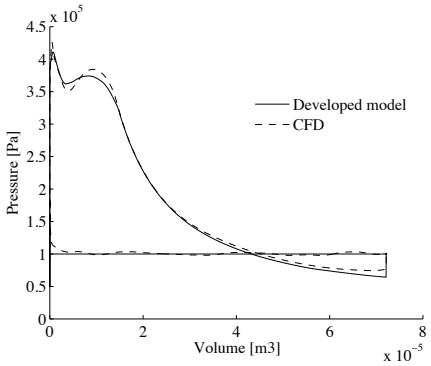

(c) Pressure ratio 4

Figure 5: Model predicted and CFD calculated results

5.2 Evaluation with speed change

The performance of the expander was also examined with variations in speed (Figure 6). With change in speed, the P-V indicator shows a difference during the filling phase. Due to the shorter duration of the filling period with the rise in rotational speed, it can be seen that the throttling loss increases. The difference between the developed model and the CFD analysis is around 4% for a rotational speed of $8000rpm$ and around 2% for a rotational speed of $4000rpm$.

5.3 Mass in the chamber

The comparison of the total mass in the chamber between the developed model and the CFD results is shown in Figure 7. This parameter is very important because it shows if the mass in the chamber after the filling is close to CFD results. This shows if the filling process in the developed model is described correctly. But also, it shows if the leakage flows are reducing the mass in the chamber in the same way as in CFD results.

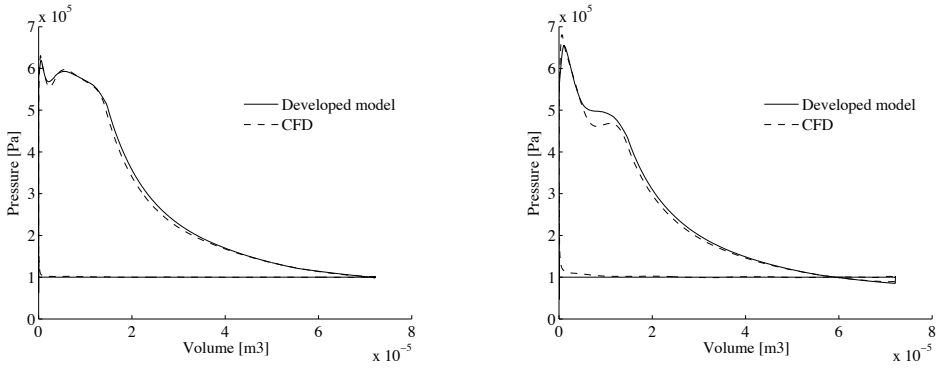

(a) 4000rpm **(b) 8000rpm**

Figure 6: Model predicted and CFD calculated results for changes in rotational speed

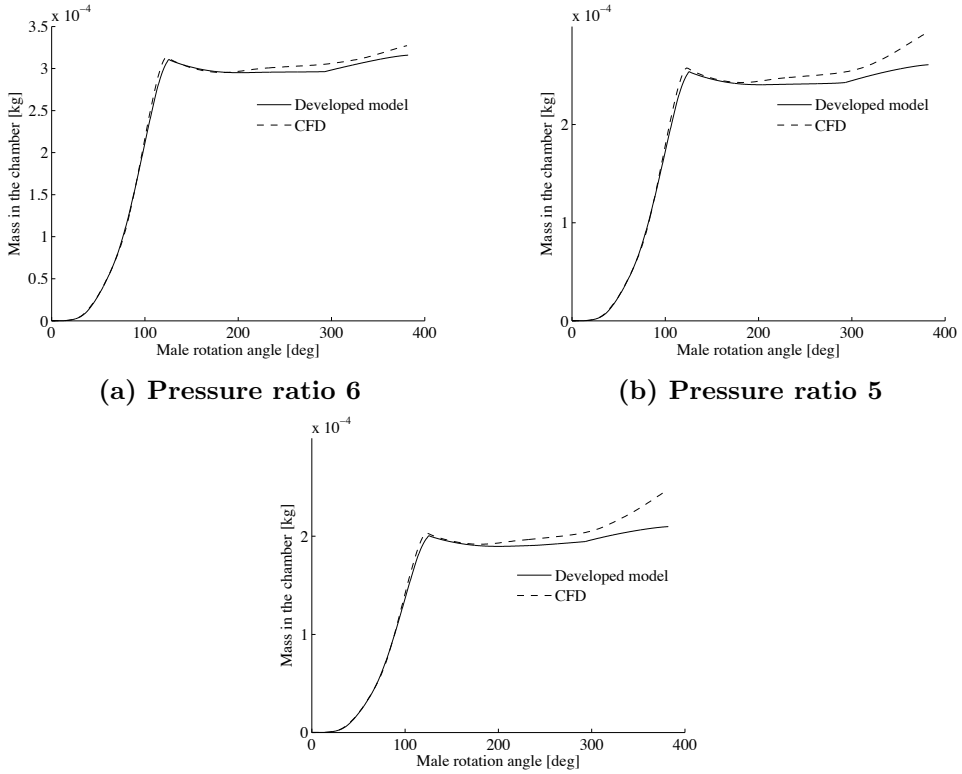

(a) Pressure ratio 6 **(b) Pressure ratio 5**

(c) Pressure ratio 4

Figure 7: Model predicted and CFD calculated results of the mass in a chamber for changes in pressure ratio

5.4 Leakage flows

The last two parameters are the mass flow rates through the tip and sealing leakage path (Figure 8). Here it is very important to see if using the constant flow coefficient derived from the CFD calculations can estimate these flows correctly. It can be clearly seen that the trend of these curves is matching well with CFD results. Although slight deviations are present, it should be noted that mass flow rates through the leakage gaps are already very low comparing to the total mass flow rate.

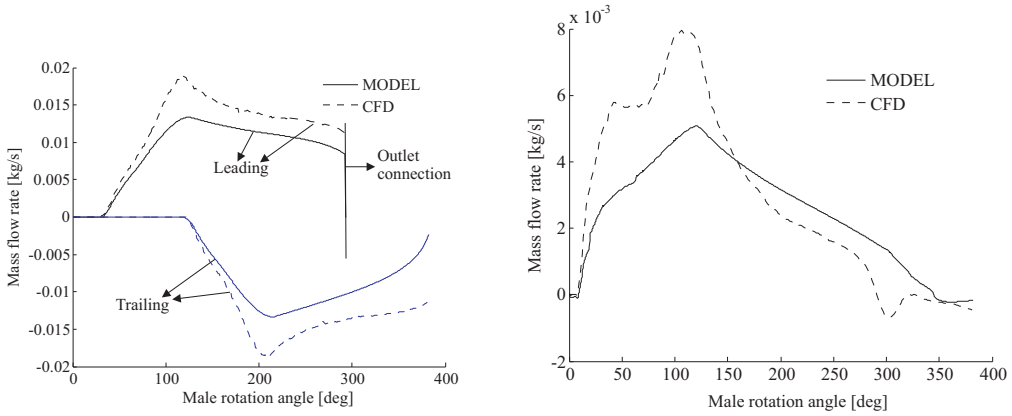

(a) Tip Leakages **(b) Sealing leakage**

Figure 8: Model predicted and CFD calculated results in the screw expander with pressure ratio 6 and rotational speed of 6000rpm

6. CONCLUSION

A mathematical model for the performance prediction of a twin screw expander has been developed. From the mass and energy conservation laws, differential equations are derived which are then solved together with the Aungier Redlich-Kwong Equation of State for R245fa in the instantaneous control volumes. The mathematical model employs all geometrical parameters such as chamber volume, suction and leakage areas. To calculate the mass flow rates through the leakage paths formed inside the screw expander, flow coefficients are derived from CFD analysis. All geometrical inputs in terms of rotational angle of male rotor are employed in the model. It is shown that the developed model accurately predicts the performance of the expander.

7. NOMENCLATURE

NOMENCLATURE

Symbols

$\dot{m}$	Mass flow rate (kg/s)
ρ	Density (kg/m^3)
A	Area of the leakage path/inlet area (m^2)
C	Flow coefficient $(-)$
h	Specific enthalpy (kJ/kg)
k	Specific heat ratio $(-)$
m	Mass (kg)
n	Rotational speed (rpm)
P	Power (W)
T	Temperature (K)
V	Volume (m^3)
W	Work (J)
z	Number of lobes $(-)$

Subscripts

ch	Chamber
$down$	Downstream
i	Number of boundaries of the working chamber
in	Indicated
up	Upstream

REFERENCES

Lemort V., Guillaume L., Legros A., Declaye S. and Quoilin S., 2013, A comparison of piston, screw and scroll expanders for small scale Rankine cycle systems In Proc. 3rd Int. Conf. on Microgeneration and Related Technologies

Papes I., Degroote J. and Vierendeels J., 2014, Analysis of a Twin Screw Expander for ORC Systems using Computational Fluid Dynamics with a Real Gas Model Int. Compressor Engineering Conf. at Purdue University

Papes I., Degroote J. and Vierendeels J., 2013, 3D CFD Analysis of an Oil Injected Twin Screw Expander ASME International Mechanical Engineering Congress and Exposition

Margolis D. L., 1978, Analytical Modelling of Helical Screw Turbines for Performance Prediction ASME J. Engr. for Power, **100**, 482

Wang Z., Zhang Y., Sun T. and Wei L., 2010, Numerical simulation and experimental study on the performance of screw expander ASHRAE Transactions part 2, **116**, 218-225

Aungier R. H., 1995, A fast, accurate real gas equation of state for fluid dynamic analysis applications J. of Fluids Engineering, **117**, 277-281

Vande Voorde J., Vierendeels J., Dick E., 2004, Development of a Laplacian-based mesh generator for ALE calculations in rotary volumetric pumps and compressors Computer Methods in Applied Mechanics and Engineering, **193**, 39-41, 4401-4415

Bell I. 2011, Theoretical and Experimental Analysis of Liquid Flooded Compression in Scroll Compressors *PhD Thesis*

ACKNOWLEDGEMENT

The results presented in this paper have been obtained within the frame of the IWT SBO-110006 project The Next Generation Organic Rankine Cycles (www.orcnext.be), funded by the Institute for the Promotion and Innovation by Science and Technology in Flanders. This financial support is gratefully acknowledged.

COMPARISON OF ORGANIC RANKINE CYCLE SYSTEMS UNDER VARYING CONDITIONS USING TURBINE AND TWIN-SCREW EXPANDERS

M. Read*, A. Kovacevic, I.K. Smith and N. Stosic

City University London,
Northampton Square, London EC1V 0HB, United Kingdom
e-mail:m.read@city.ac.uk

* Corresponding Author

ABSTRACT

A multi-variable optimization program has been developed to investigate the performance of Organic Rankine Cycles (ORCs) for low temperature heat recovery applications. This cycle model contains detailed thermodynamic models of the system components, and the methods used to match the operation of the expander to the requirements of the cycle are described. Two types of ORC system are considered; one containing a turbine to expand dry saturated or superheated vapour, and one with a twin-screw machine allowing expansion of partially evaporated fluid.

Modelling of the ORC system with a twin-screw expander has been described previously (Read et al. 2014a, 2014b). The performance of the turbine in the superheated ORC has been modelled using available operational data for single stage, reaction turbines, where correlations have been used to estimate the efficiency of the turbine at 'off-design' conditions using either fixed or variable nozzle geometries.

The capability of the cycle model has been demonstrated for the case of heat recovery from a source fluid at 120°C. The system parameters are optimised for a typical operating condition, which determines the required size of heat exchangers and the expander characteristics. Performance at off-design conditions can then be optimized within these constraints. This allows a rigorous investigation of the effect of air temperature variation on the system performance, and the seasonal variation in net power output for the turbine and twin-screw ORC systems is estimated.

1. INTRODUCTION

The Organic Rankine Cycle (ORC) provides a means of recovering useful energy from low temperature heat sources. In comparison with conventional high temperature steam Rankine cycles, the low temperature of these heat sources means that the attainable cycle efficiency is much lower, while the required surface area of the heat exchangers per unit power output is much higher. The lower latent heat of evaporation of organic fluids relative to steam also means that the feed pump work required in ORCs is a significantly higher proportion of the gross power output.

Maximising the net power output from an ORC is a compromise between increasing the mean temperature of heat addition (which, in accordance with Carnot's principle, can increase cycle efficiency) and increasing the amount of heat extracted from the source, which requires a lower evaporation temperature.

Especially at lower source temperatures, up to approximately 120°C inlet, the only cycle normally considered is that where the working fluid enters the expander as dry saturated vapour, as shown in Figure 1a. However, in most cases, this leads to the working fluid leaving the expander with some superheat, which must be removed before condensation begins. By the use of a screw expander, instead of the more conventional turbine, it is possible to admit the working fluid to the expander as

wet vapour and thereby eliminate both the need to de-superheat the vapour after expansion and, simultaneously to raise the evaporation temperature, as shown in Figure 1b, thus improving the cycle efficiency. The potential cost and performance benefits of using screw expanders in ORC systems have been extensively studied for geothermal applications by Smith et al. (2001, 2004, 2005).

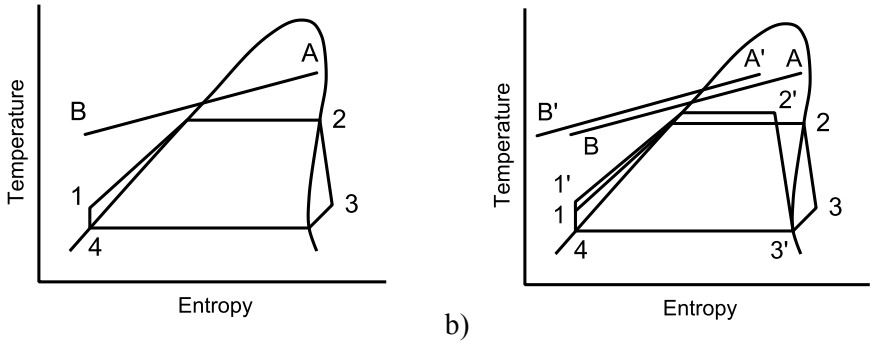

Figure 1: Illustrative T-s diagrams showing a) conventional ORC with dry saturated vapour at the expander inlet, and b) how the expansion of wet vapour can avoid superheated vapour

However, screw expander efficiencies are more sensitive to expansion pressure ratio than turbines and the expansion ratio increases as the expander inlet vapour dryness fraction decreases. To determine the value of inlet dryness fraction that leads to the maximum system power output, it is therefore necessary to include estimates of how both the screw expander and the feed pump performance vary as the inlet dryness fraction of the working fluid is changed in such a wet ORC (WORC) system. The performance of these systems has previously been studied for operation at both design and off-design conditions (Read et al., 2014a, 2014b). In order to gain more insight into the performance of these systems, they must however be assessed in comparison with equivalent optimised ORC systems using convention turbine expanders. This requires an understanding of how turbine efficiency varies with inlet conditions and required mass flow rate of the working fluid. The aim of this study is to present a comparative analysis of the design and off-design performance of twin-screw WORC and turbine ORC systems.

2. ORC MODEL FOR OPTIMISATION ANALYSIS

The performance of ORC systems has been assessed using a computational model of the cycle. This has been written as an object-oriented program in the C# language, which provides a convenient structure as it allows a generic description of heat sources, heat sinks and cycle components. Each of these cycle elements contains definitions for all the necessary input and output parameters along with the required calculations. Both simple cycles such as those shown in Figure 1, and more complex cases (including multiple heat source streams, multiple paths for the working fluid or varying working fluid composition) can be analysed by creating models of the required components and providing the necessary input parameter values. The key cycle components are discussed in more detail below.

2.1 Turbine model

Single stage radial inflow reaction turbines are commonly used in ORC applications. These turbines must be sized for specified design point conditions. The flow of working fluid is choked at the throat of the turbine inlet nozzle, and the cross-sectional area at this point must be chosen in order to achieve the required mass flow rate. The operation of the turbine can be characterised by considering the conditions at the throat (denoted by the superscript *) assuming isentropic expansion from turbine inlet conditions (subscript $turb, i$) as described by Wendt and Mines (2013). The pressure, density, enthalpy and velocity of the working fluid at the throat can be calculated using the relationships in equations (1)-(3), where the critical conditions of the working fluid are denoted by the subscript c.

$$p^* = 0.67\, p_{turb,i} \left(\frac{p_{turb,i}}{p_c}\right)^{0.2} \left(\frac{T_c}{T_{turb,i}}\right) \quad (1)$$

$$\rho^*, h^* = f\left(p^*, s_{turb,i}\right) \text{ , where values can be found using an appropriate equation of state} \quad (2)$$

$$u^* = \sqrt{2\left(h_{turb,i} - h^*\right)} \quad (3)$$

For the mass flow rate required at design conditions (denoted by subscript d), the cross-sectional area at the throat of the nozzle can then be calculated using equation (4).

$$\dot{m}_d = (\rho^* A^* u^*)_d \quad (4)$$

The mass flow rate of the working fluid in the cycle will vary at off-design conditions, and two possibilities have therefore been considered for the turbine design:

i. Fixed nozzle geometry, with constant throat area of $(A^*)_d$,
ii. Variable nozzle geometry, allowing the value of A^* to be adjusted.

For the fixed geometry case, an upstream throttle valve is required to reduce the turbine inlet pressure to a value which achieves the required mass flow rate through the fixed design throat area. Using variable geometry, the value of A^* may be varied between zero and a specified maximum value to achieve the required mass flow rate.

To characterise the effect of varying inlet and exhaust conditions on turbine performance, the turbine isentropic efficiency can be related to a velocity ratio, r_u, for the turbine. The velocity ratio is the ratio of the turbine tip speed, u_{tip}, to the spouting velocity, defined as the velocity achieved if the enthalpy change for an isentropic expansion were entirely converted to kinetic energy, as shown in Equation 5 (where $h_{turb,os}$ is the isentropic turbine outlet enthalpy).

$$r_u = u_{tip} \Big/ \sqrt{2\left(h_{turb,i} - h_{turb,os}\right)} \quad (5)$$

The correlations proposed by Wendt and Mines (2013) have been used to characterise the change in turbine efficiency as a function of both the change in the nozzle throat area resulting from manipulating the nozzle geometry, and the change in the velocity ratio for the expansion process. In the current study, a constant turbine rotational speed has been used in all cases. As the power output of the turbine is in the region of 100 kW, a representative maximum isentropic efficiency of 75% has been assumed, rather than the 82% proposed for much higher power systems (Wendt and Mines, 2013). The REFPROP database developed by NIST has been used to calculate all thermodynamic properties of the working fluid. The working fluid used in this study is the refrigerant R245fa, which has a critical temperature of 154°C. This is sufficiently high to ensure sub-critical pressure in the evaporator. While using fluids with higher critical temperature may increase the achievable net power output by reducing the pressure difference across the feed pump and expander, the reduced vapour density at condenser pressure would significantly increase the size and cost of cycle components. The cost of the R245fa fluid itself is relatively low, and it is widely used for low temperature ORC applications.

The aim of this study is to understand how changes in operating conditions affect the performance of the conventional ORC system and compare this with the results of previous analysis of a WORC system. Using the method described above, the actual size and operating speed of the turbine are not required to estimate cycle performance, and the detailed design of the turbine has therefore not been considered.

2.2 Heat exchanger models

A discretized approach has been taken to the calculation of the required surface area in the heat exchangers. Once the temperatures of the source, sink and working fluids have been defined, the heat exchangers are split into a number of short sections and the heat transfer and the log-mean temperature difference (LMTD) are calculated. Representative values for the overall heat transfer coefficient in conventional shell and tube heat exchangers with different fluid phases (Roetzel and Spang, 2010) are shown in Table 1, and have been used to calculate the heat transfer surface areas. These are then lumped into two overall heat exchanger areas for 'heat addition' (combined feed-heater, evaporator and, if required, super-heater) and 'heat rejection' (combined de-superheater, condenser and sub-cooler) which can be sized for design-point conditions. The calculation of heat exchanger areas is essential for the analysis of off-design system operation, and while this simple approach is not expected to be highly accurate for design purposes, it can be used to gain some insight into the requirements of the different cycles.

Table 1: Representative values of overall heat transfer coefficient for ORC shell and tube heat exchangers with different states for the heat transfer fluids

State of the heat transfer fluids:		Approximate overall heat transfer coefficient (W/m^2K):
Liquid or 2-phase	Liquid	1200
Liquid or 2-phase	Gas	70
Gas	Gas	35

2.3 Integrated cycle model and optimisation analysis

There are two important aspects to applying the component models in an integrated cycle model. Firstly, the mass flow rate identified by consideration of the heat transfer between the source fluid and the working fluid must be matched to the mass flow rate in the expander itself. However, the expander mass flow rate is calculated as a function of the inlet conditions (which may be throttled) and the turbine geometry; an iterative approach is therefore required in order to bring the error between these two calculated mass flow rates below an acceptable value, and identify the required operating conditions for the expander. For turbines with either fixed or variable nozzle geometry, if the required mass flow rate cannot be achieved by the turbine through throttling and/or nozzle area control then the isentropic efficiency is set to zero.

Secondly, although the heat transfer surface area of the heat exchangers can be calculated for the design point optimisation, during off-design operation these values must remain fixed. The varying cycle conditions cause changes in the integrated LMTD and the heat transferred in each heat exchanger. Two separate iterative loops are therefore required to identify the pinch point temperature differences required to achieve the require area of the boiler/evaporator and the de-superheater/condenser/sub-cooler units to within an allowable error. If, for any reason, the required heat exchanger areas cannot be achieved with particular cycle conditions, the expander efficiency is again set to zero.

Applying these iterative subroutines allows the cycle to be completely defined, and the net power output can be calculated. An evolutionary algorithm has been used to identify the optimum operating conditions for the cycle model. This is a flexible and stable numerical approach which allows for optimisation with any number of variables and is particularly good for distinguishing global from local maxima and coping with discontinuities in the target function. A population of solutions is defined in which each individual solution has a unique 'gene' consisting of a 'chromosome' for each of the cycle optimisation variables under consideration (e.g. boiler pressure, condenser pressure, degree of superheat). The values of the chromosomes are initially randomly generated, and a function (in this study, the net power output of the cycle) is defined in order to calculate the 'fitness' of a

particular solution. Over successive generations of the calculation procedure, 'fitter' genes are used to create new solutions through both combination and random mutation of the chromosomes. In this study, the optimisation method was implemented as follows:

i. An initial estimate was made of the optimal system operating conditions.
ii. An initial population of 5000 randomly generated solutions were created, centred on the estimated values.
iii. The combination and mutation algorithm was implemented for 5000 generations, and the best solution identified.
iv. A check was performed by creating a random population of 5000 centred on the best solution, and if a new best solution was identified the procedure was repeated.

3. LOW TEMPERATURE HEAT RECOVERY CASE STUDY

In order to demonstrate the cycle analysis described in Section 2, a simple case study has been performed for the recovery of heat from a geothermal brine source fluid. This liquid stream has an inlet temperature of 120°C and contains a recoverable heat content of 2.7 MW if cooled to an ambient temperature of 10°C; however, a minimum allowable brine temperature of 70°C has been imposed as this represents a typical limit for controlling the formation of precipitates.

The study presented below has investigated the generation of power from this heat source using an ORC with the following characteristics:

- The working fluid is refrigerant R245fa.
- An air cooled condenser is used with 2°C sub-cooling of the working fluid at the exit.
- Minimum pinch point temperature differences of 5°C and 10°C respectively have been applied for the boiler and condenser for the design-point optimisation.
- The efficiency of the feed pump has been characterised as a function of volumetric flow and pressure difference rate using data from manufacturers.
- An efficiency of 95% has been assumed for the electrical generator and 90% for pump/fan motors.

For this type of application, where the minimum allowable source temperature is well above the feed pump exit temperature when operating at design conditions, cycle efficiency and hence power output can be improved via recuperation, although the close temperature matching between the superheated vapour and sub-cooled liquid often necessitates a relatively large heat exchanger. In order to simplify the system analysis and the matching of the heat exchanger areas at off-design conditions, this study assumes that no recuperation is used to recover heat from the superheated turbine exit vapour.

Operation of the ORC system has been considered for average climate conditions in Nevada, USA where there are significant geothermal resources of this type. The annual mean temperature is 10.5°C, with monthly variations in the average maximum and minimum temperatures shown in Figure 2. A design-point optimisation has been performed for the annual mean temperature; the fixed parameters for this optimisation are shown in Table 2, and the results are shown in Table 3.

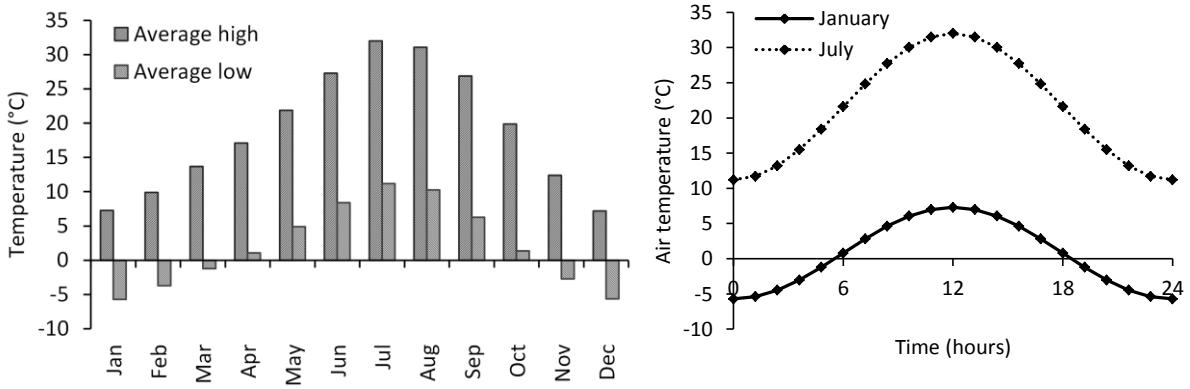

Figure 2: Monthly average maximum and minimum air temperatures in Nevada USA, and examples of assumed daily sinusoidal variation of air temperature

Table 2: Fixed parameters for design point optimisation of ORC system

Working fluid	-	R245fa
Boiler design pinch point	°C	5
Condenser design pinch point	°C	10
$T_{air,design}$	°C	10.5
$T_{source,in}$	°C	120
$T_{source,min}$	°C	70

Table 3: Optimised parameters for ORC with turbine expander operating at the design point conditions stated in Table 2

$p_{evaporator,in}$	bar	8.3
$p_{condenser,in}$	bar	1.7
$\Delta T_{superheat}$ at turbine inlet	°C	0
$\Delta T_{superheat}$ at turbine exit	°C	16
$\dot{m}_{wf}$	kg/s	5.4
$T_{brine,out}$	°C	70
$P_{expander}$ (electrical)	kWe	103
$P_{condenser\ fan}$ (electrical)	kWe	18.1
$P_{feed\ pump}$ (electrical)	kWe	4.6
P_{net} (electrical)	kWe	81.0

3.1 Off-design analysis of ORC with turbine

The off-design performance of the optimised ORC has been investigated by identifying the conditions required to achieve maximum net power output from the system defined in Table 2 for a range of air temperatures from -10 to 40°C. In all cases, the off-design analysis has achieved an error of less than 0.1% between the design-point and off-design values of the heat transfer surface area for the boiler and condenser heat exchangers. Reducing this allowable error was found to have negligible effect on the net power output from the system; with an air temperature of 30°C for example, a maximum error

of $1x10^{-6}$ in the heat exchanger areas was found to change the calculated net power output by less than 0.05%. The resulting system performance for off-design operation is shown in Figures 3 and 4, where the heat recovery efficiency refers to the fraction of available heat that is transferred into the cycle, and the cycle efficiency is the net power output divided by the heat input, as defined in equations (6) and (7).

$$\eta_{heat\ recovery} = \frac{T_{source,i} - T_{source,o}}{T_{source,i} - T_{air}} \tag{6}$$

$$\eta_{cycle} = \frac{P_{net}}{\dot{m}_{source}\left(h_{source,i} - h_{source,o}\right)} \tag{7}$$

3.2 Comparison of results for turbine ORC and twin-screw WORC

In order to assess the effect that the off-design performance has on the operation of the ORC system throughout the year, it has been assumed that for a typical day, the temperature has a sinusoidal variation between the average monthly maximum and minimum temperatures as shown in Figure 2. The variation in power with temperature through the course of a typical day in each month can then be calculated, and the mean power output for each month can be found. Figure 5 shows the time-averaged power output from the ORC for each month. The values of net power output calculated for both design-point and time-averaged annual conditions are compared in Figure 6. In Figures 3-6, results are also shown for the WORC using a twin-screw expander, as described by Read et al. (2014b). Finally, Figure 7 shows a comparison between the calculated heat transfer areas for heat addition and reject in both the WORC and ORC systems.

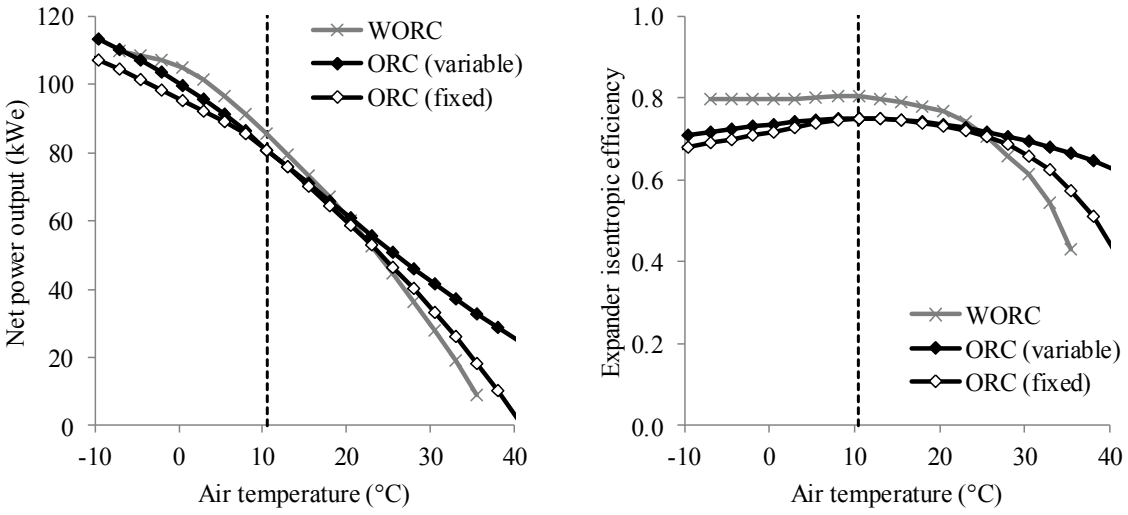

Figure 3: Maximum net power output as a function of air temperature and corresponding expander isentropic efficiency for WORC using twin-screw and ORC using fixed and variable nozzle turbines

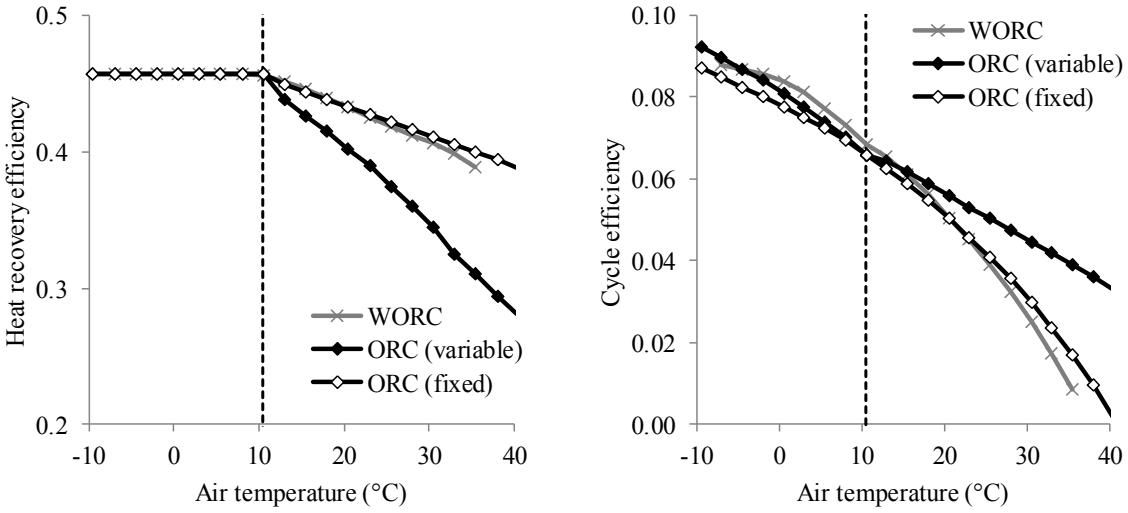

Figure 4: Heat recovery efficiency and cycle efficiency as functions of air temperature for WORC using twin-screw and ORC using turbine with fixed and variable nozzle geometry

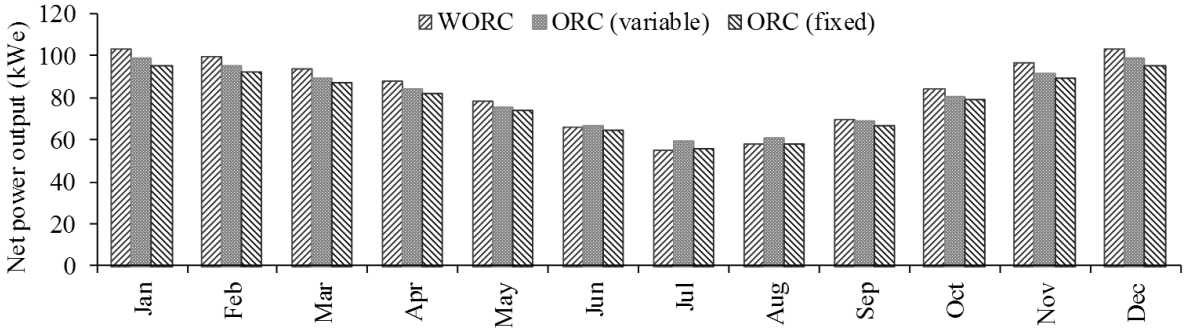

Figure 5: Comparison of monthly time-averaged net power output for the WORC, and ORC using turbine with fixed and variable nozzle geometry

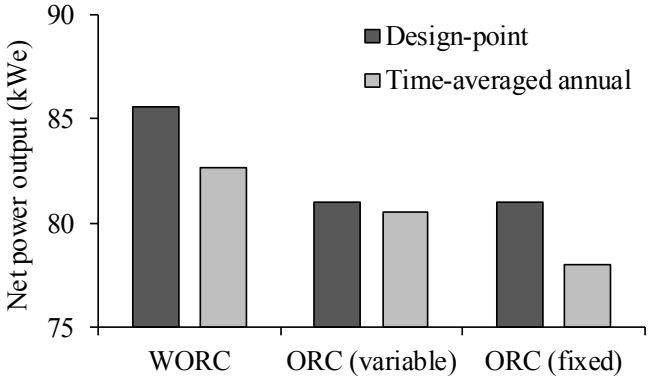

Figure 6: Comparison of net power output from WORC and ORC systems (with fixed and variable turbine nozzle geometries) for design-point and time-averaged annual conditions

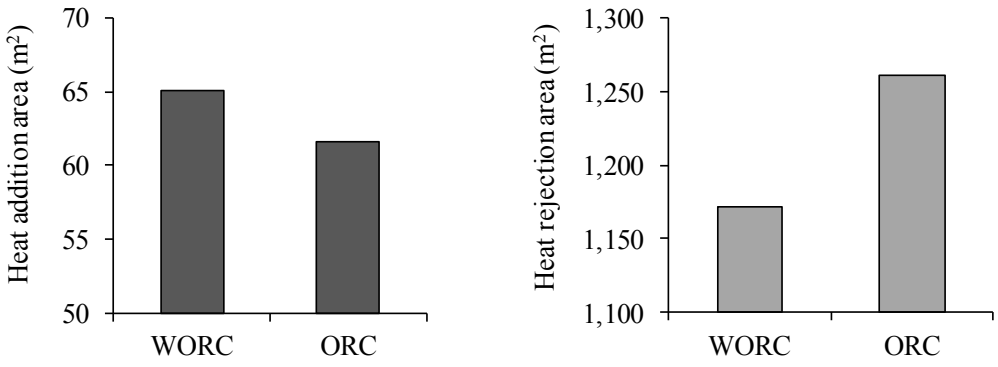

Figure 7: Comparison of predicted heat exchanger areas for WORC and ORC systems sized for design-point conditions

4. DISCUSSION

The results in Figures 3-7 show that similar overall performance is achieved by different ORC systems. The design-point net power output is largest for the WORC, largely due to the slightly higher expander isentropic efficiency predicted for the twin-screw machine, which was also able to maintain higher efficiency at off-design conditions with lower air temperature. The fixed geometry turbine was seen to achieve a lower efficiency than the variable geometry machine at all off-design conditions, but this decrease in efficiency was largely offset by a higher relative recovery of heat from the source fluid at higher air temperatures. The efficiency of the twin-screw machine in the WORC is seen to drop rapidly at higher air temperatures, due to the fixed built-in volume ratio of the machine leading to over-expansion of the working fluid. It may therefore be possible to improve the high temperature performance of the WORC system by allowing optimisation of the expander speed and/or built-in volume ratio in order to better match the volume ratio of the expansion process; the increase in net power output is however expected to be small due to the limited periods of time spent operating at these higher air temperatures. The time-averaged net power output from all cycles is seen to be very similar for all systems, at around 80 kWe, and the use of the average annual temperature to perform the design point calculations is seen to provide a good initial estimate of the real-world system performance.

The results presented above also give some insight into cost implications for the ORC systems. Compared to the optimised WORC, the area required for heat addition in the ORC is reduced by 5%, but the heat rejection area is increased by 8% due to the requirement to cool the superheated vapour at the turbine exit. As the air-cooled condenser is likely to represent a significant proportion of the total system cost due to its large size, this difference could be economically significant. However, more detailed consideration of the design and performance of heat exchangers and the associated heat transfer coefficients would be required to confirm this. The possible economic benefits of using twin-screw machines in WORC systems has already been discussed in detail (Leibowitz et al., 2006), and the results here suggest that performance can match or exceed conventional ORCs for relatively low power applications. It is however worth noting that the isentropic efficiency of turbines increases with power up to a maximum of around 83% for large-scale geothermal applications (Wendt and Mines, 2013). While the efficiency of twin-screw machines also generally improves with size and power output (due to the relative reduction in leakage flows), there is a practical limit of around 0.5 metres for the maximum rotor diameter. Applied to a WORC, isentropic efficiencies of around 84% and a net power output of around 590 kWe are predicted (Read et al., 2014b) and represent an upper limit to WORC operation using twin-screw expanders.

5. CONCLUSIONS

In this paper, the optimisation and part-load simulation of low temperature heat recovery systems has been demonstrated. The case study considered above suggests that similar overall performance can be achieved by ORC systems using both twin-screw and turbine expanders. The results indicate that for the application considered (where the heat source conditions remain constant) there is little benefit, in terms of average power output, in using a variable geometry turbine over the fixed type. While the efficiency of the screw expander is seen to decrease more rapidly than the turbine at higher air temperatures, the WORC is predicted to achieve comparable design-point and time-averaged performance and offers the potential for a low cost and low complexity system. The model described can be used for a wide range of applications, and allows comparative studies of the technical and economic performance of low temperature heat recovery systems and their components.

REFERENCES

Leibowitz, H., Smith, I.K., Stosic, N., 2006, Cost Effective Small Scale ORC Systems for Power Recovery from Low Grade Heat Sources, *Proceedings of IMECE2006*, ASME, p. 521-527

Read, M.G., Smith, I.K., Stosic, N., 2014a, Multi-Variable Optimisation of Wet Vapour Organic Rankine Cycles with Twin-Screw Expanders, 22nd International Compressor Engineering Conference at Purdue, Paper 2359.

Read, M.G., Smith, I.K., Stosic, N., 2014b, Effect of Air Temperature Variation on the Performance of Wet Vapour Organic Rankine Cycle Systems, Transactions of the 38th GRC Annual Meeting, Portland OR .

Roetzel, W., Spang, B., 2010, VDI Heat Atlas: C3 Typical Values of Overall Heat Transfer Coefficients, pp 75-78, Springer Berlin Heidelberg

Smith, I.K., Stosic, N., Aldis, C.A., 1996, Development of the Trilateral Flash Cycle System: Part 3: The Design of High-Efficiency Two-Phase Screw Expanders, *Proceedings of the Institution of Mechanical Engineers, Part A: Journal of Power and Energy*, 210(1): 75-93.

Smith, I.K., Stosic, N., Kovacevic, A., 2001, Power recovery from low cost two-phase expanders, *Transactions of Geothermal Resource Council*, p. 601-606.

Smith, I.K., Stosic, N., Kovacevic, A., 2004, An improved System for Power Recovery from Higher Enthalpy Liquid Dominated Fields, *GRC Annual Meeting, Indian Wells*.

Smith, I.K., N Stosic, N., Kovacevic, A., 2005, Screw expanders increase output and decrease the cost of geothermal binary power plant systems, *Transactions of Geothermal Resource Council*, p. 25-28.

Stosic, N., Hanjalic, K., 1997b, Development and Optimization of Screw Machines with a Simulation Model - Part I: Profile Generation, *Journal of Fluids Engineering*, 119(3): 659-663.

Wendt, D.S., Mines, G.L., 2013, Simulation of Air-Cooled Organic Rankine Cycle Geothermal Power Plant Performance, Report number: INL/EXT-13-30173, prepared for U.S. Department of Energy.

EXPERIMENTAL INVESTIGATION OF EFFECT OF OPERATING CONDITIONS ON PERFORMANCE OF ORC SYSTEM BASED ON OIL FLOODED TWIN SCREW EXPANDER

Abhijeet Chougule[1,2]*, Charles Philominraj[1], Dr. Ramakrishna R. Sonde[1]

[1]Thermax Limited,
D-13, MIDC Industrial Area, R D Aga Road, Chinchwad, Pune - 411019, India
E-mail: abhijeet.chougule@thermaxindia.com

[2]Savitribai Phule Pune University,
Ganesh Khind, Pune - 411007, India

* Corresponding Author

ABSTRACT

The paper discusses the following aspects on the experimental investigation of effect of operating conditions on volumetric expander (oil flooded twin screw expander) based ORC system.

- Experimental investigation of oil flooded twin screw expander performance in an ORC system
- Experimental investigation and analysis of oil separator pressure drop and its effect on volumetric/isentropic efficiency of the expander
- Variable speed versus constant speed operation - Effect on isentropic efficiency of expander and cycle efficiency. The variable speed operation gives optimum isentropic efficiency (80 to 85%) at all loads of low potency heat recovery for power generation.
- Field experience of 30 and 100 kW screw expander based ORC system

1. INTRODUCTION

Organic Rankine Cycle (ORC) is emerging as one of the most suitable technology for harnessing low potency (low temperature) heat for electrical power generation.

Currently it is needless to emphasize the importance of harnessing low potency heat since it has become "the need" for any industry. However there are several challenges in harnessing low potency heat (Goel *et al.,* 2014):

- Higher cost of heat recovery due to low logarithmic mean temperature difference (LMTD)
- The conversion efficiency is low as the heat source becomes lower and lower. Although very high isentropic efficiencies of the organic fluid expander/turbines is achieved, the cycle efficiency has always remained low since the limiting Carnot efficiency is itself low at these temperatures.
- Availability of equipment in terms of reliability and uninterrupted operating hours

This paper discusses/reports the investigations carried out in overcoming some of these challenges to make ORC more and more viable. The experimentally investigated ORC system consists of a volumetric expander (oil flooded twin screw expander).

The investigation is based on understanding the mechanical and thermal performance of the ORC system, with respect to thermodynamic parameters of operating fluid and variable conditions of heat source and heat sink. The key experiments investigated are the effect of operating shaft speed on the expander performance at part load conditions and the effect of oil separator pressure drop on performance of the system (Mujic *et al.,* 2010).

The later part of the paper covers the challenges involved to make the ORC technology viable and reliable for various applications (Goel *et al.,* 2014). It also focuses on identifying the key areas of development to make the ORC system cost competitive and reliable in operation.

2. EXPERIMENTAL INVESTIGATION

The ORC experimental facility is designed for testing ORC system and its different components. The system uses low temperature saturated seam (at around 130°C) as the heat source and wet cooling tower (with water cooled condenser) for heat rejection. It is designed to test various capacities of ORC expanders/ turbines from shaft power capacity of 10 to 100 kW. The shaft power is measured by using an eddy current dynamometer (capacity 110 kW). The system is also designed for different operating fluids ranging from HCFC, HFC families to pure Alkanes. The photograph of the test facility is as shown in Figure 1.

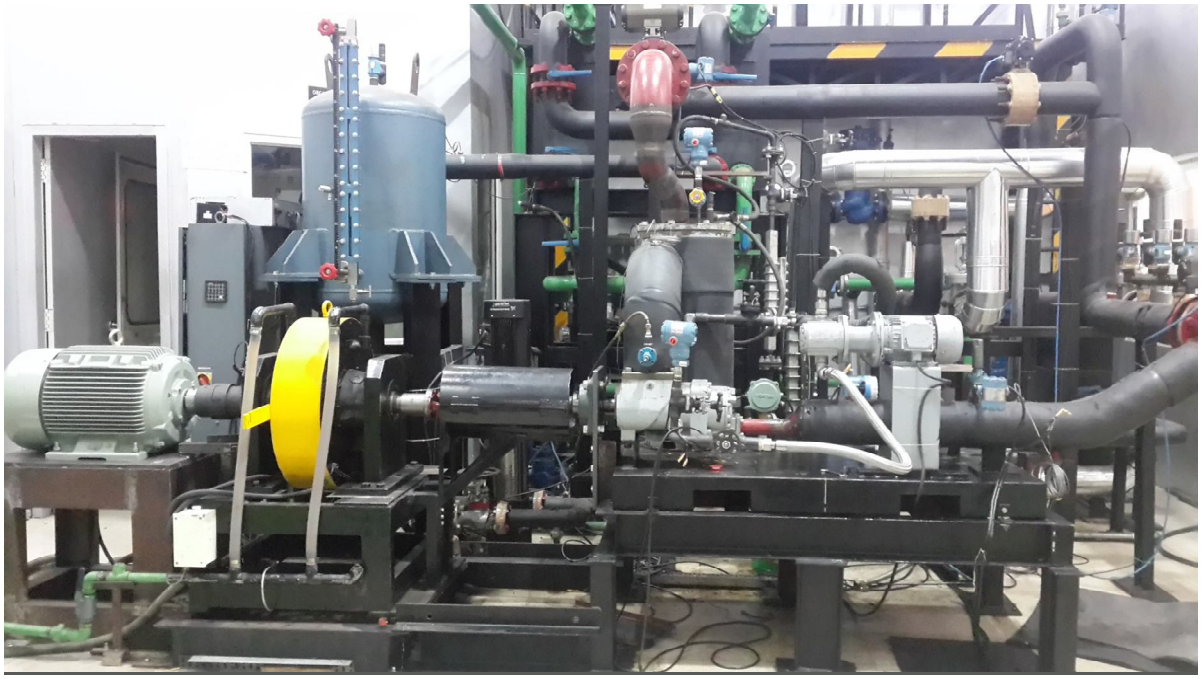

Figure 1: ORC test facility (with screw expander)

The current research work is oriented towards investigation of oil flooded twin screw expander for addressing the parametric performance of twin screw expander. The selected expander is a 4/5 lobe type design with designed displacement volume of 0.00292 m^3 per revolution with volumetric compression ratio of 4.5. The rotor length is 245 mm. The maximum withstanding pressure of the expander casing is 18 bar abs. Hence during operational trials, the expander inlet pressure is limited up to 16 bar abs. The operating fluid used is R245fa (1,1,1,3,3 pentafluoropropane). The expander was tested for variable speed as well as constant speed operation. The variable speed operation was tested in the operating speed range of 1000 to 4500 rpm. The Constant speed operation was tested at 1500, 2000 and 3000 rpm. The experimental investigation was conducted with maintaining a superheat vapor condition (degree of superheat at 20°C) at expander inlet. The lube oil for bearing weas pumped inside the expander using a positive displacement pump with constant flow rate.

Experimental results obtained from the performance testing of the expander operating at a constant shaft speed condition of 1500 rpm and 2000 rpm with steady state heat source and heat sink parameters of full load capacity, are presented in Figure 2 and 3 respectively. The experiments were conducted at steady state conditions of heat sink and heat source. The performance of the expander was monitored at steady conditions of constant flow of cooling water (heat sink fluid) and steam (heat

source fluid). The expander performance is observed though the isentropic efficiency of the expander. The isentropic efficiency of the expander is calculated from Equation (1).

$$\eta_{isentropic} = \frac{h_1 - h_2}{h_1 - h_{2'}} \quad (1)$$

The performance of the expander was monitored on the calculated isentropic efficiency based on measured operating parameters of pressure and temperature at expander inlet and outlet.

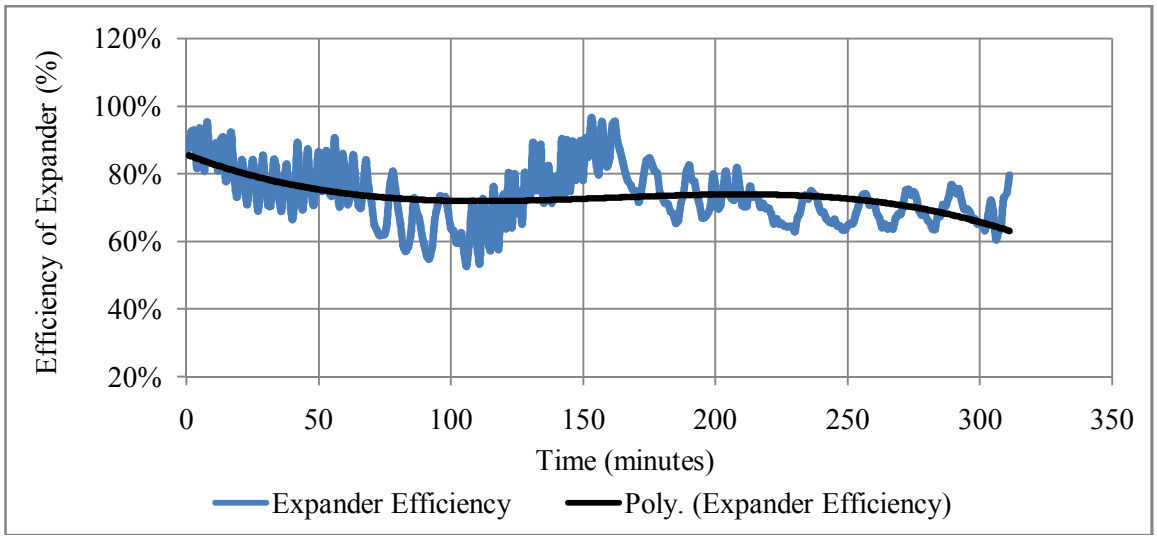

Figure 2: ORC experimental analysis (1500 rpm) - Expander isentropic efficiency

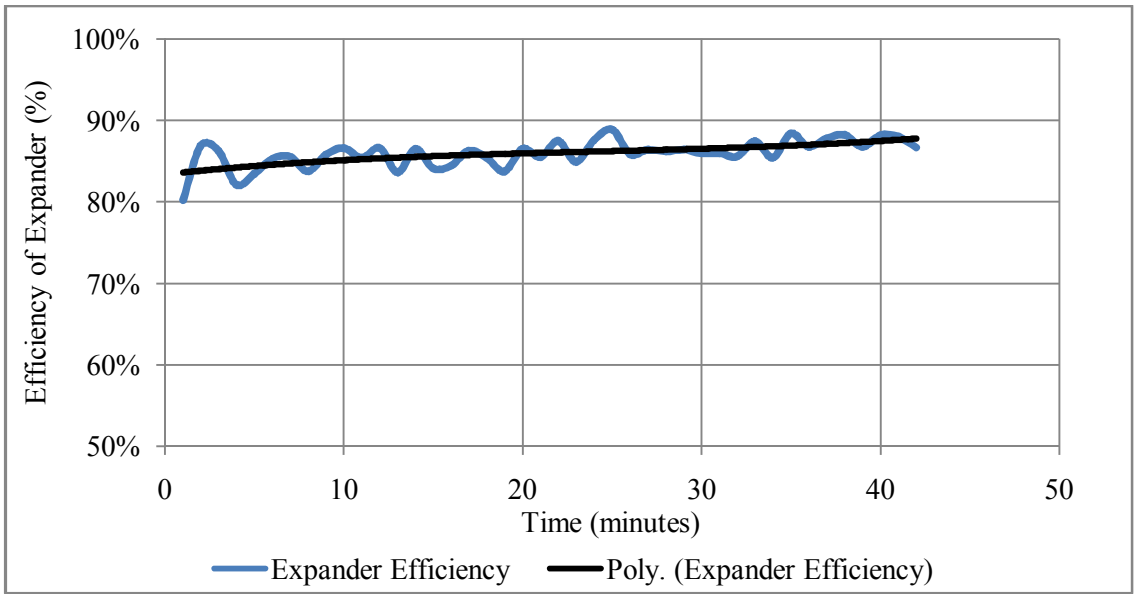

Figure 3: ORC experimental analysis (2000 rpm) - Expander efficiency

From Figure 2, it can be observed that the isentropic efficiency of expander operating at constant speed of 1500 rpm was in the range of 60 to 95%. The stable zone of operation indicated the expander isentropic efficiency in the range of 60% to 80%. Similarly from Figure 3 it can be observed that the isentropic efficiency of the expander operating at constant speed of 2000 rpm is in the range of 80% to 88%. This investigation indicates that the isentropic efficiency of the expander increases with increase in shaft speed. The cyclic variations in the isentropic efficiency graph of expander are due to

the dynamometer loading and unloading to maintain the expander shaft speed constant and with the feed pump operating to maintain constant degree of superheat at expander inlet.

2.1 Comparison of variable speed versus constant speed operation

In scenarios where heat source is varying (ORC system operating at part load conditions), the ORC system can be operated in two modes: constant speed and variable speed. The impact of operating mode on the isentropic efficiency of expander is experimentally investigated. The tests were conducted for the constant condensing temperature of 40°C (saturation pressure of 2.5 bar abs.) and variable heat input. The system was operated in constant speed mode at 1500 rpm and in variable speed mode. The shaft speed was varying between 1000 to 3000 rpm in variable speed mode operation. The experimental results obtained during this investigation are shown in figure 4.

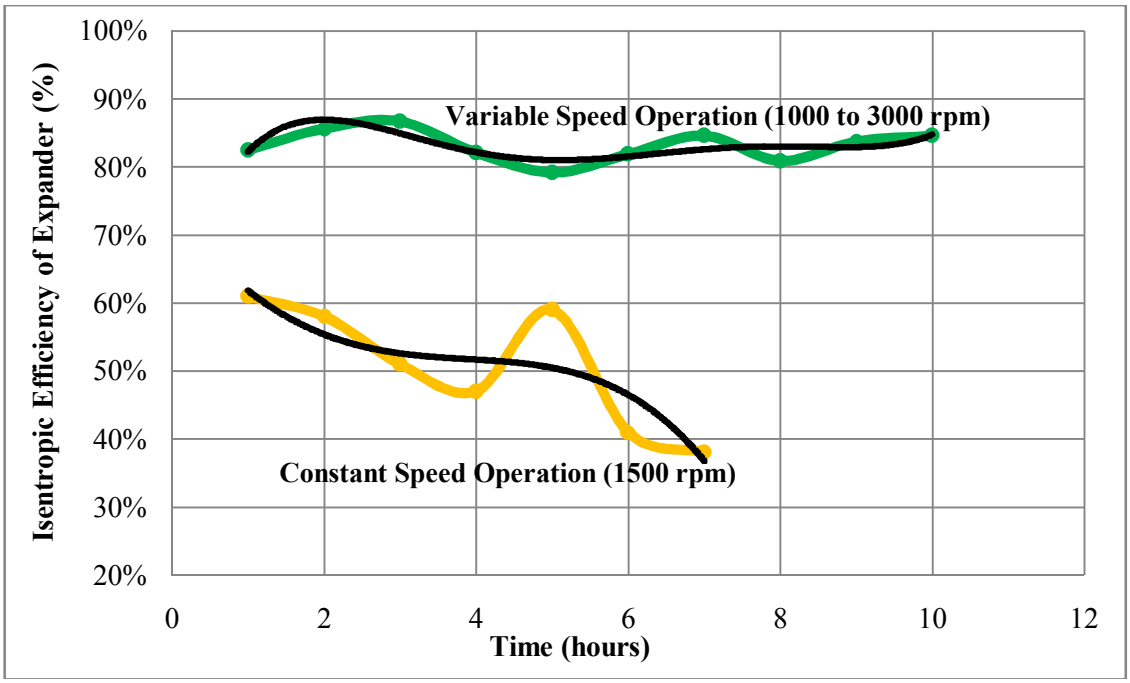

Figure 4: ORC Test result - Constant speed versus variable speed

From Figure 4, it is observed that the isentropic efficiency of the expander started reducing from 60% to less than 40%, at constant shaft speed mode with respect to reduction in heat input. The expander shaft speed was forced to be maintained at 1500 rpm using a dynamometer. The speed was maintained constant by varying the breaking torque on the expander shaft. That resulted in reduction of expander inlet pressure from 14.3 bar abs. to 5.7 bar abs. (expander pressure ratio decreased from 3.58 to 1.43) with respect to heat input reduction from 100% to 30%. The reduction in pressure ratio has resulted in poor expander efficiency.

In variable speed mode, the Shaft was allowed to vary by maintaining constant breaking torque on the dynamometer. The shaft speed variation was resulted by reduction in heat input from 100% to 30% load. The reduction in heat input actually resulted in reduced mass flow of operating fluid (as the pump flow modulated to maintain required degree of superheat at expander inlet). The effect of this change in mass flow resulted in fairly constant expander inlet pressure in the range of 13.6 to 14.3 bar abs. The obtained expander isentropic efficiency in this mode of experiment is in the range of 80 to 85%.

The conclusion drawn from this investigation is that, the operating pressure ratio of the expander impacts the expander isentropic efficiency. Higher pressure ratio is possible in variable speed operation and not is constant speed operation. Hence for part load operations and varying heat input

conditions, the performance of the system is efficient at variable speed mode operation and not with constant speed mode operation.

2.2 Effect of oil separator pressure drop

The lube oil is injected inside the oil flooded twin screw expander which is required for lubrication of bearings and for providing the sealing between two helical screws. Majority quantity of lube oil is pumped to the bearings mounted at both the ends of expander shafts (main rotor and gate rotor). A small quantity of lube oil gets mixed with operating fluid inside expander and then provides the required sealing between two screws. After lubrication the oil from bearings also gets mixed with the operating fluid and it comes out from low pressure port along with operating fluid. This oil has to be separated and circulated back to the expander for continuous lubrication and sealing. The oil separator performs the function of oil separation and also provides the required head for lube oil pump. The location of oil separator in the ORC system is between the expander outlet and condenser inlet. It is as shown in figure 5.

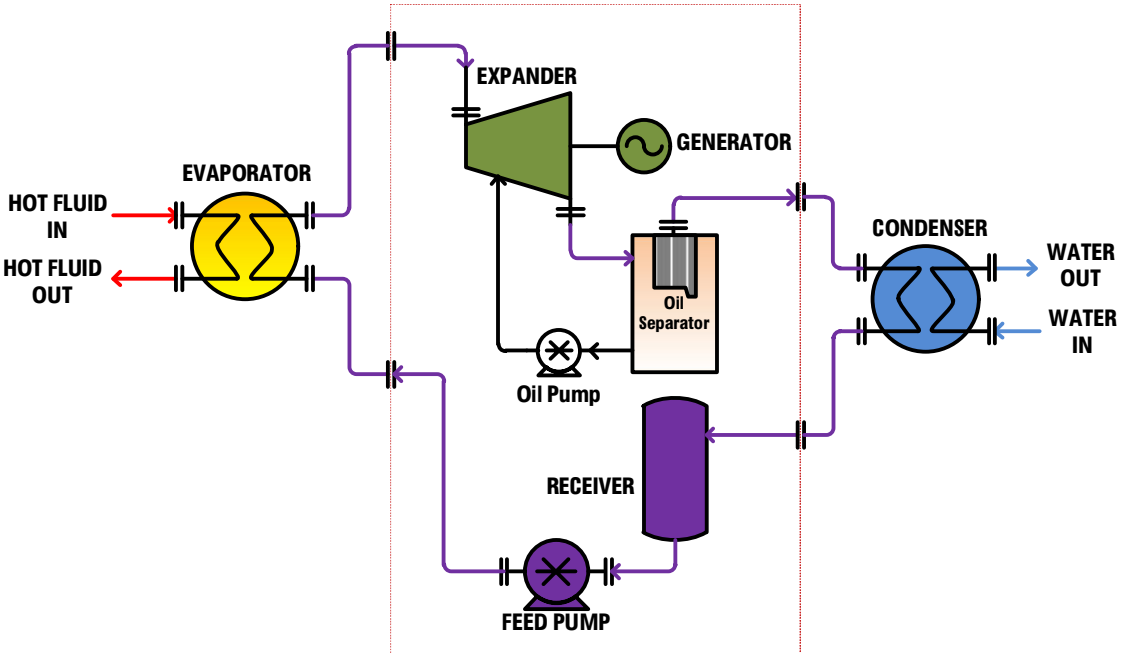

Figure 5: ORC system block diagram (with oil separator)

The oil separator tank is provided with two stage oil separation. In first stage, the bigger droplets of oil are separated by centrifugal action which is supported by the tangential entry of fluid oil mixture coming out from expander. After the first stage separation, the direction of flow is reversed and then the fluid is filtered using a clothed filter element for small oil droplet removal. This filter element is installed in the inner cavity of the oil flow reversal chamber. The smaller oil droplets are captured in the walls of filter element. These captured oil droplets trickle down, and get collected at the inner cavity of the element. Due to these changes in flow direction and filter element, the oil separator has an inherent pressure drop of the process fluid.

The conventional design of oil separator which is used along with screw compressors was incorporated in the experimental investigation. In experimental study the pressure drop observed across the oil separator was in the range of 2.4 to 2.6 bar. This resulted in increased expander outlet pressure (i.e. reduced pressure ratio) which caused reduction in power output from the expander. To decrease this pressure drop and to increase the pressure ratio across the expander, the oil separator inlet and outlet ports along with interconnecting piping was redesigned for low pressure parameters of operating fluid. After redesign, the pressure drop across the oil separator was observed to be reduced by 40%.

The effect of oil separator redesign is experimentally investigated (for improvement in expander efficiency) and compared with the results obtained with original oil separator design. The obtained results are shown in Figure 6. The reduced pressure drop across oil separator resulted in improved expander efficiency by 5%.

The experimental investigation of pressure drop across the oil separator was carried in term of its effect on the isentropic efficiency of the expander while operating at constant condensing conditions which are maintained by constant flow of heat sink and heat source fluid. The experiment was carried out at steady operating conditions of operating parameters across the expander. It was compared with earlier performance of the expander which had higher pressure drop across the oil separator.

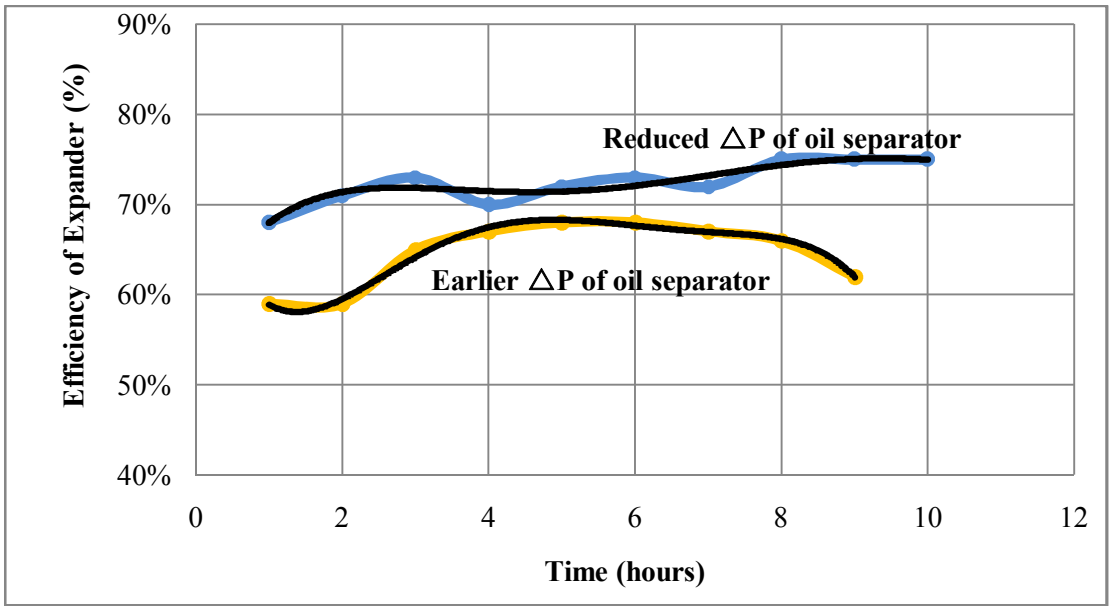

Figure 6: ORC Test result - Effect of oil separator pressure drop

Based on this experimental investigation, it can be inferred that, reduction in pressure drop across the oil separator has reduced the irreversibility from the expander and improved the expander isentropic efficiency. It can also be inferred that removal of oil separator will further enhance the expander efficiency and thus the overall efficiency of the system. This improved isentropic efficiency of expander is effect of improved pressure ratio across the expander as the expander outlet pressure has approached towards the condenser pressure. The higher pressure ratio resulted in increased power output and better efficiency.

However, in the absence of oil separator, the lube oil will be carried over to condenser. The oil carry over to condenser will foul the heat transfer surface. This is not an issue while the ORC system is operating at full load condition, as the oil percentage in operating fluid will be less than 3%. (http://handbooks.swep.net/) But at part load, the oil percentage in operating fluid will be more than 35% which affects heat transfer in side condenser. Therefore it is required to have sufficient over surface area in condenser design. The oil collection and recirculation to the expander also need to be addressed in this case.

2.3 Mechanical performance

Experimental set-up was initially designed with a velocity range of 20 m/s at expander inlet port. However during experimentation, the vibrations were noted at expander inlet piping. The cause of these vibrations was the increased velocity at expander inlet due to convergent nozzle to reduce pipe diameter of 114.3 mm to 60.3 mm neat the inlet port of expander. The nozzle was initially located close to the expander inlet port which did not provide enough straight length of pipe to stabilize the

operating flow. The redesign for flow stabilization resulted in reduction of these vibrations and improved the expander reliability.

3. 100 kW PROTOTYPE

The learning from all these experimental investigations of ORC system, are implemented in first prototype of capacity 100 kW, which is under commissioning and testing at a solar thermal based power plant. The photograph of this prototype ORC system is as shown in Figure 7.

Figure 7: First prototype of ORC system: Capacity 100 kW

The key features included are the variable speed operation for part load conditions to keep higher pressure ratio across the expander and improved design of oil separator to get lower expander outlet pressure. The expander inlet flow stabilization is also implemented to reduce the vibration at the expander. The mechanical vibration from the rotary systems i.e. expander and electrical generator are decoupled from each other by implementation of timing belt drive arrangement.

The experimental investigation of 100 kW prototype system are yet to be carried out as the system is under commissioning stage and will be produced in further work to improve the next version of the ORC systems.

4. CONCLUSION

- The ORC system is more efficient at operations with variable speed for varying source heat input and at part load conditions. The isentropic efficiency of the expander at variable speed mode of operation is 80-85%, which is at least 30% higher than that in constant speed mode. The variable speed operation improves the viability of ORC system.
- The redesigned oil separator improved the expander efficiency by 5% due to reduction in pressure drop across it by 40%. Inclusion of any additional component between expander outlet and condenser reduces the expander efficiency as well as cycle efficiency due to the pressure drop across the component.

- The removal of oil separator will certainly improve the efficiency of the system as pressure ratio across the expander. However this will increase the heat transfer area required in condenser. This has to be further investigated to arrive at an optimum system design.
- The performance of the expander was improved by reducing the flow induced vibrations at expander inlet. The availability and reliability of the screw expander for enhanced mechanical performance has to be further investigated by implementing vibration mitigation techniques, shaft seal development and arriving at optimized mechanical design parameters.

NOMENCLATURE

η	efficiency	(%)
h	enthalpy of fluid	(kJ/kg)
N	number	(–)

Subscript

1	expander inlet
2	expander outlet
‘	isentropic condition

REFERENCES

Velez F., Segovia J., Martin M., Antolin G., Chejne F., Quijano A., Nov 2012, “Comparative study of working fluids for a Rankine cycle operating at low tem-perature”, *Fuel Processing Technology*, vol. 103, p 71-77.

Stosic N., Smith I., Kovacevic A., 2005, *“Screw Compressors - Mathematical modelling and performance calculation”*, ISBN-10,3-540-24275-9 Springer, New York, 138 p.

Quoilin S., Lemort V., 2009 “Technological and economic survey of organic Rankine cycle systems”, *5th European conference Economic and Management of Energy in Industry,* p 1-12

Quoilin S., Aumann R., Grill A., Schuster A., Lemort V., Spliethoff H., 2011, “Dynamic Modelling and optimal control strategy of waste heat recovery Organic Rankine Cycles”, *Applied Energy*, vol. 88, p 2183-2190

National Institute of Standards & Technology, REFPROP 9.0, Fluid property database

Mujic E., Kovacevic A., Stosic N. and Smith I., 2010 “Advanced design environment for screw machines”. *International compressor engineering conference*, 1243, p 1-8.

Karl, J. 2004, "Decentralized energy systems, new technologies in liberalized energy market", "Dezentrale Energiesysteme, (Neue Technologien im liberalisierten Energiemarkt) Oldenbourg Wissensschaftsverlag, Munchen", (in German)

Goel S., Herzog O., Datta A., Sonde R., Deshpande K., Fink J., Schumacher T., June 2014, *“Market potential study for organic Rankine cycle technology in India - A Publication on Industrial Energy Efficiency"* Indo-German Energy Forum Support Office (IGEF-SO), New Delhi, 68 p.

Charles P., Dec 2013, “Compacting heat transfer systems in new and advanced power cycle systems: Addressing major challenge in waste and renewable energy technologies” Proceedings of Indo-US workshop on “*Recent advances in micro/ nano-scale heat transfer and applications in clean energy technologies”*

Bianchi M., De Pascale A., 2011, “Bottoming cycle for electric energy generation: Parametric investigation of available and innovative solutions for the exploitation of low and medium temperature heat sources”, *Applied Energy*, vol. 88, p 1500-1509

EXPERIMENTAL STUDY ON ORGANIC RANKINE CYCLE SYSTEM WITH SINGLE-SCREW EXPANDER FOR WASTE HEAT RECOVERY FROM DIESEL ENGINE EXHAUST

Yuting Wu*, Biao Lei, Wei Wang, Yeqiang Zhang, Chongfang Ma

Key Laboratory of Enhanced Heat Transfer and Energy Conservation of Ministry of Education and Key Laboratory of Heat Transfer and Energy Conversion of Beijing Municipality, College of Environmental and Energy Engineering, Beijing University of Technology, Beijing 100124, PR China

Contact Information：wuyuting@bjut.edu.cn

ABSTRACT

A single-screw expander prototype with 155 mm diameter screw was developed. An ORC (organic Rankine cycle) experimental system for waste heat recovery from diesel engine exhaust was built. Experiments were conducted for different expander torque and diesel engine loads. The experimental results indicated:(1) Single-screw expander is suitable for small/medium scale ORC system, and it can obtain good performance at low-medium rotational speed. The maximums of power output 10.38 kW andshaft efficiency 57.88% are achieved at 1538 rpm.(2) The maximums of volumetric efficiency, adiabatic efficiency and expansion ratio of single-screw expander are 90.73%, 73.25% and 4.6, respectively.(3) The performance of ORC system is affected not only by the working case of diesel, but also by the torque of single-screw expander. The biggest ORC efficiency is 6.48%, which is gotten at 250 kW diesel power output and 64.43 Nm of single-screw expander.(4) With ORC system, the specific fuel consumption of diesel is effectively decreased. When the power output of diesel is 250 kW, the specific fuel consumption is decreased by 3.5%, and the overall system efficiency is 43.8%, which is increased by 1.53%.(5) With the reducing of mass flow rate pumped into evaporator, the dryness of vapor is accelerated, and heat exchange quantity almost linearly decreases. Volumetric flow rate of vapor into single-screw expander increases with increase of inlet vapor dryness but volumetric efficiency decreases with that. The rising of expansion rate is due to increase of inlet pressure and decease of outlet pressure with the increase of inlet vapor dryness and the biggest expansion ratio is 4.7. With the increase of inlet vapor dryness, torques and power outputs of single-screw expander are rising.

1. INTRODUCTION

Over the past century,the diesel engine has been a primary power source for automobiles, long-haul trucks, locomotives, and ships. The efficiency of a modern diesel engine is about 30%~40% in an ideal case,Theother energy dissipated is lost bytransmission to the environment through exhaust gas,cooling water, lubrication oil and radiation.In driving conditions, energylost is even close to 80%. Improving the utilization of low temperature energy can significantlyincrease the integrated energy efficiency and remarkablyreduce the fuel consumption, so it is apromising path forenergy saving and consumption reducing for diesel engine.Of interest, manyresearchers recognize that waste heat recovery (WHR) fromengine exhaust has the potential to decrease fuel consumptionwithout increasing emissions, and recent technological advancementshave made these systems viable and cost effective (Chammas et al., 2005).

The ORC is a Rankine cycle in which an organic substance is used instead of water-vapor. ORC system is an environmentally friendly system with no emissions of exhaust gases such as CO, CO_2, NO_X, SO_X and other atmospheric pollutants. The most important feature for an ORC is its capability of utilizing various kinds of low-grade heat sources for power generation. Most studies choose ORC for WHR due to its simplicity and ability to operate with low to moderate temperature differences. Another primary advantage of ORC is the use of widely available and affordable components.

In an ORC system, there are two main types of expanders: the velocity-type expanders, such as axial turbine expander, and the volume-type expanders, such as screw expander, scroll expander and reciprocal piston expander (Qiu et al., 2011).Turbine expander has many advantages, but it is generally applied in power cycles with power output greater than 50kW, because its efficiency would

be unacceptable in small scale power cycles (Peterson et al., 2008). Turbine expander is suitable for superheated vapor. With saturated steam, the problems of using turbine expander are water erosion to blades and low shaft efficiency of the unit. In addition, turbine has faster rotational speed, and an excess gear box is indispensable if it is utilized in a small scale ORC. Compared with the velocity-type expanders, volume-type expanders are suitable for the ORC-based waste heat recovery because they are characterized by lower flow rates, higher expansion ratios and much lower rotational speeds.

Recently, scroll expander has been gaining some interests as the expanders in small scale ORC(Peterson et al., 2008, Lemort et al.,2009). This device does not require inlet or exhaust valves which reduces noise and improves the durability of the unit. Another advantage is that the rolling contacts provide a seal such that large volumes of oil used as a sealant are not required and the leakage is reduced. Compared with other volume-type expanders, scroll expander may be applied in a very small scale power system, such as 0.1~10kW.

There are two types of screw expanders: twin-screw expander and single-screw expander. Twin-screw expander has been widely used in Rankine cycle system, especially for geothermal and waste heat applications. Twin-screw expander depends on precise numerically-controlled machining to achieve a leak-resistant fit. Compared with twin-screw expander, the single-screw expander has a lot of advantages, such as long service life, balanced loading of the main screw, high volumetric efficiency, low noise, low leakage, low vibration and simple configuration, and so on. Single-screw expander can realize 1-200 kW range of power output, and it is more suitable for low temperature and small scale of ORC system for waste heat recovery. Recent studies have reported the performance of in-house built single screwexpander for low power capacity. Wang et al. (2011) presented a 5 kWe machine with an isentropic efficiency of up to59%. He et al. (2013) built and tested a 22 kWe single screw expander reaching a maximum isentropic efficiency of55% at 2800 rpm. Wang et al. (2013) analyzed the influence of the gaterotor/shell and the screw/shell gap by buildingand testing three different single screw expanders.Desideri et al (2013) described experimental results of a small scale ORC system which utilizes a single-screw expander modified from a single-screw compressor. In total, 120 steady-state experimental data points have been measured and the adiabatic efficiency of expander is from 27.3% to 56.35%.

According to the power output of different type of expanders, turbine is suitable for waste heat recovery from exhaust of diesel engine which power output is more than 1MW, and scroll expander is suitable for that with diesel engine power output less than 100kW. For the power output of ORC for waste heat recovery from exhaust of 100kW~1MW diesel engine is generally from 1kW to 10's of kW, single-screw expander is the most appropriate candidate.

In this paper, an ORC experimental system with single-screw expander was developed for waste heat recovery from exhaust of a 336hp diesel engine. Experiments were carried out to investigate the influence of engine condition and expander torque on the performance of ORC system and overall engine system with ORC.

2. DEVELOPMENT OF ORC SYSTEM

2.1 The single-screw expander

A single-screw expander has been developed by our team, as shown by fig.1. The reference of this prototype's design is a single-screw compressor. Then the arrangement of screw and gaterotors, the installment of bearings, and the apparent structure are similar to a single-screw compressor. In order to simplify the construction and reduce the friction resistance, packing seal with PTFE is used as the shaft seal. The balance hole which connects high pressure leakage room with low pressure discharge volume of this expander is drilled on the shell which is different to that drilled on the screw or main shaft. The parameters of this single-screw expander used in the test are shown in table 1.

2.2 Evaporator

A spiral-tube type evaporator has been developed for the waste heat recovery system. In the evaporator, a spiral titanium tube is placed in a cylinder and baffles are also inserted in the cylinder to enhance heat transfer in the evaporator.In order to reduce the weight of this evaporator, titanium tube

is used instead of stainless steel tube. Heat is transferred from exhaust to spiral titanium tube, and working fluid is heated by spiral titanium tube and is evaporated in the tube. The design temperature is 550℃, and the design capacity is 150kW. The design pressures of organic substance side and the gas side are 2.5MPa and 0.1MPa, respectively. Because the organic substance volume continuously increases for being heated, the cross section area needs to increase correspondingly. The evaporating process is divided into 5 tube sides. The first and second tube sides both have 8 tubes, the third tube side has 16 tubes, the forth tube side has 24 tubes and the fifth tube side has 32 tube. The length of each tube is 6.8m and the wall thickness is 1.2mm. The parameters of the evaporator are shown in Table. 2.

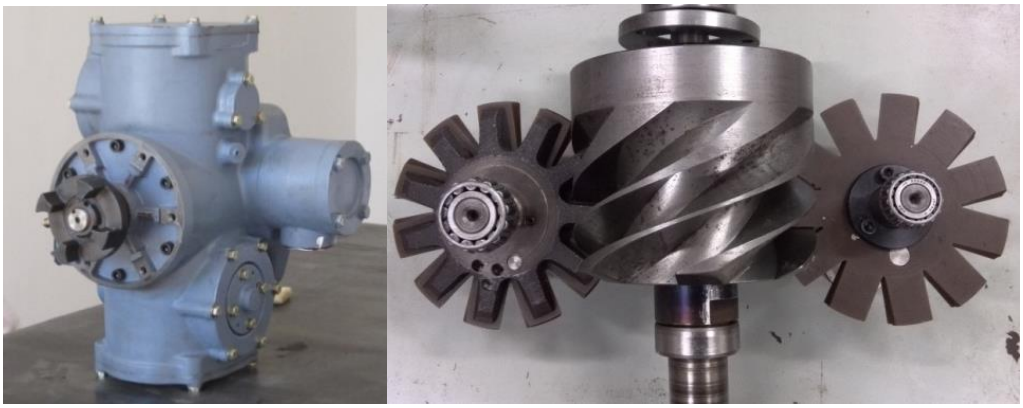

Fig.1: Photograph of the single-screw expander

Table.1: The parameter of single-screw expander

Parameters	Value	Parameters	Value
Diameter of screw(mm)	155	Diameter of gaterotor(mm)	155
Groove number of screw	6	Tooth number of gaterotor	11
Center distance(mm)	124		

Table.2: The parameter of the spiral-tube evaporator

parameters	value	parameters	value
Diameter of spiral tube(mm)	16	Wall thickness of shell (mm)	4
Wall thickness of spiral tube(mm)	1.2	Evaporator weight (kg)	147
Shell diameter (mm)	500	Heat exchange area (m^2)	12
Shell length (mm)	1500	Heat input capacity (kW)	142

2.3 Condenser

An aluminum multi-channel parallel type condenser has been developed for the waste heat recovery system. In order to enhance the heat transfer on air side, high performance louvered fins are used. While, the application of aluminum multi-channel tubes strengthens the ability of heat transfer from working fluid to air. Fig.3 shows the photograph and configuration of the aluminum multi-channel parallel type condenser. The working fluid enters the header and flows through tubes. It is important to reduce the flow resistance because of the significanteffect on the power output of single-screw expander. In the design, parallel structure of dual-condenser is used and the total flow process is divided into two tube sides. The working fluid is averaged to 70 tubes in each first tube side, and then averaged to 48 tubes in each second tube side after working fluid condensation from the first tube sides. The calculation results that the total flow resistance is less than 0.1MPa. A fan is used to

enhance the air flow and the bending type construction of the condenser would improve its utilization. The parameters of the evaporator are listed in Table. 3.

Table.3: The parameter of the parallel type condenser

parameters	value	parameters	value
Tube width (mm)	25.47	Heat transfer area in air side (m^2)	1.02
Tube thickness (mm)	2	Size of condenser (mm)	980×980×1255
Fins spacing (mm)	1.4	Condenser weight (kg)	78
Fins height (mm)	6.85	Heat rejection capacity (kW)	150
Louvered angle(℃)	27	Fan size (m)	φ860×64

2.4 Pump

The pump is a multistage centrifugal pump called CR5-32 and is provided by GRUNDFOS. The pump was running at rated speed. In order to adjust the flow rate of working fluid, a throttling bypass valvewas installed between the pump and the storage tank of working fluid. The parameters of the pump are shown in Table. 4.

Table.4: The parameter of the pump

parameters	value	parameters	value
Rotational speed (rpm)	2919	Stages	32
Designed volume flow (m^3/h)	2.98	Net weight (kg)	81.9
Designed head (m)	205		

2.5 Configuration of the ORC system

The prototype of ORC system for WHR is shown in fig.2. The ORC system included a single-screw expander, an evaporator, a condenser, a storage tank of working fluid, a multistage centrifugal pump, etc. R123 was used as the working fluid because of its outstanding ability to improve the ORC performance. R123 was first heated to vapor by exhaust waste heat of engine in the evaporator, and then the vapor expanded and generated power output in the single-screw expander. The vapor from expander was condensed into liquid by ambient air in the condenser. The R123 liquid in condenser was pumped to the evaporator. There wasa storage tank in the ORC system for supplying working fluid.

Fig.2: ORC system prototype

3. EXPERIMENTAL APPARATUS AND DATA DERIVATION

3.1 Experimental system

Fig.3 illustrates the concept of experiment. Heat source is the exhaust of a diesel engine whose power output can reach 336 horsepower. Operations start at the firing of the diesel engine. Pump begins to work when the power output of engine rises to 40 kW, then working fluid is circling in the system. It does not directly flow into the expander because a bypass is opened. When the power output of engine is over 80 kW, valves at inlet and outlet of the expander are opened, while a valve at the bypass is closed and the fan of condenser is switched on to start the working cycle. Working fluid passes through the expander, and the expander rotates. The power output of diesel engine increases gradually to the preset point. After the temperature of exhaust at inlet of the evaporator becomes steady, different torque of expander is adjusted, and experimental data are collected until the end of experiment. Pump in ORC system rotates at rated speed. In order to adjust the flow rate of working fluid into evaporator, a throttling bypass valve is installed. In the test, by adjusting the excitation of an eddy current dynamometer linked with the shaft of single-screw expander, the torque of single-screw expander can be changed.

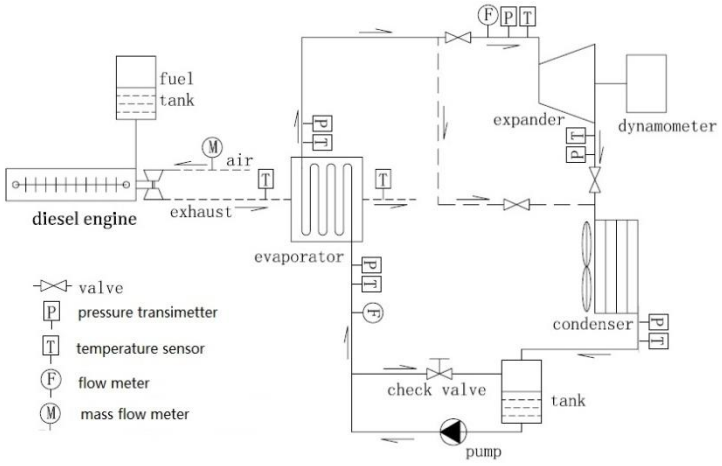

Fig.3: ORC system diagram

The power output and rotational speed of the single-screw expander are recorded by the dynamometer.Temperature probes and pressure transducers were installed on the organic substance side at inlet and outlet of the evaporator, expander, and outlet of condenser to determine the state of the working fluid. Temperature probes were installed on the exhaust side of the inlet and outlet of evaporator to determine the temperature of the exhaust. Temperature probes use PT100 with an accuracy of ±0.5℃ besides the temperature probes on the exhaust side which are N-type thermocouple with an accuracy of ±1.5℃. The pressure sensors of SMP131 with an accuracy of ±0.5%FS and measurement range of 0~2MPa were used to measure the working fluid pressure, and a pressure sensor of SMP121 is used to measure the exhaust pressure with an accuracy of ±0.2%FS and measurement range of 0~0.1MPa. These temperature probes and pressure sensors are provided by Shanghai Leeg Instruments CO., LTD. The mass flow rates of working fluid were measured using a rotameter(model H250) with an accuracy of ±1.0%FS which was installed on the organic substance side at inlet of evaporator and a vortex flow meter (model VFM4070G) with the accuracy of ±0.5%FS installed at inlet of expander. These two instruments are manufactured by KROHNE. The exhaust mass flow is calculated by the fuel consumption meter of FC2210 with the accuracy of ±0.4%FS supplied by Hunan xiangyi dynamic test instrument CO., LTD and the air mass flow measured by thermal gas mass flow meter of 20N150 with the accuracy of ±1%FS provided by Shanghai ToCeil Engine Testing Equipment CO., LTD installed at inlet of engine. In order to measure the rotational speed and power output of expander, an eddy current dynamometer of GW40 supplied by Hunan xiangyi dynamic test instrument CO., LTD. was installed. The maximum measurement of torque and rotational speed are 160N·m with an accuracy of ±0.2%FS and 10000rpm with an accuracy of

±1rpm,respectively. All the output signals of experimental data weretransported to a computer and stored as a function of time there.

3.2Dataderivation

(1)Power output: this indicates the ability of single-screw expander to output power, and is defined as

$$Pe = \frac{N \cdot \omega}{1000} \tag{1}$$

(2)Dryness is defined as the fraction of the total mixture which is vapor, based on mass. That is

$$x = \frac{\dot{m}''}{\dot{m}} = \frac{\dot{m}''}{\dot{m}' + \dot{m}''} \tag{2}$$

(3)Shaft efficiency of single-screw expander: this is the ratio of power output to enthalpy drop of working fluid in an ideal adiabatic process, which is defined as

$$\eta_{\exp} = \frac{Pe_{\exp} \times 3.6}{\dot{m}_{R123} \Delta h_{s,\exp}} \times 100\% \tag{3}$$

(4)The effect of leakage in expansion process can be evaluated by volumetric efficiency, which is defined by

$$\eta_V = \frac{V_i}{V_m} \tag{4}$$

(5)ORC efficiency: this is the ratio of available energy to overall energy obtained from thermal source, and is expressed as

$$\eta_{ORC} = \frac{(Pe_{\exp} - Pe_{pump}) \times 3.6}{\dot{m}_e (h_{e,in} - h_{e,out})} \times 100\% \tag{5}$$

(6)Specific fuel consumption: this indicates the economic performance of engine, which is defined by

$$d = \frac{\dot{m}_{fuel}}{(Pe_{\exp} + Pe_{engine})} \times 10^3 \tag{6}$$

(7)Overall system efficiency

$$\eta_{t,system} = \frac{3.6 \times (Pe_{\exp} + Pe_{engine} - Pe_{pump})}{\dot{m}_{oil} \times H_{oil}} \times 100\% \tag{7}$$

4. EXPERIMENTAL PERFORMANCE ANALYSES

In the test, temperature and mass flow of exhaust werevaried by changingin the power output and the rotational speed of diesel engine. Table 5 lists detailed specification and temperature and mass flow for different conditions of diesel engine (denoted as different cases), and table 6 gives the influences of the ORC system to diesel engine.

Table.5: Parameters of different conditions of diesel engine

item	Unit	Case1	Case2	Case3	Case4	Case5	Case6
Power output	kW	140	160	180	200	220	250
Rotational speed	rpm	1800	1800	1800	1900	1900	1900
Temperature of exhaust	℃	417	430	448	425	451	485
Mass flow of exhaust	kg/h	958	1024	1092	1205	1272	1315

Table.6: Influences of the ORC system to diesel engine

Case	Power output	Rotational speed	Specificoil consumption without ORC	Specificoil consumption with ORC	Increment of specific oil consumption	Exhaust overpressure without ORC	Exhaust overpressure with ORC	Increment of exhaust overpressure
	kW	rpm	kg/h	kg/h	%	kPa	kPa	%
1	140	1800	28.7	29	1.05	6.4	7.3	14.06
2	160	1800	32.2	32.8	1.86	7.3	8.6	17.81
3	180	1800	36.6	37.1	1.37	8.3	9.8	18.07
4	200	1900	39.4	40	1.52	9	10.7	18.89
5	220	1900	43.3	44	1.62	10.2	12.7	24.51
6	248	1900	49.5	50.1	1.21	11.6	13.3	14.65

Note: in case 6the power output of diesel engine is 250kW with ORC system.

Fig.4 shows the changes of temperature drop of exhaust with torque of single-screw expander. In the first three cases, the temperature drop decrease linearly and the changes are very small; however, the changes of temperature drop in the other cases are much larger.It is obvious that the temperature drop does not increase with the increase of diesel power output. In case 4 and case 5, some points are lower than ones in the first three cases. The influence ofexpander's torque onthe heat quantity absorbed from exhaust is shown in fig.5. The decreases of the quantity of exchanged heat are too little to consider in the first three cases, while it decreases obviously in cases 4 through 6 with the increase of torque of single-screw expander. Because the mass flow of exhaust keeps steady at a case, the quantity of exchanged heat is mainly affected by temperature drop. From this figure, it is shown that the quantity of exchanged heat increases with the increase of the power output of diesel engine also.Although the temperature drop does not increase with the increase of diesel power output, the quantity of exchanged heat keeps increasing due to the increase of the mass flow of exhaust.

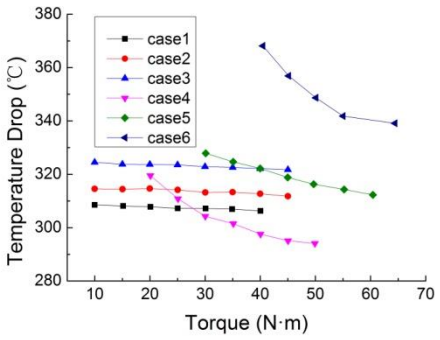

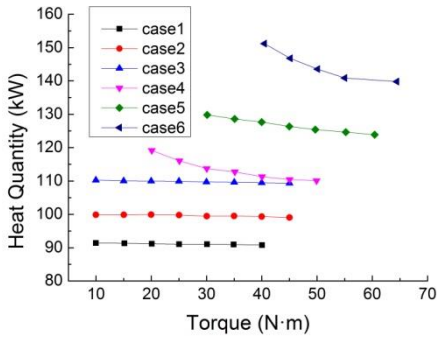

Fig.4: Temperature of exhaust gas vs. torque**Fig.5:**Quantity of exchanged heat vs. torque

Power output of single-screw expander can be calculated and its changes with the torque are shown in fig.6. It is shown that the power output of single-screw expander increased in the form of a parabola with rising expander torque. In the first four cases of experiments, when the torques of the expander are 30N·m, 40N·m, 40N·m and 50N·m, the maximums of power output of the expander are 3.63kW, 4.69kW, 5.55kW and 6.64kW, respectively. In case 5 and case 6 the maximums of power output of the expander are not achieved due to the restriction of the experimental conditions. But the increase of the power output becomes slow with the increase of the torque, and the maximums obtained are 7.81kW and 10.38kW, respectively.

Fig.7 shows the change of the shaft efficiency of the single-screw expander. From the figure, there are maximums of the shaft efficiency in every group of data in the first five cases, they are 41.45%, 46.73%, 47.59%, 49.90 and 49.93%, respectively. The shaft efficiency increases with the torque of expander in case 6, and the maximum is 57.88% at 64.43N·m of torque. The inflection point of the shaft efficiency in case 6 doesn't occur, because the increase of lubricating oil's temperature is too fast and it soon exceeds 105℃, then the engine could not go on working.

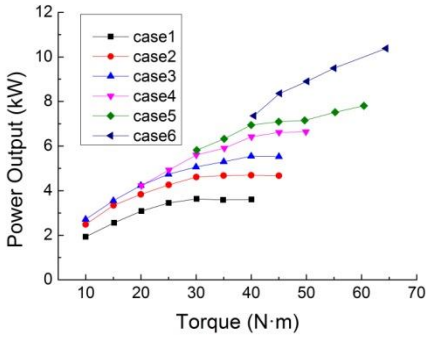

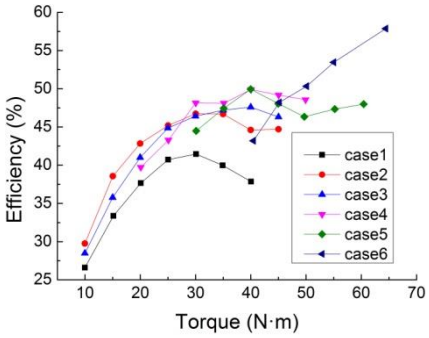

Fig.6:Power output vs. torque**Fig.7**:Total efficiency vs. torque

Fig.8 shows the variation of ORC efficiency. From this figure, the maximums of ORC efficiency are obtained in the first four cases; they are 3.04%, 3.74%, 4.04% and 5.13%, respectively, corresponding to the expander's torque of 35Nm, 40Nm, 40Nm and 50Nm. In case 5 and case 6, the power output of the single-screw expander increases with the torque while the quantity of exchanged heat decreases with the torque, so, the ORC efficiency increases with the torque, and the maximums obtained in the test are 5.34% and 6.48%, respectively.

The overall system efficiency of diesel engine with ORC is an improvement over that of diesel engine without ORC, as shown in fig.9. From the figure, the smallest improvement is 0.81% at 140kW, and the biggest improvement is 1.53% at 250kW. It is obvious that 43.80% is the highest overall system efficiency with ORC system when the power output of diesel engine is 250kW.

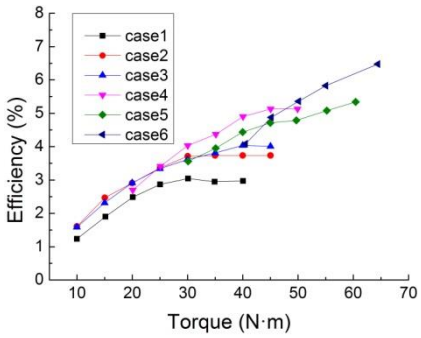

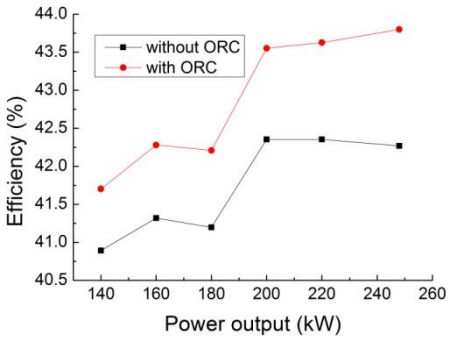

Fig.8: ORC efficiency vs. torqueFig.9: Overall system efficiency vs. power output of diesel engine

Power output indicates the performance of work output for single-screw expanders. Fig.10 shows that power output increases with dryness. The increase is faster at low dryness than it is at high dryness. But there is little difference between the values of power output for different rotational speed at the same dryness, and the biggest power output is 5.12kW, which is shown in fig.10.

Although the power output increases with the increase of inlet vapor dryness, the shaft efficiency of single-screw expander decreases with the increase of dryness, and the maximum is 7%~8% bigger than the minimum, as shown in fig.11. From this figure, it can also be observed that the shaft efficiency at 1200rpm is bigger than that at 900rpm, and the biggest efficiency is nearly 50%.

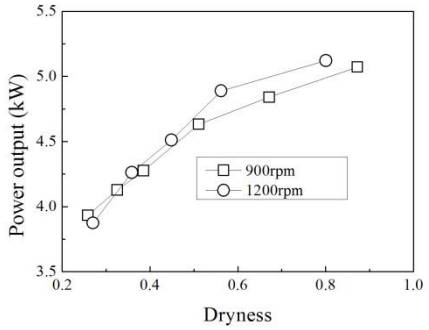

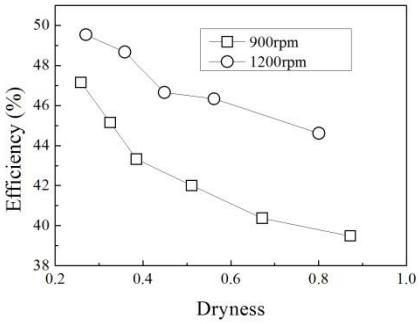

Fig.10: Power output versus inlet vapor dryness**Fig.11**:Shaft efficiency versus inlet vapor dryness

5. CONCLUSION

In this study, the influence of torque of single-screw expander on the performance of ORC used in waste heat recovery is obtained for different conditions of diesel engine. The effects on performance indices of single-screw expander and heat-work conversion efficiency are investigated. Based on the present analysis, the following results are concluded:

(1) Single-screw expander is suitable for small/medium scale ORC system, and it can obtain good performance at low-medium rotational speed. The maximums of power output 10.38kW and shaft efficiency 57.88% are gotten at 1538rpm.

(2)The maximums of volumetric efficiency, adiabatic efficiency and expansion ratio of single-screw expander are 90.73%, 63.46% and 4.6, respectively.

(3) The performance of ORC system is affected not only by the working case of diesel, but also by the torque of single-screw expander. The biggest ORC efficiency is 6.48%, which is gotten at 250kW diesel power output and 64.43N.m of single-screw expander.

(4) With ORC system, the specific fuel consumption of diesel is effectively decreased. When the power output of diesel is 250kW, the specific fuel consumption is decreased by 3.5%, and the overall system efficiency is 43.8%, which is increased by 1.53%.

(5)With the increase of inlet vapor dryness, torque and power output of single-screw expander are rising and the biggest power output is 5.5kW, but the shaftefficiencyof single-screw expanderis decreased by 7%~8%.

In summary, the results of test basically reach the expectation. Meanwhile, it also has great room for improvement. On the one hand, increasing the rotational speed to 2800~3000rpm and decreasing the outlet pressure of the single-screw expander can obtain more power output. On the other hand, optimizing the layout of system and decreasing the weight of main equipment can realize the compact and lightweight design for utilization in a truck. With the continuous improvement of equipment and testing, the system for waste heat recovery from exhaust of fixed and moving internal combustion engine would have great prospects in saving fuel and improving overall system efficiency.

Nomenclature

Variables		Subscripts	
d :	specific oil consumption [kg/(kW·h)]	e :	exhaust gases
h :	specific enthalpy [kJ/kg]	$engine$:	diesel engine
H :	heating value [kJ/kg]	exp :	expander
$\dot{m}$:	mass flow rate [kg/h]	i	ideal
N :	torque [N·m]	in :	inlet
P :	pressure [bar]	is :	isentropic

Pe :	power [kW]	m	measurement
t :	time [s]	oil :	diesel oil
V :	volume flow rate [m^3/h]	ORC :	ORC system
x	vapor dryness	out :	outlet
ε :	expansion ratio [-]	$pump$:	pump in ORC system
η :	efficiency [-]	$R123$:	R123
Δ :	difference [-]	sys :	system
ω :	angular velocity [rad/s]	$total$:	total

REFERENCES

Chammas. R. El, Clodic.D, Combined Cycle for Hybrid Vehicles. SAE Int. Publication 2005-01-1171 (2005).

Qiu, G. Q., Liu, H., Riffat, S., 2011. Expanders for micro-CHP systems with organic Rankine cycle.*Appl. Therm Eng*.,Vol. 31: p. 3301-3307.

Peterson, R.B., Wang,H.,Herron, T.,2008. Performance of small-scale regenerative Rankine power cycle employing a scroll expander, *Proceedings of the Institution of Mechanical Engineers Part A-Journal of Power and Energy*,Vol. 222:p.271-282.

Lemort,V., Quoilin,S.,Cuevas, C., Lebrun,J., 2009. Testing and modeling a scroll expander integrated into an Organic Rankine Cycle, *Appl. Therm Eng.*,Vol. 29: p. 3094-3102.

Wang,W.,Wu, Y. T.,Ma, C. F.et al., 2011.Preliminary experimental study of single-screw expander prototype.*Appl. Therm Eng.*,Vol. 31: p.3684-3688.

He, W., Wu, Y., Peng, Y., Zhang, Y., Ma, C., and Ma, G. (2013). Influence of intake pressure on the performance ofsingle screw expander working with compressed air. *Applied Thermal Engineering*, Vol. 51:p. 662 -- 669.

Wang, W.,Wu, Y.,Ma, C.,Xia, G. andWang, J.,2013. Experimental study on the performance of single screw expanders by gap adjustment, Energy Vol. 62: p. 379-384.

Desideri,A.,Broek M. van den, GusevS. et al.,2014.Experimental campaign and modeling of a low-capacity waste heat recoverysystem based on a single screw expander. *22nd International Compressor Engineering Conference at Purdue*, Paper ID: 1451, P.1-10.

ACKNOWLEDGEMENTS

The authors are also grateful to the financial support by the National Basic Research Program (also called 973 Program) of China under grant number 2011CB707202 andNational Key Technology Support Programof China under grant number 2014BAJ01B05.

EXPERIMENTAL COMPARISON OF A SINGLE SCREW EXPANDER UNDER DIFFERENT OPERATING CONDITIONS AND WORKING FLUIDS

Sergei Gusev*, Davide Ziviani, Martijn van den Broek

Department of Flow, Heat and Combustion Mechanics, Ghent University,
Ghent, Belgium
servei.gusev@ugent.be, davide.ziviani@ugent.be, martijn.vandenbroek@ugent.be

* Corresponding Author

ABSTRACT

During the last years, one of the most popular ways to recover low-grade waste heat is the organic Rankine cycle (ORC). This technology is widely studied and continuously optimized and, as a result, there are many efficient installations available on the market utilizing heat with stable parameters such as from geothermal sources or from the biomass combustion process. However, if a variable hot source in terms of either temperature or flow rate is introduced, the expansion devices have to work at non-optimal conditions, which decrease the global efficiency of ORC installations, e.g. in the case of waste heat recovery. In order to characterize the performance of a positive displacement expander close enough to the optimum, the influence of pressure ratios, filling factor, and working fluid properties on power output is studied. In this paper, experimental results obtained on a small-scale ORC test setup based on an 11 kWe single-screw expander are presented. Two working fluids are used during the tests, i.e. R245fa and SES36 (Solkatherm). These working fluids are common for ORC installations exploiting low-temperature waste heat. The waste heat source is simulated by an electrically heated thermal oil loop with adjustable temperature and flow rate. Various waste heat inlet flow rates are considered in order to find an optimal evaporation pressure and to maximize the power output with different heat source profiles. Based on the experimental data, the expander model is developed. For each working fluid, optimal working conditions are determined. In most cases, there is under-expansion due to a relatively small built-in volume ratio, causing certain losses. By means of the model, the ideal expansion process is simulated and compared with the real one obtained experimentally to quantify these losses and conclusions can be drawn whether significant benefits can be offered by using an optimized expander instead of an ”off-the-shelf” reversed compressor.

1. INTRODUCTION

The organic Rankine cycle (ORC) is mainly used to produce electricity or useful work from heat at lower temperature, which are renewable energy sources, such as solar or geothermal, and low-grade heat produced in an industrial process which cannot be recovered (van den Broek et al., 2012). Solar, with exception of concentrated solar technologies, and geothermal applications are often also characterized by relatively low temperature levels. The ORC technology utilizes this heat, reducing the use of primary energy and CO_2 emission.

A test rig (Fig. 1) was built to demonstrate the ORC technology in the frame of a project granted by IWT Flanders and it is currently used in the ORCNext project (www.orcnext.be) aiming to improve the ORC technology by introducing new types of expanders, advanced cycles, model based predictive control algorithms in combination with an economical analysis. The results obtained during extensive experiments are introduced in this paper in order to contribute to the study on the working fluids behavior in actual installations, e.g. Bracco et al. (2013) and Farrokhi et al. (2013), and to evaluate the impact of different working fluids on the same installation (Huck et al., 2013). While theoretical investigations on

(a) (b)

Figure 1: (a) ORC at UGent, Campus Kortrijk; (b) close view of the single screw expander installed.

the comparison of fluid properties can be found in literature e.g. Badr et al. (1985); Saleh et al. (2007); Quoilin et al. (2011), publications about practical use of different fluids and the relative performance are still rare. In this work, the performance of a unit built from "off the shelf" components and filled subsequently with two working fluids SES36 (Solkatherm) and R245fa is mapped and analyzed, the maximum power output regimes are indicated.

2. ORC TEST SETUP

The ORC test setup is shown in Fig. 1(a). A standard single-screw air compressor has been adjusted by BEP Europe (Ziviani et al., 2014) to operate as an expansion device and connected to an asynchronous generator with 11 kWe nominal electric power. A closer view of the expander is shown in Fig. 1(b). The electrical power produced by the generator is injected into the electric grid by means of a four-quadrant inverter, which also allows to vary the generator rotational speed from 0 to 3600 rpm. The speed of a circulating 14-stage centrifugal pump can also be varied from 0 to 3000 rpm introducing a variable evaporation pressure up to 14 bar. The evaporator, internal heat exchanger and the condenser are three identical brazed plate heat exchangers. A more detailed description of the setup and the sensors installed can be found in a previous publication (Gusev et al., 2014). Thermodynamic parameters which can not be measured directly are calculated in real time using the CoolProp library (Bell et al., 2014). In this analysis, the power consumed by auxiliary equipment is neglected. The thermal power input, $\dot{Q}_{T66,ev,in}$, is guaranteed by a controllable 250 kW electric heater with Therminol 66 (T66) as working medium. The electric power injected to the grid is measured by the inverter. The net power produced by the ORC is obtained by subtracting the pump power from the electric power measured at the grid:

$$\dot{W}_{el,net} = \dot{W}_{el,grid,exp} - \dot{W}_{pp} \tag{1}$$

Due to the absence of a torque meter to measure the expander shaft power, an overall isentropic efficiency that includes the expander and the generator/inverter is defined as follows:

$$\eta_{is,oa,meas} = \frac{\dot{W}_{el,grid,exp}}{\dot{W}_{is,exp}} = \frac{\dot{W}_{el,grid,exp}}{\dot{m}_{r,exp}\left(h_{su,exp} - h_{ex,is,exp}\right)} \tag{2}$$

In order to obtain the isentropic efficiency at the shaft, the generator efficiency and the inverter effectiveness should be accounted for as follows,

$$\eta_{is,sh,exp} = \frac{\dot{W}_{sh,exp}}{\dot{W}_{is,exp}} = \frac{\dot{W}_{el,grid,exp}}{\eta_{mech,gen}\,\epsilon_{el,inv}\left[\dot{m}_{r,exp}\left(h_{su,exp} - h_{ex,is,exp}\right)\right]} \tag{3}$$

The correlations for the generator and the inverter efficiency have been obtained from Melotte (2012). The filling factor is given by:

$$\Phi_{FF} = \frac{\dot{m}v_{su,exp}}{\dot{V}_{swept,th}} = \frac{\dot{m}v_{su,exp}}{2\,z_{sr}\,V_{g,su}\,\left(N_{rot,exp}/60\right)} \tag{4}$$

where the volume of the groove at suction closure, $V_{g,su}$, is determined by the geometric model described in details in Ziviani et al. (2015). Finally, the net cycle efficiency can be expressed as:

$$\eta_{ORC,net} = \frac{\dot{W}_{el,grid,exp} - \dot{W}_{pp}}{\dot{Q}_{T66,ev,in}} \tag{5}$$

The main measured and calculated parameters for both working fluids are summarized in Table 1.

3. EXPERIMENTAL RESULTS

The choice of the experiment operating conditions is based on some typical solar and geothermal applications described in literature (Barbier, 2002; Tchanche et al., 2009; Liu et al., 2013; Zhou, 2014). The temperature of the heat source in many cases is stable over time and therefore has been kept constant during the experiments. Typical temperature range of the heat source considered is between 90 °C and 125 °C. However, the maximum temperature of the heat carrier (Therminol66) is limited to 125 °C because of the expander design that does not allow higher operating temperatures. Another limitation is represented by the maximum pressure that the expander can handle safely. Throughout the tests, the maximum pressure never exceeded 14 bar. The operating conditions of the working fluids are shown in Fig. 2. It can be noted that the condensing pressure of SES36 is typically below atmospheric pressure. Challenges arise to avoid air infiltration in the system, in particular during the idle state. In fact, the design of the installation does not allow to completely prevent leakages because the components are designed for general purposes.

The first experiments were performed with SES36 and successively the installation has been charged with R245fa. Due to the fact that the installation relies on an air-cooler installed on the roof top, the cooling capacity strongly depends on the weather conditions. The fluids have been tested in different months of the year and therefore it is not possible to draw general conclusions on the maximum performance achievable by the system. However, a comparison of the operating conditions of the ORC with the different working fluid has been carried out. Two typical thermodynamic plots (T-s diagram) of the cycle with SES36 and R245fa are shown in Fig. 3.

In order to maintain a stable operation of the setup, a certain superheating level of 10-15 K before the expander was kept, in the case of SES36. The maximum achievable evaporating pressure in this case was about 8 bar, therefore the same pressure was used during the R245fa experiments in order to have a fair comparison. The superheating level of R245fa at the same conditions is much higher, up to 40 K. This cycle configuration leads to a significant exergy loss. Potentially, the heat source can be cooled down much deeper if a lower flow rate is chosen. As a result, a lower power output is detected. Moreover, during the experiments with SES36, a significant subcooling was detected.

One of the aims of the experimental campaign was the characterization of the expander with two different fluids and under different operating conditions. To this end, the mass flow rate is imposed by adjusting the frequency of the pump. However, it was noted that also the rotational speed of the expander influences the mass flow rate of the system. One of the reasons is that the pump is a centrifugal-type and as a consequence the mass flow rate is dependent on the evaporation pressure. Instead the expander is a volumetric machine and the volumetric flow rate is only dependent on the rotational speed. The tests were conducted by varying the frequency of the pump from minimum to maximum at a fixed expander rotational speed. The same procedure has been applied for all the considered expander rotational speeds. In particular, for SES36 only 2000 rpm and 3000 rpm have been tested. Four different speeds have been

Table 1: Summary of the minimum and maximum measured values of the variables considered for both working fluids.

	$p_{su,exp}$ (kPa)	$p_{ex,exp}$ (kPa)	$T_{su,exp}$ (°C)	$\dot{m}_r$ (kg/s)	$\dot{W}_{el,grid}$ (W)	$T_{ex,exp}$ (°C)	T_{cd} (°C)	ΔT_{sh} (K)	ΔT_{sc} (K)	$\eta_{is,oa,exp}$ (-)	η_{ORC} (-)	Φ_{FF} (-)
SES36												
Min	450	90.6	91.65	0.150	1283	73.99	30.91	0.13	9	0.135	0.010	0.897
Max	1028	177.9	125	0.406	7865	102.0	50.87	28	14	0.647	0.092	1.117
R245fa												
Min	566	120	106.7	0.12	1283	75.5	18.82	26	1.9	0.205	0.014	1.038
Max	1230	232	124.9	0.37	7364	104.6	37.12	56	3.7	0.519	0.077	1.331

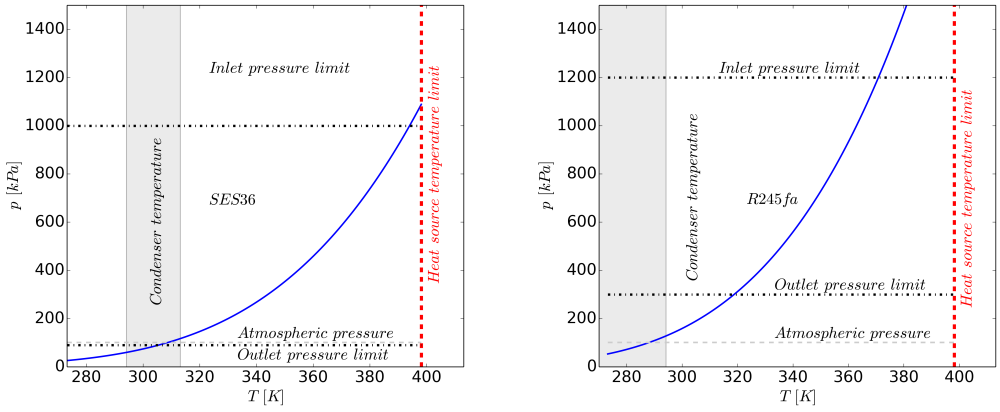

(a) (b)

Figure 2: Working fluid operating conditions during the tests: (a) SES36; (b) R245FA.

tested in the case of R245fa, i.e. 2000 rpm, 2500 rpm, 3000 rpm and 3300 rpm. A total of 43 and 59 steady-state points have been determined for SES36 and R245fa, respectively. The comparison of the fluids is proposed in terms of operating maps as function of power output, isentropic efficiency, mass flow rate, pump and expander rotational speeds as well as ORC efficiency.

4. COMPARISON OF THE WORKING FLUIDS PERFORMANCE

As it can be seen in Fig. 2, an ORC unit filled with R245fa operates at higher working pressures compared with SES36, resulting in lower pressure ratios within the same temperature region. As a consequence, the thermodynamic efficiency of the ORC running with R245fa is slightly lower. The condenser pressure is very close to the expander limit of 3 bar, especially during summer. This pressure corresponds to a temperature of about 45 °C. Taking into account a certain temperature difference between the condenser and the ambient temperatures caused by the air-type cooling loop, the current combination of working fluid and expander is not appropriate for regions with a hot climate. An expander suitable to withstand higher working pressures is needed in order to avoid emergency shut-downs if R245fa is used. An advantage of R245fa over SES36 is that the condensing pressure is higher than the ambient which prevents non-condensable gases in the system. On the other hand, higher working pressures mean in general higher leakage flows and the loss of working fluid through flanges and shaft seals. The cost of the low-GWP working fluids is non-negligible especially for larger installations. The absence of subcooling caused by non-condensable gasses in the condenser is an advantage from a thermodynamic point of view but increases the duty of the circulating pump. A saturated working fluid can start boiling in the suction line due to a certain local pressure drop preventing pump to work properly. In some cases under a variable

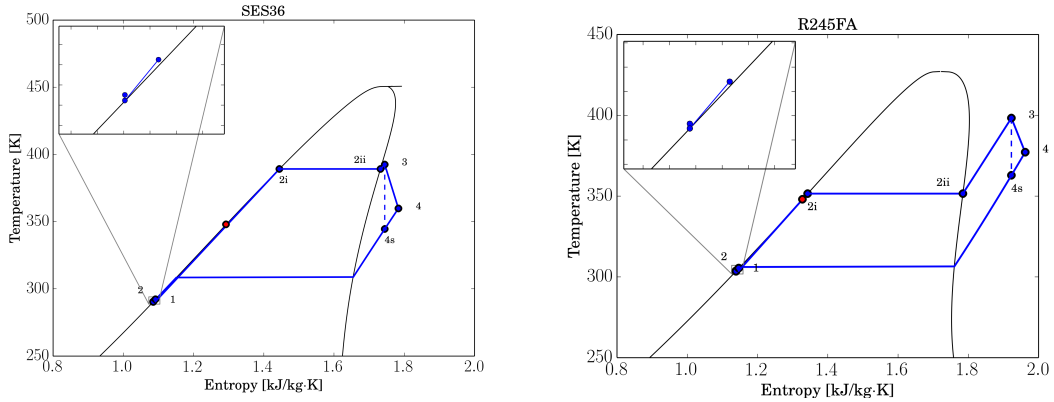

(a) (b)

Figure 3: Examples of thermodynamic plots obtained from the experiments:(a) **SES36 ;**(b) **R245fa. The outlet state of the regenerator prior entering the evaporator is marked with a red dot.**

cooling temperature this phenomenon can completely block the flow.

The steady-state points obtained for both fluids are plotted in Fig. 4, where the power output of the expander, $\dot{W}_{el,grid}$, is given as function of the pressure ratio, $r_{p,exp}$, for different rotational speeds. The isentropic efficiency is indicated by a color scale. It is possible to notice that there is a quasi-linear trend between power output and pressure ratio.

For most of the points, the power output increases with the increase of both pressure ratio and rotational speed. This can be easily observed by considering the rotational speeds of 2000 rpm and 3000 rpm. Regarding the rotational speeds of 2500 rpm and 3300 rpm for R245fa, shown in Fig. 4(b), a similar consideration can be made, i.e. the higher the rotational speed and the pressure ratio, the higher the power output, by keeping in mind that these steady-state points were obtained during a very warm day which affected the condensing pressure. The pressure ratio range achievable was limited both at high pressure side (limit set by maximum pressure of expander) and low pressure side because of high external temperature.

The ORC installation operates most of the time at pressure ratios higher than the pressure ratio corresponding to the built-in volume ratio of the expander, $r_{v,built-in}$ = 4.7 (Ziviani et al., 2015), causing an over-expansion. While the power output at the same pressure ratio is similar for both fluids, the expander isentropic efficiency is slightly higher in the case of SES36. At low pressure ratios and power, the influence of the expander rotational speed is limited. Maximum and minimum values of the performance of each fluid are listed in Table 1.

The operating conditions of both working fluids are presented with three performance maps shown in Fig. 5, 6, 8. In Fig. 5, 6, the mass flow rates of SES36 and R245fa and the isentropic efficiency versus the expander and the pump rotational speeds are shown , respectively. A higher mass flow of R245fa at the same conditions is caused by its lower density in comparison with SES36. The influence of the expander rotational speed is less significant than the pump rotational speed for both fluids. The trend for the pump rotational speed is almost linear, as shown in Fig. 7, so higher rotational speeds can be recommended in order to achieve a higher performance. The maximum isentropic efficiency of the expander is achieved at the nominal speed of 3000 rpm for both fluids. The third set of performance maps, in Fig. 8, assesses the optimum operating conditions, in terms of cycle efficiency, η_{ORC}, of the ORC system for different thermal input, $\dot{Q}_{T66}$, and degree of superheating, ΔT_{sh}. The cycle efficiency is related to the degree of superheating and the working fluid. In particular, in the case of SES36, the maximum cycle efficiency is observed with a range of the degree of superheating of 5-10 K, as shown in Fig. 8(a). Instead, in the

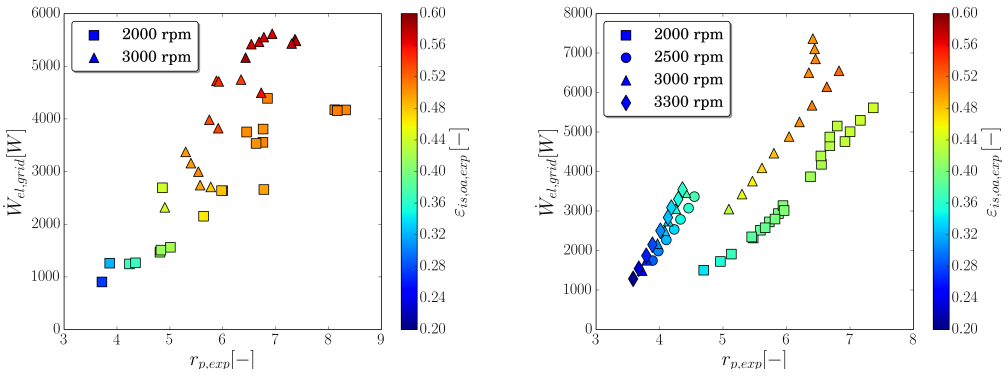

Figure 4: Power output as a function of different pressure ratios: (a) SES36 ;(b) R245fa. The color scale indicates the overall isentropic efficiency.

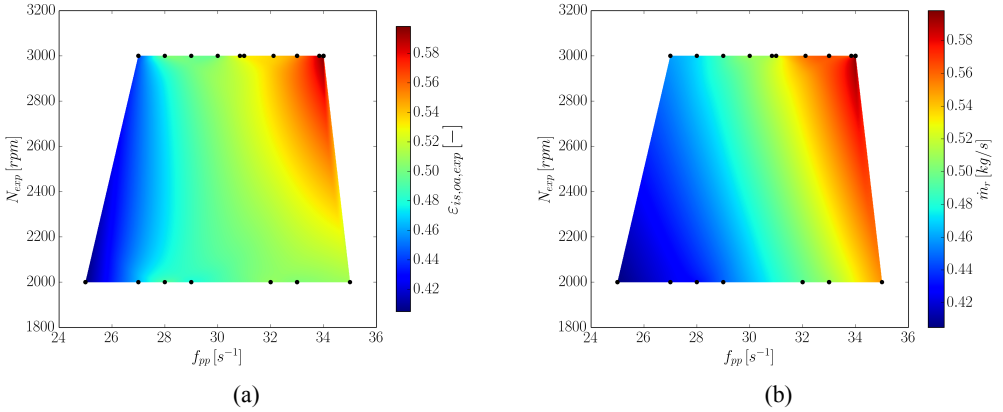

Figure 5: Operating maps of SES36: (a) overall isentropic efficiency as function of pump and expander rotational speeds; (b) mass flow rate as function of pump and expander rotational speeds.

case of R245fa, the cycle efficiency is maximized at higher values of the superheating, 30-35 K, Fig. 8(b).

The operating stability of the system and different conditions have also been investigated. During the experiments, an unstable operation characterized by a fluctuating mass flow rate of the working fluid was detected when the working fluid was entering the expander close to the vapor saturation point. A decrease of the evaporation pressure resulted in an increase of the mass flow rate, which is a sign of a wet expansion. A drop in both power output and isentropic efficiency occurred.

5. CONCLUSIONS

In this paper, the performance of an non-optimized ORC unit operating subsequently with two different working fluids under the same conditions is mapped. The efficiency of the ORC system components is not constant during operation and it is influenced by the dynamic behavior of each component. Based on the experimental results, an optimal rotational speed of the circulating pump and the expander can be found for each typical working condition such as the flow rate, the temperature of the heat source and the ambient temperature. These settings could be implemented in a feed-forward control of an installation the operates with a variable heat input.

For the given temperature level and the current installation, SES36 is more optimal than R245fa. For

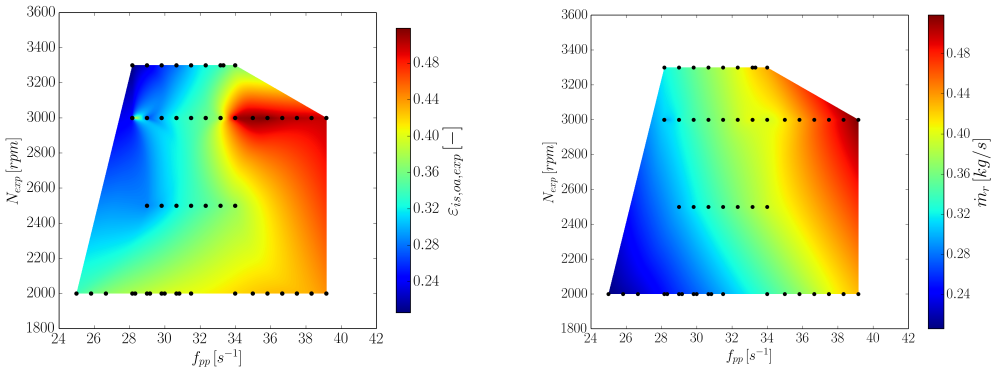

Figure 6: Operating maps of R245fa: (a) overall isentropic efficiency as function of pump and expander rotational speeds; (b) mass flow rate as function of pump and expander rotational speeds.

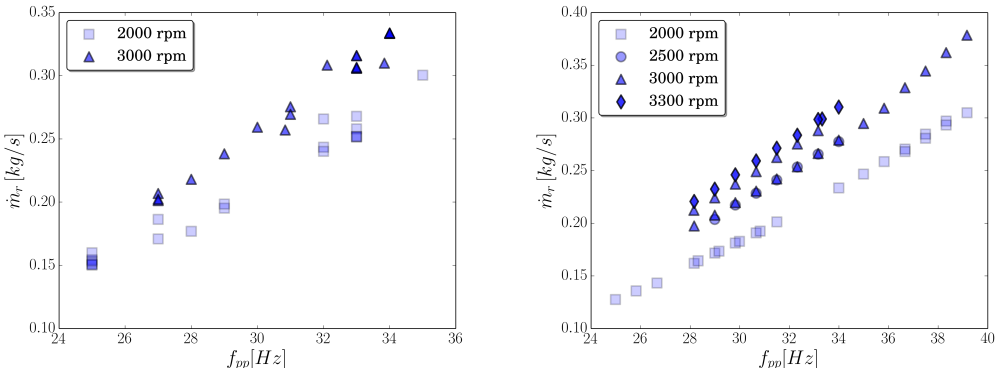

Figure 7: Influence of the pump frequency on the mass flow rate at different expander rotational speeds: (a) SES36; (b) R245fa.

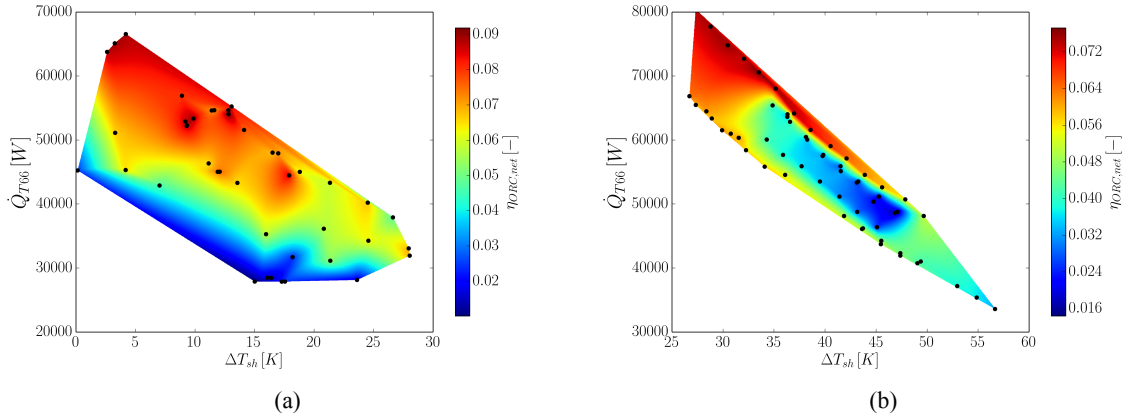

Figure 8: Net cycle efficiency as function of thermal power and degree of superheating: (a)SES36; (b) R245FA.

both fluids, operation at superheating levels lower than 5 K should be avoided due to difficulties in maintaining a stable mass flow rate.

REFERENCES

Badr, O., Probert, S. D., and O'Callaghan, P. (1985). Selecting a working fluid for a Rankine cycle engine. *Applied Energy*, 21:1–42.

Barbier, E. (2002). Geothermal energy technology and current status: an overview. *Renewable and Sustainable Energy Reviews*, 6:3–65.

Bell, I. H., Wronski, J., Quoilin, S., and Lemort, V. (2014). Pure and pseudo-pure fluid thermophysical property evaluation and the open-source thermophysical property library CoolProp. *Industrial & Engineering Chemistry Research*, 53(6):2498–2508.

Bracco, R., Clemente, S., Micheli, D., and Reini, M. (2013). Experimental tests and modelization of a domestic-scale ORC (organic Rankine cycle). *Energy*, 58(1):107–116. ISSN 0360-5442.

Farrokhi, M., Noie, S. H., and Akbarzadeh, A. A. (2013). Preliminary experimental investigation of a natural gas-fired ORC-based micro-CHP system for residential buildings. *Applied Thermal Engineering*, 7. ISSN 1359-4311.

Gusev, S., Ziviani, D., Bell, I., De Paepe, M., and van den Broek, M. (2014). Experimental comparison of working fluids for organic Rankine cycle with single-screw expander. In *Proceedings of the International Refrigeration and Air Conditioning Conference*. Paper 1548.

Huck, P., Laursen, A. L., Zia, J., and Woolley, L. (2013). Identification and test of low global warming potential alternatives to HFC-245fa in organic Rankine cycles. In *Proceedings of the 2nd International Seminar on ORC Power Systems*, Rotterdam, Netherlands.

Liu, Q., Duan, Y., and Yang, Z. (2013). Performance analyses of geothermal organic Rankine cycles with selected hydrocarbon working fluids. *Energy*, 63:123–132. ISSN 0360-5442.

Melotte, N. (2012). Experimental study and dynamic modeling of a waste heat recovery organic Rankine cycle. Master's thesis, University of Liege.

Quoilin, S., Declaye, S., Tchanche, B. F., and Lemort, V. (2011). Thermo-economic optimization of waste heat recovery organic Rankine cycles. *Applied Thermal Engineering*, 31(14):2885–2893.

Saleh, B., Koglbauer, G., Wendland, M., and Fischer, J. (2007). Working fluids for low temperature organic Rankine cycles. *Energy*, 32:1210–1221.

Tchanche, B. F., Papadakis, G., Lambrinos, G., and Frangoudakis, A. (2009). Fluid selection for a low-temperature solar organic Rankine cycle. *Applied Thermal Engineering*, 29:2468–2476.

van den Broek, M., Vanslambrouck, B., and De Paepe, M. (2012). Electricity generation from biomass: Organic Rankine cycle versus steam cycle. In *Proceedings of the Conference and Exhibition on Biomass for Energy*, Jönköping, Sweden.

Zhou, C. (2014). Hybridisation of solar and geothermal energy in both subcritical and supercritical organic Rankine cycles. *Energy Conversion and Management*, 81:72–82. ISSN 0196-8904.

Ziviani, D., Bell, I., van den Broek, M., and De Paepe, M. (2014). Comprehensive model of a single-screw expander for ORC-systems. In *Proceedings of the International Compressor Engineering Conference*. Paper 2357.

Ziviani, D., Bell, I. H., De Paepe, M., and van den Broek, M. (2015). Update on single-screw expander geometry model integrated into an open-source simulation tool. In *9th Int. Conf. on Compressors and their Systems, City University of London, London*, number 39.

NOMENCLATURE

c_p	specific heat at constant pressure	(J/kg-K)	**Subscript**	
$\dot{m}$	mass flow rate	(kg/s)	exp	expander
f_{pp}	pump frequency	(Hz)	el	electric
N	rotational speed	(rpm)	ev	evaporator
p	pressure	(Pa)	gen	generator
$\dot{Q}$	heat rate	(W)	is	isentropic
r_p	pressure ratio	(-)	in	inlet
T	temperature	(K, °C)	inv	inverter
v	specific volume	(m^3/kg)	meas	measured
V	volume	(m^3)	oa	overall
$\dot{W}$	power	(W)	pp	pump
z_{sr}	number of starwheel tooth	(-)	r	refrigerant
Φ_{FF}	filling factor	(-)	sc	subcooling
ϵ	effectiveness	(-)	su	supply
η	efficiency	(-)	sh	superheating
Subscript				shaft
cd	condenser		th	theoretical
ex	exhaust		T66	Therminol66

ACKNOWLEDGEMENT

The financial support is provided by the Institute for the Promotion and Innovation by Science and Technology in Flanders. All data and results presented in this survey have been obtained in the frame of the IWT SBO-110006 project “The Next Generation Organic Rankine Cycles”: www.orcnext.be

PERFORMANCE ANALYSIS OF ORC SYSTEM WITH IHE USING THE ZEOTROPIC MIXTURE AND THE PURE WORKING FLUID FOR VEHICLE CNG ENGINE

Songsong Song[1,2]*, Hongguang Zhang[1,2]

[1]College of Environmental and Energy Engineering, Beijing University of Technology, Pingleyuan No.100, 100124 Beijing, China
e-mail: qihesong@126.com
[2]Collaborative Innovation Center of Electric Vehicles in Beijing, Pingleyuan No.100, 100124 Beijing, China
* Corresponding Author

ABSTRACT

In order to improve the thermal efficiency of compressed natural gas (CNG) engine, a set of organic Rankine cycle (ORC) system with internal heat exchanger (IHE) is designed to recover exhaust waste heat from the CNG engine. The working fluids under investigation are the pure working fluid R245fa and the zeotropic mixture R416A. Subsequently, the influence of the two different working fluids on performance parameters such as net power output, thermal efficiency, exergy efficiency and output energy density of working fluid are analyzed. The results show that the zeotropic mixture R416A performs better. Finally, a combined CNG engine and ORC system with IHE is defined to evaluate the performance improvement. Results show that compared with the CNG engine, the thermal efficiency of the combined system can be increased by a maximum 7%.

1. INTRODUCTION

The thermal efficiency of most compressed natural gas (CNG) engines are 30% or so and they are lower than that of diesel engines, large amount fuel energy are rejected from CNG engines to the surroundings as waste heat, with a significant fraction through the exhaust. Therefore, recovering the exhaust waste heat from CNG engine so as to improve thermal efficiency and save fuel has become a hot focus of recent research work (Wang et al., 2014).

The organic Rankine cycle (ORC) is a promising method to recover waste heat from internal combustion engines (ICE) exhaust gas (Chiew *et al*., 2011, Wang *et al*., 2011, Zhang *et al*., 2014). Vaja *et al*. (2010) designed a power cycle equipment to match a stationary internal combustion engine, and accordingly chose three pure working fluids to examine three different ORC schemes separately. The analysis demonstrated that a 12% increase in the total efficiency could be achieved with respect to the engine with no ORC cycle. Yang *et al*. (2014) designed a set of dual loop ORC system to recover exhaust energy, waste heat from the coolant system, and released heat from turbocharged air in the intercooler of a six-cylinder diesel engine. R245fa was selected as the working fluid for both loops. The results showed that the dual loop ORC system achieves the largest net power output at 27.85 kW at the engine rated condition. Compared with the diesel engine, the thermal efficiency of the combined system can be increased by 13%.Yu *et al*. (2013) built an ORC system to recover waste heat both from engine exhaust gas and jacket water using R245fa as working fluid. Results indicated that the ORC system performances well under the rated engine condition with expansion power up to 14.5 kW, recovery efficiency up to 9.2% and exergy efficiency up to 21.7%. Combined with bottoming ORC system, thermal efficiency of diesel engine can be improved up to 6.1%.

For the working fluids of ORC system, the match of working fluids with heat source and systems significantly affects system performance. Zeotropic mixtures have a property called "temperature glide" in evaporation and condensation process and this can reduce exergy destruction rate due to heat transfer temperature difference (Wu *et al*., 2012). Radulovic and Castaneda (2014) proposed six zeotropic mixtures for conducting a parametric optimisation of supercritical Rankine cycle powered by low temperature geothermal heat source. And then a comparative analysis between the zeotropic mixtures and pure R-143a was studied. The results showed that the cycle efficiency can be improved by 15% at the same operational conditions. Lecompte *et al*. (2014) examined the thermodynamic performance of non-superheated subcritical organic Rankine cycles (ORCs) with zeotropic mixtures as working fluids based on a second law analysis. The results showed that an increase in second law efficiency in the range of 7.1% and 14.2% is obtained compared to pure working fluids. Furthermore, between optimized ORCs with zeotropic mixtures as working fluid the difference in second law efficiency varies less than 3 percentage points.

According to abovementioned analysis, zeotropic mixtures have bigger potential in optimizing the ORC system performances than pure working fluids, whereas few scholars use zeotropic mixtures for an ORC system in recovering the exhaust energy from a CNG engine.

2. EVALUATION OF EXHAUST WASTE HEAT FROM CNG ENGINE

To design an optimal ORC system that can efficiently recover the exhaust waste heat from CNG engine, it is necessary to analyze the energy distribution in the running process of the engine. In this paper, a six-cylinder four-stroke CNG engine was employed, and the main performance parameters were listed in Table 1. Based on the performance test data of engine experimental system, the running performances and exhaust energy of the CNG engine under various operating conditions were analyzed. During the experiment, the CNG engine speed ranged from 1800 r/min to 2200 r/min at an interval of 200 r/min. The eleven operating condition points were selected and tested under each engine speed.

Table 1: Main technical performance parameters of the CNG engine

Items	Parameters	Units
Cylinder number	6	
Rated power	206	kW
Displacement	8.3	L
Stroke and cylinder bore	135×114	mm
Compression ratio	10.5	
Maximum torque	1050	N.m

The universal characteristic of CNG engine is shown in Figure 1. As seen in this figure, the blue contour lines indicate the variations in the effective power output of the engine under engine various operating conditions. The black contour lines indicate the variations in the brake specific fuel consumption (BSFC) of the engine under engine various operating conditions. At the engine rated condition, the effective power output of the CNG engine is 206.9 kW. In addition, the brake specific fuel consumption (BSFC) is relatively low in the engine's medium speed with medium-high load regions. On the contrary, the brake specific fuel consumption (BSFC) is relatively higher in the engine's low load region, particularly in the high speed region. When the engine speed is 1400 r/min and engine torque is 1050 N.m, the CNG engine achieves the optimal fuel economy, and the BSFC is 199 g/(kW.h).

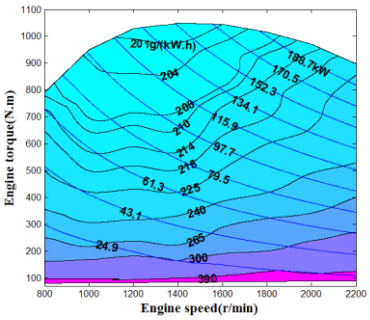

Figure 1: Universal characteristic of CNG engine

Figure 2 shows the thermal efficiency under engine various operating conditions. The thermal efficiency η_{en} can be calculated using the following equation:

$$\eta_{en} = \frac{\dot{W}_{en}}{\dot{Q}_f} \tag{1}$$

Where, $\dot{W}_{en}$ is the effective power output of CNG engine, $\dot{Q}_f$ is the fuel combustion energy which can be calculated using the fuel consumption rate and fuel lower heating value. In this paper, the fuel lower heating value is 50050 kJ/kg.

As seen in the Figure 2, the thermal efficiency increases with the engine torque. On the other hand, the thermal efficiency firstly increases and then decreases with engine torque, whereas the variation trend is not especially obvious in the engine's low load region. When the engine speed is 1400 r/min and engine torque is 1050 N.m, the thermal efficiency of CNG engine can reach up to a maximum of 36.14%.

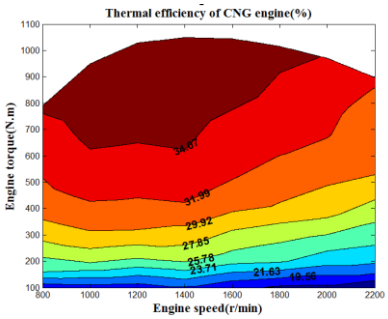

Figure 2: Thermal efficiency of CNG engine

Figure 3 illustrates the variation of exhaust temperature in different engine speed with the engine torque. As shown in Figure 3, exhaust temperature is relatively low under low speed with low torque conditions, and relatively high under both medium-high speed and medium-high torque conditions. But the overall variation trend is complex. From Figure 3 it can be seen that exhaust temperature is in the range of 730 K to 900 K.

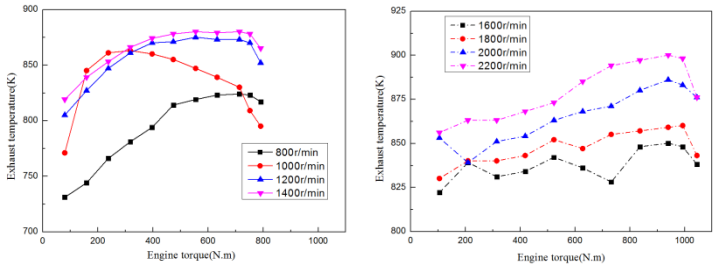

Figure 3: Exhaust temperature of CNG engine

When calculating exhaust energy, methane is assumed to be the natural gas fuel and other substances contained in the natural gas are ignored for this study. Air-fuel ratio of the CNG engine is set to 17.2 (by mass). According to chemical reaction equation for the combustion process, mass fraction of the exhaust components CO_2、H_2O and N_2 is 15.1%、12.4% and 72.5%, respectively. Subsequently, the specific enthalpy of the exhaust under a specific temperature is calculated using the thermodynamic calculation method of ideal gas and REFPROP 9.0 software. In addition, exhaust mass flow rate $\dot{m}_{\mathrm{exh}}$ can be calculated using air-fuel ratio and fuel consumption which measured by experiment. Finally, the exhaust energy $\dot{Q}_{\mathrm{exh}}$ of CNG engine can be calculated using equation (2).

$$\dot{Q}_{\mathrm{exh}} = \dot{m}_{\mathrm{exh}} h_{\mathrm{exh}} \tag{2}$$

Where, h_{exh} is the specific enthalpy of the exhaust.

In practical ORC system, exhaust energy can not be totally absorbed by working fluids (Yu *et al.* 2013). Therefore, in this paper, the exhaust temperature and pressure at the outlet of evaporator are set to 378 K and 97.8 kPa, respectively. Subsequently, specific enthalpy of the exhaust under the set exhaust temperature and pressure is calculated using REFPROP 9.0 software. Finally the available exhaust energy rate can be calculated using equation (3).

$$\dot{Q}_{ava} = \dot{m}_{\mathrm{exh}} (h_{\mathrm{in}} - h_{\mathrm{out}}) \tag{3}$$

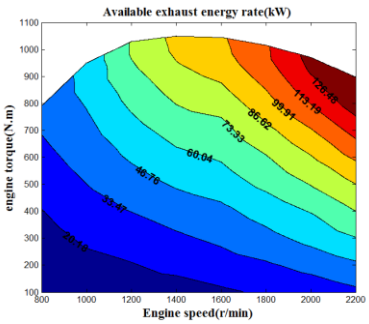

Figure 4: Available exhaust energy rate of CNG engine

According to the performance test data of CNG engine, the variation tendency of available exhaust energy rate under engine various operating conditions is shown in Figure 4. It is evident that available exhaust energy rate increases over the engine whole operating range, achieving 139.58 kW at the engine rated condition.

3. EXHAUST WASTE HEAT RECOVERY SYSTEM BASED ON ORC WITH IHE

3.1 System Description

In order to recover the exhaust waste heat from CNG engine efficiently, the ORC system with IHE is designed as shown in Figure 5. The system consists of an evaporator, a condenser, an expander, a recuperator (namely IHE), a pump, a reservoir and a generator. At first, the exhaust gas exchanges heat with the organic working fluid in the evaporator, then the exhaust gas is released through evaporator into the atmosphere. Meanwhile the organic working fluid turns into high-temperature and high-pressure gas and soon enters expander to generate electricity. Later, the organic working fluid exhausted from the expander goes into the recuperator to exchange heat with the liquid organic working fluid which exported from the pump. Subsequently, the cooled working fluid that is exhausted from recuperator condenses into a saturated liquid state and flows into the reservoir. The organic working fluid is pressurized by using pump and then absorbs heat in the recuperator. Finally, the organic working fluid flows into the evaporator to absorb the heat from engine exhaust.

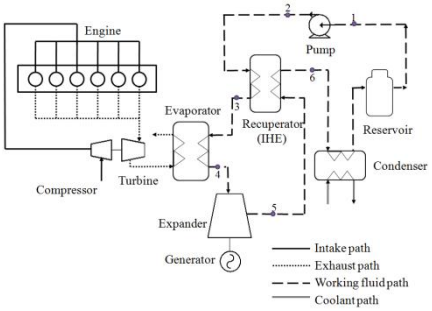

Figure 5: Schematic diagram of ORC system with IHE

3.2 Working Fluid Selection

The selection of working fluids has an important impact on thermodynamic performances of the ORC system. In this paper, there are two kinds of working fluids have been selected to study the performances of ORC system. Therein R245fa has performed well as the working fluid in ORC systems in many studies (Wang *et al*. 2011, Wang *et al*. 2012). In addition, because of the good environment friendliness and safety, zeotropic mixture R416A with property of temperature glide has been selected from the existing serial-numbered refrigerant for this study. The properties of R416A and R245fa are listed in Table 2.

Table 2: Properties of R416A

Parameters	R416A	R245fa
Components	R134a/R124/R600	~
Composition (mass fraction)	0.59/0.395/0.015	~
Critical temperature (K)	380.23	427.16
Critical pressure (MPa)	3.98	3.651
Glide temperature (K)	1.86	~
Safety	A1	B1
Environment friendliness (Yes/No)	Yes	Yes
Fluid type	Wet	Dry

Glide temperature: standard atmospheric pressure.

3.3 Thermodynamic Model

Figure 6 is the *T-s* diagram of the working fluid. Therein Process 1-2 is the actual pressurization process of pump, process 1-2s is the isentropic pressurization process. Process 2-3 is the isobaric endothermic process of the working fluids in the recuperator. Process 3-4 is the isobaric endothermic process, Process 4-5s is the isentropic expansion process, while the process 4-5 is the actual expansion process. Process 5-6 is the isobaric exothermic process of the organic working fluid in the recuperator. Process 6-1 is the isobaric condensation process. Process $T_{\text{exh\_in}}$ - $T_{\text{exh\_out}}$ is the heat transfer process of the engine exhuast in the evaporator, $T_{\text{exh\_in}}$ is the exhaust gas temperaturte at the inlet of the evaporator, $T_{\text{exh\_out}}$ is the exhaust gas temperaturte at the outlet of the evaporator.

Based on the first and second laws of thermodynamics, the performance parameters of ORC system with IHE are calculated using the following equations:

In the process 1-2, the power consumption $\dot{W}_{\text{p}}$ is calculated with the equation below.

$$\dot{W}_{\text{p}} = \dot{m}(h_2 - h_1) = \frac{\dot{m}(h_{2s} - h_1)}{\eta_p} \tag{4}$$

Where, $\dot{m}$ is mass flow rate of organic working fluid, η_p is isentropic efficiency of pump.

In the processes 2-3 and 5-6, the heat transfer rate $\dot{Q}_{\text{r}}$ of the recuperator is calculated using the following equation:

$$\dot{Q}_{\mathrm{r}} = \dot{m}(h_3 - h_2) = \dot{m}(h_5 - h_6) \tag{5}$$

ε is the effectiveness of recuperator, which can be calculated using equation (6):

$$\varepsilon = (T_5 - T_6)/(T_5 - T_2) \tag{6}$$

In the process 3-4, the heat transfer rate $\dot{Q}_{\mathrm{e}}$ of the evaporator is calculated using the following equation:

$$\dot{Q}_{\mathrm{e}} = \dot{m}(h_4 - h_3) \tag{7}$$

In the processes 4-5 and 4-5s, the power output $\dot{W}_{\mathrm{s}}$ of the expander is calculated using the following equation:

$$\dot{W}_{\mathrm{s}} = \dot{m}(h_4 - h_5) = \dot{m}(h_4 - h_{5\mathrm{s}})\eta_{\mathrm{s}} \tag{8}$$

Where, η_{s} is isentropic efficiency of expander.

In the process 6-1, the heat transfer rate $\dot{Q}_{\mathrm{c}}$ of the condenser is calculated using the following equation:

$$\dot{Q}_{\mathrm{c}} = \dot{m}(h_6 - h_1) \tag{9}$$

In the all equations, h and its subscripts represent the specific enthalpy value of each state point in the *T-s* diagram.

According to the above analysis, the net power output, thermal efficiency and exergy efficiency of ORC system with IHE are respectively calculated using the following equations:

$$\dot{W}_{\mathrm{n}} = \dot{W}_{\mathrm{s}} - \dot{W}_{\mathrm{p}} \tag{10}$$

$$\eta_{\mathrm{th}} = \frac{\dot{W}_{\mathrm{n}}}{\dot{Q}_{\mathrm{e}}} \tag{11}$$

$$\eta_{\mathrm{ex}} = \frac{\dot{W}_{\mathrm{n}}}{\dot{Q}_{\mathrm{e}}(1 - \frac{T_{\mathrm{L}}}{T_{\mathrm{H}}})} \tag{12}$$

Where, T_{H} is the temperature of the high temperature heat source that can be calculated using equation (13). $T_{\mathrm{exh\_in}}$ can be measured through engine test. $T_{\mathrm{exh\_out}}$ is the exhaust temperature at the outlet of evaporator. T_{L} is the temperature of the low temperature heat source.

$$T_{\mathrm{H}} = (T_{\mathrm{exh\_in}} - T_{\mathrm{exh\_out}}) / \ln(T_{\mathrm{exh\_in}} / T_{\mathrm{exh\_out}}) \tag{13}$$

In addition, output energy density of working fluid ρ is defined to evaluate the capability to produce useful work for per unit of mass of working fluids. Its calculation equation as follows:

$$\rho = \frac{\dot{W}_{\mathrm{n}}}{\dot{m}} \tag{14}$$

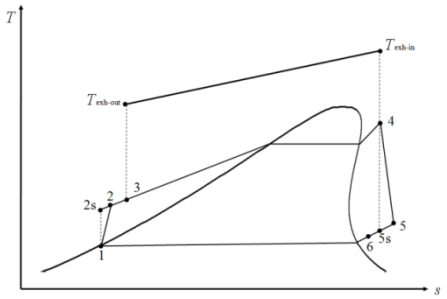

Figure 6:*T-s* diagram of ORC system with IHE

4. RESULTS AND DISCUSSION

4.1 Boundary Conditions

In order to analyze the effects of R416A and R245fa on the performance of ORC system with IHE, in this paper, the boundary conditions are set as follows:

(1) Pressure drop and heat loss in each component as well as pipelines are neglected.
(2) Evaporation pressure is set to 2.5 MPa.
(3) The degree of superheat and T_L are set to 30 K and 293 K, respectively.
(4) The isentropic efficiencies of the expander and the pump are both set to 0.8.
(5) The working fluid releases heat in the condenser and then turns into a saturated liquid state.
(6) The expansion ratio of expander is set to 4.
(7) The effectiveness of recuperator is set to 0.85.

4.2 Results Analysis

Figure 7 illustrates how the net power output of the ORC system with IHE using the two different working fluids changes over the engine whole operating range. As shown in Figure 7(a) and (b), the variation tendency of the net power output using the two different working fluids are consistent, while the values are different. The net power output of the ORC system with IHE using the two working fluids increases with the increase of the engine's speed and load. At the engine's rated condition, the net power output for R416A reaches a maximum of 16.6 kW and a maximum of 16.0 kW for R245fa. Additionally, comparing Figure 7(a) and (b) shows that the net power output for R416A is larger than that of R245fa for each engine operating conditions. Therefore, by employing zeotropic mixture R416A, the performance of ORC system with IHE has better characteristics of power output.

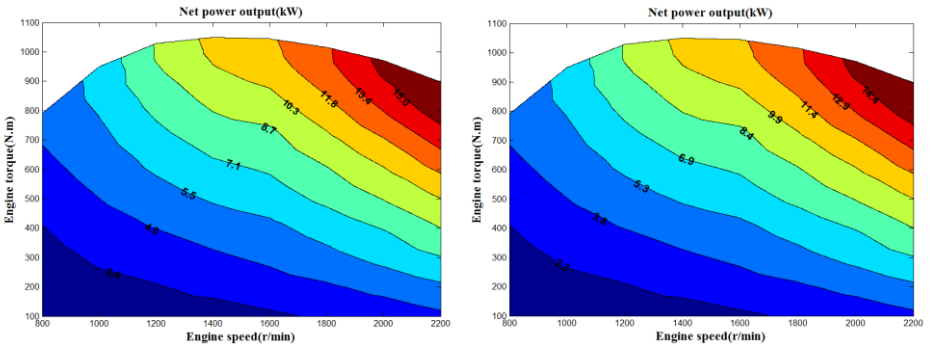

(a) Net power output of R416A (b) Net power output of R245fa

Figure 7: Net power output of ORC system with IHE

The results of the ORC system with IHE using the two different working fluids are summarized in Table 3. As shown in Table 3, the thermal efficiency and output energy density of working fluid for R416A are all larger than that of R245fa. For the same net power output of ORC system with IHE, the higher output energy density of working fluid, the less mass flow rate of working fluid is required for ORC system that can obviously reduce the working fluid mass filled in the ORC system. The total weight of the ORC system not only can be reduced but also the risk of environmental pollution can be significantly decreased.

Table 3: The results of two different working fluids

Performance parameters	Working fluids	
	R416A	R245fa
Thermal efficiency (%)	11.9%	11.4%
Condensing temperature (K)	299.7	344.1
Output energy density of working fluid (kJ/kg)	22.8	21.8

On the other hand, as listed in Table 3, we can see that the condensing temperature for R416A is lower than that of R245fa. As we all know, condensing temperature is one of the key factors which

can influence the running performance of ORC system. Although the lower condensing temperature is beneficial for the running of ORC system, in practical application, the lower condensing temperature needs the higher-performance cooling system which can increase the cost of ORC system.

Figure 8 illustrates the variation of exergy efficiency with CNG engine speed and load. As shown in the Figure 8 (a) and (b), the variation tendencies of exergy efficiency using the two different working fluids are consistent. Namely, the exergy efficiency of ORC system with IHE is higher in the engine's low speed with low load regions. Whereas the exergy efficiency is lower in the engine's medium-high speed with medium-high load regions. The reason can be analyzed as follows: according to the equation (12), for the selected working fluid, exergy efficiency only depends on the exhaust temperature on the condition that the temperature of low temperature heat source is constant. Moreover, the variation trend of exhaust temperature is shown in Figure 3.

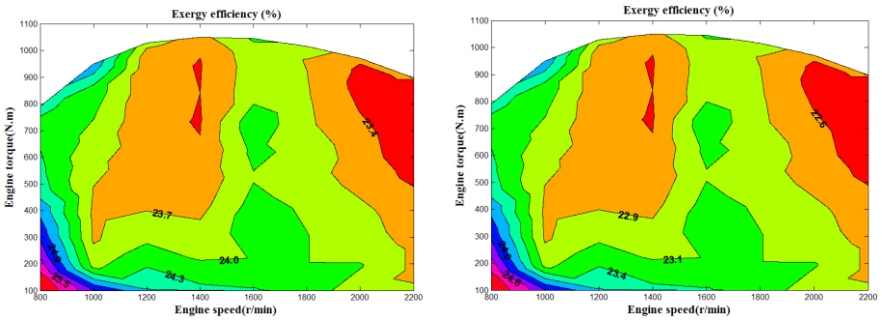

(a) Exergy efficiency of R416A (b) Exergy efficiency of R245fa

Figure 8: Exergy efficiency of ORC system with IHE

According to all of the results described above, we can conclude that the ORC system with IHE using R416A as the working fluid displays superior thermodynamic properties. Therefore, in order to optimize the power system as a whole and evaluate the improvement in overall power output, a ''combined CNG engine and ORC system with IHE'' is defined. The thermal efficiency of combined system η_{com} is calculated using the following equation:

$$\eta_{\mathrm{com}} = \frac{\dot{W}_{\mathrm{n}} + \dot{W}_{\mathrm{en}}}{\dot{Q}_{\mathrm{f}}} \tag{15}$$

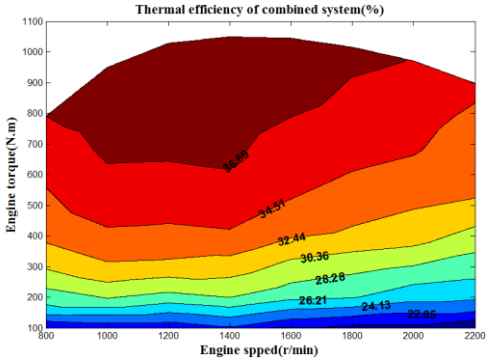

Figure 9: Thermal efficiency of combined system

The thermal efficiency of combined system is shown in Figure 9. When the engine speed is constant, the thermal efficiency of combined system increases with engine torque. On the other hand, when the engine torque is constant, the thermal efficiency of combined system firstly increases and then decreases with engine speed. When the engine speed is 1400 r/min and engine torque is 1050 N.m, the maximum thermal efficiency of combined system is 38.67%, which is higher than that of CNG engine by 7.0%.

5. CONCLUSIONS

- When evaporation pressure is 2.5 MPa and expansion ratio of expander is 4, the output energy density of working fluid, net power output, thermal efficiency, and exergy efficiency of ORC system with IHE using zeotropic mixture R416A are all superior to the same system using R245fa. Therefore, zeotropic mixtures have bigger potential in optimizing the ORC system performances than pure working fluids
- For the ORC system with IHE, condensing temperature for R416A is lower than that of R245fa. Although the lower condensing temperature is beneficial for the running of system, in engineering application, extremely low condensing temperatures cause difficulties in economically providing a low temperature heat source.
- The thermal efficiency of combined system increases with engine load, which is higher than that of CNG engine by 7.0%. From the viewpoint of power performance, the ORC system with IHE is a promising scheme to recover the exhaust waste heat from a CNG engine.

NOMENCLATURE

h	enthalpy	(kJ/kg)
s	entropy	(kJ/kg·K)
$\dot{m}$	mass flow rate	(kg/s)
$\dot{W}$	power	(kW)
T	temperature	(K)
$\dot{Q}$	heat transfer rate	(kW)
η	efficiency	(–)
ε	effectiveness of recuperator	(–)

Subscript

1,2,2s,3,4,5,5s,6	state point in cycle
p	pump
e	evaporator
s	expander
r	recuperator
n	net
c	condenser
exh	exhaust gas
in	inlet
out	outlet
L	low temperature heat source
H	high temperature heat source
th	thermal
com	combined system
en	engine
ex	exergy
f	fuel
ava	available

REFERENCES

Zhang, J., Zhang, H.G., Yang, K., et al, 2014, Performance analysis of regenerative organic Rankine cycle (RORC) using the pure working fluid and the zeotropic mixture over the whole operating range of a diesel engine, Energy Convers Manage, vol. 84, p. 282-294.

Yang, F.B., Dong, X.R., Zhang, H.G., et al, 2014, Performance analysis of waste heat recovery with a dual loop organic Rankine cycle (ORC) system for diesel engine under various operating conditions, Energy Convers Manage, vol. 80, p. 243-255.

Yu, G.P., Shu, G.Q., Tian, H., et al, 2013, Simulation and thermodynamic analysis of a bottoming Organic Rankine Cycle(ORC) of diesel engine(DE), Energy,vol. 51, p. 281-290.

Wang, E.H., Zhang, H.G., Fan, B.Y., et al, 2011, Study of working fluid selection of organic Rankine cycle (ORC) for engine waste heat recovery, Energy, vol. 36, p. 3406-3418.

Wang, J.L., Zhao, L., Wang, X.D., 2012, An experimental study on the recuperative low temperature solar Rankine cycle using R245fa, Appl Energ, vol.94, p. 34-40.

Wang, T.H., Zhang, Y.J., Zhang, J., et al, 2014, Comparisons of system benefits and thermo-economics for exhaust energy recovery applied on a heavy-duty diesel engine and a light-duty vehicle gasoline engine, Energ Convers Manage, vol. 84, p. 97-107.

Wang, T.H., Zhang, Y.J., Peng, Z.J., et al, 2011, A review of researches on thermal exhaust heat recovery with Rankine cycle, Renew Sustain Energy Rev, vol. 15, p. 2862-2871.

Wu, W., Zhao, L., Ho, T., 2012, Experimental investigation on pinch points and maximum temperature differences in a horizontal tube-in-tube evaporator using zeotropic refrigerants, Energy Convers Manage, vol. 56, p. 22-31.

Vaja, I., Gambarotta, A., 2010, Internal Combustion Engine (ICE) bottoming with Organic Rankine Cycles (ORCs), Energy,vol. 35, p. 1084-1093.

Radulovic, J., Castaneda, B.I.N., 2014, On the potential of zeotropic mixtures in supercritical ORC powered by geothermal energy source, Energy Convers Manage, vol. 88, p. 365-371.

Lecompte, S., Ameel, B., Ziviani, D., et al, 2014, Exergy analysis of zeotropic mixtures as working fluids in Organic Rankine Cycles, Energy Convers Manage, vol. 85, p. 727-739.

Chiew, L., Clegg, M.W., Willats, R.H., et al, 2011, Waste heat energy harvesting for improving vehicle efficiency, SAE paper:2011-01-1167.

ACKNOWLEDGEMENT

This work was sponsored by the Scientific Research Key Program of Beijing Municipal Commission of Education (Grant No. KZ201410005003), National Natural Science Foundation of China (Grant No. 51376011), Beijing Natural Science Foundation Program (Grant No. 3152005).

A NEW ULTRA-LOW GWP ORC WORKING FLUID

Gregory L. Smith*, Abdennacer Achaichia† and Raymond H. Thomas*

*Honeywell International
20 Peabody Street, Buffalo, NY
USA
Gregory.Smith2@Honeywell.com
Raymond.Thomas@Honeywell.com

†Honeywell Belgium N.V.
Interleuvenlaan 15, 3001 VB, Heverlee
Belgium
Nacer.Achaichia@Honeywell.com

ABSTRACT

Organic Rankine Cycle system designs that operate with hydrofluorocarbon working fluids such as HFC-134a (1,1,1,2-tetrafluoroethane) and HFC-245fa (1,1,1,3,3-pentafluoropropane) have been operating in the field for a number of years, and HFC-245fa has emerged as a leading working fluid choice.

These systems have demonstrated environmental benefits that validate their current and future use. Even so, there is great interest among system OEMs, equipment end-users, regulatory agencies, and the public to embrace new low global warming technologies. Honeywell has developed a fluid that can serve as a replacement for HFC-245fa in foam expansion, aerosols, and organic Rankine cycle applications, which has an ultra-low global warming potential of 1. This working fluid is fluorinated olefin R-1233zd(E) (1-chloro-3,3,3-trifuoroprop-1-ene). The environmental and thermo-physical properties of this fluid are reviewed, and theoretical thermodynamic efficiency and ORC system calculations are presented for R-1233zd(E) and are compared to HFC-245fa. Thermal stability data for R-1233zd(E) is also presented, along with the results of a high-temperature material compatibility study.

REVERSE ENGINEERING OF FLUID SELECTION FOR ORCS USING CUBIC EQUATIONS OF STATE

D. Roskosch[1]*, B. Atakan[2]

[1]University of Duisburg-Essen, IVG, Thermodynamics,
Duisburg, Germany
dennis.roskosch@uni-due.de

[2] University of Duisburg-Essen, IVG, Thermodynamics
Duisburg, Germany
burak.atakan@uni-due.de

* Corresponding Author

ABSTRACT

Fluid selection for thermodynamic cycles like organic Rankine cycles remains an actual topic. Generally the search for a working fluid is based on experimental approaches or on a not very systematic trial and error approach. An alternative theory based reverse engineering approach is proposed and investigated here: The process should start with a model process, designed with respect to the boundary conditions and with (abstract) properties of the fluid needed to fit into this process, best described by some general equation of state and the corresponding fluid-describing parameters. These should be analyzed and optimized with respect to the defined model process, which also has to be optimized simultaneously. The degrees of freedom of the process are restricted to some crucial state variables with variation regimes defined with respect to the boundary conditions like the heat source, heat sink, technical restrictions etc.
Knowing the optimal fluid parameters, real fluids can be selected or even synthesized which have fluid defining properties in the optimum regime like critical temperature T_c or ideal gas capacities of heat c_p, also allowing to find new working fluids, not considered so far. The number and kind of the fluid-defining parameters is mainly based on the choice of the used equation of state (EOS). In the present work the cubic Peng-Robinson equation was chosen due to its moderate numerical expense, sufficient accuracy and a general availability of the fluid-defining parameters for many compounds.
The considered model-process is designed for a typical geothermal heat source with a temperature level of 423.15 K. The objective function is the thermal efficiency as a function of critical pressure p_c, T_c, acentric factor and c_p. Also, some crucial process variables have to be regarded as a problem variable. The results give clear hints regarding optimal fluid parameters of the analyzed process and deepen the thermodynamic understanding of the process. Finally, a strategy for screening large databases is explained. Several fluids from different substance groups were found to have high thermal efficiencies. These fluids will also have to fulfill further criteria, prior to their usage, but the method appears to be a good base for fluid selection.

1. INTRODUCTION

In the context of the expanded use of renewable energies and the increased use of low-temperature heat sources (geothermal, solar thermal, waste heat etc.) for electric power generation, ORCs find wider application. A crucial step in the development process of an ORC is the fluid selection according to different, criteria. Quoilin et al. have listed in their review [1] the most important criteria of fluid selection. Here the focus will be on thermodynamic criteria only, like a high thermal efficiency η and net power output P_{net} as well as acceptable pressures (evaporator and condenser).

Today, the basic thermodynamic approach of fluid selection starts with a model process, designed to defined boundary conditions like heat source and heat sink temperatures. Several preselected fluids, for which thermodynamic data are available, are tested with respect to a specific process parameter like thermal efficiency, exergy loss etc. and finally, the fluid which performs best is selected. For this approach, ample literature is available e.g.: [2,3]. An advanced approach is to combine the fluid selection step with the process optimization (e.g.: [4–6]); fitting the process to the respective working fluid improves the results considerably. Most of these studies are theoretical and use thermodynamic databases or EOS (equation of state) to calculate properties like enthalpy, entropy etc. Due to the ample scientific literature regarding fluid selection, a broader range of compounds were discussed as potential candidates, however, only a few are actually used in commercial ORC power plants [1]. The number of chemical compounds, which are in principle suitable as working fluids, will surely be larger. One problem of the basic approach is the high experimental or computational cost for every fluid to be tested, limiting the number of tested fluids and thus, there is the risk of neglecting potentially good fluids in the preselection step. Furthermore, the fluid rating is not objective; it is only based on the investigated fluid group or on results of other studies. An objective reference point, like the performance of an optimal fluid is missed.

An alternative for fluid selection is a reverse engineering approach with simultaneous process optimization, proposed and investigated here for ORCs. Very recently, we have applied this approach to heat pump cycles [7]; the main procedure has already been described in detail there, thus, here only a brief overview of the method is given. The main idea is to find the optimal properties a fluid should have for the considered process with the defined boundary conditions. Therefore, fluid-descriptive parameters are regarded as continuous variables which are simultaneously optimized with chosen process parameters and with respect to an objective function like thermal efficiency or net power output. Every variable is restricted to physically reasonable values; furthermore, the optimization of process and fluid parameters is constrained by boundary conditions like temperature levels of heat source and heat sink, temperature differences at the pinch point, pressure limits, steam quality at the turbine outlet etc. The type of fluid-descriptive parameters depends on the chosen EOS (equation of state). It can either be defined on the macroscopic scale like critical point values combined with capacities of heat, as used e.g. in cubic EOS or based on a molecular description, as used by the PC-SAFT EOS [8]. After optimizing both, these abstract parameters and the process, the found optimal parameter combination, generally will not fit to real fluids. Thus, the approach continues with the search of real fluids with parameters near to the optimal values. One of the advantages is that also fluids would be considered which would not be investigated in the standard approach.

Comparable approaches for pure fluid selection for ORCs with various heat source temperatures, using some kind of reverse-engineering approach, are found in: [9–11]. Furthermore, a reverse-engineering approach was also used to find optimal fluid mixtures for ORCs [12,13]. All of these investigations are based on a Computer-Aided Molecular Design (CAMD) method; thus, the molecular structure is the optimized parameter. The calculation of the fluid properties is usually done via a group contribution method. A common intermediate step in all is the calculation of critical properties and of heat capacities. In the present work, those fluid parameters are directly optimized. The fluid property model is based on the less complex cubic Peng-Robinson EOS [14], also because the needed fluid parameters (see section 2.1**)** are known for many fluids. Often it was assumed that the cubic EOS are not accurate enough to describe the performance of fluids as working fluids. Analysis of our own and of others [15,16] for several refrigerants using a typical refrigeration cycle have shown that a fluid property model based on the Peng-Robinson EOS combined with the heat capacity of the ideal gas is accurate enough for the first step of fluid selection (see section 2.1). The reverse engineering approach for ORC-processes shall be investigated in the present paper for a simple ORC with a geothermal heat source at 423.15 K. The fluid and process optimizations are carried out regarding the thermal efficiency.

2. METHODS

The optimization is based on a simple Rankine cycle (see Figure 1) as found in any standard thermodynamic textbook (e.g.: [17]). It consists of a pump, an evaporator, a turbine and a condenser.

The process works between two fluid and temperature dependent pressure levels, with the high pressure in the evaporator and the low in the condenser. The condensation temperature is chosen to be 303.15 K and a mass flow of $\dot{m}_{gw} = 100$ kg/s of geothermal water with a constant heat capacity of 75 J/(mol·K) enters the evaporator at 423.15 K. According to a scenario that can be used for combined heat and power generation, the outlet temperature is 403.15 K, constantly. Condenser and evaporator are isobaric and the isentropic efficiencies of pump and turbine are chosen to be $\eta_p^s = 0.6$ and $\eta_t^s = 0.8$.

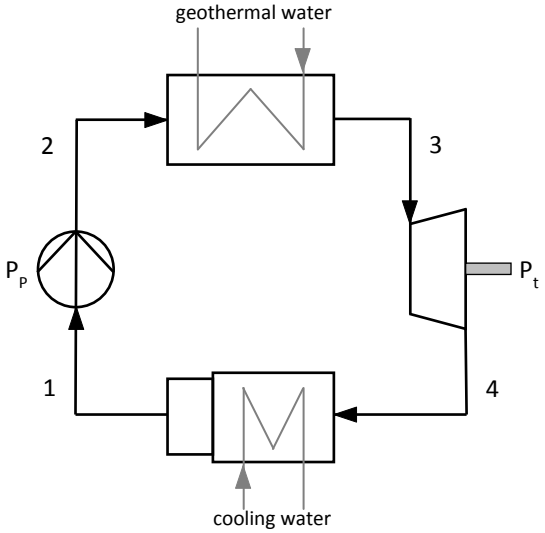

Figure 1: Working principle of the model process

The working fluid leaves the condenser at the condensation temperature and the fluid-dependent pressure as saturated liquid ($x_l = 0$). From state 1 to 2 the fluid is pumped to the evaporator pressure which depends on the evaporation temperature, which is also a problem variable, constrained by the temperature profile of the geothermal water and a minimum pinch-temperature of 10 K. After heat is supplied (st2 – st3), the fluid is expanded in the turbine and finally, condensed from st4 to st1. Based on the inlet states of pump and turbine (st1, st3), the isentropic efficiencies and by means of the isentropic outlet states ($st2^s$, $st4^s$) the real outlet states can be calculated. The procedure as well as the respective equations can be found in any thermodynamic textbook (e.g.: [17]). Finally, the enthalpies at the outlet states apply to:

$$h_2 = \frac{h_2^s - h_1}{\eta_p^s} + h_1 \tag{1}$$

$$h_4 = h_3 + \eta_t^s (h_4^s - h_3) \tag{2}$$

State 3 can be saturated or superheated steam; it is defined by the temperature in state 3 which is also a degree of freedom for process optimization. It is constrained by the evaporation temperature and the geothermal water inlet temperature, taking into account the minimum pinch-temperature. The lower limit of the steam quality at state 4 is restricted to 0.9. From the energy balances for the various components the net power output and the input heat flow are calculated by:

$$|P_{net}| = |P_t| - P_p = \dot{n}_f [(h_3 - h_4) - (h_2 - h_1)] \tag{3}$$

$$\dot{Q}_{in} = \dot{n}_f (h_3 - h_2) \tag{4}$$

The molar flow rate of the working fluid is calculated from the energy balance of the geothermal water and equation (4):

$$\dot{n}_f = \frac{\dot{n}_{gw} \cdot c_{p,gw} (T_{gw,in} - T_{gw,out})}{h_3 - h_2} \tag{5}$$

Equations (3) and (4) lead to the well known expression of the thermal efficiency η:

$$\eta = \frac{|P_{net}|}{\dot{Q}_{in}} \tag{6}$$

By means of the energy balance $|P_{net}| = \dot{Q}_{in} - \dot{Q}_{out}$, the Gibbs equation $Tds = dh - vdp$ and the thermodynamic mean temperatures it can also be written as:

$$\eta = 1 - \frac{T_{m,low}(s_4 - s_1)}{T_{m,high}(s_3 - s_2)} \tag{7}$$

2.1. The fluid property model

The calculations of the objective function η requires the determination of the different thermodynamic properties temperature T, pressure p, specific volume v, enthalpy h, entropy s and the steam quality x for the different states.

The property model used here is based on the Peng-Robinson EOS and the T dependent ideal gas heat capacity. Within the simulations only a linear temperature dependence of the heat capacity was used, since it turned out that this is accurate enough for the small considered temperature ranges (T_3-T_4). In order to find real fluids based on the optimal values the heat capacity were taken at 350 K together with the linear gradient at this temperature. Overall, the fluid descriptive parameters within the optimizations are T_c, p_c, ω, together with A and B for the temperature dependent ideal gas heat capacity $c_p(T) = A + B \cdot T$. All equations used in our property model can be found in Sandler's book [17]. The vapor liquid equilibrium calculation is done by means of the Ambrose-Walton method [18]; it is an empirical method and also based on T_c, p_c and ω. The Peng-Robinson EOS based property model is a good basis for fluid optimizing and screening, since it is easily and quickly solved, numerically and is sufficiently accurate, as shown earlier [7] the accuracy of our model appears to be reasonably good to be used in fluid screening purposes.

Table 1: Variable range for optimization, process parameters and constraints

parameter	value / range
critical temperature	$430 \leq T_c \leq 700$ K
acentric factor	$0.05 \leq \omega \leq 0.8$
heat capacity (ideal gas) at 350 K	$35 \leq c_p \leq 150$ J/(mol·K)
slope of heat capacity at 350 K	$0.01 \leq B \leq 0.6$ J/(mol·K²)
evaporation temperature	T_{evap} [a]
temperature in state 3	T_3 [a]
critical pressure	$3.0 \leq p_c \leq 12.0$ MPa
system pressure limits	$0.01 \leq p_{sys} \leq 2$ MPa
minimum steam quality in St 4	$x_{4,min} = 0.9$

[a] Depending on the actual fluid parameter and a minimum pinch of 10 K

2.2. The optimization routine

The computer programs for optimizing and calculating the fluid properties are written in the programming language Python [19]. The optimization routine was the NLP-algorithm (Non-Linear-Problem) combined with the solver "ralg" taken from the OpenOpt package [20] which can handle both non-linear and non-smooth functions; furthermore, every optimizing parameter can be box-bounded and the optimization might be generally constrained.

2.3. Boundary conditions

It turned out, that the critical pressure has only an indirect impact on the thermal efficiency; the critical pressure influences the suitability range of the critical temperature with respect to the system pressure limits, and thus, it has a mediate impact on the thermal efficiency. As a result, p_c cannot be optimized with the chosen solver, and the optimizations are repeated for 10 values of pc between 3.0

and 12.0 MPa with 1.0 MPa steps. Thus, the optimization parameters are Tc, ω, the evaporation temperature, the temperature at state 3 and the coefficients A and B of the linear temperature dependent function of the ideal gas heat capacity. Only subcritical processes are considered, therefore, the difference between T_c and the evaporation temperature must always be larger than 20 K. Besides this restriction, the evaporation temperature and the temperature in state 3 are limited by the temperature profile of the geothermal water and a minimum pinch of 10 K. Furthermore, T_3 has to be larger than T_{evap}. The parameter ranges of the ideal gas heat capacity at 350 K as well as the gradient were chosen so that values of most real fluids are within the limits. Here, the variable A is calculated from the slope of the linear equation and the value of c_p at 350 K. Table 1 gives an overview of the defined parameter limits and also over the remaining process variables, now.
As in the literature [9], the system pressures (p_{evap}, p_{cond}) are constrained between 0.01 and 2.0 MPa; they depend on the corresponding temperature levels, on the critical point and the acentric factor. Furthermore, for protection of the turbine the minimum steam quality ($x = m_v/m_{total}$) at the turbine outlet has to be larger than 0.9.

3. RESULTS AND DISCUSSION

Fluid and simultaneous process optimizations with the discussed parameters and constraints were carried out with the thermal efficiency η as objective function.
Table 2 shows the results of the η optimizations with respect to each critical pressure. It gets clear, that the optimal values of the thermal efficiency are always larger than 0.17 and increase with the critical pressure, marginally. The same is true for the associated critical temperatures, which increase from 602.75 K to 646.07 K. The optimal values of T_c correspond in combination with the optimal acentric factors to the respective maximum of T_c, which fulfills the pressure limits. However, investigations showed that p_c has no direct impact on η; in fact, it influences only the suitability limit of the critical temperature with respect to the lower pressure limit. Higher critical pressures allow higher values of T_c, which lead to higher thermal efficiencies. The optimal acentric factor also increases with the critical pressure from 0.07 to 0.13; the values are near the lower boundary of ω ($\omega_{min} = 0.05$). This investigation showed that the direct impact of ω on the thermal efficiency is marginal; however, ω influences the suitability range of T_c with respect to the pressure limits. Lower values of the acentric factor lead to a shift of the T_c suitability limit to higher critical temperatures, which results in increased thermal efficiencies. Regarding the optimizations, a further reduction of ω is in conflict with the pinch condition at the starting point of evaporation; thus, smaller values of ω

Table 2: Results from η optimization

p_c [MPa]	T_c [K]	ω [ ]	A [J/(mol·K)]	B [J/(mol·K²)]	c_p(350K) [J/(mol·K)]	T_{evap} [K]	T_3 [K]	x_4 [ ]	η [ ]
3.0	602.75	0.07	0.01	0.10	35.01	396.62	413.15	0.92	0.175
4.0	607.75	0.09	0.00	0.10	35.00	396.57	413.15	0.92	0.175
5.0	619.91	0.09	0.00	0.10	35.00	396.47	413.15	0.92	0.176
6.0	625.36	0.10	0.03	0.10	35.03	396.43	413.15	0.92	0.176
7.0	626.54	0.12	0.01	0.10	35.01	396.42	413.15	0.91	0.176
8.0	638.33	0.10	0.00	0.10	35.00	396.33	413.15	0.91	0.176
9.0	647.55	0.09	0.04	0.10	35.04	396.27	413.15	0.91	0.176
10.0	645.16	0.11	0.00	0.10	35.00	396.28	413.15	0.91	0.177
11.0	647.56	0.12	0.02	0.10	35.02	396.26	413.15	0.91	0.177
12.0	646.07	0.13	0.00	0.10	35.00	396.27	413.15	0.91	0.177

lead to the need of decreasing the evaporation temperature, which results in a significant decrease of η, again. Therefore, the optimal acentric factors are slightly shifted to higher values. Regarding the molar heat capacity at the reference temperature (T = 350 K), the optimal value of $c_p(350K) = 35$ J/(mol·K) is independent of p_c, which correspond to the lower boundary of the c_p(350K)-domain. This

is also true for the parameter A which is always at the lower boundary. The optimal value of the parameter B (c_p gradient) is constantly 0.1, corresponding to the lowest value fulfilling the c_p(350K) restriction with respect to A = 0. The optimizations lead to evaporation temperatures slightly higher than 396 K; which is the respective maximum with regards to the minimum pinch point-temperature difference at the inception of evaporation. The temperature in state 3 is 413.15 K which is the maximum temperature which fulfills the pinch point requirement. All steam qualities at the turbine outlet (state 4) are larger than 0.91 and thus, above the boundary ($x_{4,min}$ = 0.9). The results of former fluid optimizations by Lampe et al. [9], Palma Flores et al. [11] and Papadopoulos et al. [10] show a different picture with respect to the optimal fluid properties. Although similar temperature domains were regarded here, fluids with lower critical temperatures and higher heat capacities reach the highest thermal efficiencies. As main difference to our scenario the authors did not specify the outlet temperature of the heat carrier; their objective was generating the highest possible net power output with respect to a defined heat carrier mass flow with fixed inlet temperature. Regarding such a scenario, our approach also leads to fluids with lower values of T_c and higher heat capacities. Thus, the exact design of the process influences the optimal fluid, essentially and a fluid recommendation based only on the heat source temperature seems to be not reasonable.

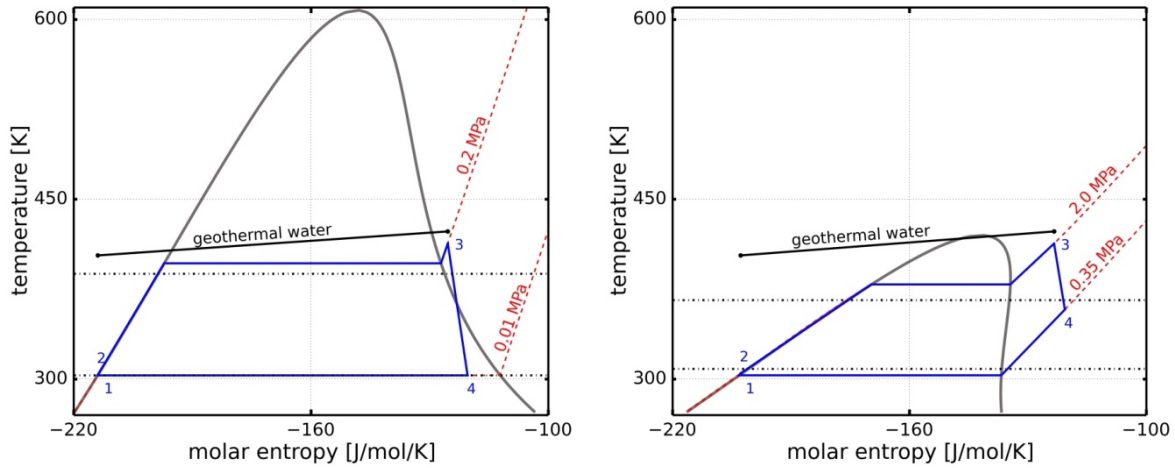

Figure 2: T-s plots of the η optimized fluid for p_c = 4.0 MPa (left) and of butene (right)

Butene is one of the recommended fluids for a heat source temperature between 420 and 445 K [21] and has a critical pressure of 4.04 MPa and thus, it is interesting to compare it with the optimal fluid at 4 MPa. Further fluid properties of butene can be found in Table 3. Figure 2 shows the Ts-diagram of the η optimized fluid for p_c = 4.0 MPa (left) and for the optimized process using butene as working fluid (right). Isobars (dashed lines), lines for the resultant thermodynamic mean temperatures (dash-dotted lines) and the temperature regime of the geothermal water are included. With respect to the discussed boundary conditions and based on the optimized process with butene a thermal efficiency of η = 0.1245 is reached, while the optimal fluid has a thermal efficiency of η = 0.175. First of all, a direct comparison of the two fluids shows a significantly elongated saturation regime for the optimal fluid, which results mainly from the higher critical temperature. The lower value of T_c (for butene) leads also to increased vapor pressures (η-opt: p_{cond} = 0.01 MPa, butene: p_{cond} = 0.35 MPa) and a significantly increased pressure difference (η-opt: Δp_{12} = 0.19 MPa, butene: Δp = 1.65 MPa), although the temperature difference ($T_{evap} - T_{cond}$) is smaller. Furthermore, smaller evaporation entropies at constant temperature levels are constituted by lower values of T_c. The flatter slope of the saturated liquid line and the partially negative gradient of the saturated steam line for butene result mainly from the higher value of the heat capacity (η-opt: c_p(350K) = 35 J/(mol·K), butene: c_p(350K) = 103.86 J/(mol·K). The small slope of the isobaric line at evaporation pressure in the domain of the subcooled liquid, the smaller evaporation entropy and the decreased evaporation temperature lead to a significantly reduced thermodynamic mean temperature at the higher pressure level. Based on the superheating in st3 and the regime of the saturated steam line, butene leaves the turbine as superheated steam resulting in a higher value of the thermodynamic mean temperature at

condensation pressure. The spreading of either thermodynamic mean temperature is directly related to the thermal efficiency of the process (eq. (7)); therefore, a higher spreading results in larger values of η, in general. Due to it, the smaller spreading for butene, compared to the optimal fluid, leads to a strongly reduced thermal efficiency.
Finally, the optimizations of the thermal efficiency lead to fluids with small values of c_p(350K), highest possible critical temperatures and small acentric factors. Such fluids are wet fluids with an elongated saturation regime, typically.

3.1. (Real) fluid selection

After having found optimal fluid parameters, real fluids with similar parameters must be found or could even be synthesized. A detailed description of the fluid selection process was discussed for heat pumps and is found in [7]. Here, we give only a brief description of the selection process. A small fluid database with 284 records taken from different sources [22–24] was used here. It contains values of T_c, p_c, ω and 4 or 5 coefficients for an equation for the isobaric ideal gas heat capacity for every record. In order to compare with optimization results, the value of c_p(350) as well as the gradient at this temperature were calculated. The fluid selection process is ordered in three steps and can also be efficiently applied to large databases:

Step 1 – Preselection with respect to the pressure limits
Using the Ambrose-Walton equation [18], vapor pressures at given temperatures can be calculated, analytically. The aim of step I is the exclusion of fluids, which do not fulfill the pressure restrictions at the given temperature levels. While, the condensation temperature is clearly defined as 303.15 K and the vapor pressure can directly be calculated; the evaporation temperature is a problem variable and is not defined, explicitly. However, it is assumed that fluids not fulfilling the higher pressure limit at the poor condensation temperature of 340 K will not reach good thermal efficiencies and are omitted. Additionally, it was found that fluids with good thermal efficiencies have vapor pressures significantly below the limit. In the present work with the used database, the above-mentioned temperature levels and the boundary conditions ($0.01 \leq p_{sys} \leq 2$ MPa), from this step the number of potential fluids was reduced from 284 to 106.

Step II – Fit of a function for η estimation
From the presented optimizations it was found that small values of c_p(350K) and ω as well as critical temperatures between 600 and 650 K (depending on p_c) lead to high values of η. Further investigations pointed out that T_c and c_p(350K) are the critical and most sensitive variables for the thermal efficiency. The critical pressure has no direct impact and the effect of ω is marginal and can be neglected. Basically, with respect to this knowledge, fluids with properties near the optimum can be chosen for further investigation. However, finding a fluid with properties very close to the optimum is not probable, thus, fluid selection represents usually a compromise. Because of the unknown sensitivity of η with respect to the individual parameters, the fluid selection along this path is always in danger of missing attractive combinations of the parameters. Thus, by means of the optimization algorithm a function for η estimation as a function of T_c, c_p(350K) and the optimized process parameters (T_{evap}, T_3) was fitted to 100 combinations of T_c and c_p(350K). Ten critical temperatures between 360 and 600 K as well as 10 values of c_p(350K) between 35 and 150 J/(mol·K) were selected. The critical pressure was fixed at 4.0 MPa and the acentric factor was set to 0.10, which is the mean value resulting from the optimizations. Here, pressure restrictions were not considered, since in step I all fluids not fulfilling the restrictions were excluded. Four polynomials, each of degree 3, with overall 12 coefficients were fitted to the optimization results. A comparison between the values of η estimated by the polynomials and calculated by our fluid property model results in an absolute mean percentage error of 7.6 %, from the 106 fluids remaining from step I. However, the largest errors are found for fluids with poor η; comparing only fluids with $\eta > 0.16$ (35 records) the absolute mean percentage error is decreased to 1.96 %. Finally, by means of the fit also large databases can be screened efficiently for good fluids.
The 2nd step requires the greatest computational effort of the 3 matching steps. The 100 optimizations for the fit can be done by a common computer (CPU: i5-3750, RAM: 8 GB) in about 30 minutes.

Step III - Final fluid selection for further investigation

With the results of step II, fluids with probably high thermal efficiencies can be chosen for further investigations, regarding other fluid criteria. Besides the estimation by the polynomials, the process optimization should be repeated once again for this limited number of fluids, to obtain the correct values. In step II 35 fluids with $\eta > 0.16$ were found; Table 3 shows 10 of them, exemplarily. Furthermore, the 5 fluids recommended by Wang et al. [21] for heat source temperatures between 420 and 445 K are also listed (No. 11 – 15). Those fluids all have thermal efficiencies smaller than 0.1245 and are with respect to the process regarded in this work much less efficient than the fluids resulting from our selection. Using our approach for a similar process as regarded in this work, but without fixing the heat source outlet temperature (regarding only power generation) leads also to the fluids 11-15 as top ranked. It follows, that besides the heat source temperature, further process parameters influence the choice of optimal fluids. Among the top-ranked fluids are conventional refrigerants like R150, R20 or R30 as well as fluids like bromine or acetonitrile, which are extremely toxic and/or corrosive compounds. However, this investigation is only meant as an example and perhaps some of the fluids like methanol, ethanol or acetone appear to be worth further investigations regarding other suitability criteria.

Table 3: Top-ranked fluids resulting from the fluid selection (No. 1-10), as well as fluids recommended by [21]

No.	Fluid	η [ ]	T_c [K]	p_c [MPa]	ω [ ]	c_p(350K) [J/(mol·K)]
1	Bromine	0.1737	584.1	10.30	0.129	36.47
2	Acetonitrile	0.1711	545.5	4.83	0.334	59.46
3	Methanol	0.1700	512.5	8.08	0.565	50.35
4	1,2-Dichloroethane (R150)	0.1693	566.0	5.36	0.250	88.77
5	Chloroform (R20)	0.1685	536.5	5.55	0.229	71.49
6	Ethanol	0.1685	514.0	6.15	0.645	77.86
7	Dichloromethane (R30)	0.1676	510.1	6.08	0.198	57.49
8	Benzene	0.1673	562.0	4.90	0.210	106,00
9	Fluorobenzene	0.1655	560.0	4.55	0.248	118.38
10	Acetone	0.1654	508.3	4.70	0.306	88.62
11	Butene	0.1245	419.9	4.04	0.189	103.86
12	Isobutene	0.1237	417.9	4.00	0.199	100.44
13	1,1,1,2,3,3-Hexafluoropropane (R236ea)	0.1218	412.4	3.50	0.379	140.81
14	1-Chloro-1,1-difluoroethane (R142b)	0.1145	409.6	4.33	0.251	94.73
15	Isobutane (R600a)	0.1122	407.8	3.64	0.184	118.52

4. CONCLUSIONS

In this work the reverse engineering approach for fluid selection, recently introduced for heat pump cycles, is now applied to ORCs. It appears to be a more promising approach to first start thinking about an optimal process with optimal fluid parameters, instead of screening well investigated fluids. Furthermore, based on the reverse engineering approach, fluids that were not well investigated so far, can be found, and also more is learned about the fluid properties which are important for the cycle. This also leads to an objective value which represents the performance of a hypothetic best fluid.

The presented approach consists of the simultaneous numerical optimization of fluid-descriptive parameters and some process parameters, the latter could easily be extended. Here, the fluid property model is the cubic Peng-Robinson equation of state and a linear equation for the temperature dependent isobaric ideal gas heat capacity. Thus, the needed fluid-descriptive parameters are the

critical temperature, the critical pressure, the acentric factor and two coefficients for the heat capacity. These values are not too numerous and available for many compounds and could in future also be extended to apply group additivity methods to search for further fluids or for calculations of other fluid properties like thermal conductivity and viscosity, without increasing the number of parameters to be optimized.

First of all, it was shown, that the reverse engineering approach also can applied to ORCs, efficiently. It was pointed out, that the results of the optimization are thermodynamically reasonable and lead to a deeper understanding of the interrelation of fluid and process parameters. Based on the optimized fluid parameters a procedure was presented to find real fluids near the optimum. Therefore, an equation for the prediction of η based on the most important variables was fitted.

Several fluids with higher values of η than the usually recommended ones for the here defined heat source temperature were found. Some of them, like bromine or acetonitrile will probably never be used as working fluids, but other like acetone or methanol may be worth further investigation. Comparing the optimal fluid parameters found in this work to the results of fluid optimizations by other authors allow the conclusion, that, besides the heat source temperature, also other criteria and parameters influence the optimal fluid choice, clearly. Further investigations regarding the influence of the process design or boundaries on the optimal fluid parameters are needed for a deeper insight.

NOMENCLATURE

A	coefficient of the molar isobaric heat capacity (intercept)	(J/mol/K)
B	coefficient of the molar isobaric heat capacity (gradient)	($J/mol/K^2$)
c_p	molar isobaric heat capacity	(J/mol/K)
h	molar enthalpy	(J/mol)
$\dot{m}$	mass flow rate	(kg/s)
$\dot{n}$	molar flow rate	(mol/s)
P	power	(MW)
P	pressure	(MPa)
$\dot{Q}$	heat flow	(MW)
s	molar entropy	(J/mol/K)
st	state	(-)
T	temperature	(K)
$\dot{V}$	volume flow rate	(m^3/s)
v	molar volume	(m^3/mol)
w	molar work	(MJ/mol)
x	steam quality	(-)
η	thermal efficiency	(-)
ω	acentric factor	(-)

Subscripts

c	critical
cond	condensation
evap	evaporation
gw	geothermal water
f	working fluid
p	pump
s	isentropic
sys	system
t	turbine

REFERENCES

[1] Quoilin S, Broek, Martijn Van Den, Declaye S, Dewallef P, Lemort V; 2013; Techno-economic survey of Organic Rankine Cycle (ORC) systems; Renewable and Sustainable Energy Reviews:168–86.

[2] SALEH B, KOGLBAUER G, WENDLAND M, FISCHER J; 2007; Working fluids for low-temperature organic Rankine cycles; Energy(7):1210–21.

[3] Siddiqi MA, Atakan B; 2012; Alkanes as fluids in Rankine cycles in comparison to water, benzene and toluene; Energy(1):256–63.

[4] Tchanche BF, Papadakis G, Lambrinos G, Frangoudakis A; 2009; Fluid selection for a low-temperature solar organic Rankine cycle; Applied Thermal Engineering(11-12):2468–76.

[5] Long R, Bao YJ, Huang XM, Liu W; 2014; Exergy analysis and working fluid selection of organic Rankine cycle for low grade waste heat recovery; Energy:475–83.

[6] Heberle F, Brüggemann D; 2010; Exergy based fluid selection for a geothermal Organic Rankine Cycle for combined heat and power generation; Applied Thermal Engineering(11-12):1326–32.

[7] Roskosch D, Atakan B; 2015; Reverse engineering of fluid selection for thermodynamic cycles with cubic equations of state, using a compression heat pump as example; Energy(81):202–12.

[8] Gross J, Sadowski G; 2001; Perturbed-Chain SAFT: An Equation of State Based on a Perturbation Theory for Chain Molecules; Ind. Eng. Chem. Res.(4):1244–60.

[9] Lampe M, Stavrou M, Bücker HM, Gross J, Bardow A; 2014; Simultaneous Optimization of Working Fluid and Process for Organic Rankine Cycles (ORCs) using PC-SAFT; Ind. Eng. Chem. Res.(53(21)):8821–30.

[10] Papadopoulos AI, Stijepovic M, Linke P; 2010; On the systematic design and selection of optimal working fluids for Organic Rankine Cycles; Applied Thermal Engineering(6-7):760–9.

[11] Palma-Flores O, Flores-Tlacuahuac A, Canseco-Melchor G; 2015; Optimal molecular design of working fluids for sustainable low-temperature energy recovery; Computers & Chemical Engineering:334–49.

[12] Papadopoulos AI, Stijepovic M, Linke P, Seferlis P, Voutetakis S; 2013; Toward Optimum Working Fluid Mixtures for Organic Rankine Cycles using Molecular Design and Sensitivity Analysis; Ind. Eng. Chem. Res.(34):12116–33.

[13] Molina-Thierry DP, Flores-Tlacuahuac A; 2015; Simultaneous Optimal Design of Organic Mixtures and Rankine Cycles for Low-Temperature Energy Recovery; Ind. Eng. Chem. Res.(13):3367–83.

[14] Peng DY, Robinson DP; 1976; A New Two-Constant Equation os State; Ind. Eng. Chem. Fundam.(15(1)).

[15] Brown JS; 2007; Predicting performance of refrigerants using the Peng-Robinson Equation of State; International Journal of Refrigeration-Revue Internationale du Froid(8):1319–28.

[16] Brown JS, Brignoli R, Daubman S; 2014; Methodology for estimating thermodynamic parameters and performance of working fluids for organic Rankine cycles; Energy:818–28.

[17] Sandler SI; 2006; Chemical, biochemical, and engineering thermodynamics. Hoboken, N.J (USA): John Wiley; xiv, 945.

[18] Ambrose D, Walton J; 1989; Vapour pressures up to their critical temperatures of normal alkanes and 1-alkanols; Pure and Applied Chemistry(8).

[19] Python.org; Available from: www.python.org/. [19/05/2015].

[20] OpenOpt; Available from: www.openopt.org. [19/05/2015].

[21] Wang D, Ling X, Peng H, Liu L, Tao L; 2013; Efficiency and optimal performance evaluation of organic Rankine cycle for low grade waste heat power generation; Energy:343–52.

[22] Poling BE, Prausnitz JM, O'Connell JP; 2001; The properties of gases and liquids. New York (USA): McGraw-Hill; 1 v. (various.

[23] 2006; VDI-Wärmeatlas. Berlin (GER), Heidelberg (GER), New York (USA): Springer; 1432 S. in getr. Zählung.

[24] Lemmon, E.W., Huber, M.L., McLinden, M.O; 2023; NIST Standard Reference Database 23: Reference Fluid Thermodynamic and Transport Properties-REFPROP. Gaithersburg: National Institute of Standards and Technology.

STUDY OF RECIPROCATING PUMP FOR SUPERCRITICAL ORC AT FULL AND PART LOAD OPERATION

Arnaud Landelle[1,2,3,4]*,Nicolas Tauveron[1,2],Philippe Haberschill[3],Rémi Revellin[3],Stephane Colasson[1,2]

[1] Université Grenoble Alpes, F-38000 Grenoble, France

[2] CEA, LITEN, LS2T, F-38000 Grenoble, France

[3] Université de Lyon, CNRS, INSA-Lyon, CETHIL, UMR5008, Villeurbanne F-69621, France

[4] ADEME, 20 Av. du Grésillé, BP90406, 49004 Angers Cedex 01, France

* arnaud.landelle@cea.fr

ABSTRACT

Recovery of waste heat in industrial processes is an important component of energy savings worldwide. At low temperature levels, thermodynamics prevents any high efficiency in the heat-to-electricity conversion; such dedicated systems have to be optimized and should achieve a maximum heat recovery, at partial and full load. These technical and technological problematic are also common with renewable natural resources use (solar, geothermal, biomass). Supercritical organic Rankine cycle is quite well investigated in the scientific community, but rarely experimentally studied, especially off-design and dynamic behaviors of such systems. The CEA/LITEN is developing a 10kWe prototypes of supercritical ORC to investigate experimental potential of such technology for low grade power generation. The first task is to characterize various components behavior in supercritical regimes. In such cycles, the pump plays a strategic role, as for supercritical operations the back work ratio is a key parameter to consider. Performance data of a reciprocating pump drive by an induction motor with variable speed drive are measured. Maximum pump efficiency achieve is 82% and maximum global efficiency (pump & drive) achieve is 41%. Losses are evaluated and a power model is proposed and compared with experimental data. Results of this work aim to give a better knowledge for ORC pump design and optimization.

1. INTRODUCTION

Organic Rankine Cycles (ORC) are known since the 19th century, but in recent decades research and commercial development increased exponentially (Quoilin *et al*., 2013).Most research focused on nominal steady-state optimization, screening working fluid and operating conditions. Optimization criteria vary from study to study (energetic efficiency, exergetic analysis, power, or cost). Several study shows supercritical ORC have a high potential (Schuter *et al*., 2010; Shu *et al*. 2013) especially in the low temperature range (~150°C) (Astolfi *et al*., 2014; Toffolo *et al*., 2014) but supercritical conditions mean high pressure and more constrains on components. For components optimization, most research focuses on the expander that is the critical components (Bao and Zhao, 2013), heat exchangers and evaporators especially are also investigated, but few researchers discuss of the pump. However, Quoilin *et al*. (2013) describes the pump as a key component that should be carefully chosen according to its controllability, tightness, Net Positive Suction Head (NPSH) and efficiency. Pump efficiency becomes a crucial parameter for low temperature and supercritical cycles. Back Work Ratio defines as the ratio between pump electrical consumption and expander outlet power is introduced to evaluate pump impact. In supercritical ORC, Maraver *et al*. (2014) shows that pump efficiency have a major impact on cycle exergetic efficiency. Using R-134a, cycle exergetic efficiency decrease from 46

to 40% if the pump efficiency decrease from 75 to 50 %. From authors' point of view, it is therefore essential to investigate the pumping system for on and off design ORC operation. The author listed only two pump efficiency correlation used for ORC models. A correlation is proposed by Lippke (1995) for centrifugal pump, losses related to the driver are also discussed. Quoilin *et al.* (2011) uses an empirical correlation proposed by Vetter (2006) for rotary positive displacement pump and add a constant electromechanical efficiency for driver losses. While most of feed pumps used in experimental ORC are reciprocating positive displacement pumps. Furthermore, as Miao *et al.* (2015) emphasized, confusions and simplifications are made about pump power consumption and efficiency. Results of this study aim to propose an experimental approach for pump characterization, a behavioural off-design reciprocating pump model for losses and efficiency that can be used for ORC system model, and provide knowledge assets for pump selection and optimal use.

2. EXPERIMENTAL SETUP

An experimental investigation is carried out on a diaphragm pump integrated into an experimental bench using R-134a as fluid. The test bench described in Figure 1 is use for subcritical and supercritical heat transfer investigation. This paper only focuses on the pumping system.

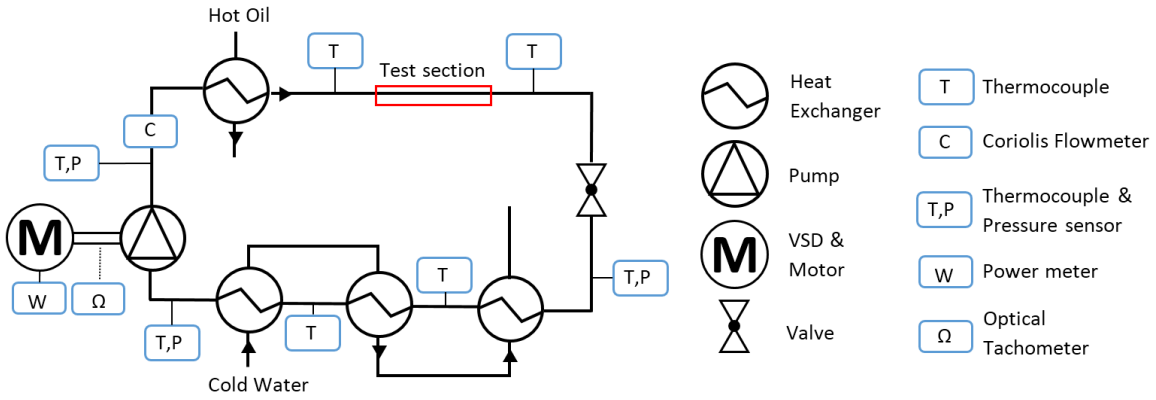

Figure 1: Scheme of the test bench

2.1 Test Bench

The pumping system is composed by a diaphragm pump (Wanner Hydra-Cell, model G03X), using a triplex single-acting reciprocating positive displacement technology. This technology is often used in small supercritical ORC because of its tightness and high efficiency at high pressure, low flow rate. And, a three-phase induction motor (Leroy-Sommer, model LS90L 1,8kW) integrating a Variable Speed Drive (VSD) (Leroy-Sommer, model Varmeca 32). The frequency can vary from 10 to 50 Hz, corresponding to a shaft rotational speed from 300 to 1500 revolutions per minute (rpm). At nominal speed (1500 rpm), the volume flow is around 0,58 m^3/h and the maximum outlet pressure is 70 bar. The pump is located at the bottom of the bench after all condensers to increase the NPSH. The fluid is evaporate and expanded through a valve that control the pressure differential at the pump ends. The electrical consumption is measured by a power quality clamp meter. The mass flow rate is measured by a Coriolis flowmeter. The shaft rotational speed is measured by an optical tachometer. Measurement accuracy are shown in Table 1.

2.2 Test Description

In order to characterize the pump, different kinds of tests are done. Since there is no torque meter between the motor and the pump, uncoupled motor tests are done to characterize the motor and VSD. Experimental data cover the full speed range, with 52 points. Unloaded pump test are done to estimate the unloaded volume flow ($\dot{V}_0$), valves are open to reduce the pressure differential at the pump ends (ΔP), 48 points cover the full speed range. For pump on load, total of 87 experimental points are achieved, covering a ΔP range from 0 to 35 bar at five different speed shaft (350 to 650 rpm). For each point, measurement are averaged during 1-2 minutes, to smooth variations. NPSH is kept as high as possible to reduce its impact on the volumetric efficiency (Miller, 1988).

Table 1 : Measuring range and accuracy

Variable	Range	Uncertainty
Supply pressure	0-17 bar	± 0,3 bar
Exhaust pressure	0-50 bar	± 0,1 bar
Temperature	0-120 °C	± 0,5 °C
Shaft rotational speed	0-1500 rpm	± 1 rpm
Electrical power	0-700W	± 20 W
Mass flow rate	0-0,1 kg/s	± 5.10^{-4} kg/s

3. DATA REDUCTION

3.1 System Energetic Model

An energetic model of the pumping system is proposed in Figure 2 to identify losses. $\dot{W}_{el}$ is the measured electrical consumption, $\dot{W}_{mech}$ is the mechanical shaft power, $\dot{Q}_{los}$ are powers dissipated by different components in the ambient environment. Fluid pumping is assumed to be fast enough to consider no heat transfer between the pump and the fluid. $\dot{W}_{flu,pp}$ the power transferred by the pump to the fluid is made of $\dot{W}_{hyd} = \int v.dP$ the hydraulic power (ie. useful) and internal frictions which are represented by a fictive heat power $\dot{Q}_{los,flu}$. Different efficiencies are defined from these power: the global efficiency of the pumping system $\eta_{global} = \dot{W}_{hyd}/\dot{W}_{el}$, the pump efficiency $\eta_{pump} = \dot{W}_{hyd}/\dot{W}_{mech}$ and the isentropic efficiency of the pump $\eta_{is} = \dot{W}_{hyd}/\dot{W}_{flu,pp}$.

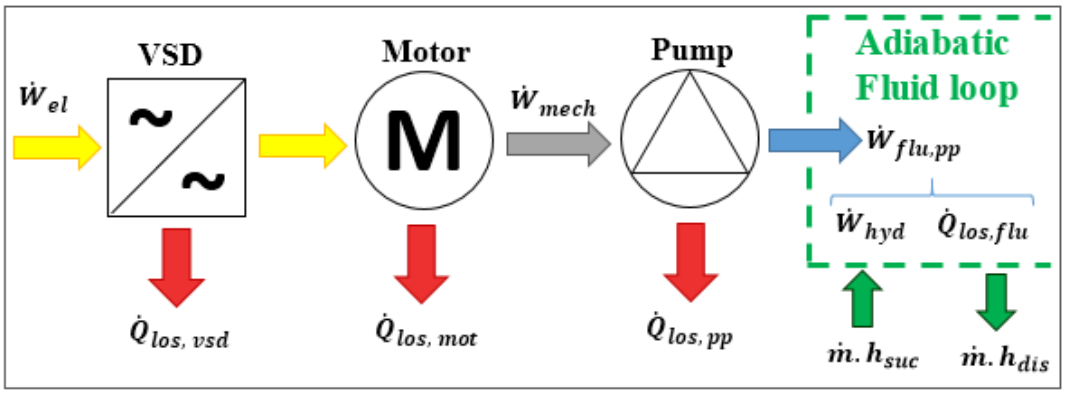

Figure 2: Energetic conceptual scheme of the pumping system

3.2 Motor and VSD Losses

Motor and VSD dissipated power should be estimated to get the mechanical power. Assumptions are made based on the literature review. De Almeida *et al*. (2014) and IEC 60034-31 explained that losses in VSD is a sum of constant loss and loss proportional to the output power. Kari (2009) performed tests and showed that in modern VSDs, losses increase with speed and torque. At low torque, losses are nearly constant and independent of the rotational speed. In tests performed for this study, motor and VSD operate under 50 % of the nominal torque. It is assumed that VSD losses ($\dot{Q}_{los,vsd}$) are constant, as did Deprez *et al*. (2010) for its VSD and motor losses approximation.

Induction motors have been more widely studied and normalized, even under variable speed and load. The IEC 60034-31 provide a part load efficiency formula based on manufacturer motor data. In this formula, motor losses are a linear function of $\dot{W}^2_{mech}$. Li *et al*. (2015) improved it with a new correlation for motor efficiency drive by a VSD, assuming the voltage is proportional to the frequency at the VSD output. From this correlation and assuming a constant power factor over the test, motor losses are expressed as: $\dot{Q}_{los,mot} = C_2.\dot{W}^2_{mech} + C_3.\dot{\Omega}^2$ with C_2 and C_3 constant parameters function of motor design. Figure 3 shows estimated losses for the motor used in this study, with both correlations. Correlations show small differences at nominal speed, correlation developed by Li is used for motor losses estimation. Therefore, the shaft power is estimated with one empirical constant (C_1) for VSD losses. $\dot{W}_{mot,n}$;$\eta_{mot,n}$;$\dot{\Omega}_n$ are respectively the nominal motor power, the efficiency and the rotational

speed, provided by the manufacturer. $\dot{W}_{el}$ and $\dot{\Omega}$ are measured parameters. The quadratic equation (1) is solved to find $\dot{W}_{mech}$.

$$\dot{W}_{mech} = \dot{W}_{el} - \dot{Q}_{los,vsd} - \dot{Q}_{los,mot} = \dot{W}_{el} - C_1 - \left[\left(\frac{1}{\eta_{mot,n}} - 1\right)\dot{W}_{mot,n}\left(0{,}7\,\frac{\dot{W}_{mech}^2}{\dot{W}_{mot,n}^2} + 0{,}3\,\frac{\dot{\Omega}^2}{\dot{\Omega}_n^2}\right)\right] \quad (1)$$

From uncoupled motor tests, assuming $\dot{W}_{mech} = 0$, experimental value of C_1 is find to be *240W*.

3.3 Pump Data

Volume flow rate is estimated from the mass flow rate and the fluid density using pressure and temperature at the pump outlet. Density, as other fluid properties, are computed with R-134a property equations provided by Tillner-Roth and Baehr (1994) used on EES. $\dot{W}_{flu,pp} = \dot{m}_{flu}.\Delta h_{pp}$ and enthalpy is computed from pressure and temperature. Hydraulic power is define as: $\dot{W}_{hyd}\ [W] = \dot{V}\ [m^3/s].\Delta P\ [Pa]$. Therefore, $\dot{Q}_{los,pp}$ and $\dot{Q}_{los,flu}$ are estimated. Volumetric efficiency is the ratio between the real volume flow ($\dot{V}$) and the theoretical flow, product of displaced volume by rotational speed ($\dot{V}_{th} = V_{disp}.\dot{\Omega}$). When the pump runs unloaded ($\Delta P = 0$), η_{vol} is near 100%. Therefore, manufacturer theoretical flow is compared with experimental no load flow ($\dot{V}_0$). Manufacturer displaced volume (V_{disp}) is estimated at 6,84 cm^3, experimental at 7,15 cm^3. Since the same method is used to estimate the volume flow on load and unloaded, experimental no load flow is taken to compute the volumetric efficiency: $\eta_{vol} = \dot{V}/\dot{V}_0$.

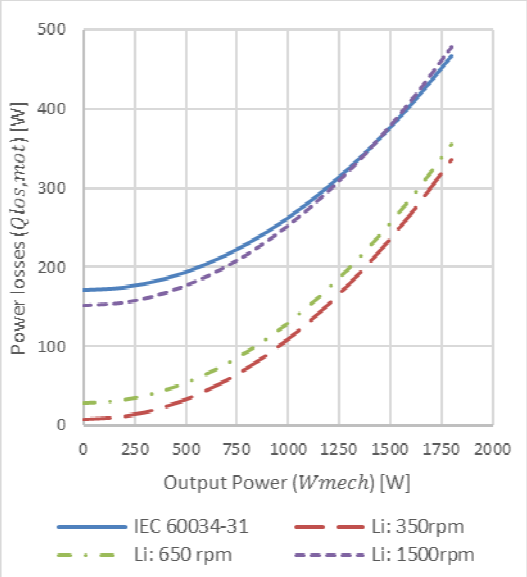

Figure 3: Motor losses function of load

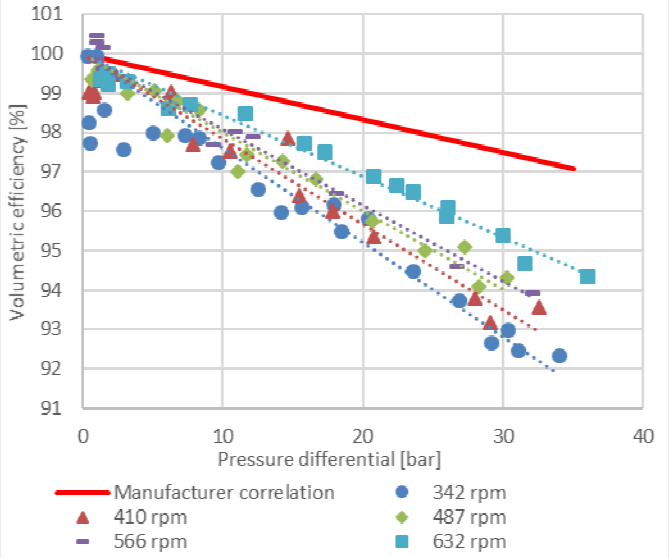

Figure 4: Effect of ΔP on volumetric efficiency for different mean rotational speed

4. RESULTS & ANALYSIS

4.1 Volumetric Efficiency

On load tests are performed at constant speed reference. Since an induction motor is used, slip increases between the speed reference and the real shaft speed when load increase. Therefore, the rotational speed should be measured at every step to compute corresponding no load flow and volumetric efficiency. As shown in Figure 4 volumetric efficiency if found to be dependent of the pressure differential and rotational speed while in theory, manufacturer data shown it is only proportional to the ΔP. Manufacturer and experimental result should be compared with caution since manufacturer data are mainly computed for cold water.

Literature shows different factors affecting the volumetric efficiency. As previously noted, NPSH affects the volumetric efficiency (Miller, 1988). For reciprocating pump, the NPSHr is defined by ANSI/HI 6.1-6.5 and 6.6 as a reduction of 3 % in the volumetric efficiency compared to the max

efficiency, at the same speed and pressure differential. Therefore, sub-cooling is essential to keep a good volumetric efficiency. Here, NPSH impact is neglected. Reciprocating pumps use valves, Miller (1995), Singh and Madavan (1987) and Johnston (1991) mentioned continuous valve leakage under high pressure and backflow when piston changes direction due to delays in the valves closing. If the closing delays is assumed to be inversely proportional to the rotational speed and since the number of cycle is proportional to the rotational speed, the average backflow time is considered constant. Therefore, backflow and continuous leakage are approximated by a continuous leakage flow rate using the equation proposed by De Chargeres and Rey (2009): $\dot{V}_{leak} = A.\Delta P/\mu$ with A an empirical geometric coefficient.

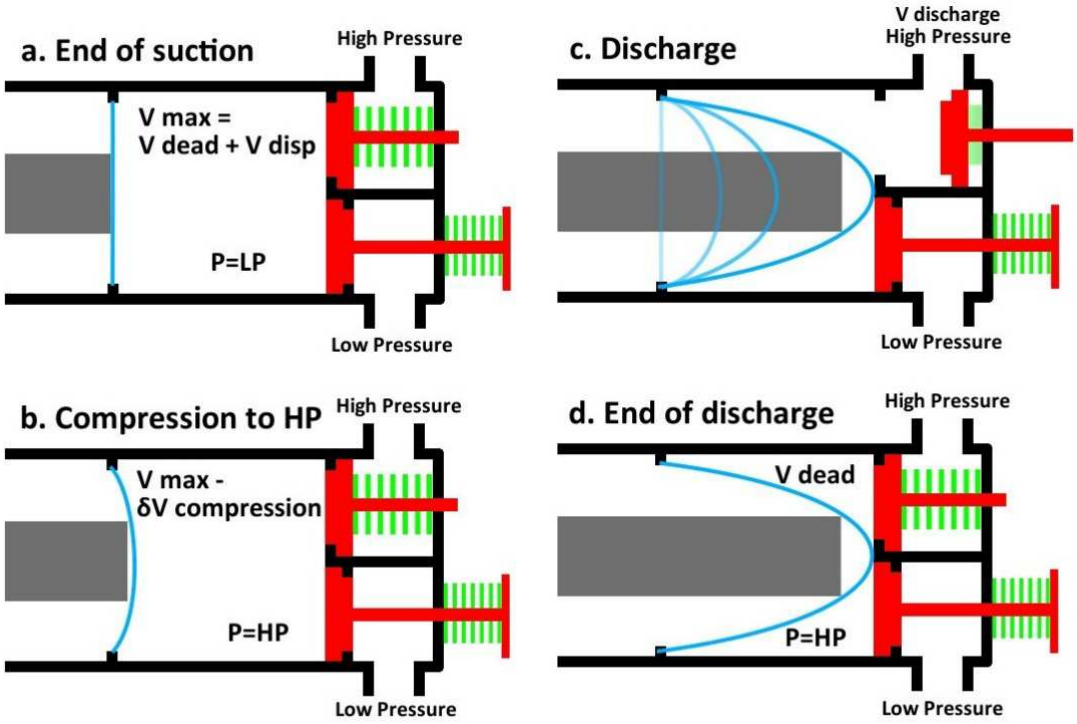

Figure 3: Reciprocating pump discharge process

Fluid compressibility is the third and most important factor. This factor creates a likelihood of confusion: the volumetric efficiency could be defined using the suction (Tackett *et al.*, 2008) or the discharge volume flow rate (Miller, 1995). Since outlet conditions are used to compute the volume flow, the second formulation is used. Figure 5 presents steps of the discharge process. Isothermal compressibility factor $\beta_T = -\frac{1}{V}.\left(\frac{\delta V}{\delta P}\right)_T$ is introduced to write the volume discharge per stroke:

$$V_{dis} = \left(V_{max} - \Delta V_{compression}\right) - V_{dead} = V_{disp} - \Delta P.\beta_T.(V_{disp} + V_{dead}) \quad (2)$$

Adding valve leakage, discharge flow and volumetric efficiency equations are:

$$\dot{V}_{dis} = \Omega.V_{disp}.\left(1 - \Delta P.\beta_T.\left(1 + \frac{V_{dead}}{V_{disp}}\right)\right) - A.\frac{\Delta P}{\mu} \quad (3)$$

$$\eta_{vol} = \frac{\dot{V}_{dis}}{\Omega V_{disp}} = 1 - \Delta P.\beta_T\left(1 + \frac{V_{dead}}{V_{disp}}\right) - \frac{A.\Delta P}{\mu.V_{disp}.\Omega} \quad (4)$$

$$= 1 - \left(\frac{C_4}{\Omega} + C_5\right).\Delta P \quad \text{with } C_4 = \frac{A}{\mu.V_{disp}} \quad \text{and } C_5 = \beta_T.\left(1 + \frac{V_{dead}}{V_{disp}}\right) \quad (5)$$

Slope coefficients of Figure 4 are reported in Figure 6 corresponding to $(a/\Omega + b)$ coefficient. V_{disp} is known from 3.3, μ and β_T are fluid properties computed from outlet conditions. Therefore, geometrical leakage coefficient is estimated $A \cong 1{,}3.10^{-10}\ cm^3$ and the dead volume $V_{dead} \cong 5{,}5\ cm^3$. Uncertainties on those values are high since there are only five data points used. Data at nominal speed will give more confidence in those results. However, manufacturer slope is constant, which could be explained if valve leakages were neglected (C_4=0), and leads to a single coefficient C_5=0,000835 bar^{-1}, close to the experimental one (C_5=0,000837).

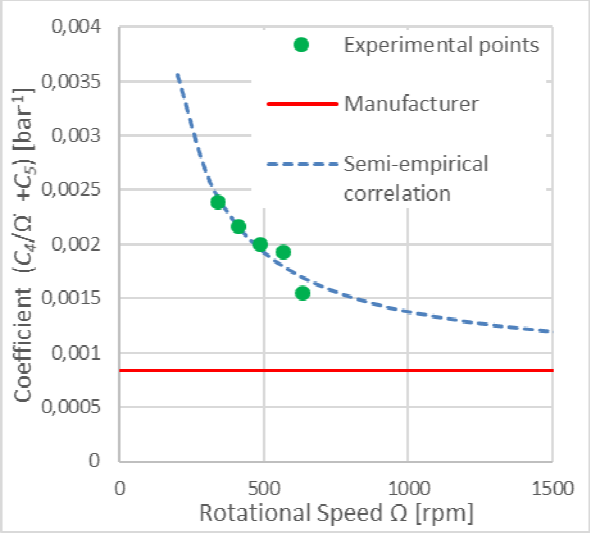

Figure 6: Volumetric efficiency slope coefficient

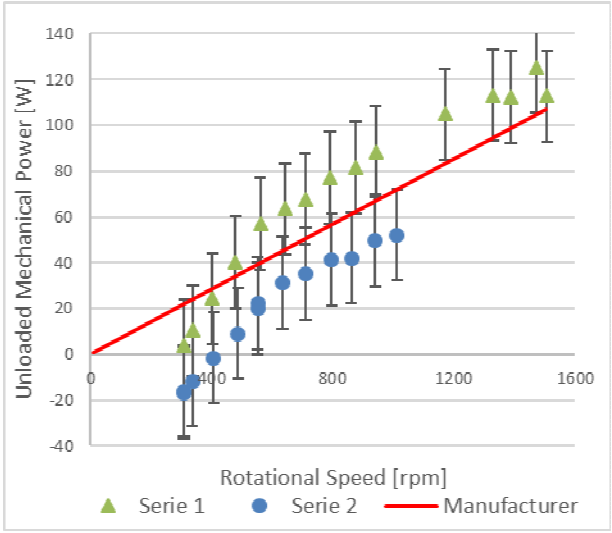

Figure 7: Unloaded mechanical power

4.2 Power & Pump Efficiency

Manufacturer proposes an equation to estimate the required power:

$$\dot{W}_{mech} = C_6.\dot{\Omega} + C_7.\dot{W}_{hyd} \quad (6)$$

The first term corresponds to friction losses, the second to pumping work efficiency. Manufacturer coefficient values are compared with experimental data. Coefficient C_6 is estimated from unloaded tests, the hydraulic power is neglected. For more accuracy, VSD and motor losses are not computed from Equation (1) to estimate $\dot{W}_{mech}$. Instead, experimental losses from uncoupled tests is used. In addition, the hydraulic power, even low, is subtracted (assuming C_7=*1*). Figure 7 shows two series of test and the linear interpolation, C_6 is estimated at *0,0723 W/rpm* with the same order of magnitude as the manufacturer value: *0,0711 W/rpm*. From on load tests, coefficient C_7 is estimated at *1,212* (manufacturer: *1,174*). Mechanical power computed from motor & VSD model (Equation 1 with experimental $\dot{W}_{elec}$) and pump model (Equation 6 with experimental $\dot{W}_{hyd}$) are compared in Figure 8.

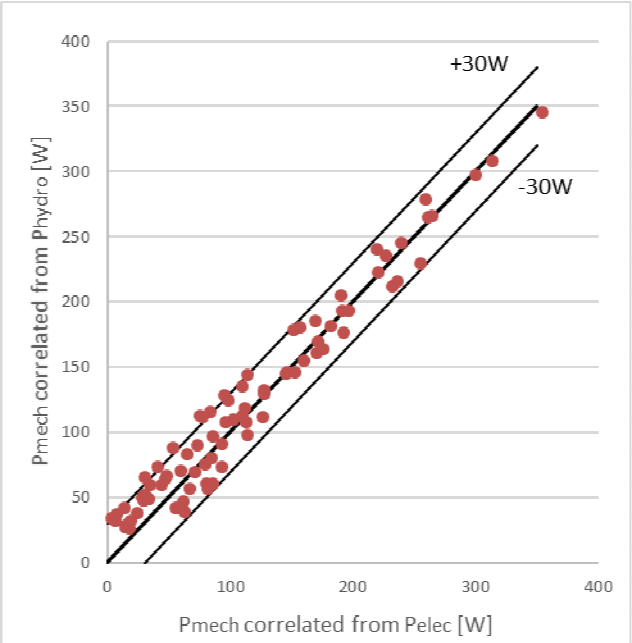

Figure 8: Correlated Mechanical Power: Pump model (equation 6) *vs* Motor model (equation 1)

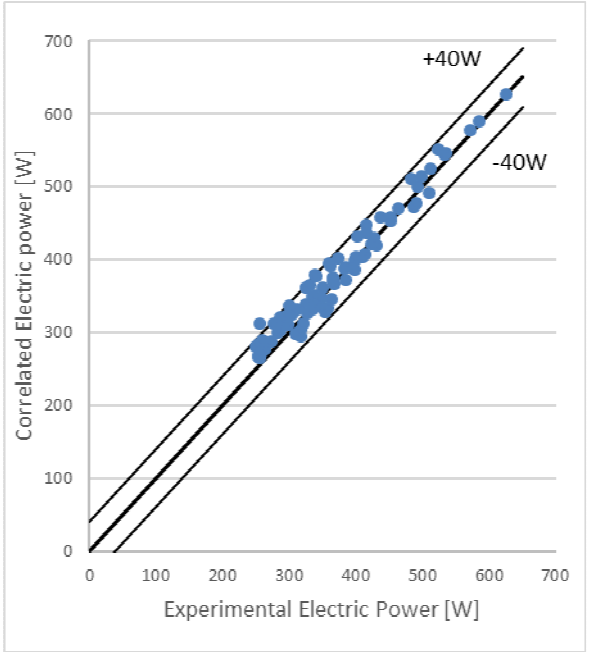

Figure 9: Experimental vs Correlated Electric Power

From Equation (6), pump efficiency becomes $\eta_{pump} = \dot{W}_{hyd}/(C_6.\dot{\Omega} + C_7.\dot{W}_{hyd})$ Miller (1995) and Tackett (2008) have the same kind of pump efficiency dependence with the load. The maximum pump efficiency is directly revealed: $\eta_{pump,max} = 1/C_7 = 82{,}5\%$. Power consumption $\dot{W}_{el}$ is estimated from $\dot{W}_{hyd}$ and $\dot{\Omega}$ using Equation (1) and (6), experimental and correlated values are compared in Figure 9.

Enthalpies are not known with enough accuracies to provide accurate $\dot{W}_{fluid}$ and therefore isentropic efficiencies values. A solution should be to use more accurate temperature sensors or use a calorimeter to estimate $\dot{Q}_{loss,pp}$. However, the isentropic efficiencies mean trend seems similar to the pump efficiency trend. If $\dot{Q}_{loss,pp}$ is assumed negligible, then, as a first approximation $\eta_{is} \cong \eta_{pump}$.

4.2 Model Overview

Table 2 summarize the main equation useful for the pumping system modelling. The first equation provide a relation between the volume flow (or the volumetric efficiency), the shaft rotational speed and the pressure drop. It could be used for flow control purpose or volume flow rate estimation. The second equation provide a relation between the pump mechanical shaft power, the rotational speed, the pressure drop and the flow rate. The flow rate could be compute from the first equation. This equation is use for pump losses and efficiency. The third equation provide a relation between the electric consumption, the rotational speed and the motor shaft power. When each equation are combined, it provide the net electric power request for a given pressure drop and rotational speed (or flow rate). This is useful for modelling or design purpose.

Table 2 : Models equations and parameters overview

Volume Flow Rate	$\dot{V}_{dis} = \dot{\Omega}.V_{disp}\left[1 - \left(\frac{A}{\dot{\Omega}.\mu.V_{disp}} + \beta_T.\left(1 + \frac{V_{dead}}{V_{disp}}\right)\right).\Delta P\right]$			
Input parameters	$\dot{\Omega}$	rpm	Rotational speed	
	ΔP	bar	Pressure differential	
Model coefficients	V_{disp}	m^3	Displaced volume	*Experimental*: Unloaded pump test
	A	m^3	Leakage coefficient	*Experimental*: On-load pump test
	V_{dead}	m^3	Dead volume	
Fluid properties	μ	Pa.s	Dynamic viscosity	Computed from outlet pressure & temperature
	β_T	Pa^{-1}	Isothermal compressibility	
Pump power	$\dot{W}_{mech} = C_6.\dot{\Omega} + C_7.\dot{W}_{hyd} = C_6.\dot{\Omega} + C_7.\dot{V}_{dis}.\Delta P$			
Input parameters	$\dot{\Omega}$	rpm	Rotational speed	
	ΔP	Pa	Pressure differential	
	$\dot{V}_{dis}$	m^3/s	Volumetric flow	
Model coefficients	C_6	W/rpm	Friction coefficient	*Experimental*: On-load pump test
	C_7	-	Efficiency coefficient	
VSD & Motor power	$\dot{W}_{el} = C_1 + \dot{W}_{mech} + C_2.\dot{W}_{mech}^2 + C_3.\dot{\Omega}^2$			
Input parameters	$\dot{\Omega}$	rpm	Rotational speed	
	$\dot{W}_{mech}$	W	Mechanical power	
Model coefficients	C_1	W/rpm	VSD losses coefficient	*Experimental*: Uncoupled motor test
	C_2	W^{-1}	Part-load coefficient	*Motor data* : $C_2 = 0{,}7.\frac{(1/\eta_{mot,n} - 1)}{\dot{W}_{mot,n}}$
	C_3	W/rpm^2	Motor friction coefficient	*Motor data* : $C_3 = 0{,}3.\dot{W}_{mot,n}.\frac{(1/\eta_{mot,n} - 1)}{\dot{\Omega}_n^2}$

6. CONCLUSIONS

An energetic analysis of a pumping system for ORC is proposed. For each component, a semi-empirical power model based on literature and experimental analysis is presented. This model could be used for the design or simulation of a reciprocating pump integrated into an Organic Rankine cycle, at part and full load. The volumetric efficiency equation could be used for simulation, process control or flow rate estimation if no flowmeter is available. Clarification of the different efficiencies useful for ORC design or simulation is proposed. The method and model deserve a deeper investigation for validation, as torque measurement between motor and pump or VSD electric power output. Measurement are in progress on a bigger pump for comparison and scale-up. .Experimental analysis shows that reciprocating pump can achieve good efficiency at high pressure (more than 80%), but falls when the pressure decrease. Pump driver should be carefully chosen and designed as well as the pump. Oversize leads to lower efficiency, especially when the process runs often at part-load operation. The electric motor should be chosen according to the process nominal power and not the pump maximum power, avoiding a motor oversizing due to pump oversize. It should also be noted that new legislation on motor minimal efficiency are implemented in most countries.

NOMENCLATURE

h	specific enthalpy	(J/kg)	$\dot{W}$	power	(W)
$\dot{m}$	mass flow rate	(kg/s)	β_T	isothermal compressibility	(Pa^{-1})
P	pressure	(bar)	Δ	difference	(-)
$\dot{Q}$	heat power	(W)	η	efficiency	(-)
V	volume	(m^3)	μ	dynamic viscosity	(Pa.s)
$\dot{V}$	volume flow rate	(m^3/h)	$\dot{\Omega}$	rotational speed	(rpm)

Subscript

0	unloaded	mech	mechanical
dis	discharge	mot	motor
disp	displaced	n	nominal
el	electrical	pp	pump
flu	fluid	suc	suction
hyd	hydraulic	th	theory
is	isentropic	vol	volumetric
los	losses	vsd	variable speed drive

REFERENCES

Astolfi, M., Romano, M.C., Bombarda, P., Macchi, E., 2014. Binary ORC (Organic Rankine Cycles) power plants for the exploitation of medium–low temperature geothermal sources – Part B: Techno-economic optimization. *Energy*, vol. 66: p. 435–446

Bao, J., Zhao, L., 2013. A review of working fluid and expander selections for organic Rankine cycle. *Renewable and Sustainable Energy Reviews*, vol. 24: p. 325–342

De Almeida, A., Falkner, H., Fong, J., Jugdoyal, K., 2014. EuP lot 30 - Electric motors and drives (Final Report). for European Commission: 209p.

De Chargeres, B., Rey, R., 2009. Pompes volumétriques pour liquides, *Techniques de l'Ingénieur*.

Deprez, W., Lemmens, J., Vanhooydonck, D., Symens, W., Stockman, K., Dereyne, S., Driesen, J., 2010. Iso efficiency contours as a concept to characterize variable speed drive efficiency. *10th International Conference on Electrical Machines*, Rome.

Maraver, D., Royo, J., Lemort, V., Quoilin, S., 2014. Systematic optimization of subcritical and transcritical organic Rankine cycles (ORCs) constrained by technical parameters in multiple applications. *Applied Energy*, vol. 117: p. 11–29.

Miao, Z., Xu, J., Yang, X., Zou, J., 2015. Operation and performance of a low temperature organic Rankine cycle. *Applied Thermal Engineering*, vol. 75: p. 1065–1075

Miller, J.E., 1988. Characteristic of the reciprocating pump. *Proc. of the 5th International Pump Users Symposium*, Houston.

Miller, J.E., 1995. *The Reciprocating Pump Theory, Design, And Use*, Krieger Publishing Co: 484 p.

Johnston, D.N., 1991. Numerical modelling of reciprocating pumps with self-acting valves. *Proceedings of the Institution of Mechanical Engineers, Part I: Journal of Systems and Control Engineering*, vol. 205: p. 87–96.

Kari, R., 2009. AC Drive comes with losses - Technical Description. ABB.

Li, Y., Liu, M., Lau, J., Zhang, B., 2015. A novel method to determine the motor efficiency under variable speed operations and partial load conditions. *Applied Energy*, vol. 144: p. 234–240

Lippke, F., 1995. Simulation of the part load behavior of a 30 MWe SEGS plant. Sandia National Laboratories

Quoilin, S., Aumann, R., Grill, A., Schuster, A., Lemort, V., Spliethoff, H., 2011. Dynamic modeling and optimal control strategy of waste heat recovery Organic Rankine Cycles. *Applied Energy*, vol. 88: p. 2183–2190

Quoilin, S., Broek, M.V.D., Declaye, S., Dewallef, P., Lemort, V., 2013. Techno-economic survey of organic rankine cycle (ORC) systems. *Renewable and Sustainable Energy Reviews*, vol. 22: p. 168–186

Schuster, A., Karellas, S., Aumann, R., 2010. Efficiency optimization potential in supercritical Organic Rankine Cycles. *Energy*, vol. 35: p. 1033–1039

Shu, G., Liu, L., Tian, H., Wei, H., Xu, X., 2013. Performance comparison and working fluid analysis of subcritical and transcritical dual-loop organic Rankine cycle (DORC) used in engine waste heat recovery. *Energy Conversion and Management*, vol. 74: p. 35–43.Astolfi, M., Romano, M.C.,

Singh, P.J., Madavan, N.K., 1987. Complete Analysis and Simulation of Reciprocating Pumps Including System Piping. *Proc. of the 4th International Pump Users Symposium*, Houston, p. 53–73.

Tackett, H.H., Cripe, J.A., Dyson, G., 2008. Positive Displacement Reciprocating Pump Fundamentals - Power and Direct Acting Types. *Proc. of the 24th International Pump Users Symposium*.

Tillner-Roth, R., Baehr, H.D., 1994. An International Standard Formulation for the Thermodynamic Properties of 1,1,1,2-Tetrafluoroethane (HFC-134a) for Temperatures from 170 K to 455 K and Pressures up to 70 MPa. *Journal of Physical and Chemical Reference Data*, vol. 23: p. 657.

Toffolo, A., Lazzaretto, A., Manente, G., Paci, M., 2014. A multi-criteria approach for the optimal selection of working fluid and design parameters in Organic Rankine Cycle systems. *Applied Energy*, vol. 121: p. 219–232.

Vetter, G., 2006. *Rotierende Verdrängerpumpen für die Prozesstechnik*, Vulkan-Verlag GmbH. 337 p.

ANSI/HI 6.1-6.5, 2000. Reciprocating Power Pumps for Nomenclature, Definitions, Application and Operation. American National Standards Institute.

ANSI/HI 6.6, 2000. Reciprocating Pump Tests. American National Standards Institute.

IEC 60034-31, 2010. Guide for the selection and application of energy efficient motors including variable-speed applications. International Electrotechnical Commission.

ACKNOWLEDGEMENT

This work was supported by the French Environment and Energy Management Agency (ADEME) and the Atomic Energy Commission (CEA)

INVESTIGATION OF A MASSIVE ELECTRICITY STORAGE SYSTEM BY MEANS OF A GEOTHERMAL HEAT TRANSFER PROCESS INVOLVING CO2 TRANSCRITICAL CYCLES

Fadhel Ayachi[1], Thomas Tartière[2], Nicolas Tauveron[1]*, Stéphane Colasson[1], Denis Nguyen[3]

[1]CEA, LITEN – DTBH/SBRT/LS2T, 17 rue des Martyrs, 38054 Grenoble, France
fadhel.ayachi@cea.fr, nicolas.tauveron@cea.fr; stephane.colasson@cea.fr

[2]Enertime, 1 rue du Moulin des Bruyères, 92400 Courbevoie, France
thomas.tartiere@enertime.com

[3]BRGM Languedoc-Roussillon, 1039 rue de Pinville, 34000 Montpellier, France
d.nguyen@brgm.fr

* Corresponding Author

ABSTRACT

This work presents a specific application of the Rankine cycle and heat pump technologies: electricity storage. A multi-megawatt thermo-electric energy storage based on thermodynamic cycles is studied as a promising alternative to PSH (Pumped-Storage Hydroelectricity) and CAES (Compressed Air Energy Storage) systems. As a preliminary work, the main objective is to assess the performances of the massive storage technology based on transcritical CO_2 heat pump for charging and transcritical CO_2 Organic Rankine Cycle for discharging, with power output in the 1-10 MWe range.

The general concept of the system is presented, along with its thermodynamic modeling. A parametric analysis is carried out showing that it is possible to reach roundtrip efficiencies up to 53% that are competitive with other technologies. This work also shows the strong dependency between the different parameters of the system, and how an economic optimization will have to take all the subcomponents into account.

1. INTRODUCTION

Organic Rankine Cycles (ORC) have been used in a wide range of applications, including geothermal, biomass or solar power plants, waste heat recovery from industrial processes or combustion engines, ocean thermal energy conversion… and a wide range of power outputs from a few kW to tens of MW. The possibility to use ORC to produce electricity from heat that has been previously stored as a large-scale electricity storage technology remains more confidential but has been the subjects of recent studies [1].

As it is well-known, the massive integration of intermittent renewable energy production generates new challenges for the supervision and regulation of electric grids. The use of flexible but carbon-intensive technologies such as gas turbines has been the main solution in order to ensure the balance between demand and supply, maintaining grid frequency and power quality. However, large-scale electricity storage is a promising alternative with a much lower environmental impact. In addition, it would enable a decentralized access to electricity and lower the dependency on fossil fuels. If storage is still expensive today, it could become increasingly viable as the price of carbon rises.

Several technologies exist or are under development for large-scale energy storage. Pumped Hydro Storage (PHS) is the most common one, accounting for more than 99% of the worldwide bulk storage capacity, representing around 140 GW over 380 locations [2]. When there is an excess of power supply, water is pumped to an upper reservoir, from where it can be discharged to drive a turbine

when power demand is high. Reported roundtrip efficiencies are typically between 70% and 85%. Despite having a long lifetime and being the most cost-effective energy storage technology, these systems have a low energy density and require the construction of large reservoirs, leading to a high environmental impact. In addition, the most suitable locations have already been used in developed countries. Other possibilities would be to include pre-existing dams or the ocean, as in the 30 MW Yanbaru project in Japan [3].

In a Compressed-Air Energy Storage (CAES) system, ambient air is compressed and stored underground. Reported roundtrip efficiencies are around 50%. The capital cost of CAES power plants is competitive with PHS and their power output can reach hundreds of MW. In contrast to PHS, only 2 CAES power plants exist in the world: a 290 MW plant in Huntorf, Germany (1978) [4], and a 110 MW plant in McIntosh, USA (1991) [5]. A much higher efficiency of up to 70% could be achieved by storing the heat of compression before the pressurized air is sent to the cavity [6][7]. This Advanced Adiabatic CAES (AA-CAES) technology is still under development. As for PHS, CAES systems require very specific sites and cannot be installed everywhere.

Thermo-electric energy storage (TEES) is a promising alternative to existing technologies that would allow widespread and large-scale electricity storage. It has a high energy density and is independent from geological or geographical constraints. During periods of excess electricity generation, a vapor compression heat pump consumes electricity and transfers heat between a low-temperature heat source and a higher temperature heat sink. The temperature difference between the heat sink and the heat source can be maintained for several hours, until a power cycle is used to discharge the system and generate electricity during peak consumption hours.

Mercangöz [1] gave references of thermo-electric energy storage studies as old as 1924 and described the general concept of this technology, based on two-way conversion of electricity to and from heat. He stated that the main challenges of TEES are to closely match the heat source and heat sink with the working fluid, and to find an optimum between roundtrip efficiency and capital cost. He analyzed a TEES system with transcritical CO_2, hot water and ice as storage materials. The ABB Corporate Research Center [8][9] described a way to store electricity using two hot water tanks, ice storage and transcritical CO_2 cycles. For similar systems, Morandin [10][11][12] defined a design methodology based on pinch analysis and calculated a 60% maximum roundtrip efficiency for a base case scenario with turbomachinery efficiencies given by manufacturers.

Sensible heat storage with hot water tanks is often considered, since water has high thermal capacity, is very cheap and environmental-friendly. Latent heat storages based on phase change materials (PCMs) have also been widely investigated. The heat sink of the system can be either the ambient or ice. This second option ensures a constant low-pressure for the process that is favorable to turbomachines. A mixture of salt and water can be used to adjust the heat sink temperature between 0°C and -21.2°C (corresponding to the eutectic point with 23.3% of NaCl in the mixture) [10].

Different working fluids can be considered for the thermodynamic cycles. Desrues [13] presented a TEES process based on Argon in forward and backward closed Brayton cycles. Henchoz [14] analyzed the combination of solar thermal energy with TEES based on Ammonia cycles. Kim [15] reviewed current TEES systems and showed that using transcritical CO2 cycles instead of Argon Brayton cycles leads to a higher roundtrip efficiency even if the required temperature difference between the heat storages is much smaller. He also proposed an isothermal energy storage system based on transcritical CO_2 cycles and liquid piston compressors/expanders.

Carbon dioxide is a natural refrigerant with many advantages. It is a low-cost fluid that is non-toxic, non-flammable, chemically stable, and readily available. In addition, the high fluid density of supercritical CO2 leads to very compact systems. Many studies have been published to evaluate the potential of supercritical CO_2 as working fluid in power cycles and heat pumps [16][17]. Cayer carried out an analysis [18] and optimization [19] of transcritical CO_2 cycle with a low-temperature

heat source. More recently, the use of CO_2 for multi-megawatt power cycles has reached a commercial step with the American company Echogen [20].

The purpose of this article is to introduce a new type of electro-thermal energy storage process for large scale electric applications, based on transcritical CO_2 cycles and ground heat storage. The conceptual design of the TEES system is addressed here only from a thermodynamic point of view and economic analysis are left for future works.

2. THERMODYNAMIC MODELING

The electro-thermal energy storage system is a high-capacity storage concept that includes:

i- a hot reservoir made of a set of ground heat exchangers in a low diffusivity rock ;
ii- a cold reservoir using either ice ($T_{cold} \leq 0°C$) or a phase-change material ($T_{cold} > 0°C$);
iii- two thermodynamic cycles as charging and discharging processes, both using carbon dioxide as working fluid;

The layouts of the thermodynamic cycles are given by Fig. 1 and Fig. 2. Due to the high storage capacity (typically 100 MWh of heat) and the rock low diffusivity, this technology is suitable for long discharge durations (typically >10 hours) and will not offer the same kind of services to the grid than batteries. Therefore, the parameters of the system will vary very slowly with time, and provided that the system is not discharged further than a certain point, can be considered as constant, as a preliminary step. Therefore, the processes are assumed to be at steady state and the system parameters are reported in Table 1. The thermodynamic model is implemented with Engineering Equation Solver (EES) [21].

During off-hours, a transcritical heat pump is used for charging the system: the working fluid leaves the cold reservoir heat exchanger as a saturated vapor at $T_1 = T_{cold} - \Delta T_{min}$ and is preheated ($1 \rightarrow 2$) through a regenerator, before being adiabatically compressed ($2 \rightarrow 3$) with isentropic efficiency $\eta_{s,c}$. At the compressor outlet, the fluid at $T_3 = (T_{hot})_{max} + \Delta T_{min}$ and supercritical high pressure $P_3 = P_H$ is cooled through the hot reservoir exchangers ($3 \rightarrow 4$) and releases heat to the ground, before being subcooled in the regenerator ($4 \rightarrow 5$). The liquid is then expanded ($5 \rightarrow 6$) to subcritical low pressure P_L and is finally evaporated in the cold reservoir exchanger ($6 \rightarrow 1$).

Table 1. Input parameters

Storage	
Hot storage max temperature	Variable
Cold storage temperature	Variable
Min temperature difference between heat reservoir and CO_2 ΔT_{min}	1 K
Charging cycle	
Compressor isentropic efficiency $\eta_{s,c}$	0.85
Motor efficiency η_m	0.98
$(T_4)_{min}$	30°C
Regenerator pinch	5 K
Discharging cycle	
Net power output $\dot{W}_{el}'$	1 – 10 MW_{el}
Pump isentropic efficiency $\eta_{s,p}$	0.80
Turbine isentropic efficiency $\eta_{s,t}$	0.90
Generator efficiency η_g	0.98
Regenerator pinch	5 K
Chiller	
Compressor isentropic efficiency	0.85
Motor efficiency	0.98
Condensing temperature	20°C
Evaporating temperature	Same than for discharge cycle

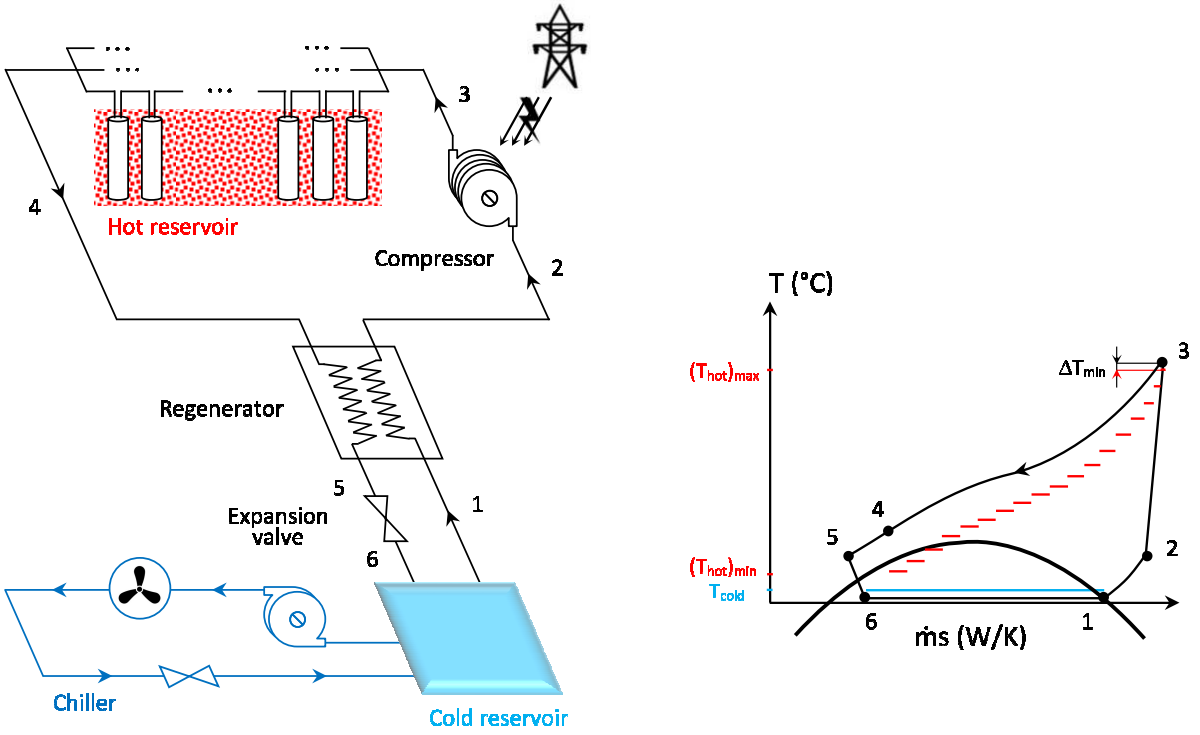

(a) *(b)*

Fig. 1. Charging process: a) process layout, b) (T, ṁs) diagram.

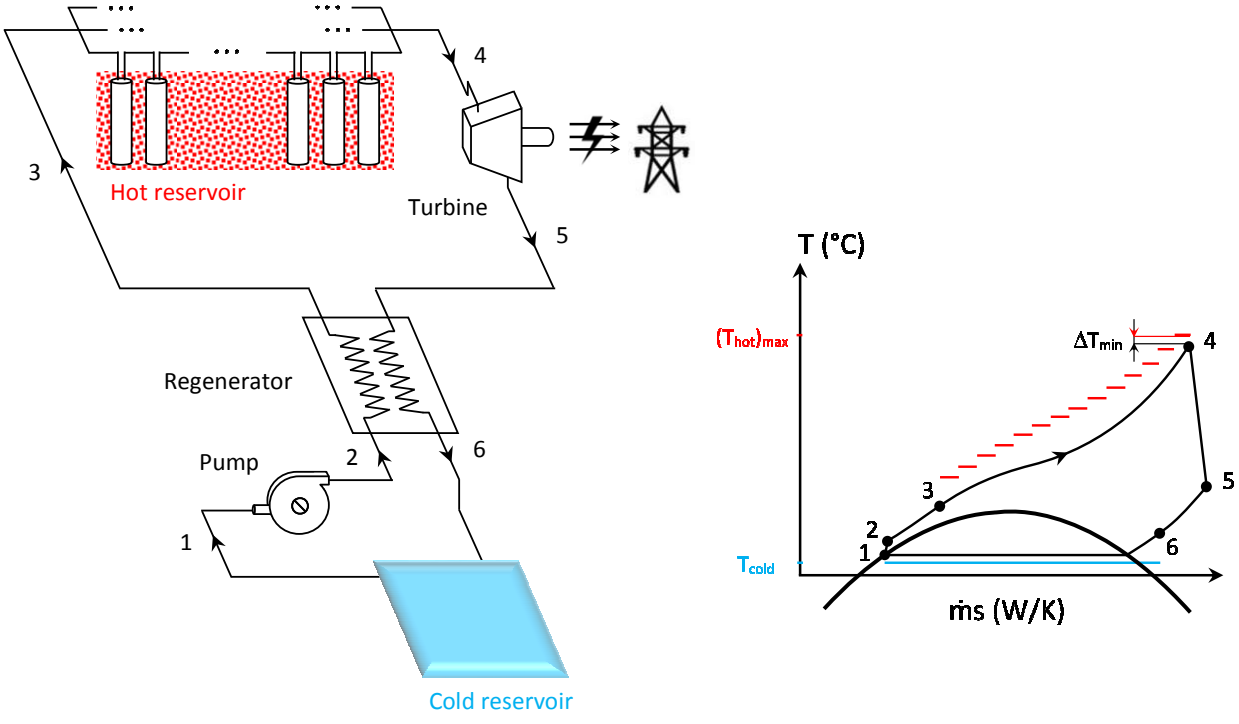

(a) *(b)*

Fig. 2. Discharging process: a) process layout, b) (T, ṁs) diagram.

High pressures in the range 100-150 bars will require the use of Printed-Circuit Heat Exchangers (PCHE) [22] or more unlikely costly tubular heat exchangers for the regenerator heat exchanger.

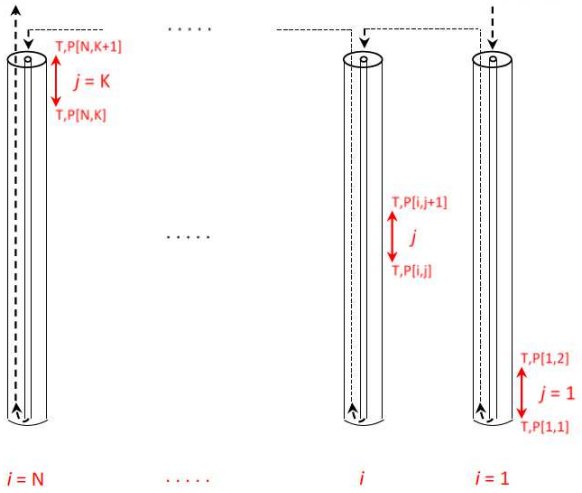

Fig. 3. Principle of the ground heat exchangers

Fig. 3 shows the general principle of the ground heat storage. The fluid at supercritical pressure is injected at the bottom of each column through a central tube and then flows up to an annular exit, transferring heat with the surrounding rock. Several series of ground heat exchangers are installed in parallel in order to reach the required thermal input/output. Detailed simulations of the overall ground heat storage system are being investigated and will enable to estimate the head losses in that component and adjust the cycle parameters. As a preliminary work, pressure losses in the thermodynamic cycles are neglected.

Given the cold storage temperature T_{cold} and ΔT_{min} as input parameters, it is possible to calculate the saturation temperature T_1 and thus the saturation pressure P_L. Similarly, knowing the hot storage temperature, ΔT_{min} and the compressor isentropic efficiency, it is possible to calculate the high pressure P_H. The thermodynamic states of the charging cycle can be obtained from the energy balances of each components:

$$(h_1 - h_2) + (h_4 - h_5) = 0 \quad (1)$$

$$\dot{W}_c + \dot{m}(h_2 - h_3) = 0 \quad (2)$$

$$\dot{Q}_{hot} + \dot{m}(h_3 - h_4) = 0 \quad (3)$$

$$h_5 - h_6 = 0 \quad (4)$$

$$\dot{Q}_{cold} + \dot{m}(h_6 - h_1) = 0 \quad (5)$$

h_i (J/kgK) and $\dot{m}$ (kg/s) being respectively the specific enthalpy at state i and the mass flow rate in the charging cycle. $\dot{W}_c = \dot{m}(h_{3s} - h_2)/\eta_{s,c} > 0$, $\dot{Q}_{hot} < 0$ and $\dot{Q}_{cold} > 0$ are respectively the compressor power, the heat flux transferred to the hot reservoir and the heat flux transferred from the cold reservoir.

Adding equations 1 to 5 leads to the energy balance of the charging cycle:

$$\dot{W}_c + \dot{Q}_{hot} + \dot{Q}_{cold} = 0 \qquad (6)$$

During peak-hours, a transcritical Organic Rankine Cycle is used for discharging the system: the working fluid leaves the cold reservoir heat exchanger at saturation $T_1' = T_{cold} + \Delta T_{min}$ and is pumped ($1 \rightarrow 2$) with isentropic efficiency $\eta_{s,p}$. At the pump outlet, the fluid at supercritical high pressure $P_2' = P_H'$ is preheated in the regenerator ($2 \rightarrow 3$), then heated in the hot reservoir exchanger ($3 \rightarrow 4$) where it recovers heat from the ground and reaches $T_4' = (T_{hot})_{max} - \Delta T_{min}$. The fluid is then adiabatically expanded ($4 \rightarrow 5$) with isentropic efficiency $\eta_{s,t}$ to the subcritical pressure P_L', producing mechanical power. Finally, the fluid is cooled in the regenerator ($5 \rightarrow 6$) before being condensed through the cold reservoir exchanger ($6 \rightarrow 1$).

The reservoir temperatures T_{cold} and $(T_{hot})_{max}$ and the hot pressure $P_H' \approx P_H$ being known, the thermodynamic states can be obtained from the energy balances of each component:

$$\dot{W}_p' + \dot{m}'(h_1' - h_2') = 0 \qquad (7)$$

$$(h_2' - h_3') + (h_5' - h_6') = 0 \qquad (8)$$

$$\dot{Q}_{hot}' + \dot{m}'(h_3' - h_4') = 0 \qquad (9)$$

$$\dot{W}_t' + \dot{m}'(h_4' - h_5') = 0 \qquad (10)$$

$$\dot{Q}_{cold}' + \dot{m}'(h_6' - h_1') = 0 \qquad (11)$$

h_i' (J/kgK) and $\dot{m}'$ (kg/s) being respectively the specific enthalpy at state i and the mass flow rate of the discharging cycle. $\dot{W}_p'(W) = \dot{m}'(h_{2s}' - h_1')/\eta_{s,p} > 0$, $\dot{W}_t(W) = \dot{m}'(h_{5s}' - h_4')\,\eta_{s,t} < 0$, $\dot{Q}_{hot}'(W) > 0$ and $\dot{Q}_{cold}'(W) < 0$ are respectively the pump power, the turbine power, the heat flux transferred from the hot reservoir and the heat flux transferred to the cold reservoir.
Adding equations 7 to 11 gives the energy balance of the discharge cycle:

$$\dot{W}_p' + \dot{Q}_{hot}' + \dot{W}_t' + \dot{Q}_{cold}' = 0 \qquad (12)$$

As an example, the Temperature-Entropy diagram of the charging and discharging cycles, for hot storage at 130°C and cold storage at 0°C, are given in Fig. 4.

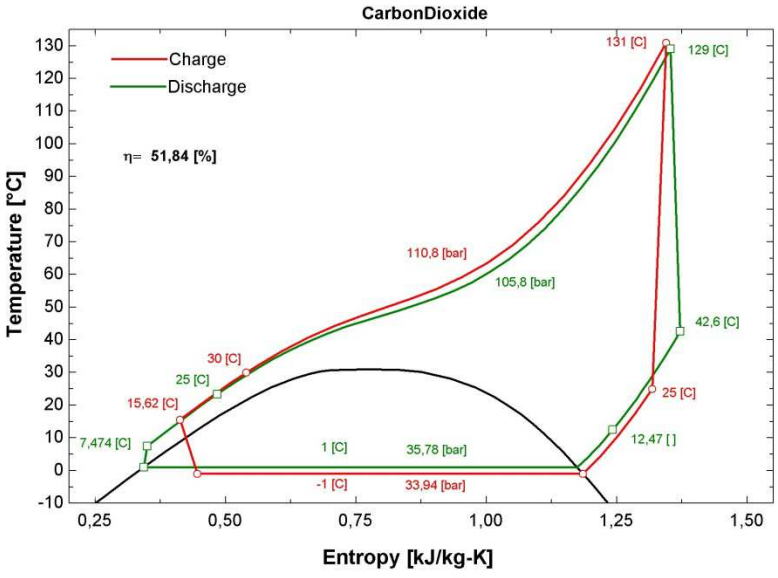

Fig. 4. T-S diagram for hot storage at 130°C and cold storage at 0°C (ΔT_{min} = 1K).

The net power output of the discharge cycle $\dot{W}'_{el} = \eta_g \cdot \dot{W}'_t - \dot{W}'_p$ is defined as an input parameter, in the range 1-10 MWel. The thermal energy stored in the ground heat exchangers is $\dot{Q}'_{hot} \cdot t_{discharge} = -\dot{Q}_{hot} \cdot t_{charge}$. As a first step, we assume similar charging and discharging time so $\dot{Q}_{hot}' \cong -\dot{Q}_{hot}$. This gives the mass flow rates ṁ and ṁ′ and then the net power input of the charging cycle $\dot{W}_{el} = \dot{W}_c / \eta_m$. Having a different charge duration would only change the mass flow rate of the charging heat pump cycle, and therefore its power input, but does not affect the thermodynamic analysis.

Furthermore, by adding equations 6 and 12 and using $\dot{Q}_{hot}' = -\dot{Q}_{hot}$, it follows that:

$$\dot{W}_c + \dot{Q}_{cold} + \dot{W}_p' + \dot{W}_t' + \dot{Q}_{cold}' = 0 \qquad (13)$$

Based on Equation 13, we can define the thermal asymmetry of the system such as:

$$\delta\dot{Q}_{cold} = \dot{Q}_{cold} + \dot{Q}_{cold}' = -(\dot{W}_c + \dot{W}_p' + \dot{W}_t') < 0 \qquad (14)$$

The charging and discharging cycles are not perfectly reversible. Even if the discharging cycle can consume the same amount of heat than provided by the charging cycle ($\dot{Q}_{hot}' = -\dot{Q}_{hot}$), the amount of cold produced by the heat pump cycle is smaller than the amount needed during the discharge. Therefore, the thermal asymmetry of the system represents the amount of additional cooling that is needed to discharge the system and that should be provided by an auxiliary CO_2 chiller working in parallel with the charging cycle (Fig. 1a).

A thermodynamic model of a single-stage chiller, with parameters given in Table 1, is developed using EES in order to calculate this additional electrical consumption $\dot{W}_{el}''(W)$, expressed by equation 15.

$$\dot{W}_{el}'' = \frac{-\delta\dot{Q}_{cold}}{COP} \qquad (15)$$

Finally, assuming similar charging and discharging durations, the overall roundtrip efficiency of the system can be defined as:

$$\eta_{sys} = \frac{\dot{W}_{el}'}{\dot{W}_{el} + \dot{W}_{el}''} \qquad (16)$$

This steady-state analysis provided a limited but useful first analysis of the system, in order to assess the main characteristics of each component and the dependency between the charging and discharging cycles. A time-dependent model of the system is under development but requires a detailed simulation of the diffusion through the ground heat exchangers, and a thorough understanding of the convection heat transfer coefficient between the supercritical CO_2 and the rock. These two topics are being investigated and will be detailed in future works.

3. PARAMETRIC ANALYSIS

Based on this preliminary thermodynamic modeling, it is possible to carry out a parameter analysis of the system. Figure 5 shows the efficiency of the system with respect to the temperature of the heat storages. As we can see, it is possible to reach roundtrip efficiencies up to 53% with high storage temperatures and 1 K-temperature difference between the charging and discharging cycle (ΔT_{min}).

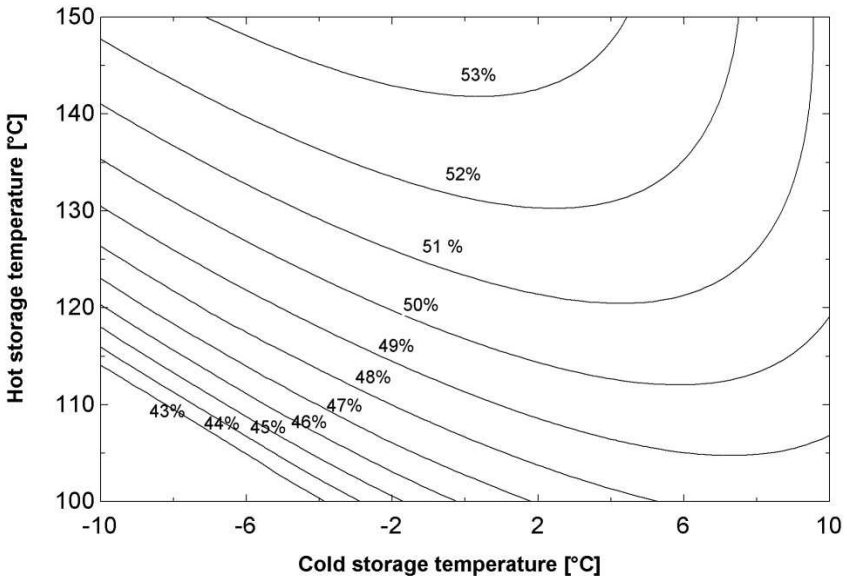

Fig. 5. Overall efficiency of the storage system with respect to the design storage temperatures (ΔT_{min} = 1K).

The choice of temperatures for the hot and cold storages will not only impact the overall electrical efficiency but also the size of the storages and the initial investment cost. For example, Fig. 6 gives the roundtrip efficiency as a function of the cold storage temperature for a hot storage at 130°C. In that case, it is possible to reach a maximum overall efficiency of 51.8% for a cold storage at 2°C. This is mainly due to the fact that the heat pump COP increases significantly when the cold storage temperature is increased, thus decreasing the electricity consumption of the system. In addition, this also reduces the pressure ratio in the two thermodynamic cycles and therefore simplifies the design of the turbomachines.

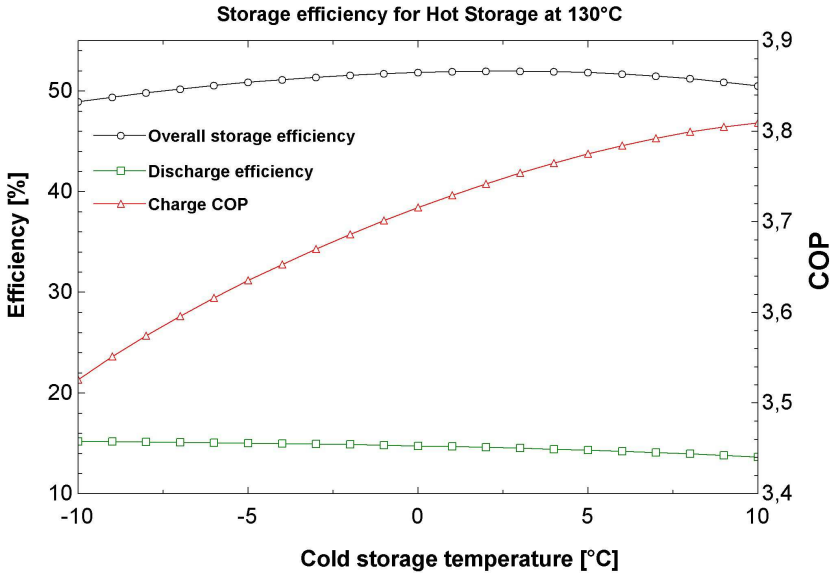

Fig. 6. Storage efficiency as a function of cold storage temperature ($(T_{hot})_{max}$ = 130°C, ΔT_{min} = 1K).

Figure 7 shows the thermal asymmetry of the system, as defined by Equation 13, as a function of the cold storage temperature, for a hot storage at 130°C. We can see that the increase in storage efficiency shown in Figure 6 when changing the cold storage temperature from -10°C to 0°C is also due to a smaller asymmetry between the charging and discharging cycles. In addition, the performance of the chiller that provides this additional cooling is improved with higher cold storage temperatures.

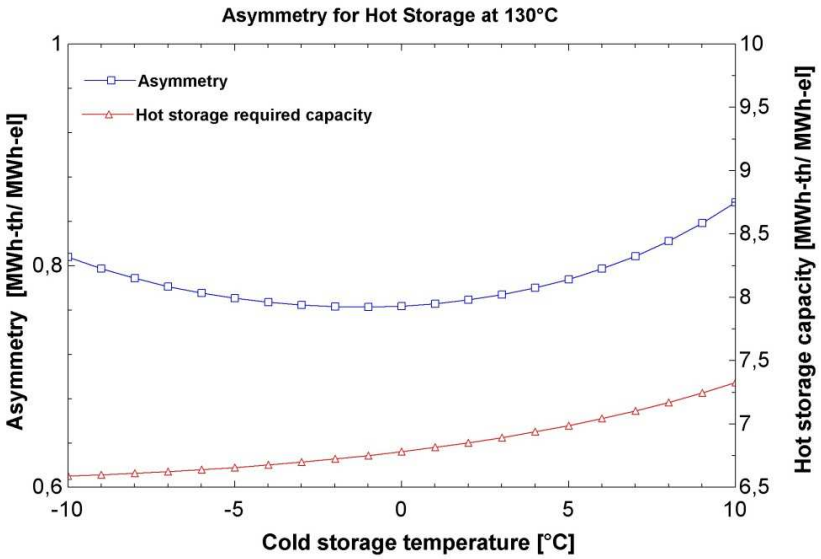

Fig. 7. Asymmetry as a function of cold storage temperature ($(T_{hot})_{max}$ = 130°C, ΔT_{min} = 1K).

However, decreasing the temperature difference between the two storages reduces the power cycle efficiency. This means that the discharging cycle has to consume more heat in order to produce the same electrical power output. Therefore, the hot storage has to be bigger, leading to an increase of about 11% between the cases of cold storage at -10°C and 10°C. In addition, for a given hot storage temperature, the high pressure of the system increases with warmer cold storage temperatures, as shown in figure 8.

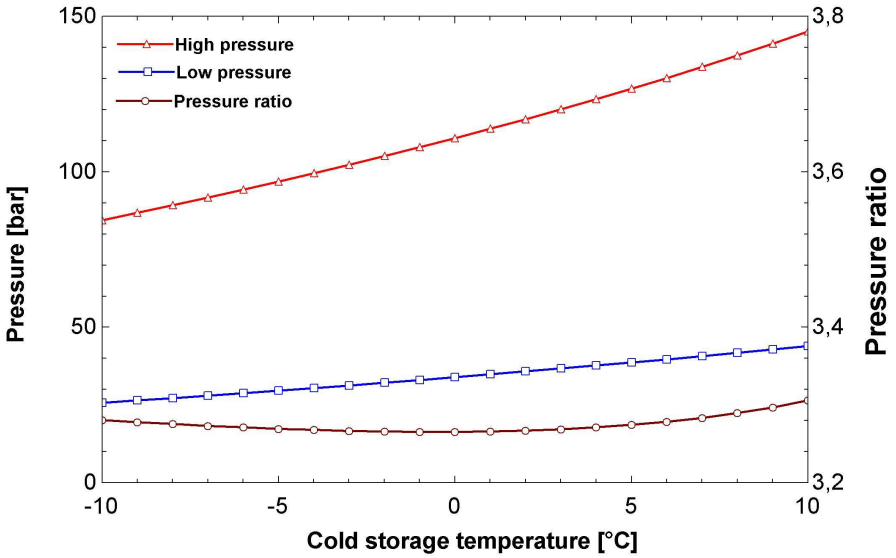

Fig. 8. Pressures of the system as a function of cold storage temperature ($(T_{hot})_{max}$ = 130°C, ΔT_{min} = 1K).

As we can see, the system optimization has to take all these elements into account in order to find a trade-off between efficiency and investment cost. Further works will take turbomachinery and heat storage designs into account in the process design, enabling a cost optimization of the storage system.

4. CONCLUSION

This work carries out the analysis of a novel system storing electricity in the form of ground heat and ice, using transcritical Heat Pump and transcritical ORC cycles for the charging and discharging processes. A thermodynamic modeling is presented and a parametric analysis shows roundtrip efficiencies of up to 53% that are competitive with other technologies. Further work through the SELECO2 project will include turbomachinery and heat storage designs in order to have a more detailed overview of the system and of the dependency between the charging and the discharging processes which can represent large off-design conditions. Furthermore transient simulations of the complete charging/discharging cycle will be performed and confirm (or not) the efficiency value and the general interest of the device.

REFERENCES

[1] Mercangöz M, Hemrle J, Kaufmann L, Z'Graggen A, Ohler C. Electrothermal energy storage with transcritical CO2 cycles. Energy 2012; 45: 407–415.
[2] ENEA Consulting, Facts & Figures : Le Stockage d'Energie. 2012; Available at: <http://www.enea-consulting.com/wp-content/uploads/ENEA-Consulting-Le-Stockage-dEnergie.pdf > [accessed 22.01.2015].
[3] Fujihara T, Imano H, Oshima K. Development of Pump Turbine for Seawater Pumped-Storage Power plant. Hitachi Review 1998 : 47 (5): 199-202.
[4] Crotogino F, Mohmeyer K-U, and Scharf R. Huntorf CAES: More than 20 Years of Successful Operation. Proc of SMRI Spring Meeting, Orlando, Florida, USA, 15-18 April 2001.
[5] PowerSouth Energy Cooperative, CAES McIntosh Alabama. Available at: <http://www.powersouth.com/mcintosh_power_plant/compressed_air_energy> [accessed 23.01.2015]
[6] Chris Bullough, Christoph Gatzen, Christoph Jakiel, Martin Koller, Andreas Nowi, Stefan Zunft, Advanced adiabatic compressed air energy storage for the integration of wind energy, in: Proceedings of the European Wind Energy Conference, London UK, 2004.
[7] Grazzini G, Milazzo A. Thermodynamic analysis of CAES/TES systems for renewable energy plants. Renewable Energy 2008;32:1998-2006.
[8] Mercangoez M, Hemrle J, Kaufmann L. Thermoelectric energy storage system having two thermal baths and method for storing thermoelectric energy. Patent EP2241737 (A1) [Internet]. 20.10.2010. Available at: www.google.com/patents/EP2241737A1 [accessed 22.05.15].
[9] Ohler C, Mercangoez M. Thermoelectric energy storage system and method for storing thermoelectric energy. Patent EP2182179 (A1) [Internet]. 05.05.2010. Available at: www.ipo.gov.uk/p-ipsum/case/PublicationNumber/EP2182179 [accessed 22.01.15].
[10] Morandin M, Maréchal F, Mercangöz M, Buchter F. Conceptual design of a thermo-electrical energy storage system based on heat integration of thermodynamic cycles - Part A: Methodology and base case. Energy 2012;45:375e85.
[11] Morandin M, Maréchal F, Mercangöz M, Buchter F. Conceptual design of a thermo-electrical energy storage system based on heat integration of thermodynamic cycles - Part B: Alternative system configurations. Energy 2012;45:386-96.
[12] Morandin M, Mercangöz M, Hemrle J, Maréchal F, Favrat D. Thermoeconomic design optimization of a thermo-electric energy storage system based on transcritical CO2 cycles. Energy 2013; 58: 571–587.
[13] Desrues T,Ruer J,Marty P,Fourmigué JF. A thermal energy storage process for large scale electric applications. Applied Thermal Engineering 2010;30(5):425-32
[14] Henchoz S, Buchter F, Favrat D, Morandin M, Mercangoez M. Thermoeconomic analysis of a solar enhanced energy storage concept based on thermodynamic cycles. Energy 2012;45(1):358e65.
[15] Kim YM, Shin DG, Lee SY, Favrat D. Isothermal transcritical CO2 cycles with TES (thermal energy storage) for electricity storage. Energy 2013; 49: 484–501.

[16] Kim YM, Kim CG, Favrat D. Transcritical or supercritical CO2 cycles using both low- and high-temperature heat sources. Energy 2012; 43: 402–415.
[17] Li M, Wang J, Li S, Xurong Wang, He W, Dai Y. Thermo-economic analysis and comparison of a CO2 transcritical power cycle and an organic Rankine cycle. Geothermics 2014; 50: 101–111.
[18] Cayer E, Galanis N, Désilets M, Nesreddine H, Roy P. Analysis of a carbon dioxide transcritical power cycle using a low temperature source. Applied Energy 2009;86:1055–63.
[19] Cayer E, Galanis N, Nesreddine H. Parametric study and optimization of a transcritical power cycle using a low temperature source. Applied Energy 2010:87:1349-1357
[20] Held T., Initial Test Results of a Megawatt-class Supercritical CO2 heat engine. The 4th International Symposium – Supercritical CO2 Power Cycles; 2014 Sept 9-10; Pittsburgh, USA.
[21] S.A. Klein, Engineering Equation Solver. F-Chart Software, Middleton, WI, 2010.
[22] Le Pierres R., Southall D., Osborne S. Impact of Mechanical Design Issues on Printed Circuit Heat Exchangers, in: Proceedings of SCO_2 Power Cycle Symposium, Boulder, 2011

ACKNOWLEDGEMENT

The authors acknowledge the support of the French Agence Nationale de la Recherche (ANR), under grant ANR-13-SEED-0004 (project SELECO2).

AN AUTOMATIC ADJUSTING DEVICE OF THE SPIRAL GROOVE FACE SEAL USED ON ORC TURBINE SHAFT END AND THE ESTABLISHMENT OF CONTROL MODEL

Ya Zheng[1], Yue Cao[2], Dongshuai Hu[3], Xurong Wang[4], Yiping Dai[5]*

[1,2,3,4,5]Xi'an Jiaotong University, Institute of Turbomachinery,
Xi'an, Shaanxi, China
ypdai@mail.xjtu.edu.cn

* Corresponding Author

ABSTRACT

ORC system has to solve the seal problem for the inflammable, explosive, corrosive and toxic working fluids. The real-time monitoring of seal systems is particularly important to ensure 'zero-leakage'. In recent decades, the development of automation technology, testing and measurement technology, advanced process technology and some related regulations for the rotating machinery promote the research and application of monitoring technology of the spiral groove face seals. This paper mainly focuses on the real-time response of the seal system to the change of working parameters. A new method is proposed to achieve the automatic control of seal pressure. The experiment and numerical simulation is conducted at first to obtain the maximum differential pressure between inlet and outlet, which can ensure zero leakage of the seal system in different working parameters. Then, the control system of pump is established to adjust the pressure of feed pump in real time when the pressure of sealed medium (the pressure of end face outlet) changes. Consequently, the pressure of end face inlet is adjusted to make the differential pressure between inlet and outlet less than or equal to the maximum differential pressure.

1. INTRODUCTION

Organic Rankine Cycle system has been confirmed to be an efficient approach to utilize low grade waste heat and this system is considerable mature for immense amounts of concrete research during these years. However, the leakage of organic fluid is still the persistent problem of the ORC system which can cause toxic substances diffusion and efficiency decrease. The spiral groove seal using liquid as sealed medium was proposed by Josef (1980) firstly. Then researchers mainly use the advanced virtual instrument technology on testing system of spiral groove face seals. It is creative to combine the machinery and electricity on the basis of virtual instrument technology, which contribute to build a complete set of testing and monitoring system of spiral groove face seals. The appropriate sensors can ensure the stable operation of turbine units. Since the concept of controlled end face seal was proposed, it has been researched by many scholars. Wolff and Salant (1995) used electronic technique to control mechanical seal for aerospace applications. Heilala (1987), Etsion *et al*. (1991) tried to prevent mechanical seal from dry running and severe wear through adjusting and controlling the end face temperature. Zou *et al*. (2000) monitored the non-contacting mechanical face seal in real time, Zhou and Gu (2009) focused on the controllability of spiral groove face seals, and concluded the relationship between sealing performance and the fluid film. Zheng *et al*. (2012) built detailed models of spiral groove face seal in commercial computational software ANSYS/FLUENT to analyze the effect of structural and operational parameters of spiral groove face seals.

According to the various characteristic parameters tests of seals, the measurement and control of liquid film pressure is vitally important to monitor the status of seals and ensure it operates stably

and safely. In general, engineers use pressure tap to measure the pressure of liquid film on the surface, however it may cause the change of flow distribution around the pressure tap which draws into error to the measurement results finally. In order to solve this situation, this paper proposes to install sensors at different positions of the end face to measure pressure of each point. Firstly, these sensors will be fitted like a parabolic curve. Secondly, they will be integrated in the whole face which can calculate the opening force of liquid film. Therefore, the seal system can be stable and safe by controlling the opening force and closing face of the spring.

2. THE STRUCTURE AND PRINCIPLE OF AUTOMATION SPIRAL GROOVE FACE SEAL

The structure of spiral groove face seal is similar to the mechanical seal, as shown in Figure 1. And the affiliated automatic control system is also illustrated in this figure.When the rotating ring begins to turn, it will pump sealed media of low voltage side to the side of the high pressure seal chamber. The razor-thin liquid film (micron-scaled) is produced between the moving and static rings what plays a significant role in preventing leakage.

In order to make the fastest response timelier according to the changes of sealed medium pressure and avoid leakage to the most extent on the seal system, it is necessary to install a sensor on the static ring for shaft position. By real-time measurement of sealing medium (water) pressure in the spiral groove end face inlet and the cover, two pressure values can be obtained. To compare the two pressure values and feed back to the controller. At last, the results will be used to adjust the speed of the motor through the controller, thereby, it can adjust the pressure of feed pump to make sealing medium pressure of end face inlet rise or fall.

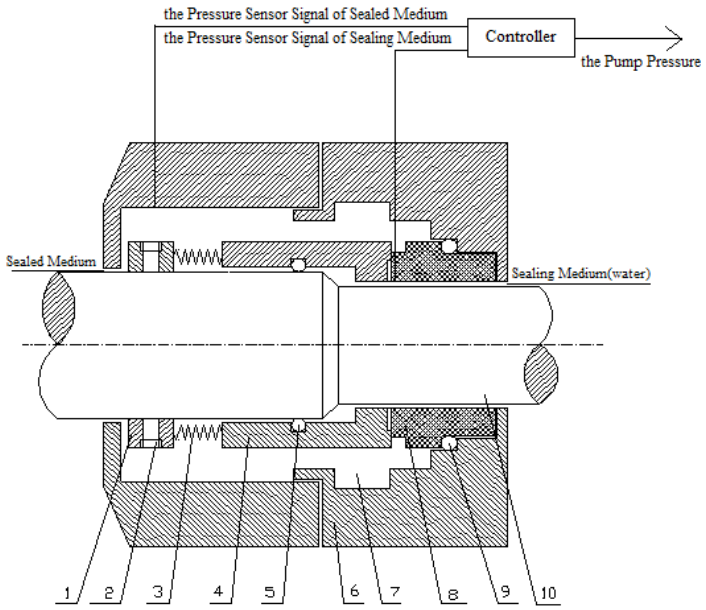

1-coil spring, 2-fastening screw, 3-spring, 4-rotating ring, 5-seals of rotating ring, 6-gland, 7-seal chamber, 8-stationary ring, 9-seals of stationary ring, 10-shaft

Figure 1: Structure and automatic control system of the spiral groove face seal

ORC system uses organism as working medium, such as R245fa, R134, and R123 (Dai *et al*., 2009). The various working medium is considered as sealed medium in the automation spiral groove face seal system. Therefore, their physical properties should be considered including toxicity, water solubility and so on. It can be easily ingored that the sensor and other materials face the risk of corrosion. In this paper, water is used as the sealing medium due to it can decrease

complexity of computation and it should be realized that lubricating oil will be used in the practical industry.

3. SIMULATION OF SPIRAL GROOVE FACE SEAL

The CFD analysis provides a visual insight to the sealed and sealing medium behavior inside the spiral groove face seal. However, the flow complexity caused by high rotation speed and micro-scale need to be solved by accurate equation approach and flow model.

3.1 Governing Equations

The simple criterion of distinguishing laminar flow and turbulent flow is the Reynolds Number. The method of calculating *Re* is given as:

$$Re = \frac{\rho L u}{\eta} \tag{1}$$

By the calculation, *Re* number is 102 and it is greater than the *Re* number used to determinate the laminar and turbulent flow on engineering which is 2600 (Moxey et al., 2010) It could be considered that the flow is in laminar motion. ANSYS/FLUENT provides four segregated types of algorithms: SIMPLE, SIMPLEC, PISO, and (for time-dependant flows using the Non-Iterative Time Advancement option (NITA)) Fractional Step (FSM). In ANSYS/FLUENT, both the standard SIMPLE algorithm and the SIMPLEC (SIMPLE-Consistent) algorithm are available. SIMPLE is the default, but many problems will benefit from using SIMPLEC, particularly because of the increased under-relaxation that can be applied. The governing equations are fllowing:

(a) The equation for conservation of mass, or continuity equation, can be written as follows:

$$\frac{\partial \rho}{\partial t} + \nabla \cdot (\rho \bar{v}) = 0 \tag{2}$$

(b) Transport of momentum in an inertial (non-accelerating) reference frame is described by

$$\frac{\partial}{\partial t}(\rho \bar{v}) + \nabla \cdot (\rho \bar{v}\bar{v}) = -\nabla p + \nabla \cdot (\bar{\tau}) + \rho \bar{g} + \bar{F} \tag{3}$$

where p is the static pressure, $\bar{\tau}$ is the stress tensor (described below), and $\rho \bar{g}$ is the gravitational body force, $\bar{F}$ contains other source terms that may arise from resistances, sources, etc.

(c) The energy equation for a fluid region can be written in terms of sensible enthalpy *h* as

$$\frac{\partial}{\partial t}(\rho h) + \nabla \cdot (\rho h \bar{v}) = \nabla \cdot [(k + k_t)\nabla T] + S_h \tag{4}$$

where *k* is the molecular conductivity, k_t is the conductivity due to turbulent transport, and the source term S_h includes any volumetric heat sources you have defined.

3.2 Simulation Model

The two dimensional structure of sealing ring is presented in Figure 2. Software of Gambit and ANSYS/Fluent were used to accomplish geometric modeling and numerical simulation of internal flow field of spiral groove respectively.

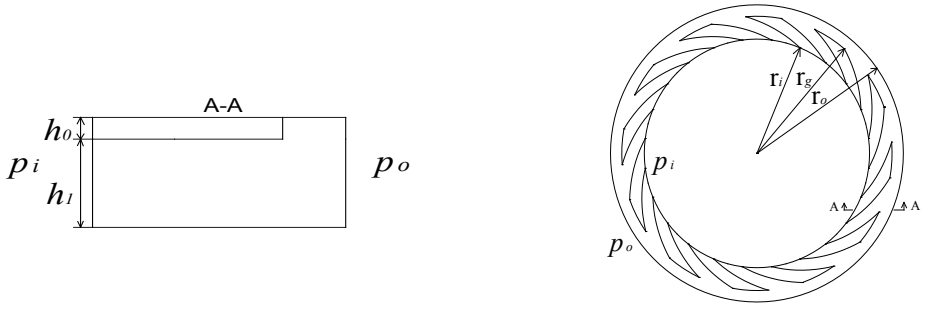

Figure 2: Structure of slotted end face of spiral groove face seal

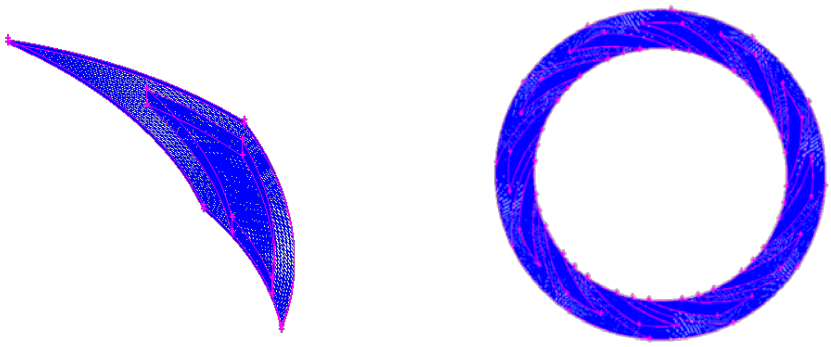

Figure 3: Computational mesh of spiral groove face seal

The spiral groove seal was modeled by the professional 3D modeling software-Gambit, and used CFD codes together with structured hexahedral mesh o as shown in Figure 3. The grid number of single spiral groove is 129536 and the grid number of whole circle is 1554432.

3.3 Simulation Results

To combine the design of sealing device and the given medium (water) parameters, the spiral groove face seal was simulated under different working parameters in this paper to ensure the differential pressure without leakage. When the seal structure and the shaft rotate, the sealing medium is constant. To calculate the pressure of end face inlet based varying sealing medium pressure (the pressure of end face outlet) within 2 to 3 MPa. In all working conditions, using the minimum value among the maximum differential pressure regarded as safety limits to be control value which can ensure no leak. The specific working parameters are presented in Table 1.

The inlet pressure is assumed to be 0.1MPa and increasing the outlet pressure gradually, it can be found that the end face has backflow when the outlet pressure p_0 is 0.6413MPa. The backflow becomes more serious as p_0 increases, what illustrates the happen of leakage. The simulation results are shown in Figure 4.

Table1: The value and range of all prameters

Items	Value	Items	Value
Inner diameter r_i / mm	25	Spiral angle/ °	21
External diameter r_o /mm	32.5	Length ration of Slot and dam L_g	0.67
Thickness of film h_0 / mm	0.003	Rotate speed n/r·min^{-1}	3000
Groove width ratio γ_g	0.5	Medium	water
Number of grooves N	12	Working temperature T /℃	20
Groove depth h_1 / mm	0.0125	Inlet pressure/MPa	0.1~2
Radius of the junction of slot and dam r_g / mm	30	Outlet pressure/MPa	0.1~3

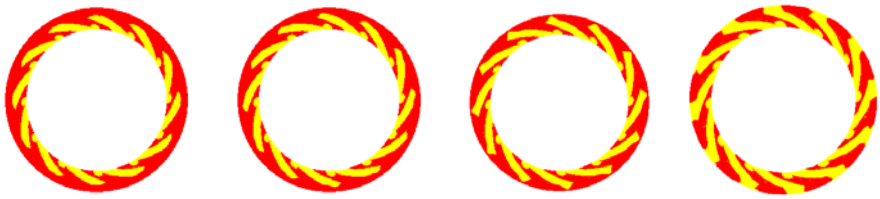

p_o=0.3MPa p_o=0.5MPa p_o=0.6413MPa p_o=1MPa

Figure 4: Radial velocity contours with different outlet pressures

Figure 4 shows the radial velocity contours when the inlet pressure is 0.1MPa and the outlet pressure is 0.3MPa, 0.5MPa, 0.6413MPa, 1MPa respectively. The yellow section represents the radial velocity direction of flow that points the center of a circle, and the red section represents the radial velocity direction of flow that points the back to center of a circle. When the outlet pressure p_0 is 0.6413MPa, the yellow section penetrates the whole circle what demonstrates the medium flows from the external to the inner, the sealing medium begins leaking. And the backflow is intensified with the increasing outlet pressure. To calculate the corresponding outlet pressure without leakage respectively when the inlet pressure is 0.1MPa, 1MPa and 2MPa. Finally we can get the differential pressure with leakage happening under these three working conditions, using the minimum value of these three differential pressures (0.54MPa) to be the control condition in this paper.

4. THE AUTOMATIC CONTROL SYSTEM OF SPIRAL GROOVE FACE SEAL

The automatic control system used for the spiral groove face seal cannot be establishment without high precision and micro sensor, extremely refine processing technic, and the sensitive controller. Moreover, the control condition which is the major part in the system has been calculated through CFD simulation in the above section. The control system mentioned in the paper need to prevent leak from happening with the differential pressure becomes 0.54MPa suddenly under all working conditions, therefore, it is vitally important for the control system to make timely and accurately responses.

4.1 Control Model

The control model of the automatic control system is shown in Figure 5. Comparing the feed pump output pressure P_V (the pressure of sealing medium) with seal medium pressure P_S, the controller transfer signal to change the valve opening of pump outlet to regulate the flow, thereby the differential pressure can be stay at 0.54MPa.

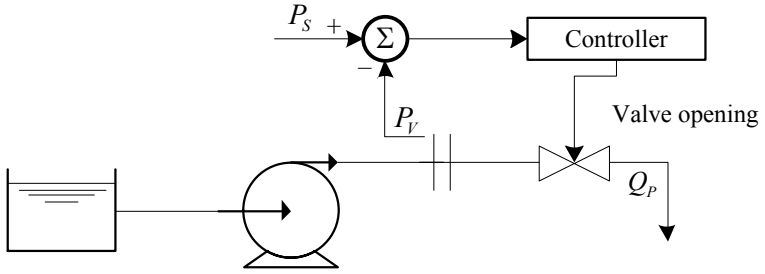

Figure 5: Pressure control model of automation spiral groove face seal

The mathematical model of centrifugal pump was established based on the characteristic curve of the pump as shown in Figure 6. Figure 6 shows the relationship between the capacity and head of the pump (Hu *et al*., 2015).

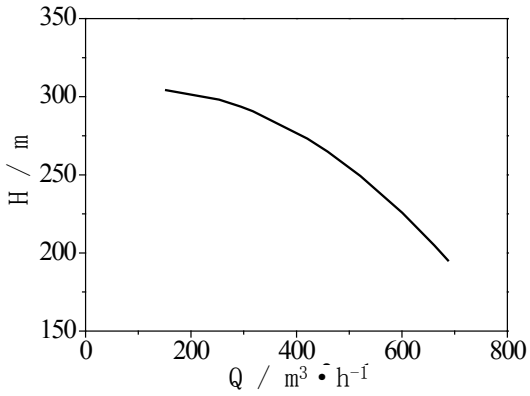

Figure 6: Characteristics curve of the feed water pump

The pump flow is determined by the valve opening and pressure difference between the front and behind of the valve and the relationship is given in Equation (5)

$$Q = k\sqrt{P_V - P_a} \tag{5}$$

Where, k represents the valve opening, P_V and P_a represent the pressure of front and behind of valve respectively. In this system, the P_a is just atmosphere pressure. When P_V is gage pressure, the Equation can be expressed as:

$$Q = k\sqrt{P_V} \tag{6}$$

The Bernoulli equation (Shames, 1982) used for the pump without considering frictional resistance and flow losses is given as:

$$\frac{P_{in}}{\rho g} + \frac{v_{in}}{2g} + z_1 + H = \frac{P_{out}}{\rho g} + \frac{v_{out}}{2g} + z_2 \tag{7}$$

To the system in this paper, $z_1 = z_2$, $v_{in} = v_{out}$, the lift of pump is:

$$H = \frac{P_{out} - P_{in}}{\rho g} \tag{8}$$

When P_V is gage pressure, the pressure of the inlet of seal end face is :

$$P_V = \alpha \rho g H \tag{9}$$

Where α represents partial loss coefficient of the pump outlet and the valve inlet what is equivalent to the flow loss of working medium in the process of the whole flow.

4.2 Control Strategy

According to the theories above, the detailed automation spiral groove end face seal model was established in MATLAB/SIMULINK as shown in Figure 7. And, the PI controller was used to control the pressure of sealing medium. To increase the proportionality coefficient can reduce static error, but oversize proportionality coefficient can take unstableness to the closed-loop system. The principle of PI controller is presented in Equation (10),

$$G_C = K_P e(t) + K_I \int_0^t e(\tau) d\tau \tag{10}$$

where $e(t)$ represents the deviation between set value and actual value, K_P and K_I represent proportionality coefficient and integral coefficient, respectively.

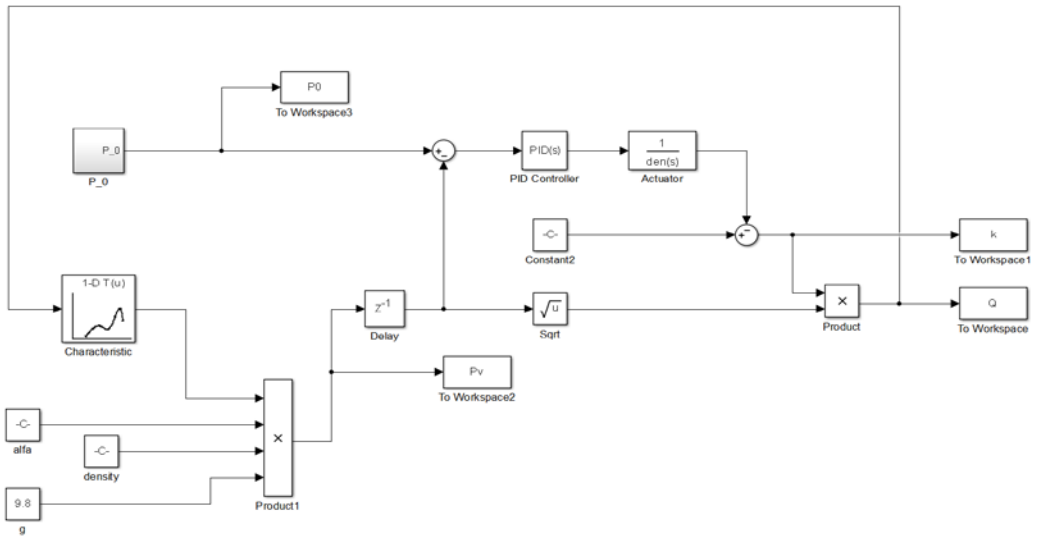

Figure 7: Control model and program of automation spiral groove face seal

4.3 Results

The paper designs proportional-integral (PI) control (Byung-Su and Edgar, 1998) for the system. For the dynamic response characteristic simulation of the system, to compare the pressure (p_i) of sealing medium provided by the feed pump with the value ($p_0^{'}$) of the sealed pressure subtracts 0.54MPa. Assuming the initial pressure of the feed pump is 2.5 MPa, and $p_0^{'}$ changes from 2.5MPa to 3MPa through stepping. After setting controller parameters, the variation of pressure provided by pump under PI control is shown in Figures 8 and 9. Figure 8 shows the pressure step disturbances (0.1MPa, 0.3MPa and 0.5MPa) of sealed medium and Figure 9 shows the pressure responses of sealing medium under the controller.

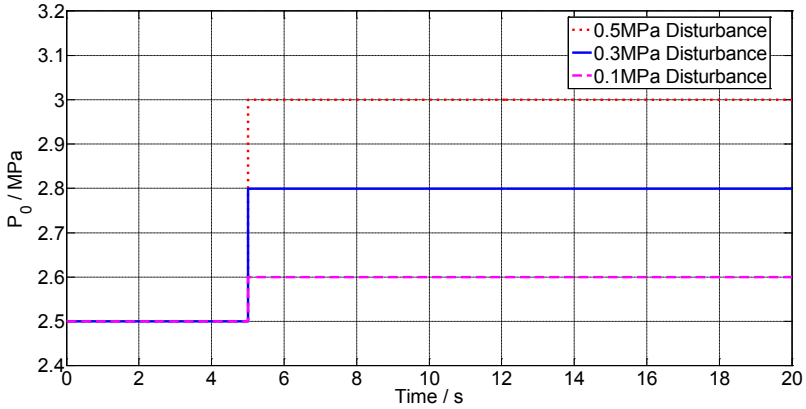

Figure 8: Pressure step disturbance of sealed medium

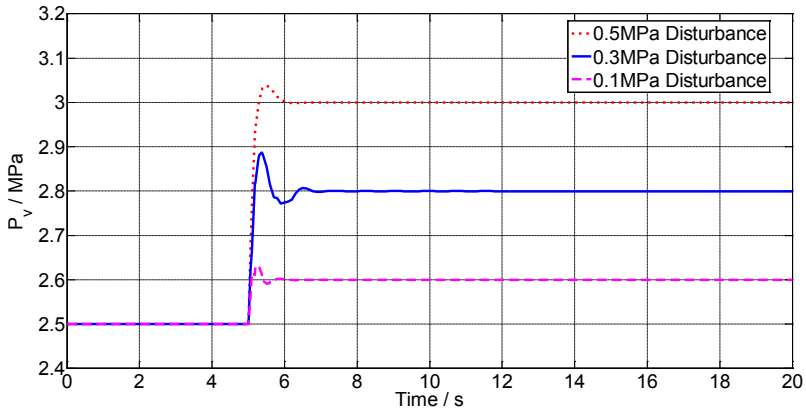

Figure 9: Pressure responses of sealing medium under varying disturbances

It can be seen that when p_0' changes from 2.5MPa to 3MPa through stepping, the sensor accepts the variation of p_0' and comparing with the pressure of the front of outlet valve. The controller adjusts the outlet valve opening by accepting the signal of differential pressure. However, more flow makes the pressure provided by pump smaller when the rotating speed of pump is constant. Figure 9 proves PI control has no static error and system overshoot. From the dynamic process of adjusting, the PI control is immediately reacting for deviation. As long as there is deviation, the integral accumulation will affect control until the deviation is zero.

The dynamic response curves of flow and valve opening are shown in Figures 10 and 11, respectively.

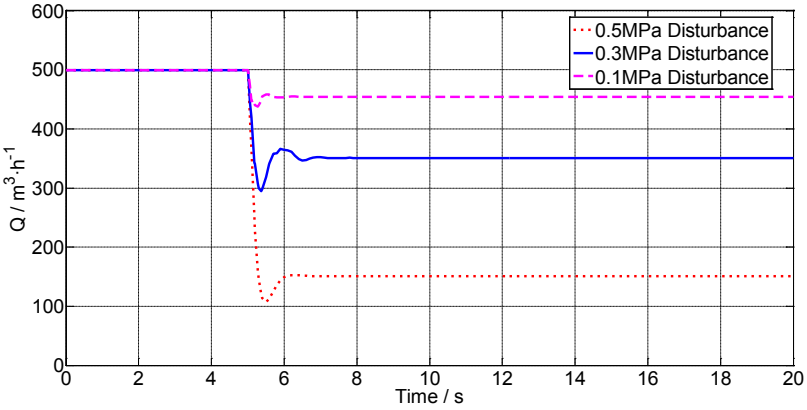

Figure 10: Dynamic response curves of flow under varying disturbances

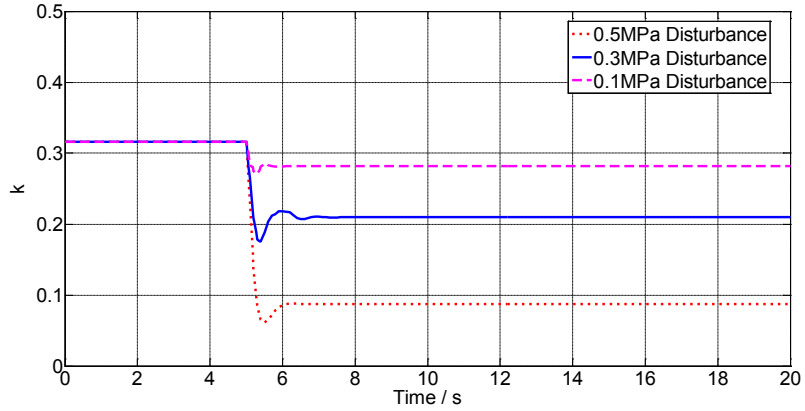

Figure 11: Dynamic response curves of valve opening under varying disturbances

The original state of system: the pressure provided by pump is 2.5MPa, the valve opening is 0.316 by calculating. To reduce the deviation from p_0' in order to increase the pressure provided by pump. Thereby the valve opening should decrease gradually by the controller. Figure 11 shows the PI control can achieve the zero static error with p_0' through adjusting valve opening. The flow variation is determined by valve opening and pressure difference on both ends of valve. According to Equation (5), it can be calculated that the flow with the pressure provided by pump and valve opening at some point. The flow decreases with valve opening decreasing. However, the relationship between the flow and pressure provided by pump is nonlinear according to the pump characteristic curve.

The working points curve of the pump under the control above as shown in Figure 12. It can be seen that A point is the original value of working point, B, C and D are the working points after PI control making system steady under different disturbances respectively. The PI control makes the working point move from A to the terminal points (B, C and D) in a curve of the second degree, the growth rate of pressure become slower with the decrease of flow.

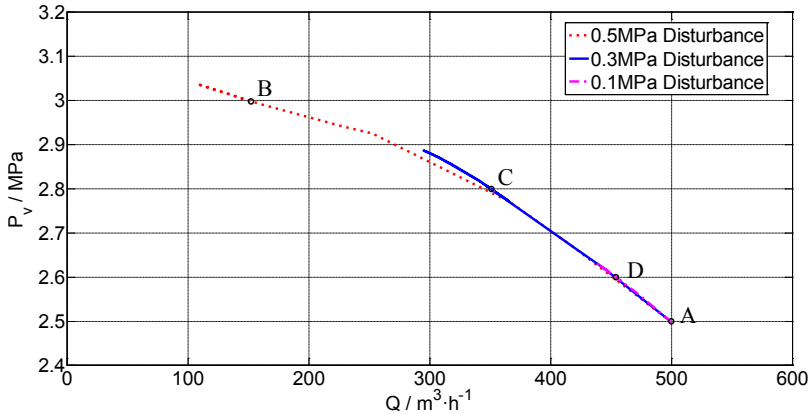

Figure 12: Dynamic response curve of the pump working points under varying disturbances

5. CONCLUSIONS

The paper proposes an automatic adjusting device of the spiral groove face seal used on ORC turbine shaft end. It can achieve zero leakage through a complete automatic control system. This paper mainly includes two parts: using CFD to simulate the spiral groove face seal in order to ensure the differential pressure, using SIMULINK to establish the automatic control model. Based on the analytical and simulative investigations presented in this paper, the following conclusions can be drawn:

1 The spiral groove face seal with automatic control system can achieve zero leakage which can be used for the ORC turbine.

2 The CFD method provides an insight way to investigate the internal flow of the spiral groove seal and calculates the differential pressure (0.54MPa).without leakage. Additionally, the outlet pressure contributes to the backflow.

3 This control system with PI controller has good robustness and strong resistance for disturbance under the off-design conditions.

NOMENCLATURE

g	gravitational acceleration	(m/s^2)
h	mean specific enthalpy	(J/kg)
k	valve opening	(m)
L	length	(m)
P_{in}	inlet pressure of pump	(Pa)
P_{out}	outlet pressure of pump	(Pa)
p	pressure	(Pa)
u	velocity	(m/s)
v_{in}	inlet velocity of pump	(m/s)
v_{out}	outlet velocity of pump	(m/s)
z_1	inlet height of pump	(m)
z_2	outlet height of pump	(m)

Greek symbol

ρ	density	(kg/m^3)
η	absolute viscosity	(kg/m·s)
τ	time	(s)

REFERENCES

Sedy J., 1980, *U.S. Patent No. 4,212,475*, Washington, DC: U.S. Patent and Trademark Office.

Wolff P.J., Salant R.F., 1995, Electronically controlled mechanical seal for aerospace applications-Part II: Transient tests, *Tribol. trans.*, vol. 38, no. 1: p. 51-56.

Heilala A. J., Kangasneimi A., 1987, Adjustment and control of a mechanical seal against dry running and severe wear, *Proc. 11th Int. Conf. Fluid Sealing,* p. 548-575.

Etsion I. Z. J. N., Palmor Z. J., HARABRI N., 1991, Feasibility study of a controlled mechanical seal, *Lubr. Eng.*, vol. 47, no. 8: p. 621-625.

Zou M., Dayan J., Green I., 2000, Dynamic simulation and monitoring of a non-contacting flexibly mounted rotor mechanical face seal, *Proc. Inst. Mech. Eng., Part C: J. Mech. Eng. Sci.*, vol. 214, no. 9: p. 1195-1206.

Boqin Z. J. G., 2009, Controllability of Spiral Groove Mechanical Seal, *Chin. J. Mech. Eng.*, *1*, p. 20.

Ya Z., Ying W., Yiping D., 2012, Numerical simulation and characteristics analysis of the turbine shaft end spiral groove mechanical seal, *Digital Manuf. Autom. (ICDMA), 2012 Third Int. Conf.* IEEE: p. 558-561

Dai Y., Wang J., Gao L., 2009, Parametric optimization and comparative study of organic Rankine cycle (ORC) for low grade waste heat recovery, *Energy Convers. Manage.*, vol. 50, no. 3: p. 576-582.

Moxey D., Barkley D., 2010, Distinct large-scale turbulent-laminar states in transitional pipe flow, *Proc. Nat. Acad. Sci.*, vol. 107, no. 18: p. 8091-8096.

Hu D., Li S., Zheng Y., Wang J., Dai Y., 2015, Preliminary design and off-design performance analysis of an Organic Rankine Cycle for geothermal sources, *Energy Convers. Manage.*, vol. 96: p. 175-187.

Shames I.H., Shames I.H., 1982, *Mechanics of fluids*, p. 359, New York, NY: McGraw-Hill.

Ko B.S., Edgar T.F., 1998, Assessment of achievable PI control performance for linear processes with dead time, *Am. Control Conf., 1998. Proc. 1998* vol. 3: p. 1548-1552.

ACKNOWLEDGEMENT

The authors gratefully acknowledge the financial support by the National High-tech Research and Development Program (Grant No.2012AA053002) and the National Key Technology R&D Program (Grant No.2011BAA05B03).

FACTOR ANALYSIS OF EXPANSION RATIO FOR SINGLE SCREW EXPANDERS

Wei WANG*, Li-li SHEN, Liang CHEN, Yu-ting WU, Chong-fang MA

* Beijing University of Technology,
College of Environmental and Energy Engineering,
Key Laboratory of Enhanced Heat Transfer and Energy Conservation, Ministry of Education and Key Laboratory of Heat Transfer and Energy Conversion, Beijing municipality,
100 PIN LE YUAN, Chaoyang District, Beijing, P R China
E-mail: wang_wei@bjut.edu.cn

*Wei WANG

ABSTRACT

For low temperature waste heat recovery, Organic Rankine Cycle (ORC) is generally considered the most promising choice in varieties of potential technologies, and become a hotspot of research and development in international academic and industrial fields. However, reviewing the research results related ORC system in recent years, the actual situation was not optimistic. There were many technical bottlenecks hindered the application of ORC, especially for small scale system. Among those problems, the performance of expander was the key issue, and how to improve it was two aspects. First one was improving the shaft efficiency of expander, and it was the common sense of the researchers in this field. Second one was controlling appropriate expansion ratio (ε), and it was special requirement of small scale ORC system. Due to relative small expansion ratio, the thermal efficiency of ORC was low even if high efficiency of expanders. In actual conditions, the high efficiency and expansion ratio of expanders were hardly obtained simultaneously. So, it is necessary to carry out the special discussion about expansion ratio. Single screw expander was a type of volumetric prime mover. Due to special configuration, it had the potential of realized relative high expansion ratio. So, it makes possible getting high thermal efficiency of ORC. In this paper, we tried to analyze the influence factors of internal expansion ratio for single screw expanders. Firstly, the thermodynamic model of ORC was described, and the analysis of expansion ratio influenced cycle thermal efficiency was carried out. From the calculation results, it was found that thermal efficiency was increased with expansion ratio, but the accelerated velocity was decreased gradually. Considering the actual efficiencies of expander and pumps, appropriate expansion ratio should be existed. Secondly, the analysis of the influence factors of internal expansion ratio for single screw expanders was carried out, from the aspects of configuration, process and condition. From the results, high expansion theoretically could be obtained by changing the configuration of screw and gaterotor, inlet and outlet structure. The maximum volumetric ratio could above 20, and it could completely cover the temperature range of low temperature waste heat recovery. However, in actual condition, different meshing and fit clearances would influence leakage and cause expansion ratio reduced. So, configuration design and clearance control were key issues to improve the expansion ratio of single screw expanders.

1. INTRODUCTION

Nowadays, research and development of low temperature heat efficient thermal power conversion system becomes a hot research field in the world. Among the research of different type thermodynamic cycles, ORC was considered the most potential technology and obtained the most attention in the world.

For ORC research, thermodynamic cycle analysis was the most popular field all over the world, and the most academic articles focused on it. Reviewing most articles in this topic, the result was still existed the problems of ideal and bad suitable for actual situation. Especially for small scale low temperature heat source, the restriction of expander was the key problem, and it was indicated overestimating expander efficiency and ignoring the influence of expansion ratio. Referring the efficiency of large scale steam turbine, expander efficiency was usually assumed above 0.8. Moreover,

the actual performance of working fluid pump was another key problem, and the pump efficiency was significantly overestimated in many articles, the value was about 0.65-0.85. Hence, the performance indexes of ORC were overestimated obviously, and thermal efficiency of ORC was higher than 10%, even above 15%.

For experimental study of ORC system, we can get quite different situation. There are many articles carried out the research of this topic, we just took some examples. The result data of some experimental study articles was showed in Table 1. From the results of those articles, we can find that the types of working fluid pump were included diaphragm and multistage centrifugal, although most of the articles did not gave actual pump efficiency, but the data of Quoilin et al. (2010) could reflect the real situation, it was only 15%. In other words, the actual pump efficiency was very lower than assumption, but we had to choose diaphragm and multistage centrifugal pumps because of high pressure requirement. It was very difficult to obtain high pressure, small flow rate and high efficiency at the same time, so how to improve the efficiency of working fluid pump was a key issue for ORC, especially for small scale system. We also can find that the types of expander were included scroll, rolling piston, radial turbine and single screw. Actually, every type expanders have been studied. From the results, it was obvious that radial turbine had the biggest capacity, second was single screw, and scroll and rolling piston was smaller. The working conditions of each article were quite different, but the temperature difference of evaporation and condensation were all about 30-50℃. Because several articles did not mentioned the degree of supercooled, so the actual temperature difference between expander's inlet and outlet should below above value. It indicated that the real energy utilization percentage of ORC was significantly lower than analyzed results, it was also indicated that the limitation of expander was a key bottleneck for sufficiently utilization low temperature thermal energy. From the data of table 1, we can find that the expansion ratio was about 2.5 to 6.6. Considering the thermophysical property of working fluid, the temperature difference between inlet and outlet for expander was estimated about 40-60℃, and it was obviously lower than the temperature difference between low temperature heat source and surrounding. Meanwhile, if expander efficiency was not good enough, the performance of ORC would be worse than desired. Unfortunately, the real efficiency of expanders was not satisfied, it was just about 40%-60%. Kang et al. (2012) presented the tested efficiency of radial turbine beyond 80%, but its expansion ratio was below 2.72, so the maximum value of thermal efficiency was about 5.65%, lower than the case of higher expansion ratio. The results of unsatisfied expansion ratio and expander efficiency were unacceptable thermal efficiency of ORC.

Reviewing the research results related small scale ORC system, we can get three bottlenecks for ORC performance: expander efficiency, expansion ratio and the efficiency of pump and fan. For small scale expanders, improving efficiency was a tuff job, and working fluid pump had similar situation. So, improving expansion ratio was an easier measure for obtaining higher thermal efficiency at present. There are many factors influencing expansion ratio, such as working fluid types, expander configurations and working conditions, etc.

Single screw configuration is composed of a screw and several gaterotors, and generally divides into four types of PC, PP, CC and CP. C and P were the abbreviations of cylinder and plate, respectively. The first abbr. means the shape of screw and the second one means the shape of gaterotor. CP type is the most common configuration of single screw because of easily processing. A single screw expander mainly consists of screw, gaterotors and shell. The screw groove, the internal wall of shell and the profile surfaces of the gaterotor teeth constitutes a closed space, which was to change the volume with the rotation of screw and gaterotor. In this paper, we tried to analyze the influence factors of expansion ratio for single screw expanders, and try to provide the technical measures to improve it.

Table 1: List of the performance indexes of some experimental study articles

Author	Work fluid pump	Expander	Working fluid	W_G/kW	T_{eva}/℃	T_{con}/℃	η_E/%	ε	η_H/%	η_P/%
Li et al. (2013)	Diaphragm	Radial turbine	R123	6.07	90.7	39.4	58.53	4.19	7.98	No
Bracco et al. (2013)	Diaphragm	Scroll	R245fa	1.1-1.8	85.4-101.4	27-30	60-74	4.6-6.6	8.8-9.8	No
Quoilin et al. (2010)	Diaphragm	Scroll	R123	0.5-1.8	-	-	42-68	2.7-5.4	Max. 7.4	15%
Zheng et al. (2013)	Diaphragm	Rolling piston	R245fa	0.16-0.32	72.4-82.6	14.6-33.2	Max. 44	4	2-6	No
Zhou et al. (2013)	Multistage centrifugal	Scroll	R123	Max. 0.645	85.5-114.9	34.9-49.6	Max. 57	5	Max. 8.5	No
Kang et al. (2012)	Multistage centrifugal	Radial turbine	R245fa	24.5-31.2	77-83	44.5-47.3	76-82.2	2.62-.2.72	5.05-5.65	No
Gu et al. (2009)	Multistage centrifugal	Scroll	R600a	Max. 1.1	-	-	Max. 50.1	-	Max. 2.9	Assumed 85%
Zhang et al. (2014)	Multistage centrifugal	Single screw	R123	Max. 10.38	123.6-140.2	79-101	Max. 57.9	2.5-4.6	Max. 6.5	No

2. INFLUENCE FACTORS FOR ORC SYSTEM

Due to the limitation of expanders, low temperature heat energy could not make full use for small scale ORC system. A remarkable phenomenon was outlet temperature of working fluid higher than condensation temperature, and it was caused by relative lower expansion ratio of expanders. In this section, we tried to analysis expansion ratio how to influence the performance of ORC system.

2.1 Thermodynamic model

Firstly, a thermodynamic model was described, and specific information was showed in Figure 1.

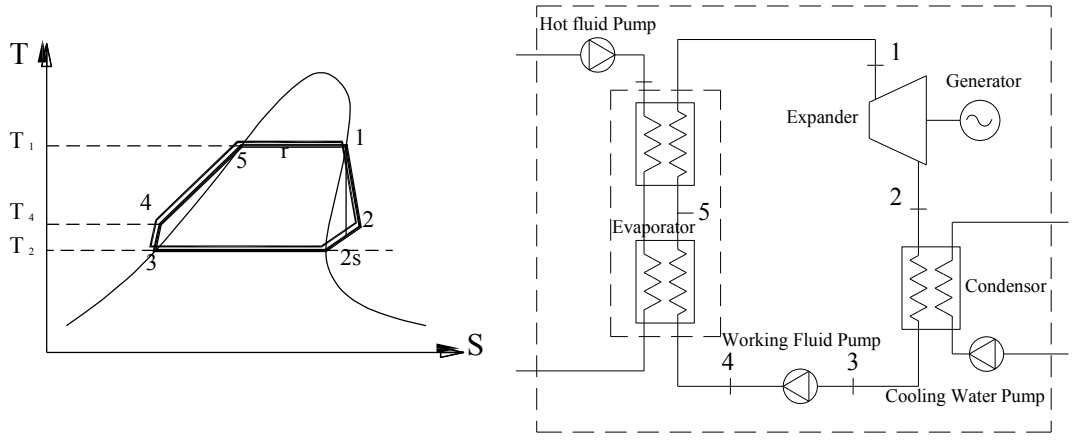

(a) (b)

Figure 1: Organic Rankine cycle
(a) T-S chart; (b) Schematic diagram of thermal system

The thermodynamic model of power generation system was described as follow. Point 1, 3 and 5 were assumed to saturation state.

The absorption heat of working fluid in evaporator is calculated by

$$Q_1 = m(h_1 - h_4) \tag{1}$$

The generating capacity of expander is calculated by

$$w_G = (h_1 - h_{2s})\eta_a \eta_M \eta_G \tag{2}$$

The consumption of working fluid pump is calculated by

$$w_P = \frac{v_3(p_4 - p_3)}{\eta_P \eta_{EM}} = \frac{(h_4 - h_3)}{\eta_P \eta_{EM}} \tag{3}$$

The net generation of ORC is calculated by

$$W_{net,ORC} = W_G - W_P = m(w_G - w_P) \tag{4}$$

The thermal efficiency (thermodynamic first law efficiency) of ORC is defined as

$$\eta_{H,ORC} = \eta_{\mathrm{I},\mathrm{ORC}} = \frac{W_{net,ORC}}{Q_1} = \frac{(h_1 - h_2) - (h_4 - h_3)}{h_1 - h_4} \tag{5}$$

The thermodynamic second law efficiency of ORC is defined as

$$\eta_{\mathrm{II},\mathrm{ORC}} = \frac{\eta_{H,ORC}}{1 - \frac{T_3}{T_1}} \tag{6}$$

Because of the limitation of expansion ratio (ε), when working fluid type and evaporation temperature was assumed, outlet pressure was calculated by expansion ratio. So, the relationship between inlet pressure and outlet pressure is defined as

$$\varepsilon = \frac{p_1}{p_2} \tag{7}$$

2.2 Result and discussion

Before calculated, we must assume some conditions. Here, R123 was selected by working fluid, because it had higher critical point. Generator efficiency and electric motor efficiency of working fluid pump was assumed 0.95, respectively.

2.2.1 Expansion ratio

Here, adiabatic and mechanical efficiency were assumed about 0.7 and 0.95, respectively. So the total efficiency of expander was about 0.65, and it was very near experimental results. Working fluid pump efficiency was assumed 0.8. Condensation temperature was assumed 30℃.

Figure 2 was the variation of thermal efficiency with expansion ratio of R123. At the same evaporation temperature, thermal efficiency increased with expansion ratio, until the condensation temperature was near environmental temperature. At the same expansion ratio, thermal efficiency decreased very slightly with the increase of evaporation temperature. However, with the absolute pressure rising, pump efficiency would be reduced in actual condition. So, it was indicated that lower evaporation temperature should be adopted at the condition of determined expansion ratio.

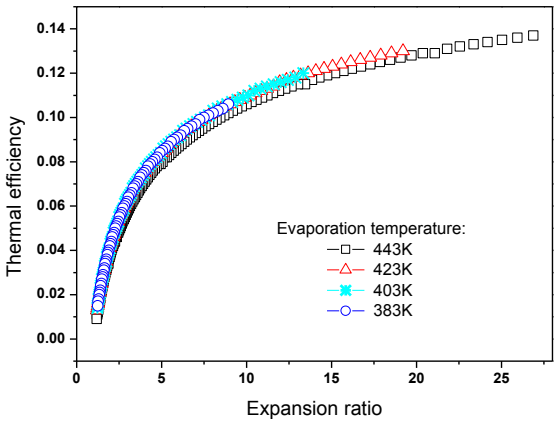

Figure 2: Variation of thermal efficiency with expansion ratio of R123

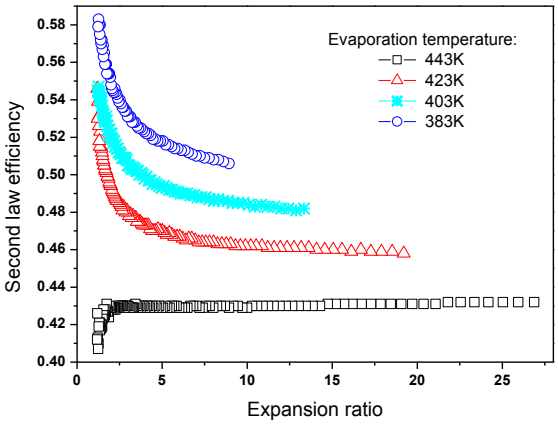

Figure 3: Variation of Second law efficiency with expansion ratio of R123

Figure 3 was the variation of second law efficiency with expansion ratio of R123. At the same evaporation temperature, second law efficiency decreased quickly with expansion ratio, until the condensation temperature was near environmental temperature. With the increase of evaporation temperature, the decrease velocity become gently. The reverse trend occurred with evaporation temperature closing critical point. At the same expansion ratio, second law efficiency accelerated declined with the increase of evaporation temperature. Summary above calculating result, it was indicated that improving expansion ratio was an effective method to increase the thermodynamic performance of ORC, however, if considering expander and pump efficiency would decrease with the increase of expansion ratio, so expansion ratio should existed suitable range.

2.2.2 Adiabatic efficiency

Here, mechanical efficiency was assumed 0.95. Expansion ratio was assumed 6. Working fluid pump efficiency was assumed 0.8.

Figure 4 was the variation of thermal efficiency with adiabatic efficiency of R123. At the same evaporation temperature, thermal efficiency lineal increased with adiabatic efficiency. At the same adiabatic efficiency, thermal efficiency decreased slightly with the increase of evaporation temperature, the trend was more obvious in the situation of lower adiabatic efficiency. So, it was indicated that improving evaporation temperature should not a reasonable method if expansion ratio fixed. Figure 5 was the variation of second law efficiency with adiabatic efficiency of R123. It has similar trend compared with thermal efficiency, just a little different. With the increase of adiabatic efficiency, the difference of second law efficiency was gradually added among different evaporation temperature. The phenomenon could explain that thermodynamic perfection will be improved with the increase of adiabatic efficiency and far away from critical point.

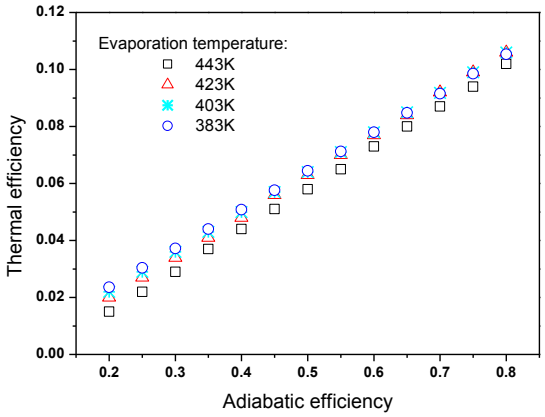

Figure 4: Variation of thermal efficiency with adiabatic efficiency of R123

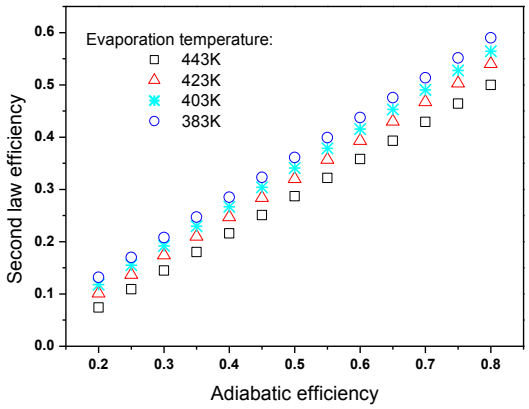

Figure 5: Variation of second law efficiency with adiabatic efficiency of R123

2.2.3 Pump efficiency

Here, adiabatic and mechanical efficiency were assumed about 0.7 and 0.95, respectively. Expansion ratio was assumed 6.

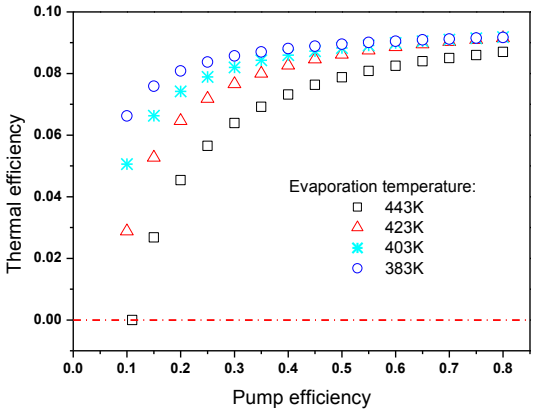

Figure 6: Variation of thermal efficiency with pump efficiency of R123

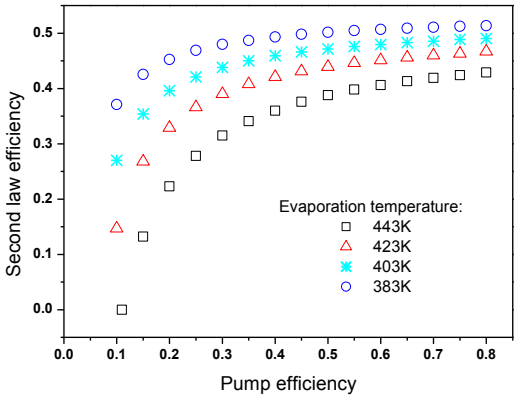

Figure 7: Variation of second law efficiency with pump efficiency of R123

Figure 6 was the variation of thermal efficiency with pump efficiency of R123. At the same evaporation temperature, thermal efficiency accelerated declined with pump efficiency decrease. At the same pump efficiency, thermal efficiency decreased accelerated with the increase of evaporation temperature, the trend was more obvious in the situation of lower pump efficiency. From the result, it was also found that the influence of pump efficiency was weakened at relative lower evaporation temperature, even lower than 0.3. So, it was indicated that improving evaporation temperature should not a reasonable method if low pump efficiency. Figure 7 was the variation of second law efficiency with pump efficiency of R123. It has similar trend compared with thermal efficiency.

Summary above calculating result, it could be found that improving expansion ratio could increase thermodynamic performance of ORC system. If expansion ratio could not be improved, increase evaporation temperature was no use to improve performance.

3. EXPANSION RATIO OF SINGLE SCREW EXPANDERS

According to the different working principles, expanders can be classified two types: velocity and positive displacement. Velocity expanders mainly include single stage and multi-stage axial turbine, single stage and multi-stage radial turbine, etc. Positive displacement expanders mainly include piston, scroll, twin screw and single screw, etc. According to the different movement forms, positive displacement expanders can be classified two types: reciprocating and rotary. Piston expander is the former, and scroll, twin screw and single screw are the latter.

For velocity expanders, increasing rotational speed could improve expansion ratio. But, if the rotational speed was increased too high, mechanical loss would be significantly raised. So, multi-stage configuration was adopted usually in order to improve expansion ratio. Generally speaking, expansion ratio of single stage for axial turbine was lower than radial turbine. So, the stage numbers of axial turbine should be more than radial turbine if obtained the same expansion ratio.

For positive displacement expanders, expansion ratio (ε) was influenced by internal volumetric ratio (τ) and adiabatic index of working fluid. The function existed in ideal condition:

$$\varepsilon = \left(\frac{V_{out}}{V_{in}} \right)^{\kappa} = \tau^{\kappa} \tag{8}$$

For reciprocating expanders, expansion ratio could be changed through controlling inlet and exhaust phases. However, if the expansion ratio was improved too high, adiabatic efficiency would greatly decrease due to the clearance volume. For rotary expanders, if the configuration and working fluid has been determined, expansion ratio was fixed. There are two methods to improve it: the one is modify the configuration of expanders, and the other is added capacity adjustment mechanism, for example, slide valve.

Single screw expander is positive displacement type, and belongs to rotary type too. Considering actual situation, mainly influence factors of expansion ratio included three aspects: internal volumetric ratio, working fluid type and working condition.

3.1 Internal volumetric ratio

Because CP type single screw configuration was the simple and widely use among different single screw types, so it was selected for the case to analysis. Geometric structure of single screw meshing pair was showed on Figure 8. Mainly parameters include screw radius R_1, gaterotor radius R_2, the center distance between screw and gaterotor A, meshing angle α_1, discharge angle α', half angle of teeth width δ, teeth width of gaterotor b_0, minimum thickness of screw rib Δb. When R_1, R_2, A, b_0 were assumed, other parameters could be calculated.

In order to obtain internal volumetric ratio, intake and exhaust volume should be calculated. Exhaust volume was the maximum volumetric element. Making reference to the handbook (Yu et al, 2012), the maximum volumetric element can be calculated by

$$V_1 = \int_{\alpha_1-\delta}^{\alpha_1+\delta} \int_{-\frac{b_0}{2}}^{R_2 \sin(\alpha_1-\alpha)} \frac{R_1^{\,2} - (A - \sqrt{R_2^{\,2} - b^2}\cos\alpha + b\sin\alpha)^2}{2\cos\alpha} \omega db d\alpha \tag{9-1}$$

$$V_2 = \int_{\alpha''}^{\alpha_1-\delta} \int_{-\frac{b_0}{2}}^{\frac{b_0}{2}} \frac{R_1^{\,2} - (A - \sqrt{R_2^{\,2} - b^2}\cos\alpha + b\sin\alpha)^2}{2\cos\alpha} \omega db d\alpha \tag{9-2}$$

$$V_t = V_1 + V_2 \tag{9-3}$$

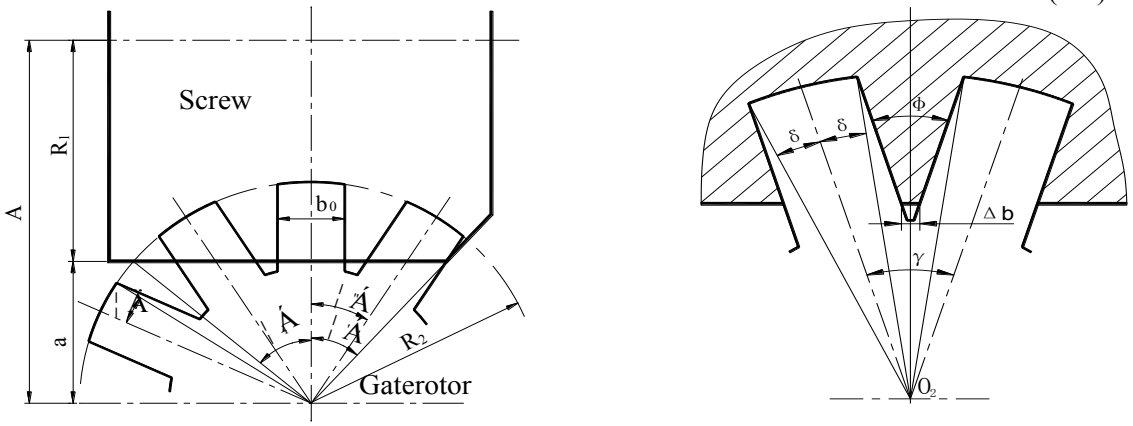

(a) Meshing pair (b) Gaterotor teeth and screw grooves

Figure 8: Geometric structure of meshing pairs

Intake volume was determined by intake triangle port and screw groove width (equal to gaterotor teeth width). When the arc length of the circumferential direction of intake triangle port was assumed, the rotary angle of screw could be calculated. Then, it was converted into the rotary angle of gaterotor. So, the rotary angle of gaterotor of intake process was the angle above sentence mentioned plusing teeth width angle (2δ). Thus, intake volume could be calculated by equation (9). Of course, the limits of integration should be changed.

Obviously, if we want to improve expansion ratio, intake volume should be reduced. According to above describe, there were two measures to realize it: the one was reduced the dimension of intake triangle port, and another was reduced screw groove width. The minimum dimension was zero, so the maximum internal volumetric ratio should be existed when screw groove width as certain value. Reducing screw groove width also can improve internal volumetric ratio, but it was limited by the requirement of gaterotor mechanical strength.

Here, we give an example to analysis. R_1, R_2, A, b_0 were assumed as 58.5mm, 58.5mm, 96mm and 17.1mm, respectively. Variation of maximum volumetric element and maximum internal volumetric ratio with minimum thickness of screw rib was showed on Figure 9. With the increase of minimum thickness of screw rib, maximum volumetric element was declined linearly, and maximum internal volumetric ratio was increased accelerated. From calculation result, appropriate reducing screw groove width could make maximum internal volumetric ratio to reach above 30. Considering the dimension of intake triangle port, internal volumetric ratio could be easy to realize above 20. Summery above analysis, for single screw expanders, internal volumetric ratio could be improved theoretically by configuration adjustment to satisfy the requirement of ORC system.

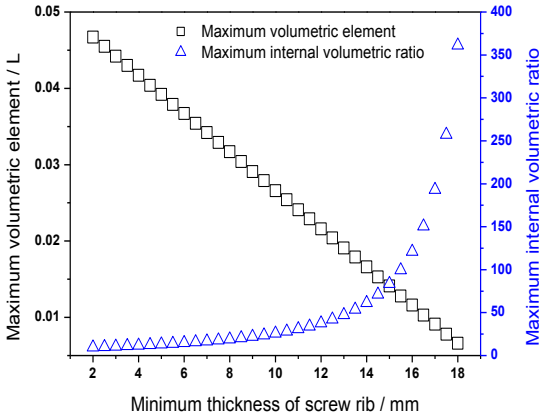

Figure 9: Variation of maximum volumetric element and maximum internal volumetric ratio with minimum thickness of screw rib (Screw diameter = 117mm)

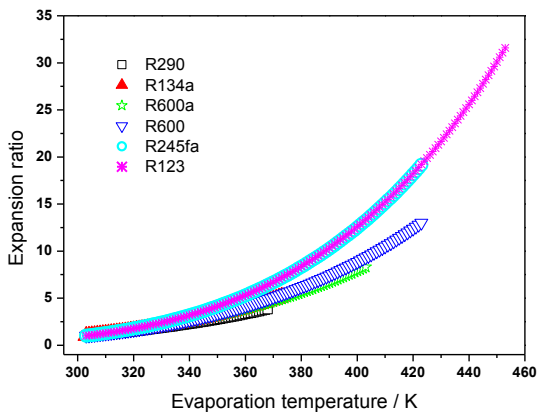

Figure 10: Variation of expansion ratio with evaporation temperature for six working fluids

3.2 Working fluids

Thermophysical properties of working fluid influencing expansion ratio was reflected in two aspects. The one was pressure ratio between evaporation and condensation temperature. Assuming condensation temperature was 303K, R290, R134a, R600a, R600, R245fa and R123 were selected to analyze. Figure 10 was the variation of expansion ratio with evaporation temperature for six working fluids. From the results, at the same temperature difference between evaporation and condensation, working fluid of higher critical point has higher expansion ratio, however, for working fluid of lower critical point, the absolute pressure was significantly higher than the former. In addition, expansion ratio of higher critical point working fluids can beyond 20, even 30 in subcritical region. So, if we want to sufficiently use low temperature heat source, expansion ratio of expanders should be improved.

On the other hand, adiabatic index of working fluids was another important factor. In common sense, working fluid has more complex of molecular structure, the adiabatic index has smaller. Furthermore, from some research result of, adiabatic index of many Freon was significant declined with pressure increase, and it was slightly changed with temperature increase in the situation of lower pressure

(about 200kPa), but it was decreased with temperature increase in higher pressure. For example, the adiabatic index of air was 1.4, R22 was about 1.12-1.19 and R600a was about 1.02-1.05. It was showed that adiabatic index of Freon was obviously lower than air. For refrigeration, it was a good characteristic because of reducing compression power consumption. But for expansion, the situation was opposite. Lower adiabatic index caused lower expansion ratio at the same configuration of expanders.

3.3 Working conditions

The above analysis was based on ideal conditions. But in actual working condition, the situation was more complex. For single screw expanders, many leakage passes were existed due to clearance fit requirement, and leakage will cause the increase of discharge temperature and pressure, so the possess index was lower than adiabatic index, at last, expansion ratio reduced. However, experimental study of this field was much lacked.

4. CONCLUSIONS

In this paper, expansion ratio influencing single screw expanders was discussed. Firstly, a simple thermodynamic model was described, and then expansion ratio influencing ORC system was analyzed. Secondly, the influence factor of expansion ratio for single screw expanders was analyzed. Through those works, five conclusions are obtained:

(1) With the increase of expansion ratio, thermal efficiency of ORC was improved, and improving speed was fast firstly, and then slowed down. Considering the actual efficiencies of working fluid pump and expander, appropriate improving expansion ratio was the effective technical measure to improve ORC performance.

(2) At the same expansion ratio, increase intake temperature was no use improving thermal efficiency, and could reduce second low efficiency. So, increase intake parameters were not a good measure to improving ORC performance when the configuration of expander was fixed or regulation system was not existed.

(3) For a certain configuration of single screw expander, maximum internal volumetric ratio was existed. Through adjusting the demission of intake triangle port and screw groove width, internal volumetric ratio could be changed.

(4) Thermophysical properties of working fluid would influence expansion ratio, especially adiabatic index. In next research, process index should be obtained by experimental study.

REFERENCES

Li M, Wang J, He W, et al, 2013. Construction and preliminary test of a low-temperature regenerative Organic Rankine Cycle (ORC) using R123. *Renew. Eng.*, vol.57: p. 216-222.

Bracco R, Clemente S, Micheli D, et al, 2013. Experimental tests and modelization of a domestic-scale ORC (Organic Rankine Cycle). *Eng*., vol.58: p. 107-116.

Quoilin S, Lemort V, Lebrun J, 2010. Experimental study and modeling of an Organic Rankine Cycle using scroll expander. *Appl*. *Eng*., vol.87, no.4: p.1260-1268.

Zheng N, Zhao L, Wang X D, et al, 2013. Experimental verification of a rolling-piston expander that applied for low-temperature Organic Rankine Cycle. *Appl*. *Eng*., vol.112: p.1265-1274.

Zhou N, Wang X, Chen Z, et al, 2013. Experimental study on Organic Rankine Cycle for waste heat recovery from low-temperature flue gas. *Eng*., vol.55: p. 216-225.

Kang S H, 2012. Design and experimental study of ORC (organic Rankine cycle) and radial turbine using R245fa working fluid. *Eng*., vol.41: p. 514-524.

Gu Wei, 2009. Theoretical and Experimental Study of Organic Rankine Cycle for Low and Medium Grade Heat Source Utilization [D]. School of Mechanical Engineering, Shanghai: Shanghai Jiao Tong University

Zhang Ye-Qiang, Wu Yu-Ting, Xia Guo-Dong, et al, 2014. Development and experimental study on organic Rankine cycle system with single-screw expander for waste heat recovery from exhaust of diesel engine. *Eng*., vol.77: p. 499-508.

Yu Yong-zhang, Jiang Pei-zheng, Sun Si-ying, 2012. *Compressor Engineering Handbook*. China Petrochemical Press, Beijing, 1070p.

ACKNOWLEDGEMENT

The work was supported by China National Natural Science Foundation (51006002) and the 973 Program' Project (2011CB707202 and 2011CB710704).

IMPLEMENTAION OF A SMALL SCALE ORGANIC RANKINCE CYCLE TEST BED SYSTEM USING STEAM AS HEAT SOURCE

Muhammad Usman[‡†], Muhammad Imran[‡†], Dong Hyun Lee[†] and Byung-Sik Park[*‡†]

‡Korea University of Science and Technology, 217 Gajeong-ro, Yuseong-gu, Daejeon 305-350, South Korea
usman@ust.ac.kr / usman7@live.com
Web page: http://www.ust.ac.kr/

[†]Korea Institute of Energy Research,
152 Gajeong-ro, Yuseong-gu, 305-343, Daejeon, South Korea
[*]Corresponding Authur e-mail: bspark@kier.re.kr
Web page: http://www.kier.re.kr

ABSTRACT

Organic Rankine cycle based power systems are well known for waste heat recovery application due to their adaptability to follow heat source variations. Industrial exhaust steam has an appreciable potential for the installation of waste heat recovery units. Korea Institute of Energy Research has developed waste heat recovery units which can generate power in the range of hundreds of kilowatts. In order to, rigorously test new cycle configurations and control strategies with least cost for heat source, a small-scale organic Rankine cycle test bed was implemented which a has steam condensing heat exchanger for using steam as a heat source in similar configurations as of larger units. The test bed was equipped with data logging and standalone control system and was configured for the electrical output around 1kW using R245fa as a working fluid. The system is composed of plate type heat exchangers, scroll type expansion machine, screw type working fluid pump and control valves with actuators. This work will present the difficulties, solutions and operational results in terms of design, equipment selection, fabrication and operational experience of system for small-scale power generation with efficiency over 5.2 % for a temperature difference of 120^{o}C. Complexities involved in superheat control of working fluid for the system powered by steam will also be discussed.

INTRODUCTION

Organic Rankine cycle system (ORC) is the accepted viable technology for low-temperature heat conversion to electricity (Lecompte et al. 2015). Statistical analysis suggests that low-grade waste heat accounts for more than 50% of the total heat generated in the industry (Hung et al. 1997). Utilization of this waste heat energy to harness electrical power output will be a necessity of future to stay within energy budget allocations, to compete with the growing economies of the world. Low-grade waste heat power generation has been experimentally tested in many studies, where (Zhang et al. 2014), (Wenzhi et al. 2013), (Peris et al. 2015) & (Minea 2014) are the few works to mention in low-grade waste heat recovery works. Most of the published works presented their heat source as hot water or exhaust gas.

Korea Institute of Energy Research has implemented 100kW class ORC systems for low-grade industrial waste heat. The implementation of a very small-scale ORC system was to be tested for performance, controllability, and net power output using low-temperature exhaust steam (<135°C), as a heat source. As this system will be operated for 1kW power output with condensing steam as a heat source, already published literature rarely contain information for such configuration of a small power system with such heat source. The implemented test bed system will be used to test thermodynamic parameters and control strategies by using negligible operational costs as compared to the already installed 100kW scale system. It is suggested that for a small-scale power generation system (under 5kW) scroll machine is the best choice (Quoilin et al. 2012). Following the previous findings, a scroll machine is used in this work. The working fluid is an important factor of choice for ORC power system design, R245fa is known for its safety levels and environmental impacts for waste heat application (Wang et al. 2011). R245fa is also the best choice based on the criteria of net power and suitable working pressure (He et al. 2012). Thus, R245fa is selected as the suitable working fluid for the proposed system.

This work describes the design, fabrication and technical difficulties involved in the implementation of ORC system of such small power out using available components from the market. The test results are presented with performance evaluation for different degrees of superheating of the working fluid at expander inlet.

Materials & Method

The system's operational success is dependent upon its design and implementation. For small scale systems, it is customary to design the thermodynamic cycle for optimum performance at given source and sink conditions to obtain required power output and then finding the equipment (expansion machine, pump, heat exchangers, etc.) from the market, which can operate at required conditions of the power cycle. Contrarily, for bigger systems, it is common to design the components to strictly fulfil the performance requirements. For smaller systems, it is not viable to design and manufacture every single component as per requirements. In that case, components which match closely are selected and can be operated at slightly off design, compromising on performance. Component sizing & selection is difficult when the unusually small power requirement and cycle configurations are imposed. The mismatched components cause a lower overall performance of the system.

The system was designed to be operated by steam in the pressure range of 0~2 bar gauge pressure and the sink temperature at 12°C was available. Numerous working fluids have been under investigation for the usage in organic Rankine cycle based system for low-grade waste heat recovery. R245fa was selected for its closest match of required thermodynamic properties for available heat source and sink conditions and favorable environmental impact. The design procedure was initiated by fixing the pinch point temperature difference in heat exchangers (evaporator and condenser). Having fixed the pinching temperatures allowed to fix evaporation and condensing temperature of the organic Rankine cycle. The pressure ratio was calculated from evaporation and condensing pressures. Although when optimizing the performance of the waste heat ORC system, an optimum evaporating temperature exists that maximizes the output power (or overall efficiency) (Quoilin et al. 2011) but for prototypes and small systems it is more feasible to follow the equipment specifications. In current case, the expander inlet pressure for required output was selected as evaporation pressure. Isentropic enthalpy change was calculated at the calculated pressure ratio. Isentropic efficiency of the scroll type expansion machine was estimated from published literature (Song et al. 2014). The mass flow rate for the proposed system can be calculated from Equation (1).

$$\dot{W}_{shaft} = \dot{m}.(h_1 - h_{2s})\eta_{isen} \quad (1)$$

Power output for net electric power includes the mechanical losses in expander, coupling and generator. Also the generator efficiency reduces the generator output. In order to obtain 1kW electric output, W_{shaft} is estimated to be higher than 1kW. After performing the design calculations for the system, the scheme was modelled in cycle tempo software (Cycle Tempo) for verification and ease of study for

various operational parameters. Major thermodynamic parameters at design point are presented in Table 1.

Table 1: Thermodynamic parameters at design point from design calculation and verified by cycle-tempo software simulation

Parameters	**Value**
Evaporator pressure	12.5bar
Condenser pressure	1.1bar
Expander Isentropic efficiency	50%
Working fluid mass flow rate	0.051kg/s
Heat source temperature (saturated steam)	120°C
Sink Temperature	16°C
Sink mass flow rate	0.73kg/s
Expander inlet temperature	101.5°C
Condenser subcooling	3°C

Table 2: Details of Equipment selected for implementation of test bed

Sr. no	**Equipment**	**Details**
1	Expander	Scroll Type expander (Airsquared Inc.), 12cc/rev, 1kW Nominal output, Magnetic coupling linked to 60Hz Generator 110V AC generator
2	Evaporator & Condenser	Braze plate heat exchangers (Janghan Engineers, Inc.) 60 & 50 plates, area of 6.5 & 5.38 square meter for evaporator & condenser, respectively
4	Feed Pump	Screw type pump (Tuthill Pump Company). Displacement of 2.6ml/rev Magnetic coupling linked to 0.75kW 3 phase 380V motor
5	Load Bank	Electric Bulbs of various power ratings were connected to the generator using single push single throw (SPST) type relays. Bulbs for 110V, were used in different power rating combination. 200W, 100W, 60W, 30W watt bulbs are used to obtain various step of resistive load connected to the generator
6	Heat Sink	Cooling tower already installed in facility
7	Heat Source	LNG based boiler with steam generation capacity of 500 kg/hr maximum
8	Flow rate meters	Working fluid with Coriolis type flow meter, sink flow rate measurement with electromagnetic flow rate meter, sink flow rate measurement with vortex type flow meter
9	Valves	Butterfly valves and globe valve for steam flow control (actuator controlled)
10	Temperature Measurement	T -type thermocouples for temperature measurement & RTD (PT100) for evaporator and expander inlet/exit
11	Pressure Transduces	Pressure Transducers with range of 0~16bar
12	Data Acquisition & Control	NI - cRIO 9074 with 8 slot integrated controller, NI I/O C-series model and Labview software

Condenser

Table 2 presents the detail of selected equipment for test bed construction. Very few off the shelf expansion machines are available in the market, which can be used directly without alteration, but in this work a scroll machine designed for ORC application was available. Pump selection is another tough choice because of low flow rate, and large pressure head, no suitable centrifugal machine was found. A screw pump was able to cater our requirement with confidence as far pressure and flow rate requirements were required, but resulted in poor efficiency (<30%). Load bank was made by connecting electric bulbs of various power ratings to generator circuit and connections were controlled by relay operation.

Figure 1 presents the piping and instrumentation diagram for the test rig which was constructed according to the CAD diagram of system presented in Figure 2. Figure 3 presents the test rig in final fabricated form and under organic Rankine cycle system operation for power output.

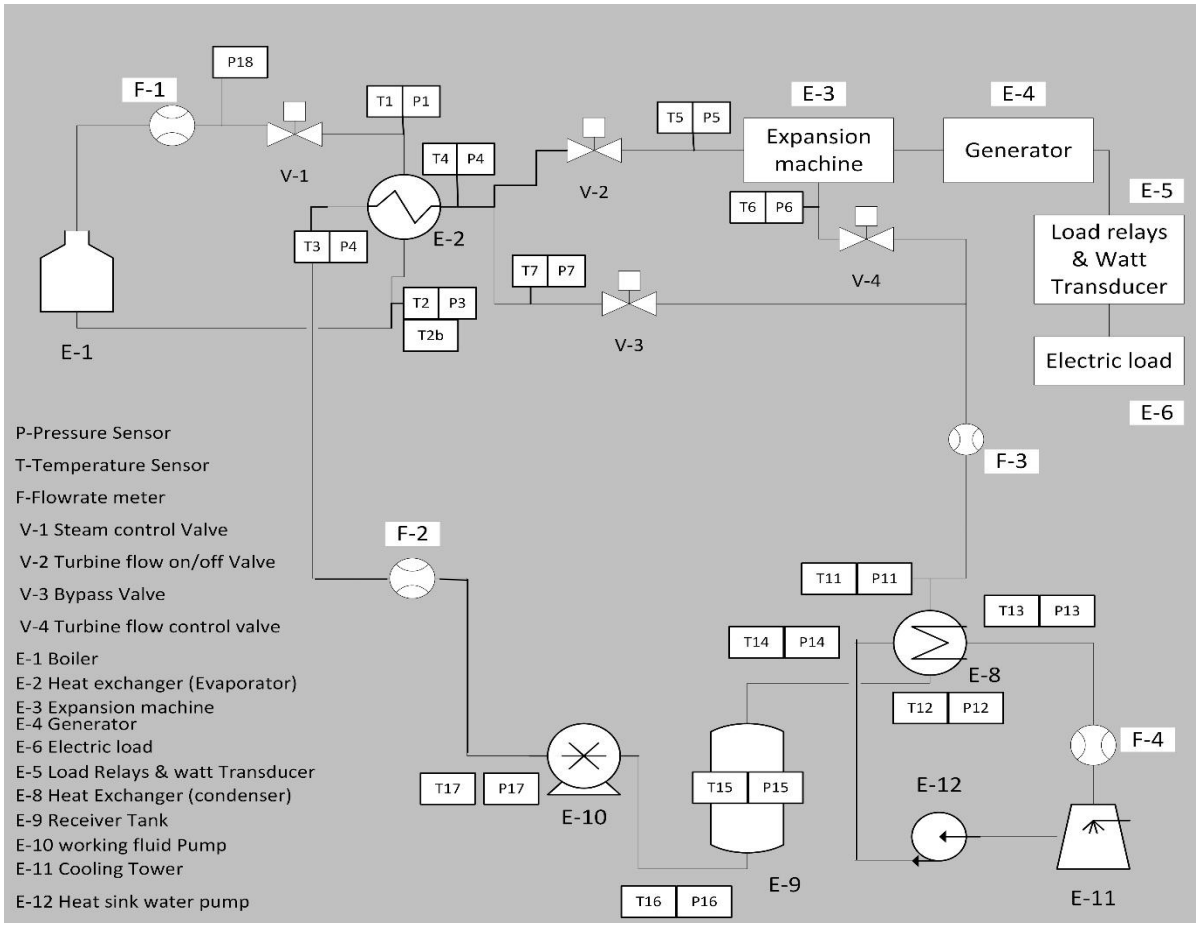

Figure 1: P&ID Scheme for proposed system

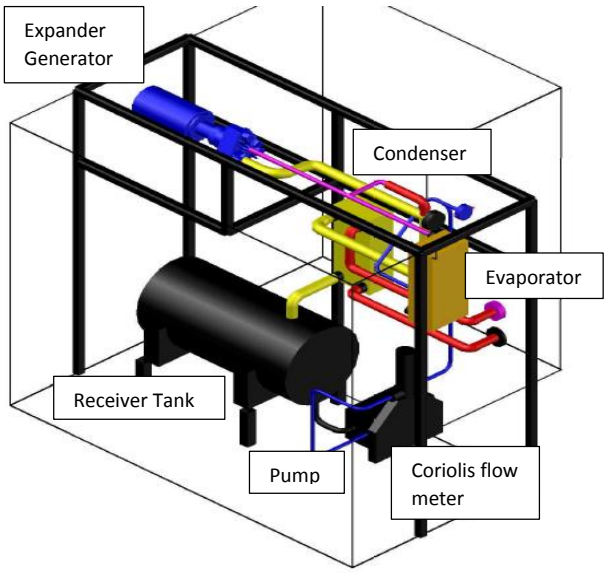

Figure 2: Isometric view of implemented system

Figure 3: System under operation

Results & Discussion

Figure 4 presents organic Rankine cycle test bed operational parameters for 20 minutes of its operating time. The system was operated in a way that the expander speed was kept below 3600RPM to follow safety recommendations from the manufacturer. Electric bulbs were connected to the load circuit one after another until a total of load of 1060W was imposed to the electric generator. After increasing the electric load, the pump speed controlled by variable frequency drive was increased to increase the mass flow rate and increase the evaporator pressure which increase the expander speed. After attaining the expander speed around 3600RPM, next electric bulb was connected which would reduce the expander speed as the torque on generator increased and for the same power output the rotational speed was decreased. Increasing the mass flow rate further, increased the evaporator pressure which allowed higher power output from the expander. The Figure shows that the evaporator pressure follows the pump speed (Mass flow rate). Generator power output increased to a maximum value of 1020W, when evaporator pressure is around the maximum operating design point of 11.5 barg. Expander speed was 3400 RPM while the generator was connected to a circuit of 8 bulbs (200W x 4, 100W x 2, 30W x 2) rated at 110V which summed up to yield 1060W resistive load.

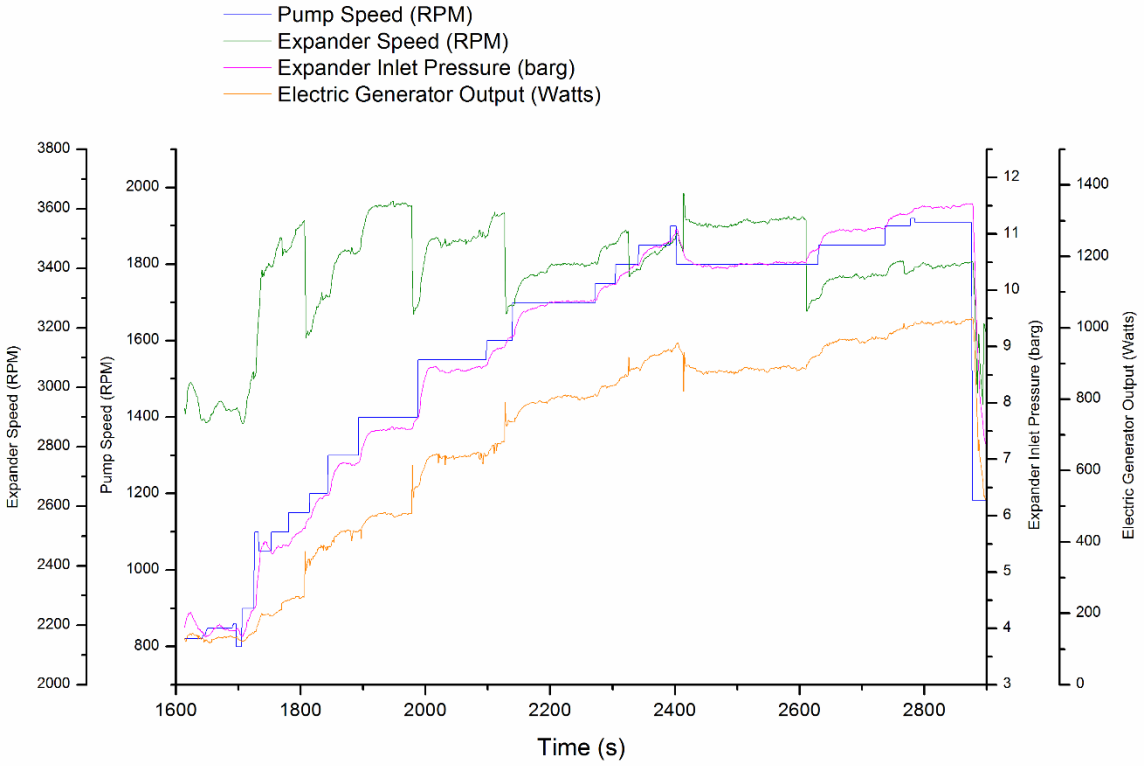

Figure 4: Organic Rankine cycle system operational parameters for different power output range

The sharp spikes in generator power output data occurred at the same time when expander speed was reduced at constant pump speed, increasing the imposed torque reduced the expander speed for the same power output. This was due to the connection of the relay with bulb. When the applied load increased as a step change the expander speed was reduced, to get back to recommended expander speed, pump speed was carefully adjusted to carry higher loads.

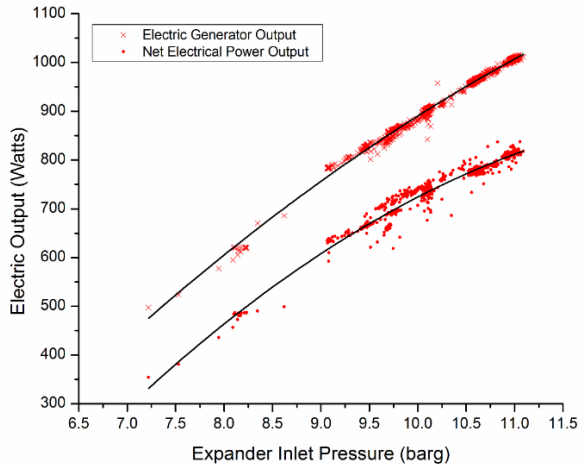

Figure 5: Electric Generator Output and Net Output vs Expander Inlet Pressure

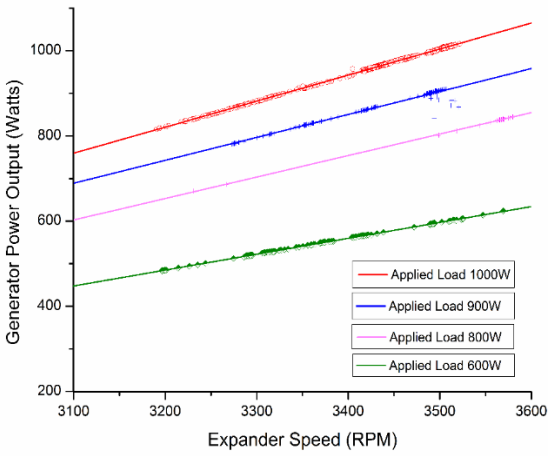

Figure 6: Electric Generator Power Output power vs Expander Speed

Figure 5 presents the electric output of generator with respect to the evaporator pressure while condenser conditions were held constant at 0.3barg. The figure also presents the net electric power output from the system. The pump electric power consumption was measured and used for evaluation. Both data plots are fitted with a 2nd order polynomial for analysis. Figure 6 presents generator output at various electric loading conditions. An applied load of 1000W refers to the connected electric bulbs with a combined power rating of 1000W to the electric generator circuit.

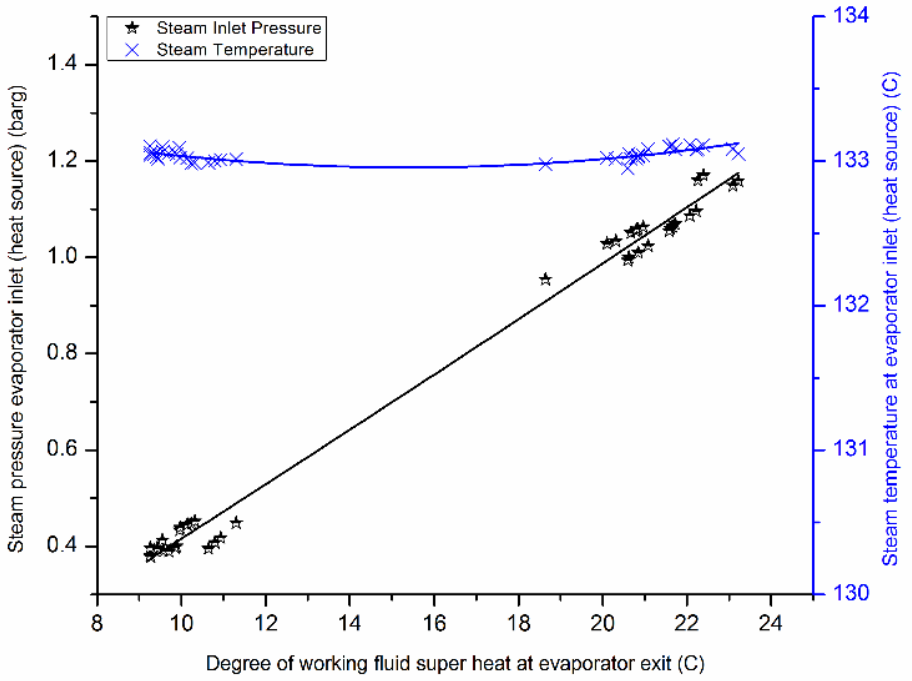

Figure 7: Variation of degree of super heat of working fluid at evaporator exit with respect to steam (heat source) pressure at heat source inlet side.

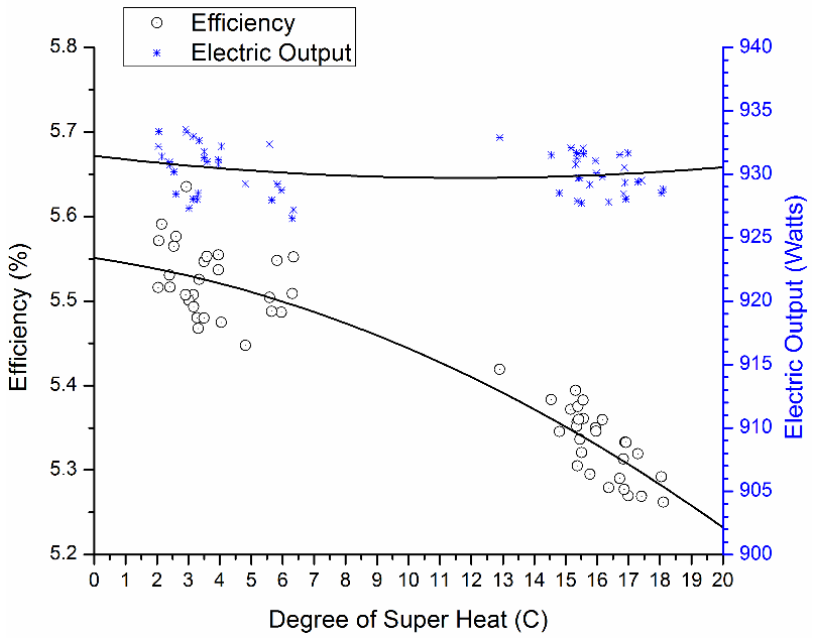

Figure 8: Effect of degree of super heat of working fluid at expander inlet vs electrical efficiency for same power output

An experiment to investigate the effects of superheat of the working fluid at expander inlet was performed. Extensive research and theoretical background suggested the lesser the degree of superheating, the better would be the performance for a system without recuperator using R245fa working fluid. In reality to maintain, superheat value of 0 would be ideal but is very challenging task to maintain a stable working fluid output with all vapor exit quality without any superheating. The ability to maintain the minimum superheating degree depends on various equipment and control characteristics. Evaporator type, size& geometry, plays an important role in this regard. In case of plate heat exchanger, the number of channels, aspect ratio, port design & thermal inertia influence the performance in such a way that to obtain a superheat of 0 is very difficult. The heat source type is also an important factor when considering the controllability of superheating of the working fluid at evaporator exit. In case of current system the heat source is steam, which is condensed in evaporator and subcooled to certain level.

Control of heat source was performed by using a globe valve which has been carefully sized and custom manufactured for the current conditions of steam pressure & flow rates. The actuator controlled valve allowed control of heat source for a steam requirement of less than 40 kg/hr. Figure 7 presents the controllability of working fluid superheat at evaporator exit. The globe valve which has an upstream steam pressure of 1.95 ~ 2barg was opened in such a way that the downstream pressure of globe valve was increased. As a result, condensing pressure in evaporator (heat source side/steam) was increased. Superheat at evaporator exit (Working fluid side) was observed as 10^{O}C when source pressure was 0.4barg, when steam pressure was increased to 1.1barg the super heat value was observed around 21^{O}C. While the source temperature was observed around 133^{O}C in both cases. Figure 8 presents superheating degree at expander inlet and cycle efficiency for same electrical power output. Figure 7 and Figure 8 present data from same experiment, but the Figure 8 presents superheat value at expander inlet while Figure 7 presents the superheat value for evaporator exit. The difference in super heat values is due to heat loss in piping network when the working fluid flows from evaporator to expander. The data in Figure 9 and 8 is used to plot 2nd order polynomial fits for analysis. Electrical efficiency of system was obtained by equation (2).

$$\eta_{elec} = \frac{Electric\ Generator\ Power\ Output\ (kW)}{\dot{Q}_{evaporator.\ working\ fluid}\ (kW)} \quad (2)$$

Where

$$\dot{Q}_{e,wf}\ (kW) = \dot{m_{wf}}\ (h_{eo} - h_{ei}) \tag{3}$$

Figure 8 data results used to obtain 2nd order polynomial relation which suggest the drop in efficiency of system with increasing super heat value. The relation is presented as Equation (4)

$$\zeta = 5.55084 - 0.00542(\theta) - 0.0005245(\theta)^2 \tag{4}$$

Where

$$\zeta - electric\ efficiency\ (percentage)\ as\ a\ function\ of\ superheat$$

$$\theta -\ is\ degree\ of\ superheat\ (Celcius)\ at\ expander\ inlet$$

Equation 4 can be used to estimate the reduction in efficiency with respect to superheating degree for the same electrical power generated. In this case power output was held constant by maintaining a constant expander speed to hold power output around 930W and heat source carefully adjusted to obtain different superheat values. It was noted that for current system an increase in 1°C of super heat will reduce 0.011% in electric efficiency if evaporator superheat is around 10°C. As the relation is nonlinear curve it suggests reduction in electric efficiency of 0.025% with increase of 1°C after super heat at heat exchanger exit is above 20°C. The relation is only valid for current system and is a basis for the future research work to be carried out to establish relationship for efficiency and superheating degree for various systems of various power range.

Conclusion

In this work, design, equipment selection and fabrication of a small scale organic Rankine cycle test bed system, using steam as heat source was performed. The fabricated test rig was operated and following conclusion were made:

- 1kW scale organic Rankine cycle system can be designed and fabricated with major components available from market.
- Design requirement of components and availability causes mismatching in component selection, whereas losses (isentropic, frictional, electrical etc.) involved in components should be carefully analyzed to achieve required performance.
- A 1kW scale ORC system is capable of producing net electrical output if components are precisely selected
- The system was able to produce 1kW electric output with efficiency value of 5.2%.
- The best efficiency points are not at the highest output power.
- Using a steam condensing evaporator for small flow rates of steam and working fluid superheat control at constant pressure is difficult procedure.
- Efficiency depreciation with increasing superheat level can go as high as 0.02% per degree Celsius for this system.
- An attempt to establish a practical approach for relating efficiency depreciation with higher superheat is initiated. The future work will incorporate various types of systems at various power range will be studied for efficiency drop due to superheat to highlight how much research attention and work will be required for improvement of control systems and heat exchangers to obtain minimum super heat levels.

NOMENCLATURE

ORC	Organic Rankine Cycle
$\dot{W}_{shaft}$	Expander shaft power output
$\dot{m}_{wf}$	Working fluid mass flow rate (R245fa)
h_{eo}	Working fluid enthalpy at evaporator outlet
h_{ei}	Working fluid enthalpy at evaporator inlet
η_{isen}	Expander Isentropic efficiency
η_{elec}	Thermal to electric conversion efficiency
$\dot{Q}_{e,wf}$	Heat transfer to the working fluid

REFERENCES

Cycle Tempo. TU Delft (Delft University of Technology), http://www.asimptote.nl/

He, C. et al., 2012. The optimal evaporation temperature and working fluids for subcritical organic Rankine cycle. *Energy*, 38(1), pp.136–143.

Hung, T.C., Shai, T.Y. & Wang, S.K., 1997. A review of organic rankine cycles (ORCs) for the recovery of low-grade waste heat. *Energy*, 22(7), pp.661–667.

Lecompte, S. et al., 2015. Review of organic Rankine cycle (ORC) architectures for waste heat recovery. *Renewable and Sustainable Energy Reviews*, 47, pp.448–461.

Minea, V., 2014. Power generation with ORC machines using low-grade waste heat or renewable energy. *Applied Thermal Engineering*, 69(1-2), pp.143–154.

Peris, B. et al., 2015. Experimental characterization of an ORC (organic Rankine cycle) for power and CHP (combined heat and power) applications from low grade heat sources. *Energy*, 82, pp.269–276.

Quoilin, S. et al., 2011. Thermo-economic optimization of waste heat recovery Organic Rankine Cycles. *Applied Thermal Engineering*, 31(14-15), pp.2885–2893.

Song, P. et al., 2014. A review of scroll expanders for organic Rankine cycle systems. *Applied Thermal Engineering*, 75, pp.54–64.

Wang, E.H. et al., 2011. Study of working fluid selection of organic Rankine cycle (ORC) for engine waste heat recovery. *Energy*, 36(5), pp.3406–3418.

Wenzhi, G. et al., 2013. Performance evaluation and experiment system for waste heat recovery of diesel engine. *Energy*, 55, pp.226–235.

Zhang, Y.-Q. et al., 2014. Development and experimental study on organic Rankine cycle system with single-screw expander for waste heat recovery from exhaust of diesel engine. *Energy*, 77, pp.499–508.

ACKNOWLEDGEMENT

This work was conducted under the framework of Research and Development program of the Korea Institute of Energy Research and University of Science & Technology (b4-5524).

THERMODYNAMIC STUDY OF INFLECTION POINT OF SATURATED VAPOR CURVE FOR DRY AND ISENTROPIC WORKING FLUIDS

Xinxin ZHANG[1]*, Congtian Zhang[1], Jingfu WANG[1], Maogang HE[2]

[1]Key Laboratory of Enhanced Heat Transfer and Energy Conservation, Ministry of Education
Key Laboratory of Heat Transfer and Energy Conversion, Beijing Municipality
College of Environmental and Energy Engineering, Beijing University of Technology
Beijing 100124, P R China
xinxinzhang@bjut.edu.cn

[2]Key Laboratory of Thermo-Fluid Science and Engineering, Ministry of Education
School of Energy and Power Engineering, Xi'an Jiaotong University
Xi'an, Shaanxi 710049, P R China
mghe@mail.xjtu.edu.cn

* Corresponding Author Xinxin ZHANG

ABSTRACT

In this paper, the definition of inflection point on saturated vapor curve of dry fluid and isentropic fluid was given according to the shape of the saturated curve of working fluids in a T-s diagram. On this basis, the model of near-critical region triangle was established. Using this model, the effect of inflection point on saturated vapor curve on performance of organic Rankine cycle(ORC) was studied when 38 kinds of dry and isentropic organic working fluids was adopted in ORC. The performance includes relationship between the inflection point temperature and the area of near-critical region triangle, the relationship between the exergy at the inflection point and the area of near-critical region triangle, and the relationship between the area of near-critical region triangle and reciprocal value of slope of saturated vapor curve. On this basis, if the type of heat source is taken into account, the theoretical analysis results show that heptane, cyclohexane, octane, nonane, decane, and dodecane are the suitable working fluids for open-type heat source utilization.

1. INTRODUCTION

The organic Rankine cycle(ORC) which applies the principle of the steam Rankine cycle, but uses organic working fluids with low boiling points was first invented and introduced by Ray and Moss (1966) who used fluorochemicals as working fluid in small Rankine cycle power units. Since then, the ORC technology has become more and more popular in both the waste heat recovery and renewable and sustainable energy utilization field.

As known to all, working fluid plays a very important role in thermodynamic cycle. The efficiency, the operation condition, the impact on the environment, and the economic feasibility of thermodynamic cycle are greatly affected by working fluid selection and the nature of the working fluid. In ORC, organic working fluid plays a decisive role. It is the lower boiling point of organic working fluid compared with water that makes a higher saturation pressure at lower temperatures. Accordingly, work can be produced at a lower temperature because of good thermodynamic performance of organic working fluid.

Organic working fluid can be classified into three categories according to the slope of the saturated vapor curve in a T-s diagram. They are dry fluid with a positive slope(e.g. isopentane), wet fluid with a negative slope(e.g. R22), and isentropic fluid with a vertical slope(e.g. R11)(Hung, 2001; Liu *et al*.,

2004; Chen *et al*., 2010). The working fluids of dry or isentropic type are more appropriate for ORC systems(Liu *et al*., 2004). The literature shows extensive researches on organic working fluid selection under certain predefined temperature conditions and certain operation conditions. If we observe the shape of saturated vapor curve of dry and isentropic fluid in a T-s diagram, we will find an inflection point on saturated vapor curve. In this paper, we defined this inflection point and established a model of near-critical region triangle. Using this model, the effect of inflection point on saturated vapor curve on performance of organic Rankine cycle(ORC) was studied when 38 kinds of dry and isentropic organic working fluids was adopted in ORC. On this basis, taking the type of heat sources into account, the suitable working fluid was analyzed and selected through theoretical calculation.

2. DEFINITION OF INFLECTION POINT ON SATURATED VAPOR CURVE

2.1 Type of Working fluid

As mentioned in Section 1, a working fluid can be classified as a wet, dry, or isentropic fluid according to the slope of the saturated vapor curve (dT/ds) in its T-s diagram as depicted in Figure 1. Considering the value of dT/ds is infinity for an isentropic fluid, the reciprocal value of the slope(e.g ds/dT) is used to judge the type of a working fluid. Here we define ξ= ds/dT, if ξ>0, then it is a dry fluid, and $\xi\approx$0 for an isentropic fluid and ξ<0 for a wet fluid. Near critical point, there is an inflection point on saturated vapor curve of dry and isentropic working fluid. In order to study the effect of this inflection point on the performance of organic Rankine cycle for waste heat recovery, first we have to judge the type of a working fluid according to its value of ξ and the shape of its T-s diagram.

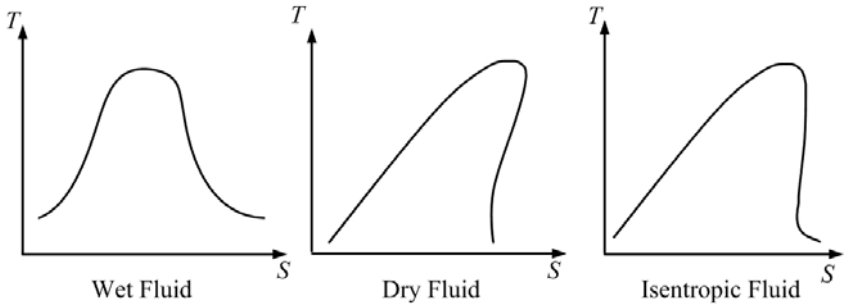

Figure 1: Temperature-entropy (T-s) diagrams of different fluids

Liu *et al.*(2004) introduced an equation for calculating the value of ξ, which is:

$$\xi = \frac{c_p}{T_H} - \frac{[(n \cdot T_{rH}) / (1 - T_{rH})] + 1}{T_H^2} \Delta H_H \qquad (1)$$

where, ξ (ds/dT) denotes the reciprocal value of the slope of saturated vapor curve in a T-s diagram, n is suggested to be 0.375 or 0.38(Poling *et al*., 2001), T_{rH}(=T_H/T_c) denotes the reduced evaporation temperature, and ΔH_H is the enthalpy of vaporization.

The calculation value of ξ according to Equation (1) and corresponding type of a working fluid is listed in Table 1. The calculation values have a good agreement with the shape of saturated vapor curves in a T-s diagram.

2.2 Definition and Determination of Inflection Point on Saturated Vapor Curve

From the classification of working fluid introduced in the last subsection, it can be seen that in a T-s diagram, a significant difference between dry(or isentropic) fluid and wet fluid is the existence of a point on its saturated vapor curve on which the entropy value reaches the maximum. This point is located near the critical point. After passing this point, the entropy value on saturated vapor curve of

dry fluid decreases. For isentropic fluid, the entropy value basically keeps unchanged. However, we cannot find out such a point on saturated vapor curve of wet fluid.

Table 1: The calculation value of ξ and corresponding type of a working fluid

Working Fluid	Calculation Value of ξ	Fluid Type
Water	-13.1818	Wet
Ethanol	-5.4299	Wet
R11	-0.3903	Isentropic
R123	0.1202	Isentropic
HFE7100	1.8252	Dry
n-Pentane	1.2835	Dry
Iso-pentane	1.1801	Dry
Benzene	0.3316	Isentropic
Toluene	1.0600	Dry
p-Xylene	1.5390	Dry
butane	0.0083	Dry
butene	0.0065	Dry
cis-butene	0.0059	Dry
cyclohexane	0.0112	Dry
decane	0.0146	Dry
dodecane	0.0149	Dry
heptane	0.0121	Dry
hexane	0.0106	Dry
isobutane	0.0083	Dry
isobutene	0.0071	Dry
isohexane	0.0113	Dry
nonane	0.0124	Dry
octane	0.0121	Dry
pentane	0.0098	Dry
perfluorobutane	0.0051	Dry
perfluoropentane	0.0056	Dry
R113	0.0030	Isentropic
R114	0.0033	Isentropic
R115	0.0032	Isentropic
R124	0.0030	Isentropic
R141b	0.0030	Isentropic
R142b	0.0029	Isentropic
R218	0.0045	Isentropic
R227ea	0.0042	Isentropic
R236ea	0.0043	Isentropic
R236fa	0.0038	Isentropic
R245ca	0.0046	Isentropic
R245fa	0.0044	Isentropic
R365mfc	0.0056	Dry
RC318	0.0043	Isentropic
trans-butene	0.0067	Dry

Considering this unique characteristic of dry and isentropic fluid, here we define an inflection point on saturated vapor curve of dry or isentropic fluid as a point whose entropic reaches the maximum value ranging from freezing point to critical point. Figure 2 illustrates the inflection point on saturated vapor curve of dry and isentropic fluid.

According to the definition of inflection point on saturated vapor curve, its location is determined by the entropic value of dry or isentropic fluid given by REFPROP 8.0 software developed by the National Institute of Standards and Technology Laboratories (NIST)(Lemmon et al., 2007). Dry and isentropic working fluids are selected from all the working fluids in REFROP 8.0 according to the

calculation value of ξ. The *T-s* diagrams of these two types of working fluids are made by software. Observe the shape of saturated vapor curve in *T-s* diagram, and obtain the entropy value under each temperature from the critical point to freezing point using 0.5K as a step. For dry fluid, it can be seen that on saturated vapor curve the entropy value increases with the temperature decrease from critical point until inflection point. As for isentropic fluid, the entropy value basically keeps constant when temperature is around the inflection point. Therefore, we define the inflection point of isentropic fluid as the closest point to critical point with the maximum entropy value on saturated vapor curve. Table 2 lists the temperature on inflection point of 38 working fluids(dry and isentropic) studied in this paper.

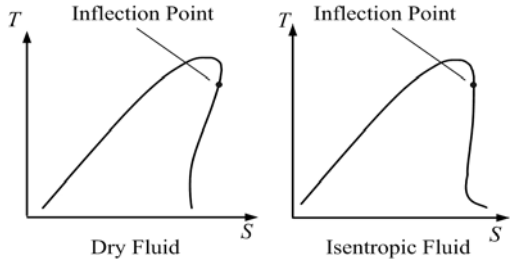

Figure 2: Inflection point on saturated vapor curve of dry and isentropic fluid

3. DEFINITION AND AREA OF NEAR-CRITICAL REGION TRIANGLE

Figure. 3 describes the typical process(1-2s-2'-3-4-5) of an organic Rankine cycle with dry working fluids. The thermal efficiency of an ideal ORC can be calculated from the following equation.

$$\eta_{\mathrm{i}} = \frac{w}{q_1} = \frac{w - w_{\mathrm{p}}}{h_1 - h_4} = \frac{h_1 - h_{2\mathrm{s}} - (h_4 - h_3)}{h_1 - h_4} \tag{2}$$

where, *h* denotes enthalpy value, *w* denotes work, and *q* denotes heat. The number on subscript stands for the state point of the ORC.

The thermal efficiency of a practical ORC can be calculated from the following equation.

$$\eta_{\mathrm{r}} = \frac{w}{q_1} = \frac{w_{\mathrm{r}} - w_{\mathrm{p}}}{h_1 - h_4} = \frac{h_1 - h_2 - (h_4 - h_3)}{h_1 - h_4} \tag{3}$$

From the above two equations, it can be seen that the enthalpy value of point 1 significantly effects the thermal efficiency of an ORC. Therefore, the inflection point introduced in this paper focuses on the characteristics of point 1 in an ORC. The inflection point usually has a relatively high temperature. Moreover, latent heat of vaporization reaches the maximum value at the inflection point for dry and isentropic fluid(In the range between critical point and inflection point). However, the temperature between critical point and inflection point doesn't offer any help for improving the thermal efficiency of an ORC. In order to study the effect of inflection point on saturated vapor curve on the thermal efficiency of an ORC, we have to define a parameter to measure the meaningless part surrounded by saturated curve of dry or isentropic fluid for improving the cycle thermal efficiency. This meaningless part will be described by the area of near-critical region triangle.

In *T-s* diagram, draw a line through the inflection point and make it parallel to the *s* axis. This straight line will make two intersections with the saturated liquid curve and saturated vapor curve. These two intersections, with the critical point, make a triangle. This triangle is defined as the near-critical region triangle. The base of the near-critical region triangle stands for the entropy difference between the

saturated liquid state and the saturated vapor state at the inflection point temperature. The height of the near-critical region triangle stands for the temperature difference between the critical point and the inflection point. Figure. 4 illustrates the near-critical region triangle of dry and isentropic fluid. The unit of entropy difference is kJ/kg·K(triangle base), and that of temperature difference is K(triangle height), therefore, the area of near-critical region triangle has a unit of kJ/kg which is the same as the unit of enthalpy.

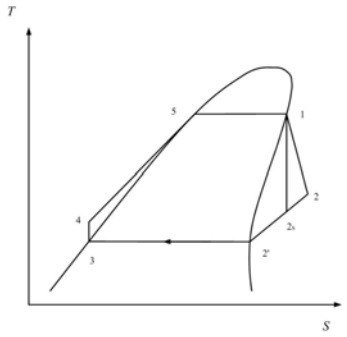

Figure 3: Typical process of an organic Rankine cycle with dry working fluids

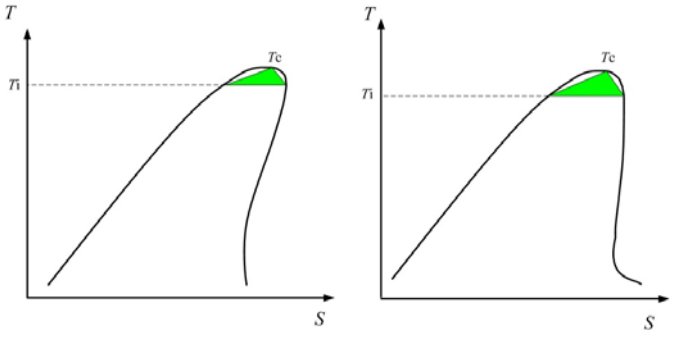

Figure 4: Near-critical region triangle of dry and isentropic fluid

From the database of REFPROP 8.0 software, 38 kinds of dry and isentropic fluids are selected for calculation and analysis. Table 2 lists the basic thermophysical characteristics of these 38 kinds of fluids. According to these parameters and the definition of near-critical region triangle, the areas of near-critical region triangle of these 38 kinds of working fluids were calculated. Figure 5 depicts the relation between the inflection point temperature and the area of near-critical region triangle. From the figure, it can be seen that dodecane and perfluoropentane has the smallest area of near-critical region triangle. However, dodecane has the highest inflection point temperature among these 38 kinds of working fluids. Most of working fluids have inflection point temperatures ranging from 350K to 500K. Here it has to be mentioned that the critical temperature of R116(hexafluoroethane) is 293.03K which is much lower than the operation temperature of an ORC which is from 353K to 673K. Therefore, R116 will not be included in the following analysis.

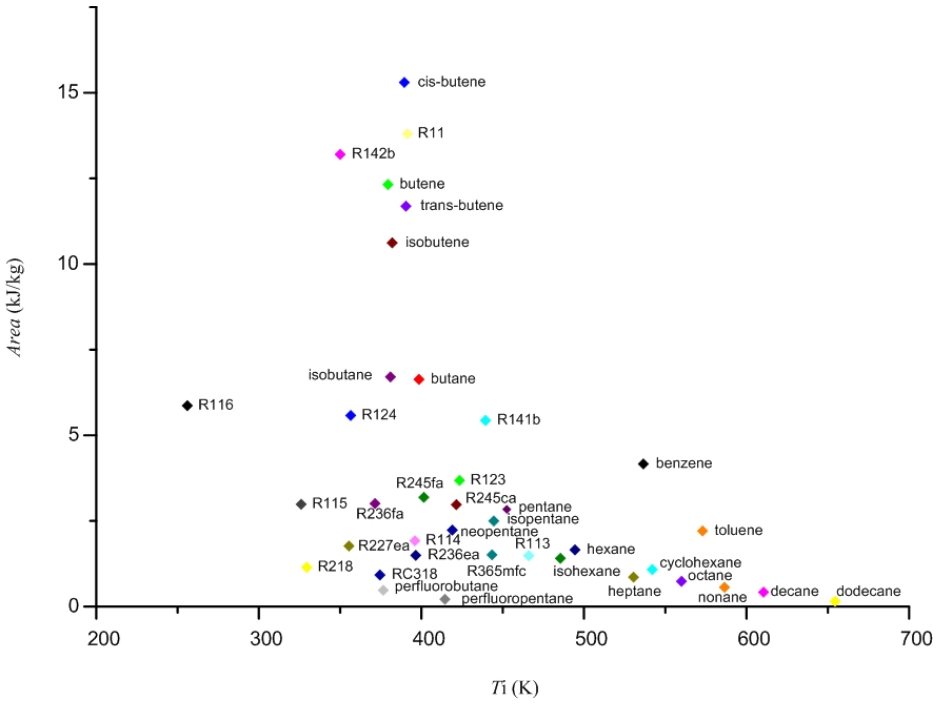

Figure 5: Relation between the inflection point temperature and the area of near-critical region triangle

Table 2: Basic thermophysical characteristics of 38 working fluids

Working Fluid	Critical Temperature/ K	Temperature on inflection point/ K	Vapor entropy on inflection point/ kJ·(kg·K)$^{-1}$	Liquid entropy on inflection point/ kJ·(kg·K)$^{-1}$
benzene	562.05	536.5	1.3865	1.0710
Butane	425.13	398.5	1.357	1.0539
Butene	419.29	379.5	1.1707	1.0303
cis-butene	435.75	389.5	1.2149	1.0565
Cyclohexane	553.64	542	1.4009	1.0711
Decane	617.7	610.5	0.47934	0.3824
Dodecane	658.1	654.5	0.4546	0.3836
Heptane	540.13	530.5	1.6772	1.3305
Hexane	507.82	494.5	1.6776	1.5374
Isobutane	407.81	381	1.5635	1.3951
Isobutene	418.09	382	1.4151	1.1946
Isohexane	497.7	485.5	1.2371	0.9202
Isopentane	460.35	444.5	1.7003	1.4793
Neopentane	433.74	419	1.5991	1.3125
Nonane	594.55	586.5	1.8847	1.5986
Octane	569.32	560	1.7887	1.3505
Pentane	469.7	452.5	1.369	1.2213
perfluorobutane	386.33	376.5	1.5087	1.3263
perfluoropentane	420.56	414.5	1.6921	1.5041
R11	471.11	391.5	1.6371	1.4109
R113	487.21	466	1.8634	1.6349
R114	418.83	396	1.7999	1.5510
R115	353.1	326	1.9259	1.7425
R116	293.03	256	1.5085	1.3759
R123	456.83	423.5	1.2	0.9647
R124	395.43	356.5	1.5067	0.8932
R141b	477.5	439.5	1.3865	1.0710
R142b	410.26	350	1.357	1.0539
R218	345.02	329.5	1.1707	1.0303
R227ea	374.9	355.5	1.2149	1.0565
R236ea	412.44	396.5	1.4009	1.0711
R236fa	398.07	371.5	0.47934	0.3824
R245ca	447.57	421.5	0.4546	0.3836
R245fa	427.16	401.5	1.6772	1.3305
R365mfc	460	443.5	1.6776	1.5374
RC318	388.38	374.5	1.5635	1.3951
Toluene	591.75	573	1.4151	1.1946
trans-butene	428.61	390.5	1.2371	0.9202

4. EFFECT OF INFLECTION POINT ON PERFORMANCE OF AN ORC

Exergy is used to evaluate the quality of energy. Under ambient condition, the energy that can be converted into useful work is called exergy. Through exergy analysis of an ORC, we can find out the part that needs to be improved. As for an ORC, the exergy loss caused by expansion process cannot be ignored. Based on this consideration, the exergy at inflection point temperature of working fluid and its area of near-critical region triangle is compared. Figure. 6 depicts this comparison result. From the figure, it can be seen that heptane, cyclohexane, octane, nonane, decane, and dodecane has a relatively small area of near-critical region triangle but a high exergy.

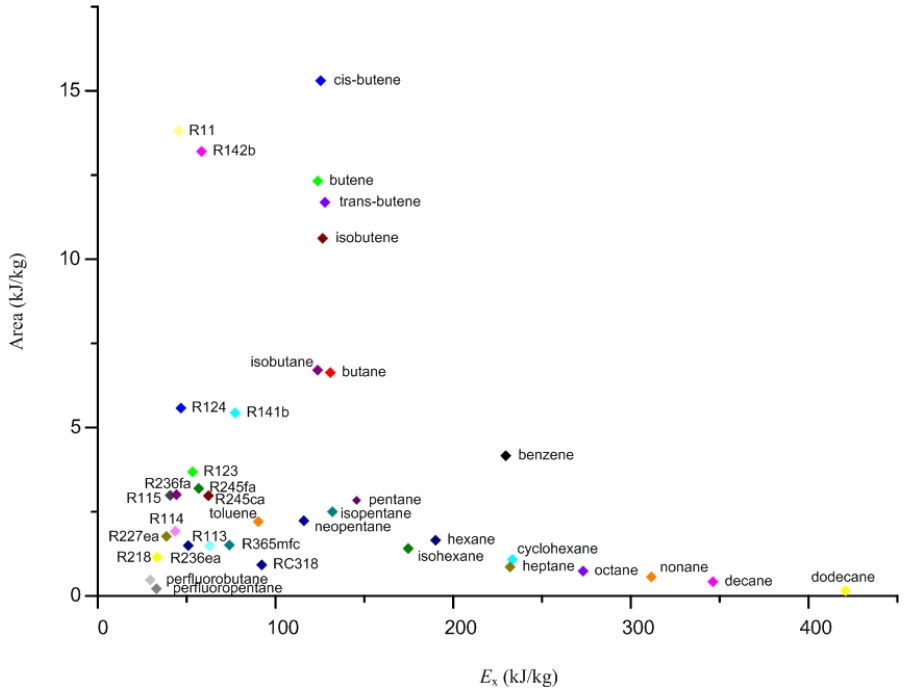

Figure 6: Relation between the area of near-critical region triangle and the exergy at inflection point temperature

From the previous discussion, it is known to all that the drier working fluid is, the more benefit an ORC gets from an expander's perspective. What is the relation between the area of near-critical region triangle of a working fluid and its type. Figure. 7 depicts this relation. The value of ξ can be used to judge the type of a working fluid. The dry fluid has a positive value of ξ. From the figure, it can be seen that compared with other working fluids, decane and dodecane has a relatively big value of ξ and a relatively small area of near-critical region triangle. These two working fluids are good candidates for selection.

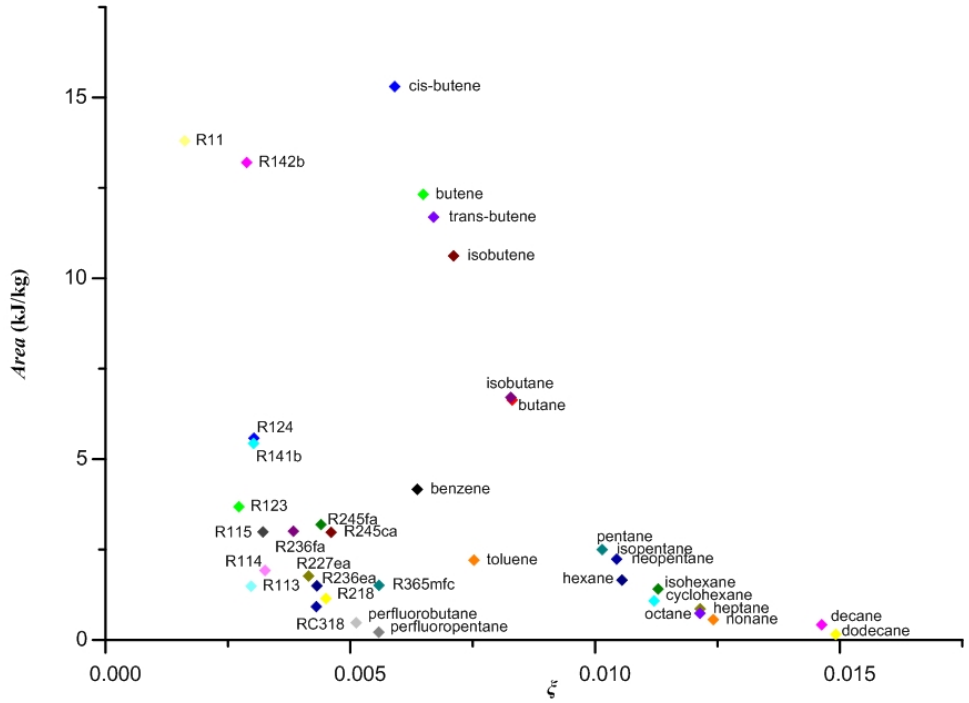

Figure 7: Relation between the area of near-critical region triangle and the type of working fluid

There are two types of waste heat(Yan, 1982; Zhao and Qian, 1984; He *et al*. 2014). One is called open type. The other is called closed type. For the open type, the inlet temperature and the mass flow rate are known, and the working mass of the heat source is directly discharged after being used. For the closed type, the heat release is specific and the working mass of the heat source is usually recycled after releasing heat. Therefore, the standards used to measure the waste heat recovery of these two types of heat source are different(Yan, 1982; Zhao and Qian, 1984). For the open type, the maximum net power output is used as the criterion. However, for the closed type, the maximum thermal efficiency is the criterion. Accordingly, the selection principle of working fluid for waste heat recovery with different heat source is different(Yan, 1982; He *et al*. 2014). For the open type, the working fluids with high liquid specific heat and low latent heat of evaporation should be selected as the working fluids. In contrast, the working fluids with low liquid specific heat and the high latent heat of evaporation are better for the closed heat source.

According to the above conclusion, the liquid specific heat at the inflection point temperature and the latent heat of evaporation at the inflection point temperature for 38 kinds of organic working fluids are listed in Table 3. Moreover, Figure 8 depicts the relation between these two parameters.

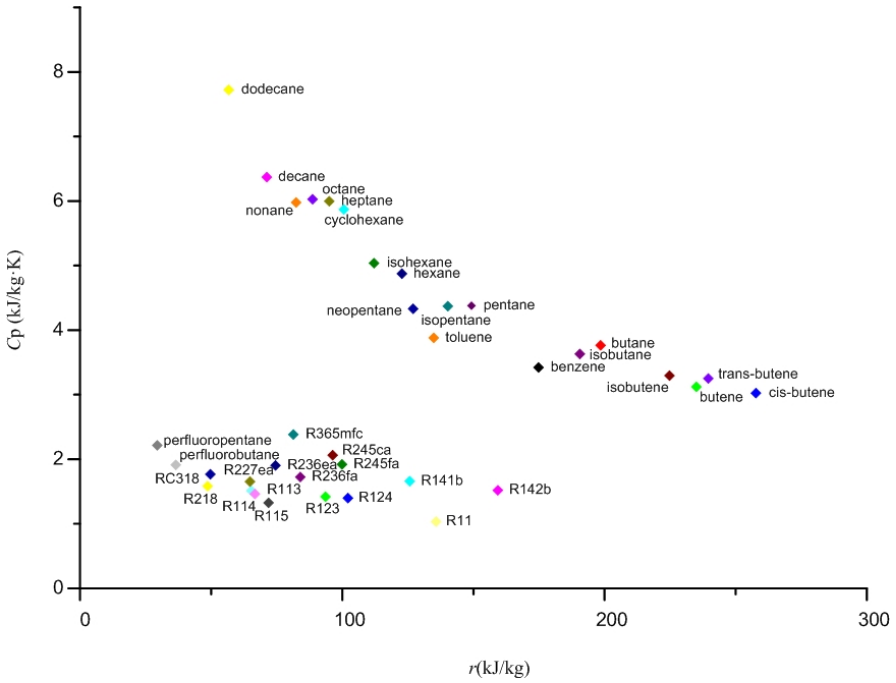

Figure 8: Relation between the liquid specific heat at the inflection point temperature and the latent heat of evaporation at the inflection point temperature

Scanning the figure carefully, it can be seen that the working fluids at the upper left corner should be selected for waste heat recovery of open type heat source. In contrast, the working fluids at the bottom right corner are better for the closed type heat source. The working fluids at the upper left corner (heptane, cyclohexane, octane, nonane, decane, and dodecane) are just the ones we have selected through the previous discussion. However, butene and its isomers which are at the bottom right corner are not selected due to their big areas of near-critical region triangle.

5. CONCLUSIONS

Through scanning the shape of saturated curve of dry and isentropic fluid, it can be seen that there is an inflection point on its saturated vapor curve. We define an inflection point on saturated vapor curve of dry or isentropic fluid as a point whose entropic reaches the maximum value ranging from freezing point to critical point. On this basis, we define the near-critical region triangle which is used to measure the meaningless part surrounded by saturated curve of dry or isentropic fluid.

Table 3: Liquid specific heat and latent heat of evaporation at the inflection point temperature of 38 working fluids

Working Fluid	Liquid specific heat at the inflection point temperature, C_p / kJ·(kg·K)$^{-1}$	Latent heat of evaporation at the inflection point temperature, / kJ·kg^{-1}
Benzene	3.4216	174.84
Butane	3.7638	198.48
Butene	3.1208	235.01
cis-butene	3.0254	257.72
Cyclohexane	5.8695	100.62
Decane	6.3693	71.25
Dodecane	7.7228	56.71
Heptane	5.9967	95.04
Hexane	4.8754	122.74
Isobutane	3.6316	190.56
Isobutene	3.2953	224.77
Isohexane	5.0375	112.11
Isopentane	4.3709	140.24
Neopentane	4.3319	126.99
Nonane	5.9777	82.37
Octane	6.0278	88.7
Pentane	4.378	149.26
perfluorobutane	1.9117	36.51
perfluoropentane	2.2151	29.42
R11	1.036	135.75
R113	1.5117	65.34
R114	1.4625	66.67
R115	1.3247	71.88
R123	1.419	93.57
R124	1.3982	102.14
R141b	1.6606	125.71
R142b	1.5201	159.3
R218	1.5841	48.68
R227ea	1.6539	64.82
R236ea	1.9049	74.52
R236fa	1.7247	84.03
R245ca	2.0641	96.31
R245fa	1.9207	99.91
R365mfc	2.3851	81.37
RC318	1.7678	49.66
Toluene	3.8798	134.84
trans-butene	3.2499	239.57

Using these two model, the effect of inflection point on saturated vapor curve on performance of organic Rankine cycle(ORC) was studied when 38 kinds of dry and isentropic organic working fluids was adopted in ORC. The analysis results show that heptane, cyclohexane, octane, nonane, decane, and dodecane are the suitable working fluids. On this basis, if the type of heat source is taken into account, a same theoretical analysis results is gotten for open-type heat source utilization. However, for the closed-type heat source, there is no suitable working fluid if using these two models for analysis due to the big areas of near-critical region triangle of butene and its isomers.

REFERENCES

Ray, S.K., Moss, G., 1966, Fluorochemicals as working fluids for small rankine cycle power units, *Adv. Energy. Convers.*, vol. 6, no.2: p. 89-102.

Hung, T. C., 2001, Waste heat recovery of organic Rankine cycle using dry fluids, *Energy. Convers. Manage.,* vol. 42: p. 539-553.

Chen, H., Goswami, D.Y., Stefanakos, E.K., 2010, A review of thermodynamic cycles and working fluids for the conversion of low-grade heat, *Renew. Sust. Energ. Rev.,*vol. 14: p.3059-3067.

Liu, B.T., Chien, K.H., Wang, C.C., 2004, Effect of working fluids on organic Rankine cycle for waste heat recovery, *Energy*, vol.29: p.1207-1217.

Poling, B.E., Prausnitz, J.M., O'Connell, J.P., 2001,The properties of gases and liquids, 5th ed., McGraw-Hill, New York.

Lemmon, E.W., McLinden, M.O., Huber, M.L., 2007, NIST reference fluid thermodynamic and transport properties-REFPROP version8.0, National Institute of Standard Technology, Boulder.

Yan, J.L., 1982, Thermodynamic principles and formulas for choosing working fluids and parameters in designing power plant of low temperature heat. *J. Eng. Thermophys.*, vol. 3, no.1: p.1-7.[In Chinese]

Zhao, G., Qian, L., 1984, Exergy analysis and its application, Higher Education Press, Beijing.[In Chinese]

He, C., Liu C., Zhou, M. et al., 2014, A new selection principle of working fluids for subcritical organic Rankine cycle coupling with different heat sources, *Energy*, vol.68: p. 283-291.

ACKNOWLEDGEMENT

This work was supported by the National Key Basic Research Program of China (973 Program, No.2013CB228306). The authors gratefully acknowledge them for financial support of this work.

DESIGN AND NUMERICAL ANALYSIS OF PROCESSES IN SILOXANE VAPOR DRIVEN TURBINE

A. Sebelev*[1], R. Scharf[2], N. Zabelin[1], M. Smirnov[1]

[1]Peter the Great St. Petersburg Polytechnic University (SPbPU),
Department "Turbines, Hydro machines and aero-engines"
St. Petersburg, Russia;
[2]Leibniz Universität Hannover,
Institut für Kraftwerkstechnik und Wärmeübertragung
Hannover, Germany
e-mail: a.sebelev.turbo@mail.ru

ABSTRACT

The problem of decreasing of fossil fuel consumption and energy efficiency is one of today's major conceptions in the field of energy economics. Waste heat recovery is one of the promising solutions for this problem. One of the ways to increase efficiency of the waste heat recovery process is using siloxanes as working fluids for organic Rankine cycles (ORC).

SPbPU scientists have analyzed peculiarities of the steady-state expansion process in the siloxane vapor driven turbine. The design of the nozzle and the blade wheel of the turbine is supersonic due to the low speed of sound of siloxanes. Initial parameters of siloxane were subcritical; a pressure ratio of the turbine was 25. Progressive steps of the initial temperature, pressure ratio and rotational velocity were used to obtain convergence of the solution process. The changings of positions of the nozzle and blade wheel critical sections were established. The details of the supersonic vortices interaction in the blade wheel flow range were analyzed.

The efficiency and power output of the investigated turbine stage were estimated as 0.699 and 309.1 kW, respectively.

1. INTRODUCTION

Waste heat recovery is one of the promising solutions to increase efficiency of different plants and industrial processes (Larjola (1995), Vescovo (2009)). The highest volume of waste heat resources takes place at different thermal power plants, cement, metallurgical and chemical productions. In Russia it is also the gas transport industry. The estimation of waste heat thermal power at the all gas compressor stations of "Gazprom" is 87.9 GW (Lykov *et al.* (2013)). Rough estimations of waste heat thermal power at different productions in Russia, made on the base of Key World Energy Statistics (2014), are: 3.9 GW at the all cement production plants, 2.8 GW at the all metallurgical production plants and 1.9 GW at the all chemical production plants. In the other words, all this waste heat may be turned to 14.5 GW of electrical power by the most conservative estimate.

In most cases using of organic Rankine cycles (ORC) for recovery plants provides higher efficiency of the recovery plants in comparison with water steam Rankine cycle due to low temperature levels of the waste heat streams (Larjola (1995), Hung *et al.* (1997), Vescovo (2009)). The average temperature level of the waste heat streams in the whole Russian gas transport system is 390ºC by the estimation of Lykov *et al.* (2013). The average temperature level of the waste heat streams at other productions in Russia varies from 150ºC to 350ºC. One of the most important questions in the recovery plant designing is the choosing of a working fluid. Nowadays the aspects of using of various hydrocarbons, freons and alcohols in ORC are widely researched by different authors (Iqbal *et al.* (1977), Hung *et al.* (1997), Shuster *et al.* (2010), Gao *et al.* (2012)). Modern requirements for environment safety determine ozone depletion potential (ODP) and global warming potential (GWP) as main criteria for

choosing of a working fluid. It was shown that in this case the most promising alternatives to different hydrocarbons, freons and alcohols are zeotropic mixtures and siloxanes (Heberle *et al.* (2012), Chys *et al.* (2012), Weith *et al.* (2014)). The aspects of using of siloxanes in ORC were investigated by Lai *et al.* (2011), Fernandez *et al.* (2011), Uusitalo *et al.* (2013). It was shown that in this case the efficiency of ORC may be increased up to 23 – 25%.

The turbines for organic working fluids have essential differences in details of the expansion process in comparison with typical gas and steam turbines. The special supersonic design is required for such turbines due to low speed of sound of different organic working fluids. The aspects of designing of the ORC driven turbines were outlined by different authors. Yamamoto *et al.* (2001) designed and tested R-123 centripetal turbine; Kang (2012) designed and tested R-245fa radial-inflow turbine; Casati *et al.* (2014) described designing method of the ORC centrifugal microturbines. Guardone *et al.* (2013) described the influence of molecular complexity on nozzle design.

Despite the high volume of investigations in the area of organic working fluids expansions the peculiarities of siloxanes behavior during the expansion process still haven't been outlined. Thus, the scope of the present paper is to investigate the siloxane expansion process and to outline its peculiarities.

2. INVESTIGATION OBJECT

2.1. Initial parameters of the expansion process

Hexametyldisiloxane (MM) was chosen as working fluid for the expansion process. The initial pressure p_0 was set as 1 MPa. The initial temperature T_0 was set as a vapor saturation temperature at chosen initial pressure. The turbine pressure ratio has been chosen as 25 to provide the required turbine enthalpy drop upon the condition of 300 kW power output of the turbine stage. Trans- and supercritical initial parameters were not considered.

Positive slope of MM vapor saturation curve provides inability of intersection between expansion process curve and two-phase region as shown in figure 1. It means that there is no possibility of droplet formation in the turbine stage.

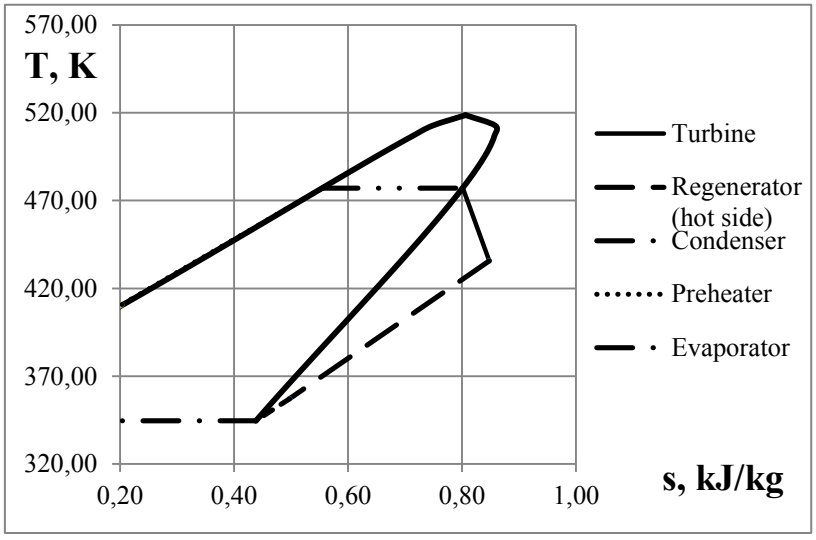

Figure 1: T-s diagram of the expansion process

2.2. The turbine

A single-stage double-flow axial turbine was chosen as the expander machine. The choice of the double-flow design was made due to high axial forces acting on the turbine rotor. The subsonic part of the nozzle was designed according to Vitoshinski profile. The supersonic part of the nozzle was designed using the SPbPU high pitch-chord ratio design. The main features of the high pitch-chord ratio design, described in details by Rassokhin (2004), are:

- small angles α_1 (3..5º) and β_1 (8..14º);

- high blade wheel flow turning angle (Ω = 151..164º);
- high pitch-chord ratio for the nozzle and blade wheel blades ($t_N/b_N > 4$, $t_{BW}/b_{BW} > 1.1$);
- high enthalpy drops at one turbine stage (up to 800 kJ/kg).

The supersonic blade profile C9022B was chosen for the blade wheel. This blade profile was described in details by Dejch *et al.* (1965). The reason to use blade profile with thick leading edge is strong changing of MM properties with relation to thermodynamic parameters. The design of the nozzle and blade wheel is supersonic due to low MM speed of sound. Involutions of the nozzle and blade wheel at the mean diameter are shown in figure 2. The blade wheel of the turbine has a tip shroud. The main geometric parameters of the single-flow turbine stage are given in table 1.

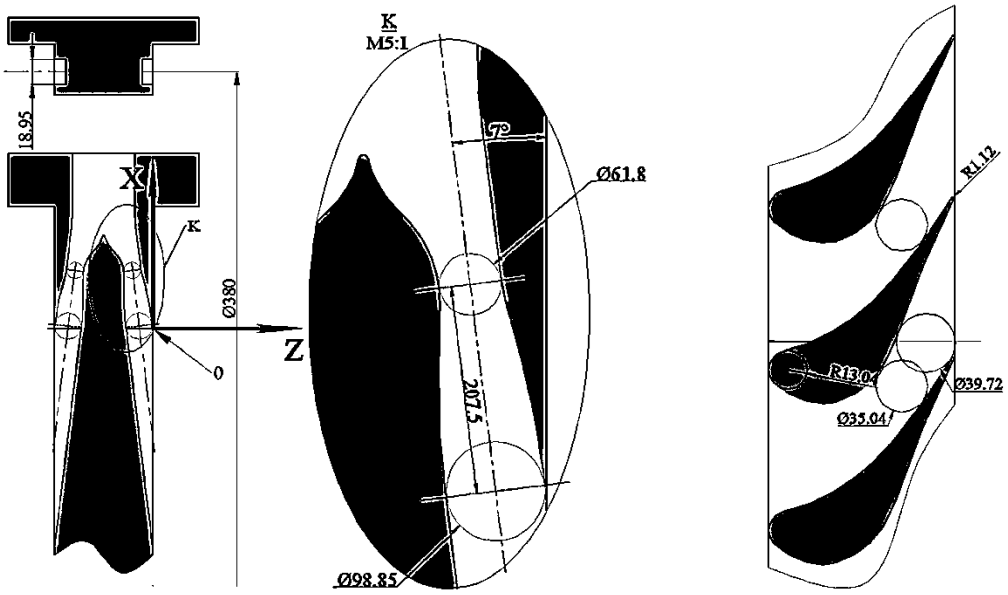

a) b)

Figure 2: Involutions of the nozzle (a) and blade wheel (b) at the mean diameter

Table 1: The main geometric parameters of the one-flow turbine stage

Parameter	Dimensions	Value	Parameter	Dimensions	Value
D_m	mm	380	α_1	deg.	7.00
n	rev/min	12000	ΔL_{ax}	mm	7.00
H_0	kJ/kg	66.26	ΔL_{tc}	mm	0.30
G	kg/s	6.86	β_1	deg.	90.00
C_{ax}/u	-	1.52	Z_2	-	55
ε	-	0.97	l_2	mm	24.75
Z_1	-	7	β_2^*	deg.	30.00
l_1	mm	18.95	Ω	deg.	60.00

3. NUMERICAL SIMULATION METHOD

The SPbPU method for numerical simulation of processes in supersonic turbines, described by Zabelin *et al.* (2013), was used. ANSYS CFX was used to provide the numerical simulation.

The original relation between the number of nozzles and number of working blades is 7/55. The relation 1/8 and periodic boundary conditions were used in the computational model. This assumption is correct to be used with Frozen Rotor interface between the nozzle and blade wheel areas because the relation between connecting areas in this case is 1:1.018. The modeling of blade wheel tip shroud was also considered in numerical model in assumption of rotating motion of tip shroud domain. The computational model of the single-flow turbine stage is presented in figure 3.

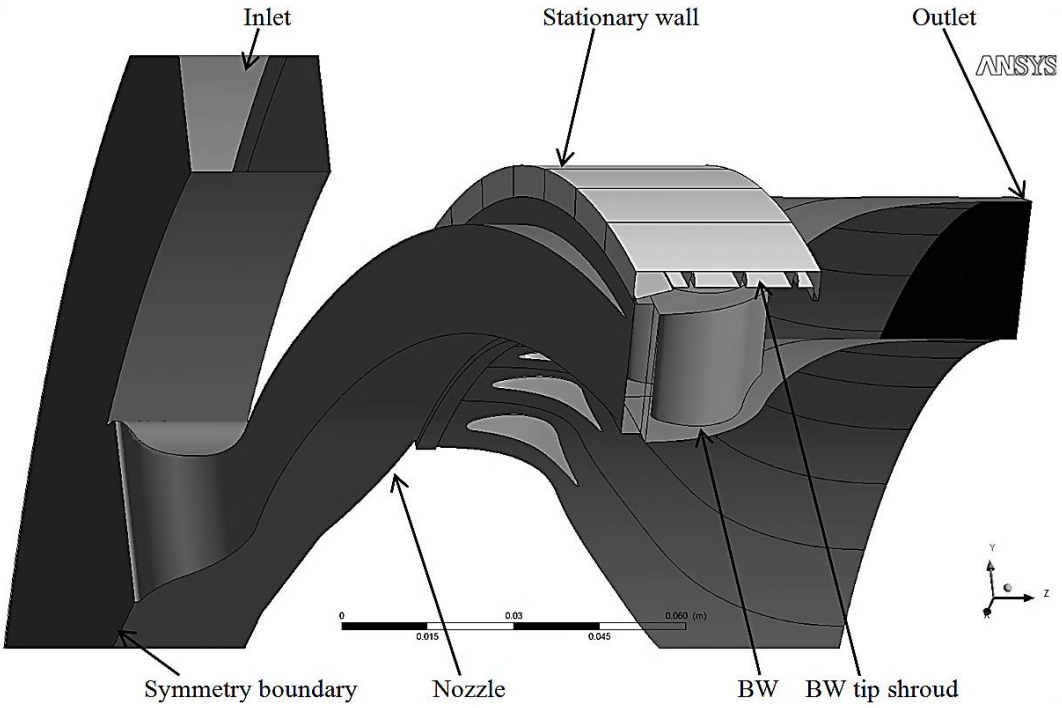

Figure 3: Computational model of the single-flow turbine stage

High-Reynolds version of the k-ω SST turbulence model was used. Steady-state Frozen rotor interface between the nozzle and blade wheel areas was used to model rotor-stator interaction. Flow parameters of the turbine stage were obtained by averaging of their values for 4 positions of blade wheel relatively to the nozzle in the range of blade wheel pitch angle.

Aungier Redlich Kwong real gas equation of state was used to model thermodynamic properties of MM during the expansion process. The main parameters need to be specified are: molar mass, critical temperature and pressure, acentric factor and boiling temperature. Zero pressure polynomial coefficients were obtained with using REFPROP databases to evaluate specific heat capacity of MM. Kinetic Theory models were used to model transport properties of MM. Rigid Non Interacting Sphere model was used to model MM dynamic viscosity behavior.

Total parameters at inlet (p_0 = 1 MPa, T_0 = 477.1 K) and static pressure at outlet (p_0 = 0.04 MPa) were specified as boundary conditions in computational model. Progressive steps of the boundary conditions were used to obtain convergence of the solution process. The iteration steps between the changings of boundary conditions were different to decrease their negative influence on the solution process. Monitoring of the RMS residuals, imbalances and turbine efficiency and power output were used to control convergence of the solution process. The criteria of the convergent solution in present research were:

- drop of the RMS residuals more than 10^2;
- imbalances less than 0.5%;
- fluctuation of the turbine efficiency and power output less than 5%.

Three different types of computational domains discretization were compared to obtain grid independent solution. The results of the grid independency study are presented in table 2.

Table 2: The results of the grid independency study

Grid type	1 nozzle sector, millions of nodes	8 blade wheel sectors, millions of nodes	8 tip shroud sectors, millions of nodes	Difference in the turbine efficiency with the previous grid, %	Difference in the turbine power output with the previous grid, %
Coarse	0.68	3.21	3.15	-	-
Medium	1.15	6.85	4.26	10.2	15.4
Fine	1.98	10.64	5.32	4.2	4.8

The medium grid was used in further calculations. The grid structure is presented in figure 4.

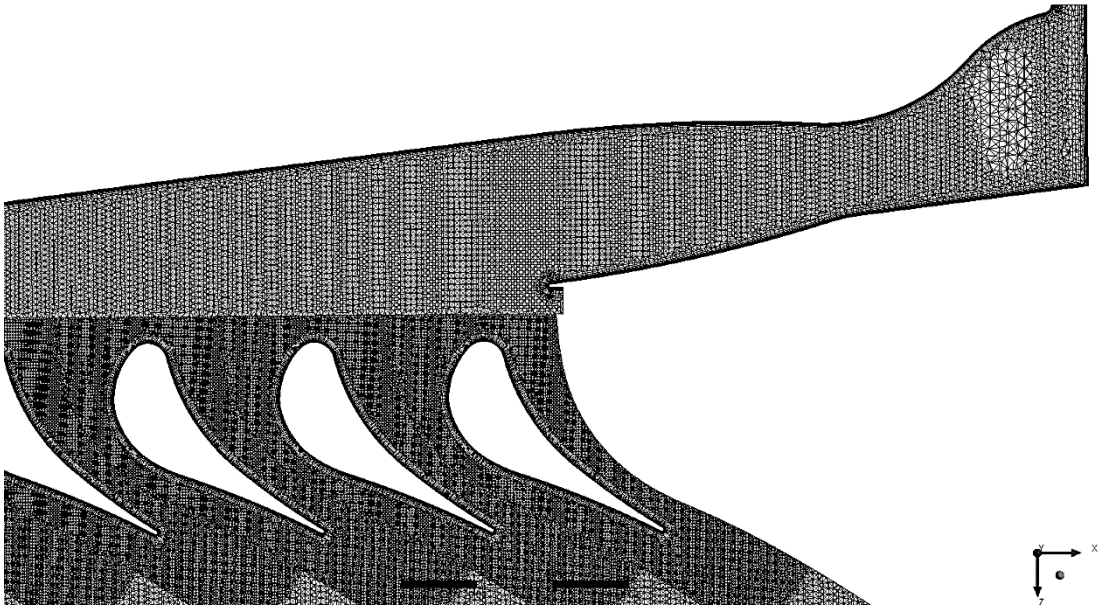

Figure 4: The grid structure

4. DISCUSSION OF THE RESULTS

The values of the calculated thermodynamic and transport properties were compared with the values obtained with using REFPROP databases to estimate tolerance of the obtained results. Maximum deviation between CFX and REFPROP results was less than 5% for specific heat capacity and dynamic viscosity. It is noteworthy that isentropic exponent of MM has a strong nonlinear dependence on temperature and pressure in superheated vapor area as shown in figure 5a. In this case it is incorrect to use constant isentropic exponent in preliminary turbine calculations. Rough boundary in figure 5a is a consequence of discrete steps of temperature and pressure.

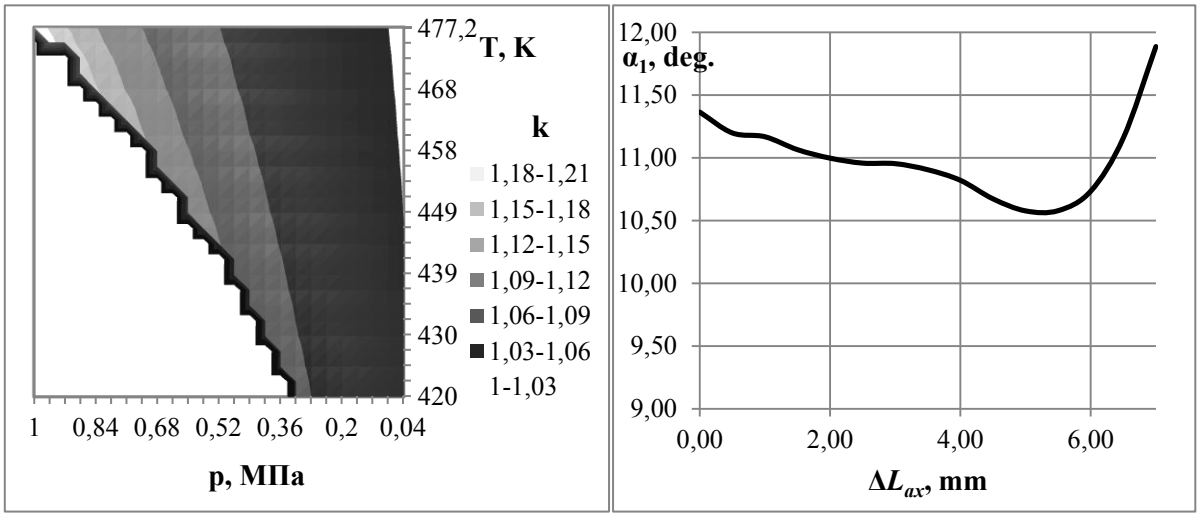

a) b)

Figure 5: MM isentropic exponent dependence on temperature and pressure in superheated vapor area (a) and varying of the nozzle outlet angle outbound of the nozzle (b)

The analysis of Mach number field in the nozzle (figure 6) shows that the flow in the critical section is not fully supersonic. It can be seen in details in figure 7. Physically, it means that the position of real critical section changed to the downstream direction in comparison with its design position. This

phenomenon was established by Reichert and Simon (1997). This fact means that the theoretical mass flow rate through the supersonic nozzle, defined as:

$$G_t = \frac{p_0 \cdot S_{cs}}{\sqrt{T_0}} \sqrt{\frac{k}{R}\left(\frac{2}{k+1}\right)^{\frac{k+1}{k-1}}}, \tag{1}$$

should be based on the cross-sectional area of the real critical section. Additionally, the velocity profile near the critical section is highly distorted towards to the straight nozzle wall. This is a consequence of the non-symmetric shape of the nozzle and was also outlined by Reichert and Simon (1997). The same situation takes place near the blade wheel critical section.

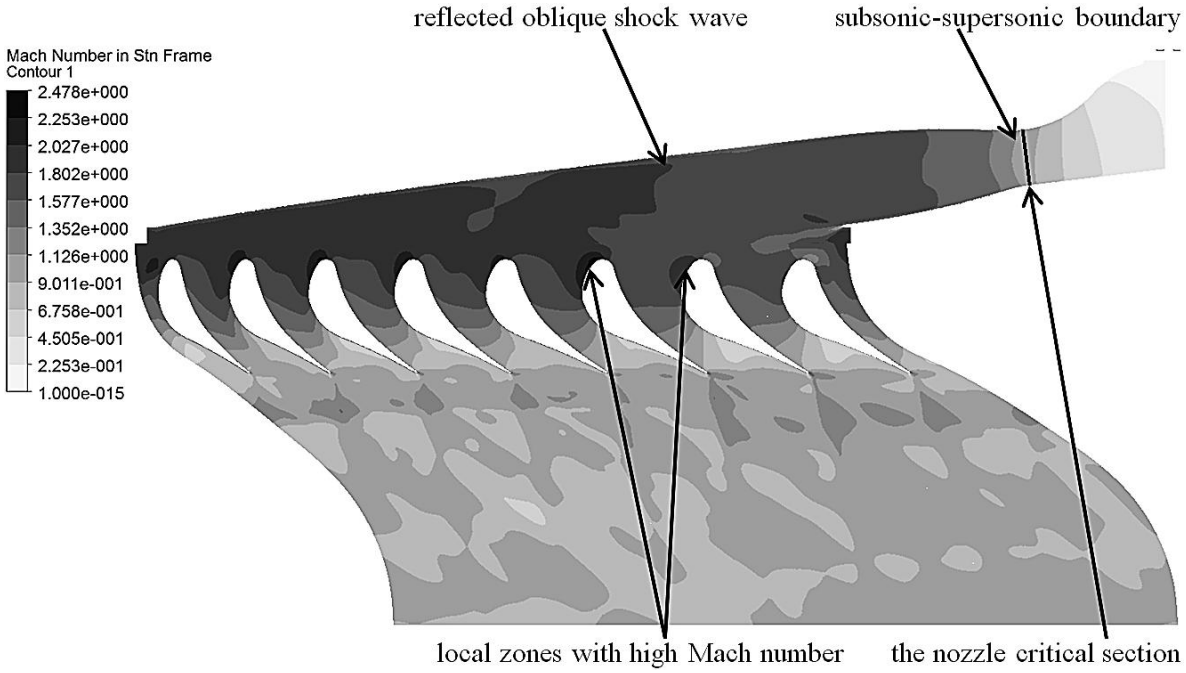

Figure 6: Mach number field in the turbine stage at the mean diameter

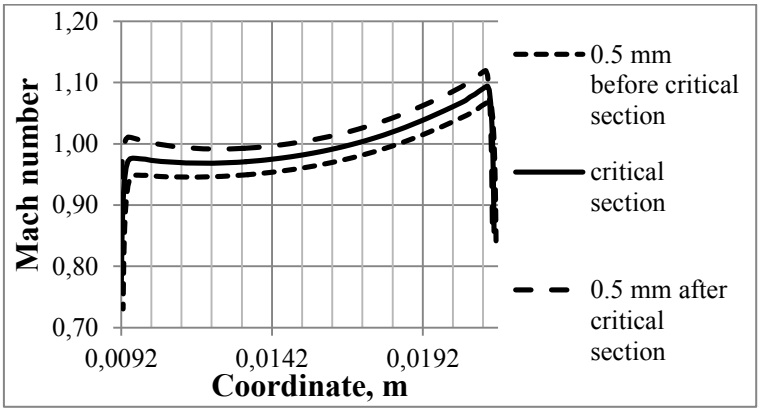

Figure 7: Velocity profiles near the nozzle critical section at the mean diameter

The oblique shock wave from the nozzle reflects from the nozzle wall and then impinges on the leading edge of the blades. This leads to the appearing of the local zones with high Mach number (up to 2.5 in stationary frame) at the blades leading edges. Such flow behavior is typical for axial supersonic turbines and was described in details by Kirillov (1972) and Traupel (1977). It should be outlined that the nozzle outlet angle, defined as:

$$\alpha_1 = arctg\left(\frac{G \cdot D_m \cdot c_{1z}}{2M_N}\right), \tag{2}$$

has a decreasing value outbound of the nozzle as shown in figure 5b. Zabelin *et al.* (2013) showed that this phenomenon is a consequence of the blade wheel influence on the nozzle in trans- and supersonic turbines. The nozzle torque in equation (2) was calculated directly in CFD-Post.

The analysis of the flow structure in the blade wheel shows that double vortex structure appears at the blade wheel inlet as shown in figure 8. It is a consequence of complex phenomena which take place at the edges of the nozzles active flow sectors. These phenomena related to the flow separation and were described by Natalevich (1979). The hub vortex rotates clockwise and rests against the blade wheel hub. The shroud vortex has a counterclockwise rotation and rests against the blade wheel shroud because of the inertial forces. This flow separation leads to additional energy loses at the boundary of vortices interaction as shown in figure 9.

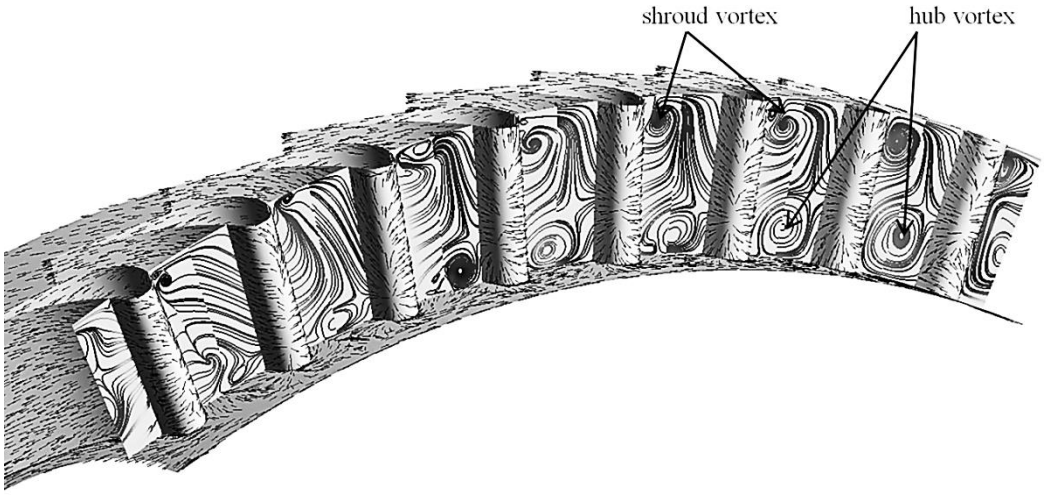

Figure 8: Flow structure at the blade wheel inlet

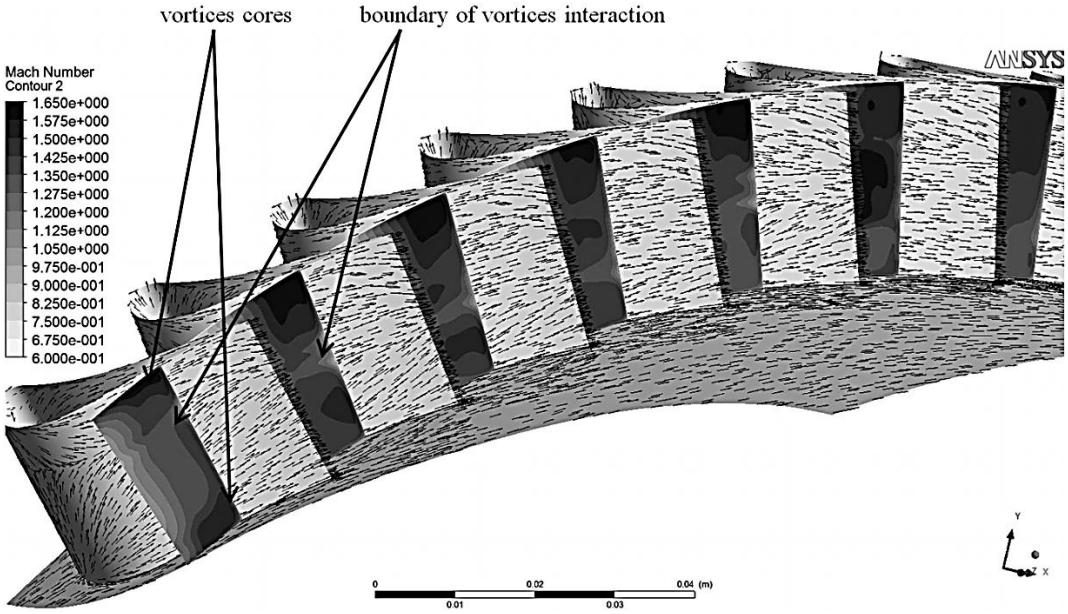

Figure 9: Flow structure at the blade wheel outlet

Another peculiarity that should be highlighted is a specific shape of the shock wave after the blade wheel. As it can be seen in figures 8 and 9 the hub vortex increases as it drew in the blade wheel flow range. This leads to the decreasing of the shroud vortex and increasing of the Mach number at the blade wheel shroud. This process is illustrated in figures 9 and 10. The zones with low velocities at the blade wheel shroud in figure 10 are the zones of the tip shroud leakage interaction with the main flow. High volume of the hub vortex together with strong dependence of the MM density on thermodynamic parameters leads to appearing of the normal shock wave at the blade wheel outlet as

shown in figure 10. The intensity of the normal shock wave decreases from hub to shroud due to low volume of the shroud vortex in comparison with the hub vortex. This is also the reason for the high Mach number zones appearing at the blade wheel shroud. The volume of the high Mach number zones increases with distance from the blade wheel. It means that shroud vortex is underexpanded and continues its expansion after the blade wheel.

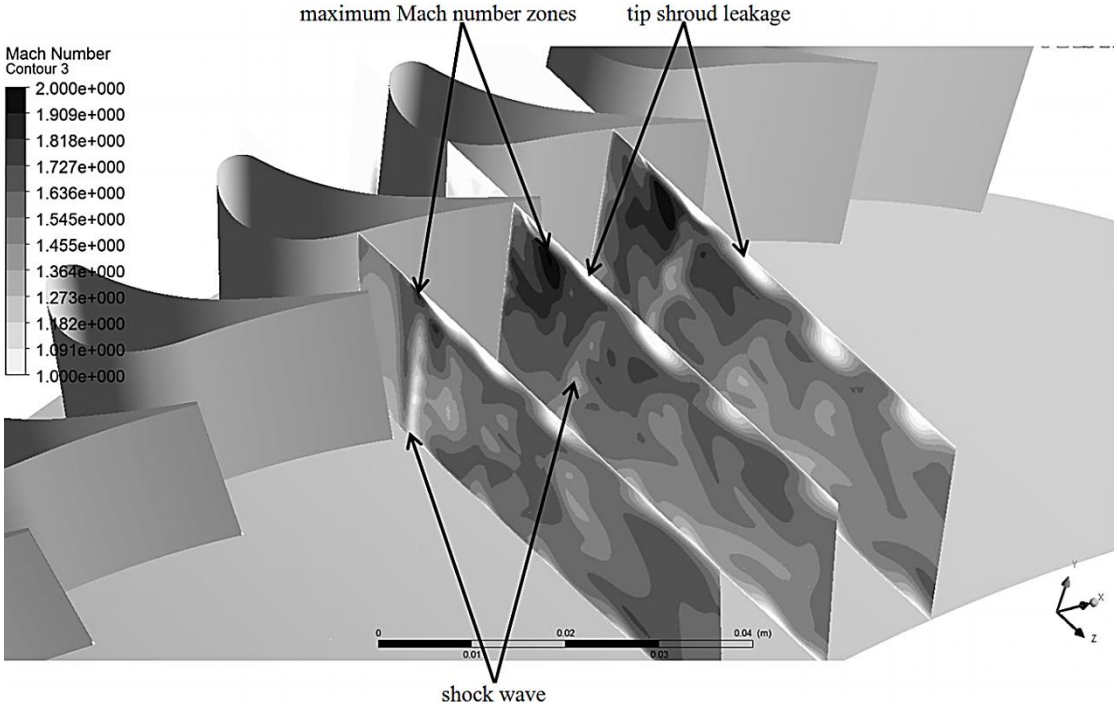

Figure 10: Shock wave at the blade wheel outlet

The efficiency and power output of the investigated turbine stage were calculated with using following equations:

$$\eta_i = \frac{M_{BW} \cdot \pi \cdot n}{30 \cdot G \cdot H_0}, \tag{3}$$

$$N = \frac{M_{BW} \cdot \pi \cdot n}{30}. \tag{4}$$

The calculated values of the efficiency and power output for investigated single-flow turbine stage are 0.699 and 309.1 kW respectively.

5. CONCLUSIONS

The expansion process in the siloxane vapor driven turbine was modeled. The peculiarities of the siloxane expansion process were outlined. The important conclusions about the calculations of theoretical mass flow rate through the supersonic nozzles were made. It was shown that in case of the supersonic nozzles the equation for theoretical mass flow rate should be based on the cross-sectional area of the real critical section. It was also shown that it is inacceptable to use constant isentropic exponent in case of the preliminary ORC turbines calculations.

Most of the outlined peculiarities are typical for the supersonic axial microturbines because of subcritical initial parameters of the siloxane vapor. However, the strong relation of the siloxane properties to the thermodynamic parameters determines its nonconventional behavior during the expansion in the blade wheel. Complex interaction between two supersonic vortices in the blade wheel leads to additional energy losses and appearing of the normal shock wave after the blade wheel. As a result, calculated efficiency of the investigated turbine stage is 0.699. This value is close to the efficiency of the water steam microturbines with mean diameter up to 500 mm.

NOMENCLATURE

GW	Gigawatt	
GWP	Global Warming Potential	
kW	Kilowatt	
MM	Hexametyldisiloxane	
ODP	Ozone Depletion Potential	
ORC	Organic Rankine Cycle	
SPbPU	Peter the Great St. Petersburg Polytechnic University	
C_{ax}/u	stage load coefficient	
c_{1z}	axial component of velocity at the nozzle outlet	m/s
D_m	mean diameter	m
G	mass flow rate	kg/s
H_0	isentropic enthalpy drop	kJ/kg
k	isentropic exponent	
l_1	nozzle height	mm
l_2	blade height	mm
M	torque	N·m
n	rotational speed	rev/min
p_0	nozzle inlet pressure	MPa
p_2	blade wheel outlet pressure	MPa
R	individual gas constant	J/(kg·K)
S	cross-sectional area	m^2
T_0	nozzle inlet temperature	K
Z_1	number of nozzles	
Z_2	number of blades	
α_1	nozzle outlet angle	deg.
β_1	blade wheel inlet angle in relative frame	deg.
β_2^*	blade wheel outlet angle in relative frame	deg.
ΔL	clearance value	mm
ε	partial admission ratio	

Subscript

BW	blade wheel
N	nozzle
ax	axial
cs	critical section
i	internal
t	theoretical
tc	tip clearance

REFERENCES

[1] Casati, E., Vitale, S., Pini, M., Persico, G., Colonna, P., 2014, Centrifugal turbines for mini-organic Rankine cycle power systems, *Journal of Engineering for Gas Turbines and Power*, vol. 136, 122607.

[2] Chys, M., van den Broek, M., Vanslambrouck, B., De Paepe, M., 2012, Potential of zeotropic mixtures as working fluids in organic Rankine cycles, *Energy*, vol. 44, pp. 623 – 632.

[3] Dejch, E.M., Filipov, A.G., Lazariev, J.L., 1965, *Atlas profilej reshetok osevyh turbin*, Mashinostroyenie, Moscow, 96p.

[4] Fernandez, F.J., Prieto, M.M., Suarez, I., 2011, Thermodynamic analysis of high-temperature regenerative organic Rankine cycles using siloxanes as working fluids, *Energy*, vol. 36, pp. 5239 – 5249.

[5] Gao, H., Liu, Ch., He, Ch., Xu, Xi., Wu, Sh., Li, Y., 2012, Performance Analysis and Working Fluid Selection of a supercritical Organic Rankine Cycle for low grade waste heat recovery, *Energies*, vol. 5, pp. 3233 – 3247.

[6] Guardone, A., Spinelli, A., Dossena, V., 2013, Influence of molecular complexity on nozzle design for an organic vapor wind tunnel, *Journal of Engineering for Gas Turbines and Power*, vol. 135, 042307.

[7] Heberle, F., Preißinger, M., Brüggemann, D., 2012, Zeotropic mixtures as working fluids in Organic Rankine Cycles for low-enthalpy geothermal resources, *Renewable Energy*, vol. 37, pp. 364 – 370.

[8] Hung, T.C., Shai, T.Y., Wang, S.K., 1997, A review of Organic Rankine Cycles (ORCs) for the recovery of low-grade waste heat, *Energy*, vol. 22, pp. 661 – 667.

[9] Iqbal, K.Z., Fish, L.W., Starling, K.E., 1977, Isobutane geothermal binary cycle sensitivity analysis, Proceedings *Oklahoma Academic Science*, The University of Oklahoma, pp. 131 – 137.

[10] Kang, S.H., Design and experimental study of ORC (organic Rankine cycle) and radial turbine using R245fa working fluid, 2012, *Energy*, vol. 41, pp. 514 – 524.

[11] Key World Energy Statistics, *International Energy Agency*, 2014.

[12] Kirillov, I.I., 1972, *Teorija turbomashin*, Mashinostroyenie, Leningrad, 533p.

[13] Lai, N.A., Wendland, M., Fischer, J., 2011, Working fluids for high-temperature organic Rankine cycles, *Energy*, vol. 36, pp. 199 – 211.

[14] Larjola, J., 1995, Electricity from industrial waste heat using high-speed organic Rankine cycle (ORC), *International journal of production economics*, vol. 41, pp. 227 – 235.

[15] Lykov, A.V., Zabelin, N.A., Rassokhin, V.A., 2013, Estimation of waste heat resources in Russian unified system of gas supply, *St. Petersburg State Polytechnical University Journal*, vol. 183 (4), pp. 136–145.

[16] Natalevich, A.S., 1979, *Vozdushnye mikroturbiny*, Mashinostroyenie, Moscow, 192p.

[17] Rassokhin, V.A., 2004, Turbiny konstrukcii LPI: preimushhestva, harakteristiki, opyt razrabotki i primenenie, *St. Petersburg State Polytechnical University Journal*, vol. 491, pp. 152 – 161.

[18] Reichert, A.W., Simon, H., 1997, Design and flow field calculations for transonic and supersonic radial inflow turbine guide vanes, *Journal of turbomachinery*, vol. 119 (1), pp. 103 – 113.

[19] Shuster, A., Karellas, S., Aumann, R., 2010, Efficiency optimization potential in supercritical Organic Rankine Cycles, *Energy*, vol. 35, pp. 1033 – 1039.

[20] Traupel, W., 1977, *Thermische Turbomaschinen*, 3. Aufl., Springer, Berlin, 579p.

[21] Uusitalo, A., Turunen-Saaresti, T., Honkatukia, J., Colonna, P., Larjola, J., 2013, Siloxanes as working fluids for mni-ORC systems based on high-speed turbogenerator technology, *Journal of Engineering for Gas Turbines and Power*, vol. 135, 042305.

[22] Vescovo, R., 2009, ORC recovering industrial heat, *Cogeneration and On-Site Power Production*, vol. 2, pp. 53 – 57.

[23] Weith, T., Heberle, F., Preißinger, M., Brüggemann, D., 2014, Performance of siloxane mixtures in a high-temperature Organic Rankine Cycle considering the heat transfer characteristics during evaporation, *Energies*, vol. 7, pp. 5548 – 5565.

[24] Yamamoto, T., Furuhata, T., Arai, N., Mori, K., 2001, Design and testing of the organic Rankine cycle, *Energy*, vol. 26, pp. 239 – 251.

[25] Zabelin, N.A., Rakov, G.L., Rassokhin, V.A., Sebelev, A.A., Smirnov, M.V., 2013, Investigation of fluid flow highlights in low flow-rated LPI turbine stages, *St. Petersburg State Polytechnical University Journal*, vol. 166 (1), pp. 45–53.

HIGH-TEMPERATURE SOLAR ORGANIC RANKINE CYCLE – ANNUAL SIMULATION OF VARIOUS SYSTEM DESIGNS

Björn Hunstock[1]*, Sabine Strauch[2], Wilhelm Althaus, Björn Bülten, Johannes Grob, Ralf Paucker

Fraunhofer UMSICHT
Department Energy Systems Engineering
46047 Oberhausen, Germany
[1]bjoern.hunstock@umsicht.fraunhofer.de
[2]sabine.strauch@umsicht.fraunhofer.de

* Corresponding Author

ABSTRACT

This paper deals with the simulation of high-temperature solar organic Rankine cycles. In contrast to previous simulations the diurnal variations and the effect of charging and discharging the thermal energy storage are taken into account. Furthermore, the presented simulations cover one full year. The simulations use discrete time steps with a constant operation over a period of one hour. Considering a full year, 8 760 connected simulations have been carried out to describe the full and part load operation of one plant. Annual simulations allow a detailed evaluation of a solar organic Rankine cycle. The work describes the effect of varying solar field area and thermal energy storage capacity with different design points. High values of irradiance result in small solar fields. These fields often cannot provide enough thermal energy to produce the nominal electrical power at time steps with low irradiance. Design points using a low value for irradiance allow full load operations during the winter season. On the other hand, they generate a large percentage of waste heat during summer, which cannot be used due to limited storage and power capacity. The presented annual simulations show that different design points for a solar organic Rankine cycle cause various results for the plant performance over a full year. A design point in December leads to a large solar field and a thermal energy storage with a high capacity. The annual simulations show the continuous operation over a full year and are used to evaluate the plant designs.

1. INTRODUCTION

A comprehensive use of solar energy for power production is one approach for global sustainable electricity generation. Many rural areas with high potential of solar radiation (e. g. Northern Africa) are still supplied with power from stand-alone diesel generators (Szabó *et al.*, 2011). Hence, small decentralized power plants using renewable energies can reduce the consumption of fossil fuels in such areas. Concentrated solar power (CSP) is a promising technology to generate power in areas with high direct solar radiation that is non-scattered radiation. Small CSP plants are able to replace or support existing diesel generators.

The organic Rankine cycle (ORC) efficiently converts heat into power and can be used as a decentralized power plant. High-temperature ORC (evaporation temperatures of more than 200 °C) utilizing solar thermal power suits to be combined with the state-of-the-art mid- or high-temperature parabolic trough collectors. These solar driven ORC is called solar organic Rankine cycle (SORC) Providing high evaporation temperatures, parabolic trough collectors enable ORC to operate at high

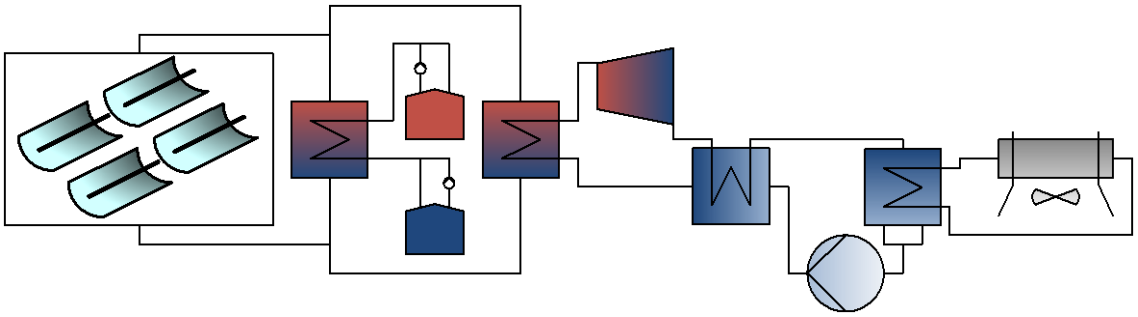

Figure 1: Scheme of a SORC plant

cycle efficiencies. Furthermore, an additional thermal energy storage (TES) increases the full load hours of the power plant. In consequence a SORC can theoretically cover a continuous load if a well-sized TES is integrated and the solar field is sufficiently large. Figure 1 shows the scheme of a SORC plant. The plant consists of two different cycles. The first one is the solar field which converts solar irradiation into thermal energy. The second one utilizes this thermal energy to generate electricity. The first cycle includes the TES which consists of two tanks (one hot and one cold tank). The indirect storage system is charged and discharged by a heat exchanger. During times with sufficient irradiance the solar field charges the TES and at the same time supplies the ORC with thermal energy. At night the stored thermal energy is used to evaporate the ORC working fluid.

Only a few high-temperature SORC plants have been built yet. Most of these SORC originate from research projects. Stine and Geyer (2001) mentioned three different SORC plants with the electrical power of 19 kW, 37 kW and 150 kW which were used to supply the pumps for wells. In 2006 a SORC with an electrical gross power of 1.35 MW started operation at Arizona Public Service in the USA (Sinai and Fisher, 2007; Canada *et al.*, 2004). A thermocline storage was planned for a future expansion of this SORC to store the thermal energy for a full load operation of six hours. Orosz *et al.* (2010a) developed a small scaled SORC with 1 kW_{el} for decentralized power generation tested in Lesotho, Africa. Kane (2003) presented operation data of a 15 kW_{el} ORC connected to linear Fresnel collectors, whereas Moustafa *et al.* (1984) showed a SORC plant that uses parabolic dishes to produce thermal energy for a 100 kW_{el} ORC.

The academic research focuses on the simulation of SORC. For different applications the cycle has been simulated and optimized to achieve a high cycle efficiency. Delgado-Torres and García-Rodríguez (2007a) and (2007b) simulated different SORC and compared different ORC working fluids. The simulations used a constant direct normal irradiance (DNI). The steady-state simulations did not consider a TES and determined the collector area taking into account different condensation temperatures for recuperative and non-recuperative ORC. Several other works dealt with the simulation of SORC systems, for example Bruno *et al.* (2008), Nafey and Sharaf (2010), Orosz *et al.* (2010b) and Quoilin (2011). A thermal energy storage is considered by Price and Hassani (2002), McMahan (2006), He *et al.* (2012) and Al-Sulaiman *et al.* (2011), but the operation for different values of irradiance was not included. Orosz *et al.* (2010b) developed a design tool for small scaled SORC on the basis of the plant design described in Orosz *et al.* (2010a). The continuing impact of the hourly varying direct irradiance during a full year on a SORC has not been focused by research yet.

Hence, this paper deals with the annual simulation of SORC plants considering the charge and discharge of an integrated TES. Different SORC configurations are analyzed. Plant parameters are varied to show the effects in operation. Technical or economic interests are not taken into account. An ORC power capacity of 500 kW_{el} serves as an example for decentralized power supply applications. SORC of this plant size are considered to be technically mature and available (Dürr Cyplan, 2015).

First of all, it is shown how the design of a SORC can differ depending on varying values of DNI. For different solar field sizes and TES capacities the daily variation of produced energy is computed to preselect design points. The parameters are varied to show the influence on the annual solar capacity

factor. Considering these results annual simulations with hourly time steps for three different designs are carried out and main results of the annual simulations are analyzed.

2. EVALUATING DESIGN POINTS FOR SORC PLANTS

2.1 Basics for simulations

The simulation of the SORC including solar field, TES and power block are carried out with the commercial software THERMOFLEX. The program allows modeling several thermal systems, e. g. steam power plants, gas turbines etc. Thermodynamic properties for various fluids are included in the model. Therefore different working fluids for an ORC can be taken into account. The software allows predicting the part load behavior of an energy system with an off-design simulation mode.

At first, a design is specified and simulated. The chosen design is used to simulate the off-design behavior, for example the part load operation caused by low irradiance. Discrete time steps are used to calculate time dependent results. Each time step represents one hour. A higher time step resolution would increase the duration of calculation. The direct normal irradiance as input parameter does not cause fast load changes. Only for sunrise and sunset a higher time step resolution would increase the precision. Therefore, one steady state simulation runs for each hour of the day. The state of charge (SOC) of the TES depends on the previous SOC and on the actual charging or discharging rate. Therefore, the SOC of the TES at the end of a time step is used as input value for the following time step. Heat capacity of plant material and flow simulation are not taken into account.

To simplify, the ambient temperature for every simulation is fixed at 15 °C. This satisfies the requirements of the approach chosen in this paper, which does not consider exact efficiency losses caused by high ambient temperatures. For an economic analyze it must be kept in mind.

The size of a solar field is often specified as dimensionless factor, the solar multiple. According to the definition in Montes *et al.* (2009) the solar multiple SM equals the ratio between the thermal power of solar field at design point and the thermal power required for full load operation of the power block.

$$SM = \frac{\dot{Q}_{\text{th, SF}}}{\dot{Q}_{\text{th, ORC}}} \tag{1}$$

According to this approach for this ORC application the SM is calculated by dividing the thermal power required for full load operation of the ORC $\dot{Q}_{\text{th, ORC}}$ by the thermal power of the solar field $\dot{Q}_{\text{th, SF}}$ (compare Equation (1)). Following this definition, a solar field with a solar multiple $SM = 2$ causes a collector area twice as much as a solar field with $SM = 1$. The solar multiple mainly depends on the used irradiance and the power capacity of the power block.

A calculation shows the impact of the amount of DNI on the required solar field area. For this calculation all losses are assumed to be negligible during energy conversion to prove the direct interrelationship between solar field area and direct normal irradiance. Table 1 demonstrates the dependency of the solar field area and the normal component of the beam irradiance. Equation (2) outlines this correlation.

$$\dot{Q}_{\text{th, SF}} = \eta_{SF} \cdot G_{bn} \cdot A_{ap} \tag{2}$$

The thermal power of the solar field is calculated by multiplying the solar field efficiency η_{SF}, the

Table 1: Required solar field area to produce 2 MW_{th} for different values of irradiation

DNI	Solar field area
400 W/m²	5 000 m²
600 W/m²	3 333 m²
800 W/m²	2 500 m²

collected direct normal irradiance G_{bn}, and the aperture area of the solar field A_{ap}. Hence, assuming a high irradiance, e. g. in the summer season, the calculation results in a small solar field. A solar field at that size might not be able to provide sufficient thermal energy to operate the ORC during winter times. In Table 1 each solar field area delivers a thermal power of 2 MW. Assuming that an ORC requires the same thermal power, each solar field would have a SM of 1, although the area differs.
The annual performance of a CSP plant can be described with the annual solar capacity factor CF_{sol}. Equation (3) shows this ratio between the electrical energy yield and the product of the DNI on aperture and the aperture collector area.

$$CF_{sol} = \frac{\sum_{i=1}^{8\,760} P_i \cdot \Delta t_i}{\sum_{i=1}^{8\,760} G_{bn,i} \cdot A_{ap} \cdot \Delta t_i} \tag{3}$$

2.2 SORC without a TES

To show the influence on the plant design and operation three different dates of the year are used to design a SORC with the same process parameters.

The site location is assumed to be at a longitude of 30° north of the equator. Table 2 summarizes the main design parameters of the SORC. The design points are on March 21th (spring equinox) as well as June 21st and December 21st (summer and winter solstice). The irradiance on the spring and autumn equinox is identical, therefore only March 21st is taken into account. For every design point a solar time of 12:00 o'clock is assumed to estimate the irradiance.

The ORC uses toluene as working fluid and an internal heat exchanger to recuperate the thermal energy of the superheated steam after expansion. Previous research studies favored toluene as working fluid, which allows a high cycle efficiency compared to other fluids (Delgado-Torres and

Table 2: Relevant simulation parameters for comparison of different design points without a TES

	March 21st	**June 21st**	**December 21st**	
Site				
Longitude		30		° north
Solar time (decimal)		12.00		h
Direct normal irradiance on aperture area	719.1	869.8	429.2	W/m²
Day of the year	80	172	355	-
ORC				
ORC Gross power		500		kW_{el}
Working fluid		Toluene (C7H8)		-
Evaporation pressure		25.00		bar
Condensing pressure		0.14		bar
ORC gross efficiency		24		%
Solar field				
Heat transfer fluid		Therminol 66		-
Aperture area	4 624	3 542	9 756	m²
Solar multiple		1		-
Thermal power		2 039		kW
Outlet temperature		320		°C
Inlet temperature		250		°C
Solar field efficiency	61.3	66.2	48.7	%

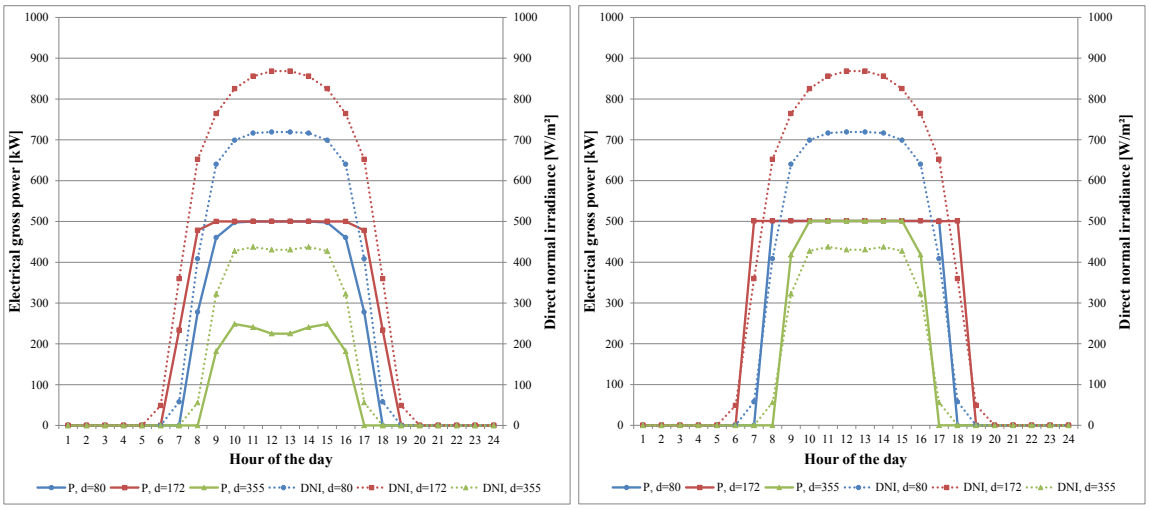

Figure 2: Electrical gross power of the SORC for the design point March 21st (left) and December 21st (right)

García-Rodríguez, 2007a). The inlet pressure of the turbine is 25 bar at about 280 °C. This prevents thermal decomposition that may occur above 300 °C. The condensing pressure of the cycle is 0.14 bar at about 53 °C. For the design point a turbine isentropic efficiency of 75 % is used and a feed pump isentropic efficiency of 75 %. With a gross power of 500 kW_{el} the ORC achieves a gross efficiency of 24 %.

Each design uses a solar field with $SM = 1$. Due to the different direct normal irradiance, the required area of the solar field varies. The used heat transfer fluid is Therminol 66 and the thermal power of each configuration is about 2 039 kW. A TES is not considered in the first run, but will be added in following simulations. The solar field efficiency depends among other parameters on the ambient temperature and solar irradiance, which is the reason for varying efficiencies presented in Table 2.
Hourly off-design simulations are carried out for each design on all design dates. The irradiance for one time step is constant. The value is determined at the middle of one hour. This means, that for the twelvth hour of a day (11:00 to 12:00) the solar time 11:30 is used to estimate the irradiance for the entire time step.

Figure 2 shows the results of the off-design simulations using March 21st ($d = 80$) and December 21st ($d = 355$) as design points (right chart). On the left ordinate the electrical gross power of the SORC in kW is plotted, while the right ordinate gives the DNI on the aperture area in W/m². The March design allows six hours of full load operation on the design day and eight hours on June 21st ($d = 172$). The higher irradiance in June and the long sunshine duration allow two more hours with full load operation for the ORC. In contrast, the available solar fiel area does not allow a full load operation on December 21st. In this case, a solar field of a larger area with $SM > 1$ is necessary to satisfy the required thermal power of a 500 kW_{el} ORC. As shown in Table 2 the solar field size nearly doubles, but it allows full load operation with a low irradiance at the design point in December. On the other side, this large solar field causes a great amount of excess thermal energy in March and June. This waste heat can only utilized when using a TES.

Chosing the optimal design point for the SORC is essential to satisfy a local power demand. Increasing the solar field size causes more full load hours during sunshine duration especially in times of low DNI. A TES or an auxiliary boiler allow operation after sunset. In conclusion, a TES is considerd in the following simulations.

2.3 SORC with a TES

For these simulations the design point is March 21st. A TES of 17.7 MWh capacity is included to enable a 500 kW_{el} ORC for six hours of full load operation. The solar multiple takes the values 1, 2 and 4 to size the solar field. The off-design simulations are carried out for March 21st, June 21st and December 21st. Each of these days is analyzed on the SOC and electrical power. The SOC of the TES at the end of the last time step is equal to the SOC at the beginning of the first time step. This condition ensures realistic behavior of the plant for sequent days with nearly the same irradiance profile.

Figure 3 shows the trend for three different days for a SORC plant with a solar multiple of 1 and 2. The system design with $SM = 1$ leads to a small solar field and, therefore, not sufficient thermal energy is supplied to the storage on December 21st and March 21st. On June 21st there are higher irradiance and more sunshine hours available to increase the SOC. The peak of the storage level is at the 17th hour with a value of approximately 30 %. A solar field with $SM = 1$ does not allow charging the TES. The solar field is too small to use a TES appropriately. A solar field twice as big ($SM = 2$) enables a more effective use of the TES in March and June, and it allows full load operation in December. The TES is charged between morning and afternoon while the ORC is supplied directly. When the irradiance decreases, the TES is discharged and the ORC operates nearly at 90 % load. The reason for this is the lower temperature of the heat transfer fluid after discharging due to the temperature difference at the pinch point. The TES is integrated as an indirect system and uses a heat exchanger to store the thermal power of the solar field. In storage mode the heat exchanger reduces the temperature twice for the reason of charging and discharging. The bigger solar field allows a full load operation during sunshine in December, whereas operation during that time is not possible at $SM = 1$.

In Figure 4 the performance of two storage capacities, namely six and twelve hours, are compared with each other. The design point is March 21st and the SM is 4. The off-design simulations are carried out for the same days as in Figure 2 and under the same cycle conditions for each day. Compared to the results of the simulations for $SM = 2$ the full load operation on December 21st is increased by using a large solar field. This even allows operation of 90 % load in the evening.

In March and June the TES is already fully charged in the morning, but at the beginning of the day the storage is totally discharged. This shows that the storage capacity is too small for 24 hours of operation and an increased solar field does not result in more full load hours. The TES with a capacity of 12 hours in chart of Figure 4 allows this operation in March and June. The solar field size does not

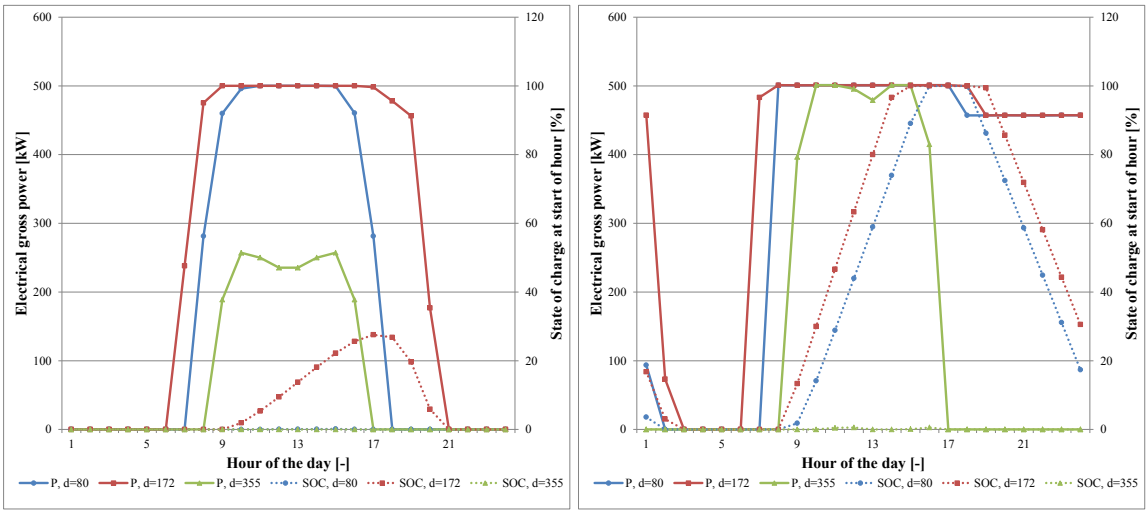

Figure 3: Electrical gross power (left ordinate) and state of charge at start of hour (right ordinate) for off-design simulations with $SM = 1$ (left chart) and $SM = 2$ (right chart).

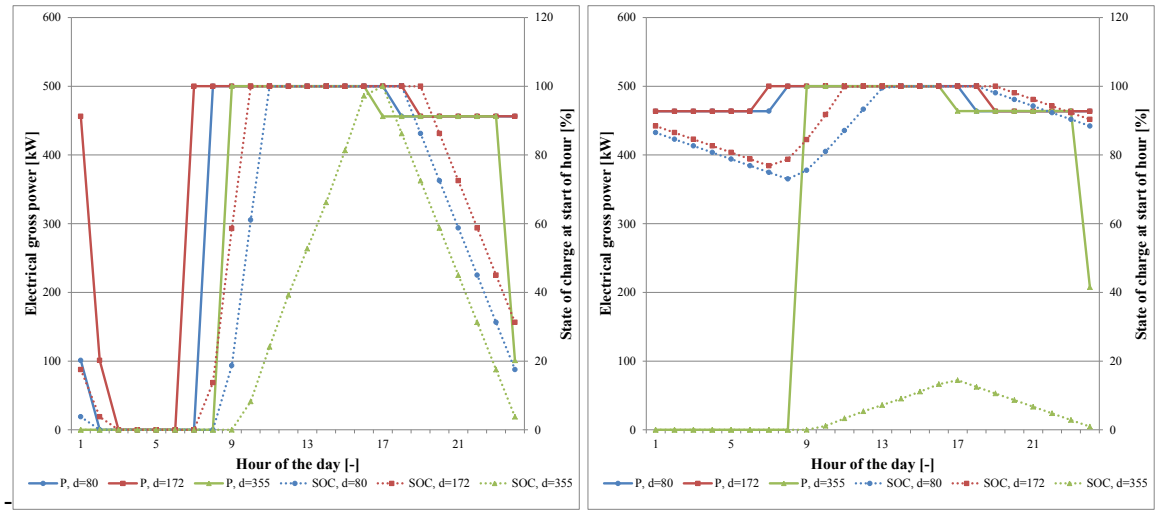

Figure 4: Electrical gross power (left ordinate) and state of charge at start of hour (right ordinate) for off-design simulations with a storage capacity of 6 hours (left chart) and 12 hours (right chart).

change and the excessive thermal energy is stored in the TES. On December 21st the collected thermal energy does not suffice to operate the ORC from the beginning of the day. For this amount of irradiance the solar field is too small and the storage cannot be charged sufficiently. At the charge peak only 15 % of the capacity is used. On March 21st and June 21st the TES is not discharged totally. The minimum SOC reaches only 72 % (March 21st) and 75 % (June 21st). Hence, in these cases the designed storage is oversized and does not suit the solar field size. Furthermore, this design does not suffice for continuous operation on December 21st.

The previous simulations made it possible to evaluate different designs on independent days. However, these daily simulations are not suitable to predict the real behavior of a SORC on successional days, but they are essential to specify characteristic design points. This approach is beneficial regarding aspects of time required for computing and simulating. The preselection using the characteristic design points helps to avoid surplus annual simulations.

Hence, annual simulations for three different design points are carried out in a case study to evaluate the annual performance of a SORC plant.

3. CASE STUDY – ANNUAL SIMULATION OF A SORC

Considering the results of the simulations prior to this, three different annual simulations are carried out. Case 1 refers to the 21st of March (80th day of the year), case 2 to June 21st (172nd day of the year) and case 3 to December 21st (355th day of the year). As in the previous simulations, the ORC has an electrical nominal gross power of 500 kW. The TES is sized with a capacity of 12 full load hours for the ORC and the solar field has a *SM* of 4. The DNI at 12:00 o' clock solar time is used as design point. Table 3 shows the main results of the annual simulation for each design point.

The different DNI on aperture of collector influences the solar field area. In December the low irradiance results in the need of a big solar field, nearly twice as big as the solar field with design point in June. The sunshine duration of an entire year is 4 382 hours. Hence, a TES has to cover the remaining hours for continuous operation. As shown in Figure 4, the design points in March and June lead to the fact that the solar field is too small to charge the TES in winter times when the irradiance is low. The bigger solar field in case 1 allows more operation hours compared to case 2. Whereas, the solar field in case 3 allows 8 760 operation hours for the SORC. The amount of hours out of operation is a theoretical value since e. g. no maintenance stops are taken into account for these simulations. For case 3 the annual electrical energy yield is 4 202 MWh. The solar field and thermal energy storage

Table 3: Case study: results of annual simulation

	Case 1	**Case 2**	**Case 3**	**Unit**
Design point	March 21st	June 21st	December 21st	-
Aperture direct normal irradiance	719.1	869.8	429.2	W/m²
Solar field aperture area	18 596	14 418	39 286	m²
Sunshine duration	4 382			h
Hours out of operation	485	1 022	0	h
Annual aperture direct normal irradiation	2.306			MWh/m²
Annual collected normal irradiation	42 885	33 248	90 597	MWh
Annual collected thermal energy	18 596	14 882	16 580	MWh
Annual electrical energy yield	3 955	3 690	4 202	MWh
Annual solar capacity factor	9.2	11.1	4.6	%

allow SORC operation in every simulated time step. However, the huge solar field causes a low annual solar capacity factor of 4.6 %. The annual solar capacity factor of case 1 is about 9.2 % and for case 2 11.1 %.

To evaluate one SORC design in detail an in-depth view has to be carried out. An annual simulation can be reviewed by looking closely at single days. Hence, in Figure 5 the course of various parameters for March 21st and June 21st of the annual simulation of case 3 is presented. For both entire days the electrical gross power, the direct normal irradiance and the SOC of the TES at the beginning of every time step are plotted. The solar field and the TES ensure the continuous power production of the SORC plant. The TES is charged within a few hours. This is caused by the fact that the simulation allows a higher heat flux than the nominal thermal heat flux for the ORC. If this heat flux is limited, charging times will become longer. The trend of the SOC shows that only about 30 % of the TES load are used on December 21st. Therefore, the storage capacity and the solar field size are not regarded to be well designed for this plant since in this case a huge percentage of the storage fluid is not needed during most of the year. Finding a more suitable design will need several more simulations of further designs which on their part again have to evaluated by annual simulations.

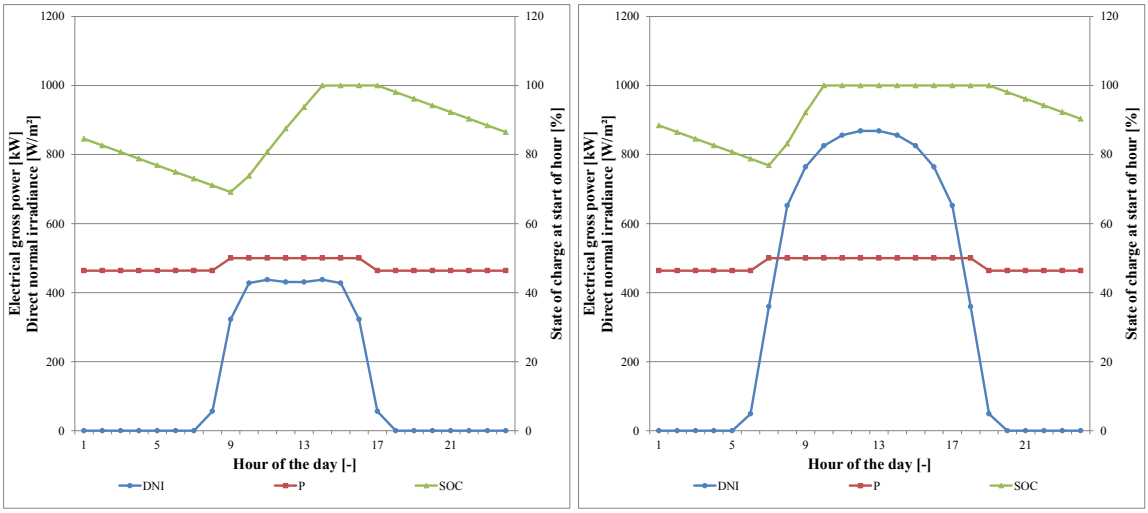

Figure 5: Gross power P, DNI (both left ordinate) and SOC (right ordinate) for December 21st (left chart) and June 21st (right chart), all charts are created with the results of case 3 plant design

4. CONCLUSIONS

Many options exist to design and engineer a SORC. The size of TES and of solar field are directly linked to plant availability and the number of annual operation hours at full and part load. The solar field size and the TES size influence the capacity factor of the SORC. For sizing the solar field and the TES an appropeiate design point has to be chosen. Annual simulations describe accurately the full and port load behavior of a SORC plant. With these simulations the chosen design can be evaluated.

In detail, the simulations carried out in this paper conclude in the following:

- A time step approach is used to describe the full and part load behavior of a SORC. A steady-state simulation is not considered to be a suitable approach.
- Choosing an appropriate design point is essential when designing and evaluating a SORC plant with annual simulations.
- The available irradiance and the required thermal power for the ORC influence the solar field size significantly.
- When sizing the TES, the following parameters have to be taken into account at least: the solar field size, full load hours, demand profile and direct normal irradiance over a period of one year.
- Specifying the most suitable design for solar field and TES with simulations results in an optimization problem characterized by a large number of degrees of freedom.
- To determine the best SORC plant design (including economic parameters) an optimization is required.

The simulations described in this paper do not consider economic constraint, auxiliary equipment such as boilers or load profile for power demand. In these cases the simulation needs to be extended by the relevant parameters to optimize a design and to compare it to a diesel generator.

Further works focus on the design of an optimization model. This model will aim at finding the most suitable basic engineering parameters, e. g. capacity of ORC and TES and size of solar field, for a SORC design as adecentralized power plant. The optimization model will contain an economic objective function and uses, among others things, a power demand and an irradiance profile as constraints. The modell will include part load behavior for the SORC to satisfy a load dynamic.

NOMENCLATURE

A_{ap}	aperture area	(m²)
d	day of year	(-)
G_{bn}	beam (direct) normal irradiance	(W/m²)
P	electrical power	(kW)
$\dot{Q}$	thermal power	(kW)
SM	solar multiple	(-)
Δt	duration of time step	(h)
η	efficiency	(-)
CF	capacity factor	(-)

Subscripts

el	electrical
i	time step ‘i’
sol	solar
th	thermal

Abbreviations

DNI	direct normal irradiance
ORC	organic Rankine cycle
SF	solar field
SORC	solar organic Rankine cycle
SOC	state of charge
TES	thermal energy storage

REFERENCES

Al-Sulaiman, F. A., Dincer, I., Hamdullahpur, F., 2011, Exergy modeling of a new solar driven trigeneration system, *Solar Energy*, vol. 85, no. 9: p. 2228-2243.

Bruno, J. C., López-Villada, J., Letelier, E., Romera, S., Coronas, A., 2008, Modelling and optimisation of solar organic rankine cycle engines for reverse osmosis desalination, *Applied Thermal Engineering*, vol. 28, 17-18: p. 2212-2226.

Canada, S., Cohen, G., Cable, R., Brosseau, D., Price, H., 2004, Parabolic Trough Organic Rankine Cycle Solar Power Plant, *Proceedings of the 2004 DOE Solar Energy Technologies Program Review Meeting*, National Renewable Energy Laboratory:

Delgado-Torres, A. M., García-Rodríguez, L., 2007a, Comparison of solar technologies for driving a desalination system by means of an organic Rankine cycle, *Desalination*, vol. 216, 1-3: p. 276-291.

Delgado-Torres, A. M., García-Rodríguez, L., 2007b, Preliminary assessment of solar organic Rankine cycles for driving a desalination system, *Desalination*, vol. 216, 1-3: p. 252-275.

Dürr Cyplan, 2015, Hochtemperaturanlagen ohne Wärmenutzung, http://www.durr-cyplan.com/de/energietechnik-produkte/ht-anlagen-ohne-waermenutzung/, last access: 18 May 2015.

He, Y.-L., Mei, D.-H., Tao, W.-Q., Yang, W.-W., Liu, H.-L., 2012, Simulation of the parabolic trough solar energy generation system with Organic Rankine Cycle, *Applied Energy*, vol. 97: p. 630-641.

Kane, M., 2003, Small hybrid solar power system, *Energy*, vol. 28, no. 14: p. 1427-1443.

McMahan, A. C., 2006, *Design & Optimization of Organic Rankine Cycle Solar-Thermal Powerplants*, Masterthesis, Madison (Wisconsin).

Montes, M. J., Abánades, A., Martínez-Val, J. M., Valdés, M., 2009, Solar multiple optimization for a solar-only thermal power plant, using oil as heat transfer fluid in the parabolic trough collectors, *Solar Energy*, vol. 83, no. 12: p. 2165-2176.

Moustafa, S., Hoefler, W., El-Mansy, H., Kamal, A., Jarrar, D., Hoppman, H., Zewen, H., 1984, Design specifications and application of a100 kW_{el}(700 kW_{th}) cogeneration solar power plant, *Solar Energy*, vol. 32, no. 2: p. 263-269.

Nafey, A. S., Sharaf, M. A., 2010, Combined solar organic Rankine cycle with reverse osmosis desalination process: Energy, exergy, and cost evaluations, *Renewable Energy*, vol. 35, no. 11: p. 2571-2580.

Orosz, M. S., Mueller, A., Quoilin, S., Hemond, H., 2010a, Small Scale Solar ORC System for Distributed Power, *Eurosun 2010: 2nd International Congress on Heating, Cooling and Buildings*.

Orosz, M. S., Quoilin, S., Hemond, H., 2010b, SORCE: A design tool for solar organic Rankine cycle systems in distributed generation applications, *Eurosun 2010: 2nd International Congress on Heating, Cooling and Buildings*.

Price, H., Hassani, V., 2002, *Modular Trough Power Plant Cycle and Systems Analysis,* National Renewable Energy Laboratory, 118 p.

Quoilin, S., 2011, *Sustainable Energy Conversion Through the Use of Organic Rankine Cycles for Waste Heat Recovery and Solar Applications*, Dissertation, Liège, 138 p.

Sinai, J., Fisher, U., 2007, 1 MW Solar Power Plant using Ormat® Energy Converter, *Proceedings of the 14th Sede Boqer Symposium on Solar Electricity Production*, Ben-Gurion University of the Negev:p. 53-56.

Stine, W. B. and Geyer, M., 2001, Power From The Sun, Online book, http://powerfromthesun.net/book.html, last access: 27 January 2014.

Szabó, S., Bódis, K., Huld, T., Moner-Girona, M., 2011, Energy solutions in rural Africa: mapping electrification costs of distributed solar and diesel generation versus grid extension, *Environ. Res. Lett.*, vol. 6, no. 3: p. 1-9.

EXPERIMENTAL STUDY ON A LOW TEMPERETATURE ORC UNIT FOR ONBOARD WASTE HEAT RECOVERY FROM MARINE DIESEL ENGINES

Aris-Dimitrios Leontaritis[1], Platon Pallis[1], Sotirios Karellas[1]*, Aikaterini Papastergiou[1], Nikolaos Antoniou[1], Panagiotis Vourliotis[1], Nikolaos Matthaios Kakalis[2], and George Dimopoulos[2]

[1]Laboratory of Steam Boilers and Thermal Plants, School of Mechanical Engineering, National Technical University of Athens, 9 Iroon Polytechniou, 15780, Athens, Greece.
Web page: http://www.lsbtp.mech.ntua.gr/

[2]DNV GL Strategic Research & Innovation East Med., Black & Caspian Seas/ Piraeus Hub

* Corresponding Author
e-mail: sotokar@mail.ntua.gr

ABSTRACT

The aim of this work is the experimental study of an ORC prototype unit which has been designed as a waste heat recovery system for the jacket water of marine diesel auxiliary internal combustion engines (ICEs). In order to simulate the operating characteristics of such engines, the heat input is in the order of 90kWth at low-temperature (90 ^{o}C) and is supplied by a natural gas boiler. The ORC unit produces 5 kWel of net electrical power, using as working medium the refrigerant R134a at a design cycle pressure of 25 bar and a temperature of 82 ^{o}C.
The experimental evaluation of the unit focuses more on operational issues than overall performance which has already been experimentally studied by a number of researchers. Accordingly, this study includes the investigation of the behaviour of the whole ORC system as well as of its key components under varying operational parameters, such as the occurrence of cavitation in the system feed pump and optimal scroll expanders operation. These outcomes contribute to an optimized configuration of the ORC system components and of the necessary measuring equipment as well as to the development of an efficient automatic control strategy of a dedicated ORC test bench which could then be directly coupled to an adequately sized marine auxiliary ICE for real time operation assessment.

1. INTRODUCTION

The energetic consumption of a commercial ship consists of propulsion and internal consumption electricity needs, which are entirely covered by specially designed marine diesel engines (main and auxiliary respectively). For large ships, the fuel expenses constitute about 30-55% of the total operational costs, depending on the type of vessel (Kalli et al., 2009). Strong motivation exists within the marine sector to reduce fuel expenses and to comply with ever stricter efficiency regulations, e.g. the EEDI -Energy Efficiency Design Index (Larsen et al., 2014a). Moreover, regarding emissions of CO_2 and oxides of sulfur and nitrogen (SO_x and NO_x) the international regulations are changing towards stricter limits (IMO, 2011). Currently, emphasis is being put on the improvement of the thermal efficiency of engines by optimizing their configuration in order to achieve lower fuel consumption (Jaichandar and Annamalai, 2012; Park, 2012). Also, research has been focused on advanced combustion technologies, such as the HCCI (Gan et al., 2011; Yao et al., 2009), the lean combustion (Zheng and Reader, 2004), and the stratified combustion (Park et al., 2012; Lu et al., 2011), in order to achieve a higher overall efficiency and reduce overall emissions. However, as these technologies have achieved quite a matured stage, it becomes harder to achieve further improvements by using these methods and thus a valuable alternative approach to improve overall energy efficiency is to capture and reclaim the ‘‘waste heat’’ (Shu et al., 2013). Hence, in times of high fuel prices,

there are significant economic advantages associated with investing in marine diesel engine waste heat recovery (WHR) systems (MAN, 2012; Shu et al., 2013). WHR systems for electrical or mechanical power production can significantly contribute to dealing with these issues, with the ORC (Organic Rankine Cycle), the Kalina cycle and the steam Rankine cycle receiving the majority of attention in the literature. The steam Rankine cycle is focused on higher temperature WHR mainly from the exhaust gases of the main engines of a ship, while the ORC/Kalina cycles are more suitable for smaller engines (MAN, 2012), like the marine auxiliary ones, while at the same time they can also be used for WHR from lower temperature heat sources (e.g. the jacket water of diesel engines). However, optimisation results suggest that the Kalina cycle possess no significant advantages compared to the ORC or the steam cycle (Larsen et al., 2014a).

Although the Diesel process is highly efficient, large marine diesel engines are particularly well suited to be coupled with a WHR system (Larsen et al., 2014b), as the engine loses a large part of the fuel energy to the environment, mainly with the exhaust gases (up to 25% of the input energy) and the jacket water (up to 5.1% of the input energy; MAN, 2012). However, both of these heat sources, originating from the main engine, are used for covering the internal heating needs of a ship (e.g. heavy fuel oil pre-heating, fresh water generation, exhaust gas boiler), while the respective ones from the auxiliary engines remain unused. Several researchers have proposed WHR systems for main marine diesel engines (Larsen et al., 2014a-2014b; Bounefour and Ouadha, 2014; MAN, 2012; Yang and Yeh, 2014), but no experimental study or even a theoretical analysis has ever been conducted regarding the jacket water of auxiliary engines. In this perspective, the present work focuses on the recovery of heat from the auxiliary engines and more specifically from their jacket water. For the scale and heat source temperature level considered, both the ORC and the Kalina could be used as bottoming cycles. Bombarda et al. (2010) compared the two processes applied for WHR on large marine engines and found that both cycles, when optimized, produced equal power outputs. In the present paper, an ORC WHR system, specially designed for the jacket water of a marine auxiliary diesel engine is experimentally studied.

2. THE MARINE ORC PROTOTYPE TEST BENCH

The marine ORC prototype unit is based on a conventional low-temperature subcritical Organic Rankine Cycle using R134a as working medium. This experimental unit has been designed as a waste heat recovery system for the jacket water of marine diesel auxiliary internal combustion engines (ICEs). In order to simulate the operating characteristics of such engines, the heat input is in the order of 90kWth at a low-temperature (90^{o}C), and is supplied by a natural gas boiler via an intermediate plate heat exchanger (evaporator). The boiler thermal output is adjustable and thus part load operation can be simulated as well. A schematic diagram of the unit is presented in **Figure 1**.

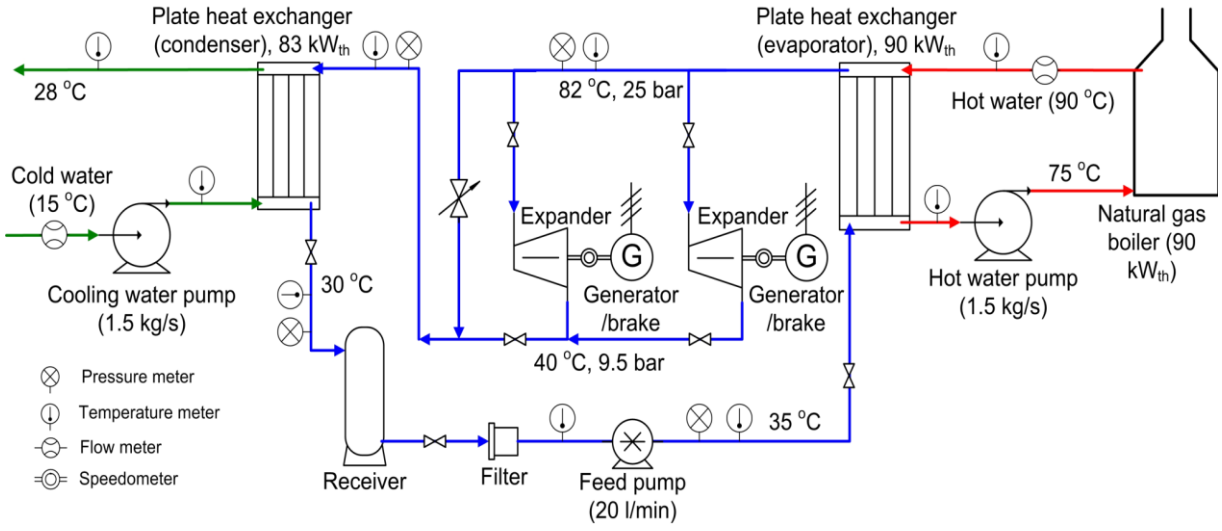

Figure 1: Schematic diagram of the ORC prototype unit.

2.1 Operation and control parameters of the experimental unit

The cycle is fed by a receiver (feed tank) at an average pressure of 9.5 bar and an average temperature of 30 ^{o}C. These parameters are controlled by the cold water flow in the condenser, which is adjusted by a regulatory valve.

The feed pump is a positive displacement multi-diaphragm pump that subsequently raises the pressure of the fluid at about 22-25 bar, depending on the operational conditions, and leads it to the evaporator. At a nominal speed of 960rpm a flow rate of 20lt/min is achieved. The rotational speed of the pump is controlled by a frequency drive. As a result, the refrigerant mass flow rate can be adjusted according to the unit load and the desired superheating temperature of the vapor, given the fact that the delivered volume flow rate of diaphragm pumps is in most cases a linear function of their rotational speed.

The high pressure vapor is expanded in two parallel scroll expanders, while a by-pass section controlled by an electromagnetic valve can alternatively lead the flow directly to the condenser. Actually, these expanders are two open-drive scroll compressors in reverse operation as it is thoroughly explained in the next paragraph. Each scroll expander drives an asynchronous motor/generator through a 1:1 belt drive, which can be coupled and uncoupled by an electromagnetic clutch. Both generators are connected to the 50Hz/400V electrical grid via a regenerative inverter module, which provides both grid stability and rotational speed control of the generators and hence of the expanders. For a given pump rotational speed (and thus mass flow rate), the inlet pressure of the scroll expanders is directly adjusted by their rotational speed, since the processed mass flow rate for volumetric machines is given by the product of the inlet density (ρ_{in}) multiplied by the swept volume (V_H) and the rotational speed (N_{rot}) of the machine (1).

$$\dot{M} = \rho_{in} \cdot V_H \cdot N_{rot} \quad (1)$$

An increase (decrease) of the rotational speed allows for a decrease (increase) of the density of the refrigerant at the expander inlet and thus causes a decrease (increase) of the respective inlet pressure. Finally, the expanded vapor is led to the condenser (plate heat exchanger), the condensate returns to the feed tank, and the cycle starts over.The ORC unit (**Figure 2**) produces 5 kWel of net electrical power, at a design cycle pressure of 25bar and a temperature of 82^{o}C.

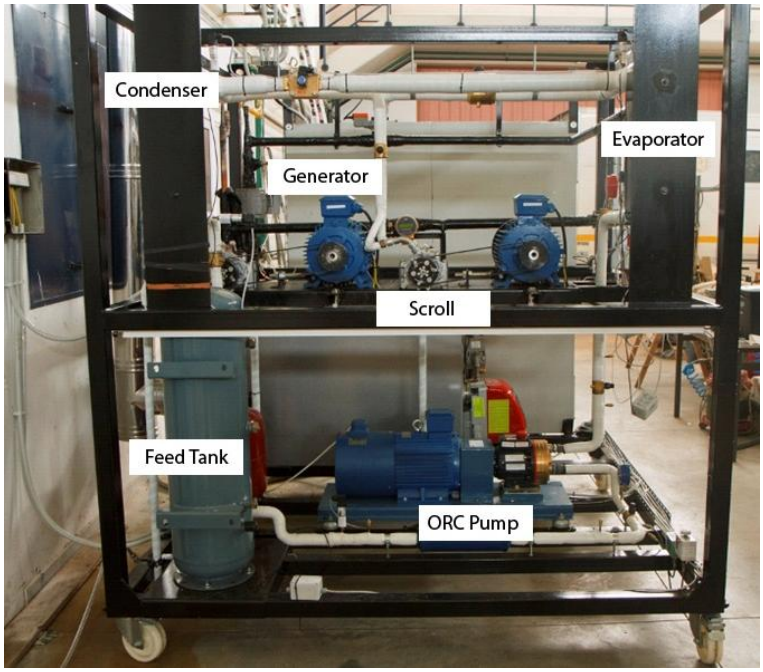

Figure 2: The Marine-ORC experimental unit

Various instruments have been mounted at all key-points of the cycle (**Figure 1**), in order to evaluate the performance of the different components of the ORC unit. Thermocouples and pressure transducers record the thermodynamic procedure; an electromagnetic flow-meter supervises the hot

water volume flow rate and two tachometers the scrolls' actual rotational speed. All important parameters regarding the electrical motors of both the pump and the generators, such as the consumed/produced active power are retrieved by the respective frequency drives.
It is noted that the automatic control of the system (including the frequency drives), the measurements and the data logging is materialised with the use of an industrial PLC (Programmable Logic Controller) and a SCADA (Supervisory Control and Data Acquisition) environment, which constitutes an important step towards the standardization and commercialization of such micro-scale units.

2.2 The scroll expanders

The expansion machine of an ORC system is a key component with critical influence on the overall system performance. Volumetric expanders are mostly suitable for micro-scale ORC systems (Declaye et al., 2013) as they are characterized by low mass flows, relatively high pressure ratios and much lower rotational speeds compared to turbo-machines (Quoilin, 2011). Scroll machines, in particular, are more favorable for such applications due to high performance and reliability, reduced number of moving parts, low price and broad availability at a wide power output range (Zanelli and Favrat, 1994).
In the power range of micro scale ORCs (up to a few kWs) there are currently no dedicated commercial scroll expanders available at an affordable price. Therefore, a viable solution is the use of a modified commercial scroll compressor (hermetic or open drive), designed either for air compression or for refrigeration applications, at reverse operation (Declaye et al., 2013).
In this study, two identical commercial open drive scroll compressors, originally designed for trucks' A/C systems were used as expanders. Their modification mainly focused on the inlet/outlet connectors and on the removal of the outlet (at compressor mode) check-valves so that they don't block the flow at reverse operation (expander mode).

Table 1: Scroll expanders characteristics

Swept volume (compressor mode)	121 cm^3/rev
Maximum Pressure	35bar
Built-involume ratio	≈2.3
Nominal Power output (expander mode)	3.5 kW

3. RESULTS and DISCUSSION

3.1 Cavitation effect on the ORC pump operation

A typical problem in micro scale ORC systems is the cavitation effect on the feed pump. Indeed, this problem was faced during the first steps of operation of the presented experimental unit, causing serious oscillations in its operation (mass flow rate, cycle pressure and temperature). In order to thoroughly understand this problem and finally solve it, an analysis of the pump operational conditions was conducted and is presented next.
First of all, in order to ensure stable operation of a pump, the **available** Net Positive Suction Head (**NPSHa**) at the pump inlet should exceed the respective **required** Net Positive Suction Head (**NPSHr**), given by the operation curves provided by the manufacturer, by at least 100mbar or an equivalent of 1 mH_2O. The NPSHa (mH_20) is calculated by the following equation:

$$NPSHa = Pt + Hz - Hf - Ha - Pvp \quad (2)$$

Where:
Pt = Pressure at the pump inlet
Hz=Vertical distance from liquid surface to pump center line
Hf = Friction losses in suction piping
Ha = Acceleration head at pump suction
Pvp = Absolute pressure of liquid at pumping temperature

The acceleration head factor (Ha) is calculated by equation (3).

$$\mathrm{Ha} = \frac{C \cdot L \cdot V \cdot N}{K \cdot G} \tag{3}$$

Where:

C = Constant determined by type of pump (in our case Wanner Engineering, Hydra Cell D/G10)
L = actual length of suction line
V = Velocity of liquid in suction line
N = RPM of crankshaft
G= Gravitational constant
K = Constant to compensate for compressibility of the fluid

For the operation conditions at the design point of the experimental unit the NPSHr is 500mbar, Hz=0.3m, Ha≈200mbar, and Hf=200mbar.

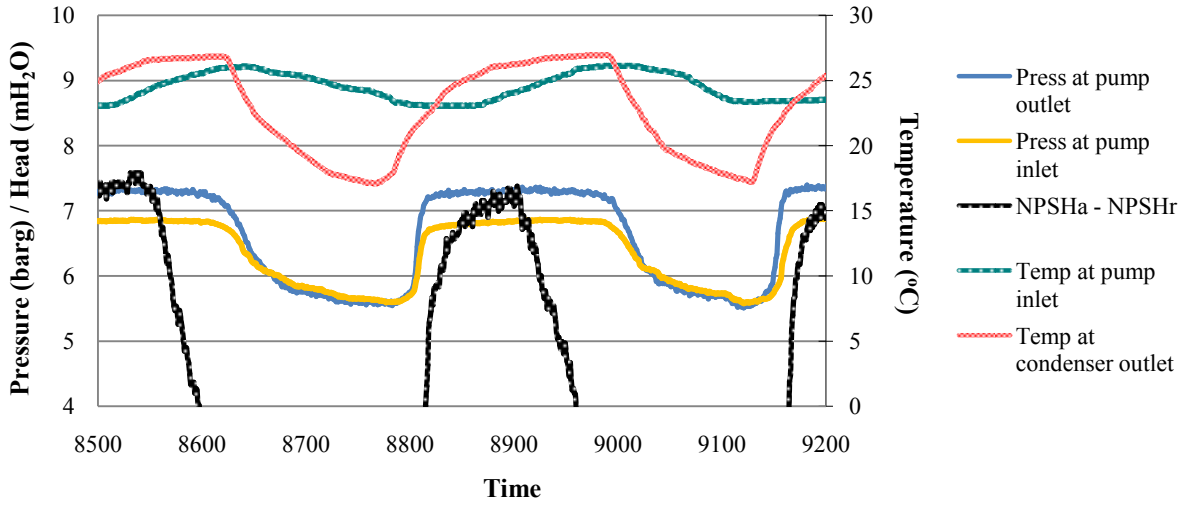

Figure 3: Cavitation effect on ORC pump operation.

The main parameters of the ORC feed pump under operation with cavitation effect are depicted in **Figure 3**. In fact, the ORC pump was tested while just circulating the refrigerant around the ORC circuit via the scroll by-pass section and thus practically no pressure raise is implemented by the pump. Analyzing the pump operation at the first oscillation cycle (cold start), it is observed that initially the pressure at the pump inlet/outlet remains constant with time, indicating a constant mass flow rate, and that the NPSHa - NPSHr difference is maintained well above the threshold of 100mbar (1 mH_2O). As the whole system is ramping up, the temperature at the condenser outlet raises due to the increase of the evaporator outlet temperature. Consequently, the temperature at the pump inlet raises but with a significant time lag caused by the thermal inertia of the feed tank, which stands between the condenser outlet and the pump inlet. With raising temperature at the pump inlet, the absolute pressure of the refrigerant (factor Pvp of equation (2)) raises and as a result the NSPHa drops. When the difference NPSHa – NPSHr reaches a critical value of around 100mbar (1 mH_2O), the cavitation effect is initiated and the circulating mass flow rate drops significantly. Simultaneously, the pressure of the circuit (controlled by the condensation temperature which drops due to the reducing refrigerant mass flow rate) also drops (factor Pt of equation (2)) and the unit's operation practically collapses. To make things worse, even though at this point the refrigerant temperature at the condenser outlet drops dramatically, since there is practically a zero mass flow rate, the feed tank needs time to cool down and keeps feeding the pump at relatively high temperature (and thus high Pvp); at this point the NPSH difference is strongly negative. Eventually the feed tank cools down, lowering the pumping temperature and thus raising the NPSH difference. Gradually the cavitation effect fades, the mass flow rate raises, and a new cycle starts over.

In order to solve this problem a water cooled heat exchanger was installed in the suction line of the ORC pump, downstream of the liquid receiver, so that the pumping temperature and thus the absolute

pressure of the refrigerant (factor Pvp of equation (2)) are maintained at lower values, ensuring stable pump operation. The main parameters of the ORC pump under operation with the additional sub-cooling heat exchanger are depicted in **Figure 4**. The measurements have been obtained at similar operation conditions with **Figure 3**, allowing their direct comparison. The sub-cooling heat exchanger causes an average 2K temperature drop at the suctioned refrigerant which has proved to be sufficient for the stable operation of the unit. As it can be seen in the diagram, the NSPHa is constantly kept above 17 mH_2O with a required NPSH of 5 mH_20. Its main fluctuations are caused by the suction pressure, which in turn depends on the cooling water mass flow at the condenser (or equivalently on the condenser outlet temperature) and naturally by the temperature at the pump inlet which affects the factor Pvp as already discussed. Accordingly, between t=300 and t=690 the NPSHa is slightly dropping even though the suction pressure is slightly raising, due to the greater influence of the raising temperature at the pump inlet (factor Pvp). The evident drops of NPSHa at t=700, t=840 and 1040 are caused by marginal steps of increasing cooling water mass flow rate at the condenser which directly influence the pressure at the pump inlet and thus the NPSHa. At the respective intervals the observed NPSHa raise is caused by the slightly decreasing temperature at the pump inlet. It is finally noted that the stable operation of the feed pump can be confirmed by the observation of the almost constant delivered Head of the pump over time (Pout-Pin).

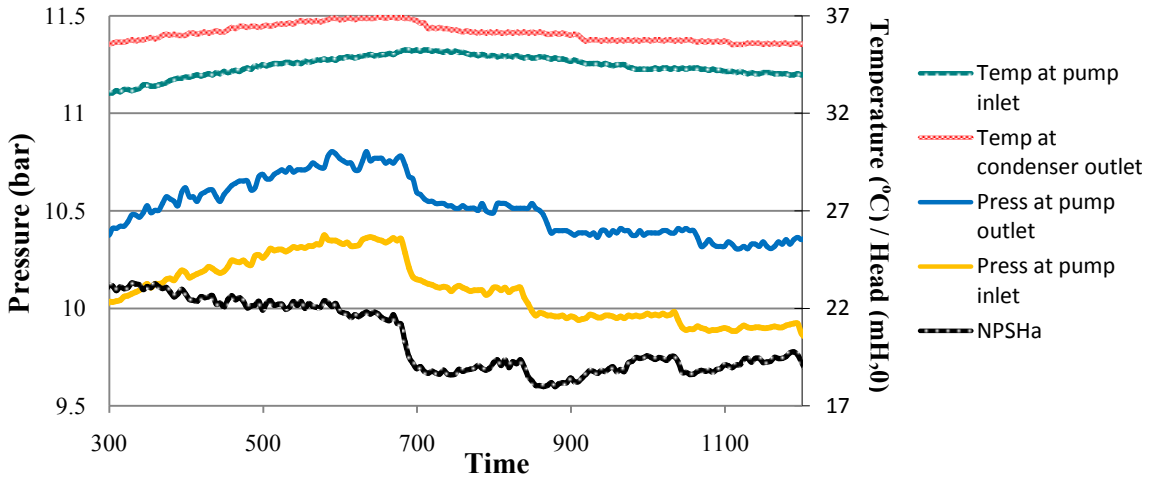

Figure 4: Cavitation free ORC pump operation with the addition of a sub-cooling heat exchanger

Extensive testing under different load and other operational conditions proved this solution as sufficiently effective to ensure the stable operation of the ORC pump and thus of the whole system. All the results presented from this point on in this paper refer to the experimental unit with the fitted additional heat exchanger. However, there are indications of partial cavitation occurrence at high pump rotational speeds which need to be further studied. As cavitation can be detected by the reduced delivered mass flow under constant pump rotational speed, a coriolis type mass flow meter has to be installed to the test rig in order to further investigate this issue, while the influence of the sub-cooling degree also requires to be studied.

3.2 Scroll expanders' operation

In this section the scroll expander's operation is presented through diagrams of its main operational parameters. It is noted that at this point of studying, the presented data can be used for a qualitative analysis of the behavior of the used scroll expanders under various conditions and its comparison with the findings of other researchers. **Figure 5** depicts the influence of the **scroll rotational speed** ($Nrot_{exp}$) and the **supply (inlet) temperature** (Tsu) of the refrigerant on the **overall isentropic efficiency** ($epsilon_s$). The presented surface has been produced by the statistical fitting of the experimental data. $Epsilon_s$ is defined as:

$$\text{epsilon}_s = \frac{Pel_{gross}}{\dot{M}_{in} \cdot (h_{su} - h_{ex,is})} \qquad (4)$$

Where:

Pel_{gross} the gross electrical power output of the ORC unit (equal to the net electrical power output of the two scroll expanders)
$\dot{M}_{in}$ the total circulating mass flow rate
h_{su} the suppy enthalpy of the refrigerant at the expander inlet
$h_{ex,is}$ the enthalpy at the ideal isentropic expansion point at the measured exhaust pressure

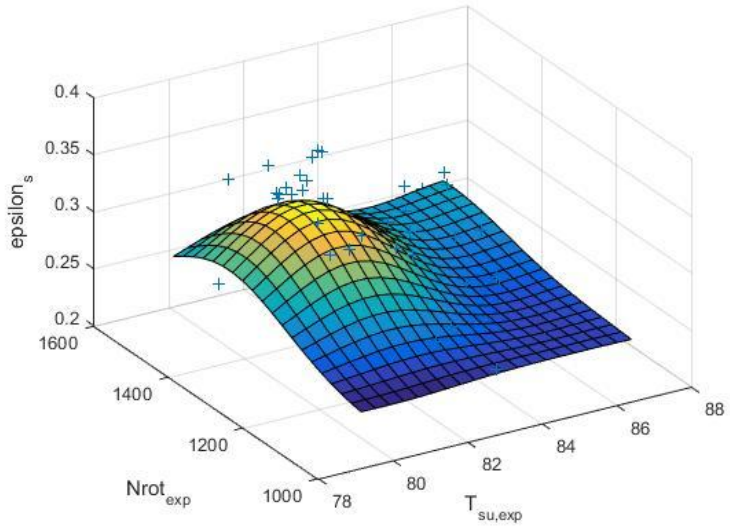

Figure 5: Scroll expander overall isentropic efficiency as a function of supply temperature ($Tsu_{,exp}$) and rotational speed ($Nrot_{exp}$)

Using this definition for the isentropic efficiency, all electromechanical losses, which can account for up to 40% of the gross generated electircal power, are included and that is the reason why the efficiency appears to be quite low.. The use of inverter frequency drives and induction motors/generators gives much room for improvements which is part of the work planned ahead. This was confirmed by low measured values of the power factor which indicates the low electrical efficiency of the generators. In order study the behaviour of the expander itself separately a dyno-meter or torque meter should be installed directly on its shaft. At any case, the results are useful for the qualitative analysis of the system. Analysing this diagram, the first obvious observation is that the isentropic efficiency is maximised near the nominal design conditions ($Nrot_{exp}$=1500 rpm / Tsu=82^{o}C). From a thermodynamic point of view, this was expected since the optimisation objective during the design of this system (as in most heat recovery systems) was the power output and not the cycle thermal efficiency (Braimakis et al., 2015; Quoilin et al., 2011). Moreoever, the expander itself is expected to have a better efficiency near its design point (i.e.when the imposed volume/pressure ratio is near the built in volume ratio of the expander) where over-expansion and under-expansion losses are minimized.

Focusing on the influence of the supply temperatue, it is concluded that a 4 to 5K degree of superheating of the live vapor gives the optimum results (at 25 bar the saturated vapor has a temperature of 77.5^{o}C). As other researchers have pointed out (Quoilin et al., 2011; Mago et al., 2008; Yamamoto et al. 2001), the superheating at the evaporator exhaust should be at low levels when using high molecular weight organic fluids, such as R134a .

The impact of the rotational speed can be better understood by the explanation of Figure 6,which presents the overall isentropic efficiency of the expander as a function of the filling factor (Φ) under various rotational speeds. The filling factor expresses a relative measure for the internal mass flow leakages and the respective power losses. The filling factor is defined as:

$$\Phi = \frac{\dot{M}_{in}}{V_{swept} \cdot N_{rot} \cdot \rho_{su}} > 1 \qquad (5)$$

Where:

$\dot{M}_{in}$ the total circulating mass flow rate
V_{swept} the bulit in swept volume of the scroll machine at expander mode
N_{rot} the expander rotational speed
ρ_{su} the suppy density of the refrigerant at the expander inlet

As expected, the rotational speed highly affects Φ, and as it can be observed in the diagram, the lower the rotational speed is the higher the filling factor gets due to the larger relative impact of the internal leakages. This effect has also been noted by Lemort et al. (2009) in an experimental analysis of an open drive scroll expander. Other operational parameters such as the inlet pressure and the imposed pressure ratio also affect the filling factor and that is the reason why its value varies for constant rotational speeds. Naturally, Φ in turn affects the overall isentropic efficiency which gets reduced by increasing internal leakages.

.

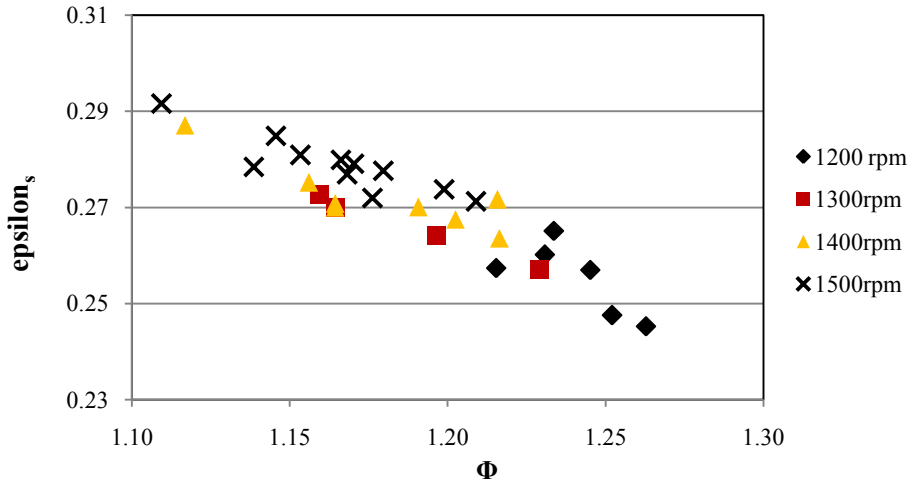

Figure 6: Scroll expander overall isentropic efficiency as a function of the filling factor (Φ)

Another interesting issue is the actual mass flow rate that circulates through the ORC circuit. Currently this value is calculated through the heat balance in the evaporator. The temperature and pressure of the heat source (water) as well as the volume flow rate are measured so the heat input rate ($\dot{Q}_{in}$) is known. At the same time the inlet and outlet conditions (pressure and temperature) of the refrigerant are also measured and thus considering zero heat exchange losses the circulating mass flow rate ($\dot{M}_{in}$) can be calculated by the following equation:

$$\dot{M}_{in} = \frac{\dot{Q}_{in}}{(h_{out} - h_{in})_{refrigerant}} \quad (6)$$

A cross-check of this value can be done through the heat balance at the system condenser. For this purpose an ultrasonic mass flow meter and two thermocouples (condenser inlet-outlet) were installed at the cooling water circuit and the dissipated heat rate was this way indirectly measured. In the following diagram (**Figure 7**), the values of the measured condenser dissipated heat rate (Qmeas) vs the respective calculated values (Qcalc) using the above-mentioned value (equation 6) of the mass flow rate ($\dot{M}_{in}$) are presented. The relative declination (ΔQ%) between these values is within 2-8% which is satisfactory for the needs of the present study. Moreover, the total system heat balance ($Q_{tot} = Q_{evap} + W_{pump} - W_{scrolls} - Q_{cond} - Q_{subcooler} - Q_{amb}$) gives a calculated Qamb of about 600W which is a realistic value for the non calculated ambient heat losses through the pipes of the system. However, in order to investigate certain operational issues such as the occurence of partial cavitation in the ORC pump and the filling factor of the expander, accurate measurements of the mass flow meter with a coriolis mass flow meter are absolutely necessary.

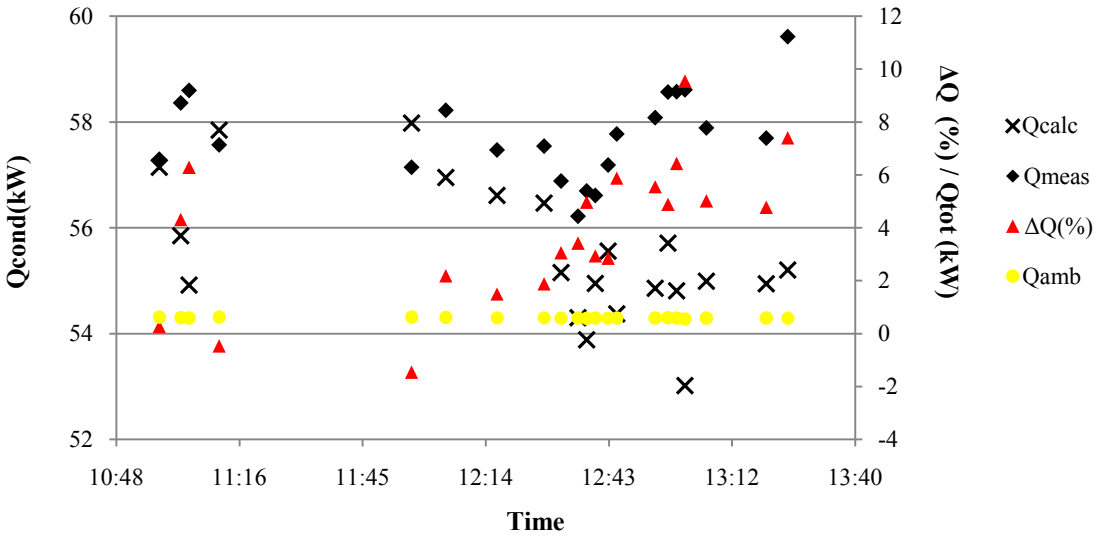

Figure 7: Condenser and overall heat balance

4. CONCLUSIONS

- A coriolis mass flow meter is an indispensable part of the measuring equipment of such experimental benches.
- Cavitation effect in ORC feed pumps can be dealt with the addition of a sub-cooling heat exchanger at the suction line of the pump. The effect of the sub-cooling degree on the cavitation effect as well as on the system performance needs further investigation.
- Partial cavitation at high pump loads and/or rotational speeds and its effect on the feed pump as well as on the overall system efficiency is another issue that requires further studying.
- The relatively low overall scroll expanders isentropic efficiency implies a low conversion of mechanical power into electrical. This was confirmed by low measured values of the power factor. Much room for performance enhancement through the optimization of the main operational parameters of the the induction motors/generators, such as the motor control method and its relative slip speed.
- A torque meter has to be installed directly on the expander's shaft in order to evaluate its performance separately. This is also necessary for the performance optimization of the electrical power generation sub-system.

REFERENCES

.

Bombarda, P., Invernizzi, C.M., Pietra, C., 2010, Heat recovery from diesel engines: a thermodynamic comparison between Kalina and ORC cycles. *Applied Thermal Engineering*, vol.30, no 2-3: p. 212-219.

Bounefour,Ouadha, a., 2014, Thermodynamic analysis and thermodynamic analysis and working fluid optimiazation of a combined ORC-VCC system using waste heat from a marine diesel engine,*Proceedings of the ASME 2014 International Mechanical EngineeringCongress and Exposition IMECE2014 November 14-20, 2014, Montreal, Quebec, Canada.*

Braimakis, K., Preißinger, M., Brüggemann, D., Karellas, S., Panopoulos, K., 2015, Low grade waste heat recovery with subcritical and supercritical Organic Rankine Cycle based on natural refrigerants and their binary mixtures, *Energy*, In Press, Corrected Proof, doi: 10.1016/j.energy.2015.03.092

Declaye, S., Quoilin, S., Guillaume, L., Lemort, V., 2013, Experimental study on an open-drive scroll expander integrated intoan ORC (Organic Rankine Cycle) system with R245fa as working fluid, *Energy*, vol.55, no.1: p. 173-183.

Gan, S., Ng, H.K., Pang. K.M., 2011, Homogeneous Charge Compression Ignition (HCCI) combustion: implementation and effects on pollutants in direct injection diesel engines. *Applied Energy* ,vol88, no.1: p.559–67.

IMO, The International Maritime Organisation, 2011,IMO and the environment, URL: *imo.org*

Jaichandar, S., Annamalai, K., 2012, Effects of open combustion chamber geometries on the performance of pongamia biodiesel in a DI diesel engine. *Fuel*, vol. 98, no. 1: p.272–279.

Kalli, J., Karvonen, T., Makkonen, T., 2009,Sulphur content in ships bunker fuel in 2015, Technical Report, Helsinki, Finland: Ministry of Transport and communications.

Larsen, U., Nguyen, T., Knudsen, T., Haglind, F., 2014b, System analysis and optimisation of a Kalina split-cycle for waste heat recovery on large marine diesel engines, *Energy*, vol. 64, no. 1: p. 484-494.

Larsen, U., Sigthorsson, O.,Haglind., F., 2014a, A comparison of advanced heat recovery power cycles in a combined cycle for large ships, *Energy*, vol. 74, no.1 : p. 260-268.

Lemort, V., Quoilin, S., Cuevas, C., Lebrun, J., 2009, Testing and modeling a scroll expander integrated into an Organic Rankine Cycle, *Applied Thermal Engineering*, vol. 29,no.1: p. 3094–3102.

Lu, X., Shen, Y., Zhang, Y., Zhou, X., Ji, L., Yang, Z., 2011, Controlled three-stage heat release of stratified charge compression ignition (SCCI) combustion with a two-stage primary reference fuel supply. *Fuel*, vol. 90, no. 1: p. 2026–38.

Mago, P.J., Chamra, L.M., Srinivasan, K., Somayaji, C., 2008, An examination of regenerative Organic Rankine Cycles using dry fluids, *Applied Thermal Engineering*, vol. 28, no. 1: p. 998-1007.

MAN, Diesel & Turbo, Denmark, 2012, Waste heat recovery systems (WHRS). URL: *www.mandieselturbo.com* [accessed 30.08.13].

Park, C., Kim, S., Kim, H., Moriyoshi, Y., 2012,Stratified lean combustion characteristics of a spray-guided combustion system in a gasoline direct injection engine. *Energy*, vol. 41, no. 1 : p. 401–407.

Park, S., 2012, Optimization of combustion chamber geometry and engine operating conditions for compression ignition engines fueled with dimethyl ether. *Fuel*,vol. 97, no.1: p. 61–71.

Quoilin S., 2011, Sustainable Energy Conversion through the use of Organic Rankine Cycles for waste heat recovery and solar applications, Liege, PhD Dissertation: p.12-15.

Quoilin S., Lemort, V., 2011, Thermo-economic optimization of waste heat recovery Organic Rankine Cycles, *Applied Thermal Engineering*, vol. 31, no.1: p. 2885-2893.

Shu, G., Liang, Y., Wei, H., Tian, H., Zhao, J., Liu, L.,, 2013, A review of waste heat recovery on Two-stroke IC engine aboard ships,*Renewable Sustainable Energy Review 2013*, vol. 19, no.0: p. 385-401.

T. Yamamoto, T., Furuhata, T., Arai, T., Mori, T., 2001, Design and testing of the Organic Rankine Cycle, *Energy,* vol. 26, no. 1: 239-251.

Yang, M.H., Yeh, R.H., 2014, Analyzing the optimization of an organic Rankine cycle system for recovering waste heat from a large marine engine containing a cooling water system, *Energy Conversion and Management*, vol. 88, no. 1:p. 999-1010.

Yao, M., Zheng, Z., Liu, H., 2009, Progress and recent trends in homogeneous charge compression ignition (HCCI) engines. *Progress in Energy and Combustion Science* 2009,vol. 35, no.1: p. 398–437.

Zanelli R., Favrat D., 1994, Experimental investigation of a hermetic scroll expander generator. In: *Proceedings 12th international compressor engineering conference at Purdue:* p. 459-64.

Zheng, M., Reader, G.T., 2004, Energy efficiency analyses of active flow aftertreat- ment systems for lean burn internal combustion engines, *Energy Conversion and Management*, vol. 45, no1. : p. 2473–93.

(Quoilin et al., 2011; Mago et al., 2008; Yamamoto et al. 2001)

ACKNOWLEDGEMENT

This study has been conducted within the Marine-ORC project funded by “DNV GL, Strategic Research & Innovation East Med., Black & Caspian Seas/ Piraeus Hub”.

REDUCING FUEL CONCUMPTION BY UP TO 10 % FOR DIESEL-BASED POWER GENERATION BY APPLYING ORC

Quirijn Eppinga & Jos P. van Buijtenen

Tri-O-Gen B.V.,
PO Box 25, 7470 AA Goor, The
Netherlands E-mail:
Jos.vanbuijtenen@triogen.nl

ABSTRACT

A high efficiency Organic Rankine Cycle (ORC) power unit has been developed by Tri-O-Gen B.V. of The Netherlands. The ORC system is based on a thermally stable hydro-carbon as a working fluid, hence suitable for direct use of intermediate temperature heat sources. The unit is capable of transforming heat flows at temperatures between 350 and 600 ºC into electricity. Typical applications involve the exhaust gasses of gas- or diesel engines and small gas turbines. These can be either fuelled by bio-gas, landfill gas, mine gas, or by natural gas as CHP units, where the power-to-heat ratio can be improved considerably. Unit power ranges from 65 to 165 kWe. Generally, the power produced by the ORC is considered as extra (renewable) power.

This paper describes the effect of applying this technology to Diesel engine based power generation, by recovering the heat in the exhaust gas and converting it into electricity. Here, the effect is a direct saving on fuel, as the power output is generally a number dictated by the grid. For a given amount of power, the Diesel engine can run in part-load, reducing its fuel consumption by up to 10 % and increasing its life, and also reducing its emissions of CO_2 and other harmful constituents. Applications are in decentralized and remote power, where fuel costs are generally high.

An economic evaluation will be given, together with some application examples and recent operating experience.

TORQUE RESEARCH OF SINGLE SCREW EXPANDERS

Ruiping Zhi[1]*, Yuting Wu[1], Yeqiang Zhang[1], Biao Lei, Wei Wang[1], Guoqiang Li[1] and Chongfang Ma

[1]Key Laboratory of Enhanced Heat Transfer and Energy Conservation of Ministry of Education and [1]Key Laboratory of Heat Transfer and Energy Conversion of Beijing Municipality, College of Environmental and Energy Engineering, Beijing University of Technology, Beijing 100124, PR China

*E-mail: Zhiruiping@gmail.com

ABSTRACT

In recent years, people have paid much attention to single screw expanders. Many experiments have been carried out on the performance of single screw expanders in fundamental applications such as industry waste heat recovery, compressed air power system, and pressure energy recovery. This paper presents a theoretical torque model of single screw expander under the conditions of ideal adiabatic expansion and air as working fluid. It was found that the torque ratio is independent of inlet pressure of single screw expander and is close to 1. It indicates that the single screw expander runs smooth. Besides, the calculated output power based on the theoretical torque model was close to the measured output power by experiments, if the shaft efficiency from experiments results and output work loss under over-expansion process were considered. And it demonstrates that this model can be used to estimate the output power of single screw expander before designing it according to the diameter of main rotor, volume ratio, inlet and back pressure of single screw expander.

1. INTRODUCTION

In recent years, with heavy fog and haze dominating our life, people realized the bad effects of PM2.5, such as coughs, asthma, sore throats and other respiratory illnesses. Many researchers and industries have realized the importance of using low-grade energy so that we can contribute to a permanent "Beijing Blue". Without doubt, ORC system is a great technology to save energy and keep the energy clean. A whole ORC system is basically composed of evaporator, expander, condenser and working fluid pump. Among these components, the selection of expander type is crucial to this efficiency of the system because the expander decides how much pressure energy is converted to power.

Among piston expanders, turbo expanders, scroll expanders and screw expanders, single screw expanders (SSEs) have received much attention in recent years due to its unique advantages, such as balanced loads, long working life, simple structure, low vibration and so on. In 2008, Ma Chongfang and his team [1] first reported the SSEs with 10kW and 40kW in Science Times. He et al. [2] carried out the study on the power system of compressed air based on three-stage SSEs. By programming and mathematical modeling results, it is shown that the single screw expander (SSE) has a good potential to be used in power systems. Liu et al. [10] verified the feasibility of SSE on ORC system with heat source of flue gas. Wang et al. [3] used compressed air as working fluid to verify the performance of SSE prototype. The designed flow rate of SSE is 1.1Nm³/min. The performance tests were conducted under different conditions including different intake flow, different humidity, constant torque and constant rotational speed. According to the experimental results, it is shown that the output power is 5kW at rotary speed of 2850r/min, discharge temperature is -45℃, the maximum temperature drop was about 62℃, and the maximum of adiabatic efficiency and total efficiency were 59% and 32.5% respectively. And it also shows that this SSE prototype has good part-load performance. And lubrication may be a factor to cause low adiabatic efficiency. He et al. [4] carried out experiments on the performance of the SSEs with compressed air as working fluid under different intake pressures and showed that the measured torque has a large increase as the intake pressure increases and has a slight decrease as the rotational speed increases. Desideri et al. [5] evaluated the SSE modified from a standard compressor and developed a steady-state model of the whole ORC unit. In this experiment,

the working fluid is Solkatherm (the azetropic mixture of HFC365mfc and YR-1800), the volume ratio of the expander is 5 and the diameter of main rotor is 155mm. The results show that the maximum expander isentropic efficiency and generated power are 64.78% and 7.8 kWe respectively. The whole cycle efficiency peaked at 9.8% with the evaporating temperature of 108℃. Ziviani et al. [6] established a detailed model of SSE based on the geometric parameters, heat transfer model and governing equations. And then verified the calculated data using experiment data between mass flow rates and output power.

Although the performance of SSE have been carried out in the ORC system and power system, little attention has been paid to the theoretical torque model of SSE which can be used to predict if the SSE works in a good state and also can be used to estimate how much output power are produced. The paper presents a detailed torque model of single screw expander and gives out comparison of calculated torque and experimental data.

2. Theoretical torque calculation of single screw expander

2.1 Main Parameters of Single Screw Expanders

The main rotor and a pair of gate rotors are the key components in SSE (shown in Figure 1). In this paper, the SSE is designed by our laboratory team. The single screw expander belongs to CP type. It means that the main rotor is machined by a cutting tool with straight line like a single tooth of gate rotor. The gate rotor is generated by envelope of main rotor. The main rotor and gate rotor are machined by special purpose machine developed by our team (shown in Figure 2). Their meshing relations are just like worm gears. The main structure parameters of meshing pair are the foundation to calculate the basic volume, the volume ratio and the whole design of SSE. The main parameters are illustrated in Figure 3.

Figure 1: Single screw expander

Figure 2: Main rotor and gate rotor

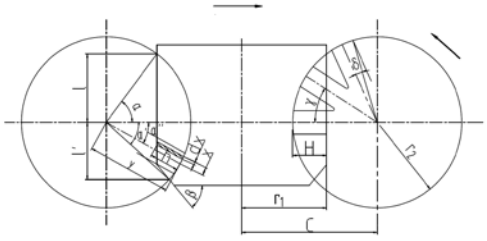

Figure 3: Structure of single screw meshing pair

$$i = \frac{\theta_1}{\theta_2} = \frac{z_2}{z_1} \tag{1}$$

$$\gamma = \frac{2\pi}{z_2} \tag{2}$$

$$k_0 = \frac{r_2}{r_1} \tag{3}$$

$$k = \frac{H}{r_1} \tag{4}$$

$$C = r_1(1 + k_0 - k) \tag{5}$$

$$l = \mathrm{r}_1\sqrt{2k_0k - k^2} \tag{6}$$

$$\alpha = \arcsin(\frac{\sqrt{2k_0k - k^2}}{k_0}) \tag{7}$$

$$\alpha' = \arcsin(\frac{l'}{r_1k_0}) \tag{8}$$

$$l' = 0.7l \tag{9}$$

$$\xi = \frac{\mathrm{e}}{2\mathrm{r}_1} \tag{10}$$

$$b = 2r_1[(k_0 - k)\sin(\frac{\gamma}{2}) - \xi\cos(\frac{\gamma}{2})] \tag{11}$$

$$b_s = \frac{b}{2r_2} = \frac{(k_0 - k)\sin(\frac{\gamma}{2}) - \xi\cos(\frac{\gamma}{2})}{k_0} \tag{12}$$

$$\delta = \arcsin(b_s) \tag{13}$$

2.2 Swept Volume Equation

In this paper, based on the method used by Sun Guangsan (1988), we calculate the whole single groove basic volume of the main rotor. The method mainly refers to the area of the gate rotor and the centroid of the gate rotor when meshing with the main rotor. The whole single groove basic volume is divided into two parts. One part is the volume of the gate rotor sweeping the groove of the main rotor from the front edge of the gate rotor just coming into the groove to the back edge of the gate rotor just coming to the groove (in Figure 4). The other part is the volume of the gate rotor sweeping the groove from the back edge of the gate rotor just coming into the groove to just beginning discharge. However, there is some difference between the volume equation inferred by Sun Guangsan and this volume equation in this paper. This volume equation of this paper is mainly expressed by non-dimensional coefficients of k and k_0 and the radius (r_1) of main rotor. The formulae are as follows:

$$V = V_1 + V_2 = \int_{\alpha-\delta}^{\alpha+\delta} A \cdot i\bar{R}_1 d\theta_2 + \int_{\alpha_{ds}}^{\alpha-\delta} A \cdot i\bar{R}_2 d\theta_2 \tag{14}$$

$$A_{\alpha-\delta} = k_0{}^2 r_1^2 \arcsin(b_s) + b_s\sqrt{1 - b_s{}^2} - 2b_sk_0r_1^2(k_0 - k)\sec(\alpha - \delta) \tag{15}$$

$$\begin{cases} A = A_{\alpha-\delta} \cdot \left(\dfrac{\alpha + \delta - \theta_2}{2\delta}\right)^2; \alpha - \delta \le \theta_2 \le \alpha + \delta \\ A = \int_{\frac{-b}{2}}^{\frac{b}{2}} (\sqrt{k_0{}^2 r_1^2 - x^2} - (k_0 r_1 - H)\sec\theta_2 + x\tan\theta_2)dx; \theta_{db} \le \theta_2 \le \alpha - \delta \end{cases} \tag{16}$$

(a) Cross-section **(b)** Primary view

Figure 4: Movement relations of single screw meshing pair

For the single screw expander, the whole expansion process is divided into three phases. It is suction, closed expansion and discharge respectively. The first part volume (V_1) is an inherent suction volume for every main rotor when the angle of gate rotor is between $\alpha - \delta$ and $\alpha + \delta$. So when we calculate the expander suction volume at any time during the suction phase, the formula is as follows:

$$V=\begin{cases}V_1=\int_{\alpha-\delta}^{\alpha+\delta}A\cdot i\bar{R}_1 d\theta_2,\alpha-\delta\le\theta_2\le\alpha+\delta\\ V_1+V_2=\int_{\alpha-\delta}^{\alpha+\delta}A\cdot i\bar{R}_1 d\theta_2+\int_{\theta_2}^{\alpha-\delta}A\cdot i\bar{R}_2 d\theta_2,\theta_{se}\le\theta_2<\alpha-\delta\end{cases} \tag{17}$$

When we calculate the closing expansion volume at any time during the closing expansion phase, the formula is as follows:

$$V=\int_{\alpha-\delta}^{\alpha+\delta}A\cdot i\bar{R}_1 d\theta_2+\int_{\alpha-\delta}^{\theta_2}A\cdot i\bar{R}_2 d\theta_2,\theta_{db}\le\theta_2<\theta_{se} \tag{18}$$

When we calculate the discharge volume at any time during the discharge phase, the formula is as follows:

$$V=\begin{cases}\int_{\alpha-\delta}^{\alpha+\delta}A\cdot i\bar{R}_1 d\theta_2+\int_{\alpha-\delta}^{2\theta_{db}-\theta_2}A\cdot i\bar{R}_2 d\theta_2,2\theta_{db}-\alpha+\delta\le\theta_2<\theta_{db}\\ \int_{\alpha-\delta}^{\alpha+\delta}A\cdot i\bar{R}_1 d\theta_2,2\theta_{db}-\alpha-\delta\le\theta_2<2\theta_{db}-\alpha+\delta\end{cases} \tag{19}$$

2.3 Calculation of Instantaneous and Average Torque

For the single screw expander, the instantaneous torque of main rotor is equal to product of the force on the gate rotor tooth area and the distance from the centroid of the gate rotor tooth area to the center of main rotor. Assuming that the pressure on the lower teeth surface of gate rotor is equal to the discharge pressure and the instantaneous torque is divided into three phases according to the operation process of single screw expander. Assuming that the expansion is a perfect adiabatic process and that the working fluid is compressed air, the formulae of the instantaneous torque are as follows:

$$\begin{cases}F=(p_{in}-p_{out})A,\alpha-\delta<\theta_2\le\alpha+\delta\\ F=(p_{in}-p_{out})A,\theta_{se}<\theta_2\le\alpha-\delta\\ F=p_{in}\left(\frac{V_2}{V_1}\right)^k A,\theta_{db}<\theta_2\le\theta_{se}\\ F=(p_{out}-p_{out})A=0,2\theta-\alpha-\delta\le\theta_2\le\theta_{db}\end{cases} \tag{20}$$

$$\begin{cases}T=(p_{in}-p_{out})A\bar{R}_1,\alpha-\delta<\theta_2\le\alpha+\delta\\ T=(p_{in}-p_{out})A\bar{R}_2,\theta_{se}<\theta_2\le\alpha-\delta\\ T=p_{in}\left(\frac{V_2}{V_1}\right)^k A\bar{R}_2,\theta_{db}<\theta_2\le\theta_{se}\\ T=(p_{out}-p_{out})A\bar{R}_2=0,2\theta_{db}-\alpha-\delta\le\theta_2\le\theta_{db}\end{cases} \tag{21}$$

Therefore, the average torque is given by the following equation (22):

$$T_{a1}=\frac{\int_{t_1}^{t_2}Tdt}{t_2-t_1} \tag{22}$$

The theoretical output power can be written as

$$P_{e1}=\frac{T_{a1}n}{9550} \tag{23}$$

2.4 Output Power Loss Percentage of Over or Under Expansion Process

It is known that the single screw expander is a positive displacement expander without discharge valve. As a result, there is a built-in volume ratio (η_{iv}) for the single screw expander. If the inlet pressure of expander (P_{in}) is certain, the internal outlet pressure (P_{iout}) is a certain value when the expansion ends and the expander begins discharging. But the internal outlet pressure finally needs to be equal to the back pressure (P_d) of the discharge pipe, so that the working fluid can be discharged. The internal and external expansion ratio (ε_i and ε_d) can be obtained in the following equation (24-25). If the internal outlet pressure P_{iout} is equal to the external outlet pressure P_d, the expansion process is called as 'full expansion' (shown in Figure 5a). If the internal outlet pressure P_{iout} is less than the external outlet pressure P_d, the expansion process is called as 'over expansion' (shown in figure 5b). If the internal outlet pressure P_{iout} is greater than the external outlet pressure P_d, the expansion process is called as 'under expansion' (shown in Figure 5c). For the over and under expansion, there is additional power consumption and it will decrease the output power. The output work loss Δw is shown in the triangle with shadow part. The output power loss percentage η_w can be calculated in equation 26.

$$\varepsilon_i = \frac{p_{in}}{p_{iout}} \tag{24}$$

$$\varepsilon_d = \frac{p_{in}}{p_d} \tag{25}$$

$$\eta_w = \frac{\Delta w / t}{w_d / t} = \frac{\Delta w}{w_d} = \frac{\left(\frac{\kappa-1}{\kappa}\varepsilon_d^{-1}\varepsilon_i^{\frac{1}{\kappa}} - \varepsilon_d^{\frac{1-\kappa}{\kappa}} + \frac{1}{\kappa}\varepsilon_i^{\frac{1-\kappa}{\kappa}}\right)}{1-\varepsilon_d^{\frac{1-\kappa}{\kappa}}} \tag{26}$$

Hence, the output power P_{e2} after considering the output power loss under different expansion type can be written as

$$P_{e2} = P_{e1}(1-\eta_w) \tag{27}$$

Furtherly considering the shaft efficiency η_s, the output power P_{e3} is given by

$$P_{e3} = P_{e1}(1-\eta_w)\eta_s \tag{28}$$

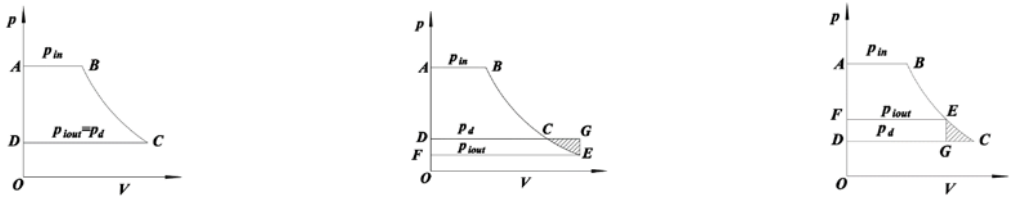

(a) Full expansion (b) Over expansion (c) Under expansion

Figure 5: Expansion type

3. Results and Discussions

3.1 Experimental Results

The single screw expander designed by our laboratory is installed in a compressed air power system. This whole system includes five parts: air intake and exhaust circuit, oil lubrication circuit, power testing system, water cooling system and data acquisition system. The air source comes from a compressed air storage tank. The rotary speed of single screw expander is 3000r/min. And the inlet air measured pressure was varied from 4.97bar to 9.975bar. The main parameters of SSE are listed in

Table 1. The measured variables and their uncertainties are shown in Table 2. And the experimental results are shown in Table 3.

The built-in volume ratio of single screw expander is 5. This experiment uses the air as working fluid. And the adiabatic exponent of air is assigned as an ideal value of 1.4. Assuming that the expansion process is an adiabatic process, according to the adiabatic equation of air, the ideal adiabatic expansion ratio is 9.518. As can be seen from Table 3, the expansion ratios calculated by experiments data are less than that of ideal adiabatic expansion ratio. So this single screw expander was in an over-expanded working state. This inlet pressure in this experiment just sets less than 10 bar, because there is an upper end of measured output power for the eddy current dynamometer (0~10 kW). That's the reason that experiments with higher inlet pressure cannot be carried out.

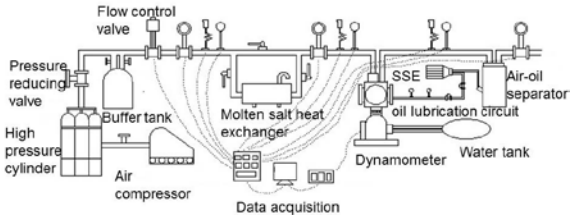

Figure 6: General layout of experimental setup with air compressor

Table 1: Main parameters of single screw expander

Parameters	
Diameter of main rotor	155mm
Diameter of gate rotor	155mm
Transmission ratio	11/6
Center distance	124mm
Volume ratio	5
Tooth width of gate rotor	23.4mm

Table 2: Measured variables and their uncertainties

Variable	**Units**	**Uncertainties**
Temperature	℃	0.5%
Pressure	bar	0.5%
flow	m^3/h	1.5%
Torque	N.m	±0.2~0.4%FS
Rotate speed	r/min	±1%

Table 3: Experimental results of single screw expander

Inlet pressure P_{in} (bar)	**Rotate speed n (r/min)**	**Torque T_{ex} (N.m)**	**Output Power P_{ex} (kW)**	**Outlet Pressure P_d (bar)**	**External expansion ratio ε_d**	**Shaft efficiency η_s (%)**
4.971	2999	11.464	3.600	0.500	3.981	48.189
5.976	3000	15.785	4.958	0.600	4.340	51.387
7.033	2999	20.166	6.333	0.700	4.725	54.046
8.010	2999	24.028	7.457	0.800	5.005	56.393
8.975	3000	27.776	8.72	0.967	5.073	57.679
9.975	3000	31.583	9.92	1.100	5.226	58.274

3.2 Calculated Torque and Torque Ratio of Single Screw Expander

Based on the equation presented in this paper, the Matlab codes are programmed and developed to calculate the instantaneous torque of single screw expander with the rotary angle changes of main rotor. Assuming that the inlet pressure is equal to the measured values by experiments, the expansion process is a perfect adiabatic expansion, and that there is no mechanical and frictional loss. From the Figure 7, the output torque value appears again with period 60 degrees. In a period, no matter how much the inlet pressure is equal to, all the relative highest point and lowest point appears at the same degrees (46degrees and 30degrees respectively). In Figure 7, it is shown that the output torque of single screw expander increases with the increase of inlet pressure. This trend is in accordance with that of experimental results.

Torque ratio is defined as theoretical torque at different angle of main rotor in to average torque of single screw expander and can be calculated in equation (shown in equation 29). Torque ratio can reflect the operation performance of single screw expander. The torque ratio is closer to 1, the single screw expander runs smoother. It can be observed in Figure 8 that the torque ratio is independent of inlet pressure, and that there is a small fluctuation for torque ration around at the horizontal line (Torque ratio of the horizontal line is equal to 1). It could be concluded that the single screw expander runs steadily.

$$\lambda = \frac{T}{T_{a1}} \tag{29}$$

3.2 Calculated and Measured Output Power of Single Screw Expander

According to the trapezoid rule of numerical integral formulas, the average torque in one period is obtained by equation (22), and then by equation (23-28), the calculated output power can be calculated (shown in Table 5). The relative error can be obtained by the following equation (30). As listed in table 5, it reveals that the over-expansion would cause great output power loss and that the output power loss percentage will decrease sharply with a slow increase of external expansion ratio.

$$Er = \frac{P_{e3} - P_{ex}}{P_{ex}} \tag{30}$$

It can be observed in Figure 9 that the output power of single screw expander increases linearly with growth of inlet pressure. The relative error of output power is given in Table 4. The difference value of output power is around at 1 and there is almost no change for ΔP, but the relative error is bigger compared to the change of difference value ΔP of it. Because the output power value itself is not a big value. Although the relative error is not much small, the output power by this mathematical model still can be accepted. That's because in this model, the leakage and friction loss are not considered.

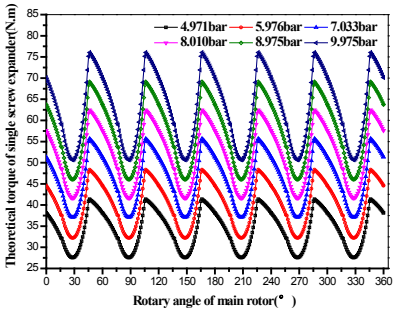

Figure 7: Theoretical torque of main rotor at different rotary angle of main rotor

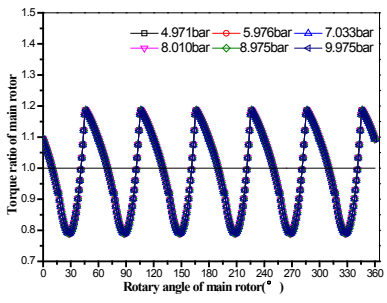

Figure 8: Torque ratio at different angle of main rotor

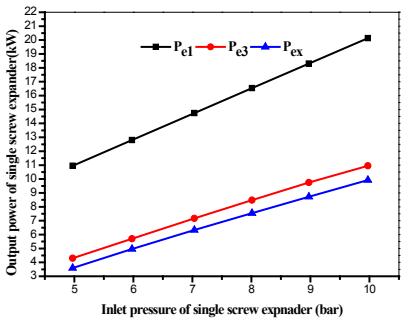

Figure 9: Output power of single screw expander with changes of inlet pressure

Table 4: The relative error, the theoretical output power, the output power after considering shaft efficiency and output power loss percentage and the measured output power

Inlet Pressure(bar)	P_{e1} **(kW)**	η_w **(%)**	P_{e3} **(kW)**	P_{ex} **(kW)**	ΔP **(kW)**	Er **(%)**
4.971	10.949	18.46	4.301	3.600	0.701	19.5
5.976	12.800	13.48	5.704	4.958	0.746	15.0
7.033	14.739	10.01	7.168	6.333	0.834	13.2
8.010	16.537	7.98	8.479	7.547	0.932	12.4
8.975	18.301	7.57	9.748	8.725	1.023	11.7
9.975	20.135	6.67	10.951	9.920	1.031	10.4

4. Conclusions

In this paper, based on the modified mathematical model of basic volume for main rotor, the theoretical model torque model of single screw expander is established under ideal adiabatic expansion process and air as working fluid. And this paper presents the output power loss percentage equation during under or over expansion process. According to the present analysis, the following results are concluded:

(1) From the torque equation, it can be found that the theoretical torque mathematical model is independent of rotation speed of single screw expander. The instantaneous torque and the torque ratio reflect that the single screw expander runs steadily.

(2) The output power loss percentage equation can also be applied to polytropic process in twin screw expanders and single screw expanders. The κ value in equation (26) is replaced by the polytropic exponent n.

(3) By comparison between calculated output power by mathematical model and measured torque by experiments, this relative error is 10%~19% while the differential value ΔP between calculated and measured output power is just around at 1. Hence, this model can be used to estimate the output power of SSE under given diameter of main rotor, inlet pressure, built-in volume ratio and back pressure when design the SSE. And there is a rapid increase for η_w with a slight decrease of external expansion ratio. So the SSE should avoid over-expansion process when design it in order to lower great output power loss.

This theoretical mathematical model can just be used to estimate the operation state and output power of SSE under ideal adiabatic expansion process and air as working fluid, if the diameter of main rotor, inlet pressure, volume ratio and back pressure are given. But there is still some room to improve. On the one hand, the inlet pressure loss should be included in the future study in order to make the

calculated torque be closer to the measured torque. On the other hand, in order to calculate the torque of SSE in ORC system, the state equation of organic fluid need to be studied. With the continuous improvement of this model, this model will be more accurate.

NOMENCLATURE

Variable	definition	units
i	transmission ratio	(–)
z	number of grooves or teeth	(–)
γ	indexing angle of gate rotor	(rad)
r	radius	(mm)
k_0	ratio of the main rotor radius in to the gate rotor radius	(–)
k	meshing depth coefficient	(–)
H	the maximum meshing depth	(mm)
C	Center distance of single screw meshing pair	(mm)
l	axial length of the discharge side	(mm)
α	meshing angle of the discharge side	(–)
α'	meshing angle of the suction side	(–)
l'	axial length of the suction side	(–)
b_s	tooth width coefficient	(–)
b	tooth width of the gate rotor	(mm)
δ	half angle of the tooth width	(rad)
e	the minimum width of the groove wall	(mm)
ξ	coefficient of the groove wall	(–)
A	area of gate rotor tooth meshing with main rotor	(mm^2)
V	volume of main rotor groove	(mm^3)
θ	rotary angle	(rad)
p	inlet or outlet pressure of single screw expander	(Mpa)
p_d	back pressure	(Mpa)
p_{iout}	internal expansion pressure of single screw expander	(Mpa)
T	instantaneous output torque of single screw expander	(N.m)
T_{a1}	theoretical average output torque	(N.m)
P	output power of single screw expander	(kW)
η_s	shaft efficiency of single screw expander	(–)
η_w	output power loss percentage of single screw expander	(–)
λ	torque ratio	
Er	relative error	(–)
ε_i	internal expansion ratio	(–)
ε_d	external expansion ratio	(–)
ΔP	differential value of output power	(kW)

Subscript

1	main rotor
2	gate rotor
e1	theoretical
e2	after considering output power loss percentage
e3	after considering shaft efficiency

ex	experimental results
in	inlet
out	outlet
se	suction ending
db	discharge beginning

REFERENCES

[1] http://news.sciencenet.cn/sbhtmlnews/2008/12/214421.html (2008) (in Chinese)

[2] HE, W., Wu, Y.T., Ma, C.F., Ma, G.Y., (2010). Performance study on three-stage power system of compressed air vehicle based on single-screw expander [J]. Science China Technological Sciences, 2010, 53(8): 2299-2303.

[3] Wang, W., Wu, Y.T., Ma, C.F., Liu, L.D., and Yu, J., (2011). Preliminary experimental study of single screw expander prototype. Applied Thermal Engineering, 31:3684 - 3688.

[4] He, W., Wu, Y.T., Peng, Y.H., Zhang, Y.Q., Ma, C.F., and Ma, G.Y., (2013). Influence of intake pressure on the performance of single screw expander working with compressed air. Applied Thermal Engineering, 51:662-669.

[5] Desideri, A., van den Broek, M., Gusev, S., and Quoilin, S., (2014). Experimental campaign and modeling of a low-capacity waste heat recovery system based on a single screw expander. In International Compressor Engineering Conference. Paper 1506.

[6] Ziviani, D., Bell, I., Paepe, D., and M., van den Broek, M., (2014). Comprehensive model of a single screw expander for orc-systems applications. In 2014 Purdue Conferences: Compressor Engineering Refrigeration and air conditioning high performance building. Paper 1451.

[7] Lu, Y.W., He, W., Wu, Y.T., Ji, W.N., Ma, C.F., and Guo, H., (2013). Performance study on the compressed air refrigeration system based on single screw expander. Energy, 55:762--768.

[8] Sun, G., (1988). The investigation of some basic geometric problems of the single screw co. In International Compressor Engineering Conference. Paper 630.

[9] ZHANG, Y.Q., WU, Y.T., XIA, G.D., Ma, C.F., Ji, W.N., Liu, S.W., Yang, K., and Yang, F.B., (2014). Development and experimental study on organic Rankine cycle system with single-screw expander for waste heat recovery from exhaust of diesel engine [J]. Energy, 77: 499-508.

[10] Liu, L.D., (2010). Research of the single screw expander and organic Rankine cycle system [D]. (in Chinese)

[11] Peng, Y.H., (2013) Performance study of the compressed-air power system based on single-screw expanders[D].(in Chinese)

[12] Peng, Y.H., Wu, Y.T., He, W., Ji, W.N. And Ma, C.F., (2014) Experimental study of single screw engine at different intake pressure.(in Chinese)

ACKNOWLEDGEMENTS

The authors are grateful to acknowledge the financial support provided by the National Basic Research Program of China with Grant Numbers 2011CB710704 and 2013CB228306，International S&T Cooperation Program of China with Grant Numbers 2014DF60600.

Thanks for experimental data supported by Yeqiang Zhang, Weining Ji and Yanhai Peng. If there is no their hard work, there will be no model validation of this paper. I am quite grateful for the guide from Biao Lei. Thanks for good suggestions from Wei Wang. Thanks them very much for their help.

EXPRIMENTAL STUDIES ON AN ORGANIC RANKINE CYCLE (ORC) SYSTEM UNDER VARIABLE CONDENSATION TEMPERATURE

Feibo Xie, Tong Zhu *, Jihua Liu, Naiping Gao, Wei An

College of Mechanical Engineering,Tongji University,
Siping Road 1239, Shanghai, China
E-mail:zhu_tong@tongji.edu.cn
Tel:86-21-65983867
* Corresponding Author

ABSTRACT

For a thermal power system the operating condensation temperature fluctuates significantly throughout the year in many areas due to the change of ambient temperature. Therefore, off-design operation of an Organic Rankine Cycle (ORC) system is unavoidable. The present paper focuses on the test and analysis of an ORC system using R123 as the working fluid under various condensation temperature conditions. A scroll expander was integrated into the ORC system and connected with a synchronous generator. The exhaust gas from a furnance and the water from the cooling tower were adopted to simulate the low-grade heat source and the cold source, respectively. The temperature of the exhaust gas was about 180°C. With the increasing of the cold water temperature from 22 °C to 42 °C, the condensation temperature of the working fluid varied from 50 °C to 65 °C and the pressure from 0.21MPa to 0.32MPa, respectively.It affected the expansion ratio and the temperature difference between the inlet and outlet of the expander.The performances of the expander, evaporator, condenser and the whole system were influenced subsequently. The measured electric power output declined from 2.36kW to 1.54kW, and the thermal efficiency fell from 7.25% to 5.52% as well. Under the operation conditions, the electric power and thermal efficiency decreased, by 34.75% and 23.86%, respectively. These results indicate that the operating condensation temperature plays a key role on the performance of the ORC system, and suggest that a proper condensation temperature is important to the design and operation of the ORC system.

1. INTRODUCTION

Energy crisis and global warming have greatly accelerated the development of low grade heat recovery technologies. An Organic Rankine Cycle (ORC) is regarded as a resonable and promising way for power generation from low grade heat sources due to its high efficiency and flexibility (Tchanche B. et al.,2011; Velez F. et al.,2012; Ziviani D. et al.,2014). Compared to steam Rankine Cycles (RC), ORCs prefer organic fluids to low boiling points to improve the efficiency in low temperature applications. Several large scale ORCs have been available on the market (Quoilin S. et al.,2013; Tchanche B. et al., 2014). However, most of small-scale ORCs are still at the initial stage and recieve increasingly striking attention due to its great market potential in low grade heat sources.
ORCs show dramatic potential in utilization of geothermal (Gu Z. et al., 2002;Franco A. et al. 2009), solar energy (Joan B. et al., 2008; Pei G. et al., 2010), industrial waste heat (Liu B. et al.,2004; Dai Y. et al.,2009; Srinivasan K. et al., 2010; Zhou N. et al., 2013), engine exhaust gas (Invernizzi C. et al., 2007) and biomass (Martina P. et al., 2010). Over the past several decades, this wide range of applications has encouraged researchers' efforts to provide suitable ORC solutions.Thus various investigations have been carried out for working fluid selections (Hung T. et al.,2001; Saleh B. et al., 2007; Tung T. et al.,2010) and parameter optimizations (Wei D. et al., 2008; Quoilin S. et al.,2010; Quoilin S. et al.,2011; Lee Y. et al.,2012; Bracco R. et al.,2013; Minea V. et al., 2014).

Unlike RCs, ORCs, especially small scale, easily suffer the influence of off-design operation conditions. Heat sources for ORCs are usually unsteady. An industrial waste heat source usually fluctuates in a certain range because of the variation of the upstream production process. The solar radiation intensity fluctuates with the time of day and the season. The variable operation has been becoming a hotspots of ORCs studies recently. Many studies indicate that the performance and operating parameters of an ORC are sensitive to the changes in the heat source temperature (Bamgbopa M. et al.,2013; Ibarra M. et al., 2014), the working fluid flow rate (Bracco R. et al.,2013;Miao Z. et al.,2015) and the load (Miao Z. et al.,2015). And variations of the entering cooling fluid temperature also have an important influence on the output power and cycle efficiency of the ORC (Lee Y. et al.,2012; Li J. et al., 2014).

Additionally the expander is a critical component of an ORC. Among positive displacement expansion machines, a scroll expander is widely regarded as a potential and promising canditate for a kW-scale ORC due to compactness, high efficency, few movement part, broad availablity and so on (Bao J. et al., 2013; Song P. et al., 2015). Generally, the scroll expander is mainly modified from a scroll compressor (Lermort V. et al.,2009; Declaye S. et al., 2013; Liu G. et al.,2015), and elaborately designed for an ORC are hardly reported.

In the present work, an ORC using an oil-free scroll expander is tested and analyzed. R123 was adopted as the working fluid. The authors focus on the steady-state expander operation characteristic and performance of the ORC system under various cooling water temperature conditions, which simulates seasonal and daily variations of the ambient temperature. Under these conditions, the key operating parameters, which mainly includes pressures and temperatures at the expander inlet and outlet, electric output power and cycle efficency, are analyzed,.

2. TEST BENCH DESCRIPTION

2.1 Experimental testing rig

In this section, the brief schematic diagram of the ORC is shown in Figure 1 (a). The thermodynamics of the ORC is similar to that of the RC. The T-*s* diagram of the thermodynamic processes is shown in Figure 1 (b). The liquid working fluid pressurized by the working fluid pump in the evaporator absorbs the heat from the low temperature heat source and becomes the high pressure superheating vapor.The high pressure and temperature vapor expands in the scroll expander to drive the sychronous generator. The low pressure superheating vapor exhausted from the scroll expander evolves through precooling to condensering to overcooling process in the condenser and is changed into liquid, and then feeds back to the evaporator via the pump.Then this process completes a power circulation.

The major components of the ORC include an evaporator, a scroll expander, a condenser, a working fluid pump, a cooling water tower, a synchronous generator, and other auxiliary equipments. R123 was selected as the working fluid. The exhaust gas from a furnance burning flue gas was utilized to simulate a low grade heat source. A cooling water tower installed in the outdoor cooled down the cooling water from the condenser.

A tube-shell heat exchanger with the heat transfer area of 4.9 m^2 was used as the condenser. And here the superheated working fluid is precooled, condensed and slightly subcooled by the cooling water.

The working fluid pump is a disphragm metering pump and its displacement can be adjusted by its stroke, which allowed controlling the R123 flow rate through the cycle. It could provide the maximum volumetric flow rate and pressure, 800L/h and 2MPa, respectively.

A finned-tube exchanger was selected as the evaporator according to the type of the low temperature heat source, and its total heat transfer area is 14m^2.

An oil-free scroll expander was used for the expansion process, which was elaborately designed for the ORC by Air Squared. Some basic parameters about the scroll expander are listed in Table 1.

An synchronous generator was driven by the scroll expander through belt- pulley couping. The rated outpower and rated rotate speed was 5kW and 1500rpm, respectively. Several bulbs was used to consume eletricity from the generator.

In the test rig, the measured parameters included the pressure and temperature at inlet and outlet of four primary devices, flow rates of the working fluid and the cooling water. In addition, the detailed information of these main measurement instruments is listed in Table 2.

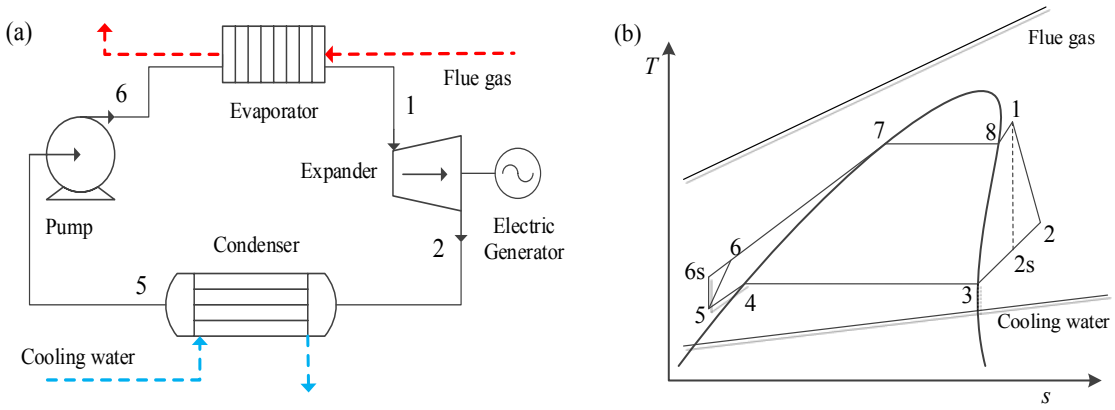

Figure 1: Schematic diagram of (a) the ORC and (b) T-*s* of the ORC

Table 1: Basic parameters of the scroll expander

Parameters	Unit	Value
Type	--	E22H38N4.25(oil-free)
Suction volume	cm^3/r	73.6
Max. rotational speed	rpm	3600
Max. inlet pressure	MPa	1.38
Max. inlet temperature	°C	175
Built-in volume ratio	--	3.5

2.2 Thermodynamic analysis equations

Sevareal diffierent parameters were used for the analysis of the experimental data obtained under the variation of the entering cooling water temperature condition.

Table 2: Main instruments used in the test rig

Parameters	Sensors	Range	Accuracy
Temperature	K-type thermocouple	0-1580K	±0.1K
Pressure	diffused silicon pressure transmitter	0-2.5MPa	±0.2%
Liquid turbine flowmeter	LWGY-2Y	1-10m^3/h	±0.1%
vortex-shedding flowmeter	BF-LUGB32246	15-150m^3/h	±1.5%

The heat absorbed by the working fluid from the low temperature heat source in the evaporator is caculated by Equation (1):

$$Q_{\text{evap}} = m_{\text{wf}}(h_{\text{wf,evap,out}} - h_{\text{wf,evap,in}}) \quad (1)$$

The heat released by the working fluid towards the cooling water in the condenser is caculated by Equation (2):

$$Q_{\text{cond}} = m_{\text{wf}}(h_{\text{wf,cond,in}} - h_{\text{wf,cond,out}}) \quad (2)$$

The working fluid pump consumption is calculated by Equation (3):

$$W_{\mathrm{p}} = m_{\mathrm{wf}}(h_{\mathrm{wf,pump,out}} - h_{\mathrm{wf,pump,in}}) \tag{3}$$

The net electric output power in the test is calculated by Equation (4):

$$W_{\mathrm{net}} = W_{\mathrm{ele}} - W_{\mathrm{p}} \tag{4}$$

where W_{ele} is the eletric power from synchronous generator which is measured by the electrodynamometer as the power consumed on the bulbs.
The cycle electric efficiency is defined by Equation (5):

$$\eta_{\mathrm{ORC}} = \frac{W_{\mathrm{net}}}{Q_{\mathrm{evap}}} \tag{5}$$

The expander isentropic efficency and electric isentropic efficiency, is defined by Equation (6) and (7), respectively:

$$\varepsilon_{\mathrm{s}} = \frac{h_{\mathrm{wf,exp,in}} - h_{\mathrm{wf,exp,out}}}{h_{\mathrm{wf,exp,in}} - h_{\mathrm{wf,exp,out,s}}} \tag{6}$$

$$\varepsilon_{\mathrm{s,ele}} = \frac{W_{\mathrm{ele}}}{m_{\mathrm{wf}}(h_{\mathrm{wf,exp,in}} - h_{\mathrm{wf,exp,out,s}})} \tag{7}$$

The pressure ratio of the expander, is defined by Equation (8):

$$r_p = \frac{P_{\mathrm{exp,in}}}{P_{\mathrm{exp,out}}} \tag{8}$$

2.3 Operating procedure

The ORC rig was tested under varying the cooling water inlet temperature. For this, as the ambient temperature cannot be controlled, different operating conditions had been achieved during the tests by replacing the higher temperature water in the outdoor cooling tower. On the other hand, the flue gas inlet temperature and flow rate kept steady by the flue gas flow rate and air-input amount, and the flow rate of the cooling water was imposed with a fixed frequency set point in the centrifugal water pump. In Table 3, it can be seen that the operating range obtained during the tests for each variable.

Table 3: The operating parameters during the tests

Parameter	Unit	Value
t_{hf}	°C	180
$V_{\mathrm{cf,cond}}$	m^3/h	20
$t_{\mathrm{cf,cond,in}}$	°C	20-45
$P_{\mathrm{exp,in}}$	MPa	0.9-1.1
$P_{\mathrm{exp,out}}$	MPa	0.2-0.35

3. RESULTS AND DISCUSSION

From the experimental data obtained during the tests, an analysis has been conducted, and these results are exposed and discussed in this section.

Figure 2 shows the variation of the pressure and saturation temperature at the condenser inlet under the different cooling water temperature.The pressure was found to be approximately proportional to the entering cooling water temperature. The saturation temperature also increased linearly. This phenomenon was in accordance with the mechanism of heat transfer at the condenser. This was because when the entering cooling water temperature increase and other parameters (for example flow rates of the working fluid and cooling water), the coefficient and area of heat transfer had little effect on. The increase of the pressure at the condenser inlet inevitably results into the increase of the pressure at the expander outlet, and this could have a great effect on the expander performance.

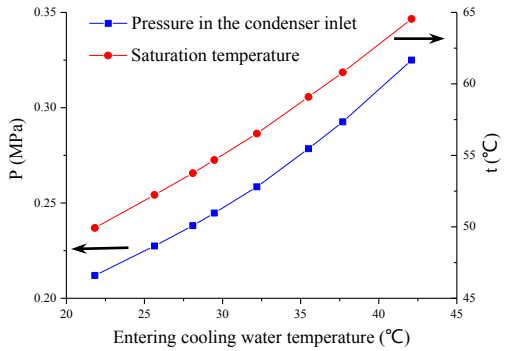

Figure 2: The pressure and saturation temperature at the conderser inlet vs. the enetering cooling water temperature

The variation of vapor pressure, temperature and superheating degree at the expander inlet are shown in the Figure 3. The vapor pressure slightly increased, and the temperature and the degree of superheating decreased with the increase of the entering cooling water temperature.This phenomenon agreed with the scroll expander characterization and the heat transfer mechanism in the evaporator.The highger scroll expander back pressure increased the discharge resistance and resulted in the higher pressure at the expander inlet. The higher vapor pressure meant the higher evaporation temperature in the evaporator. When the temperature and flow rate of the heat source at the evaporator inlet was relatively steady, it meant that the heat-transfer temperature difference decreased. The preheating and evaporating area enlarged, and the superheating area shrinked. The decrease in the superheating area led to the slight decrease of the vapor temperature at the expander inlet. And this process made the superheating degree decrease.

Figure 4 shows the variation of vapor pressure, temperature and superheating degree at the expander outlet. Generally speaking, the vapor temperature at the expander outlet decreased with the entering cooling water temperature, and the vapor pressure increased. So these reduced the superheating degree. These are because the lower heat flux in the evaporator at higher entering cooling water temperature reduced the heat transfer load of the evaporator and the temperature at the expander inlet decreased. Moreover, it is obvious that the supereheating degree at the expander outlet, about 50 °C is relatively high, especially under the lower entering cooling water temperature, and it could be a good choice to recover this part of heat by an internal heat exchanger (IHE). This could benefit to promote the thermal efficiency of the ORC.

The pressure ratio and temperature drop through the scroll expander were calculated and analyzed by using data from tests and is shown in Figure 5. The pressure ratio in Figure 5 is known as external pressure ratio because of the pressure sensors at the tubes connnecting with the expander inlet and outlet. A higher pressure ratio through the expander leads a higher driving force for the expander. When the entering cooling water temperature increased, the relative increase of the vapor pressure at the expander outlet is larger than that at the inlet. This process results in the decrease of the pressure ratio and the pressure, and the output power could decrease.

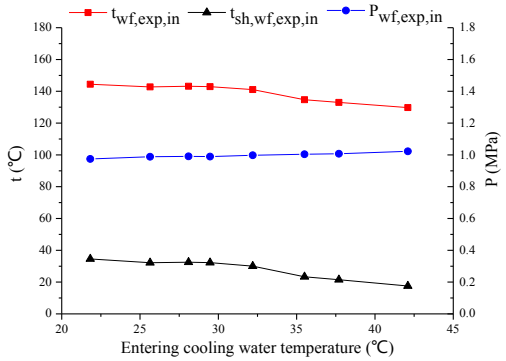

Figure 3: The key operating parameters characterization at the expander inlet during the tests

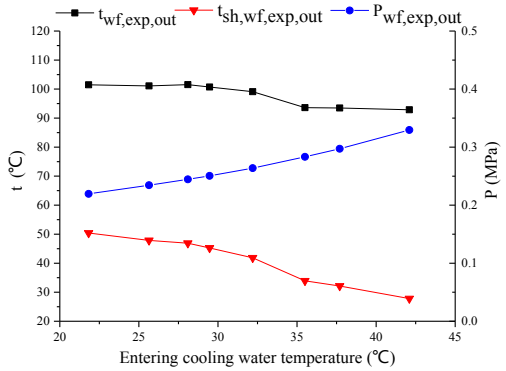

Figure 4: The key operating parameters characterization at the expander outlet during the tests

Based on the collected operating parameters of the expander, the isentropic efficiencies is calculated and shown in Figure 6. It can be shown clearly that firstly the scroll expander isentropic efficiencies slightly descended with the increase in the entering cooling water temperature, increased dramatically, and slight decreased with the further increase in the entering cooling water temperature. The maximum isentropic efficiency was obtained when the entering cooling water temperture was 35.5 °C, and at this time the volume ratio was 3.6, which was very closed to the design value 3.5. In addition, the isentropic efficiencies calculated by Equation (6) was relative too high because the heat losses the scroll expander was not negligible during the test (Declaye S. et al., 2013). So it is hardly expected to elucidate the trends only by means of the experimental results because many factors, such as pressure losses, mechanical friction and leakage, affected the isentropic effiency. Beside the scroll expander electric isentropic efficiency slightly decreased with the increase of the cooling water temperature,seen in Figure 6.

Figure 7 shows the variation of the measured electric power ouput and the cycle thermal efficiency with the increase of the entering cooling water temperature. Definitely, the electric power output and the cycle thermal efficiency decrease with the increase of the entering cooling water temperature. When the entering cooling water temperature increase from 21°C to 42°C, the measured electric power output declines from 2.36kW to 1.54kW, and the cycle thermal efficiency falls from 7.25% to 5.52% as well. These mean that when the entering cooling water temperature increases by 1°C, the electric power output decreases by 1.65%. Under the operating conditions, the electric power output and thermal efficiency decreases, by 34.75% and 23.86%, respectively. It is noted that the relative decrease in the electric power output was more important than that in the thermal efficiency.The reason is likely that the heat absorbed by the working fluid from the heat source at the evaporator also decreases with the entering cooling water temperature, but the variation slowered by lower than that of the electric power ouput. The heat absorbed by the working fluid at the evaporator decreases because the saturation temperature in the evaporator and the enthalpy at the evaporator inlet increase.

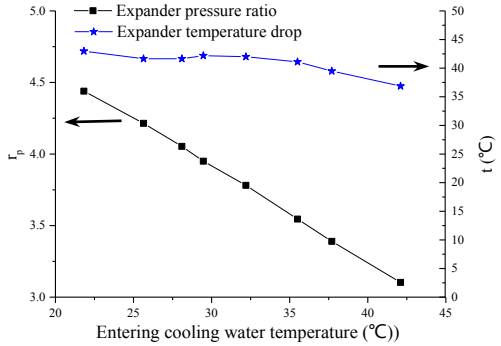

Figure 5: The pressure ratio and temperature drop through the expander during the tests

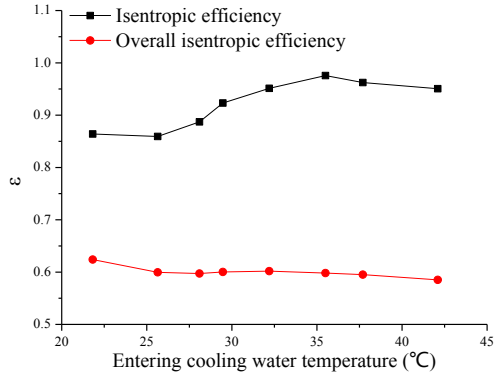

Figure 6: The isentropic efficency characteriztion during the tests

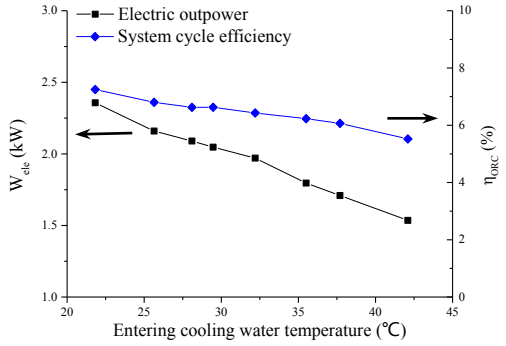

Figure 7: The ORC performance characterization during the tests

6. CONCLUSIONS

Focused on the exploration of kW-scale ORC system, this investigation presents the test and analysis of the operation characteristic and performance of an ORC rig with R123 as the working fluid. A oil-free scroll expander was adopted and then converted heat energy into mechanical power. Operation characteristics were compared under various cooling water temperatures from 22°C to 42°C,which the condensation temperature of the working fluid varied from 50°C to 65°C and the pressure from 0.21MPa to 0.32MPa, respectively.The measured electric power output declined from 2.36kW to 1.54kW, and the cycle thermal efficiency fell from 7.25% to 5.52% as well. Under the operation conditions, the electric output power and thermal efficiency decreased, by 34.75% and 23.86%, respectively.

For the tests, the entering cooling water temperature has a great effect on the electric output power and thermal efficiency by the variation of the pressure at the scroll expander outlet. And this means that the performance of the ORC could be sensitive to the seasonal and daily variation of the ambient temperature and suggest that a proper condensation temperature is important to the design and operation of the ORC system.

NOMENCLATURE

h	enthalpy	kJ/kg
m	mass flow rate	kg/s
P	pressure	MPa
Q	thermal power	kW
r_p	pressure ratio	-
r_v	volume ratio	-
s	entropy	kJ/kg/K
t	temperature	°C
V	volume	m^3
W	power	kW

Greek symbols

ε	efficiency	%
η	efficiency	%
ρ	density	kg/m^3

Subscript

cf	cooling fluid
cond	condenser
ele	electric
evap	evaporator
exp	expander
hf	heat fluid
in	inlet
oc	overcooling
out	outlet
p	pump
s	isentropic
sat	saturation
sh	superheat
wf	working fluid

REFERENCES

Bamgbopa, M., Uzgoren, E., 2013, Numerical analysis of an organic Rankine cycle under steady and variable heat input, *Applied Energy*, vol. 107 : p. 219-228.

Bao, J., Zhao, L., A review of working fluid and expander selections for organic Rankine cycle, *Renewable and Sustainable Energy Reviews*, vol. 24 : p. 325-342.

Bracco, R., Clemente, S., Micheli, D., Reini, M., 2013, Experimental tests and modelization of a domestic-scale ORC (Organic Rankine Cycle), *Energy*, vol. 58 : p. 107-116.

Dai, Y., Wang, J., Gao, L., 2009, Parametric optimization and comparative study of organic Rankine cycle (ORC) for low grade waste heat recovery, *Energy Conversion and Management*, vol. 50 : p. 576–582.

Declaye, S., Quoilin, S., Guillaume, L., Lemort, V., 2013, Experimental study on an opendrive scroll expander integrated into an ORC (Organic Rankine Cycle) system with R245fa as working fluid, *Energy*, vol. 55 : p. 173-183.

Franco, A., Villani, M.,2009, Optimal design of binary cycle power plants for water-dominated, medium-temperature geothermal fields, *Geothermics*, vol. 38 : p. 379–391.

Gu, Z., Sato, H., 2002, Performance of supercritical cycles for geothermal binary design, *Energy Conversion and Management*, vol. 43 : p. 961–971.

Hung, T., 2001, Waste heat recovery of organic Rankine cycle using dry fluids, *Energy Conversion and Management*, vol. 42 : p. 539-553.

Ibarra, M. Rovira, A., Alarcon-Padilla, D., Blanco, J., 2014, Performance of a 5kWe Organic Rankine Cycle at part-load operation, *Applied Energy*, vol. 120 : p. 147-158.

Invernizzi, C., Iora, P., Silva, P.,2007, Bottoming micro-Rankine cycles for micro-gas turbines, *Applied Thermal Engineering*, vol. 27 : p. 100–110.

Joan, B., Jesús, L., Eduardo, L., Silvia, R., Alberto, C., 2008, Modelling and optimisation of solar organic Rankine cycle engines for reverse osmosis desalination, *Applied Thermal Engineering*, vol. 28 : p. 2212–2226.

Lee, Y., Kuo, C., Wang, C., 2012, Transient response of a 50 kW organic Rankine cycle system, *Energy*, vol. 48 : p. 532-538.

Lemort, V., Quoilin, S., Cuevas, C., Lebrun, J., 2009, Testing and modeling a scroll expander integrated into an organic Rankine cycle, *Applied Thermal Engineering*, vol. 29 : p. 309-3102.

Li, J., Pei,G., Ji, J., Bai, X., Li, P., Xia, L., 2014, Design of the ORC (organic Rankine cycle) condensation temperature with respect to the expander characteristics for domestic CHP (combined heat and power) applications, *Energy*, vol. 77 : p. 579-590.

Liu, B., Chien, K., Wang, C., Effect of working fluids on organic Rankine cycle for waste heat recovery, *Energy*, vol. 29 : p. 1207–1217.

Liu, G B., Zhao, Y., Yang, Q., Wang, L., Tang, B., Li, L., 2015, Theoretical and experimental research on scroll expander used in small-scale organic Rankine cycle system, *Journal of Process Mechanical Engineering*, vol. 229 : p. 25-35.

Martina, P., Shane, W., Philip, O., 2010, Evaluation of energy efficiency of various biogas production and utilization pathways, *Applied Energy*, vol. 87 : p. 3305–3321.

Miao, Z., Xu, J., Yang, X., Zou, J., 2015, Operation and performance of a low temperature organic Rankine cycle, *Applied Thermal Engineering*, vol. 75 : p. 1065-1075.

Pei, G., Li, J., Ji, J., 2010, nalysis of low temperature solar thermal electric generation using regenerative organic Rankine cycle, *Applied Thermal Engineering*, vol. 30 : p. 998–1004.

Quoilin, S., Aumann, R., Grill, A., Schuster, A., Lemort, V., Spliethoff, H., 2011, Dynamic modeling and optimal control strategy of waste heat recovery Organic Rankine Cycles, *Applied Energy*, vol. 88 : p. 2183-2190.

Quoilin, S., Broek, M., Declaye, S., Dewallef, P., Lemort, V., 2013,Techno-economic survey of Organic Rankine Cycle (ORC) systems, *Renewable and Sustaunable Energy Reviews*, 2013, vol. 22 : p. 168-186.

Quoilin, S., Lemort, V., Lebrun, J., 2010, Experimental study and modeling of an organic Rankine cycle using scroll expander, *Applied Energy*, vol. 87 : p. 1260-1268.

Saleh, B., Koglbauer, G., Wendland, M., Fischer, J., 2007, Working fluids for lowtemperature organic Rankine cycles, *Energy*, vol. 32 : p. 1210-1221.

Song, P., Wei, M., Shi, L., Danish, S., Ma, C., 2015, A review of scroll expanders for organic Rankine cycle systems, *Applied Thermal Engineering*, vol. 75 : p. 54-64.

Srinivasan, K., Mago, P., Krishnan, S.,2010, Analysis of exhaust waste heat recovery from a dual fuel low temperature combustion engine using an organic Rankine cycle, *Energy*, vol. 35 : p. 2387-2399.

Tchanche, B., Lambrinos,Gr., Frangoudakis, A., Papadakis, G., 2011, Low-grade heat conversion into power using organic Rankine cycles – A review of various applications, *Renewable and Sustainable Energy Reviews*, vol. 15 : p. 3963-3979.

Tchanche, B., Petrissans, M., Papadakis, G., 2014, Heat resource and organic Rankine cycle machine, *Renewable and Sustaunable Energy Reviews*, vol, 39 : p. 1185-1199.

Tung, T., Wang, S., Kuo, C., Pei, B., Tsai, K., 2010, A study of organic working fluids on system efficiency of an ORC using low-grade energy sources, *Energy*, vol.35 : p. 1403-1411.

Vasile, M., 2014, Power generation with ORC machines using low-grade waste heat or renewable energy, *Applied Thermal Energineering*, vol. 69 : p. 143-154.

Velez, F., Segovia, J., Martin, C., Antolin G., Chejne F., Quijano,A., 2012, A technical, economical and market review of organic Rankine cycles for the conversion of low-grade heat for power generation, *Renewable and Sustainable Energy Reviews*, vol. 16 : p. 4175-4189.

Wei, D., Lu, X., Lu, Z., Gu, J., 2008, Dynamic modeling and simulation of an Organic Rankine Cyle (ORC) system for waste heat recovery, *Applied Thermal Engineering*, vol. 28 : p. 1216-1224.

Zhou, N., Wang, X., Chen, Z., Wang, Z., 2013, Experimental study on Organic Rankine Cycle for wate heat recovery from low-temperature flue gas, *Energy*, vol. 55 : p. 216-225.

Ziviani, D., Beyene, A., Venturini, M., 2014, Advances and challenges in ORC systems modeling for low grade thermal energy recovery, *Applied Energy*, vol. 121: p. 79-95.

ACKNOWLEDGEMENT

The authors want to acknowledge the financial support by National Fundamental Research Program 973 project (2014CB249201) "Research on the stability of complex energy system integrated natural gas and renewable energy" and ENN-Tongji Institute for Advanced Clean Energy under the project "Research on the key technologies in power generation from low-grade waste heat".

ADVANCED THERMODYNAMIC MODEL OF ORGANIC RANKINE CYCLE

Parsa Mirmobin*, Chris Sellers

Calnetix Technologies, LLC
16323 Shoemaker Ave, Cerritos, CA 90703
USA
e-mail: pmirmobin@calnetix.com, csellers@calnetix.com
Web page: http://www.calnetix.com

* Corresponding Author

ABSTRACT

Low-grade heat from geothermal or industrial processes is an eco-friendly resource for electric power production. The Organic Rankine Cycle (ORC) has become a popular means to exploit these energy sources. This growing popularity has resulted in the need for rapid, accurate simulation tools for plant design and specification.

In this paper, an advanced, steady state, thermodynamic model of an ORC is developed. The model is composed of several sub components including: an evaporator and condenser, centrifugal pump, turbine expander, and pipe elements. Each of these components is modeled independently and their inputs/outputs are combined together to form the overall system.

The model is developed using simple programming language (VBA) in excel and utilizes NIST Refprop for calculation of state properties. This medium was chosen because of its simplicity and low cost; however, the general model structure can easily be implemented in any programming language. The model predictions are validated against field data collected from ORC systems operating at several evaporating and condensing conditions.

1. INTRODUCTION

Rising energy costs, the demand for improved system efficiency, and government programs to reduce plant emissions have led to a surge in the popularity of the Organic Rankine Cycle (ORC.) Advanced modeling techniques are required to estimate the electrical power produced by an ORC system and to choose appropriate system components. The demand for simulation tools which can quickly and cheaply accomplish these tasks has grown in lockstep with ORC demand.

Commercially available process simulators (e.g. ASPEN HYSYS, CHEMCAD) are powerful but often expensive and cumbersome to work with. These “all encompassing” simulators are excellent for plant designs yet lack modeling for key components necessary to develop a high fidelity ORC system simulator. The following paper will describe the development of a low cost, flexible model written in Excel VBA. The model has been used to design over 100 plants and shows excellent agreement with field installations.

The model is divided into three main sections:
1) The working fluid loop
2) The evaporator
3) The condenser

The working fluid loop model is composed of several component models arranged in series to represent the ORC system. The following sections will describe each component model in detail.

2. MODELING METHODOLOGY

2.1 Pipe Section Model

The pipe model estimates the pressure and temperature losses experienced by the fluid as it flows through a pipe section. It links the major components (e.g. pump, evaporator, etc.) together in the working fluid loop model. The inputs are temperature, pressure, and mass flow and the outputs are temperature and pressure losses. Additionally there are several descriptive inputs: roughness, height, length, diameter, overall heat transfer coefficient, and ambient temperature. The pressure drop is found using the Darcy-Weisbach equation.

$$\Delta P = 8\pi f L \frac{\dot{m}^2}{\rho_{in,pipe} D^3} \tag{1}$$

The inlet density in Equation (1) is calculated from the inlet temperature and pressure. The Darcy friction factor in Equation (1) is found from an iterative solution to the equation below, Colebrook (1939).

$$\frac{1}{\sqrt{f}} = -2\log_{10}\left(\frac{\epsilon}{3.7D} + \frac{2.51}{\mathrm{Re}\sqrt{f}}\right) \tag{2}$$

The Reynolds number in Equation (2) is calculated using the inlet density and viscosity. These properties are calculated at the inlet temperature and pressure. Treating the pipe section as a cylinder with 1-D convective heat transfer and a constant ambient temperature, the temperature drop across the pipe section is calculated by (Incropera and DeWitt 2002):

$$\Delta T = (T_{amb} - T_{in}) e^{-\frac{\pi UDL}{\dot{m} c_p}} \tag{3}$$

The overall heat transfer coefficient in Equation (3) is adjusted based on test data of a production ORC. The specific heat is calculated at the pipe inlet temperature and pressure.

The pressure loss of system fittings within the working fluid loop (i.e. filters, valves, etc.) may be modeled as an equivalent length of pipe for a given diameter.

2.2 Pump Model

The pump model simulates the operation of a centrifugal pump as utilized in the Calnetix ORC product. The inputs are inlet temperature, inlet pressure, mass flow and outlet pressure. The outputs are the exit temperature and motor power. The calculation begins with determining the inlet density, enthalpy, and entropy at the inlet temperature and pressure. Next the volumetric flow and hydraulic head are calculated by:

$$G = \frac{\dot{m}}{\rho_{in}} \tag{4}$$

$$\Delta H = \frac{(P_{out} - P_{in})}{\rho_{in} g} \tag{5}$$

The values for volumetric flow rate and hydraulic head are input into a table map which outputs the pump efficiency, η_{pump}.

$$\eta_{pump} = MAP(\Delta H, G) \tag{6}$$

Next the ideal outlet enthalpy is calculated at the inlet entropy and outlet pressure. The true pump outlet enthalpy is calculated using:

$$h_{out} = \eta_{pump}\left(h_{out,s} - h_{in}\right) + h_{in} \tag{7}$$

Combining the output from Equation (7), the mass flow, and inlet enthalpy, the pump power is found using:

$$W_{pump} = \dot{m}(h_{out} - h_{in}) \tag{8}$$

Finally the outlet temperature may be calculated at the outlet pressure and outlet. The MAP used by Equation (6) was developed experimentally from the centrifugal pump model used in Calnetix ORC products. Maps for other types of pumps may be developed in the same manner.

2.3 Integrated Power Module (IPM)

The integrated power module, IPM, plays a pivotal role in the working fluid loop model by setting the system mass flow and determining the grid power output. The Calnetix IPM consists of a nozzle, turbine wheel, rotor, and generator stator. The rotor/wheel assembly is levitated by magnetic bearings within the generator stator, see Figure 1 below.

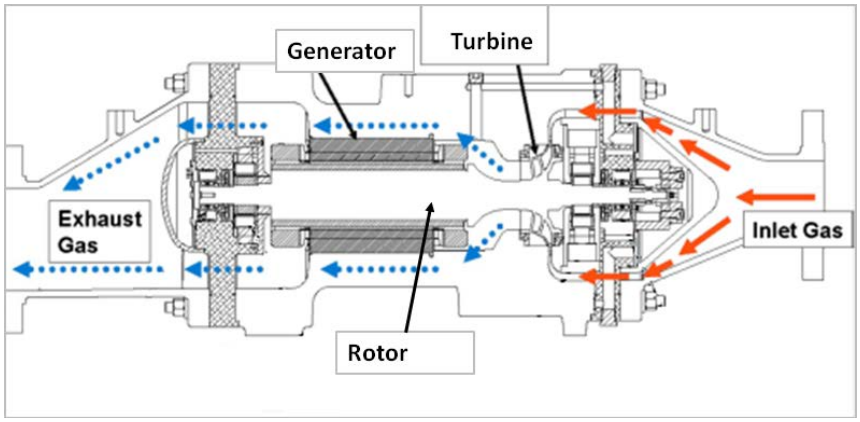

Figure 1: Calnetix IPM

The working fluid flows into the nozzle, through the turbine, over the rotor, and around the generator. Heat from turbine efficiency losses, rotor windage, and generator efficiency losses are added into the fluid stream increasing the exit enthalpy. These losses are estimated using table maps and correlations developed using CFD and empirical test data.

The inputs to the IPM model are inlet temperature, inlet pressure, outlet pressure, and turbine speed. Additionally there are several internal variables used from the previous calculation. These values are the static speed of sound at the nozzle inlet a^*, the static density at the nozzle inlet ρ^*, the dimensionless enthalpy drop across the wheel, the dimensionless wheel rotation speed, and the flow parameter at the wheel exit. The outputs are grid power, temperature at the IPM outlet, and working fluid loop mass flow.

The model calculation is carried out in several steps. Initially the internal input variables are input into map files which represent the turbine operation. The outputs are the isentropic efficiency (η_T) of the nozzle turbine system, the dimensionless inlet flow parameter (ϕ_{in}), and the turbine exit swirl angle (θ.)

$$\eta_T = MAP\left(\frac{\Delta h_s}{(a^*)^2}, \frac{N}{a^*}\right) \tag{9}$$

$$\phi_{in} = MAP\left(\frac{\Delta h_s}{(a^*)^2}, \frac{N}{a^*}\right) \tag{10}$$

$$\theta = MAP\left(\frac{\Delta h_s}{(a^*)^2}, \frac{N}{a^*}\right) \tag{11}$$

Next the turbine exit swirl angle and wheel exit flow parameter are used to find the percentage pressure drop across the generator, $\Delta P_{Gen}\%$.

$$\Delta P_{Gen}\% \ = MAP(\theta, \phi_{out}) \tag{12}$$

The pressure at the wheel outlet is determined from:

$$P_{out} = (1 + \Delta P_{Gen}\%) P_{out,IPM} \tag{13}$$

Next the entropy and enthalpy at the nozzle inlet are calculated at the IPM inlet temperature and pressure. The ideal enthalpy at the wheel exit is calculated at the wheel outlet pressure and entropy at the nozzle inlet. The true enthalpy at the wheel exit is calculated by combining values from:

$$h_{out} = h_{in} - \eta_T\left(h_{in} - h_{out,s}\right) \tag{14}$$

Next the system mass flow is calculated from the inlet flow parameter (ϕ_{in}), static speed of sound at the nozzle inlet (a^*), and static density at the nozzle inlet (ρ^*). The model accounts for turbine leakage as follows:

$$\dot{m}_T = (1 - \alpha)\dot{m} \tag{15}$$

Combining the values from Equations (14), (15), and the nozzle inlet enthalpy, the turbine work may be calculated as:

$$W_T = \dot{m}_T(h_{in} - h_{out}) \tag{16}$$

The generator converts the turbine work calculated in Equation (16) to electrical power. A portion of the mechanical work is lost due to viscous effects acting on the rotor and wheel outer surfaces. These loses are called "windage" losses and are calculated through the aid of correlations from Norris (1970) and Vrancik (1968.) Additionally there are electrical losses due to resistance in the copper windings of the stator and iron losses due to changes in the magnetic field. An energy balance across the wheel/rotor control surface results in:

$$W_{Gen} = W_T - Q_{Loss} - W_{windage} \tag{17}$$

Where Q_{loss} is the heat lost from generator due to inefficiencies. Equation (17) may be simplified by introducing the generator efficiency, η_{Gen}, which relates the portion of turbine work lost due to generator efficiencies as:

$$\eta_{Gen} = \frac{W_T - Q_{\,Loss}}{W_T} \tag{18}$$

Thus combining Equations (17) and (18) then generator work may be expressed as (19):

$$W_{Gen} = \eta_{Gen} W_T - W_{windage} \tag{19}$$

The generator efficiency is found from a map lookup with inputs turbine work and generator frequency. The final step in the grid power calculation is to account for losses due to inefficiencies in the electrical power rectification and conversion process. These losses are accounted for with the power electronics efficiency number, η_{PE}, and related to the generator power and grid power by:

$$W_{PE} = \eta_{PE} W_{Gen} \tag{20}$$

To determine the temperature at the exit of the IPM, the enthalpy at the exit of the generator must be determined. This is found by forming an energy balance for the control surface surrounding the fluid flowing into and out of the generator:

$$\dot{m}\left(h_{out,Gen} - h_{in,Gen}\right) = Q_{Loss} + W_{windage} \tag{21}$$

The enthalpy at the generator inlet is found from a mass weighted average of the enthalpy exiting the turbine and leakage enthalpy. Using Equation (15) and values for the wheel outlet enthalpy and nozzle inlet enthalpy:

$$h_{in,Gen} = (1-\alpha)h_{out} + \alpha h_{in} \tag{22}$$

Thus using Equations (18), (21), and (22) and solving for the generator outlet enthalpy, we arrive at:

$$h_{out,Gen} = (1-\alpha)h_{out} + \alpha h_{in} + \frac{\left[(1-\eta_{Gen})W_T + W_{windage}\right]}{\dot{m}} \tag{23}$$

Finally the exit temperature of the wheel is a function of the IPM outlet pressure and the enthalpy. The Calnetix ORC utilizes a reaction type turbine, thus the model is readily compatible with different types of reaction turbines. With appropriate map files, the model may be modified to accommodate other types of turbines.

2.4 Updating IPM Model Internal Variables

Once the calculations from section 2.3 are completed, the internal variables are updated for the next calculation loop. These values converge after several iterations. The first step in the update process is to calculate the static speed of sound and static density at the nozzle inlet.

The initial speed of sound is calculated at the nozzle inlet temperature and pressure. Using the value for enthalpy at the nozzle inlet found earlier, an intermediary enthalpy is found. by subtracting the square of the initial speed of sound:

$$h_i = h_{in} - \frac{a_i^2}{C} \tag{24}$$

Next the speed of sound is recalculated using the intermediary enthalpy, h_i, and the nozzle inlet entropy:

$$a_i = a(h_i, s_{in}) \tag{25}$$

The new speed of sound value is placed back into Equation (24) and the process is repeated until the value for a_i converges. This converged value is the static speed of sound at the nozzle inlet, $a^*_{in,nozzle}$. The final value of h_i is the static enthalpy at the nozzle inlet, h*. The static density is now calculated from the value h* and the entropy at the nozzle inlet.

Next the values for the static speed of sound at the nozzle inlet, nozzle inlet enthalpy, ideal nozzle exit enthalpy, and rotor speed are used to calculate the quantities $\Delta h_s/(a^*)^2$ and N/a^*. A new inlet flow parameter is calculated using the mass flow calculated by the IPM model. Finally the flow parameter at the wheel exit may be calculated using the procedure described above with the temperature, pressure, enthalpy, and entropy at the wheel exit.

2.5 Combining the Working fluid loop Components

Integrating the working fluid loop components is depicted graphically in Figure 2 below:

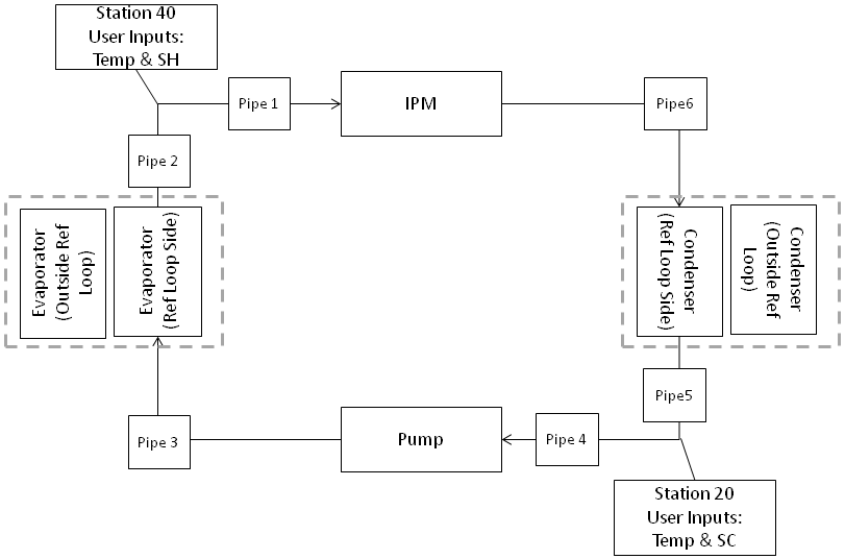

Figure 2: Working fluid loop Diagram

The overall user inputs to the working fluid loop model are temperature at station 40, superheat at station 40, temperature at station 20, and sub-cooling at station 20. From these values the pressure is calculated at stations 40 and 20 respectively. The pressure drop across each pipe element is added or subtracted from the P_{40} and P_{20}. Thus the pressure inputs to each component are calculated by:

$$P_{in,IPM} = P_{40} - \Delta P_1 \tag{26}$$

$$P_{\text{out,IPM}} = P_{20} + \Delta P_5 + \Delta P_{\text{Cond}} + \Delta P_6 \tag{27}$$

$$P_{\text{in,Pump}} = P_{20} - \Delta P_4 \tag{28}$$

$$P_{\text{out,Pump}} = P_{40} + \Delta P_2 + \Delta P_{\text{Evap}} + \Delta P_3 \tag{29}$$

The inlet temperature to each component is found using the temperature loss for each pipe section with Equation (3). In some cases the temperature loss is calculated in reverse and added to the user input temperature. The input/output temperature values are updated with each successive calculation of the working fluid loop. Convergence is achieved after several iterations.

2.6 Evaporator and Condenser Models

The evaporator and condenser models estimate the source mass flow and heat exchanger surface area needed. The user inputs are inlet temperature and pressure of the source, source side pressure loss coefficient, working fluid side pressure loss coefficient, exit temperature of the source, and overall heat transfer coefficient. Additionally these models take inputs of working fluid inlet temperature/pressure, outlet temperature/pressure, and heat exchanger duty which are all calculated by the working fluid loop model. The pressure drop on the source and working fluid sides are calculated by the minor loss equation:

$$P_{out} = P_{in} - \xi \frac{\dot{m}^2}{\rho_{in}} \tag{30}$$

The inlet density in Equation (30) is calculated at the inlet temperature and pressure. The pressure loss coefficient, ξ, is typically given by the heat exchanger manufacturer. The heat exchanger duty is calculated from the inlet enthalpy, outlet enthalpy, and mass flow on the working fluid side by:

$$Q = \dot{m}(h_{in} - h_{out}) \tag{31}$$

The source mass flow is calculated by dividing the heat exchanger duty calculated by Equation (31) by the enthalpy change between the inlet and outlet of the source:

$$\dot{m}_{Source} = \frac{Q_{HEX}}{\left(h_{out,Source} - h_{in,Source}\right)} \tag{32}$$

The inlet enthalpy for the source is calculated at the source inlet temperature and pressure. The outlet enthalpy is calculated from the source outlet temperature and pressure. The source outlet pressure is updated iteratively using Equation (30), (31), and (32).

The heat exchanger surface area is found using a discrete integration process. The process begins by determining the enthalpy and pressure step sizes for both the source side and working fluid sides of the evaporator and condensing with:

$$\Delta h = \frac{h_{out} - h_{in}}{k} \tag{33}$$

$$\Delta P = \frac{P_{out} - P_{in}}{k} \tag{34}$$

From Equations (33) and (34), a discretized pressure and enthalpy field for the source and working fluid sides is defined by:

$$h_i \in \{h_{in} + i\Delta h\}\, for\ i = 0,1,2,\dots,k \tag{35}$$

$$P_i \in \{P_{in} + i\Delta P\}\, for\ i = 0,1,2,\dots,k \tag{36}$$

By Equation (36)(37), the pressure field is evenly spaced with the enthalpy change for both the source and working fluid sides. The discrete temperature field may be calculated from each enthalpy and pressure pair as:

$$T_i \in \{T(h_i, P_i)\}\, for\ i = 0,1,2,\dots,k \tag{37}$$

The heat flux through each heat exchanger section is defined for both the source and working fluid sides as:

$$Q_{\mathrm{i}} \in \{(1/\dot{m})(h_{\mathrm{i}} - h_{\mathrm{i}-1})\}\, for\ i = 1,2,\dots,k \tag{38}$$

Next the log mean temperature difference for each section is found from:

$$\mathrm{T}_{\mathrm{i,LMD}} \in \left\{ \frac{\left(T_{i,Source} - T_{k-\mathrm{i},Ref}\right) - \left(T_{i-1,Source} - T_{k-\mathrm{i}-1,Ref}\right)}{\ln \frac{\left(T_{\mathrm{i},Source} - T_{k-\mathrm{i},Ref}\right)}{\left(T_{\mathrm{i}-1,Source} - T_{k-\mathrm{i}-1,Ref}\right)}} \right\} \tag{39}$$

The index "i" in Equation (39) takes integer values from to 0 to k. Using Equations (38) and (39) and the relationship between heat flux, the overall heat transfer coefficient, heat exchanger surface area, and log mean temperature difference:

$$(UA)_{\mathrm{i}} \in \left\{Q_{\mathrm{i}}/\mathrm{T}_{i,LMD}\right\} for\ i = 1,2,\dots,k \tag{40}$$

Finally the heat exchanger surface area is found by summing the values in Equation (40) and dividing by the user input overall heat transfer coefficient, U.

$$A = \frac{1}{U}\sum_{i=1}^{k}(UA)_i \tag{41}$$

The model described above is intentionally simple for the following reasons:

1) The model is iterated many times to arrive at the desired set point. A simpler component model reduces the overall computation time.
2) Complex models require parameters such as local friction factor which need to be determined experimentally or analytically across a broad range of fluid conditions. This data is often unavailable from heat exchanger manufacturers.

3. CASE STUDIES

The model described above is used extensively by Calnetix to assess new applications as well as validate unit performance at specific operating conditions. The data tabulated below is from 4 distinct applications in the field. The applications are all commercial, utilizing generated power within the facility or exporting power to local utilities. The working fluid in these cases was R245fa refrigerant. The model output in general shows good agreement with field data. The Gross Efficiency is defined as the gross electrical power exported to the grid divided by the rate of heat is transferred to the working fluid.

Table 1: Saturated Steam Plant- Japan

	Model	Field data
Heat Source Temp (°C)	145	145
Heat Source Pressure (Bar)	1.95	1.8
Heat Source Flow Rate (kg/s)	0.35	0.35
Coolant Temperature (°C)	26	26
Coolant Pressure (Bar)	1.38	No Value
Turbine Inlet Temperature (°C)	122	119
Turbine Inlet Pressure (Bar)	16.4	15.5
Condenser Exit Temperature (°C)	29	29.5
Condenser Exit Pressure (Bar)	1.9	1.95
Gross Power Output (kW)	100.7	101
Gross Efficiency (%)	11.1	11.0

Table 2: Hot Water from an Incineration Plant- Japan

	Model	Field data
Heat Source Temp (°C)	98.7	98.7
Heat Source Pressure (Bar)	2.9	2.9
Heat Source Flow Rate (kg/s)	7.25	12.28
Coolant Temperature (°C)	20.2	20.2
Coolant Pressure (Bar)	1.4	1.4
Turbine Inlet Temperature (°C)	67.8	67.8
Turbine Inlet Pressure (Bar)	4.9	4.9
Condenser Exit Temperature (°C)	21	21
Condenser Exit Pressure (Bar)	1.47	1.47
Gross Power Output (kW)	100.8	124.7

Gross Efficiency (%)	7.0	6.7

Table 3: Geothermal Low Pressure Steam- Japan

	Model	Field data
Heat Source Temp (°C)	125	128
Heat Source Pressure (Bar)	2.1	2.9
Heat Source Flow Rate (kg/s)	0.47	0.45
Coolant Temperature (°C)	25	24
Coolant Pressure (Bar)	1.3	1.5
Turbine Inlet Temperature (°C)	120	126
Turbine Inlet Pressure (Bar)	17.3	18.2
Condenser Exit Temperature (°C)	31.4	29.9
Condenser Exit Pressure (Bar)	2.06	1.99
Gross Power Output (kW)	125	125
Gross Efficiency (%)	12	12

Table 4: Flue Gas from Clay Factory Using Intermediate Oil Loop- Europe

	Model	Field data
Heat Source Temp (°C)	148	160
Heat Source Pressure (Bar)	7	No Value
Heat Source Flow Rate (kg/s)	20.8	20
Coolant Temperature (°C)	19	28
Coolant Pressure (Bar)	1	1
Turbine Inlet Temperature (°C)	128	130
Turbine Inlet Pressure (Bar)	18.7	18.6
Condenser Exit Temperature (°C)	25.7	30
Condenser Exit Pressure (Bar)	1.8	2.8
Gross Power Output (kW)	125	125
Gross Efficiency (%)	12.6	12.4

4. CONCLUSION

The development of an advanced thermodynamic model of an Organic Rankine Cycle was discussed. The model is implemented in Excel VBA script and uses Refprop as an equation of state. Each major component of the ORC is modeled in detail and combined together to form the completed system. The model obviates the need for complex and expensive process simulation tools, and delivers a highly accurate output. This affords a high degree of confidence to Calnetix and its customers when selecting balance of plant components and arriving at sensitive capital investment decisions.

NOMENCLATURE

α	turbine seal leakage	(%)
ϵ	roughness height	(m)
θ	swirl angle	(°)
η	efficiency	(%)
ξ	minor loss coefficient	(MPa-m^3-s^2/kg^3)
ρ	density	(kg/m^3)
Φ	flow parameter	(m^2)
A	surface area	(m^2)
a	speed of sound	(m/s)
C	unit conversion constant	(J-s^2/kg-m^2)
c_p	specific heat	(J/kg-°C)

D	diameter	(m)
f	Darcy friction factor	(-)
G	volumetric flow rate	(m^3/s)
g	gravitational constant	(m/s^2)
H	hydraulic head	(m)
h	specific enthalpy	(J/kg)
k	number of heat exchanger sections	(-)
L	length	(m)
MAP	value lookup table	(-)
$\dot{m}$	mass flow rate	(kg/s)
N	rotational speed	(RPM)
P	pressure	(MPa)
Q	heat	(Watts)
Re	Reynolds number	(-)
T	temperature	(°C)
U	overall heat transfer coefficient	(W/m^2-°C)
W	work	(Watts)

Subscript

*	static condition
amb	ambient
Cond	condenser
Evap	evaporator
Gen	generator
i	index integer
in	inlet condition
IPM	integrated power module
LMD	log mean difference
Loss	heat loss
out	outlet condition
PE	condition or item related to the power electronics
pipe	condition or item related to the pipe model
Ref	working fluid side of the condenser or evaporator
s	isentropic
Source	source side of the condenser or evaporator
T	condition or item related to the turbine
Windage	energy loss associated with windage

REFERENCES

Colebrook, C.F., 1939, "Turbulent flow in pipes, with particular reference to the transition region between smooth and rough pipe laws", Journal of the ICE, vol. 11, no. 4: P.133-156

Incropera, F.P., De-Witt, D.P., 2002, Fundamentals of Heat and Mass Transfer5th ed., John Wiley & Sons, New York, 981p

Hawkins, L., Zhu, L., Blumber, E., Mirmobin, P., and Erdlac Jr., R., 2012, "Heat-To-Electricity with High-Speed Magnetic Bearing/Generator System", *2012 GRC Annual Meeting*

Norris R., Buckland F., Fitzroy N., General Electric Company Corporate Research and Development, 1970, Heat Transfer and Fluid Flow Data Book, G408.3, G408.5

Vrancik, J., 1968, "Prediction of Windage Power Loss in Alternators", National Aeronautics and Space Administration, TN D-4849

Yuksek, E., Mirmobin P., 2015, “Electricity Generation from Large Marine Vessel Engine Jacket Water Heat", *ASME Power Energy 2015*

THERMAL EXPANSION AND STRUCTURAL BEHAVIOR OF A CLOSED LOOP THERMAL WIND TUNNEL FOR ORC FLUIDS

Maximilian Passmann, Karsten Hasselmann,
Felix Reinker, Stefan aus der Wiesche

Department of Mechanical Engineering
Muenster University of Applied Sciences,
48565 Steinfurt, Germany
e-mail: f.reinker@fh-muenster.de

ABSTRACT

The Organic Rankine Cycle (ORC) offers great potential for recovering waste heat and using low-temperature sources for power generation. However, the ORC thermal efficiency is limited by the relatively low temperature level, and therefore, designing ORC components with high efficiencies and minimized losses is of major importance. The use of organic fluids creates new challenges for turbine and component design, due to dense gas behavior and the low speed of sound leading to high Mach numbers.

Computational fluid dynamics (CFD) offers great potential for design and optimization of ORC components. But the employment of CFD methods requires careful validation by means of experimental data. For ORC components, such an experimental approach requires the use of specially designed wind tunnels for organic vapors.

The closed wind tunnel, presented in this contribution, is designed as a pressure vessel system to allow for pressure levels up to p = 10 bars and temperatures up to θ = 180°C. The investigation of heavy weight organic fluid flows at superheated state also needs for higher temperature levels. Heating and cooling units are therefore used to achieve steady state conditions inside of the test section.
In this contribution the design process of a closed loop wind tunnel is presented, focusing on the thermal expansion of the system. Thermal finite element method (FEM) analysis is applied to calculate temperature distributions, considering thermal loads and heat losses of the facility. Based on these data, linear FEM analysis is used to investigate thermal stress in the closed loop vessel system. Supporting points and critical zones are assessed in a more detailed analysis. A method to analyse the transient behavior of the structure and to determine allowable heating rates during heat-up phase is presented.

The testing facility is part of a large research project aiming at obtaining loss correlations for performance predictions of ORC turbines and processes, which is supported by the German Ministry for Education and Research (BMBF).

1. INTRODUCTION

The Organic Rankine Cycle represents a viable technical approach for conversion of low temperature sources, like waste heat or geothermal reservoirs, to electricity or to combined electricity and heat. An ORC process consists of a Rankine cycle employing an organic compound as working fluid. This technology is usually preferred over steam cycles, due to the higher thermodynamic cycle efficiency, in case of low-grade heat sources [1, 4, 9]. The design and performance prediction of steam and gas turbines have been initially based on measurements and numerical simulations of flow through two-dimensional cascades of blades [5]. In case of ORC turbines and related fluids, such an approach requires the use of specially designed wind tunnels and dedicated instrumentation. The Laboratory for Thermal and Power Engineering of Muenster University of Applied Sciences, Germany is building up

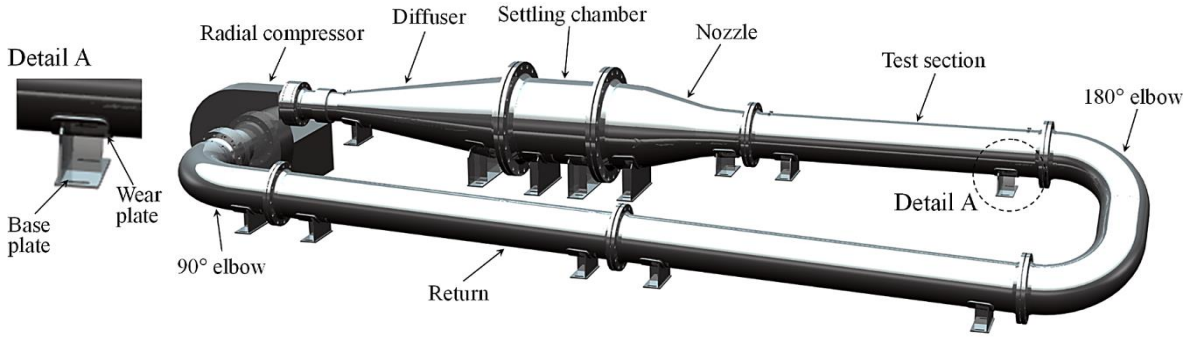

Figure 1: 3D model of the closed circuit wind tunnel for ORC fluids.

a closed loop wind tunnel for investigating real gas effects in dense gas flows of organic vapors in nozzles and axial turbine blades.

The basic test section, as shown in Fig. 1, acts as a barrel-type casing allowing for different inserted test sections like simple nozzle geometries or axial turbine blade test sections. The maximum Mach number upstream the blade section will lie in the transonic region (M = 1). Shadow schlieren visualization utilizing a high speed camera will be used for qualitative flow characterization in the test section. For local flow field investigation Laser Doppler Anemometry will be used. Besides optical measurements, classical pneumatic measurement techniques will also be performed, as for instance to measure the pressure field alongside the nozzle axis.

Subject of the present contribution is the examination of thermal expansion and structural behavior of the facility by means of structural and thermal linear finite element analysis. Fig. 1 shows a 3D model of the closed circuit wind tunnel in its current development status. To allow for operating conditions of up to p = 10 bars internal pressure at θ = 180°C, all pressurized components are laid out according to pressure rating PN16 [13]. The support saddles (cf. Fig. 1, detail A) are designed on the basis of DIN 28080 [6] with a wall thickness of 10 mm for the wear plate and 8 mm for all other components. The entire unit rests on a rigid steel subframe (not shown in Fig. 1). The saddle base plates act as bearing areas. Sliding plates will be installed between subframe and base plates, to reduce friction forces and to avoid thermal bridging to the ground.

The dimensions of the wind tunnel are approximately 7200 mm in length and 1600 mm in width. The 180° elbow is angled at 30°, resulting in a maximum level difference of 610 mm between test section and return. An overview of the dimensions is given in Tab. 1.

The first part of this paper focuses on the overall bearing concept of the unit, taking into account thermal and structural influences. A simplified shell model is used to investigate three different bearing concepts under steady-state conditions. In the second part, temperature distribution and thermal stress, occurring during heat-up phase, will be addressed based on the example of the settling chamber.

Table 1: Dimensions of the closed circuit wind tunnel for ORC fluids.

Component	**Length**	**Midsurface diameter**		**Wall thickness**
	l [mm]	d_{min} [mm]	d_{mout} [mm]	s [mm]
Diffuser	1745	216.1	601.2	8.8
Settling chamber	690	601.2		8.8
Nozzle	1073	601.2	318.5	8.8
Test section	2067	318.5		7.1
Return	5454.3	318.5		7.1
	Radius	**Midsurface diameter**	**Length in x-direction**	**Length in y-direction**
	r [mm]	d_m [mm]	l_x [mm]	l_y [mm]
90° elbow	486	318.5	648	486
180° elbow	486	318.5	1221	564

2. FINITE ELEMENT ANALYSIS OF THE STATIC SHELL MODEL

2.1 Finite Element Model

Linear finite element analysis utilizing NX Nastran version 8.5 (SOL101) [10] is used to investigate expansion and stress distribution resulting from both, thermal and structural loads under steady-state conditions. Based on the 3D solid model of the wind tunnel, as depicted in Fig. 1, a midsurface model was generated. Mapped meshing was utilized to mesh the midsurface with 8-noded shell elements (CQUAD8). For singly curved shells like cylinders this element type performs better than the 4-noded CQUAD4 element [10]. The coordinate system and calculated stresses for this type of element are shown in Fig. 2. CQUAD8 elements are isoparametric with four corner and four mid-side grid points. Stresses, as shown in Fig. 2, are evaluated at the centroid and at the vertices. For plane strain analysis the von Mises equivalent stress σ_{VFEM} is defined by:

$$\sigma_{VFEM} = \sqrt{\frac{1}{2} \cdot \left[\left(\sigma_x - \sigma_y\right)^2 + \left(\sigma_y - \sigma_z\right)^2 + \left(\sigma_z - \sigma_x\right)^2 \right] + 3 \cdot {\tau_{xy}}^2} \qquad (1)$$

with the stress component in z-direction being $\sigma_z = 0$. A thorough description of the finite element method and theoretical backgrounds concerning shell elements can be found in [3].

Multiple mesh collectors were generated, to account for different wall thicknesses and materials in pipe sections and support saddles. The meshed model is shown in Fig. 3. The pressure vessel is made from high-alloy austenitic steel (X5CrNi18-10), whereas the support saddles are made from construction steel. For both materials all physical and mechanical properties were implemented into NX as temperature dependent values [12]. Typical values are given in Section 2.2.

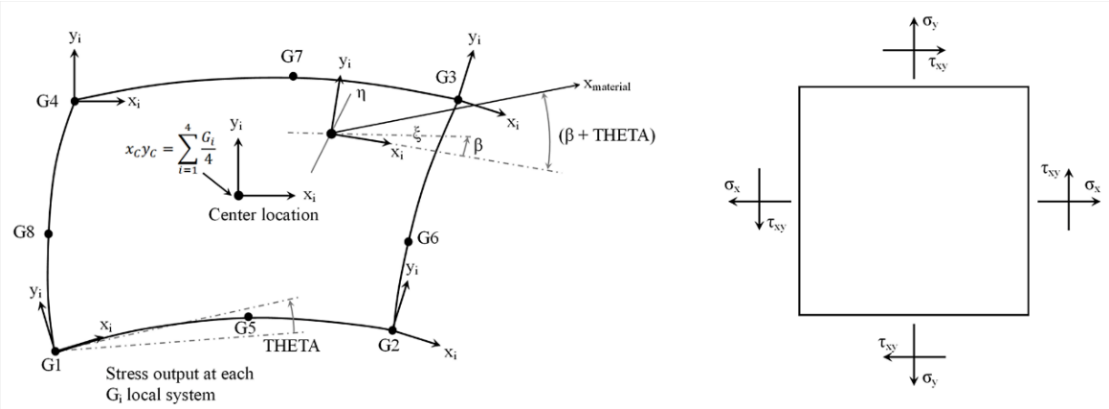

Figure 2: CQUAD8 coordinate system and stresses in shell elements.

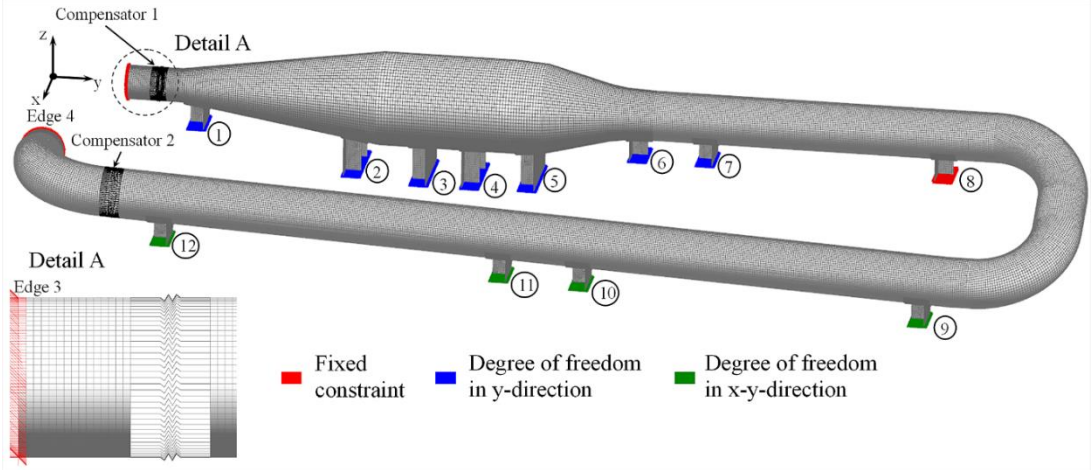

Figure 3: Meshed finite element shell model with boundary conditions.

The two axial compensators were modeled with elastic 1D elements (CELAS) which behave like simple extension or compression springs (cf. Fig. 3, detail A). The axial spring stiffness for compensator 1 and 2 were assumed as k = 257 N/mm and k = 705 N/mm respectively.

A surface-to-surface glue constraint was applied to connect each wear plate of the saddle to the pressure vessel. Glue constraints allow to join dissimilar meshes by creating weld-like connections, preventing relative motion in all directions between the glued surfaces. At the same time, displacements and loads are transferred correctly, resulting in an accurate strain and stress condition between glued surfaces [10].

The boundary conditions were modeled according to Fig. 3. All nodes on edge 3 and 4 representing the connection between pressure vessel and radial compressor were fixed, as was the lower face of the base plate of saddle 8. Support saddles 1 to 7 act as movable bearing points with a single degree of freedom (DOF) in x-direction at the lower face of the saddle base plates. For the remaining saddles 9 to 12 the base plates were fixed in all degrees of freedom but in x- and y-direction. This concept was modified later on as described in Section 2.3. The entire vessel was loaded with p = 10 bars internal pressure and a temperature of θ =180 °C.

2.2 Material Properties

Two materials were used in the simulation. The pressure vessel whose inner surface is in contact with the organic fluid is made from X5CrNi18-10. The support saddles are made from construction steel. The temperature dependency of mechanical and physical properties are taken into account in the finite element model. Typical values for both materials at θ = 20°C and θ = 180°C are given in Tab. 2.

The decisive strength parameter for both X5CrNi18-10 and construction steel is the yield strength $R_{p0.2}$ which is depicted in Fig. 4 as function of temperature θ. Especially in the case of X5CrNi18-10, the operating temperature of θ = 180°C leads to a significant decrease in strength, resulting in a value of $R_{p0.2}$ = 131 N/mm² compared to a nominal value of $R_{p0.2}$=190 N/mm² at θ = 20°C.

Table 2: Mechanical and physical properties of construction steel and X5CrNi18-10 at θ = 20°C and θ = 180°C.

Material	Temperature	Density	Young's module	Yield strength	Coefficient of linear expansion
	θ	ρ	E	$R_{p0.2}$	α
	[°C]	[kg/m³]	[N/mm²]	[N/mm²]	[10^{-6} K^{-1}]
Construction steel	20	7830	207000	140	11
	180	7830	207000	134	12.3
X5Cr-Ni18-10	20	7900	200000	190	16
	180	7900	186000	131	17

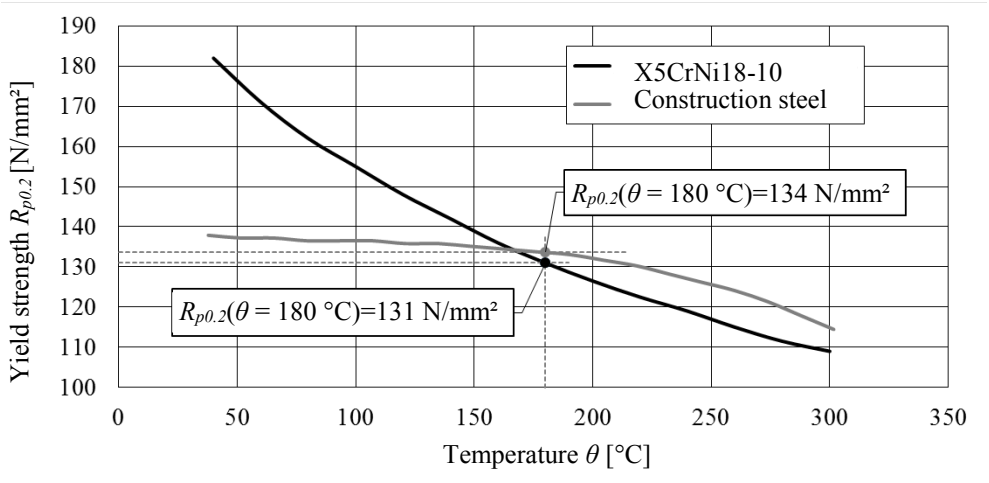

Figure 4: Temperature dependency of yield strength $R_{p0.2}$ for construction steel and X5CrNi18-10.

2.3 Results of the Static Shell Model

The decisive strength parameter for evaluating the results is the allowable stress at design temperature σ_{aDT}, with the yield strength $R_{p0.2}$ at design temperature and the safety factor S = 1.5 according to [13]:

$$\sigma_{aDT} = \frac{R_{p0.2}}{S}. \tag{2}$$

For the given temperature of θ = 180°C the allowable stress for X5CrNi18-10 results in a value of approximately σ_{aDT} = 90 N/mm². One-dimensional thermal expansion can be estimated for a given temperature difference $\Delta\theta$, thermal expansion coefficient α, and geometric dimension l from [8]:

$$\Delta l = \alpha \cdot l \cdot \Delta\theta \tag{3}$$

with values for α according to Tab. 2 and dimension l according to Tab. 1.

Three different bearing-concepts were investigated (cf. Tab. 3). Starting point for the calculations was concept a) as shown in Fig. 3. The position of saddles 8, 9 and 13 are shown in Fig. 6. For concepts a) and b) only saddles 8 and 9 were considered. In concept c) an additional saddle 13 was added in front of the 90° elbow.

Fig. 5 shows the effects of temperature, pressure and the combination of both on nodal displacements. The basis for this calculation is concept a). In the first step, only a temperature load of θ = 180°C was applied to the structure (cf. Fig. 5, left side). The resulting displacements in x- and y-direction are consistent with analytical values calculated from Eq. 3. In the second step, only an internal pressure load of p = 10 bars was applied to all pressurized parts (cf. Fig. 5, in the middle). The resulting radial stresses in the test section, diffuser, settling chamber, and nozzle compare well to the analytical values derived from standard equations as found for instance in [8, 13]. However, the major effect of the pressure load is the tendency to bend up the 180° elbow. This movement is allowed due to the fact that saddles 9 to 12 of the return section have DOFs in x- and y- direction, while saddle 8 of the test section is fixed. Therefore, the axial compensator of the return section with its low spring stiffness of k = 705 N/mm offers little resistance and acts as an extension spring. The resulting maximum displacements in the 180° elbow lie in the order of 20 mm.

In a final step the combination of temperature and pressure loads were considered (cf. Fig. 5, right side). Both individual influences can be superimposed [11]. While the tendency to straighten up the 180° elbow remains, the expansion of the axial compensator is substantially reduced. This can be attributed to the fact that the displacement of the return section, resulting from the thermal load, is in reverse direction to the displacement caused by internal pressure. The main portion of the resulting strain can be attributed to the effect of pressure. High values of strain can result in critical stress values especially in the area of the 180° elbow. Fig. 6 shows displacement and resulting stress values for different bearing concepts. For each of the three evaluated concepts the bearing concept was gradually modified to optimize strain and stress distribution. Each time the structure was loaded with a temperature of θ = 180°C and internal pressure of p = 10 bars. Average and maximum stress values for 180° elbow, return, 90° elbow, and test section are shown in Fig. 7.

Table 3: Bearing concepts for the static shell model.

Saddle	**8**	**9**	**13**
	Degree of freedom (DOF)		
Concept a)	fixed	x-y	-
Concept b)	fixed	x	-
Concept c)	fixed	x	x

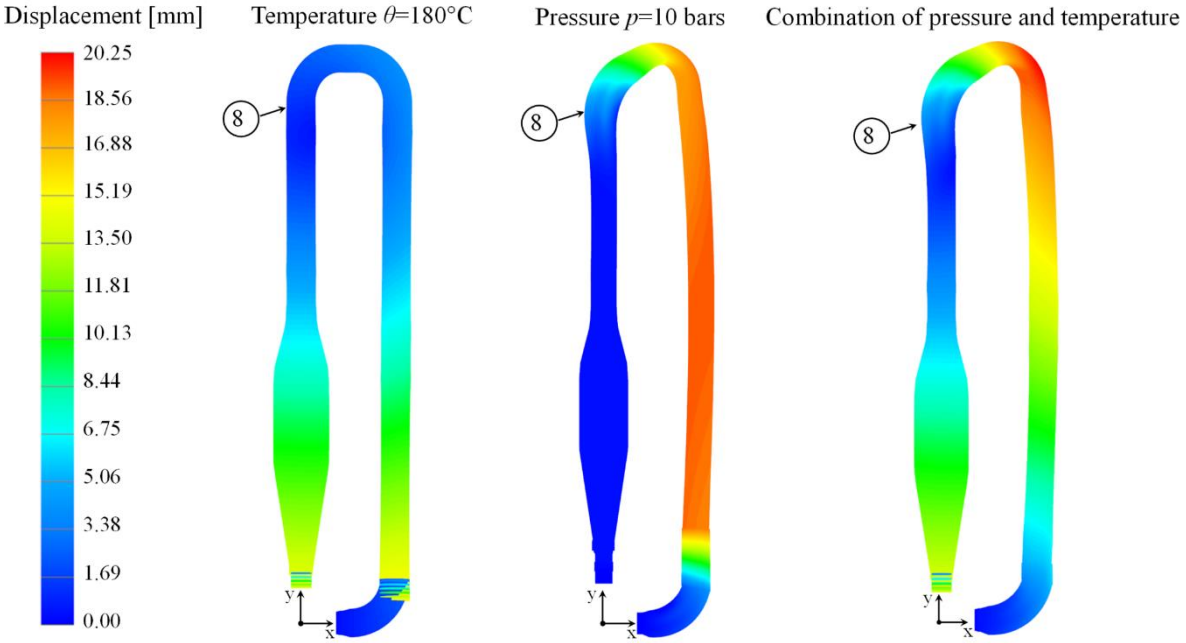

Figure 5: Effect of temperature and pressure on displacement for the basic model as shown in Figure 3.

For concept a) saddle 8 at the end of the test section was fixed. All saddles at the return section have DOFs in x- and y- direction. The results are high values of stress in the 180° elbow, test section and return. The maximum stress values in all four sections exceed the allowable stress of σ_V = 90 N/mm² by a factor of 1.3 up to 2.4. For concept b) saddle 9 in addition to saddle 8 was fixed in y-direction to prevent the tendency to straighten up the 180° elbow, allowing only for movement in x-direction. As a result, average and maximum stress values found in the 180° elbow, test section and return are greatly reduced and lie below the allowable stress level. With a maximum of σ_V = 144 N/mm² in the 90° elbow, concept b) still leads to an overloading of this section. Therefore, saddle 13 was added for concept c). By locking the DOF in y-direction, the reaction force of the axial compensator is no longer affecting the 90° elbow but is absorbed by the saddle. The resulting maximum stress of σ_V = 79.7 N/mm² was almost halved compared to the σ_V = 144.4 N/mm² from concept b).

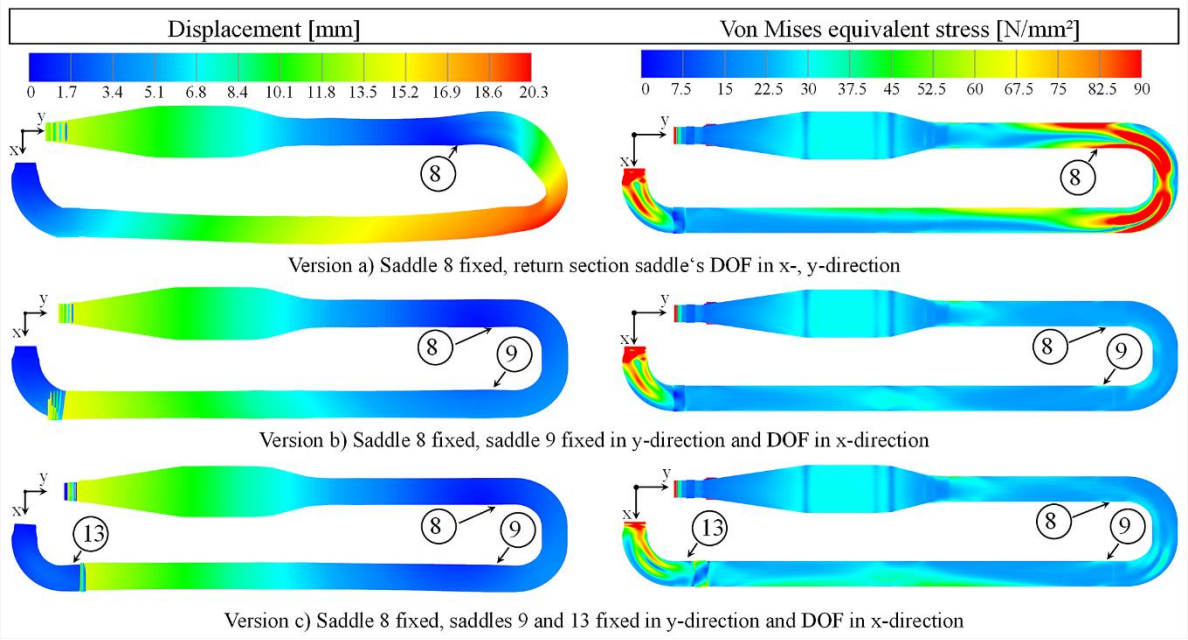

Figure 6: Effect of different bearing-concepts on displacement and von Mises stress.

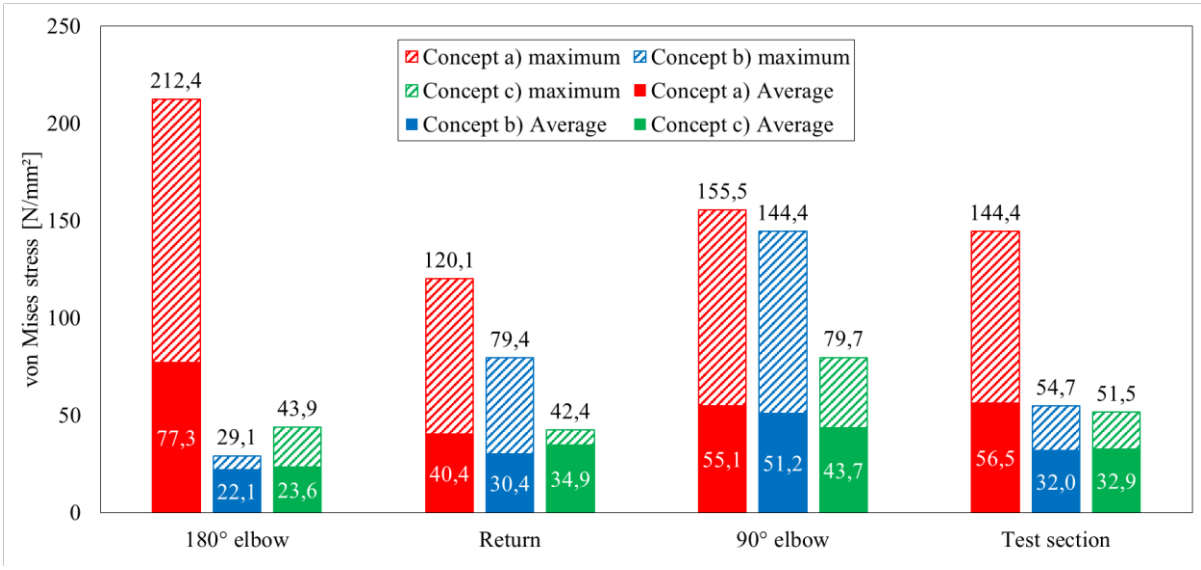

Figure 7: Maximum and average von Mises equivalent stress for concepts a), b) and c).

3. TRANSIENT ANALYSIS

During the start-up process, thick-walled parts and areas of high material accumulation lead to significant temperature differences within the material. The resulting thermal strain evokes high residual stress states [11]. In general, thermal stresses are directly proportional to the temperature difference (θ_i-θ_m) of a local temperature θ_i to the average wall temperature θ_m. Thermal stresses are also known to be proportional to the square of the wall thickness. Therefore, thick-walled components usually determine allowable heating and load change rates [11]. Thermal expansion and resulting thermal stresses during heat-up phase were investigated using the example of the settling chamber, which was assumed to be critical due to its massive flanges.

Analytical methods for estimating the maximum temperature differences and resulting thermal stresses exist for simple geometries like spheres, cylinders or plates [2, 11]. Applying the procedure given by [2], the progression of the wall temperature difference (θ_i-θ_m) in a plate, resulting from a sudden temperature change, was plotted over a period of two hours (cf. Fig. 8). According to Fig. 8, the maximum temperature difference hence the maximum thermal stress in a plate will occur within the first 30 minutes. Assuming a similar transient behavior for the settling chamber, the following investigations were confined to a time frame of 60 minutes.

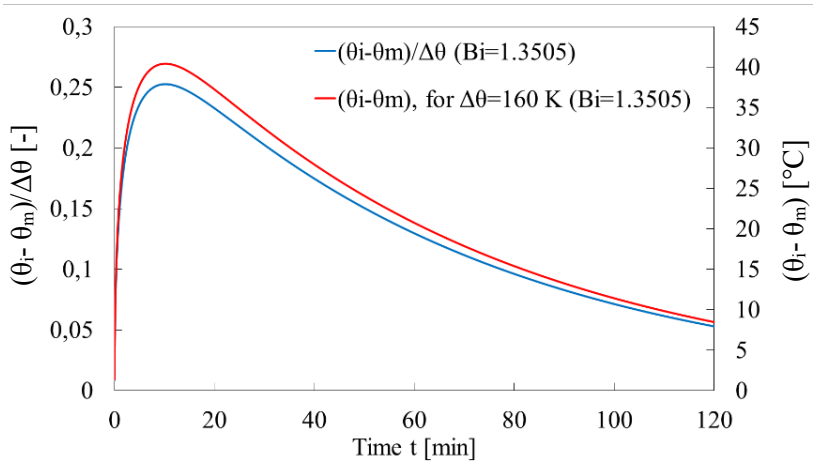

Figure 8: Wall temperature difference over time for a sudden temperature change in a plate.

3.1 Finite Element Model for Transient Analysis

In the First step, a thermal finite element model was built, which provided the temperature distribution throughout the structure. This was achieved using the NX Thermal solver in advanced transient settings [7]. In an interim step, a mapping solution mapped the nodal temperatures to the structural model, which in turn provided strain and stress distribution. For the structural computations linear finite element analysis utilizing NX Nastran (SOL 101) was used. Symmetry to the y-z-plane was exploited for all models to reduce computing time.

The thermal model, as shown in Fig. 9 on the left hand side, was meshed with 4-noded tetrahedral elements. As the whole structure will be insulated with a layer of mineral wool, a solid body of 100 mm thickness was added. The introduction of heat into the structure will be achieved by electric heating sleeves applied to the pressure vessel. A thermal load was applied to the outer surface of the pressure vessel to model the heating sleeves (cf. Fig. 9, Detail A), assuming the thermal resistance between heating sleeves and pressure vessel to be negligibly small. The thermal load is regulated by a PID controller with a specified target temperature of θ = 180°C. A number of elements from the mesh of the pressure vessel were chosen as sensors for the controller. Natural convection at the outer surface of insulation and saddle was added utilizing built in correlations provided by NX for cylinder, horizontal and vertical plate. The assumed ambient temperature is θ = 22°C. As the pressure vessel will be under vacuum during the start-up process, the inner surface of the vessel is adiabatic in this model.

The structural model was meshed utilizing mapped meshing with 20-noded hexahedral elements. Mesh refinement was carried out in the area of the pressure vessel, to ensure 4 element layers across the wall thickness. The bended wear plate of the saddle was meshed with 10-noded tetrahedral elements. In the symmetry y-z-plane a symmetrical constraint was applied (DOF in y- and z-direction). At the right end of the model the raised surface of the flange (flange gasket contact area) was fixed. The cross section of the pressure vessel at the left end was elastically supported by grounded springs. The springs represent the axial compensator with a spring stiffness of k = 257 N/mm.

For the pressure vessel and saddle the same materials as described in Section 2.1 were used. The thermal model additionally contains the insulation layer. A material file was generated using physical properties of mineral wool assuming isotropic material behavior. Mineral wool possesses an average thermal conductivity of λ = 0.05 W/(m·K), a density of ρ = 100 kg/m³ and a specific heat capacity of c_p = 0.84 kJ/(kg·K) [12].

3.2 Results of the Transient Analysis

Temperature distribution and thermal stress were evaluated for two different configurations over a period of 60 minutes. For configuration a) a thermal load of $\dot{q}$ = 2500 W/m² was applied to the outer surface of the pressure vessel as described in Section 3.1. For configuration b) the thermal load was split up into two

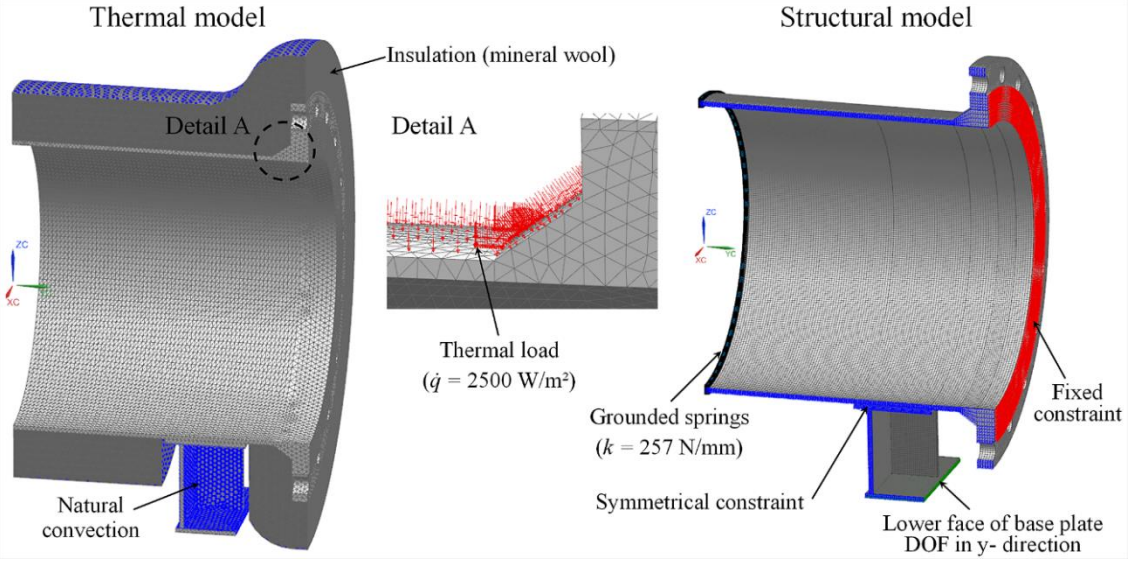

Figure 9: Meshed thermal and structural finite element model of settling chamber.

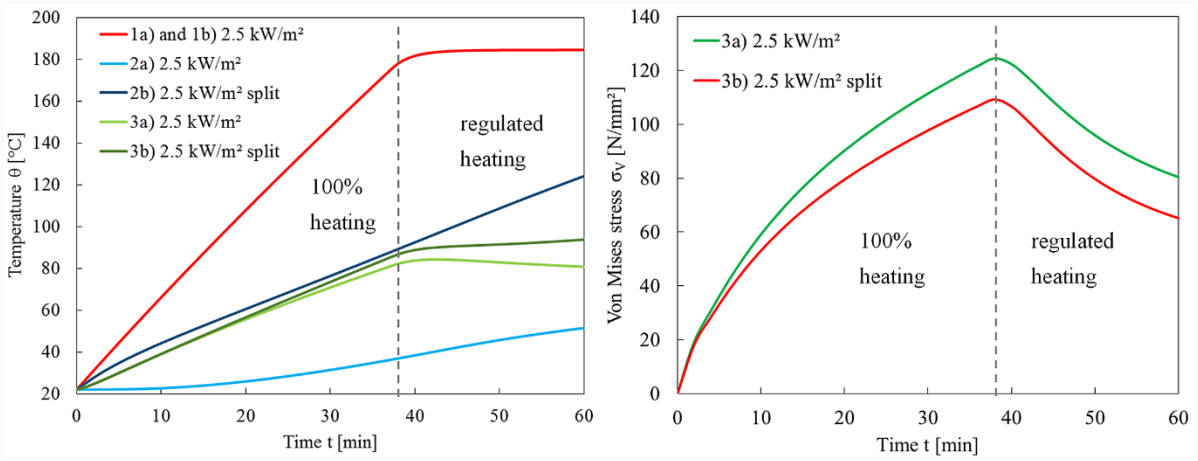

Figure 10: Development of temperature θ and von Mises stress σ_V over the first hour during heat-up phase for a thermal load of $\dot{q}$ = 2500 W/m² at different structural points.

areas. The first load was defined for the pressure vessel itself, whereas the second one only covered the surface area of the flange. The weld, joining pressure vessel and flange, was chosen as the parting line between the two areas. In this configuration each thermal load had its own PID controller assigned to it.

The development of temperature θ and von Mises stress σ_V within the first hour for a thermal load of $\dot{q}$ = 2500 W/m² is shown in Fig. 10. The positions of the points 1) to 3) are illustrated in Fig. 11. In the thin walled pressure vessel, represented by points 1a) and 1b), the temperature curve is identical for both configurations. After approximately 40 minutes this area has reached its target temperature of θ = 180°C. After that the PID controller reduces the thermal load to maintain the target temperature. A similar behavior can be observed for points 3a) and 3b).

The maximum stress values occur in the areas of the weld seam, joining pressure vessel and flange, and the weld seam, joining pressure vessel and saddle. As becomes evident from Fig. 10 (right hand side), configurations a) and b) both yield failure critical stress values of up to σ_V = 123 N/mm². However, by splitting up the thermal load and defining two separate areas a more uniform temperature distribution in vessel and flange can be achieved resulting in lower thermal stress values.

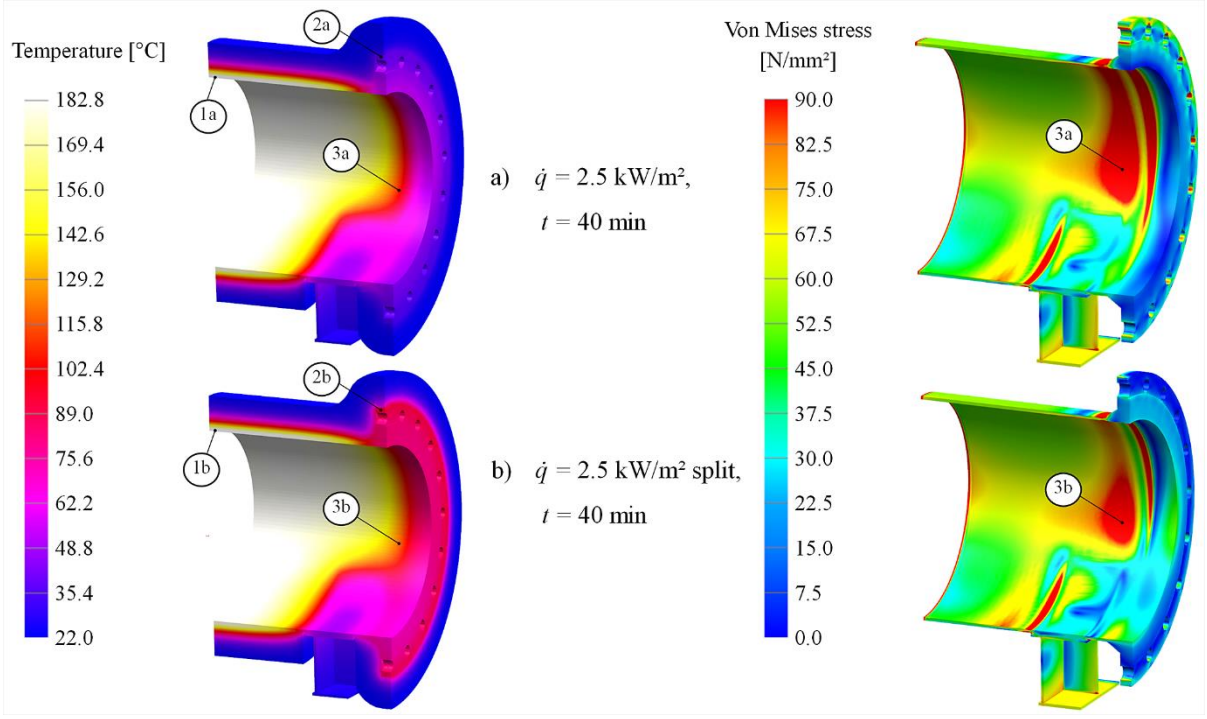

Figure 11: Temperature θ and von Mises stress σ_V distribution at t = 40 min for a thermal load of $\dot{q}$ = 2500 W/m².

4. CONCLUDING COMMENTS

This paper describes a method to design and analyse the bearing concept of a closed wind tunnel for organic fluids by means of linear finite element analysis. A simplified shell model was built up and three different concepts were considered. The basic impacts of temperature and pressure loads were identified. Based on these findings an optimized bearing concept, leading to an equal strain and stress distribution, was developed.

Temperature distribution and thermal stress during heat-up phase were investigated using combined thermal and structural finite element analysis. The thermal model provided transient temperature distributions, which were used to calculate thermal stresses. A method was presented to reduce these thermal stresses by way of achieving a uniform temperature distribution throughout the structure. As the resulting stress values presented in this paper are still above the critical yield strength, further investigations are needed. This includes the determination of permitted heating rates, the ideal configuration of the heating sleeves and their individual regulation.

5. NOMENCLATURE

c_p	Specific heat capacity	kJ/(kg·K)
d_m	Midsurface diameter	mm
E	Young's modulus	N/mm²
k	Spring stiffness	N/mm
l	Length	mm
$\dot{q}$	Heat flux	W/m²
r	Radius	mm
$R_{p0.2}$	0.2%-yield strength	N/mm²
s	Wall thickness	mm
t	Time	s
α	Coefficient of linear expansion	1/K
θ	Temperature	K
ρ	Density	kg/m³
σ_V	Von Mises equivalent stress	N/mm²
τ	Shear stress	N/mm²

6. REFERENCES

[1] Adam, A. W., ed., 1995. *Organic Rankine Cycles. Encyclopedia of Energy Technology and the Environment*, John Wiley & Sons, New York, 3024 p.

[2] Baehr, H.D., Stephan, K., 2013. *Wärme- und Stoffübertragung*, Springer, Berlin, Heidelberg, 804 p.

[3] Bathe, K.J., 2002. *Finite Elemente Methode*, Springer, Berlin, Heidelberg, 1253 p.

[4] Chen, H., Goswami, D. Y., and Stefanakos, E. K., 2010. *A review of thermodynamic cycles and working fluids for the conversion of low-grade heat*, Renewable and Sustainable Energy Reviews, 14(9), pp. 3059-3067.

[5] Dixon, S. L., 1998. *Fluid mechanics and thermodynamics of turbomachinery*, Butterworth-Heinemann, Boston, 556 p.

[6] German Institute for Standardization, 2003. *DIN 28080:2003-08, Saddle supports for horizontal apparatus - Dimensions*, Berlin, 12 p.

[7] Maya Heat Transfer Technologies Ltd., 2012. *NX Thermal Reference manual*, 544 p.

[8] Scholz, G., 2012. *Rohrleitungs- und Apparatebau*, Springer, Berlin, Heidelberg, 411 p.

[9] Schuster, A., Karellas, S., Kakaras, E., and Spliethoff, H., 2009. *Energetic and economic investigation of organic rankine cycle applications*, Applied Thermal Engineering, 29(8-9), pp. 1809-1817.

[10] Siemens Product Lifecycle Management Software Inc., 2012. *NX Reference manual.*

[11] Strauß, K., 2009. *Kraftwerkstechnik*, Springer, Berlin, Heidelberg, 522 p.

[12] VDI e.V., ed., 2013. *VDI-Wärmeatlas,* Springer, Berlin, Heidelberg, 1760 p.

[13] Verband der TÜV e.V., ed., 2006. *AD 2000 - Regelwerk*, Carl Heymanns Verlag, Berlin, 796 p.

ANALYSIS OF PURE FLUID AND ZEOTROPIC MIXTURES UESD IN LOW-TEMPERRATURE REHEATING ORGANIC RANKINE CYCLES FOR POWER GENERATION

Changwei Liu[1], Tieyu Gao[2]*, Jiamin Xu[3], Jiangnan Zhu[4], Xun Xu[5]

[1]School of Energy and Power Engineering, Xi'an Jiaotong University
Xi'an, Shaanxi, P.R.China
876180495@qq.com

[2]School of Energy and Power Engineering, Xi'an Jiaotong University
Xi'an, Shaanxi, P.R.China
sunmoon@mail.xjtu.edu.cn

[3]School of Energy and Power Engineering, Xi'an Jiaotong University
Xi'an, Shaanxi, P.R.China
88342276@qq.com

[4]School of Energy and Power Engineering, Xi'an Jiaotong University
Xi'an, Shaanxi, P.R.China
zhujiangnan1234@126.com

[5]School of Energy and Power Engineering, Xi'an Jiaotong University
Xi'an, Shaanxi, P.R.China
402270702@qq.com

ABSTRACT

The shortage of fossil energy sources boosts the development and utilization of renewable energy. Among various novel techniques, recovering energy from low-grade heat sources including industrial waste heat, geothermal energy and solar energy through power generation via organic Rankine cycle (ORC) has been one of the focuses. ORC is one of the effective methods to recover low-grade heat, which makes use of environment-friendly organics as working fluids, and low temperature thermal energy as the driving energy. Investigations have indicated that reheating ORC can improve the thermal performance of the system. In this paper, the cycle performance is measured by the system net power output. By using pure fluid R245fa, R123 and zeotropic mixtures R245fa/R21, R123/R21, R245fa/R123 as the cycle working fluids, the influences of working fluid, mixtures component ratio and reheat pressure ratio on low-temperature reheating ORC system are investigated. The optimal reheat pressure ratios of reheating ORC system using different working fluids are obtained. In addition, zeotropic mixtures R245fa/R21(0.65/0.35) is superior in the improvement of the system net power output. In practical application, the optimal reheat pressure ratio and component ratio should be determined based on the mixture and evaporation temperature to ensure the net power output of reheating ORC system maximum.

1. INTRODUCTION

As the world's energy situation becomes aggravate, the recovery of low-temperature heat sources has become one of the research focuses. Due to the fact that conventional steam Rankine cycle does not allow efficient energy conversion at low temperatures, organic Rankine cycle (ORC) has been extensively studied for the conversion of low-grade heat into power for its simplicity and relatively high efficiency (Chen *et al*., 2011).

Recently, some researchers have studied the reheating ORC system. Li *et al.* (2102) investigated the net power output and thermal efficiency of pure R245fa in reheating ORC system aiming at low-temperature heat source below 120℃. Xu *et al.* (2009) proposed a determination method for optimal reheating pressure of ORC system using R123 as working fluid, which could ensure a highest system efficiency. Li *et al.* (2013) studied the low-temperature heat source utilization of reheating ORC systems using different working fluids, then gained the variation regularity of the net power output and thermal efficiency with evaporation temperature and reheat pressure ratio. Wang *et al.* (2013) chose R601 and R245ca as the working fluids and investigated the influence of the reheat pressure ratio on the net power output, thermal efficiency and exergy efficiency of the system, then obtained the optimal reheat pressure ratios.

In order to improve the efficiency of ORC system, using mixtures has become an important method (Zheng *et al*., 2008). The temperature glide of zeotropic mixture in phase transformation zone can provide a good temperature matching of cold and heat fluids for heat-exchanges, which could reduce the irreversible entropy production caused by the heat transfer temperature difference (Maizza *et al*., 2001). Wang *et al.* (2010) compared low-temperature solar ORC systems using pure fluid and zeotropic mixture as the working fluid by experiments, and the results showed that using zeotropic mixture as working fluid could improve both output work and exergy efficiency of the system. Angelino *et al.* (1998) calculated performance of waste heat recovery ORC system and geothermal power generation ORC system using mixtures as working fluids which were composed of silicone oil and different hydrocarbon by the PRSV state equation and WS mixing rule. The results indicated that cycle performance was closely relative to the component ratio of mixtures, so the component ratio must be optimized when mixture was used.

Above studies indicate that reheating process and zeotropic mixtures can both effectively improve the thermodynamic performance of ORC system. At present, very few studies on low temperature reheating ORC system for power generation using zeotropic mixtures are reported, and the optimal component ratio of zeotropic mixtures has not been fully studied. In this paper, influences of zeotropic mixtures' kind and component ratio, as well as the reheating pressure ratio on the net power output of reheating ORC system are investigated. The results show that zeotropic mixtures can effectively improve the net power output of reheating ORC system when the mixture's kind and component ratio are suitable.

2. ANALYSIS OF REHEATING ORC SYSTEM AND SELECTION OF WORKING FLUIDS

2.1 Reheating ORC System

Compared with the simple ORC system, Reheating ORC system includes a high pressure expander and a low pressure expander instead of a single expander. A reheating ORC system includes evaporator, high pressure turbine 1, reheater, low pressure turbine 2, condenser and pump, as shown in Figure 1. The circulation specifically include the following processes:

5-6: Adiabatic compression process. The saturated liquid working fluid is compressed adiabatically into high pressure unsaturated liquid in pump, then enters evaporator.

6-1: Isobaric heating process. High pressure unsaturated liquid is heated into high temperature and high pressure saturated vapor by absorbing heat of the low-temperature heat source in evaporator, then enters high pressure turbine1.

1-2: Adiabatic expansion process. Saturated vapor expands in high pressure turbine 1 to do work and generate electricity, and the pressure and temperature of working fluid drop, then enters the reheat.

2-3: Isobaric heating process. Vapor is heated in reheater, and its temperature increases to the same value of that of state 1, then enters low pressure turbine 2.

3-4: Adiabatic expansion process. Vapor expands in low pressure turbine 2 to do work, then becomes low temperature and low pressure superheated vapor.

4-1: Isobaric condensation process. Vapor is condensed into saturated liquid by heat exchange with cooling water in condenser.

In this paper the system is in a stable flow state, and no heat exchange occurs between each thermal device and the environment. The pressure losses of evaporator, reheater, condenser and the connecting pipes are negligible. The working fluid at outlet of the condenser is saturated liquid while the working fluid at outlet of the evaporator is saturated vapor. The tephigram of reheating ORC system is shown in Figure 2.

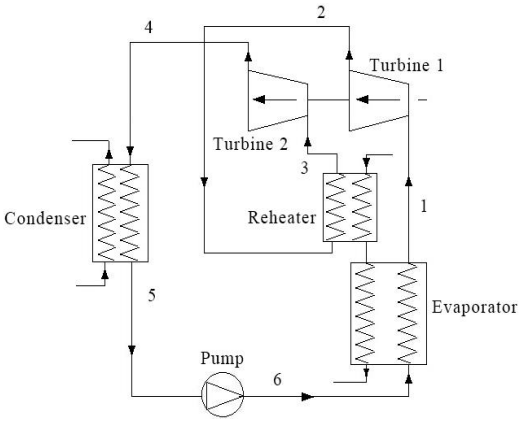

Figure 1: Reheating ORC system

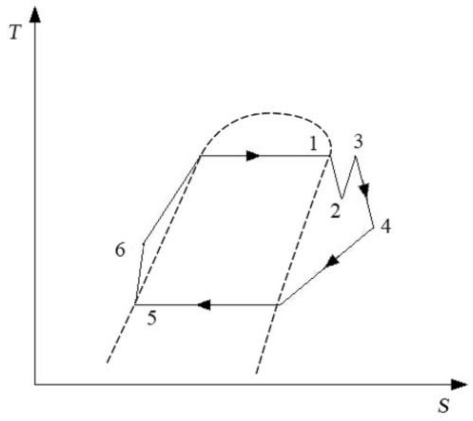

Figure 2: Tephigram of reheating ORC system

2.2 The Choice of Working Fluids

Studies of simple ORC system show that choice of the working fluid has an important influence on the system thermal performance (Ni *et al.*, 2013). The working fluid should have superior stability, good environmental protection and excellent thermal physical properties which match well with heat source (Maizza *et al.*, 1996). Drying and wetting of working fluid is an important feature in low grade heat source ORC system, which is determined by the slope of saturated vapor line in the tephigram. The slope of dry working fluid is greater than zero while the slope of wet working fluid is lower than zero, and the slope of isentropic fluid is close to zero. High temperature and high pressure vapor of dry working fluid and isentropic working fluid becomes superheated vapor after expanding in turbine, thus there is no droplet appearing in the process (Gu *et al*., 2008).

Table 1: Thermophysics property parameters of working fluids.

Working Fluid	Molecular Weight /kg·mol^{-1}	Standard Boiling Point /K	Critical Temperature /K	Critical Pressure /Mpa	ODP	GWP (100 Years)
R21	102.92	282.01	451.48	5.1812	0.04	151
R245fa	134.05	288.29	427.16	3.6510	0	1050
R123	152.93	300.97	550.0	3.6618	0.01	77

R21, R123 and R245fa are common working fluids used in ORC system, and the values of ODP (Ozone Depression Potential) and GWP (Global Warming Potential) of the three fluids are relatively small, which means they are eco-friendly (Gu *et al*., 2007). Thermophysics property parameters of three pure working fluids are shown in Table 1 (Calm *et al.*, 2011). Using R245fa/R21 as working fluid could effectively improve the net power output of the ORC system (Li *et al*., 2012). Therefore, we select R21, R123, R245fa as pure fluids and R245fa/R21, R123/R21, R245fa/R123 as zeotropic mixtures in this paper. In this study, the working fluid is set as saturated vapor at the outlet of the evaporator, and dry working fluid or isentropic working fluid should be used to avoid the water hammer at the tail of turbine (Xu *et al*., 2011). R21 is a typical wet working fluid while R245fa and

R123 are dry working fluids. To guarantee the zeotropic mixtures are dry working fluids or isentropic working fluids, the mass fraction of R21 must be no more than 0.35 in mixture R245fa/R21 and no more than 0.2 in mixture R123/R21 from REFPROP's calculations. Figure 3 is the tephigram of saturated R245fa/R21 (0.65/0.35), and Figure 4 is the tephigram of saturated R123/R21 (0.8/0.2). As shown in two figures, these two mixtures are isentropic working fluids under the corresponding proportion.

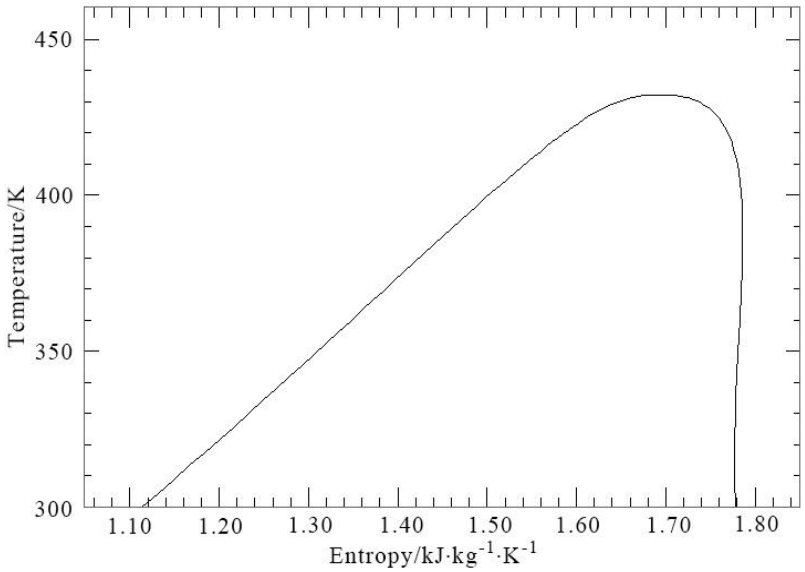

Figure 3: Tephigram of saturated R245fa/R21 (0.65/0.35)

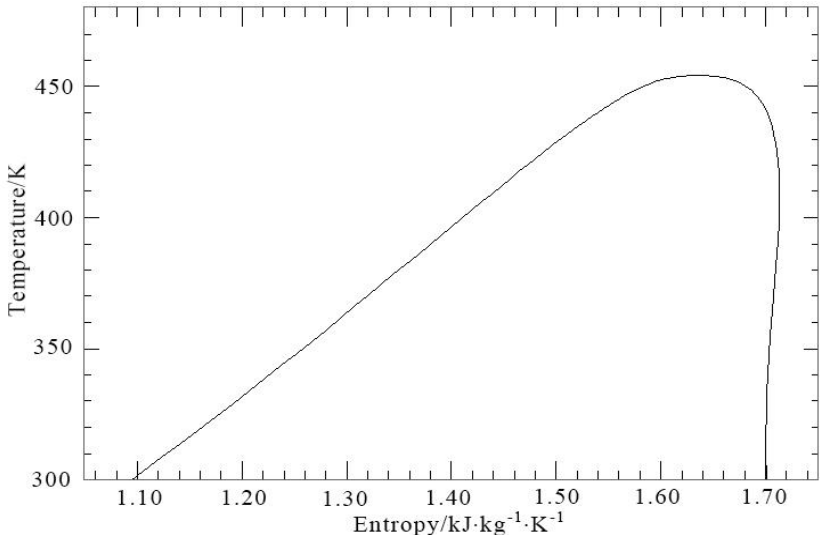

Figure 4: Tephigram of saturated R123/R21 (0.8/0.2)

3. THE PERFORMANCE ANLYSIS OF REHEATING ORC SYSTEM

3.1 System Parameters Setting and The Research Method

In this research, the condensing temperature is 300K which is constrained by environmental temperature. In the case of zeotropic mixtures, the temperature of working fluid at outlet of the condenser is regarded as the condensing temperature. The heat source temperature is 400K, and the maximal evaporation temperature is 380K which is constrained by heat source temperature. In the

case of zeotropic mixtures, the temperature of working fluid at outlet of the evaporator is regarded as the evaporation temperature. The adiabatic efficiency of the turbines is 85%, and the mechanical efficiency is 90%. The adiabatic efficiency of the pump is 80%, and the mass flow of working fluid is 1kg·s^{-1}. In addition, the working fluid is set as saturated liquid at the outlet of the condenser and saturated vapor at the outlet of the evaporator. The Reheat pressure ratio is defined as the ratio of inlet pressure of Turbine 2 and that of Turbine 1. To ensure the inlet pressure of Turbine 2 is greater than its outlet pressure, which is condensation pressure, we set the minimal reheat pressure ratio as 0.3. The parameter values of each state point are calculated by REFPROP.

For low-temperature heat energy generating system, the important thing is to improve the total output work, not the thermal efficiency. Therefore the system performance is evaluated by net power output of the reheating ORC system in this article. Fundamental equations are as follows:

Work of high pressure turbine 1:

$$W_1=\dot{m}\cdot(h_1-h_2)\cdot\eta_m \quad (1)$$

Work of low pressure turbine 2:

$$W_2=\dot{m}\cdot(h_3-h_4)\cdot\eta_m \quad (2)$$

Consumed work of pump:

$$W_p=\dot{m}\cdot(h_6-h_5) \quad (3)$$

Net power output of the system:

$$W=W_1+W_2-W_P \quad (4)$$

Where: $\dot{m}$ is mass flow of the working fluid, which is 1 kg·s^{-1} in this research; h_1 is specific enthalpy of the working fluid at inlet of high pressure turbine 1, kJ·kg^{-1}; h_2 is specific enthalpy of the working fluid at outlet of high pressure turbine 1, kJ·kg^{-1}; h_3 is specific enthalpy of the working fluid at inlet of low pressure turbine 2, kJ·kg^{-1}; h_4 is specific enthalpy of the working fluid at outlet of low pressure turbine 2, kJ·kg^{-1}; η_m is the mechanical efficiency of the turbines, which is 90% in this research; h_5 is specific enthalpy of the working fluid at inlet of pump, kJ·kg^{-1}; h_6 is specific enthalpy of the working fluid at outlet of pump, kJ·kg^{-1}.

3.2 The Performance Analysis of Reheating ORC System Using Pure Working Fluid

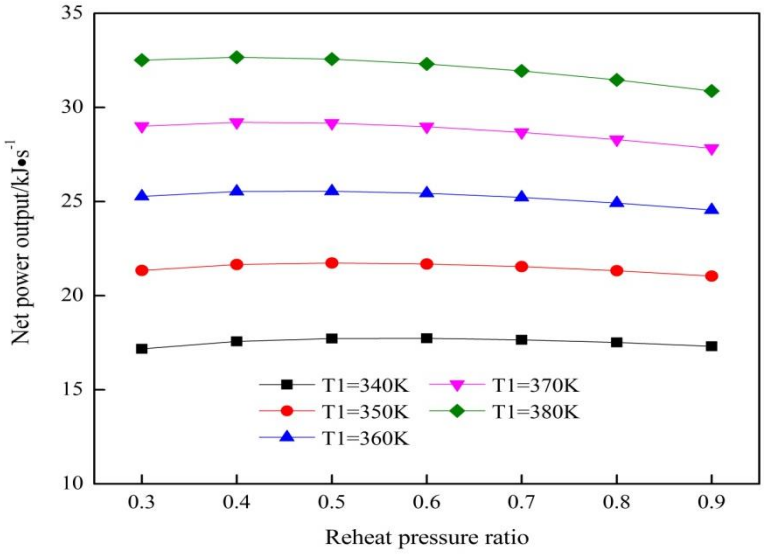

Figure 5: The influences of reheat pressure ratio and evaporator temperature on net power output (working fluid is R245fa)

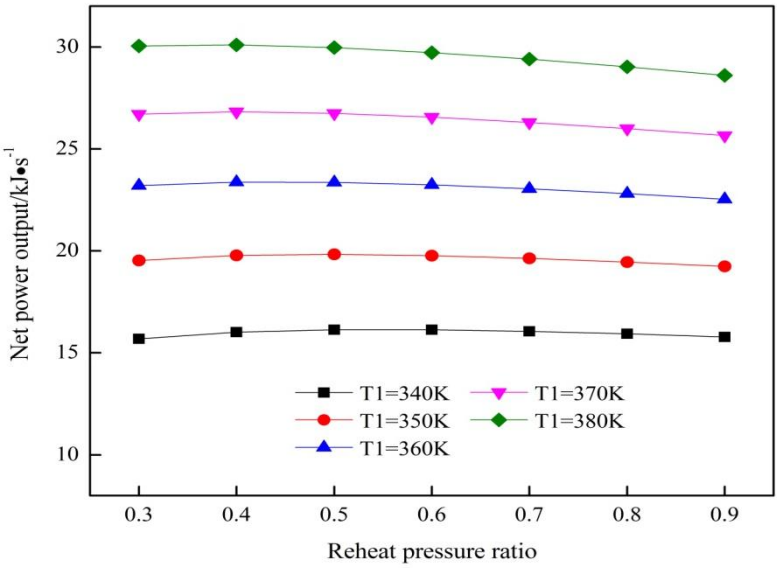

Figure 6: The influences of reheat pressure ratio and evaporator temperature on net power output (working fluid is R123)

Net power outputs of the reheating ORC system using R245fa and R123 as working fluids are calculated at different temperatures (340K-380K) and different reheat pressure ratios (0.3-0.9), and the results are shown in Figure 5 and Figure 6. T_1 denotes evaporation temperature in the figures.

As shown in the two figures, the net power output increases gradually with the increasing evaporating temperature. net power output of the reheating ORC system using R245fa as working fluid is about 9% greater than that of the reheating ORC system using R123 at the same evaporating temperature and reheat pressure ratio, indicating that the performance of R245fa is better than that of R123.

Table 2: The optimal reheat pressure ratios

Evaporating Temperature/K	Working Fluid	Optimal Reheat Pressure Ratios	Maximum Net Power Output /kJ·s^{-1}
340	R245fa	0.56	17.743
	R123	0.55	16.141
350	R245fa	0.50	21.741
	R123	0.49	19.829
360	R245fa	0.46	25.566
	R123	0.44	23.387
370	R245fa	0.43	29.211
	R123	0.40	26.895
380	R245fa	0.40	32.665
	R123	0.37	30.112

In addition, with reheat pressure ratio increases, net power outputs of reheating ORC system using different working fluids all first increase then decrease. The reheat pressure ratio which makes the net power output maximum is regarded as the optimal one and the optimal reheat pressure ratio is related to working fluid type and evaporating temperature. The optimal reheat pressure ratios under different evaporating temperatures are gained through further calculations, and the results are shown in Table 2. From Table 2 we can see that, the optimum reheat pressure ratios of reheating ORC systems using this two kinds of working fluids gradually reduce with the evaporating temperature increasing; and the optimum reheat pressure ratio is smaller when R245fa is used as working fluid at the same evaporating temperature .

3.3 The Performance Analysis of Reheating ORC System Using Zeotropic Mixtures

We select 360K as characteristic evaporation temperature and respectively calculate the net power outputs of ORC system using R245fa/R21,R123/R21 and R245fa/R123 as working fluids under different reheat pressure ratios and component ratios. The results are shown in Figure7-9.

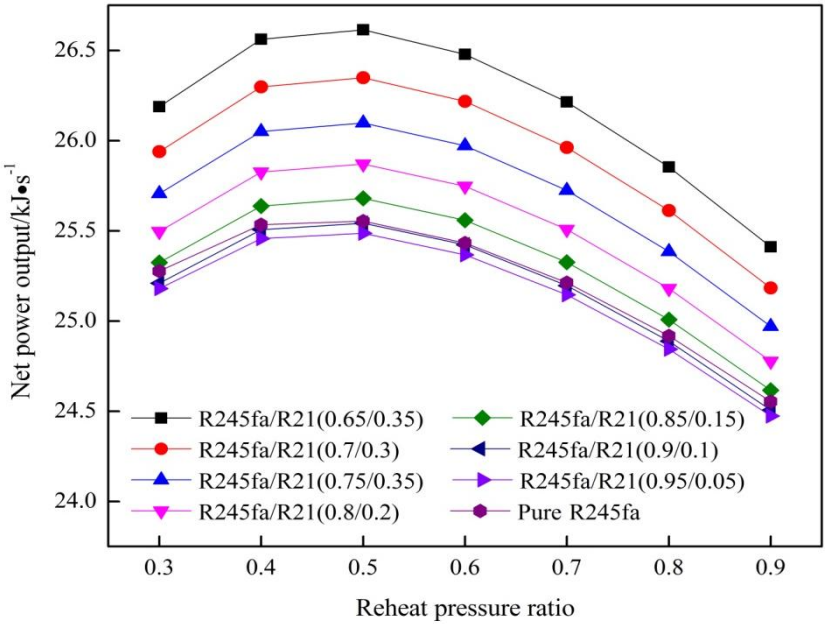

Figure 7: The influences of reheat pressure ratio and component ratio on net power output (working fluid is R245fa/R21)

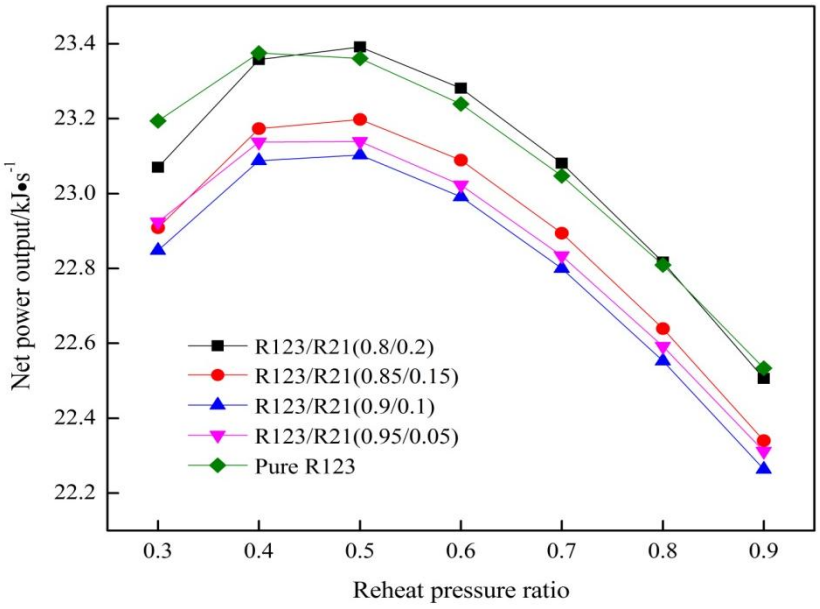

Figure 8: The influences of reheat pressure ratio and component ratio on net power output (working fluid is R123/R21)

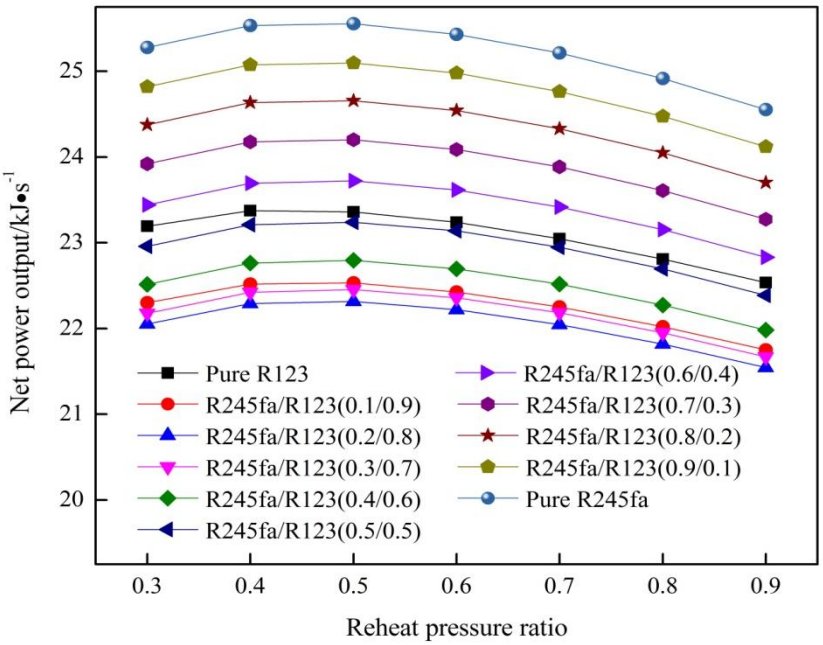

Figure 9: The influences of reheat pressure ratio and component ratio on net power output (working fluid is R245fa/R123)

Figure 7 shows that with an increase in the component ratio of R245fa, the net power output of reheating ORC system gradually decreases. As we can see from Figure 7, net power output of the reheating ORC system using R245fa/R21 as working fluid is greater than that of the reheating ORC system using pure R245fa when the component ratio of R245fa is less than 0.9. This is because that zeotropic mixtures present variable temperature profile during the phase change process, which could considerably reduce the mismatch between heating or cooling sources and the evaporating or condensing working fluid mixtures respectively, so the system irreversibilities could be minimized. Consequently, an appropriate choice of zeotropic mixtures could improve the enthalpy drop between the turbine import and export, thus raising the net power output of ORC system. Net power output of the reheating ORC system using R245fa/R21 (0.65/0.35) as working fluid is about 4% greater than that of the reheating ORC system using pure R245fa at the same reheat pressure ratio. With a further calculation, we acquire that when the evaporation temperature is 360K, the optimal reheat pressure ratio of the reheating ORC system using R245fa/R21 (0.65/0.35) as working fluid is 0.47, and the maximum net power output is 26.622kJ·s^{-1}, which is 4.13% greater than that of the reheating ORC system using pure R245fa.

Figure 8 shows that the net power output of reheating ORC system using R123/R21 (0.8/0.2) or pure R123 as working fluid is relatively large while the net power output of reheating ORC system using R123/R21 (0.9/0.1) is smallest. With a further calculation, we acquire that when the evaporation temperature is 360K, the optimal reheat pressure ratio of the reheating ORC system using R123/R21 (0.8/0.2) as working fluid is 0.47, and the maximum net power output is 23.399kJ·s^{-1}, which is 0.05% greater than that of the reheating ORC system using pure R123. We could obtain that using mixtures R123/R21 as working fluid could hardly improve the net power output of reheating ORC system.

Figure 9 shows that net power output of the reheating ORC system using R245fa/R123 as working fluid is smaller than that of the reheating ORC system using pure R245fa. It is interesting to find that when the component ratio of R123 is larger than 0.5, net power output of the reheating ORC system using R245fa/R123 as working fluid is even smaller than that of the reheating ORC system using pure R123. We could obtain that using mixtures R123/R21 as working fluid could not improve the net power output of reheating ORC system.

4. CONCLUSIONS

In this paper, the research object is reheating ORC system utilizing low temperature waste heat, and the evaluation standard is net power output of the ORC system. The reheating ORC systems using R245fa,R123, R245fa/R21,R123/R21 and R245fa/R123 as working fluids were investigated. The main conclusions can be extracted as follow:

- For reheating ORC systems using pure R245fa and R123 as working fluids, with an increase in evaporation temperature, the net power output gradually increases. Net power output of the reheating ORC system using pure R245fa as working fluid is about 9% greater than that of the reheating ORC system using pure R123 at the same temperature and reheat pressure ratio. There is an optimal reheat pressure ratio making the net power output of ORC system maximum. The optimal reheat pressure ratios of reheating ORC systems using pure R245fa and R123 as working fluids decrease with the evaporation temperature increasing. The optimal reheat pressure ratio of reheating ORC system using pure R245fa as working fluid is slightly smaller than that of reheating ORC system using pure R123 at the same evaporation temperature.
- When the evaporation temperature is 360K, the maximum net power output of reheating ORC system using mixtures R245fa/R21 as working fluid is 4.13% greater than that of reheating ORC system using pure R245fa while the maximum net power output of reheating ORC system using mixtures R123/R21as working fluid is only 0.05% greater than that of reheating ORC system using pure R123. The optimal mixtures component ratios are R245fa/R21 (0.65/0.35) and R123/R21 (0.8/0.2). Using mixture R245fa/R123 as working fluid cannot increase the net power output of reheating ORC system.
- Zeotropic mixture can effectively improve the net power output of reheating ORC system when the mixture's category and component ratio are suitable. In practical application, the optimal reheat pressure ratio and component ratio should be determined based on the mixture and evaporation temperature to ensure the net power output of reheating ORC system maximum.

REFERENCES

Angelino, G., Paliano, P., 1998, Multicomponent Working Fluids for Organic Rankine Cycles, *Energy*, vol. 23, no. 6: p. 449-463.

Calm, J M., Hourahan, G C.,2011, Physical, Safety and Environmental Data for Current and Alternative Refrigerants, *Proceedings of 23rd International Congress of Refrigeration.*, ICR.

Chen, H., Goswami, D Y., Rahman, M M., *et al*., 2011, A Supercritical Rankine Cycle Using Zeotropic Mixture Working Fluids for the Conversion of Low-grade Heat Into Power, *Energy*, vol. 36, no. 1: p. 549-555.

Gu, W., Weng, Y., Cao, G. *et al.*, 2007, The Research Status and Development Trend for Low Temperature Heat Energy Power Generation, *Journal of Engineering for Thermal Energy and Power*, vol. 22, no. 2: p. 115-119.

Gu, W., Weng, Y. *et al.*, 2008, Thermodynamic Analysis of Power Generation System Based on Closed Organic Rankine Cycle, *Acta Energiae Solaris Sinica*, vol. 29 , no. 5 p:608- 612.

Li, M., Bai, H. *et al.*, 2013, The Study on Thermodynamic Performance of Reheating Organic Rankine Circulation System, *Journal of Inner Mongolia University of Science and Technology*, vol. 32, no. 1: p. 50-53.

Li, N., Zhang, X., Bai, H. *et al.*, 2012, The Study on Thermal Performance of Power Generation System Using Organic Rankine Cycle and Reheating Cycle System, *Industrial Heating*, vol. 41, no. 2: p. 44-47.

Maizza, V., Maizza, A., 1996, Working Fluids in Non-steady Flows for Waste Energy Recovery Systems, *Applied Thermal Engineering*, vol. 16, no. 7: p. 579-590.

Maizza, V., Maizza, A., 2001, Unconventional Working Fluids in Organic Rankine Cycles for Waste Energy Recovery Systems, *Applied Thermal Engineering*, vol. 21, no. 3: p. 381-390.

Ni, Y., Zhao, L., Liu, C. *et al.*, 2013, Recovery of Waste Heat of Low Temperature Flue Gas by Parametric Optimization on Organic Rankine Cycle with Non-Azeotropic Mixtures, *CIESC Journal*, vol. 64, no. 11: p. 3985-3992.

Wang, J., Zhao, L., Wang, X., 2010, A Comparative Study of Pure and Zeotropic Mixtures in Low-Temperature Solar Rankine Cycle, *Applied Energy*, vol. 87, no. 11:p.3366-3373.

Wang, Z., Yu, Y. *et al.*, 2013, Parameter Optimization on Low Temperature Reheating Organic Rankine Cycle, *Thermal Power Generation*, vol. 42, no. 5: p. 22-29.

Xu, J., Dong, A. *et al.*, 2011, Working Fluid Selecting of Organic Rankine Cycle for Low and Medium Grade Heat Source Utilization, *Energy Conservation Technology*, vol. 29, no. 167: p. 204-210.

Xu, J., Li, X., Gu, C. *et al.*, 2009, Determination of Optimal Reheating Pressure in Organic Rankine Cycle System, *Journal of Tianjing Polytechnic University*, vol. 28, no. 2: p. 83-85.

Zheng, H., Tang, K., Jin, T. *et al.*, 2008, Advances in Working Fluids for Organic Rankine Cycle, *Energy Engineering*, no.4: p.5-11.

STRUCTURE RELIABILITY ANALYSIS AND EXPERIMENTAL VERIFICATION OF A NEW FREE PISTON EXPANDER

Gaosheng Li[1,2*], Hongguang Zhang[1,2]

[1]College of Environmental and Energy Engineering, Beijing University of Technology, Pingleyuan No.100, 100124 Beijing, China

[2]Collaborative Innovation Center of Electric Vehicles in Beijing, Pingleyuan No.100, 100124 Beijing, China
E-mail: gao.sheng2005@163.com

* Corresponding Author

ABSTRACT

A new free piston expander coupled with liner generator (FPE-LG) has been proposed in this paper, which can be used as a thermo-electric conversion device for organic Rankine cycle (ORC). Compared to other expanders, the free piston expander (FPE) seems to be the most suitable working component for small scale ORC system owing to good sealing, variable compress ratio and compact structure if the inlet/outlet control is worked out accurately. Thus, a physical prototype with a novel valve train has been manufactured, which is experimentally validated in an air test rig before it is integrated into whole ORC system.

In this paper, a general engineering methodology is adopted to analyze the structure reliability of the FPE valve train at different input frequencies. The dynamics simulation of the valve train is carried out via ADMAS software firstly, the obtained contact force results are set as boundary conditions of stress analysis. Based on elastic mechanics theory and finite element method, more precise calculation results about stress distribution on the valve train are obtained through transient structural module in ANSYS® Workbench V14.5. The results show that the maximal von Mises stress is 231.71MPa which mainly concentrate on the root of the valve slider. Although the maximal von Mises stress on the valve slider does not exceed its material allowable stress when the servomotor input frequency is 8Hz, the fluctuation of the stress is obvious, which leads to mechanical failure. FPE prototype with the valve train can realize the suction, expansion and discharge processes properly in the air test rig and can work stably in a relatively wide range of servomotor input frequency from 1Hz to 8Hz. The stress analysis and dynamics simulation results can provide a significant reference value for the mechanical performance optimization of the next generation FPE and further validation of the FPE-LG in the ORC system will be conducted in the near future.

1. INTRODUCTION

About one third of the energy which is produced by the automotive fuel combustion has been utilized, however, the majority has been wasted in the form of exhaust gases, cooling water and mechanical friction loss. Utilizing exhaust energy has recently become a more efficient and effective method by which to save energy and reduce emissions (Ou *et al*., 2013, Boretti, 2012). The organic Rankine cycle (ORC) system is not only a reliable and promising method for converting waste heat of vehicle exhaust into useful work but also a most likely industrialization technology (He *et al*., 2012).

As the core working part, the performance of expander has a direct influence on output power of automotive ORC system. Owing to small flow rate constraint and compact structure requirement, the

traditional expanders such as the turbine, screw, scroll expanders have certain difficulties in application for the small scale automotive ORC system respectively. For instance, although the screw expander is widely used in ORC system, of which helix rotor surface with high accuracy must be manufactured by special equipment and tools (Wang *et al*., 2011). Furthermore, the screw expander can't reach the end pressure as high as reciprocating piston expander when the expansion process is completed (Gao *et al*., 2013). Due to large leakage under high pressure difference, the scroll expander has a low efficiency. Hence, very tight clearance design is required in order to achieve a satisfactory efficiency, which will make the manufacturing costs increased. As for the turbine expander, the rotating speed will exceed 200,000 to meet to this small flow rate, which is a great challenge associated with the reliability and mechanical strength. However, the free piston expander (FPE) is suitable to the condition of small flow and low output power (Han *et al*., 2014, Zhang *et al*., 2007). At present, studies of free piston expander mainly focus on the refrigeration field. No public reports about using free piston expander as working part for vehicle internal combustion engine (ICE) waste heat recovery has been seen in published literatures yet. Thus, free piston expander coupled with a liner generator has been proposed in this paper, which can be used as a thermo-electric conversion device in vehicle ICE waste heat recovery. Moreover, the FPE-LG prototype is preliminary validated in the air test rig under low intake pressure and steam flow rate condition before it is integrated into the whole ORC system.

2. DESCRIPTION OF THE FPE-LG PROTOTYPE

2.1 The system description of free piston expander coupled with liner generator (FPE-LG)

The thermo-electric conversion components in conventional automotive ORC system consists of independent expander and generator, which need more space for installation and make the ORC system very difficult to application in the vehicle. The FPE-LG unit can be used as a substitute for thermo-electric conversion components in the small scale automotive ORC system owing to compact structure. The basic concept presents in this work is illustrates in Fig.1.

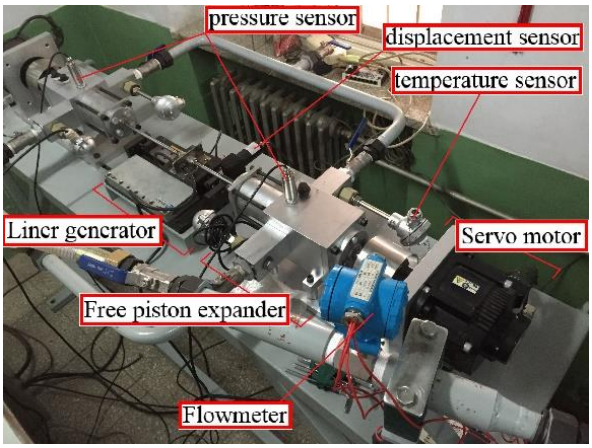

Figure 1: System diagram of FPE-LG

As shown in Fig.1, FPE-LG unit is mainly composed of four components: expander, liner generator, servomotor, measurement and control system. Compared to the opposed arrangement form with two free piston expanders, the piston returning of an independent free piston expander needs an additional return spring what will decrease the reliability in working process. Furthermore, electric energy production by the liner generator need reciprocating movement of the mover. Thus, the former scheme is adopted. Both the output ends of the two opposed FPEs are jointed together with the mover of the liner generator through two flexible joints, and enable the mover to free reciprocate without additional return springs under the support of stator which is fixed on the test-bed. Working principle of the FPE-LG is discussed in detail in the following section.

2.2 Structure layout of free piston expander

During the concept design phase of the prototype, what we mainly focus on is the total electric energy production of liner generator which is decided by piston velocity of FPE according to Faraday's electromagnetic induction law. While the pressure and flow rate of the working fluid in the small scale ORC system have a significant influence on the piston velocity of FPE. Thus, it is very important to select appropriate structure parameters in order to satisfy these design requirements. Subsequently, the diameters of the expander cylinder and the stroke are calculated according to the assumed compression ratio. Moreover, the important factors which are mentioned above have been taken into consideration overall. The final geometric parameters of the FPE are determined as shown in Table.1.

Table 1: Structure parameters of free piston expander

Items	Value	Units
Cylinder bore	80	mm
Working frequency	1-8	Hz
Stroke	102	mm
Piston rod diameter	10	mm
Compression ratio	8	
Intake/exhaust port diameter	20	mm

Fig.2 shows the structure of the free piston expander. The FPE mainly includes following components: cylinder head, piston group, cylinder, valve seat, cylinder block, valve train, valve sleeve, fixed plate, cover, guide sleeve, input shaft. Simultaneously, the output end of a 200V servomotor is connected to input shaft of the expander with a flexible coupling joint which can ensure alignment of center line. Thus, working fluid inflow and outflow of the FPE can be adjusted via the valve train which movement is controlled by the servomotor. In order to reduce the loss of friction, the closed space between the cover and fixed plate is filled with lubricating oil which can be added through a small hole on the cover. We select aluminum alloy for constituting the moving parts including valve and piston while the other main parts are constituted with 304 stainless steel, since aluminum alloy has high-strength which is used generally in ICE piston design, it can bear the high pressure and temperature in ORC system and maintain its mechanical property in these conditions while 304 stainless steel has good resistance to corrosion. Owing to the mechanical wear between the piston group and cylinder head, a guide sleeve constituted with aluminum bronze is placed in the cylinder head which can improve the service life of piston rod and meet the high precision demand of the piston group installed.

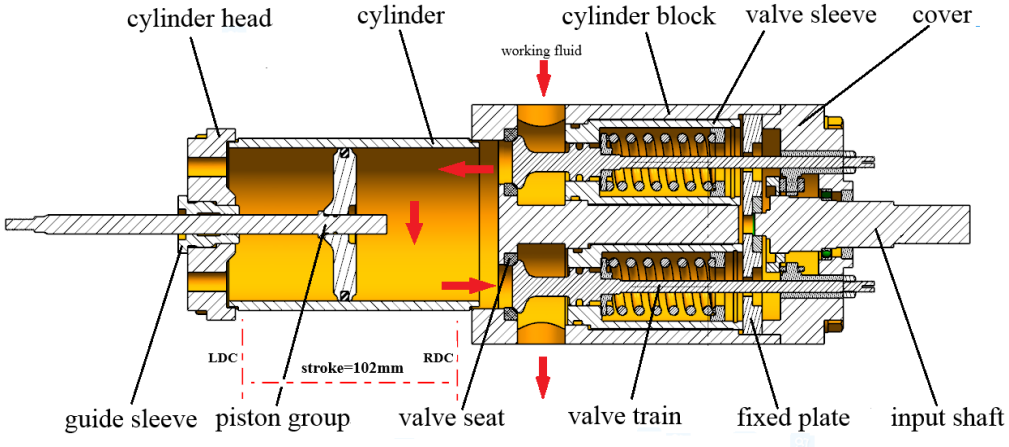

Figure 2: Structure diagram of free piston expander

Based on the description about main structure of the free piston expander and selection of key parts above, the working process of the FPE-LG prototype can be simply described as following: firstly,

two servomotors are set to certain phase difference before the FPE-LG operates, which can ensure the inlet valve of expander on one side opens while the outlet valve on other side closes. Taking the expander on the right side (as shown in Fig.2) as an example, the exhaust gas exchanges heat with the organic working fluid in the evaporator when ORC system works. Meanwhile the organic working fluid turns into high-temperature and high-pressure gas, which is injected into the expander intake port and then enters into the expander cylinder when the inlet valve opens, driving the piston to the LDC. Simultaneously, the outlet valve of the left expander opens which is controlled by another servomotor and the in-cylinder pressure is lower than the right side. So the piston is pushed to the RDC under the action of force produced by the right expander. In this process, the liner generator mover can move together with expander piston groups, cutting the magnetic induction lines to produce electric energy.

2.3 The expander inlet/outlet control method

The free piston expander seems to be the most suitable thermal-power conversion component for small scale ORC system if the inlet/outlet control is carried out successfully, since it has the greatest potential for practical application owing to the good sealing, less mechanical loss and simple structure. In fact, the development of the free piston concept at the TU Dresden seems to be the most promising one up till now, because the efficiency was reported to approach 50% and the prototype expander was verified to be feasible. The electronically controlled valve is abandoned owing to the high cost and complex control system. Thus, a novel mechanical valve train has been created for the FPE in this paper and a full scaled CAD model of the valve train which is built via CATIA V5R21® is prepared for the subsequent analyses, as shown in Fig.3.

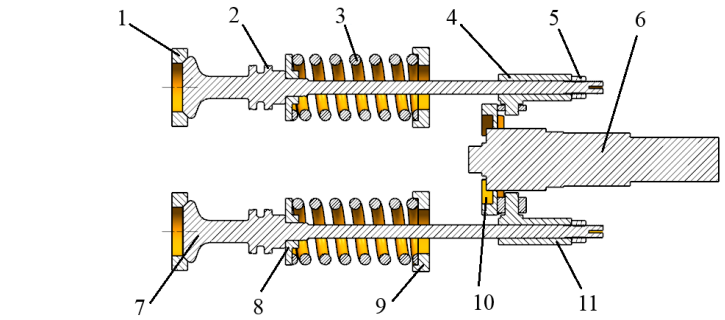

Figure 3: Structure diagram of FPE valve train

The structure of the FPE valve train is illustrated in Fig.3. It is mainly composed of several parts: valve seat, valve spring, cam plate, inlet/outlet valve slider, input shaft, inlet/outlet valve, bearing disc A and B. The cam plate is processed into stepped shape with a height difference of 3 millimeter. The surface of upward and downward position is processed into arc surface in order to reduce the resistance of the valve opening and closing. The valve spring with a pre-compressing quantity of 5.5 millimeter is fixed between bearing disc A and B when the expander is assembled. An axial hole through the center of valve slider is manufactured which can be used to fix the valve with a nut. And the gap between bearing disc B and cam plate can be adjusted by changing the mounting position of bearing disc B after the valve train is assembled into the FPE cylinder block. Through this kind of design approach, the valve slider can be compressed on the cam plate. Thus, the valve opening and closing which is driven through the rotating movement of the cam plate can be achieved.

Considering that the reliability and durability of the valve train is mainly determined by spring load, natural frequency, fatigue resistance and relaxation properties, 55CrSi has been selected for

constituting the mechanical spring of the valve train owing to wide applications in the field of high stress spring and excellent mechanical character which can insure the air tightness at the same time. According to the design parameters of the mechanical spring, as shown in Table 2, spring stiffness (*f*) can be calculated with following equation:

$$f = \frac{G \cdot d^4}{8 \cdot D^3 \cdot n} \tag{1}$$

Table 2: Mechanical spring parameters

Parameters	Mean	Value	Units
G	Shearing modulus of elasticity	8×10^4	N/mm^2
d	Spring diameter	25	mm
D	Wire diameter	5	mm
n	Effective number of turns	5.5	-
f	Stiffness	72.7	N/mm
L	Spring relaxation length	67	mm
c	damping	0.66E-003	N·s/mm

3. DYNAMICS SIMULATION OF THE FPE VALVE TRAIN

3.1 Dynamics simulation model description

The irregular contact surface between cam plate and valve slider will cause a serious problem of calculation convergence in the process of stress analysis. Owing to the diffculty of the nolinear problem in transient structural solution, we adopt a general engineering methodology. Firstly the dynamics simulation is carried out via ADMAS software, which is a professional mechanical dynamics simulation software. Then the contact force simulation results between the valve silders and cam plate are exported and be set as stress analysis boundary conditions in transient structural module of ANSYS® Workbench V14.5. Furthermore, it is also convenient to analyze the valve train movement rule and the design parameters of cam plate profile through ADMAS.

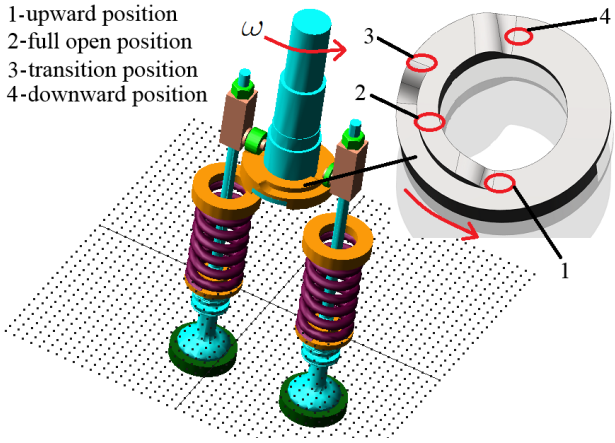

Figure 4: Dynamics simulation model of the valve train

As shown in Fig.4, aim to get the force conditions in the contact location between valve sliders and cam plate, the CAD model we prepared has been imported into the ADMAS. And then, constraints and loads are added according to the true motion. In order to obtain precise results, the spring, valve sliders and valves are set as flexible parts which are divided into suitable mesh, while the rest are set as rigid parts. Simutaneously, the time of the cam plate rotates a cycle is defined as the end time of simulation in order to observe the change of force more clearly, while the simulation steps are defined to one thousand which can ensure the accuracy of dynamics simulation results.

3.2 Analysis of the simulation results and boundary conditions extraction

Force conditions between the inlet/outlet valve sliders and cam plate at different servomotor input frequencies is analyzed. We select 2Hz, 5Hz, 8Hz, 10Hz as input simulation variables to prove the reliability of the valve train at design frequency.

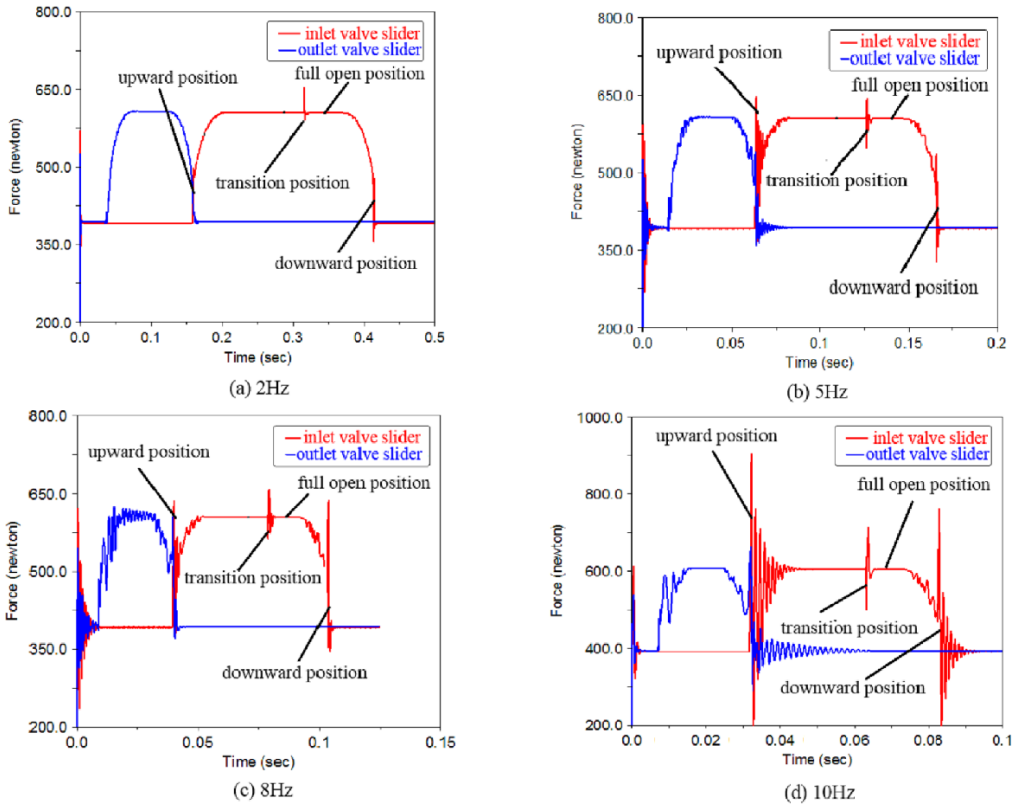

Figure 5: Total contact force of valve sliders at different servomotor input frequencies

Fig.5 shows the total contact force comparisons between the inlet and outlet valve slider at different input frequencies. The sudden change of contact force on inlet valve slider increased significantly with improvement of the servomotor input frequencies when it reaches the upward and downward positon, while the change rule of outlet valve slider is not obvious at low input frequency. There is hardly any sudden change of the force in the inlet valve opening and closing process in Fig.5(a), however, as we can see in Fig.5(b) (c) (d) the fluctuating intensities and the magnitudes of the force changes obviously. Simultaneously, a sudden change of contact force occurred at the transition positon owing to the sudden decreasing of the contact surface between inlet valve slider and cam plate. However, the contact surface between outlet valve slider and cam plate is constant, so the variation of contact force between the outlet valve slider and cam plate at the transition position is very different from it. Meanwhile, both contact force of the inlet and outlet valve slider has no significant change at the full open position. Then, the force data of inlet/outlet valve sliders in three coordinate directions is exported, which can be set as the force load in following stress analysis.

4. FINITE ELEMENT MODLE OF THE FPE VALVE TRAIN

Based on analysis of the simulation results above, the left side where inlet valve is settled as shown in Fig.4 is taken as main research object owing to the complexity of the contact force change. The finite element (FE) model of the valve train used in the numerical analysis is constructed, the assembled finite element model includes inlet valve, valve spring, inlet valve slider, nut, circular bearing disc A and B, as shown in Fig.6.

In order to precisely simulate the real contact and load conditions in stress analysis, the simplified model is meshed using SOLID187, a higher order three-dimensional solid element, which has a quadratic displacement behavior and well suited to model irregular meshes. The element is defined by 10 nodes having three transitional DOF at each node. The valve train FE model has 319795 elements and 484079 nodes.

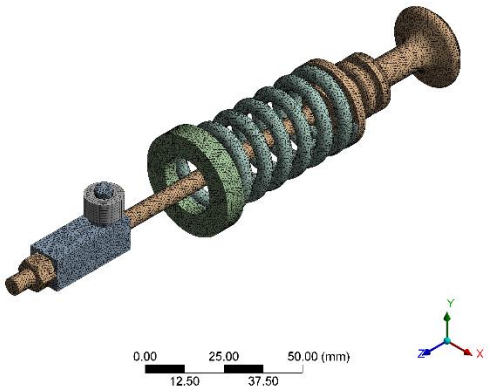

Figure. 6: Finite element model of the valve train

4.1 simplification of boundary conditions and imposing load

In order to ensure convergence of calculation, the boundary conditions such as force and displacement of each part or part contacts must be simplified according to actual conditions before the solution program of FE model has been carried out.

Based on the actual working conditions, an equivalent intake pressure which is imposed on the inlet valve head has been ignored. The total friction of contact portions has much less influence on the calculation results in the design conditions owing to splash lubrication. Then, the contact force of inlet valve slider in three coordinate directions which is obtained via ADMAS is imported into transient structural module as calculation boundary. Considering that it is approximately liner contact between the inlet valve slider and cam plate, main load is defined to nodal force which magnitude depends on the dynamic simulation results. Completely bonded contact is assigned to the interface between components. A displacement constraint which is limited the X, Y directions and free the Z direction is applied to four profiles of the valve slider and a fix constraint is assigned to the cylindrical surface of the bearing disc B. Finally, an equivalent spring contact is assigned to the contact surface between two bearing discs which stiffness, damping, preload is defined to 72N/mm, 0.66E-003Ns/mm and 400N according to the calculation results in section 2.3, respectively.

4.2 Experimental validated of FPE-LG in air test rig

In order to validate the correctness of working principle of the expander and the valve train, an air test rig has been set up. As shown in Fig.7, it includes high pressure air compressor, air receiver, connecting pipe, FPE-LG, acquisition system. Furthermore, test of the valve train in actual working conditions is conducted to validate the results of stress simulation, which is discussed in detail in the following section.

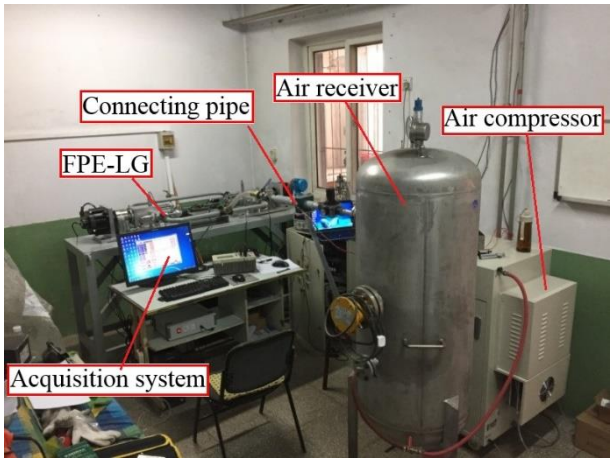

Figure. 7: FPE-LG test bench

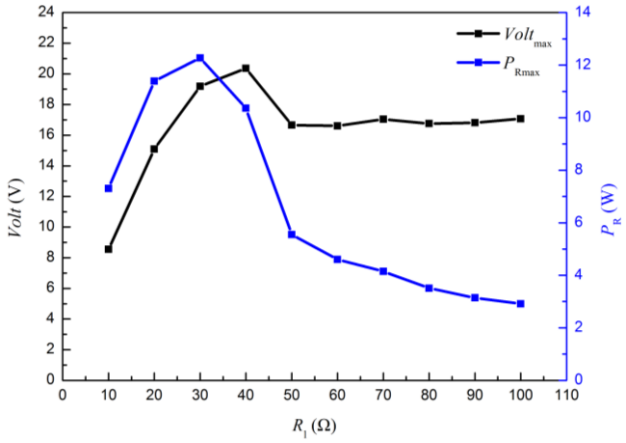

Figure. 8: Load peak voltage and peak power for different load resistance

In order to assess the thermoelectric conversion capacity of the FPE-LG, preliminary experiment is carried out at a certain condition, which intake pressure, input frequency, external load resistance is 0.2MPa, 1.5Hz and 10Ω-100Ω respectively. As illustrated in Fig.8, the maximum transient voltage is 20.4V when the external load resistance value is 40Ω. The maximum output power is 12.3W when the external load resistance value is 30Ω according to the Ohm's law. Since the compressed air is selected as working fluid in this pneumatic test, the working pressure and temperature are lower than conventional ORC system. However, the transient maximum output power of FPE-LG is considerable. More experiments about other variable factors includes intake pressure, input frequency, evaporating temperature will be conducted when the FPE-LG is integrated into a small scale ORC system.

The FPE-LG prototype can operated stably at different servomotor input frequencies from 1Hz to 8Hz. The maximal pressure in cylinder can reach 5 bar. Although the FPE-LG prototype can operate at a higher input frequency and pressure, we don't further improve it since the collision between piston and cylinder head increases obviously with input frequency improving.

5. ANALYSIS OF SIMULATION RESULTS

The prototype can operate steadily at different input frequencies in the air test rig. However, crack of the inlet valve slider mainly originates from the same region after long time running, which is marked with A in Fig.9.

Figure 9: Actual failure region of the inlet valve slider

FE analyses results illustrates that the root of inlet valve slider is subjected to stress concentration which make it easily failure region and can cause a premature failure problem. This is consistent with the actual damage conditions. Owing to high speed and frequent collision with the cam plate, a large quantities of heat is generated through friction, which can also reduce the serve life of the inlet valve slider.

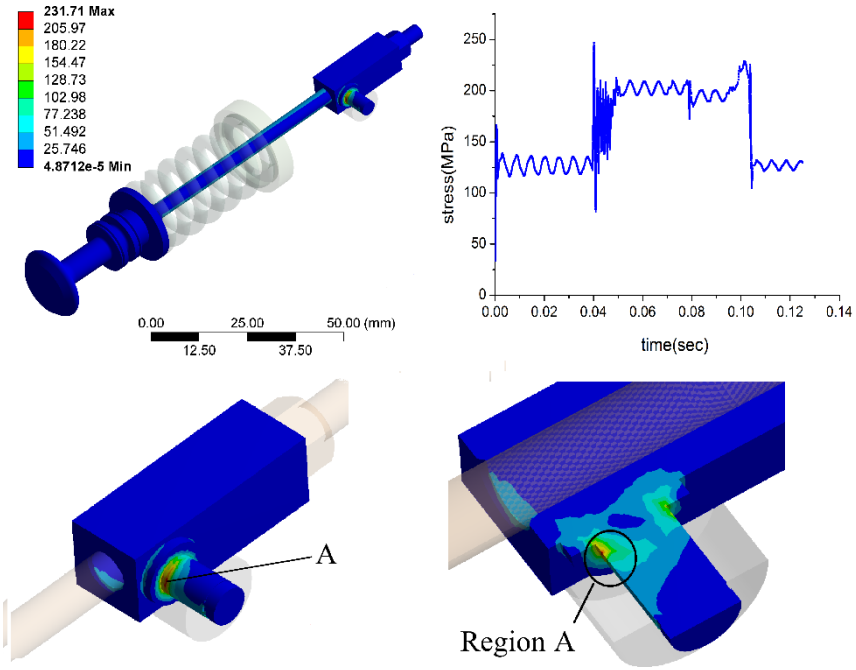

Figure 10: Equivalent von Mises stress (MPa) distribution on the inlet valve slider

Fig.10 shows equivalent von Mises stress distribution obtained from the FE analysis when the servomotor input frequency is 8Hz which is the maximum value in actual test conditions. It can be seen that the maximum von Mises stress is 231.71Mpa which mainly concentrates on the root of inlet valve slider when it moves from upward position to full open position. Simultaneously, the fluctuation of the von Mises stress is obvious in one working cycle. The results are agreement with actual situations. The maximum stress is meet limit yield of material which is selected to constitute the valve slider. However, the stress in this area (marked with A) is close to the mechanical strength of the material, which indicates that the region is a critical area and prone to be failed. Enhancement of the fatigue life of the inlet valve slider is dependent on the decreases of the stress concentration. Hence, adding a fillet to the root of inlet valve slider and taking heat treatment are both the effective methods to eliminate the stress concentration. Because of the exact value of stress distribution on the root of

valve slider is difficult to measure in practice, the proposed method of analyzing the failure of valve slider, which takes into account of several key position, is predictive and applicable.

6. CONCLUSIONS

In this paper, an engineering methodology is adopted to analyze the structure reliability of the FPE valve train. And experimentally validated of FPE-LG in an air test rig is conducted before it is integrated into whole ORC system. The main conclusions can be drawn as follows:

- The results of the stress analysis indicated that the region of stress concentration on the inlet valve slider is in coincidence with the real failure areas. The maximum value of the von stress is 231.71MPa in a working cycle. The stress concentration and fluctuation are two main factors which strongly affects the structural reliability of the valve train. The methodology is feasible and low-cost in the prototype design. And the mechanical damage of the operated prototype indicates that FPE can't work normally when it deviated from the analysis results in this paper.
- The FPE-LG with the novel valve train was validated in the air test system. The results shows that the FPE-LG can operate in a wide range of input frequencies from 1Hz to 8Hz which reveals that the inlet/outlet control scheme is feasible. Furthermore, the pressure in cylinder can reach 5 bar. The FPE-LG prototype described in this work is shown to be successful in meeting its design goals.
- Further experimental validation about the FPE-LG will be conducted in a miniature ORC system in near future.

REFERENCES

Ou, X.M., Yan, X.Y., Zhang, X., Zhang, X.L., 2013, Life-cycle energy use and greenhouse gas emissions analysis for bio-liquid jet fuel from open pond-based micro-algae under China conditions, *Energies*, vol. 6, p. 4897-4923.

Boretti, A., 2012, Recovery of exhaust and coolant heat with R245fa organic Rankine cycles in a hybrid passenger car with a naturally aspirated gasoline engine, *Appl Therm Eng*, vol. 36, p. 73-77.

He, Y.L., Mei, D.H., Tao, W.Q., Yang, W.W., Liu, H.L., 2012, Simulation of the parabolic trough solar energy generation system with Organic Rankine Cycle, *Appl Energ*, vol. 97, p. 630-641.

Wang, W., Wu, Y.T., Ma, C.F., Liu, L.D., Yu, J., 2011, Preliminary Experimental Study of Single Screw Expander Prototype, *Appl Therm Eng*, vol. 31, p. 3684-3688.

Gao, W.Z., Zhai, J.M., Li, G.H., Bian, Q., Feng, L.M., 2013, Performance evaluation and experiment system for waste heat recovery of diesel engine, *Energy*, vol. 55, p. 226-235.

Han, Y.Q., Kang, J.J., Zhang, G.P., et al, 2014, Performance evaluation of free piston compressor coupling organic Rankine cycle under different operating conditions, *Energ Convers Manage*, vol. 86, p. 340-348.

Zhang, B., Peng, X., He, Z., Xing. Z., Shu, P., 2007, Development of a double acting free piston expander for power recovery in transcritical CO2 cycle, *Appl Therm Eng*, vol. 27, p. 1629-1636.

ACKNOWLEDGEMENT

This work was sponsored by the Beijing Natural Science Foundation Program (Grant No. 3152005), the National Natural Science Foundation of China (Grant No. 51376011), and the Scientific Research Key Program of Beijing Municipal Commission of Education (Grant No. KZ201410005003).

WORKING FLUID SELECTION FOR ORGANIC RANKINE CYCLES BASED ON CONTINUOUS-MOLECULAR TARGETS

Johannes Schilling[1], Matthias Lampe[1], Joachim Gross[2], André Bardow[1*]

[1] Chair of Technical Thermodynamics, RWTH Aachen University,
Schinkelstraße 8, 52062 Aachen, Germany
E-mail: andre.bardow@ltt.rwth-aachen.de

[2] Institute of Thermodynamics and Thermal Process Engineering, Stuttgart University,
Pfaffenwaldring 9, 70569 Stuttgart, Germany

* Corresponding Author

ABSTRACT

Organic Rankine Cycles (ORCs) transform heat from low-temperature sources to electrical power. To ensure optimal use of a heat source, the cycle needs to be tailored to the specific application. Tailoring the cycle means optimizing both process and working fluid. Simultaneous optimization of process and working fluid is enabled by the Continuous-molecular targeting (CoMT) framework. Herein, working fluid properties are calculated by the perturbed-chain statistical associating fluid theory (PC-SAFT). The pure component parameters representing the working fluid are relaxed during the optimization leading to an efficient nonlinear program (NLP). The solution is an optimal combination of working fluid and process. Due to the relaxation, the pure component parameters of the optimal working fluid, in general, do not coincide with any real working fluid. Thus, real working fluids with similar properties are searched for in the following step, the so-called structure-mapping. Currently, a Taylor approximation of the objective function around the hypothetical optimal working fluid is used to estimate the objective function value of real working fluids. The Taylor approximation does not account for changes in the active set of constraints leading to occasional poor classification of the working fluids. To overcome this shortcoming, we present an adaptive structure-mapping: An additional Taylor approximation is added around a sampling point, if its approximation is poor. All Taylor approximations are combined using inverse distance weighting. The resulting adaptive structure-mapping improves the quality of the result and efficiently identifies the best working fluids. The approach is demonstrated in a case study for working fluid selection of a solar ORC.

1. INTRODUCTION

Organic Rankine Cycles enable the utilization of low-temperature heat to generate electrical power. Low-temperature heat is available from different sources, e.g., solar (Tchanche et al., 2009), geothermal (Heberle and Brüggemann, 2010), biomass (Drescher and Brüggemann, 2007) or waste heat (Wang et al., 2012). To ensure optimal use of a heat source, the cycle needs to be tailored to the specific application. For tailoring the cycle, both have to be optimized: process and working fluid.

Today, working fluid selection and process optimization are commonly carried out separately following a two-step approach (Tchanche et al., 2009; Drescher and Brüggemann, 2007; Quoilin et al., 2013): In a first step, working fluid candidates are preselected by experience and based on heuristic guidelines defining favorable working fluid properties. In the second step, the process is optimized for each preselected working fluid. For the preselection, a variety of different, partly conflicting heuristic criteria have been proposed. Papadopoulos et al. (2010) combine therefore computer-aided molecular design (CAMD) methods and multi-objective optimization for working fluid selection. Importantly, the proposed criteria can not reflect the actual operating conditions. However, if the heuristic knowledge underlying

the preselection fail, meaningful and promising working fluids are excluded leading to suboptimal solutions. Working fluid selection is inherently coupled to process optimization. Thus, recent reviews (Quoilin et al., 2013; Bao, J. and Zhao, L., 2013) recommend including working fluid selection in process optimization to obtain an overall optimal solution. However, the direct integration of these two design tasks leads to a mixed integer nonlinear program (MINLP) of prohibitive size and complexity for practical applications (Lampe et al., 2014). Recently, Papadopoulos et al. (2013) use a process-related objective function. The working fluid properties are modeled by a cubic equation of state and combined with a process model.

Simultaneous optimization of process and working fluid is achieved in the Continuous-molecular targeting framework by relaxation of the pure component parameters describing the working fluid (Bardow et al., 2010; Lampe et al., 2014; Stavrou et al., 2014). Here, in a first step, a hypothetical working fluid is identified maximizing a process-based objective function. Then, real working fluids with similar properties are identified in the second step, the so-called structure-mapping. For this purpose, a Taylor approximation around the hypothetical optimal working fluid is used to estimate the objective function value of real working fluids. However, this local approximation suffers from occasional poor classification of real working fluids. In this work, we present a method for adaptive structure-mapping to allow for efficient identification of the best working fluids.

The paper is structured as follows: in section 2, the current CoMT framework is briefly reviewed. Our method for adaptive structure-mapping is introduced in section 3. In section 4, the adaptive structure-mapping is applied to a case study and the results are analyzed. Conclusions are drawn in section 5.

2. CONTINUOUS-MOLECULAR TARGETING FRAMEWORK

Selecting a suitable working fluid is a generic problem with applications beyond ORC processes. Bardow et al. (2010) propose a generic approach, the so-called continuous-molecular targeting (CoMT). The approach was first applied to achieve simultaneous optimization of solvents and processes. Lampe et al. (2014) successfully applied the CoMT framework for the simultaneous process and working fluid optimization of ORC processes (Figure 1).

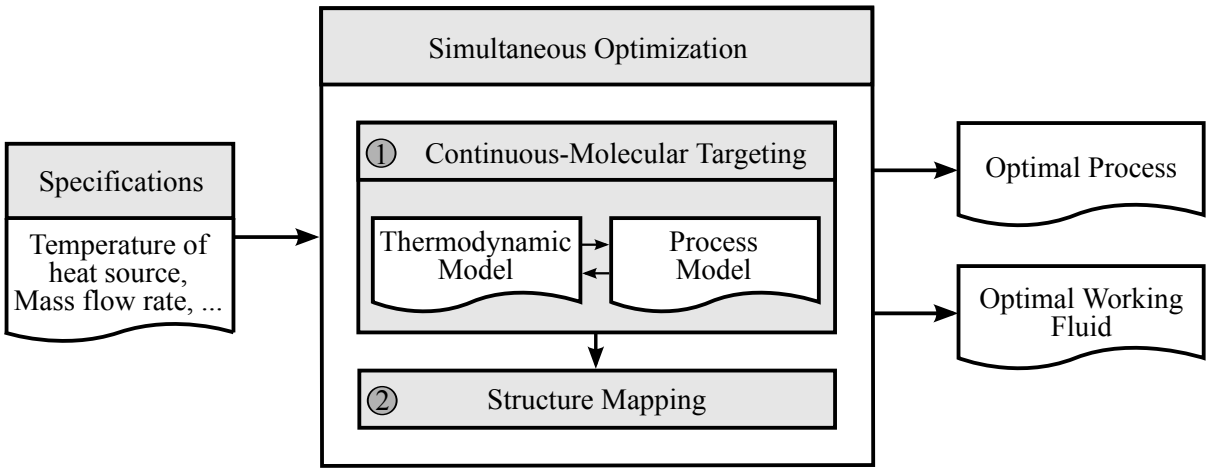

Figure 1: Simultaneous optimization of working fluid and process using the CoMT framework

To allow for the integrated process and working fluid optimization, we exploit the rich molecular picture underlying the perturbed-chain statistical associating fluid theory (PC-SAFT) equation of state (Gross and Sadowski, 2001). PC-SAFT is a model of the Helmholtz energy, which ensures a consistent picture of all equilibrium properties of the working fluid. A set of typically up to seven pure component parameters describes each working fluid (Stavrou et al., 2014). For simplicity, non-polar and non-associative

working fluids are considered in this work. Each working fluid is then described by three parameters: the segment number m, the segment diameter σ, and the segment dispersion energy ϵ/k.
A direct formulation of the integrated optimization using the pure component parameters as variables leads to a MINLP of prohibitive size and complexity, because a discrete degree of freedom is added to the problem for each real working fluid. Here, the MINLP is avoided by relaxing the pure component parameters during the simultaneous optimization of process and working fluid. Relaxation transforms the MINLP into a NLP of the form

$$\begin{aligned} &\max_{x,y} f(x,y) \\ s.t.\quad &g(x,y) \leq 0 \\ &h(x,y) = 0 \\ &Ay \leq b \\ &x_{\text{min}} \leq x \leq x_{\text{max}} \ \in \mathrm{R}^{\mathrm{n}} \\ &y_{\text{min}} \leq y \leq y_{\text{max}} \ \in \mathrm{R}^{\mathrm{m}} \end{aligned} \tag{1}$$

where x denotes the process variables, y denotes the pure component parameters and $f(x,y)$ denotes the objective function to be optimized. Here, any objective function can be employed, which is based on equilibrium thermodynamics. First approaches are available to even calculate transport properties based on PC-SAFT (Novak, 2011; Lötgering-Lin and Gross, 2015). The integration of such approaches would allow for a thermoeconomic objective function still requiring only PC-SAFT parameters to describe the working fluid. Without loss of generality, maximization is considered. The inequality and equality constraints of the process as well as PC-SAFT are formed by $g(x,y)$ and $h(x,y)$. The solution of Problem (1) is a hypothetical optimal working fluid y^* and the corresponding optimal process parameters x^*. In general, the hypothetical optimal working fluid does not coincide with a real fluid. To identify real fluids, a database of pure component parameters is used in this work. The values of the database can, in turn, be used to constrain the search space for optimization. For this purpose, a convex hull around the pure component parameters of real working fluids y_{k} of a database is used. The convex hull is represented by the set of linear constraints $Ay \leq b$ in Problem (1).
In the second step, real working fluids with similar properties as the hypothetical optimal working fluid are identified (Figure 1). Currently, a second degree Taylor approximation around the hypothetical optimal working fluid is used to estimate the objective function value of real working fluids (Bardow et al., 2010; Lampe et al., 2014; Stavrou et al., 2014). For this purpose, it is necessary to rewrite the objective function $f(x,y)$ as

$$\begin{aligned} \tilde{f}(y) \ = \ &\max_{x} f(x,y) \\ &s.t.\quad g(x,y) \leq 0 \\ &\qquad h(x,y) = 0 \\ &\qquad x_{\text{min}} \leq x \leq x_{\text{max}} \ \in \mathrm{R}^{\mathrm{n}}. \end{aligned} \tag{2}$$

From Problem (2), the Taylor approximation around optimum values y^* is calculated:

$$T(y) = \tilde{f}(y^*) + J(y^*)(y-y^*) + \frac{1}{2}(y-y^*)^{\mathrm{T}} H(y^*)(y-y^*). \tag{3}$$

Here, $J(y^*)$ denotes the Jacobian and $H(y^*)$ the Hessian of $\tilde{f}(y)$ at the sampling point y^*. Thus, the approximation of the performance for a working fluid is solely characterized by pure component parameters y_k. Based on the approximation $T(y_{\text{k}})$, a ranking of potential working fluids is obtained. Each working fluid is classified by the rank r of the ranking. However, the Taylor approximation does not account for changes in the active set of constraints (Lampe et al., 2014), whereby a substantial deviation between the Taylor approximation and the real objective function value occurs (Figure 2a). Thus, working fluids are classified wrongly. To overcome these shortcomings, an adaptive structure-mapping is presented.

3. ADAPTIVE STRUCTURE-MAPPING

The adaptive structure-mapping iteratively identifies sampling points to adapt the approximation. In section 3.1, the method for selection of additional sampling points is presented. The adaption of the current approximation is detailed in section 3.2.

3.1 Algorithm

The key idea for the adaption of approximation is to apply a Taylor approximation not only once at the hypothetical optimal working fluid, but also at additional sampling points. The individual Taylor approximations $T_{\mathrm{i}}(y)$ are combined to an adapted approximation $A(y)$ (Figure 2). The sampling points are selected in regions with a substantial deviation between the current approximation and the objective function. Through an iterative selection of suitable sampling points, the approximation, and therefore the structure-mapping, is adapted until a sufficient accuracy is achieved.

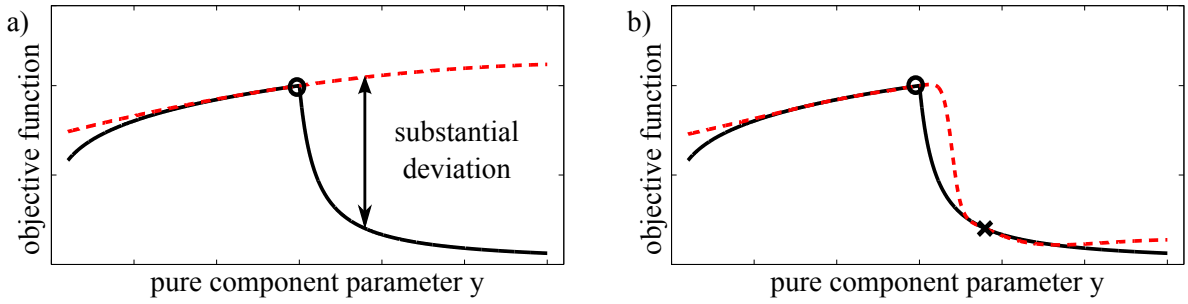

Figure 2: Qualitative illustration of the adapted approximation of the objective function $\tilde{f}(y)$ (black, solid) in the mapping step: a) Taylor approximation $T(y)$ (red, dashed) around the optimum y^* (marker ○), b) adapted approximation $A(y)$ (red, dashed) with an additional sampling point (marker ×) in a region with previous substantial deviation between the objective function and the approximation.

The starting point is the ranking based on the Taylor approximation around the hypothetical optimal working fluid (step 1 in Figure 3). The selection of the next sampling point is performed by a systematic analysis of the current ranking (step 2). Beginning with the highest ranked working fluid $r = 1$ and following the order of the ranking , the real objective function value $\tilde{f}(y_{\mathrm{r}})$ of the r-th ranked working fluid y_{r} is calculated from Problem (2) (step 2a). This procedure continues, until the absolute difference ΔA_{r} between approximation $A(y_{\mathrm{r}})$ and real objective function value $\tilde{f}(y_{\mathrm{r}})$ exceeds a threshold ΔA_{max} (step 2b)

$$\Delta A_{\mathrm{r}} = |A(y_{\mathrm{r}}) - \tilde{f}(y_{\mathrm{r}})| > \Delta A_{\mathrm{max}}. \tag{4}$$

Here, r denotes the rank of the working fluid in the current ranking. In this work, the threshold ΔA_{max} is set to $5\,\%$ of the objective function value of the hypothetical optimal working fluid. If the absolute difference ΔA_{r} exceeds the threshold, the pure component parameters of this r-th ranked working fluid are selected as additional sampling point. The approximation $A(y)$ is adapted by taking a Taylor approximation of the additional sampling point into account (step 3, see section 3.2 for details). A revised ranking of potential working fluids is obtained based on the adapted approximation (step 4). Subsequently, a termination criterion is checked (step 5). The algorithm stops, if for the first 15 ranks of the revised ranking a process optimization is performed in a previous iteration. If the termination criterion is not fulfilled, the algorithm continues at step 2. Beginning with the highest ranked working fluid $r = 1$, the algorithm analyzes the revised ranking systematically to select one more additional sampling point. Thus, the approximation is iteratively adapted to the objective function, since a region with previous poor approximation is improved by an additional Taylor approximation in each iteration. As a result, the method yields a ranking based on the real objective function values of the already calculated working fluids and the approximations of all further working fluids. The adaptive structure-mapping improves the quality of the ranking and allows for efficient identification of the best working fluids.

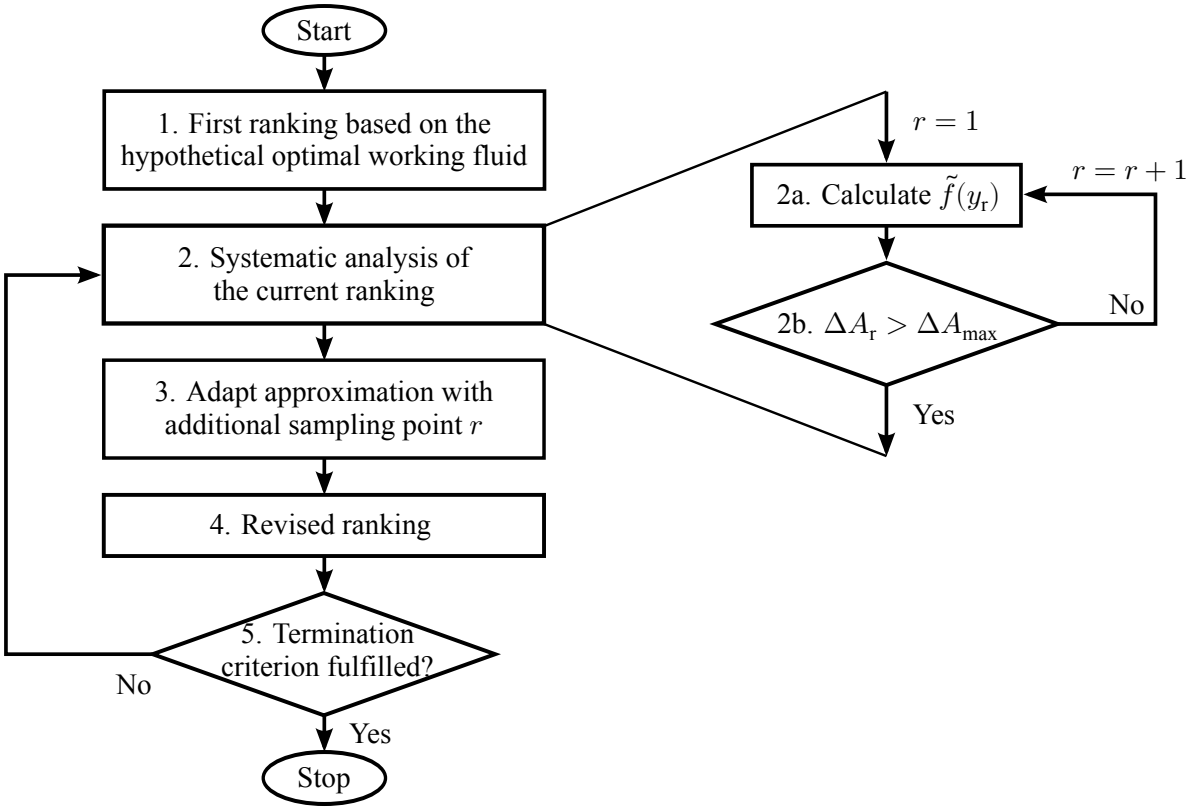

Figure 3: Flow chart for adaptive structure-mapping.

3.2 Adaptive approximation

The adaptive approximation $A(y)$ is a weighted sum of individual Taylor approximations $T_i(y)$. The Taylor approximations $T_i(y)$ are calculated by Equation (3), whereby the pure component parameters of the hypothetical optimal working fluid y^* are replaced by the sampling points y_i. The individual Taylor approximations $T_i(y)$ around the sampling points y_i are multiplied by a weighting factor $w_i^*(y)$ and combined to an adapted overall approximation $A(y)$ of the objective function

$$A(y) = \sum_{i=1}^{S} w_i^*(y) \cdot T_i(y), \tag{5}$$

whereby S denotes the number of sampling points. The weighting factor $w_i^*(y)$ increases the influence of Taylor approximation $T_i(y)$ the closer the pure component parameters y are to the corresponding sampling point y_i. A suitable method for this purpose is the so-called inverse distance weighting. In this work, the distance between two points in the three-dimensional space spanned by the pure component parameters $y = (m, \sigma, \epsilon/k)^T$ is considered. The pure component parameters have different magnitudes and units. To prevent effects of different scaling, the pure component parameters are normalized to one by

$$m_n = \frac{m - m_{min}}{m_{max} - m_{min}}, \quad \sigma_n = \frac{\sigma - \sigma_{min}}{\sigma_{max} - \sigma_{min}}, \quad (\epsilon/k)_n = \frac{(\epsilon/k) - (\epsilon/k)_{min}}{(\epsilon/k)_{max} - (\epsilon/k)_{min}}, \tag{6}$$

yielding normalized pure component parameters $y_n = (m_n, \sigma_n, (\epsilon/k)_n)^T$. Here, parameters $y_{j,min}$ and $y_{j,max}$ are the smallest and largest value of the pure component parameters of the database respectively. The inverse distance $d_i^{-p}(y)$ of the Taylor approximation $T_i(y)$ around a sampling point y_i is calculated by (Dumitru et al., 2013):

$$d_i^{-p}(y) = \frac{1}{\|y_n - y_{n,i}\|^p}. \tag{7}$$

The weighting factor depends on the so-called power parameter p. The best results are typically obtained for $p = 2$ (Dumitru et al., 2013). To ensure that the approximation at the sampling point matches the

objective function value, the sum of all inverse distances is normalized to one leading to a weighting factor $w_i^*(y)$:

$$w_i^*(y) = \frac{d_i^{-p}(y)}{\sum_{u=1}^{S} d_u^{-p}(y)}. \tag{8}$$

The approximation $A(y)$ does not explicitly account for changes in the active set of constraints. However, the adaption captures the behavior of the objective due to the changes in the active set.

The adaptive approximation improves the solution but it can also produce suspicious solution as shown in the following. Figure 4 illustrates a qualitative one-dimensional example for the objective function and its approximation. A second degree Taylor approximation around a sampling point in a region with strong convex curvature leads to unphysical approximation and slow convergence of the adaptive structure-mapping (Figure 4a). This difficulty is circumvented by using a first degree Taylor approximation instead of a second degree Taylor approximation in regions with convex curvature (Figure 4b).

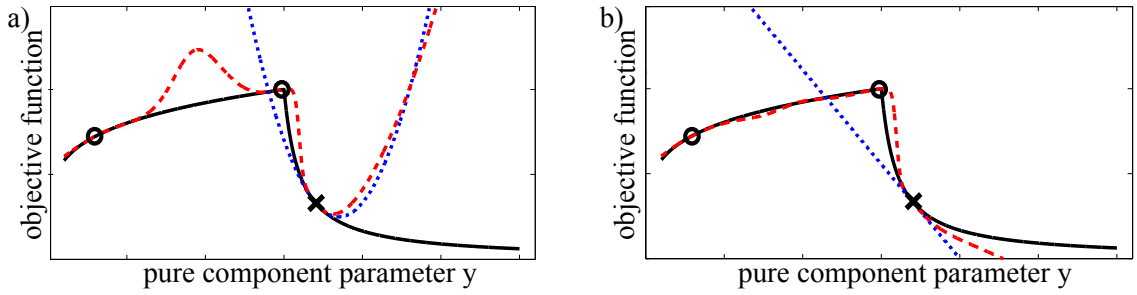

Figure 4: Approximation $A(y)$ (red, dashed) of the objective function $\tilde{f}(y)$ (black, solid) with a) second degree and b) first degree Taylor approximation $T_i(y)$ (blue, dotted) around a sampling point in a region with strong convex curvature (marker ×)

In the multidimensional case, a function is considered to be concave, if a concave curvature exists in all spatial directions. In the major part of the considered parameter space, the objective function shows both concave and convex curvatures in the various spatial directions. If first degree Taylor approximations are used whenever one spatial direction has convex curvature, a first degree Taylor approximation is chosen for almost all sampling points. This leads to slow convergence of the adaptive structure-mapping and, thus, longer computing time, since the approximation is much less accurate.
For this reason, we classify the vicinity of a sampling point as concave, if possible convex curvatures in all directions are negligible compared to the concave curvature. Curvature is evaluated from the eigenvalues of the Hessian $\tilde{H}(y_i)$ of the objective function $\tilde{f}(y)$. In order to ensure comparability of the eigenvalues, the Hessian is transformed to the normalized parameter space (Equation (6)). Positive eigenvalues characterize convex and negative concave curvature; the magnitude is a measure for the strength of the curvature. We allow convex curvature, if the highest eigenvalue λ_{max} of the normalized Hessian is at least an order of magnitude smaller than the amount of the lowest eigenvalue λ_{min}. With this restriction, the Hessian $H(y_i)$ in Equation (3) is

$$H(y_i) = \begin{cases} \tilde{H}(y_i), & \text{if } \ 10 \cdot \lambda_{max} < |\lambda_{min}| \\ 0_{3,3}, & \text{otherwise.} \end{cases} \tag{9}$$

Using this heuristic, more second degree Taylor approximations are selected, while avoiding unphysical impact of the convex curvature. This curvature approach proves suitable in all case studies.

4. CASE STUDY – SMALL-SCALE SOLAR THERMAL ORC SYSTEM

The adaptive structure-mapping is applied to the optimization of a ORC process with direct solar evaporation based on Casati et al. (2011). A recuperator is used to increase the efficiency. The net power

output P_{net} is considered as objective function. The degrees of freedom in the process model are: pressure of the condenser p_{cond}, pressure of the evaporator p_{evap}, degree of superheating ΔT_{sh} and mass flow rate of the working fluid $\dot{m}_{\text{wf}}$. We assume a fixed heat flow of the solar field $\dot{Q}_{\text{solar}}$ at the temperature T_{Q} (Table 1). A minimal temperature difference in the heat exchangers ΔT_{pinch} is imposed to ensure feasible heat transfer. The pressure levels in the cycle are further constrained by minimal and maximal absolute pressures p_{min} and p_{max}, respectively.

Table 1: Solar source specifications and constraints for the case study

Parameter	Symbol	Value
temperature of heat source	T_{Q}	380 °C
heat flow of the solar field	$\dot{Q}_{\text{solar}}$	463 kW
temperature of heat sink	T_{S}	80 °C
maximal absolute pressure	p_{max}	50 bar
minimal absolute pressure	p_{min}	0.05 bar
minimal temperature difference	ΔT_{pinch}	10 K
isentropic turbine efficiency	η_{T}	80 %
generator efficiency	η_{G}	95 %
isentropic pump efficiency	η_{P}	70 %
mechanic pump efficiency	$\eta_{\text{P,mech}}$	90 %

The adaptive structure-mapping is applied to a database of 223 working fluids. In order to evaluate the results of the structure-mapping, an individual process optimization for all working fluids of the database is performed. A real ranking is obtained, which serves as an unambiguous measure for the quality of the ranking from the adaptive structure-mapping. Thus, the database is comparatively small to allow for an efficient validation. The database can easily be extended to consider more fluids. Alternatively, computer-aided molecular design can be employed for the design of working fluids (Lampe et al., 2015). For this case study, the adaptive structure-mapping terminates after two iterations, i.e., three sampling points are used for the overall approximation. All sampling points are approximated by a second degree Taylor approximation. To evaluate the results of the adaptive structure-mapping, the ranking after each iteration is compared to the real ranking. Spearman's rank correlation coefficient ρ_{s} serves as a measure for the correlation (Puth et al., 2015): The closer the correlation coefficient ρ_{s} is to one, the better is the correlation. The corresponding real rank is plotted for the 60 highest ranked working fluids of the structure-mapping (Figure 5).

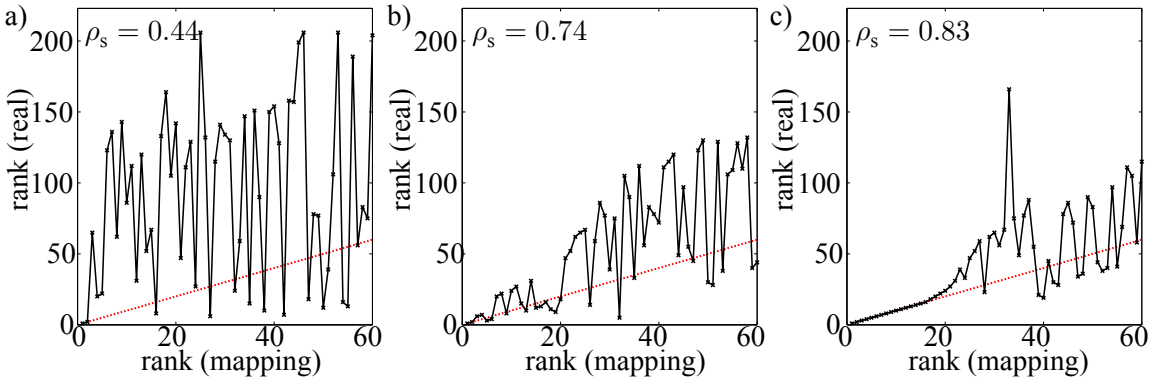

Figure 5: Comparison of result of the CoMT-CAMD approach (black, solid) with one (a), two (b) and three (c) sampling points and the ideal result (red, dotted)

The original structure-mapping with only one Taylor approximation around the hypothetical optimal working fluid identifies the best two working fluids but shows large deficits (Figure 5a): Many working fluids are overestimated and ranked too well. Here, Spearman's rank correlation coefficient is $\rho_{\text{s}} = 0.44$.

The result with two sampling points shows a better correlation ($\rho_s = 0.74$, Figure 5b). In particular, the top 20 are already well captured. The final result with three sampling points identifies the top 20 nearly in the correct order ($\rho_s = 0.83$, Figure 5c).

The original structure-mapping with one Taylor approximation around the hypothetical optimal working fluid identifies only 2 working fluids of the top 10 (4 of the top 20). This result is improved significantly by the adaptive structure-mapping: all working fluids of the top 10 and 18 of the top 20 are identified correctly. The improvement is archived by a more accurate approximation of the objective function in the relevant region. To visualize the functionality of the adaptive structure-mapping, the working fluid ethylcyclohexane is examined ($m = 3.0$, $\sigma = 4.0$ Å, $\epsilon/k = 283.8$ K). Ethylcyclohexane is ranked 9th in the real ranking. Figure 6 shows the optimal net power output $\tilde{f}$ as function of the segment number m for constant segment diameter σ and segment dispersion energy ϵ/k corresponding to the pure component parameters of ethylcyclohexane. The pure component parameters of the hypothetical optimal working fluid y^* are $m^* = 1.8$, $\sigma^* = 4.1$ Å, and $(\epsilon/k)^* = 408.6$ K and are not in the plane of Figure 6. Additionally, the approximation function $A(y)$ with one, two, and three sampling points are plotted. The Taylor approximation around the optimum is not sufficient to approximate the objective function in this region. A substantial deviation between the approximation $A(y)$ and the objective function $\tilde{f}(y)$ occurs: ethylcyclohexane is underestimated and ranked 69th. However, the approximation with three sampling points corresponds well to the objective function. Ethylcyclohexane is correctly ranked 9th in the final ranking.

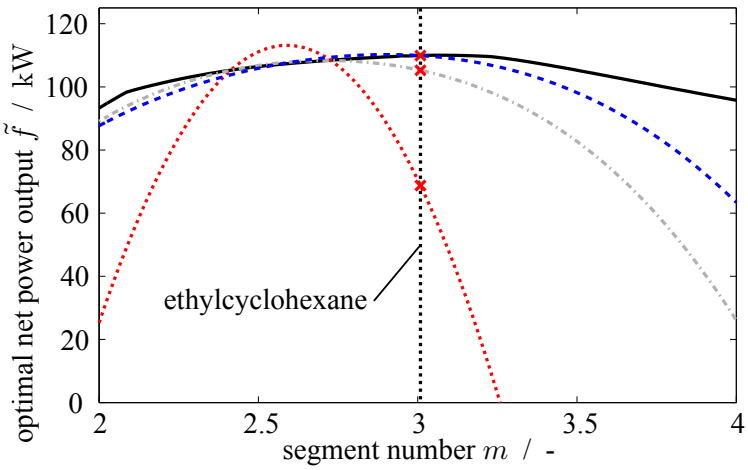

Figure 6: Optimal net power output $\tilde{f}$ (black, solid) and the approximation function $A(y)$ with one (red, dotted), two (gray, dash-dotted) and three (blue, dashed) sampling points as function of the segment number m for constant segment diameter $\sigma = 4.0$ Å and segment dispersion energy $\epsilon/k = 283.8$ K corresponding to the pure component parameters of ethylcyclohexane. The optimal values are $m^* = 1.8$, $\sigma^* = 4.1$ Å and $(\epsilon/k)^* = 408.6$ K.

Finally, the effectiveness of the method is evaluated based on the required computing effort. The number of function evaluations of the objective function in the optimizations for both the adaptive structure-mapping and the calculation of the real ranking are compared. For the adaptive structure-mapping, the function evaluations of the CoMT-optimization, the calculation of Jacobians and Hessians by finite differences, and the calculation of real objective function values are considered. For the real ranking, the function evaluations to calculate the individual process optimizations of each working fluid of the database are counted.

The calculation of the real ranking requires 31,537 function evaluations. The calculation of the case study by the adaptive structure-mapping takes 3,951 function evaluations, which corresponds to savings of 87.5 %. Thus, the adapted CoMT framework is far more efficient than an individual optimization of each working fluid to identify the best working fluids. Considering a larger database, the number

of function evaluations to calculate the real ranking would increase with the number of working fluids. In contrast, in our experience, there is no direct correlation between the number of working fluids and function evaluations in the CoMT framework, so that overall, the efficiency of the CoMT framework is expected to increase.

If the heuristic regarding the negligible convex curvature is not made (see Section 3.2), the adapted CoMT framework requires 12,805 function evaluations and 10 sampling points to identify the ten best working fluids. In this case, five first degree Taylor approximations and five second degree Taylor approximations are employed. If exclusively first degree polynomials are used, the CoMT framework requires 17,838 function evaluations and 24 sampling points. The results demonstrate the advantage of using second degree polynomials and the heuristic regarding negligible convex curvature.

5. CONCLUSIONS

Simultaneous design of ORC process and working fluid is enabled by the Continuous-molecular targeting framework. However, mapping of the targets onto real working fluids occasionally failed. For this purpose, an adaptive structure-mapping is presented to identify the best working fluids for ORC processes based on continuous-molecular targets. The approximation used for the structure-mapping is iteratively adapted by combining several Taylor approximations around different sampling points. A method to select sampling points is presented and a heuristic for the selection of the degree of the Taylor approximations is proposed. The result of the method is a ranked set of working fluids. The adaptive structure-mapping improves the quality of the ranking and allows for efficient identification of the best working fluids.

The adaptive structure-mapping is successfully applied to a case study, where the original mapping only identifies 2 working fluids out of the top 10 correctly. The adaptive method correctly identifies all working fluids of the top 10. Thereby, the adaptive structure-mapping is more efficient than an individual optimization of each working fluid: In this case study, the function evaluations are reduced by 87.5 %.

NOMENCLATURE

A	approximation function	(-)	T	Taylor approximation	(-)
d^{-p}	inverse distance	(-)	w^*	normalized weighting factor	(-)
f, $\tilde{f}$	objective function	(-)	x	process variables	(-)
g	inequality constraints	(-)	x^*	optimal process parameters of y^*	(-)
H, $\tilde{H}$	Hessian	(-)	y	pure component parameters	(-)
h	equality constraints	(-)	y^*	hypothetical optimal working fluid	(-)
J	Jacobian	(-)	ϵ/k	associating energy	(K)
m	segment number	(-)	λ	eigenvalues	(-)
p	power parameter	(-)	ρ_s	rank correlation coefficient	(-)
S	number of sampling points	(-)	σ	segment diameter	(Å)

Subscript

i	sampling point	min	minimal
k	real working fluid of the database	n	normalized
max	maximal	r	rank

REFERENCES

Bao, J. and Zhao, L. (2013). A review of working fluid and expander selections for organic rankine cycle. *Renewable and Sustainable Energy Reviews*, 24:325–342.

Bardow, A., Steur, K., and Gross, J. (2010). Continuous-molecular targeting for integrated solvent and process design. *Ind. Eng. Chem. Res.*, 49(6):2834–2840.

Casati, E., Colonna, P., and Nannan, N. R. (2011). Supercritical ORC turbogenerators coupled with linear solar collectors. In *Proceedings of the ISES solar world congress 2011, Kassel, Germany, 2011*.

Drescher, U. and Brüggemann, D. (2007). Fluid selection for the organic rankine cycle (ORC) in biomass power and heat plants. *Applied Thermal Engineering*, 27(1):223 – 228.

Dumitru, P. D., Plopeanu, M., and Badea, D. (2013). Comparative study regarding the methods of interpolation. In *1st European Conference of Geodesy & Geomatics Engineering 2013, Recent Advanced in Geodesy and Geomatics Engineering–Conference Proceedings, 45-52pp, Antalya, Oct. 8*, volume 10.

Gross, J. and Sadowski, G. (2001). Perturbed-chain SAFT: An equation of state based on a perturbation theory for chain molecules. *Ind. Eng. Chem. Res.*, 40(4):1244–1260.

Heberle, F. and Brüggemann, D. (2010). Exergy based fluid selection for a geothermal organic rankine cycle for combined heat and power generation. *Applied Thermal Engineering*, 30(11-12):1326 – 1332.

Lampe, M., Stavrou, M., Bücker, H. M., Gross, J., and Bardow, A. (2014). Simultaneous optimization of working fluid and process for organic rankine cycles using PC-SAFT. *Ind. Eng. Chem. Res.*, 53(21):8821–8830.

Lampe, M., Stavrou, M., Schilling, J., Sauer, E., Gross, J., and Bardow, A. (2015). Computer-aided molecular design in the continuous-molecular targeting framework using group-contribution PC-SAFT. *Computers & Chemical Engineering*.

Lötgering-Lin, O. and Gross, J. (2015). A group contribution method for viscosities based on entropy scaling using the perturbed-chain polar statistical associating fluid theory. *Ind. Eng. Chem. Res.*, submitted.

Novak, L. T. (2011). Fluid viscosity-residual entropy correlation. *Int. J. Chem. React. Eng.*, 9(1).

Papadopoulos, A. I., Stijepovic, M., and Linke, P. (2010). On the systematic design and selection of optimal working fluids for organic rankine cycles. *Applied Thermal Engineering*, 30(6-7):760 – 769.

Papadopoulos, A. I., Stijepovic, M., Linke, P., Seferlis, P., and Voutetakis, S. (2013). Toward optimum working fluid mixtures for organic rankine cycles using molecular design and sensitivity analysis. *Ind. Eng. Chem. Res.*, 52(34):12116–12133.

Puth, M.-T., Neuhäuser, M., and Ruxton, G. D. (2015). Effective use of spearman's and kendall's correlation coefficients for association between two measured traits. *Animal Behaviour*, 102:77 – 84.

Quoilin, S., Broek, M. V. D., Declaye, S., Dewallef, P., and Lemort, V. (2013). Techno-economic survey of organic rankine cycle (ORC) systems. *Renewable and Sustainable Energy Reviews*, 22:168 – 186.

Stavrou, M., Lampe, M., Bardow, A., and Gross, J. (2014). Continuous molecular targeting-computer-aided molecular design (CoMT-CAMD) for simultaneous process and solvent design for CO2 capture. *Ind. Eng. Chem. Res.*, 53(46):18029–18041.

Tchanche, B. F., Papadakis, G., Lambrinos, G., and Frangoudakis, A. (2009). Fluid selection for a low-temperature solar organic rankine cycle. *Applied Thermal Engineering*, 29(11-12):2468 – 2476.

Wang, Z. Q., Zhou, N. J., Guo, J., and Wang, X. Y. (2012). Fluid selection and parametric optimization of organic rankine cycle using low temperature waste heat. *Energy*, 40(1):107 – 115.

ACKNOWLEDGEMENT

We thank the Deutsche Forschungsgemeinschaft (DFG) for funding this work (BA2884/4-1).

NUMERICAL AND EXPERIMENTAL INVESTIGATION ON THE ROTARY VANE EXPANDER OPERATION IN MICRO ORC SYSTEM

Piotr Kolasiński*[1], Przemysław Błasiak[2]

[1,2]Wrocław University of Technology,
Department of Thermodynamics, Theory of Machines and Thermal Systems
Wrocław, Poland
E-mail: [1]piotr.kolasinski@pwr.edu.pl, [2]przemyslaw.blasiak@pwr.edu.pl

* Corresponding Author

ABSTRACT

Volumetric expanders are nowadays used in micro, small and medium power ORC systems. As it was indicated by Bao and Zhao (2013) most often spiral and screw machines are applied. However, it can be seen that the application of rotary vane expanders is also growing (Tchanche et al. (2011)). Rotary vane expanders are particularly interesting because of the many advantages they have. The most important features of such expanders are: very simple construction; high power in relation to the dimensions; the ability to operate in low inlet pressure and wet gas conditions; low weight; lack of clearance volume; lack of steering valves; possibility to construct an oil-free machines; ease of sealing; the ability to operate at low rotational speeds and a low price. As it was described by Gnutek and Kolasiński (2013) power range of the rotary vane expanders is 0.1—7 kW, thus these machines are particularly interesting for micro and domestic ORC systems. Vane expanders used in ORC systems are very similar to these commonly used in pneumatic systems, however, it is necessary to carry out the appropriate adaptation of the machine. This includes special hermetic sealing, lubrication and cooling. As a part of the research works on ORC power systems with vane expanders conducted by the authors on Wrocław University of Technology a research test-stand (comprehensively described by Gnutek and Kolasiński (2013)) was designed and realized. This micro power, R123 based, ORC prototype enables experimental analysis of the vane expander operation under different conditions. In this article authors present the results of numerical simulation of vane expander operation in ORC prototype and compared them with the results of experiment. 3D model of the expander was built and analyzed in ANSYS CFX based on the geometrical data obtained by complete disassembly of the machine. The numerical analysis included the same, as in the case of the experiment, expander operating conditions, i.e. pressure, temperature and R123 flow rate at the inlet and outlet of the expander.

1. INTRODUCTION

As it was indicated by Lund and Münster (2006) effective energy recovery from renewable and waste energy sources is one of the most important present-day problems. Advanced energy systems based on local waste heat, renewables and fossil fuel resources can give the opportunity for an increase of consumers energy safety and continuity of energy supply. However, implementation of local energy systems requires the relevant energy conversion technologies.

One of the promising energy conversion technologies is a ORC system. ORC power systems may differ in power, purpose and technical configuration. Available are: micro power (0.5—10 kW), small power (10—100 kW), medium power (100—500 kW) and a large power (500 kW and more) systems. As it was presented by Vanslambrouck (2009) they can operate as power plants, CHP's and multi-generation systems.

The most important problems connected with ORC system design are the suitable working fluid and expander selection. Expander selection is mainly based on the system power and its purpose. In

general, two types of expanders can be applied in ORC systems. One are the turbines, the others are volumetric machines.
Turbines are mainly applied in an large and medium power ORC systems powered by the heat sources with high thermal capacity (1 MW and more) and temperature (150 °C and more), such as large industrial waste sources e.g. steam boilers or gas turbine exhaust gases. Volumetric expanders are applied mainly in micro and small power systems such as domestic and agriculture plants. One of the most important problems in this case is the dynamic thermal characteristic of the heat source also characterized by small capacity, thermal power and temperature (up to 150 °C). Variation in the heat source properties has a negative influence on the continuity of the system operation and difficulty in system adjustment. Therefore the design and construction of small and micro power ORC systems is very difficult and most of the existing systems are still at the level of prototype or under research. In low and micro power ORCs applicability of turbines is very limited due to the machine operational characteristics requiring large flow of the working medium. Moreover microturbines are very small in dimensions what results in very high rotational speeds and difficulty of a rotor balancing and bearing. The necessity of a very precise parts fitting result in high manufacturing costs. This is the contrary to the aim of small ORC systems which should be simple, cheap and easy to use.
Volumetric expanders are a good option for systems where the low pressures and low working medium flows are expected. In general piston, screw, spiral, vane and the rotary lobe expanders can be applied in small and micro ORC plants. The general advantages of volumetric expanders resulting from comparison with the turbines were comprehensively described by Gnutek and Kolasiński (2013). Vane expanders are especially interesting for small and micro ORC systems. Currently they became a subject of different experimental and numerical scientific analyses (Montenegro et al. (2014)). Micro vane expander has a number of advantages resulting from comparison with other volumetric expanders. The most important are: very simple design, high power in relation to the dimensions, suitability for wet gas conditions, low weight, ease of gas-tight sealing and very low price. There are no ORC-dedicated vane expanders available, however, standard pneumatic air motors can be easily adapted.
As a part of the research works on ORC power systems with vane expanders, conducted by the authors on Wrocław University of Technology, a research test-stand (comprehensively described by Gnutek and Kolasiński (2013)) was designed and realized. This micro power, R123 based, ORC prototype enables experimental analysis of the vane expander operation under different conditions.
The authors decided to carry out the experiment on the test-stand and to compare the results with numerical analysis of the applied vane expander. 3D model of the expander was built and analyzed in ANSYS CFX based on the geometrical data obtained by complete disassembly of the machine. The numerical analysis included the same, as in the case of the experiment, expander operating conditions i.e. pressure, temperature and R123 flow rate at the inlet and outlet of the expander.

2. DESCRIPTION OF THE TEST-STAND, THE EXPANDER AND THE EXPERIMENTAL RESULTS

An experimental test-stand was designed and realized in order to study the influence of the different operational conditions on the operation of the rotary vane expander. Figure 1 shows a simplified construction scheme of the test-stand. The main test-stand components are: the gas central heating boiler (featuring maximal thermal power of 24 kW) (1), the shell-and-tube evaporator (2), the working fluid pump (3), the reservoir of working fluid (4), the plate condenser (5) and the micro multivane expander connected with DC generator (6). The working fluid is R123. The test stand is based on manual control of operational parameters with the help of regulation valves. The manual control helps in simulating different operational conditions e.g. it is possible to change the working medium flow direction in the evaporator from a counter-flow to the co-current. The measurements are carried out using the following methods: temperatures are measured with the use of T-type thermocouples, pressures are measured with the use of tube pressure gauges. The flow rate of R123 as well as the flow rate of cooling and heating water are measured with the use of rotameters (See Fig. 1 for the measurement sensors locations: p – manometer, t – thermocouple, V – rotameter).

The heat source for the system is hot water from the gas central heating boiler (1). The temperature of the heat source can be regulated in the range of 40—85 °C. This allows the evaluation of operational conditions of the ORC power system for variable heat sources.

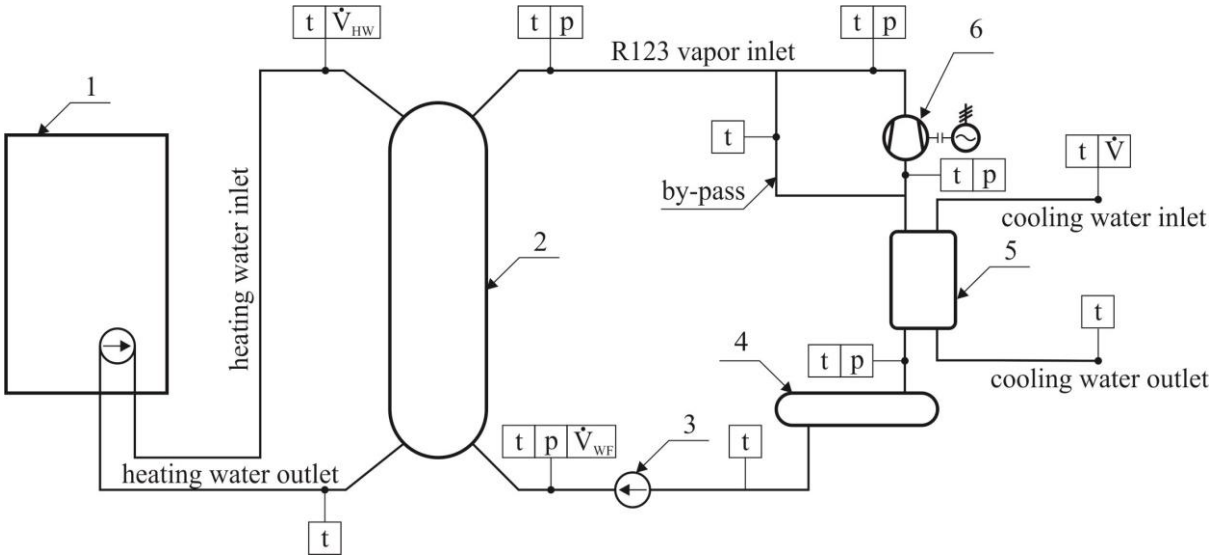

Figure 1: The simplified construction scheme of the test-stand.
1 – gas central heating boiler, 2 – shell-and-tube evaporator, 3 – working fluid pump,
4 – reservoir of working fluid, 5 – plate condenser, 6 – multivane expander with DC generator

A more detailed description of the test stand was presented by Gnutek and Kolasiński (2013). The expansion device is a micro four-vane air motor featuring a maximum power of 600 W. The expander was specially adapted for low-boiling working fluid e.g. the special seals and bearings were used. Moreover, a number of changes in the expander design were made in order to maximize the machine power. The expander is connected by gas-tight clutch with a small DC generator. Figure 2 shows a view of the expander-generator unit disassembled from the test-stand.

Figure 2: The view of the expander-generator unit disassembled from the test-stand

The design of the above described rotary vane expander is presented in figure 3. It consists of cylindrical stationary cylinder of inner diameter 37.5 mm and rotating rotor of outer diameter 34.0 mm. The rotor is placed eccentrically relative to the cylinder. Eccentricity is 1.75 mm. Length of the cylinder is 22.0 mm. Rotor is equipped with four flat vanes, which can move in the slots due to centrifugal forces. Vanes are positioned to the cylinder surface in the right angles. Thickness of each vane is 1.5 mm. Rotary vane expander is fed with R123 working fluid via cylindrical pipe of inner

diameter 8.5 mm. Pipe is tangentially located at side surface of the cylinder. On the second side there is identical outlet pipe where gas leaves the expander chamber to the condenser. The operation principle of rotary vane expander is as follows: high pressure at inlet acts on the vanes and results in rotary motion of the rotor. Due to eccentricity and moving blades, working chamber constantly changes its volume from lowest to highest. The working fluid is trapped in chamber which volume increases with increase of angle of rotation. Consequently working fluid expands and exits through the outlet to the condenser. Rotational energy of the rotor is transformed into mechanical work which is the main output of the rotary vane expander.

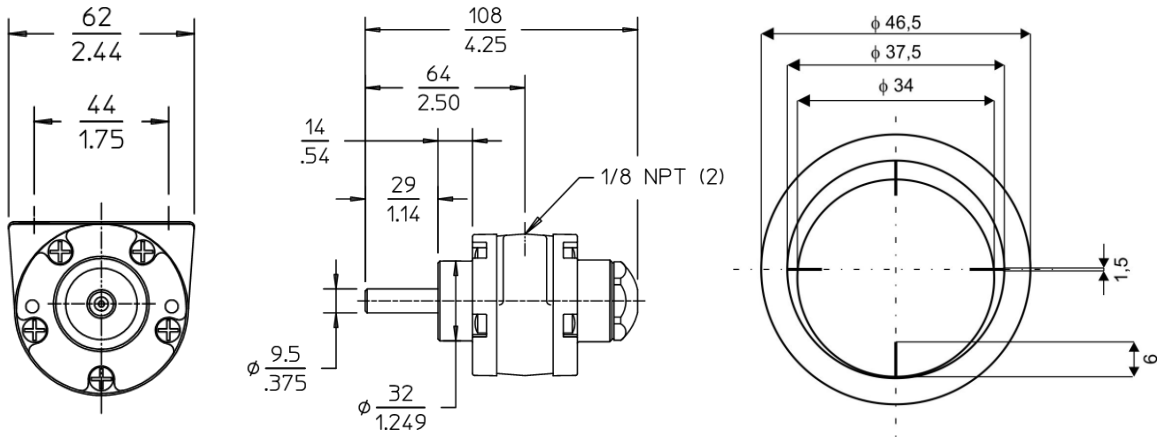

Figure 3: Dimensions of the rotary vane expander being considered.

In order to determine the working fluid thermal properties at the inlet and the outlet of the expander the experiment was carried out on the test-stand. The authors decided to carry out this experiment for the maximum temperature of the heat source (t = 85 °C) and maximum working medium pressure allowed for this expander (p = 0.5 MPa). For this conditions the measured thermal properties of the working fluid at the inlet to the expander were p_{in} = 0.5 MPa and t_{in} = 80 °C. The measured outlet temperature was t_{out} = 65 °C and the outlet pressure was p_{out} = 0.1 MPa. The measurement results together with the corresponding values of specific enthalpy and the specific entropy (determined with the SOLKANE software) are presented in table 1.

Table 1: The experimental results

$\dot{m}_{R123}$	t_{in}	p_{in}	t_{out}	p_{out}	h_{in}	s_{in}	h_{out}	s_{out}
kg/s	**°C**	**MPa**	**°C**	**MPa**	**kJ/kg**	**kJ/kgK**	**kJ/kg**	**kJ/kgK**
0.0615	81	0.5	65	0.1	429.48	1.6788	424.88	1.7472

Presented above experimental results are the input data to the described below numerical analysis.

3. NUMERICAL MODELING

3.1 Numerical domain

In the figure 4 three dimensional numerical domain and mesh are depicted. Additionally the mesh details near the tip of the vanes and inlet/outlet areas are also visible. Numerical domain consists of fluid regions only and housing walls of the rotary vane expander are modelled via boundary conditions. Additionally numerical domain was divided into two areas: stationary inlet and outlet pipes and rotating part including fluid residing in the working chambers of the rotary vane expander. Dimensions of the numerical domain are the same as described in the previous section. The inlet and outlet are in the distance 45 mm from the Y axis of the rotary vane expander. Inner cylinder surface is

represented by the CYLINDER surface and outer surface of the rotor by ROTOR surface. Due to small differences between rotor and cylinder diameter it was hard to provide good quality mesh in the case of vane thickness 1.5 mm. In order to overcome this difficulties vane thickness in the model was set up to 0.5 mm. This simplification does not introduce significant error during the calculation because impact of vane thickness on heat transfer and fluid flow is negligible. Additionally it was impossible to use gap value between vane tip and cylinder wall less than 0.15 mm due to strong curvature of the geometry. Therefore for each time step during the simulation gap was hold to 0.3 mm for each vane to avoid creation of negative volumes in the numerical mesh. It results in eccentricity 1.45 mm whereas in the real rotary vane expander it equals to 1.75 mm. Nevertheless, in the reality small gaps always exists due to sealing rings and small gaps should be taken into account in order to model leakage phenomenon (Montenegro et al., 2014). In the present study hexahedral mesh was used for rotor domain with 9 control volumes in the gap and number of hexahedrons equal to 75492. For the inlet and outlet pipes tetrahedral mesh was used with total number of tetrahedrons equal to 109383.

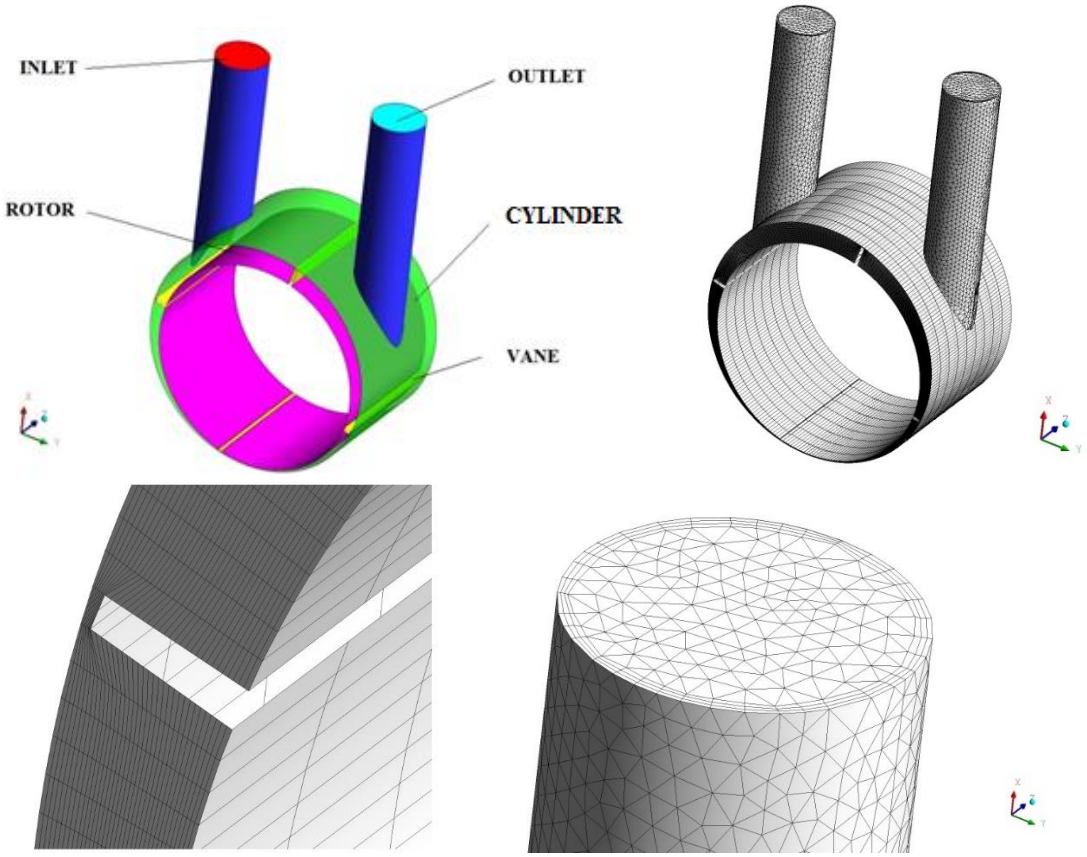

Figure 4: Three dimensional numerical domain of the rotary vane expander and numerical mesh. At the bottom mesh details near the vane tip and inlet/outlet areas

3.2 Numerical model

Non-isothermal, incompressible turbulent flow in the rotary vane expander has been considered. Transport equations of mass, momentum and energy were solved with the use of commercial solver (Ansys, 2014). In the absence of a phase change, radiation and with neglecting dissipation function term these equations can be written in the following vector form

Continuity equation

$$\nabla \cdot \mathbf{U} = 0 \tag{1}$$

Momentum equation

$$\frac{\partial \rho \mathbf{U}}{\partial \tau} + \nabla \cdot \left(\rho \mathbf{U} \mathbf{U} \right) = -\nabla p + \nabla \cdot \left[\mu \left(\nabla \mathbf{U} + \nabla \mathbf{U}^T \right) \right] \tag{2}$$

Energy equation

$$\rho c_p \left[\frac{\partial T}{\partial \tau} + \nabla \cdot \left(T \mathbf{U} \right) \right] = \nabla \cdot \left(k \nabla T \right) \tag{3}$$

where **U** stands for total velocity vector, i.e. difference between velocity vector and moving mesh velocity vector. It is due to the incorporated deforming mesh method (Ansys, 2014) in order to take into account movement of the rotor and vanes. Deforming mesh method consists in calculating in each time step the shape of the moving boundaries. Additionally the nodes distribution in the mesh is calculated according to the following diffusion equation

$$\nabla \cdot \left(\Gamma_{disp} \nabla \delta \right) = 0 \tag{4}$$

where δ is the displacement relative to the previous mesh locations and Γ_{disp} is the mesh stiffness, which determines the degree to which regions of nodes move together (Ansys, 2014). It is so-called displacement diffusion model and preserves the relative mesh distribution of the initial mesh. Deforming mesh method requires additional computational resources, but it provides most accurate results for issues with moving parts. Due to simple geometry of the rotary vane expander for each of the boundary surface equations of motion were specified via CEL expressions (CFX Expression Language). They are basically code routines written in Fortran programming language and can be easily incorporated in the solver. The deforming mesh method is inherently transient because shape of the numerical domain changes constantly and has to be determined for each time step. In the present study rotor moves at constant rotational speed n = 3000 rev/min. The time step used in the simulations corresponds to the rotation of the rotor about 0.1 degree. Very high rotational speed results in fully turbulent flow. In order to turbulent flow standard k-ε model was used. Both convection, temporal and turbulent terms in the transport equations were solved with use of high resolution scheme. For each wall no-slip boundary condition was applied. The vane and the rotor surfaces were treated as adiabatic. On the cylinder and side walls convective boundary condition was imposed with heat transfer coefficient h = 5 W/(m^{2}K) and ambient temperature t_{amb} = 20° C. Working fluid enters the inlet pipe under 0.5 MPa pressure and in temperature 81 °C and exits through outlet in temperature 65 °C. The outlet pressure is equal to 0.1 MPa. In order to provide information transfer between stationary and rotating subdomains, interface boundary condition was used. The working fluid used in the simulation was R123. It was treated as Newtonian with having constant thermo-physical properties determined from the Refprop software for the mean temperature 73 °C and presented in table 2. Calculations were conducted up to five full rotor revolutions and then periodic steady state was assumed. It was reasonable due to small differences between successive fourth and fifth rotation. In terms of residuals, within each timestep calculations were conducted to achieve convergence below 10^{-6}.

Table 2: Thermo-physical properties of R123 used in the simulation

ρ	c_p	μ	k	Pr
kg/m^3	**J/(kgK)**	**μPa·s**	**W/(mK)**	**-**
10.00	750.00	12.388	0.01201	0.77

4. NUMERICAL RESULTS AND DISSCUSION

Figure 5 shows the pressure distribution in the working chambers during rotor movement. As it can be seen from this figure the highest pressure of the working fluid is in the inlet port and filled working chamber. During the rotor movement working fluid pressure decreases with the decreasing volume of the working chamber. The lowest pressure is in the outlet port during the evacuation of the working fluid from the machine. Figure 6 shows the working fluid velocity vectors during the rotor movement. The highest velocities can be observed in the 2nd and the 3rd working chamber, where the chamber volume is minimal. Relatively low working fluid velocities can be observed in the inlet and the outlet ports. Also, in this areas, vortices can be observed. These vortices have negative influence on the expander operation, as they result in working fluid pressure changes and mixing, thus the edges of the inlet and the outlet port of the expander should be redesigned and optimized. Figure 7 shows the temperature distribution in the working fluid during the expander operation. As it can be seen in this figure the working fluid temperature decreases during the expansion. In the inlet and the outlet port the local temperature fluctuations are appearing. These fluctuations are resulting from both the leakage between the vane and the cylinder (the hot gas flowing into the 1st expander working chamber mixes with the gas in the 4th expander working chamber and the gas flowing through the outlet port) and vortices appearing in these areas (increased velocity of the fluid and change in the fluid internal energy).

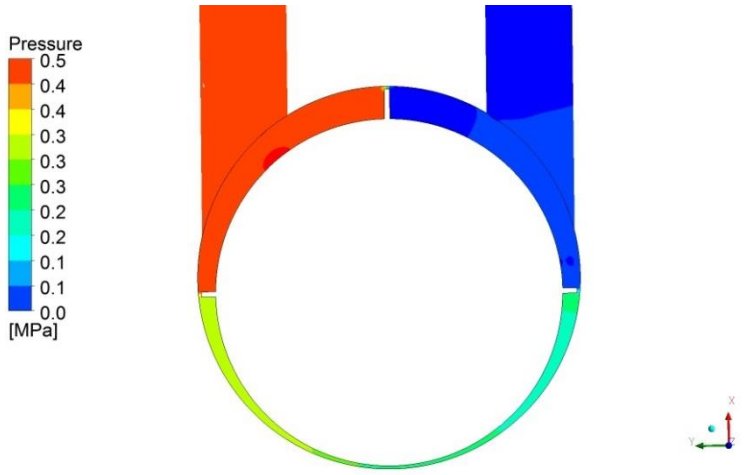

Figure 5: Pressure distribution in the plane for z = 0.011 m

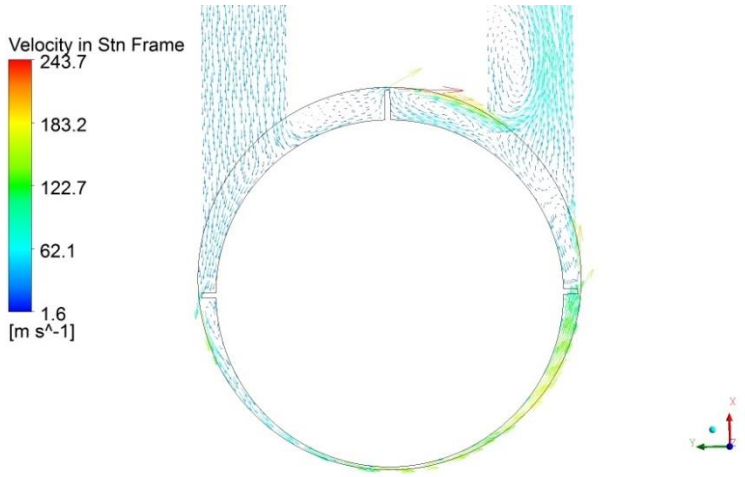

Figure 6: Vectors of velocity in the stationary frame of reference in the plane for z = 0.011 m

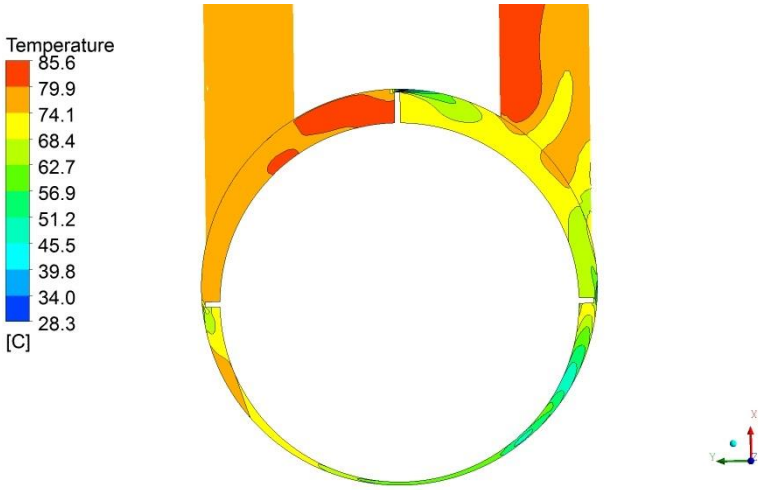

Figure 7: Temperature distribution in the plane for z = 0.011 m

5. SUMMARY AND CONCLUSIONS

In this study the numerical and experimental analysis of the micro-power rotary vane expander operation in ORC system were presented. Numerical analysis was based on 3D model of the expander which was built basing on the geometrical data obtained by complete disassembly of the experimentally tested machine. Numerical analysis of the expander operation was performed in ANSYS CFX, basing on the thermodynamic parameters measured on the test-stand.

The results of the analysis showed the distributions of the pressure, velocity vectors and the temperature of R123 in the expander working chambers. The calculated results show that in the case of volumetric machines the working fluid velocities inside the working chambers are low when compared to the turbines. Moreover, the velocity vectors distribution indicated that in the inlet and the outlet port of the expander large vortices are appearing. These vortices have negative influence on the expander operation, and should be optimized by the change in the expander design. Thus, the sharp edges of the inlet and the outlet port should be redesigned. One of the possible solutions is the change of the inlet and the outlet port diameter to the larger and rounding the edges. Also, the optimization of the expander design should include the change of the rotor diameter to the lower and the length of the cylinder to the larger, in order to increase the volume of the working chambers. Increased volume of the working chambers will result in the increase of the expander power. The authors are currently working on further numerical and experimental analyses concerning the optimization of the volumetric expanders design.

NOMENCLATURE

The nomenclature should be located at the end of the text using the following format:

δ	relative displacement	(–)
Γ	mesh stiffness	(–)
μ	dynamic viscosity	(μPa·s)
ρ	density	(kg/m^3)
τ	time	(s)
c	specific heat	(J/kgK)
h	specific enthalpy	(kJ/kg)
h	heat transfer coefficient	(W/m^{2}K)
k	thermal conductivity	(W/mK)
$\dot{m}$	mass flow	(kg/s)
p	pressure	(Pa)

Pr	Prandtl number	(–)
s	specific entropy	(kJ/kgK)
T	temperature	(K)
t	temperature	(°C)
U	total velocity vector	(–)

Subscript

amb	ambient
in	inlet
out	outlet
p	related to the isobaric process
R123	related to the R123 working fluid

REFERENCES

Ansys CFX v. 14.5, 2014, Ansys CFX Theory Guide,

Bao, J., Zhao, L., 2013, A review of working fluid and expander selections for organic Rankine cycle, *Renewable and Sustainable Energy Reviews*, Vol. 24: pp. 325-342,

Gnutek, Z., Kolasiński, P., 2013, The application of rotary vane expanders in ORC systems – 479 thermodynamic description and experimental results. *Journal of Engineering for Gas Turbines and Power*, Vol. 135(6): pp. 1-10,

Lund, H.; Münster, E., 2006, Integrated energy systems and local energy markets. *Energy Policy*, Vol. 34: pp. 1152-1160,

Montenegro , G., Della Torre, A. D., Fiocco, M., Onorati, A., Benatzky, Ch., Schlager, G., 2014, Evaluating the Performance of a Rotary Vane Expander for Small Scale Organic Rankine Cycles using CFD tools, *Energy Procedia*, Vol. 45: p. 1136-1145,

Montenegro, G., Della Tore, A., Onorati, A., Broggi, D., Schlager, G., Benatzky, C., 2014, CFD simulation of a sliding vane expander operating inside a small scale ORC for low temperature waste heat recovery, *SAE Technical Papers*, Vol.1,

Tchanche, B. F., Lambrinos, Gr., Frangoudakis, A., Papadakis, G., 2011, Low-grade heat conversion into power using organic Rankine cycles – A review of various applications, *Renewable and Sustainable Energy Reviews*, Vol. 15: pp. 3963-3979,

Vanslambrouck, B., 2009, The Organic Rankine Cycle: Technology and Applications, *International Symposium: Waste Heat Recovery by ORC*, Howest De Hogeschool West-Vlaanderen

ACKNOWLEDGEMENT

Calculations have been carried out using resources provided by Wroclaw Centre for Networking and Supercomputing (http://wcss.pl).
This work is co-financed by the European Union as part of the European Social Fund.

THE METHOD OF THE WORKING FLUID SELECTION FOR ORGANIC RANKINE CYCLE (ORC) SYSTEM WITH VOLUMETRIC EXPANDER

Piotr Kolasiński*[1]

[1]Wrocław University of Technology,
Department of Thermodynamics, Theory of Machines and Thermal Systems
Wrocław, Poland
E-mail: piotr.kolasinski@pwr.edu.pl

* Corresponding Author

ABSTRACT

Volumetric expanders are nowadays used in micro, small and medium power ORC systems. Tchanche (2011) indicated that most often spiral, screw and the rotary vane machines are applied. Volumetric machines have a number of specific features determining their operation. The most important are: the possibility of building expanders for small and very small capacities; small and moderate frequency of operating cycle - allowing for consideration of the processes taking place in the machine as a quasi-static; the ability to operate at high pressure drops in a single stage and ease of the hermetic sealing. The most important feature of the volumetric expander operation is the relationship of the expander power and the expansion ratio (the ratio of the inlet and outlet pressure). Each type of volumetric expander also has the optimum value of the expansion ratio. Unlike the turbines, volumetric expanders can operate at low working fluid flow rates and lower pressures. Thus, it is possible to apply volumetric expanders in ORCs powered by low-temperature heat sources, such as e.g. domestic waste heat. The task of a suitable working fluid selection to the ORC system with volumetric expander should be considered differently than in the case of the turbine-based systems. It is caused by low thermal parameters of the cycle and indicated earlier volumetric expander characteristic features. In this paper a new method of the working fluid selection to the ORC system working with volumetric expander was presented. The method is based on the dimensionless parameters useful for the comparative analysis of different working fluids. Dimensionless parameters were defined for selected thermal properties of the working fluids, namely the ability of heat absorption from the heat source, heat removal, mean temperature of the heat supply and the efficiency of the energy conversion. These comparative parameters were calculated for selected low-boiling ORC working fluids and selected temperature of the heat source and the heat sink. Basing on the values of these parameters the working fluids comparison was presented and applicable working fluids were selected.

1. INTRODUCTION

As it was indicated by Bao and Zhao (2013) the most important problems connected with ORC system design are the suitable working fluid and expander selection. They also showed that currently there is a wide range of applicable working fluids available. Expander selection is mainly based on the system power and its purpose. In general two types of expanders can be applied in ORC systems. One are the turbines, the others are volumetric expanders.

Turbines are mainly applied in an large power (1 MW and more) ORC systems powered by the heat sources with high thermal power and temperature (150 °C and more). Such heat sources are generated as waste heat in large industrial power machines e.g. steam boilers (waste steam) or gas turbines (exhaust gases). Lai et. al. (2011) showed that in the large power systems silicone oils (e.g. MM (hexamethyldisiloxane) or MDM (octamethyltrisoloxane)) are mainly adopted as working fluids.

Gnutek and Kolasiński (2013) indicated that volumetric expanders are applicable mainly in micro and small power systems such as domestic and agriculture plants powered by the heat sources with small capacities, thermal power and temperature (up to 150 °C). Low thermal parameters of heat source influences also the working fluid selection. Only the low-boiling working fluids are possible for application in this case. Such working fluid are the refrigerants and similar substances e.g. classical R123 ($C_2HCl_2F_3$) and R245fa ($C_3H_3F_5$), as well as new specially designed fluids e.g. R1234yf ($C_3F_4H_2$), R1234ze ($C_3F_4H_2$), or SES36 ($CF_3CH_2CF_2CH_3$/PFPE).
Volumetric expanders are a good option for systems where the low pressures and low working medium flows are expected. In general piston, screw, spiral, vane and rotary lobe expanders can be applied in ORC plants. Piston expanders are good option for the ORC systems were high (up to 20 MPa in case of the single stage expanders) inlet pressures of the working fluid are expected, as they have the high expansion ratios (the ratio of the inlet and outlet pressure). Piston expanders can be used in the ORC systems powered by heat sources with stable characteristic of the thermal power output as these expanders must work in dry vapor conditions in order to avoid liquid phase in the cylinder. Screw expanders can be applied in systems powered by heat sources with changeable characteristic (both in terms of the temperature, capacity and power) as in this type of the expanders moist vapor can be expanded without problems. The expansion ratio of the screw expander typically is in the range of $\sigma = 10—15$. Spiral expanders are applied in many of the ORC systems as they are compact and relatively cheap. Vane expanders are applied mostly in the ORC prototypes and test-stands and most of them is under research and development. The expansion ratio of the rotary vane expanders typically is in the range of $\sigma = 5—7$. Rotary lobe expanders are also under research and development, but these type of the expanders are promising because of their advantages such as e.g. ability to expand the moist vapor, low operating pressures and simple design. The range of working pressures and expansion ratios of different types of volumetric expanders are presented in table 1.

Table 1: Range of the working pressures and expansion ratios for different types of the volumetric expanders (Więckiewicz and Cantek (1985))

Expander type	$p_{in\ max}$	p_{out}	σ_{max}
	MPa	**MPa**	**-**
Piston (single stage)	20	0.1	200
Screw	1.5	0.1	15
Spiral	1.0	0.1	10
Vane	0.7	0.1	7
Rotary lobe	0.6	0.1	6

The most important feature of the volumetric expander is the relationship of the expander power and the expansion ratio. This issue was discussed in details by Gnutek and Kolasiński (2011). Each type of volumetric expander also has the optimum value of the expansion ratio. Unlike the turbines, volumetric expanders can operate at low working fluid flow rates and low pressures. The task of a suitable working fluid selection to the ORC system with volumetric expander should be thus considered differently than in the case of the turbine-based systems.

2. THERMODYNAMIC PROPERTIES OF WORKING FLUIDS SUITABLE FOR ORC SYSTEMS WITH VOLUMETRIC EXPANDERS

As it was indicated in the introduction volumetric expanders are good option for ORC systems powered by low temperature heat sources and each type of the volumetric expander has specific range of the expansion ratio. Taking into account this specific conditions (low temperature of the heat source and expander operational conditions) only the selected working fluids can be applied in ORC system with volumetric expanders. Selected working fluids that can be used in low-power ORC systems with volumetric expanders are presented in table 2.

Working fluids can be described by well-known thermodynamic relationships (equations of the state, the expressions for the specific heat, heat of a phase change or the thermodynamic functions), and the coefficients defined for the description and analysis of specific applications. The above-mentioned thermodynamic relations are presented in the form of algebraic or differential equations, tables, graphs or software. Level of completeness of this description in relation to the substances, presented in table 2, is very different, which does not facilitate the thermodynamic analyzes. Figure 1 shows the general T-s diagram for the low-boiling substance. The characteristic values of thermal properties are indicated on this graph with taking into account the ambient parameters. The areas of the individual phases can therefore be highlighted: superheated vapor, moist vapor, liquid, the area of the critical point (C_r), the dry saturated vapor line (x = 1) and the line of boiling liquid (x = 0). Working fluid with ambient temperature T_a has the pressure $p(T_a)$, typically different from the ambient pressure p_a. Evaporation temperature T_{ev} at ambient pressure (p_a) is one of the basic quantities describing the substance, just like the corresponding heat of condensation $q_c(p_a)$ (isobar, isotherm e-f). The critical point parameters – p_{cr}, T_{cr} are another key parameters describing the substance. Isobar passing through this point is important in the division of the operating range of the power plant and organization of the cycle. In contrast, the critical isotherm determines the usefulness of a substance to act as a heat transfer fluid in a power plant. If $T_c < T_a$ it would be not possible to condense the vapor and liquid compression, which is the basic principle of a power plant operation. On the background of the described T-s graph the power plant cycle was presented (red lines).

Table 2: The working fluids suitable for low-power ORC systems with volumetric expanders

No.	**Margin Position**	**Chemical formula**	**Molar mass**	**Normal boiling point**	**Critical point**			**Range of applicability**		
			M	**t_n**	**t_{cr}**	**p_{cr}**	**ρ_{cr}**	**t_{min}**	**t_{max}**	**p_{max}**
			kg/kmol	**°C**	**°C**	**MPa**	**kg/m^3**	**°C**	**°C**	**MPa**
1	R113	CCl_2FCClF_2	187.38	47.5	214.06	3.39	560.00	-36.22	251.85	200
2	R114	$C_2Cl_2F_4$	170.92	3.6	145.68	3.25	579.97	0	233.85	21
3	R123	$CHCl_2CF_3$	152.90	27.8	183.68	3.66	550.00	-107.15	326.85	40
4	R124	CF_3CHClF	136.50	-11.9	122.28	3.62	560.00	-153.15	196.85	40
5	R1234ze	$CHF=CHCF_3$	114.04	-18.9	109.37	3.63	489.24	-104.53	146.85	20
6	R134a	CH_2F-CF_3	102.00	-26.0	101.06	4.06	512.00	-103.3	181.85	70
7	R152a	CHF_2CH_3	66.05	-24.0	113.26	4.51	368.00	-118.59	226.85	60
8	R227	CF_3CHFCF_3	170.03	-16.3	101.75	2.93	594.25	-126.8	201.85	60
9	R236fa	$CF_3CH_2CF_3$	152.00	-1.4	124.92	3.20	551.30	-93.63	226.85	40
10	R245fa	$CF_3CH_2CHF_2$	134.05	15.1	154.01	3.65	516.08	-102.1	166.85	200
11	R365mfc	$CF_3CH_2CF_2CH_3$	148.07	40.1	186.85	3.22	473.84	-34.15	226.85	35
12	R409A	-	97.40	-34.2	107.00	4.60	-	-	-	-
13	SES 36	$CF_3CH_2CF_2CH_3$/PFPE	184.85	35.6	177.60	2.85	-	-	-	-

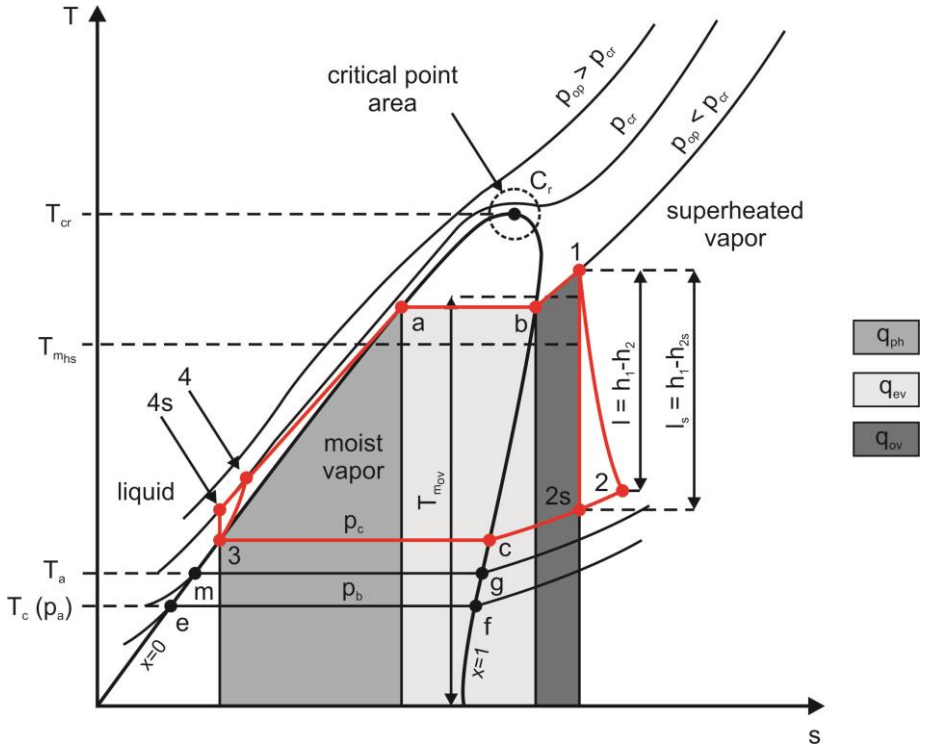

Figure 1: T-s diagram for low-boiling working fluid

Depending on the working fluid type the characteristic curve can have different shapes. Figure 2 shows the characteristic curves for selected working fluids. Also the temperature range for low potential heat sources is presented on this figure with dashed lines (90—150 °C).

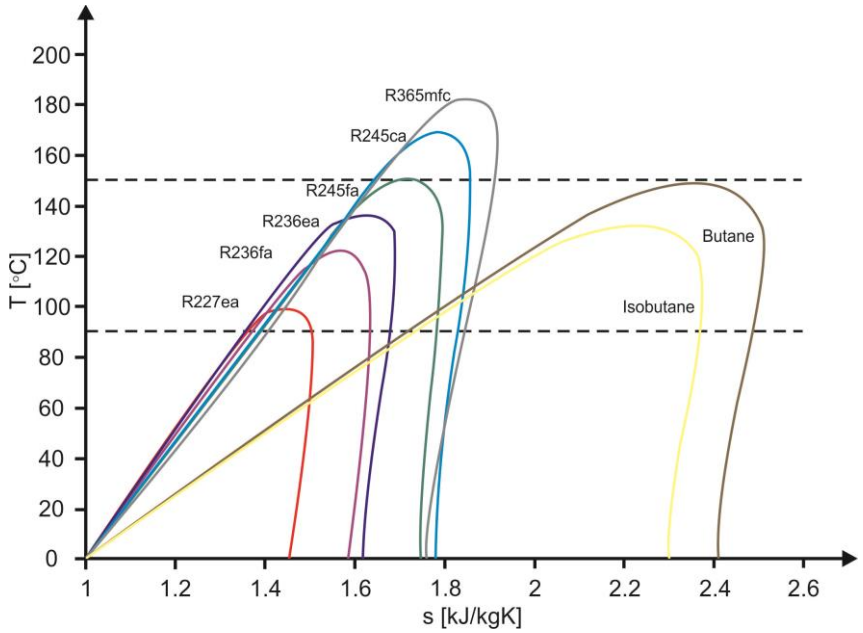

Figure 2: Characteristic curves for different working fluids (Trapp and Colonna (2013))

3. THE METHOD OF WORKING FLUID SELECTION

Figure 3 shows the comparison of two ideal power plant cycles (blue and red lines) for two different low-boiling working fluids on T-s plane, which is the basis for further considerations. This graph is

built with the assumption that both of the cycles are powered by the same heat source with the same heat supply temperature (T_{hs}). Moreover it is assumed that both of the cycles are cooled by the same heat sink with the same condensation temperature (T_c).

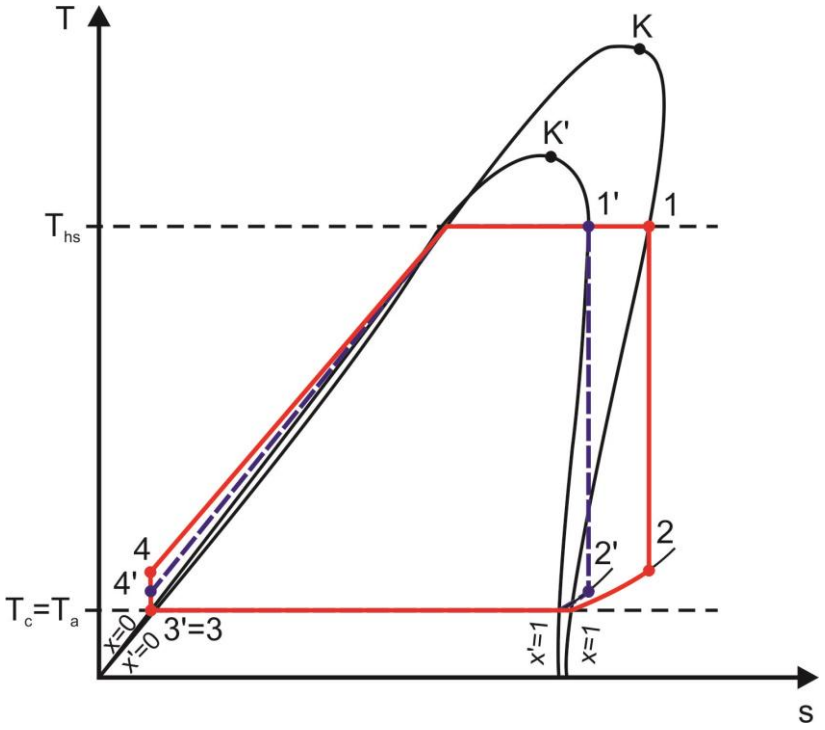

Figure 3: T-s diagram with the power plant cycles for two different working fluids

Comparison of two different substances is possible basing on many parameters (e.g. toxicity, ODP, HGWP, etc.), but the most important are the thermal properties as they have the influence on the ORC system power, efficiency and quality of operation. Thus, in this methodology, it is proposed to analyse the substances basing on the following thermal properties:

- The amount of the heat absorbed from the heat source in the evaporator,
- The mean temperature of the heat supply,
- The amount of the heat removed by the heat sink in the condenser,
- The efficiency of thermal energy conversion.

Moreover the following assumptions are needed to carry out the comparison (see Fig. 3 for details):

- The temperatures of the heat source and the heat sink are the same for both substances,
- Both working substances are thermally stable in the described on Fig. 3 temperature range,
- One of the substances is the reference.

In order to compare two substances with taking into account above mentioned properties and assumptions it is useful to define dimensionless comparative parameters, described in the following.

3.1 α_{hs} - The parameter of the absorbed heat

α_{hs} parameter characterizes the working fluid in terms of ability to absorb heat at the possible highest supply temperature (T_{hs}). This parameter can be useful when comparing the working fluids in terms of maximizing the heat amount absorbed from the heat source. The comparison of α_{hs} parameter calculated for two different working fluids and two different ORC cycles (the reference one and compared one, as presented on Fig.3) allows the selection of a working fluid with larger heat absorption capacity, i.e. one that will maximize the heat absorption from the heat source. This parameter can be defined with the expression

$$\alpha_{hs} = \left(\frac{\dot{Q}^{+}_{ORC1}}{\dot{Q}^{+}_{ORC2}} \right)_{(T_{hs}-T_a),\, p} \tag{1}$$

$$\dot{Q}^{+}_{ORC1} = \dot{m}_{ORC1} \cdot \left(h_1 - h_4 \right) \tag{2}$$

$$\dot{Q}^{+}_{ORC2} = \dot{m}_{ORC2} \cdot \left(h_{1'} - h_{4'} \right) \tag{3}$$

Where:

$\dot{m}_{ORC1}$ - the working medium mass flow in the compared cycle,

$\dot{m}_{ORC2}$ - the working medium mass flow in the reference cycle,

$\dot{Q}^{+}_{ORC1}$ - the heat transfer rate absorbed by the working fluid during the evaporation in the compared cycle,

$\dot{Q}^{+}_{ORC2}$ - the heat transfer rate absorbed by the working fluid during the evaporation in the reference cycle.

3.2 α_{mhs} - The parameter of the mean heat supply temperature

α_{mhs} parameter characterizes the working fluid in terms of ability to absorb heat at the highest possible mean heat delivery temperature T_{mhs}. This parameter can be useful for comparing the working fluids in terms of maximizing the heat delivery temperature and comparative analyses of working fluids in terms of maximizing ORC plant efficiency. This parameter can be defined with the expression

$$\alpha_{m_{hs}} = \left(\frac{T^{mhs}_{ORC1}}{T^{mhs}_{ORC2}} \right)_{(T_{hs}-T_a),\, p} \tag{4}$$

$$T^{mhs}_{ORC1} = \frac{q_{ph} + q_{ev} + q_{sh}}{\Delta s} \tag{5}$$

$$T^{mhs}_{ORC2} = \frac{q_{ph}' + q_{ev}' + q_{sh}'}{\Delta s'} \tag{6}$$

Where:

T^{mhs}_{ORC1} - mean temperature of the heat supply in the compared cycle,

T^{mhs}_{ORC2} - mean temperature of the heat supply in the reference cycle,

q_{ph} - heat of preheating,

q_{ev} - heat of evaporation,

q_{sh} - heat of superheating,

Δs - change in the medium entropy during the preheating, evaporation and superheating.

3.3 α_o - The parameter of the removed heat

α_o parameter characterizes the working fluid in terms of ability to remove the heat at the lowest possible heat removal temperature $T_c \cong T_a$. This parameter can be useful for comparing the working fluids in terms of minimizing the temperature of the heat sink. This parameter can be defined as:

$$\alpha_{hr} = \left(\frac{\dot{Q}^{-}_{ORC1}}{\dot{Q}^{-}_{ORC2}} \right)_{(T_{hs} - T_a),\, p} \tag{7}$$

$$\dot{Q}^{-}_{ORC1} = \dot{m}_{ORC1} \cdot \left(h_{ORC1}'' - h_{ORC1}' \right) \tag{8}$$

$$\dot{Q}^{-}_{ORC2} = \dot{m}_{ORC2} \cdot \left(h_{ORC2}'' - h_{ORC2}' \right) \tag{9}$$

Where:

$\dot{m}_{ORC1}$ - the working medium mass flow in the compared cycle,

$\dot{m}_{ORC2}$ - the working medium mass flow in the reference cycle,

$\dot{Q}^{-}_{ORC1}$ - the heat transfer rate removed during the condensation in the compared cycle,

$\dot{Q}^{-}_{ORC2}$ - the heat transfer rate removed during the condensation in the reference cycle.

3.4 α_e – The parameter of the efficiency of thermal energy conversion

α_e parameter characterizes the working fluid in terms of ability to maximize the efficiency of the energy conversion. This parameter can be useful when comparing the working fluids in terms of maximizing the efficiency of conversion of the heat supplied from the heat source to the other energy forms. This parameter can be defined as:

$$\alpha_e = \left(\frac{E_{ORC1}}{E_{ORC2}} \right)_{(T_{hs} - T_a),\, p} \tag{10}$$

$$E_{ORC1} = P_{ORC1} + Q_{TORC1} + Q_{LORC1} \tag{11}$$

$$E_{ORC2} = P_{ORC2} + Q_{TORC2} + Q_{LORC2} \tag{12}$$

Where:

E_{ORC1} - the energy generated and dissipated in the compared cycle,

E_{ORC2} - the energy generated and dissipated in the reference cycle,

P - electric power output (the electric power on the output of the current generator),

Q_T - thermal power output (heat generated for the central heating purposes),

Q_L - heat losses (heat losses via convection and radiation from the surfaces of the pipelines, the evaporator, the condenser and the other system devices).

The above defined parameters can be useful for comparative selection of the ORC system working fluid, when the thermal characteristic of the heat source and the heat sink (namely the heat source and the heat sink temperatures) are known. The selection criteria are the maximal values of the α_{hs}, α_{mhs}, α_{hr} and α_e parameters. Moreover, basing on the comparison of the calculated parameters and the values of the expansion ratio as well as specific expansion work it is possible to select a suitable volumetric expander to the ORC system. The importance of the α_{hs}, α_{mhs}, α_{hr} and α_e parameters is always connected with the application of the ORC system. For the example in the ORC system dedicated for heat recovery from the cooling mediums (e.g. in internal combustion engines) the heat removal from the medium is the priority. Thus, the most important parameter in this case is the α_{hs} and it should be maximized during the expander and working fluid selection. In each ORC system

cycle efficiency is also very important, thus in all of the applications α_e parameter should be maximized.

4. COMPARATIVE ANALYSIS OF THE WORKING FLUIDS

In the following the comparative analysis of the selected low-boiling working fluids suitable for application in ORC powered by low temperature heat sources is presented. The analysis was performed for working fluids listed in table 2. The values of thermal properties (i.e. specific enthalpy and the specific entropy) were calculated with the Refprop and Solkane software.
The following assumptions were taken into account in the calculations:
- The temperature of the heat source is t_{hs} = 95 °C,
- The expander internal efficiency is η_i = 0,7,
- Temperature of the heat sink is t_c = 20 °C,
- The reference substance is R123,
- There is no heat generated for central heating and heat losses in the system are negligible.

The defined earlier comparative parameters (α_{hs}, α_{mhs}, α_{hr} and α_e) together with the expansion ratio and expander specific work were calculated for each of the working fluid. Calculations were made for cycles presented in fig. 3. The results of these calculations are presented in table 3 (indexes of the thermal properties according to fig. 3).

Table 3: The results of the calculations

Working fluid	t_1	p_1	t_2	p_2	h_1	s_1	i_2	s_2	h_3'	s_3'	l	σ	α_{hs}	α_{mhs}	α_{hr}	α_e
	°C	bar	°C	bar	kJ/kg	kJ/kgK	kJ/kg	kJ/kgK	kJ/kg	kJ/kgK	kJ/kg	-	-	-	-	-
R113	95	3.87	50.26	0.37	417.07	1.6262	391.75	1.6527	218.09	1.0639	25.32	10.55	0.91	1.00	0.91	0.92
R114	95	12.83	48.42	1.82	390.81	1.5562	369.83	1.5783	219.44	1.0684	20.98	7.05	0.79	0.99	0.79	0.76
R123	95	7.02	42.45	0.76	438.19	1.6890	410.56	1.7188	220.05	1.0763	27.63	9.24	1.00	1.00	1.00	1.00
R124	95	21.54	23.65	3.27	404.41	1.5971	381.89	1.6220	222.09	1.0779	22.52	6.59	0.84	0.99	0.84	0.82
R1234ze	95	27.39	28.02	4.27	252.31	0.7610	229.22	0.7931	51.019	0.1856	23.09	6.41	0.92	0.98	0.94	0.84
R134a	95	35.91	20.00	5.72	421.12	1.6504	397.73	1.6770	227.47	1.0960	23.39	6.28	0.89	0.98	0.89	0.85
R152a	95	31.79	20.00	5.13	540.50	2.3412	501.80	2.3852	234.77	1.4755	38.70	6.20	1.40	0.99	1.40	1.40
R227	95	25.50	37.64	3.90	369.04	1.5025	352.37	1.5206	222.81	1.0806	16.67	6.54	0.67	0.98	0.68	0.60
R236fa	95	17.44	43.36	2.30	416.85	1.6370	393.91	1.6615	224.62	1.0867	22.94	7.60	0.88	0.99	0.89	0.83
R245fa	95	11.30	43.05	1.22	471.29	1.7885	440.70	1.8213	225.86	1.0912	30.59	9.21	1.13	0.99	1.13	1.11
R365mfc	95	5.20	56.16	0.46	492.00	1.8487	459.26	1.8824	226.90	1.0956	32.74	11.30	1.22	0.99	1.22	1.18
R409A	95	35.99	19.33	5.78	412.28	1.6186	387.37	1.6474	215.20	1.0495	24.91	6.23	0.90	0.97	0.90	0.90
SES 36	95	5.61	60.64	0.58	414.77	1.6176	390.30	1.6423	220.28	1.0705	24.47	9.67	0.89	1.00	0.89	0.89

As it can be seen from the calculation results, three of the working fluids (R152a, R245fa and R365mfc) have better thermal properties in comparison to R123 as the comparative parameters are greater than 1.
For the assumed ORC system working conditions, the best working fluid is R152a when compared to R123. In case of R152a the calculated values of the α_{hs}, α_{hr} and α_e are equal (1.4). This means that R152a is 40% better than R123 in the heat absorption, heat removal and thermal energy usage efficiency. The α_{mhs} parameter is lower (α_{mhs} = 0.99) in case of R152a when compared to R123, thus the mean heat supply temperature is lower for R152a. Also, the value of the expansion ratio is lowest (σ = 6.2) in case of R152a in comparison to other analyzed substances, and the specific expansion work is highest (l = 38.7 kJ/kg). However, in case of R152a the pressure on the expander inlet is high (p_1 = 31.79 bar) and the choice of the suitable volumetric expander is limited only to the piston expander (see Table 1 for maximum expansion ratio of different volumetric expanders).

The second, better than R123 working fluid, is R365mfc. In case of R365mfc the calculated values of the α_{hs}, α_{hr} and α_e are 1.22, 1.22 and 1.18 correspondingly. This means that R365mfc is 22% better than R123 in the heat absorption and heat removal and 18% better in the thermal energy usage efficiency. Similarly to the earlier described comparison α_{mhs} parameter is also lower (α_{mhs} = 0.99) in this case. The value of the expansion ratio in case of R365mfc is higher than in the case of R123 (σ = 11.3), but the operational pressures are lower (p_1 = 5.20 bar and p_2 = 0.46 bar) and the specific expansion work is higher (l = 32.74 kJ/kg) when compared to R123. Low operational pressures and the value of the expansion ratio makes that screw expander will be optimal in this case.
The third, better than R123, working fluid is R245fa. In case of R245fa the calculated values of the α_{hs}, α_{hr} and α_e are 1.13, 1.13 and 1.11 correspondingly. This means that R245fa is 13% better than R123 in the heat absorption and heat removal and 11% better in the thermal energy usage efficiency. Similarly to the earlier described comparisons α_{mhs} parameter is also lower (α_{mhs} = 0.99) in this case. The value of the expansion ratio in case of R245fa is lower than in the case of R123 (σ = 9.21), but the operational pressures are higher (p_1 = 11.30 bar and p_2 = 1.22 bar). The specific expansion work is higher (l = 30.59 kJ/kg) when compared to R123. The moderate pressures and the value of the expansion ratio in this case makes that two types of the volumetric expanders (screw and spiral) can be applied in this case. As it can be seen from the results α_{hs} and α_{hr} are similar for the analyzed substances. This is due to the similar shapes of the saturation curves for these substances and similar ratio of the heat needed for preheating, evaporation and superheating of the substance in relation to the heat of condensation. The other working fluids (R113, R114, R124, R1234ze, R134a, R227, R236fa, R409A and SES 36) have worse thermal properties when compared with R123. The calculated comparative parameters are lower for these substances in comparison to R123.

5. CONCLUSIONS

This study presents the comparative working fluid selection method for ORC system powered by low temperature heat source. This method is based on comparison of selected thermal properties of working fluids with the use of the defined parameters describing the substance in the following properties: the amount of the heat absorbed from the heat source, the mean temperature of the heat supply, the amount of the heat removed by the heat sink and the efficiency of thermal energy conversion. Described method can be useful for the working fluid selection to the ORC system with known thermal parameters (temperatures) of the heat source and the heat sink. Moreover, it is possible to select the suitable volumetric expander basing on the comparison of the calculated parameters, the expansion ratio and the specific expansion work. The comparison example presented in point 3 of this paper and valid for the ORC system powered by the low-temperature (95 °C) heat source, where R123 is the reference working fluid, shows that in considered case three different working fluids (R152a, R245fa and R365mfc) can be more efficient alternatives to R123. Also, the suitable volumetric expanders were selected using the presented method for each of the working fluids alternatives. Presented method can also easily be adopted to other working substances and other assumptions. Thus, using this method, it is possible to analyze many different ORCs powered by different heat sources.

NOMENCLATURE

The nomenclature should be located at the end of the text using the following format:

α	comparative parameter	(–)
η	efficiency	(–)
ρ	density	(kg/m^3)
σ	expansion ratio	(–)
E	energy	(J)
h	specific enthalpy	(kJ/kg)
l	specific work	(kJ/kg)
M	molar mass	(kg/kmol)

$\dot{m}$	mass flow	(kg/s)
P	power	(W)
p	pressure	(Pa)
r	heat of evaporation	(kJ/kg)
q	specific heat	(kJ/kg)
$\dot{Q}$	heat transfer rate	(W)
s	specific entropy	(kJ/kgK)
T	temperature	(K)
t	temperature	(°C)
x	vapor quality	(–)

Subscript

1, 2, …, n	1st, 2nd, … nth
a	ambient
c	condensation
cr	critical
e	efficiency
ev	evaporation
hs	heat supply
i	internal
in	inlet
L	losses
m	mean
max	maximal
min	minimal
out	outlet
op	operational
ORC1	related to the compared cycle
ORC2	related to the reference cycle
sh	superheating
ph	preheating
s	isentropic
T	thermal

REFERENCES

Bao, J., Zhao, L., 2013, A review of working fluid and expander selections for organic Rankine cycle, *Renewable and Sustainable Energy Reviews*, Vol. 24: pp. 325-342,

Gnutek, Z., Kolasiński, P., 2013, The application of rotary vane expanders in ORC systems – 479 thermodynamic description and experimental results. *Journal of Engineering for Gas Turbines and Power*, Vol. 135(6): pp. 1-10,

Lai, N.A., Wendland, M., Fischer, J., 2011, Working fluids for high-temperature organic Rankine cycles. *Energy* , Vol. 36: pp. 199-211,

Tchanche, B. F., Lambrinos, Gr., Frangoudakis, A., Papadakis, G., 2011, Low-grade heat conversion into power using organic Rankine cycles – A review of various applications, *Renewable and Sustainable Energy Reviews*, Vol. 15: pp. 3963-3979,

Trapp, C., Colonna, P., 2013, Efficiency Improvement in Precombustion CO2 Removal Units With a Waste–Heat Recovery ORC Power Plant, *Journal of Engineering for Gas Turbines and Power*, Vol. 135(4): pp. 1-12,

Więckiewicz, H., Cantek, L., 1985, *Volumetric Compressors - Atlas*, 2nd ed.; Gdańsk University of Technology Publishing, Gdańsk, Poland, pp. 380,

THERMODYNAMIC AND DESIGN CONSIDERATION OF A MULTISTAGE AXIAL ORC TURBINE FOR COMBINED APPLICATION WITH A 2 MW CLASS GAS TURBINE FOR DEZENTRALIZED AND INDUSTRIAL USAGE

René Braun[1]*, Karsten Kusterer[1], Kristof Weidtmann[1], Dieter Bohn[2]

[1]B&B-AGEMA,
Aachen, NRW, Gemany
braun@bub-agema.de

[2]Aachen University,
Aachen, NRW,Germany
Dieter.bohn@rwth-aachen.de

* Corresponding Author

ABSTRACT

The continuous growth of the part of renewable energy resources within the future mixture of energy supply leads to a trend of concepts for decentralized and flexible power generation. The raising portion of solar and wind energy, as an example, requires intelligent decentralized and flexible solutions to ensure a stable grid and a sustainable power generation.
A significant role within those future decentralized and flexible power generation concepts might be taken over by small to medium sized gas turbines. Gas turbines can be operated within a large range of load and within a small reaction time of the system. Further, the choice of fuel, burned within the gas turbine, is flexible (e.g. hydrogen or hydrogen-natural gas mixtures). Nevertheless, the efficiency of a simple gas turbine cycle, depending on its size, varies from 25% to 30%.
To increase the cycle efficiencies, the gas turbine cycle itself can be upgraded by implementation of a compressor interstage cooling and/or a recuperator, as examples. Those applications are cost intensive and technically not easy to handle in many applications. Another possibility to increase the cycle efficiency is the combined operation with bottoming cycles. Usually a water-steam cycle is applied as bottoming cycle, which uses the waste heat within the exhaust gas of the gas turbine. In small to mid-sized gas turbines the temperature and heat amount within the exhaust gas are often not sufficient to operate a water steam cycle efficiently. Further, in industrial applications, a part of the heat, within the exhaust gas, is often used in secondary processes which lower the total amount of heat, which can be transferred to a bottoming cycle.
An alternative to water-steam bottoming cycles can be given by organic Rankine cycles (ORC) based on organic fluids. An advantage of organic fluids is the characteristic of evaporating at lower temperatures and lower heat amounts and thus, the usability in a Rankine cycle even at low heat source temperatures.
This paper discusses an ORC process design for a combined application with a simple cycle gas turbine in the 2 MW class. The thermodynamic cycle configuration is shown and it will be pointed out that the cycle efficiency (simple GT) of 26.3% can be increased to more than 36% by application of a bottoming ORC cycle (simple GT+ORC). A key component within the ORC cycle is the turbine. This paper shows the results of an extended aerodynamic ORC axial turbine pre-design based on the thermodynamic cycle considerations. Within the design study the real gas properties of the organic fluid are taken into account. Based on the outcome of the pre-design a 3D aerodynamic axial turbine design is investigated. By application of CFD simulations the turbine design has been optimized and the ORC power output could be increased from 636kW (0D-design) to 659 kW (CFD-design), which lead to a combined cycle efficiency of more than 36%.

1. INTRODUCTION

During the last decade the importance of intelligent, flexible and sustainable energy conversion systems is steadily growing. Thereby the application of systems based on organic Rankine cycles (ORC) get more and more in focus in several technical disciplines as Quoilin et al. (2013) have shown in their survey of ORC systems. The technology of Organic Rankine cycles are nowadays applied to many kinds of technology fields, such as solar thermal, geothermal or biomass power plants, in offshore platform applications, waste heat recovery systems and even in heavy trucks.
This paper deals with the application of ORC system as bottoming cycles for usage of waste heat from a primary cycle. Due to the trend of decentralized power generation, as a consequence of the growing part of renewables within the future energy mixture, small to mid-sized flexible power generation systems are required. The application of gas turbines can full fill the requirements in terms of system flexibility and variable sizes. A disadvantage of simple gas turbine cycles are the low efficiencies. A possibility to increase the simple cycle efficiency is the application of a bottoming cycle. In many cases a conventional bottoming cycle based on water/steam is not economical. In such cases a bottoming cycle based on organic fluids can be a successful alternative. Nguyen et al. (2012) and Pierobon et al. (2013) have shown in their investigations the significant benefit which can be achieved by the application of ORC system as bottoming cycle to a gas turbine for offshore solution. Kusterer et al. (2013) have shown the potential of a combined cycle configuration of a 2 MW class gas turbine with an ORC within a conceptual process design study.
As various kinds of organic fluids are available, a usage-oriented working fluid selection process is necessary, in order to find the best candidate for the process of interest. As the fluid properties of organic fluids are different in a huge range and the consideration of the real gas behavior of such fluids is of highest importance within those selection analyzes, many researchers have investigated in this field (e.g. Quoilin et al. (2012); Saleh et al. (2007)) For the best choice of suitable fluids the practicability and feasibility of the thermodynamic results have to be taken into account, but also the design of the cycle, the heat transfer behavior within the heat exchanger and the relating volume flows through the expansion machines are of highest interest for an ORC fluid selection. There is a significant amount of literature dedicated to the evaluation of suitable working fluids, due to the complexity of the topic (e.g. Kusterer et al.(2014); Fernandez et al. (2011); Lai et al. (2011); Sauret et al. (2011); Chen et al. (2011)).
The calculation of ORC processes has to consider the real gas properties of the analyzed fluids, as the approximation with ideal gas equations is not valid for the most of the fluids. Therefore the development of suitable equation of states for analyzing of organic fluids is investigated by a lot of researchers (e.g. Weingerl et al. (2001), Wei et al. (2000), Miyamoto and Watanabe (2003)). Harink et al (2010) have analyzed the influence of different CFD solvers, turbulence models and equation of states to the performance of a radial ORC turbine predicted by the application of different CFD solvers. They have shown that the accuracy of the results is highly addicted to the related models and solvers.
This paper deals with the applicability of conventional steam turbine design procedures and how far those are transferrable to the design of axial turbines using organic mediums. The analyzed design is based on a thermodynamic process study of a combined application of an ORC and a simple gas turbine (2 MW class). As organic working fluid pentane is used in the ORC cycle

2. Thermodynamic Cycle Modeling

2.1 Software tool for process calculations

The thermodynamic cycle modeling of the combined gas turbine and ORC has been performed by a "Thermodynamic Design Tool" (TDT) application, developed by B&B-AGEMA. TDT supports the design and calculation of single and combined energetic processes based on a 0D thermodynamic approach, using different fluids selected by the user. Combined cycles (e.g. gas turbine + ORC) can be investigated directly and with consideration of interactions. It comprises real gas behavior of several fluids and mixtures. The thermodynamic processes can be visualized in parametric

thermodynamic diagrams, e.g. enthalpy/entropy, temperature/pressure, including precisely tabled thermodynamic values. The calculation method for compression and expansion processes under real gas behavior are based on Lüdtke (2004).

2.2 Combined Cycle Calculation (0D-TDT)

The cycle design of the combined gas turbine and organic Rankine cycle configuration is shown in Figure 1. The combined cycle contains a simple cycle gas turbine and a recuperated organic Rankine cycle. On the right hand side of the Figure the thermodynamic parameter of the single components are illustrated in order to classify the cycles. The simple gas turbine cycle results in an efficiency of 26.3%, this efficiency includes a thermal to electrical factor of 0.893, which approximates the mechanical losses of rotating parts and transmission losses within the generator.

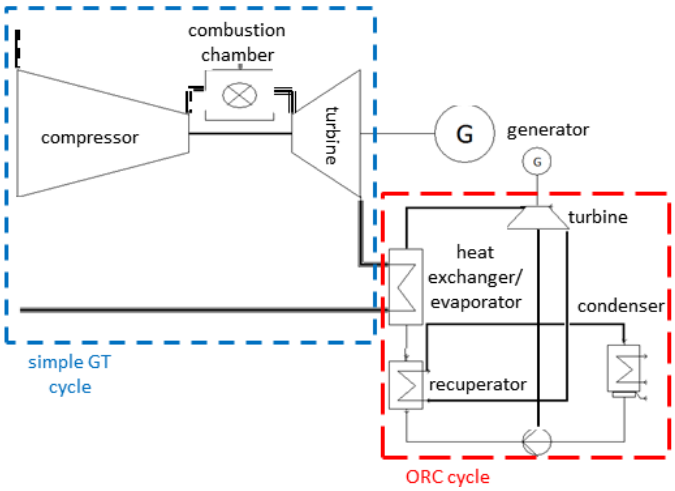

process thermodynamic parameter

GT		ORC	
compressor		pump	
η_s	81.00%	η_s	75%
π	10.4	π	23.8
mass flow	8 kg/s	mass flow	6.5 kg/s
combustor			
pressure loss	3.40%		
turbine		turbine	
η_s	89.40%	η_s	85.00%
exhaus diffusor			
pressure loss	4.5%		
Both cycles			
heat exchanger/evaporator/recuperator/condenser			
pressure loss	2%		
effectiviness	90%		
efficiency	90%		

Figure 1: combined cycle configuration of simple gas turbine and organic Rankine cycle

The resulting combined cycle efficiency is 35%, whereas the power output of the ORC is 625.6 kW (without consideration of the condenser energy consumption and an assumed thermal to electrical factor, similar as for the GT cycle, of 0.9). Thus, the efficiency of the simple cycle could be increased by more than 8%pts., by application of a bottoming ORC cycle.

As the focus of this paper is on the design of the axial turbine, the calculated turbine power within the thermodynamic 0-D process calculation (TDT) has to be seen as reference and starting point for the more detailed turbine design. The ORC 0-D net turbine power output is 707 kW which is conform to a specific work of 108.8 kJ/kg. For the further design study the specific work is set as value of comparison.

3. ORC Turbine Design

3.1 Definition of Main Turbine Parameter and Boundary Conditions

As first, a simple 1D design approach has been performed by calculating the characteristic machine parameters ψ_{yM}, δ_M and σ_M. The characteristic machine parameters are defined as:

$$\psi_{yM} = \frac{\left(\frac{n}{n-1}\right) RT\left(\pi^{\frac{n-1}{n}} - 1\right)}{\frac{1}{2}u^2} \tag{1}$$

$$\delta_M = \frac{|\psi_{yM}|^{\frac{1}{4}}}{\left|\frac{4\dot{V}u}{\pi D_B^2}\right|^{\frac{1}{2}}} \tag{2}$$

$$\sigma_M = \frac{\left|\frac{4\dot{V}u}{\pi D_B^2}\right|^{\frac{1}{2}}}{|\psi_{yM}|^{\frac{3}{4}}} \tag{3}$$

Based on the characteristic machine parameters a first assumption of rotational speed and stage numbers can be defined for the turbine by using the Cordier diagram (see Figure 2) and by variation of the reference diameter and the rotational speed. The Cordier diagram presents ranges of machine characteristic parameters and is based on empirical data of real single stage machines. The diagram has been developed by O. Cordier in 1953. The Cordier diagram and the definitions of the characteristic machine parameters are only defined for single stage compressors and turbines, but they are useful to get a first impression of the needed stage numbers, the reference diameters and the rotational speed of compressors and turbines. Thus, the diagram is used in order to determine the rotational speed and stage number for the ORC turbine.

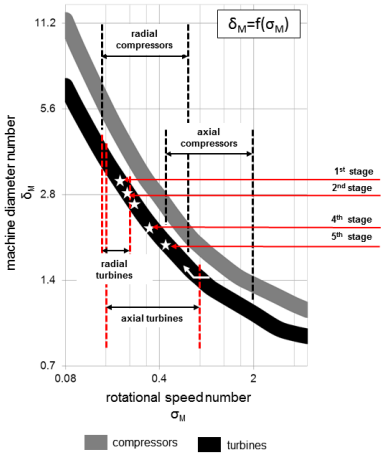

Figure 2: Cordier Diagram

The analysis based on the Cordier diagram and the related formulas (Equ.2 and 3) leads to a rotational speed of the turbine of 300 s^{-1}, which is related to a σ_M of 0.14 for the whole turbine. The number of stages is evaluated with 5, by calculating the characteristic parameters for each stage and manipulating the stage loading and influencing parameters till all stages are within the range of experienced axial machines of the Cordier diagram. By this procedure the required number of stages can be assumed and has to be verified as feasible in the detailed turbine design.
For simplification purposes the 5 stages of the turbine shall be designed as quasi-repetition stages, with constant stage flow coefficients φ

$$\varphi = \frac{c_m}{u} \tag{4}$$

where u is the circumferential velocity of the blade outlet and c_m the velocity of the flow in the meridian section. By the stage load coefficient ψ_h the loading of each stage is characterized:

$$\psi_h = \frac{\Delta h}{u^{2\,\frac{1}{2}}} \tag{5}$$

where Δh describes the difference of the specific total enthalpy between outlet and inlet of the stage. Another important parameter within the design of a turbomachine is the enthalpy reaction number ρ_h:

$$\rho_h = \frac{\Delta h_{vane}}{\Delta h_{vane} + \Delta h_{vblade}} \tag{6}$$

it describes the load distribution between the vane and the blade of a stage.
Within the iterative 1D mean line design approach φ, ψ_h, ρ_h, the rotation rate, the mass flow of the organic medium and the diameter of the hub contour are initial values. Those values are necessary, in order to start the iterative process presented within the following section. The characteristic stage parameters are given in Table 1.

Table 1: turbine stage parameter

	1. stage	2. stage	3. stage	4 stage	5. stage
φ	0,3	0,3	0,3	0,3	0,3
ρ_h	0,5	0,5	0,5	0,5	0,5
ψ_h	-2,1	-2,1	-2	-2	-1,6

3.2 1D Mean Line ORC Turbine Design

In order to evaluate the main design parameters (e.g. geometrical parameters, flow parameters, etc.) of the ORC turbine, a 1D design has to be performed. A common design practice for gas or steam turbines is the application of a 1D Mean Line approach. This paper analyses the applicability of the common design procedure for the design of the axial ORC turbine and if the conventional design laws and methods are also applicable for turbines working with organic mediums. Therefore the changes of state, which have to be calculated within the mean line approach, have been iteratively solved by consideration of real gas equations and by implementation of property tables based on the data base implemented within the thermodynamic design tool (TDT). The iterative solving of the change of state is illustrated. The iteration is done till two criteria (ϵ_P and ϵ_T) are fulfilled. The main equations (7 and 8) to solve the change of state are based on RIST (1996) and shall not be further explained here. Thus, the 1D mean Line approach for application for ORC turbines becomes more complex as for example for gas or steam turbines in cause of missing data correlations or applicable real gas models.

$$\frac{p_2}{p_1} = \left[1 + \frac{\Delta h_s + (K_T \cdot v)_{1,2} \cdot p_1 \left(\frac{\tilde{p}_2}{p_1} - 1\right)}{c_{p_{1,2S}} \cdot T_1}\right]^{\left(\frac{\kappa \cdot [1+K_T]}{\kappa \cdot [1-K_p]-1}\right)_{1,2}} \tag{7}$$

$$\frac{p_2}{p_1} = \left(\frac{T_2}{T_1}\right)^{\left(\frac{\kappa \cdot [1+K_T]}{\kappa \cdot [1-K_p]-1}\right)_{1,2}} \cdot \exp\left(-\frac{\Delta s}{(K \cdot R_N \cdot [1+K_T])_{1,2}}\right) \tag{8}$$

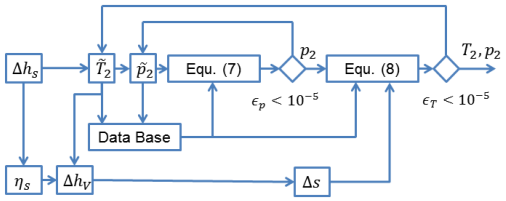

Figure 3: iterative scheme of solving the change of state

The 1D mean line process is illustrated in Figure 4. As it can be seen, due to the consideration of the real gas behavior of the organic fluid, the design process of the 1D mean line approach becomes complex and requires an iterative solutions. However, the results of the mean line approach are the flow angles in the mean line and the geometrical information about the hub and casing contour. Due to feasibility issues, additional boundary (BC) conditions have been considered within the design approach. Therefore the minimal size of a blade height is set to 5mm and additionally, in order to avoid a supersonic flow within the cascade, the inflow Mach number (Ma) should be lower than 0.3 and the outflow Ma lower than 0.9 (for each blade). Aerodynamic losses as well as profile losses have been approximated within the 1D design approach by empirical loss models (LM) with corresponding loss coefficients ξ. Those models are addicted to empirical models used for the design of steam turbines, as specific models are not available for organic mediums. The mean line approach is mainly divided into two sections, the thermodynamic (TD) and aerodynamic (AD) part as illustrated in Figure 4.

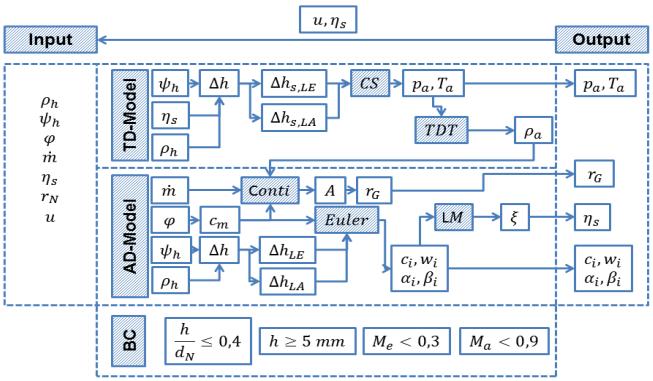

Figure 4: mean-line design process

The mean line approach results in the main geometrical information for the turbine design, as the hub and casing contour as well as the flow angles within the mean line section. Based on this information the main flow path and the profiles of the vanes and blades can be designed, as illustrated in Figure 5.

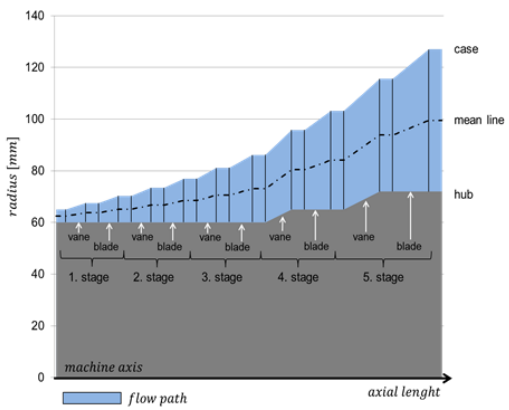

turbine cross section view

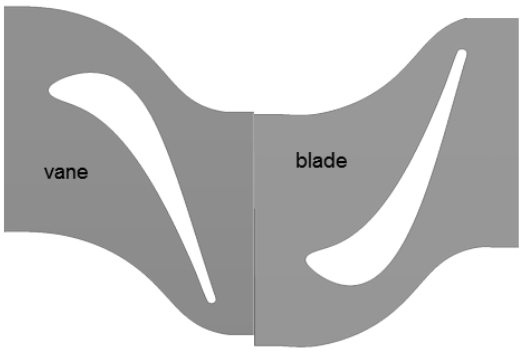

1st stage mean line profile

		vane	blade	vane	blade	vane	blade	vane	blade	vane	blade
aerodynamic mean line results											
velocity (abs. frame of reference)	in	35,350	130,662	37,222	137,367	39,206	143,180	41,525	163,851	47,954	174,503
	out	130,662	37,222	137,367	39,205	143,180	41,525	163,851	47,954	174,503	57,021
velocity (rel. frame of reference)	in	-	36,455	-	378,465	-	399,075	-	45,467	-	57,185
	out	-	133,353	-	140,667	-	147,798	-	171,435	-	187,073
angle (abs. frame of reference)	in	90,00	16,015	98,355	15,939	99,090	16,184	95,804	16,106	97,438	17,699
	out	16,015	98,355	15,939	99,091	16,184	95,804	16,106	97,438	17,699	99,266
angle (rel. frame of reference)	in	-	81,433	-	85,386	-	90,289	-	91,363	-	111,918
	out	-	163,969	-	164,026	-	163,767	-	163,897	-	162,493

Figure 5: mean line results - flow passage and flow angles

Due to the quasi-repetition stage design the mean line is not following on a constant radial position, but increasing in its radial position in axial direction. The resulting flow passage and the mean line location can be seen in on the left hand side in Figure 5. On the right hand side the contour of the vane and blade profiles of the 1st stage is exemplarily shown. Based on the resulting flow angles, the profiles have been designed within an in-house profile generator, which is not be further explained. As the hub and casing contour is known, a 3D turbine design can be evaluated. The first design considers non twisted airfoils, which means constant shapes in radial direction.
The calculated specific work is 104.54 kJ7kg, a difference of 3.9% to the 0-D process calculation. The reasons can be seen in the application of an iterative solving of the changes of state and the application of empirical loss models.

4. ORC Turbine CFD Simulation

The CFD simulations within this study are performed with the commercial code STARCCM+. The simulation set up considers the realizable k-ε turbulence model for the turbulence expression and considers the thermodynamic fluid properties of pentane as pressure and temperature depended tables for the thermal conductivity and dynamic viscosity. The specific heat has been prescribed as polynomial function. To consider the real gas behavior the Peng Robinson real gas model has been selected. The inlet conditions are prescribed as total conditions of temperature and pressure and the outlet is considered as a static pressure outlet.

4.1 CFD Simulation of first mean line design approach

The results of the numerical analysis (CFD 1st) in comparison to the 1D and 0-D design results are listed in Figure 6. It can be seen that small deviations are calculated by each approach by a direct comparison. The main key factors why there are differences are driven by two main factors: i) the consideration of the real gas behavior and ii) the consideration of losses. Within the numerical

analyses those two factors are directly connected to each other, in the 1D design there are indirect connected via loss models and in the 0-D design the losses are indirect considered by the prediction of isentropic component efficiencies. Thus, the different applications of the losses lead to small deviations, which need to be adjusted and fine-tuned.
Nevertheless, in a direct comparison of CFD and 1D design, the turbine principally shows the expected behavior by comparing the calculated pressure expansion line through the turbine, shown on the right hand side of Figure 6. The pressure lines are perfectly overlapping, whereas the static temperature distribution shows a difference. The difference of the static temperature is mainly produced within the first stage, the location where the applied real gas model within the CFD shows its highest failure in the calculation of the change of state, which has then direct influence to the prediction of the static parameters. After the first stage the static temperature lines are nearly parallel, this shows a similar prediction of CFD and 1D.
The accuracy of applicable real gas models in STARCCM+ in regard of the real gas factor determined by the real gas model versus the data base is as well illustrated in Figure 6. The failure rate is decreasing along the expansion line and has its maximum in the first stage for all models, but the Peng Robinson model shows the smallest deviations. Within the first stage the real gas factor of pentane is around 0.5 and as smaller the real gas factor as higher the failure rate of the real gas models. The models are not validated for pentane and thus have increasing failure rates for low real gas factors and this failure rate is then transported throughout the calculation of the static parameters.
Nevertheless, it can be said that the numerical investigation has shown a good performance of the turbine and the results are within an acceptable range of deviation for the first run.

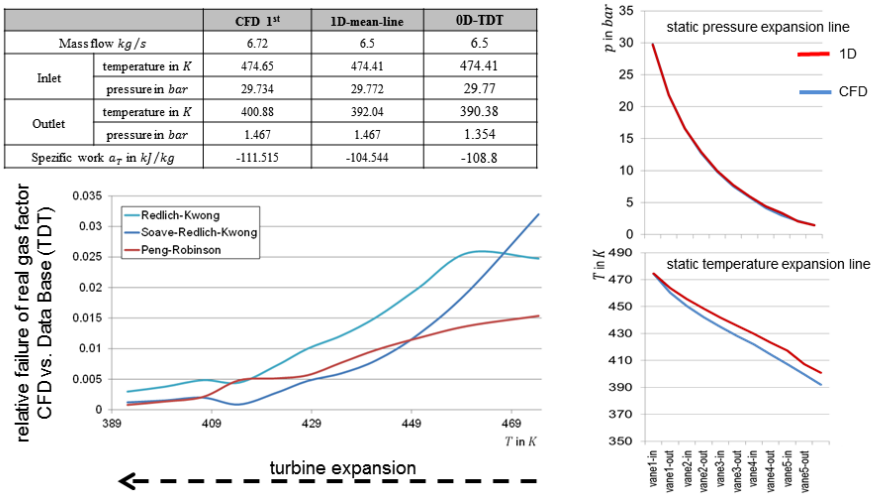

		CFD 1st	1D-mean-line	0D-TDT
Mass flow kg/s		6.72	6.5	6.5
Inlet	temperature in K	474.65	474.41	474.41
	pressure in bar	29.734	29.772	29.77
Outlet	temperature in K	400.88	392.04	390.38
	pressure in bar	1.467	1.467	1.354
Spezific work a_T in kJ/kg		-111.515	-104.544	-108.8

Figure 6: CFD results compared to 1D mean line design parameter

In order to compare the results, the specific work can be taken into account. It can be seen, that the prediction of the CFD is 6.3% higher than the estimated work by the 1D mean line design, whereas the deviation between the 1st CFD and the thermodynamic process calculation is 2.5%. Of course, a certain value of uncertainty is not avoidable but it can be assumed, that the implemented models within the 1D-design are not perfectly transferrable to the analyzed ORC turbine, as most of the correlations (especially for loss prediction, etc.) are specialized for steam turbine designs. Nevertheless, the 1D-design based on common practices of steam turbine design procedures is applicable and the resulted design is already close to a feasible design also for an organic fluid application. Based on the CFD results a turbine optimization process can be started to further increase the power output and to optimize the aerodynamic behavior. This can be done for instance by optimizing the shape of the profiles and/or to twist the blades.

4.2 CFD based optimization: consideration of radial twisting

Despite the deviations between the CFD and the 1D mean line results, an optimization of the turbine can be performed based on the results and experiences observed from the CFD analysis. Thus, a twisting of the blades has been analyzed and compared on the basis of a numerical delta analysis with

the first step CFD calculation of section 4.1. The evaluation of the twist parameters can be evaluated on two approaches: i) directly by evaluation of flow angles within the CFD or ii) by empirical models. For the determination of the twist parameters of the blades the second method has been chosen, as empirical models can be directly applied to a 1D Mean Line approach and thus show more potential to considered in an early design stage. Two models have been compared: a free vortex model and a stator outflow angle model (Schuh (2012)). The models determine the radial flow angle distribution of the blades based on the result of the mean line calculation. The twist of the blade can then be realized within the profile generator. In order to validate the applicability of the models, the predicted flow angles from the two models have been compared to the flow angles from the CFD analysis. A comparison is shown exemplarily for the outlet of the 3rd vane in Figure 7. Within the analysis the free vortex model has been evaluated as best practice for an application.

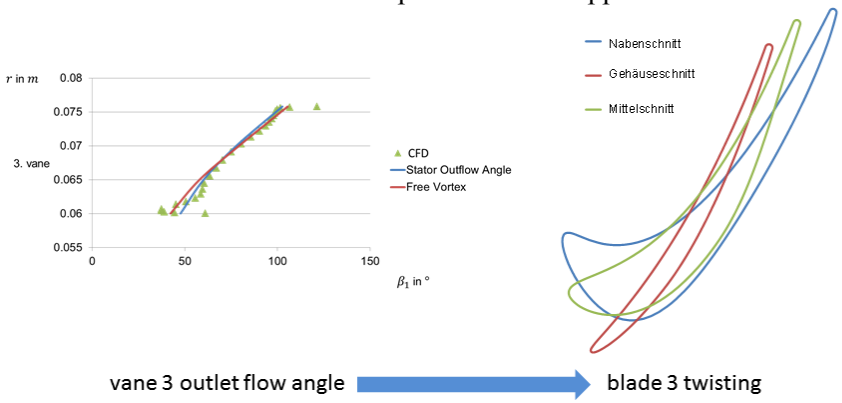

Figure 7: radial outlet flow angle distribution of vane 3 and blade 3 twist

The main results of the CFD considering the twisted profiles are shown and compared in Figure 8. Due to a twist of the profiles the flow losses induced by incidence could be reduced and thus, the specific work has been decreased by 1.4%.

		CFD twist	CFD-1st	1D-mean-line	0D-TDT
Mass flow kg/s		6.48	6.72	6.5	6.5
Inlet	temperature in K	474.76	474.65	474.41	474.41
	pressure in bar	29.81	29.734	29.772	29.77
Outlet	temperature in K	399.8	400.88	392.04	390.38
	pressure in bar	1.467	1.467	1.467	1.354
Specific work a_T in kJ/kg		-113.034	-111.515	-104.544	-108.8

Figure 8: comparison of results

6. CONCLUSIONS

Within this paper the design of an ORC turbine has been presented. Based on the results of a 0D thermodynamic process calculation a 1D turbine design has been performed on the basis of a mean line approach. The turbine has been designed as quasi repetition stages with consideration of empirical loss models and correlations applied from the design of steam turbines. The design has been transferred to a 3D turbine design and calculated by CFD. The main results of the analysis are that the design rules and methods of designing steam turbines are applicable for the design of ORC turbines. Nevertheless, some deviations and uncertainties are carried out, which require an adjustment of correlations and loss models in order to increase the accuracy of the ORC turbine design. The analysis by CFD requires a high accuracy in defining the fluid properties and the chosen physical models within the calculation. In order to minimize the design effort of an ORC turbine, it is intended to achieve a good turbine design already in early design steps, as within the 1D design approach. Therefore the implementation of empirical models and correlations are necessary. Those models are available for steam turbine design but not verified for organic turbines. The analysis of empirical

models for twisted blade designs has shown the applicability of those models as well for a pentane axial turbine.

The thermodynamic process design has shown the potential of the application of ORC systems as bottoming cycles to small and middle size gas turbines as the cycle efficiency could be increased from 26% to 36%. Especially the application of axial turbine designs offer a high potential, as high turbine efficiencies can be achieved.

NOMENCLATURE

A	specific work	[kJ/kg]
A	Flow channel area	[mm²]
c	velocity magnitude (absolute system)	[m/s]
d	diameter	[mm]
w	velocity magnitude (relative system)	[m/s]
c_m	velocity in meridian section	[m/s]
D_B	reference diameter	[m]
h	specific enthalpy	[kJ/kg]
P	static pressure	[kg/m²]
r	radius	[m],[mm]
R	specific gas constant	[J/(kg*K)
T	static temperature	[K]
u	circumferential velocity	[m/s]
$\dot{V}$	volume flow	[m³/s]
α	absolute flow angle	[°]
β	relative flow angle	[°]
δ_M	machine diameter number	
σ_M	rotational speed number	
φ	flow coefficient	
ψ_h	stage loading number	
ψ_{yM}	machine loading number	
ρ_h	enthalpy reaction number	
η	efficiency	
π	pressure ratio	

Subscript

a	outlet position
e	inlet position
G	casing
i	inlet position
N	hub
n	counting variable
s	isentropic

Abbreviation

AD	Aerodynamic
CFD	Computational Fluid Dynamics
Conti	Continuity
CS	Change of State
Euler	EULER equations
GT	Gas Turbine
LA	blade
LE	vane
LM	Loss Models
ORC	Organic Rankine Cycle
TD	Thermodynamic
TDT	Thermodynamic design Tool

REFERENCES

Chen, Y., Lundqvist, P., Johansson, A., "A comparative study of the carbon dioxide transcritical power cycle compared with an organic Rankine cycle with R123 as working fluid in waste heat recovery", Applied Thermal Engineering, 2006, 26, 17-18, 2142-2147

Cordier, O.,1953,"Ähnlichkeitsbedingungen für Strömungs-maschinen, Brennstoff-Wärme-Kraft", J. Strömungsmachinen, **5/10**

Fernandez, F.J., Prieto, M.M., Suarez, I., "Thermodynamic analysis of high temperature regenerative Organic Rankine Cycles using Silohexanes as working fluids" Energy, 2011, 36, 8, 5239-5249

Harinck, J., saaresti, T.T., Colonna, P., Rebay, S., Buijtenen, v.J., "Computational Study of a high.expansion ratio radial Organic Rankine Cycle Turbine Stator, Journal of Engineering for Gas Turbines and Power, May 2010, vol. 132 /054501-1

Kusterer, K., Braun, R., Bohn, D.,2014, Organic Rankine Cycle Working Fluid Selection and Performance Analysis for Combined Cycle Application with a 2MW class Gas Turbine, Proc. of ASME Turbo Expo 2014, GT2014-25439, Düsseldorf, Germany

Kusterer, K, Braun, R., Köllen, L., Tanimura, K., Sugimoto, T., Bohn, D., "Combined Solar Thermal Gas Turbine and Organic Rankine Cycle Application for Improved Cycle Efficiencies", Proc. of ASME Turbo Expo 2013, GT2013-94713, San Antonio, USA

Lütke, K., "Process Centrifugal Compressors: *Basics, Function, Operation, Design,* Application", Springer Verlag Gmbh, 2004

Lai, N.A., Wendland, M., Fischer, J., Working fluids for high temperature Organic Rankine Cycles", Energy, 2011, 36, 1, 199-211

Miyamoto, H., Watanabe, K., "Helmholtz-Type Equations of State for Hydrocarbon Mixtures of Propane/n-Butane, Propane/Isobutane, n-Butane/Isobutane, and Propane/n-Butane/Isobutane", International Journal of Thermophysics, Vol. 254, No. 4, 2003

Nguyen, T.V., Elmegaard, B., Pierobon, L., Haglind, F.H., Breuhaus, P., „Modeling and analysis of offshore energy systems on north sea oil and gas platforms", Proc. of the 53rd Scandinavian Simulation and Modeling Society Conference, October 4-6,2012, Reykjavik, Iceland

Quoilin S., v.d. Broek, M., declaye, S., Dewallef, P., Lemort, V., 2013, Techno-economic survey of Organic Rankine Cycle (ORC) system, Renewable and Sustainable Energy Reviews, no. 22, p.168-186

Quoilin, S., Declaye, S., Legros, A., Guillaume, L., Lemort, V.,2012, "Working fluid selection and operating maps for Organic Rankine Cycle expansion machines", International Compressor Engineering Conference at Prudue, July 16-19, 2012

Rist, D., 1996, Dynamik Realer Gase. Grundlagen, Berechnungen und Daten für Thermogasdynamik, Strömungsmechanik und Gastechnik. Springer, Berlin, 1996

Saleh, B., Koglbauer, G., Wendland, M., Fischer, J.,2007, Working fluids for low-temperature organic Rankine cycles", Journal of Energy, 32, p. 1210-1221

Sauret, E., Rowlands, A.S., "Candidate radial-inflow turbines and high density working fluids for geothermal power systems", Energy, 2011, 36, 7, 4460-4467

Schumann, J.; Sahnen, D.; Jeschke, P.; Harbecke, U.; Polklas, T.; Schwarz, M., 2012, Impact of Secondary Flow on the Accuracy of Simplified Design Methods for steam turbine stages, Proceedings of ASME Turbo Expo, 2012

Tveitaskog, A.K., Haglind, F., "Optimization of advanced liquid natural gas fuelled machinery systems for a high speed ferry", Proc. of ASME Turbo Expo 2012, GT2012-69022, Copenhagen, Denmark

Weingerl, U., Wendland, M., Fischer, J., Müller, A., Winkelmann, J., „Backone family of equations of state: 2. Nonpolar and polar fluid mixtures", Journal of AIChE , 47, 705-17, 2001

Wei, S.Y., Sadus, R.J., "Equations of State for the calculation of fluid phase equilibria", Journal of AIChE, 46, 169-196, 2000

CONTROL STRATEGIES FOR AUTOMOTIVE RANKINE SYSTEM EVALUATION USING A COSIMULATION PLATFORM

Abdelmajid Taklanti*, Jin-Ming LIU, Regine Haller, Samy Hammi, Bertrand Nicolas, Yulia Glavatskaya and Mohamed Yahia

Valeo Thermal Systems
8, rue Louis Lormand 78321 le Mesnil saint Denis
Contact Information (abdelmajid.taklanti@valeo.com)

ABSTRACT

Today, several solutions to recover wasted heat in automotive power train are considered and evaluated in order to reduce vehicle fuel consumption and to meet new emission regulation targets (El Habachi *et al.* (2010), Abbe Horst *et al.* (2014), Domingues *et al.* (2013) and Haller *et al.* (2014)). One of the solutions is to use Organic Rankine Cycle to recover waste heat from engine cooling system and/or engine exhaust gas and transform it to mechanical or electrical power. Automotive environment is very severe and very transient, the key point for operating such system is to set up and validate a suitable control strategy to maximize the recovered output power.

In automotive industry development processes the control strategies are mainly described in a control tool environment. Commonly, the control is then tested and the control parameters are set up using physical mockups and prototypes of the studied system on a test bench. Afterwards the control is coded into a control unit and integrated in a vehicle or a demo-car in order to validate and tune up the control strategies and parameters. This process is very long and time consuming because physical prototype and demo-car are needed.

In this paper, we are going to present a methodology using a virtual model of a R134a low temperature Rankine system integrated in a vehicle platform developed in a system simulation tool environment and coupled to a Rankine control system developed in a control tool environment. This methodology and co-simulation (see Taklanti *et al.,* 2013) allow us to test and evaluate different control strategies, to select the optimal one and to set up control parameters prior to physical mockup or demo car availability.

Finally, some results are presented showing the performance of a low temperature R134a Rankine system in a vehicle environment and the performance of a control strategy for constant velocities and transient driving cycles.

1 INTRODUCTION

The efficiency of an Internal Combustion Engine used in passenger cars is at maximum 45% and about 18% in average during the NEDC driving cycle. This means, 55% to 78% of the chemical energy in the fuel is emitted to the environment as heat through the exhaust line and the engine cooling system. Many investigations have been done to exploit these losses. Direct use of heat to enhance engine warm up, thermoelectricity, turbo-compound, for example, are technical solutions mainly valorizing the exhaust losses. Among those technologies, Rankine Cycle seems very promising and potentially able to use low or high temperature heat losses considering a well adapted working fluid and component technologies.

Haller *et al.* (2014) compared Rankine waste heat recovery system performance versus car velocity at high and low heat source temperature. It appears that the low temperature system is better than the high temperature one at lower engine loads which corresponds to lower vehicle speeds. An additional parameter is the ambient temperature as it affects the performance of the heat sink. The high

temperature system is well adapted for high engine load at high speed driving and less sensitive to ambient condition. Depending on the ambient temperature the crossing point is variable, but approximately at a vehicle speed of 100km/h for an ambient temperature of 22°C.

In this paper the methodology for the control strategy development of the Rankine system and the optimization of the recovered power will be presented. This methodology is applied to a R134a low temperature Rankine system integrated into a vehicle power train.

2 R134A LOW TEMPERATURE RANKINE SYSTEM

Different Rankine system architectures are possible for automotive applications. Figure 1 presents the low temperature system layout chosen for the current study. The engine coolant picks up the waste heat of the engine which is then used to evaporate the working fluid in the water evaporator (or boiler). The expansion of high pressure vapor through the refrigerant expander (RExp) produces mechanical power. Then, the low pressure vapor condenses in the water condenser cooled by a low temperature coolant circuit. Finally a subcooler guarantees sub-cooled liquid at pump inlet to prevent the pump from cavitations.

Exhaust gas heat recovery exchanger (EHR) may be considered in the high temperature coolant loop prior to the evaporator. With higher coolant temperature the potential of recovery power increases and the system efficiency may be improved.

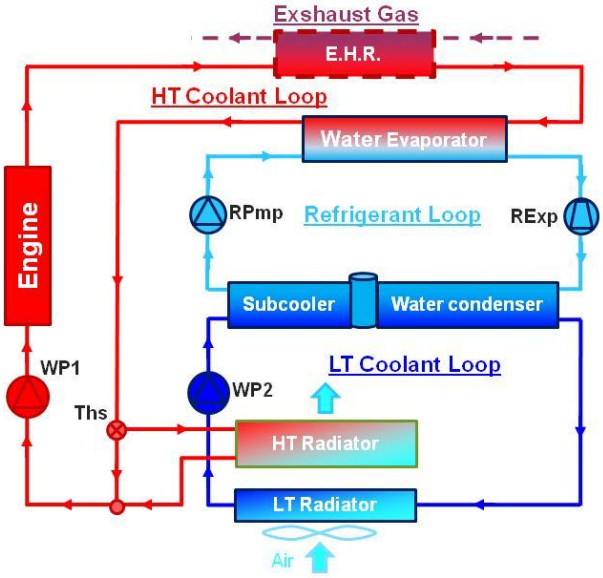

Figure 1 : Low temperature Rankine Architecture

For the integration of the Rankine system in a vehicle different solutions are possible. In the architecture considered in this study, the evaporator is placed at engine coolant outlet. The thermostat (Ths) controls the temperature setting at engine outlet by adjusting the coolant flow distribution between high temperature radiator and the radiator bypass. In the low temperature circuit, the electrical water pump WP2 ensures the coolant circulation in the water condenser and subcooler. The low temperature radiator is placed in the vehicle front end upstream, or in parallel of, the high temperature radiator.

3 SIMULATION MODEL DEVELOPMENT

3.1 R134a Rankine Cycle Model

A simulation model of a R134a Rankine cycle was developed in a multi-physics systems simulation tool. Figure 2 presents a sketch of the Rankine cycle composed of 3 main circuits: High temperature

coolant loop, refrigerant loop and low temperature coolant loop. Those loops integrate the main components of the system: evaporator, expander, condenser, receiver, subcooler, refrigerant pump, low temperature radiator and water pump.

A co-simulation block developed on control tool representing the Rankine control system is linked to the Rankine system model developed on system simulation tool.

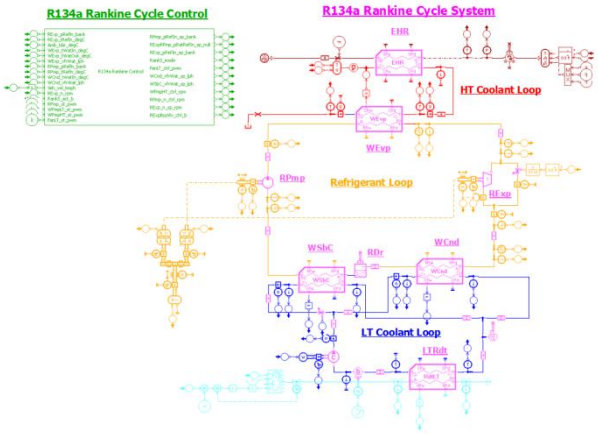

Figure 2 : R134a Rankine cycle simulation model

Large experimental investigations were performed on a low temperature Rankine cycle prototype as shown in figure 3 (see also Haller *et al* (2014)). The characteristics of this low temperature R134a Rankine prototype and part of the experimental results were used to set up the simulation model and to define and calibrate parameters of the physical component models.

4 R134A RANKINE SYSTEM CONTROL DEVELOPMENT

4.1 Rankine System Operation

Figure 3 represents a Rankine cycle operation in R134a Mollier Diagram (temperature/entropy and pressure/enthalpy). The mechanical power recovered by the Expander is:

$$Pw_{rExp} = (H_{rExpi} - H_{rExpo}) * Qm_{rExp} \quad (1)$$

$$Pw_{mExp} = Pw_{rExp} * Eff_{mExp} \quad (2)$$

To maximize the recovered power by the expander it is necessary to maximize the product of refrigerant mass flow rate Qm_{rExp} and the difference between inlet and outlet enthalpy of Expander ($H_{rExpi} - H_{rExpo}$) weighted by the Expander mechanical efficiency Eff_{mExp}. These variables depend on a set of external and internal parameters of the Rankine cycle.

The principal external parameters are:

- Temperature and volume flow rate of the high temperature coolant at evaporator inlet
- Temperature and mass flow rate of ambient air at low temperature radiator

The principal internal parameters are:

- Refrigerant pump speed
- Refrigerant expander speed

Other internal parameters which affect the Rankine system performance are the sizing of the heat exchangers and other components, the volume of the refrigerant loop and the refrigerant charge, volume and mass flow rate of high temperature and low temperature coolant loops.

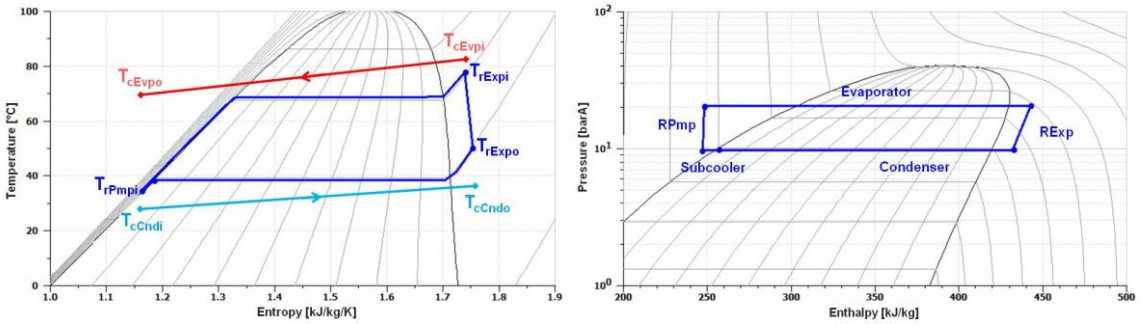

Figure 3 : R134a TS and Mollier diagram of Rankine cycle

In practice, maximizing the power Pw_{mExp} of the expander isn't enough, because the refrigerant pump has to be driven electrically or mechanically, in fact we should maximize the net power produced by the Rankine system. This is to say, for a predefined external condition, it is important to control pump and expander speeds in order to maximize the recovered net power Pw_{mNet} defined by:

$$Pw_{mNet} = Pw_{mExp} - Pw_{mPmp} \quad (3)$$

In mean time the control system should ensure the Rankine system protection for all operating points:

1. Avoid that high pressure exceeds a maximal limit $HP_{\_work\_max}$.
2. Ensure a superheat at expander inlet higher than $Sh_{\_work\_min}$ and avoid droplets formation at evaporator outlet, since it can damage the expander.
3. Avoid cooling down the coolant at the evaporator outlet below a minimum temperature limit $T_{w\_out\_min}$.
4. Ensure a minimum subcooling at pump inlet higher than $Sb_{\_work\_min}$ to avoid pump cavitations.

4.2 Optimal Rankine System operation

In order to find the best compromise of pump and expander speeds a matrix of steady state operating conditions is defined. It corresponds to ambient temperatures variation between -20°C and +45°C and vehicle speed variation from 30 to 180 km/h (low temperature radiator air velocity variation from 0.75 m/s to 7 m/s without Fan functioning).

For each external operating condition steady states simulations are performed for a set of pump speeds variation and expander speeds variation. Points with high pressure values exceeding the maximum working pressure $HP_{\_work\_max}$=32 bar are removed. The same for points with a superheat at evaporator outlet or condenser inlet lower than $Sh_{\_work\_min}$ = 5 K. The target of these simulations is to identify points with the highest Rankine mechanical net power Pw_{mNet} defined by equation 3.

Figure 4 presents an example of Rankine mechanical net power versus pump speed and expander speed obtained for an operating condition of 20°C ambient temperature, 2.5 m/s air velocity at the radiator, 90°C coolant temperature, 1500 l/h HT coolant flow rate and 1200 l/h LT coolant flow rate.

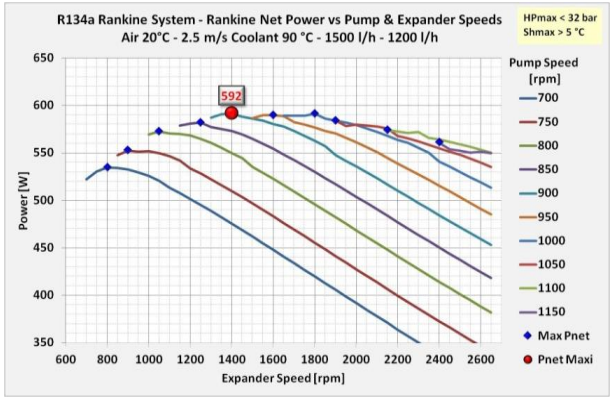

Figure 4 : Rankine net power for condition :
T_{aExt} = 20°C V_{aExt} = 2.5 m/s T_{cEvpi} = 90°C Qv_{Evp}= 1500 l/h Qv_{Cnd} = 1200 l/h

The blue dot points represent for a given pump speed, the expander speed with the maximum Rankine net power. The red dot point represents the optimal pump speed and optimal expander speed with the highest possible Rankine net power.

The next two figures present for the optimal Rankine net power obtained for different operating conditions. Figure 5a presents the effect of high temperature coolant loop temperature varying from 80°C to 115°C and for two ambient air temperatures of 20°C and 0°C. Figure 5b presents the effect of ambient air temperature variation from -20°C to 35°C for two high temperature coolant temperatures of 90°C and 110°C.

Figure 5 : Effect of operating conditions on optimal Rankine system performance
a: HT coolant temperature effect b: Ambient air temperature effect

As expected, the Rankine net power increases when the coolant temperature increases and when the ambient air temperature decreases. The Rankine net power vary from 339W at 35°C Ambient temperature and 90°C coolant temperature to 2155 W for -20°C ambient temperature and 110°C coolant temperature.

We can observe also that for a coolant temperature higher than 105°C, the slope of variation of the net power decreases. This is due to the limitations in high pressure $HP_{\_work\_max}$. For example, at ambient air of 20°C, and coolant temperature of 110°C, the maximum Rankine net power without limitation in high pressure is 1005 W with a high pressure of 37 bars to be compared to 942 W with high pressure limited to 32 bars or 815 W with high pressure limited to 28 bars.

5 RANKINE SYSTEM CONTROL ALGORITHM

As stated in §4.1, the objective of the Rankine control system is to control the refrigerant pump speed and the expander speed in order to maximize the recovered net power Pw_{mNet} and protect the system during operating.

Quoilin, S., (2011) propose three control strategy of a small-scale ORC based on the regulation of evaporating temperature and superheating in order to control the expander and the pump speeds. A relationship of optimal evaporating temperature is defined by a linear regression of optimal results obtained from a set of 31 steady state workings points where condensing temperature, working fluid mass flow rate and heat source temperature are varying in certain range. The superheating is imposed to a constant value.

The control strategies developed in this paper are based on an estimation of the optimal evaporating high pressure and the optimal condensing low pressure, and they are also based on the high pressure limit and the minimal superheat limit. To estimate the optimal working points, we write down the equation of the recovered power in the evaporator, the rejected power in condenser, the shaft power produced by the expander and the power consumed by the pump. These equations are then simplified by using a set of assumptions. An analytical treatment allows us to define optimal roots that maximize the Rankine net power.

5.1 Expander speed control.

To control the expander speed, we estimate an evaporating high pressure set point P_{rEvpo_sp} corresponding to the optimal evaporator power recovered from high temperature coolant loop $Pw_{rEvpOpt}$. To do that, we set a number of assumptions in order to simplify the equation of Pw_{mNet}. After derivation $\partial Pw_{mNet} / \partial Pw_{rEvp} = 0$ and assuming some parameters as constants, we obtain a solution Pw_{rEvp} that maximize Pw_{mNet} of the form: (f is a defined function of T_{cEvpi}, T_{aExt}, Qv_{cEvp}, Qv_{cCnd}, V_{aExt} and the system components characteristics)

$$Pw_{rEvp\_Opt} = f(T_{cEvpi}, T_{aExt}, Qv_{cEvp}, Qv_{cCnd}, V_{aExt}) \quad (4)$$

From Pw_{rEvp_Opt} of equation 4 we define the evaporating high pressure set point P_{rEvpo_sp} that will be used to control the expander speed.

5.2 Refrigerant pump speed control

To control the pump speed, we estimate a condensing low pressure set point P_{rCndi_sp} or a pressure ratio set point P_{rat_sp} corresponding to the maximum expander net power Pw_{mNet}. To do that, we used the equation of Pw_{mNet} and the high pressure set point P_{rEvpo_sp} defined in §5.1. After different mathematical manipulations and some assumptions to simplify the equations, we set the derivative $\partial Pw_{mNet} / \partial P_{ratio} = 0$ and we obtain a solution P_{ratio_sp} that maximize Pw_{mNet} of the form: (g is a defined function of P_{rEvpo_sp}, T_{aExt} and the system components characteristics)

$$P_{ratio\_sp} = g(P_{rEvpo\_sp}, T_{aExt}) \quad (5)$$

From P_{ratio_sp} of equation 5 and P_{rEvpo_sp} we define the condensing low pressure set point P_{rCndi_sp} that will be used to control the pump speed.

5.3 Control system architecture

Figure 6 presents the diagram of the Rankine control system. For this control strategy we use the following sensor data:

- From vehicle control unit:
  - T_{aExt} : Air temperature at low temperature radiator inlet
  - V_{aExt} : Air velocity at low temperature radiator inlet
  - Qv_{cEvp} : High temperature coolant volume flow rate at evaporator inlet
- From Rankine system :
  - T_{cEvpi} : High temperature coolant temperature at evaporator inlet
  - P_{rExpi} : Refrigerant pressure at evaporator outlet or at expander inlet
  - T_{rExpi} : Refrigerant temperature at evaporator outlet or at expander inlet
  - P_{rExpo} : Refrigerant pressure at expander outlet or at pump inlet

An evaporating high pressure set point P_{rEvpo_sp} and a condensing low pressure set point P_{rCndi_sp} are estimated by the control system. The high pressure is then regulated by controlling the expander speed and using the estimated high pressure set point. The low pressure set point and the condition on the minimum superheat are used to control the pump speed.

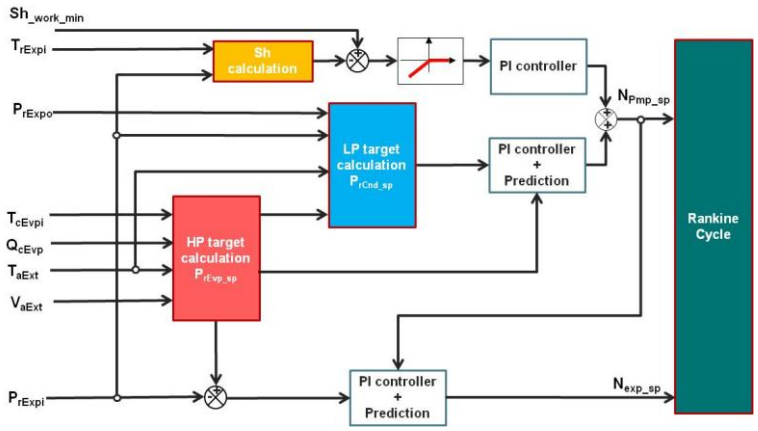

Figure 6 : Control system diagram

5.4 Rankine control system validation.

Different algorithms to estimate the optimal evaporating high pressure and condensing low pressure were tested. In order to evaluate the performance of these algorithms, we tested the Rankine control system with the Rankine system alone without the vehicle model. Steady state simulations are performed on the matrix of operating conditions defined in §4.2.

Because of the assumptions and approximations used to estimate the optimal Rankine system working points, the Rankine net power obtained with the different control algorithms is, in general, lower than the reference net power. The differences are between 0 W to 40 W.

Figure 7 illustrates the performance of the selected control algorithm. The first graph 7a shows the comparison on the effect of evaporator coolant temperature from 80°C to 110°C. Ambient temperature is 20°C. The control allows us to obtain a very good level of Rankine net power with a maximum difference of 17 W corresponding to 3% compared to the optimal power. The second graph 7b shows the comparison on the effect of radiator air velocity from 0.75 m/s to 5 m/s. The maximum difference on Rankine net power is 20 W corresponding to 4% of the optimal power.

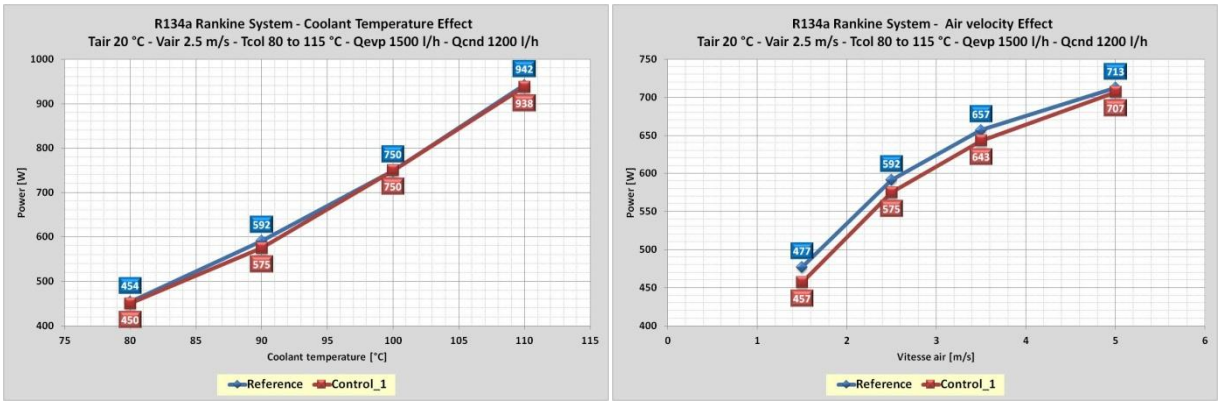

Figure 7 : Comparison of control algorithm performance on steady state conditions

6 VEHICLE INTEGRATION

6.1 Vehicle Energy and Thermal Management Simulation Platform

A simulation platform developed in the multi-physics systems simulation tool allows vehicle energy management and vehicle thermal management simulations of a vehicle equipped with a 2.0 liter turbocharged gasoline engine.

The R134a Rankine cycle model presented in Figure 2 and the control system were integrated into the Vehicle platform in order to simulate Rankine cycle with operating conditions close to real life

vehicle conditions. The interactions between vehicle and Rankine system are taken into account. However, in this study, the use of recovered power by the Rankine system electrically or mechanically by the vehicle power train is not considered. We only evaluate the recovered mechanical net power. The use of this power will be up to the carmaker strategy and will depend on the vehicle and the power train architecture and engine control strategy.

6.2 Application to constant velocities driving cycles

Figure 8 presents the Rankine net power obtained for constant vehicle velocities from 30 km/h to 180 km/h and for ambient temperature from -10°C to 25°C. The thermostat temperature setting is 90°C.

The following remarks can be stated:

- The Rankine net power increases when the vehicle speed increases. This is due to an increase of the available waste heat that can be recovered by the evaporator on one side, and an improvement of condensation performance due to the radiator air velocity increases with vehicle velocity on the other side.
- The Rankine net power is higher for low ambient temperature than for high ambient temperature. This is due to the improvement of condensation performance.
- The Rankine net power is limited by the recovered heat which is limited by the condensation side of the system, the pump and expander size.

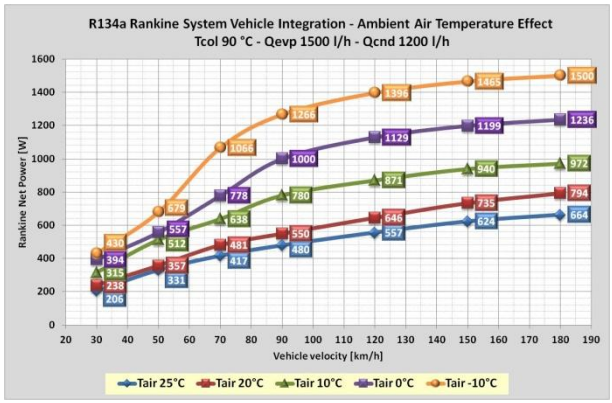

Figure 8 : Rankine net power versus vehicle speed and ambient air temperature

6.3 Application to transient driving cycle

To illustrate the performance of the Rankine control system, results are presented for transient WLTC driving cycles. WLTC is the driving cycle of the upcoming Worldwide harmonized Light vehicle Test Cycle. WLTC is more representative of real life driving in urban and sub urban conditions than driving cycles like NEDC. The duration of the WLTC cycle is 1800s and the average vehicle velocity is 46 km/h with a maximum vehicle velocity of 130 km/h. The simulations are performed for a period of 3600 s corresponding to two times the WLTC cycle duration in order to compare a WLTC with cold start engine and a WLTC cycle with warm engine.

Figure 9 presents the evolution of different Rankine cycle variables during the two WLTC driving cycles at 10°C ambient temperature. We can distinguish different phases:

- Phase I: At the start of the driving cycle, we assume that the vehicle temperature is constant and equal to the ambient temperature of 10°C. During the first 780 s period, the engine and the coolant are not hot enough and the Rankine system is switched off. The expander speed is zero and the pump speed is zero (In fact, for numerical reasons, the pump speed is set to a small value in order to ensure a minimal refrigerant circulation)
- Phase II: The coolant temperature is now higher than a coolant temperature high limit setting of 85°C, the Rankine system is activated and the pump and the expander are controlled in order to

regulate high pressure set point and low pressure set point with the constraint on minimum superheat $Sh_{\_work\_min}$.

- Phase III (highlighted zones): The vehicle speed is too low or the vehicle is stopping. There is no more sufficient energy to be recovered. The air velocity at the radiator vanishes unless we switch on the Fan. The coolant outlet temperature is decreasing and reaches a low temperature limit setting of 80°C. So, the Rankine system is switched off and the pump and the expander are stopped.

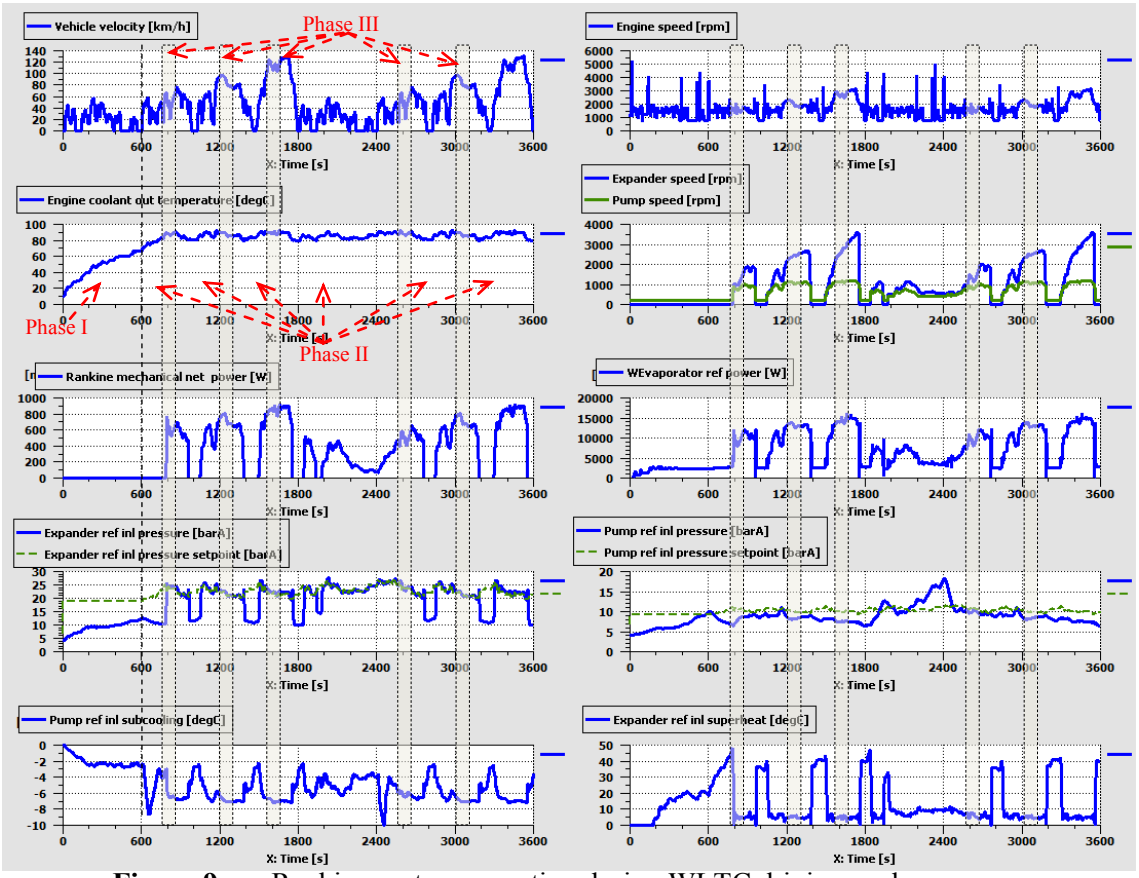

Figure 9 : Rankine system operation during WLTC driving cycle

Figure 10 presents a zoom showing the performance of the regulation of the evaporating high pressure and the condensing low pressure. The first graph shows the regulation of evaporation high pressure. The simulated high pressure follows correctly the estimated high pressure evolution defined by the control system with a delay of about 5s. The high pressure drops down when the Rankine system is switched off and the expander is stopped. The second graph presents the control of condensation low pressure. The condensing low pressure is 3 to 4 bars lower than the optimal low pressure defined by the control. In fact, to increase the level of low pressure we need to increase the pump speed. However, the superheat is very low as shown in the fourth graph. If the pump speed increases, the superheat will decrease below the $Sh_{\_work\_min}$ limitation. So, during these operating conditions the pump speed is controlled here by the superheat limit instead of by the condensation low pressure.

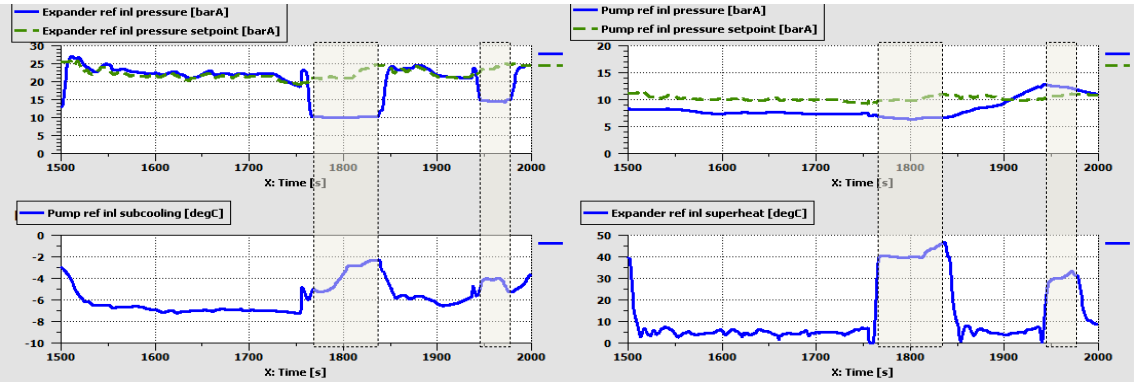

Figure 10 : Evaporating high pressure and condensing low pressure control

7 CONCLUSION

In this paper, we presented a methodology to develop and validate a control system of a low temperature waste heat recovery Organic Rankine Cycle system based on a co-simulation between a control tool and a systems simulation tool.

In the first part, a model of R134a Rankine cycle developed in a multi-physics systems simulation tool is presented. The model is based on a R134a Rankine prototype developed and tested at Valeo on a test bench. Experimental results obtained on the prototype are used to set up, calibrate and validate the models of the components and the Rankine system models.

The Rankine system model is then integrated into a global vehicle energy and thermal management model allowing simulation of Rankine system in various vehicle operating conditions corresponding to constant vehicle velocities.

A control algorithm is derived from an analytical analysis of the Rankine system equations. Different estimation of optimal evaporating high pressure and condensing low pressure are extracted and used to control the expander speed and the pump speed. The control algorithm programmed in a control tool is coupled to the physical model of a vehicle with Rankine system. The selected control algorithm was validated in steady state conditions and showed a good performance. The estimated Rankine net power obtained with the control system is no more than 20 W lower than the maximum possible net power.

Finally, the Rankine control system is applied to a transient WLTC driving cycle at different ambient conditions. It shows the ability of the control system to regulate the Rankine system with highly transient external and internal operating conditions in order to maximize the recovered mechanical net power and ensure a good conditions for a safe Rankine system functioning.

The developed control strategy and the methodology presented here can be adapted to different Rankine cycle architectures and different working fluids. It allows us also to study and evaluate different vehicle integration architectures and different options to use the mechanical power recovered by the expander directly to assist the engine and bring part of the power needed to accessories functioning or indirectly by producing electricity with an electrical generator.

NOMENCLATURE

Eff_{mExp}	Expander mechanical efficiency	[-]
$HP_{\_work\_max}$	High pressure maximal working limit	[barA]
H_{rExpi}	Refrigerant enthalpy at expander inlet	[J/kg]
H_{rExpo}	Refrigerant enthalpy at expander outlet	[J/kg]
P_{ratio_sp}	Ratio of high and low pressure set point	[-]
P_{rCndi_sp}	Refrigerant pressure set point at condenser inlet	[barA]
P_{rEvpo_sp}	Refrigerant pressure set point at evaporator outlet	[barA]

P_{rExpi}	Refrigerant pressure at expander inlet	[barA]
P_{rExpo}	Refrigerant pressure at expander outlet	[barA]
Pw_{mExp}	Expander mechanical power	[W]
Pw_{mNet}	Rankine mechanical net power	[W]
Pw_{rEvp}	Evaporator refrigerant power	[W]
Pw_{rEvp_Opt}	Optimal evaporator refrigerant power	[W]
Qm_{rExp}	Expander refrigerant mass flow rate	[kg/s]
Qv_{cCnd}	Coolant volume flow rate at condenser inlet	[m^3/s]
Qv_{cEvp}	Coolant volume flow rate at evaporator inlet	[m^3/s]
$Sb_{\_work\_min}$	Subcooling minimal working limit	[K]
$Sh_{\_work\_min}$	Superheat minimal working limit	[K]
T_{aExt}	Ambient air temperature	[°C]
T_{cCndi}	Coolant temperature at condenser inlet	[°C]
T_{cCndo}	Coolant temperature at condenser outlet	[°C]
T_{cEvpi}	Coolant temperature at evaporator inlet	[°C]
T_{cEvpo}	Coolant temperature at evaporator outlet	[°C]
T_{rExpi}	Refrigerant temperature at expander inlet	[°C]
T_{rExpo}	Refrigerant temperature at expander outlet	[°C]
T_{rPmpi}	Refrigerant temperature at refrigerant pump inlet	[°C]
$T_{w\_out\_min}$	Coolant temperature return minimal working limit	[°C]
V_{aExt}	Air velocity at low temperature radiator inlet	[m/s]

REFERENCES

El Habchi, A., Ternel, C., Leduc, P., Hetet, J.F., 2010, Potential of waste heat recovery for automotive engines using detailed simulation, *ASME-ATI Conference on Thermal and Environment Issues in Energy Systems, Sorrento, Italy, May 16-19.*

Abbe Horst, T., Tegethoff, W., Eilts, P., Koehler, J., 2014, Prediction of dynamic Rankine Cycle Waste heat recovery performance and fuel saving potential in passenger car applications considering interactions with vehicles energy management, *Energy Conversion and Management, vol. 78, p. 438-451.*

Domingues, A., Santos, H., Costa, M., 2013, Analysis of vehicle exhaust waste heat recovery potential using a Rankine Cycle, *Energy vol. 49 p. 71-85.*

Haller, R., Nicolas, B., Hammi, S., Taklanti, A., Labaste-Mauhe, L., Glavatskaya, Y., Yahia, M., 2014, Comparison of high and low temperature working fluids for automotive Rankine waste heat recovery systems, *SIA Powertrain, Rouen, France, May 21-22; 2014.*

Taklanti, A., Liu, J.M., Yahia, M., 2013, Toward verification and optimization of electrical vehicle thermal management control strategies based on virtual vehicle model, *SAE Thermal Management Systems Symposium, Troy, Michigan October 22-24; 2013.*

Quoilin, S., Aumann, R., Grill, A., Schuster, A., Lemort, V., Spliethoff, H., 2011, Dynamic modeling and optimal control strategy of waste heat recovery Organic Rankine Cycles, *Applied Energy vol. 88 p 2183-2190.*

PVT PROPERTIES AND VAPOR PRESSURES OF HFO-1336MZZ(E)

Katsuyuki TANAKA[1]*, Ryo AKASAKA[2], Eiichi SAKAUE[3]

[1]Nihon University, Department of Precision Machinery Engineering,
Chiba, Japan
ktanaka@eme.cst.nihon-u.ac.jp

[2]Kyushu Sangyo University, Department of Mechanical Engineering,
Fukuoka, Japan
ryo-a@ip.kyusan-u.ac.jp

[3]Toshiba Co. Ltd., Power System Company,
Kanagawa, Japan
eiichi.sakaue@toshiba.co.jp

* Corresponding Author

ABSTRACT

Experimental data of PVT properties and vapor pressures are presented for trans-1,1,1,4,4,4-hexafluoro-2-butene (HFO-1336mzz(E)). HFO-1336mzz(E) can be an alternative for conventional working fluids. However, reliable property information on the refrigerant is scarce at this time.
This work performed measurements of the PVT properties at temperatures from 323 K to 443 K and pressures up to 10 MPa, including supercritical region. An isochoric method was employed with a constant volume cell designed for operation at high temperatures and high pressures. The critical temperature, pressure, and density were estimated from the PVT properties in the critical region. The saturation properties were also obtained.

1. INTRODUCTION

Regarding effective energy utilization, organic Rankine cycle systems are expected for power generation systems using waste heat energy which is relatively low-temperature heat sources. And then, several kinds of working fluids should be able to be selected according to temperature of heat sources. HFO-1336mzz(E) (CAS registry no.66711-86-2, molecular weight is 164.05) is definitely one of possible candidates for the working fluid whose boiling point is near and less than room temperature. HFO-1336mzz(E) is geometrical isomer of HFO-1336mzz(Z) whose boiling point is more than room temperature. In this study, PVT properties and vapor pressures for HFO-1336mzz(E) were measured to develop the thermophysical property data base of working fluids for organic Rankine cycle systems.

2. EXPERIMENTAL

A schematic diagram of the experimental apparatus is shown in Figure 1. Sample of HFO-1336mzz(E) producted by SynQuest Laboratories, Inc. was used. Measurements of PVT (Pressure-Volume-Temperature) properties were conducted by the isochoric method. The sample was filled in a sample cell with constant volume. The mass of sample was determined from difference in the mass of a sample bomb before and after filling the sample. The density was obtained from the volume of the cell and the mass of sample. Temperature of the sample was controlled by a thermostat oil bath. Pressure of the sample was measured by a pressure sensor. PVT properties were obtained along several isochoric lines by changing the mass of sample filled in the sample cell.

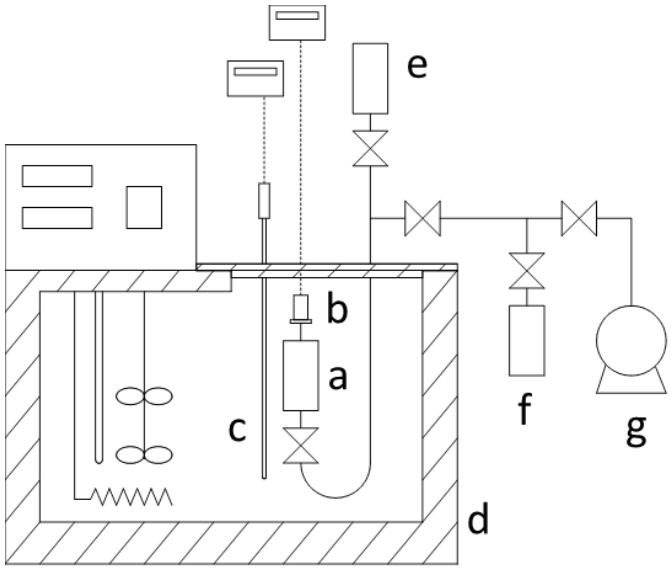

a: Sample cell, b: Pressure sensor, c: Temperature sensor, d: Thermostat oil bath,
e: Filling bottle, f: Sample bottle, g: Vacuum pump

Figure 1 Schematic diagram of the apparatus

3. RESULTS AND DISCUSSIONS

3.1 PVT properties

The data of PVT properties for HFO-1336mzz(E) was obtained at temperatures from 323 K to 443 K at 10 K interval and pressures up to 10 MPa, along 17 isochores as shown in Figure 2. The data arranged along isotherms are shown in Figure 3.

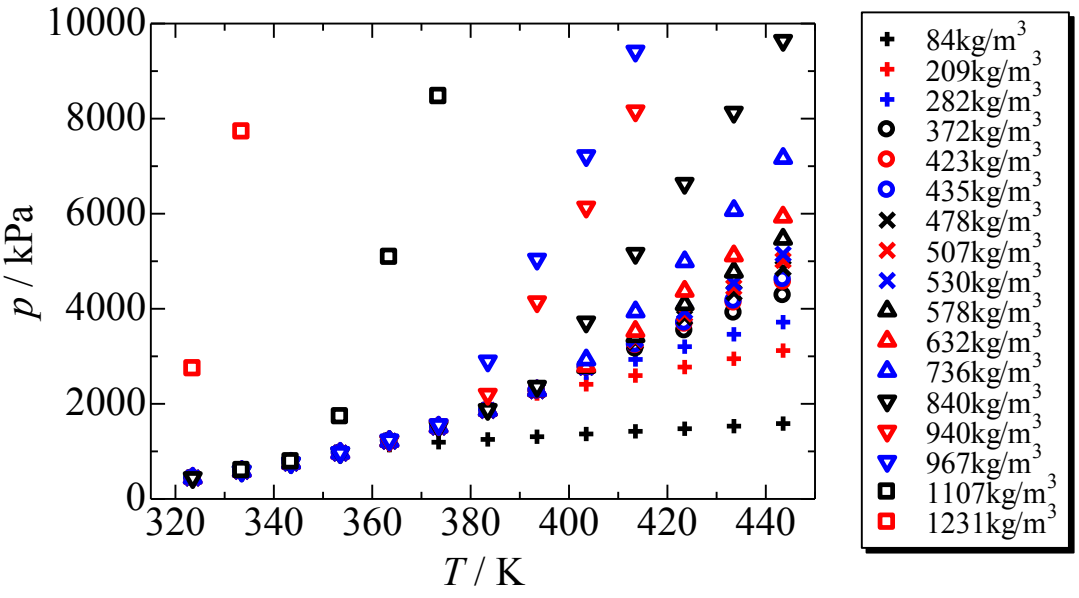

Figure 2 Experimental PVT data on pressure-temperature diagram

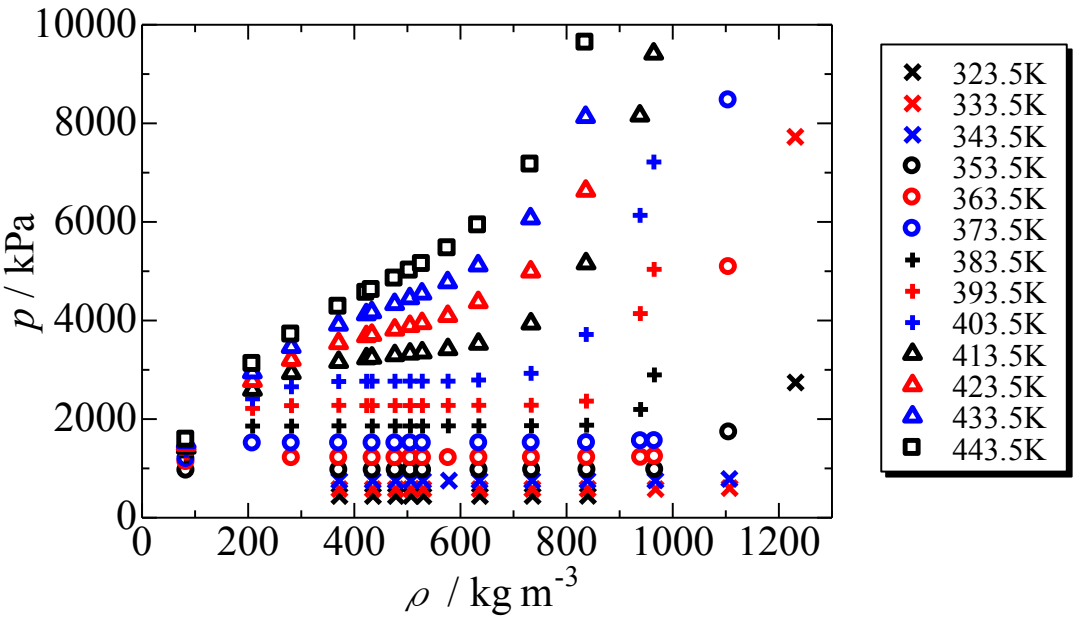

Figure 3 Experimental PVT data on pressure-density diagram

Figure 4 is an enlarged view of the critical region in Figure 3. The isotherm of 403.5 K includes data in two-phase region, because the pressure is constant in the density range from 400 kg/m^3 to 600kg/m^3. The isotherm of 413.5K consists of only data in the super critical region, because the pressure increases monotonously. These observations suggest that the critical temperature is located between 403 K and 413 K and that the critical density is to be found between 400 kg/m^3 and 600 kg/m^3.

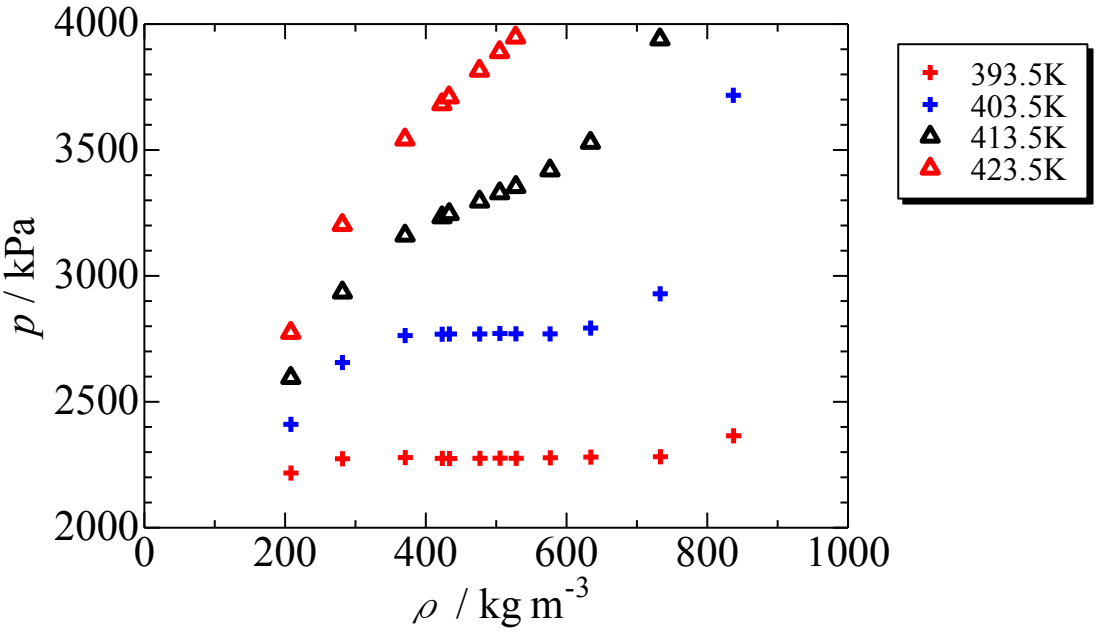

Figure 4 Experimental PVT data on pressure-density diagram in the temperature range from 393.5 K to 423.5 K

3.2 PVT properties near the critical point

In order to find more accurate location of the critical point, additional PVT measurements were performed in the critical region. PVT properties in the temperature range from 403.5 K to 413.5 K at 1K interval and in the density range from 384 kg/m^3 to 605 kg/m^3 along seven isochores were obtained. The data is shown in Figure 5 on the pressure-temperature diagram. They are also shown in Figure 6 on the pressure-density diagram, and its enlarged figure is shown in Figure 7 in the temperature range from 403.5 K to 405.5 K. These figures indicate that the critical point is located between 403.5 K and 404.5 K for temperature, between 2770 kPa and 2820 kPa for pressure, and between 476 kg/m^3 and 528 kg/m^3 for density.

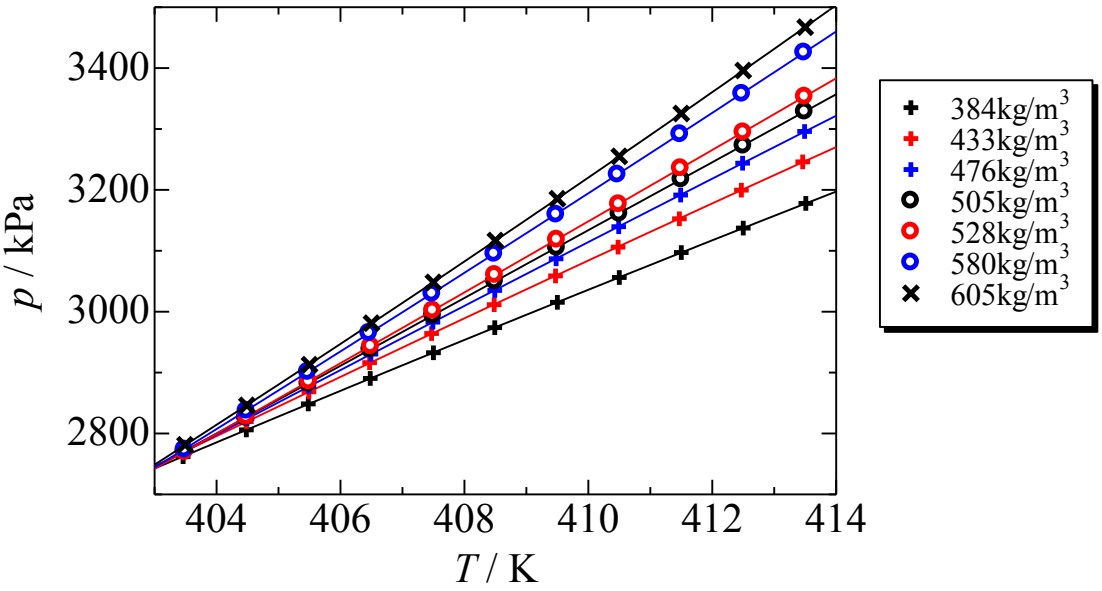

Figure 5 Experimental PVT data on pressure-temperature diagram near critical point

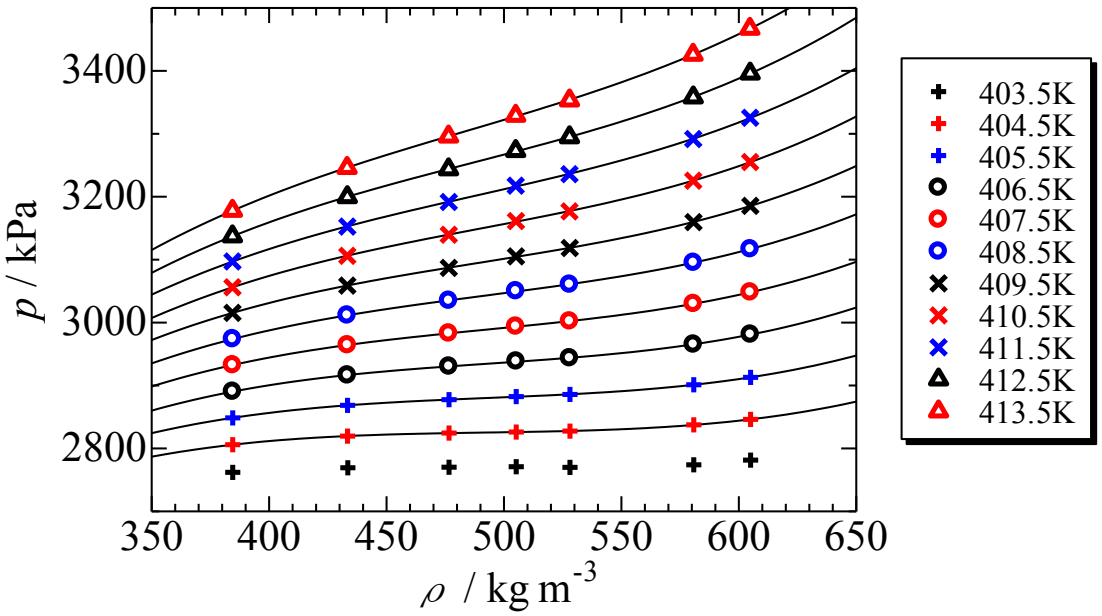

Figure 6 Experimental PVT data on pressure-density diagram near critical point

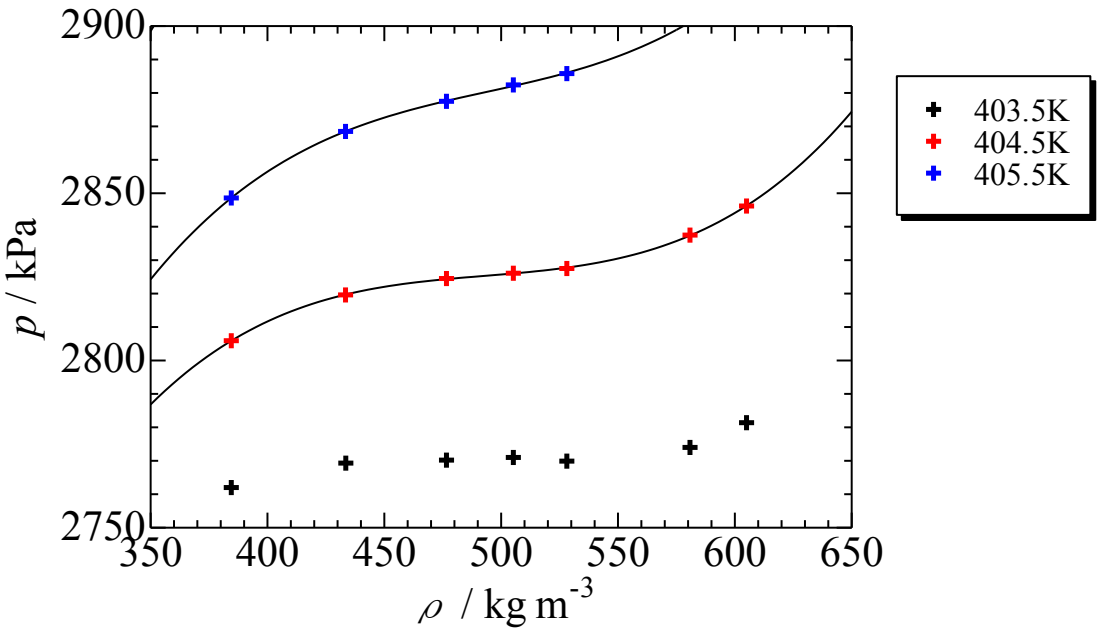

Figure 7 Experimental PVT data on pressure-density diagram near critical point (from 403.5 K to 405.5 K).

3.3 Vapor pressure

Vapor pressures are obtained from two-phase region data in the isotherms. Temperature dependence of the vapor pressures is shown in Figure 8.

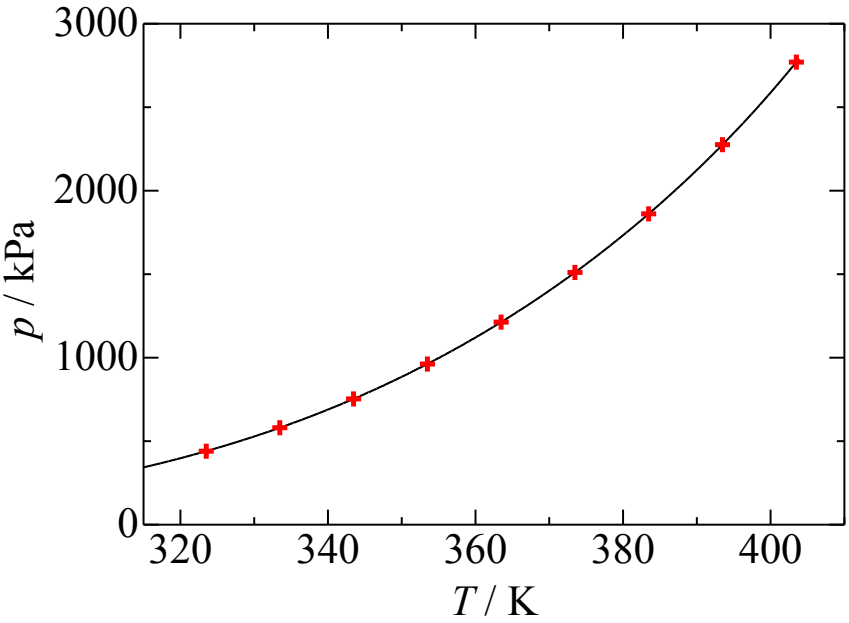

Figure 8 Vapor pressure of HFO-1336mzz(E)

3.4 Saturated densities

The saturated liquid or vapor densities were determined from intersections of the vapor pressure curve and several isochores, as shown in Figure 9. Eleven data points of saturated densities were obtained as shown in Figure 10.

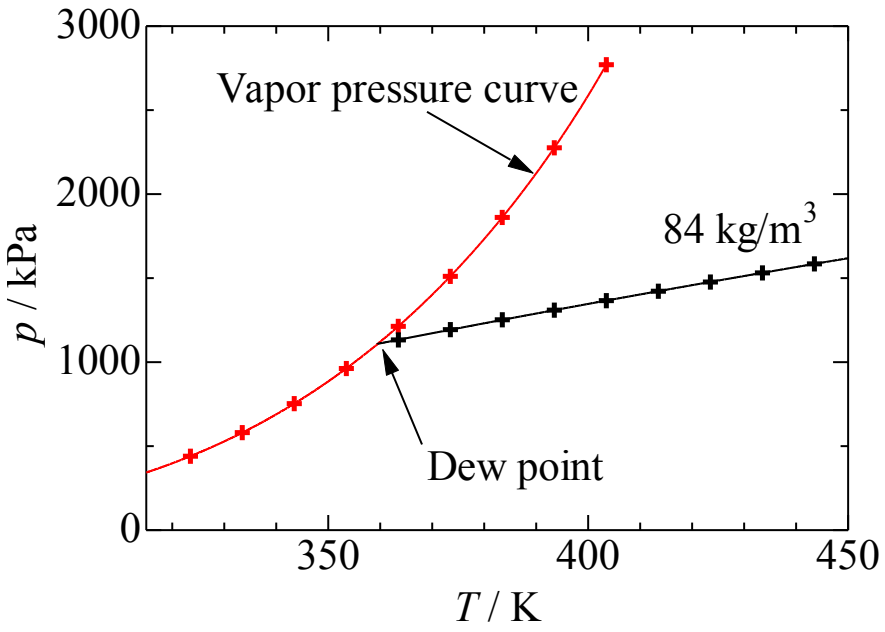

Figure 9 Determination of the saturated densities. Example for isotherm of 84 kg/m^3.

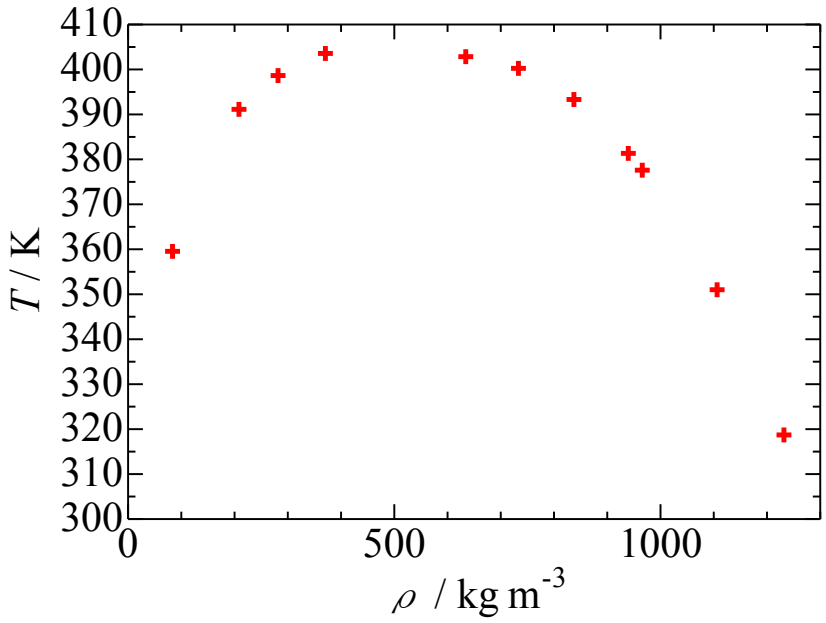

Figure 10 Saturated liquid and vapor densities of HFO-1336mzz(E)

4. CONCLUSIONS

Conclusions of this work are summarized as follows:

- Seventy seven data points of PVT properties for HFO-1336mzz(E) were obtained in a wide ranges of temperature and density, including the critical region.
- Nine data points of the vapor pressures for HFO-1336mzz(E) were obtained from two-phase region data.
- Eleven data points of the saturated densities of HFO-1336mzz(E) were determined from intersections of the vapor pressure curve and isochores.

NOMENCLATURE

p	pressure	(kPa)
T	temperature	(K)
V	volume	(m^3/kg)
ρ	density	(kg/m^3)

ACKNOWLEDGEMENT

This work was supported by the Japan Science and Technology Agency (JST) under the Strategic International Collaborative Research Program (SICORP).

ORC-DEMONSTRATION-PLANT WITH 1 KW SCROLL EXPANDER – CONCEPT, DESIGN AND OPERATIONAL EXPERIENCES

Albrecht Eicke[1]
Slawomir Smolen[2]

University of Applied Sciences Bremen
Julius Robert Mayer – Institute for Energy Technology
Neustadtswall 30, Bremen, 28199, Germany
[1] Albrecht.Eicke@hs-bremen.de
[2] Slawomir.Smolen@hs-bremen.de

ABSTRACT

The development and optimization of the ORC technology can be divided into two general groups of tasks and challenges: theoretical investigations and practical system and component improvement. One of the main practical challenges is the adoption of proper and effective expansion devices.

In this paper the current project – an ORC demonstration and test plant with an oil free expander - will be presented. The core of the micro power plant is a scroll-expander with a nominal power of 1 kW.
A commercially available scroll expander (Air Squared Inc., E15H22N4.25) with generator was used as expansion machine of the plant, in order to check the capabilities and the theoretical and practical limitations. In the first testing phase, compressed air has been used as working fluid in the expansion machine and the characteristic curves (electric power versus revolution speed with overall efficiency) have been plotted. These results can be extrapolated on other working fluids theoretically and are an indicator for the limitations of the scroll expander coupled with the electric generator. In the main phase of the project, the complete ORC-Installation with R245fa as working fluid is going to be tested and evaluated.
In the future the installation will be coupled to solar collectors, which will provide the heat to keep the ORC process running. Alternatively the heat can be generated by an electric driven thermal heater rated at a nominal power of 17 kW to demonstrate the functionality of the ORC itself without using solar energy. Disregarding the source of the heat, it is transmitted by two plate heat exchangers to the working fluid (R245fa). The extensive measurement instrumentation will be able to evaluate the entire process and the components used for the installation, especially the effectiveness of the expansion device.

1. INTRODUCTION

Organic Rankine Cycle (ORC) installations use an organic fluid instead of water as working fluid and are potentially feasible in heat recovery systems - especially for energy conversion on low and middle temperature levels. Many practical applications have been designed and installed to use low enthalpy heat sources like geothermal energy, industrial waste heat, solar energy, biomass combustion plants, small scale cogeneration systems, domestic boilers and others.
Within the framework of many projects and activities in the JRM-Institute and Laboratory for Energy Engineering at the University of Applied Sciences in Bremen, several practical and theoretical aspects of energy transformation using Organic Rankine Cycle have been investigated.
The prior activities focused on two general optimization and designing tasks. A special procedure and program has been elaborated and developed in the area of universal theoretical analysis, which facilitates working fluid selection in Organic Rankine Cycle for waste energy recovery from potential low and medium temperature level sources. In order to identify the most suitable organic fluids, several criteria have to be taken into consideration. An essential part of the program is a wide range database of organic fluids and the elaborated tool should create a support by choosing an optimal

working fluid for special applications and become a part of a bigger optimization procedure by different boundary conditions.

The theoretical research areas to develop and optimize the ORC technology can be divided into two general groups of tasks and challenges. The first big area is the thermodynamic system optimization which means not only the efficiency improvement within the cycle but also analysis of the complex system: heat source coupled with ORC-process (Smolen, 2014). This analysis should be performed by minimizing energy and exergy losses (Srinophakum, 2001, Invernizzi, 2007, Hung, 2001, and others).

The second theoretical field is the working fluid selection as optimization measure of the cycle and the entire process heat transfer from heat source. However, the selection of working fluids and operational conditions are very important to system performance. The thermodynamic properties of working fluids will affect the system efficiency, operation, and environmental impact (Smolen, 2011, Saleh, 2006, Angelino, 1998, Borsukiewicz-Gozdur, 2007, Liu, 2004 and others)

The ORC-Process is not the only alternative to use low enthalpy heat sources. Some technologies are available and efficient, some other technologies are still been developed but seem being promising. Among those technologies the water-ammonia cycle, the supercritical CO_2 cycle, the Stirling and Ericsson cycles, the Kalina cycle and the thermoelectric generator can be mentioned. There are many criteria and boundary conditions to compare the different approaches and methods of energy conversion but generally the Organic Rankine Cycle is preferred to those technologies, because of its simplicity and its limited number of components, all of them being very common and in the typical applications commercially available.

One of the practical limitations and challenges of developing of new ORC-installations are expansion devices, or lack of suitable machines for special applications in small and middle range of performance (especially micro- and mini ORC-installations). There are many approaches and practical solutions and technologies like using micro turbines, scroll expanders, screw machines, special reciprocation engines and others. The internal efficiency of expansion process is one of the biggest sources of energy and exergy losses which restrict system's efficiency. As example of practical possibilities and solutions, the application of a screw compressor as expansion device of ca. 30 kW has been investigated and the unique installation has been put into operation within a prior theoretical and practical work (Eicke, 2014). The project work presented in this paper deals with smaller range of performance and uses existing components in order to extend the practical and theoretical experiences and potential applicability.

2. OBJECTIVES AND REQUIREMENTS TO THE TEST AND DEMONSTRATION 1 KW ORC-PLANT

The general goal of the work was concept development, design, evaluation and optimization of an ORC plant in power range of ca. 1 kW. One of the practical intensions of the project was to investigate a commercially available scroll expander (Air Squared Inc., E15H22N4.25) with generator as core piece of the plant, to adopt the installation to this specific expansion device and to check the capabilities and the theoretical and practical limitations.

In the first stage of development, the heat source should be "simulated" by an electric heater but, as final solution, the test plant will be coupled with a solar installation in order to demonstrate the application as renewable energy conversion and use. Subject of the presented paper is only the first stage of the project and the relevant subsequent subtasks are:

- technical optimization by concept development and permanent improvement after the first operational experiences;
- thermodynamic process evaluation and optimization by using advanced measurement technology;
- theoretical validation and transfer of the measurement results to changeable temperature levels and different working fluids. (This possibility is limited by the existing installation and the reconfiguration require additional measures like component replacement);
- evaluation of the practical application possibilities in different energy supply systems.

Furthermore some additional aspects have been taken into consideration like flexibility by required modifications and improvement measures, safety aspects, analysis and prevention of operational

accidents, demonstration effects and others. Advanced measurement technology should facilitate thermodynamic and technical evaluation and optimization of the plant and additionally support the demonstration effect.

3. DEMONSTRATION PLANT CONCEPT AND MAIN COMPONENTS

As already mentioned, the general goal of the installation concept has been adapted to the requirements and performance of the scroll expander (Air Squared Inc., E15H22N4.25). All components and parts of the installation have been calculated and selected, in order to use the possibilities and potential of the existing expansion device in an optimal way. The temperature, pressure and flow rate sensors have been installed in all relevant points not to be able to evaluate the whole cycle but also to validate the components and the auxiliary equipment. The connection scheme of the plant is shown in figure 1.

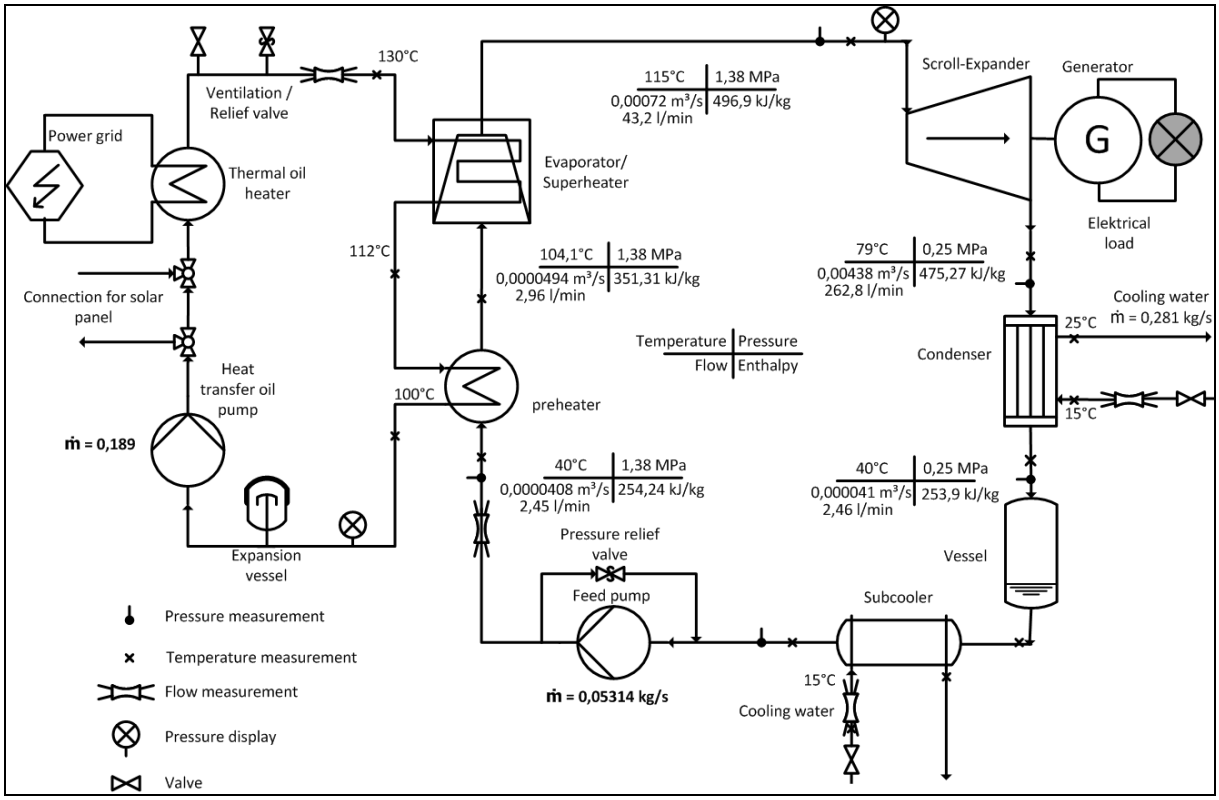

Figure 1: ORC demonstration plant – connection schema

In the first stage of the project the heat power is provided by electric heater and the heat transfer medium is thermal oil. The typical ORC-installation consists of preheater, evaporator, scroll expander, condenser and feed pump. An additional special part is the refrigerant sub cooler after the storage tank. This one facilitates the operational quality, especially by putting into operation or changeable performance (experiences from the bigger installation mentioned in the introduction).
The thermodynamic cycle is shown in figure 2 (log p–h–Diagram).

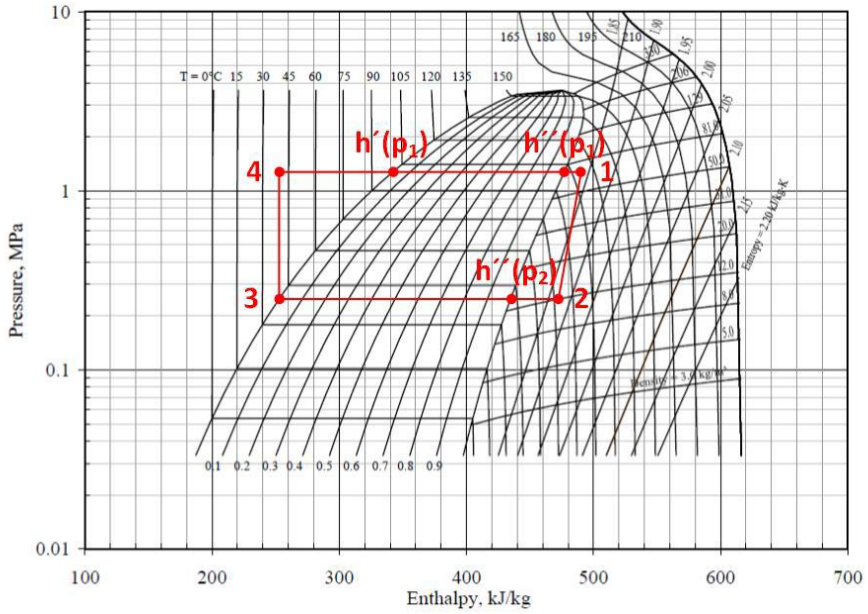

Figure 2: ORC cycle parameter in log-p-h-diagram

For the test bench the working fluid R245fa was selected but some alternatives are possible and can be taken into consideration. The calculated (expected) efficiency amounts to ca. 8.7 %. This efficiency has been calculated as total efficiency, it means electrical energy output to thermal energy input (4-1 in Fig. 2). The expected internal efficiency of expansion (1-2 in Fig. 2) has been considered as well as pumping power (3-4 in Fig. 2). Heat losses in heat exchangers (evaporator, condenser) and in connecting pipes are negligible - when good insulated - and were not calculated.

The following table specifies some important data and characteristics to the main components of the installation.

Table 1: Components of the plant – selected data and characteristics

No.	Component	Parameter
1.	Scroll expander	Air Squared Inc., E15H22N4.25, expansion ratio 3.5
2.	Generator	AB30 Hydro, 50Hz, 2400W at 3000min-^{1}
3.	Electric thermal oil heater	Typ HF/SE-20, t_{max} = 130°C, Power = 20kW
4.	Feed pump (refrigerant)	Slide pump with magnetic coupling
5.	Heat exchanger	Preheater: Plate heat exchanger, GPL 25-8 Evaporator: Plate heat exchanger, GPL 25-14 Condenser: Plate heat exchanger, GPL 1-20 Sub cooler: Pipe in pipe heat exchanger Typ HE1.5
6.	Heat transfer pump	small centrifugal pump for Therminol ADX10
7.	Electric installation (energy use)	15 Halogen bulb each 100W electrical load

4. DESIGN OF THE INSTALLATION

The installation has been designed and built in the Laboratory for Energetics of the Hochschule Bremen within a master project work (Haberkorn *et al.*, 2015). All the requirements and objectives mentioned above has been considered and as demonstration effect the front side of the box shaped stand is designed as thermodynamic part, the expander and generator is mounted on the top and the electric and control devices are placed on the back – as shown in figure 3. On the right the electrical power can be visualized by luminous halogen lamps, which are controlled by a special board. For the second stage of the project, the connections to the solar installation have been designed too.

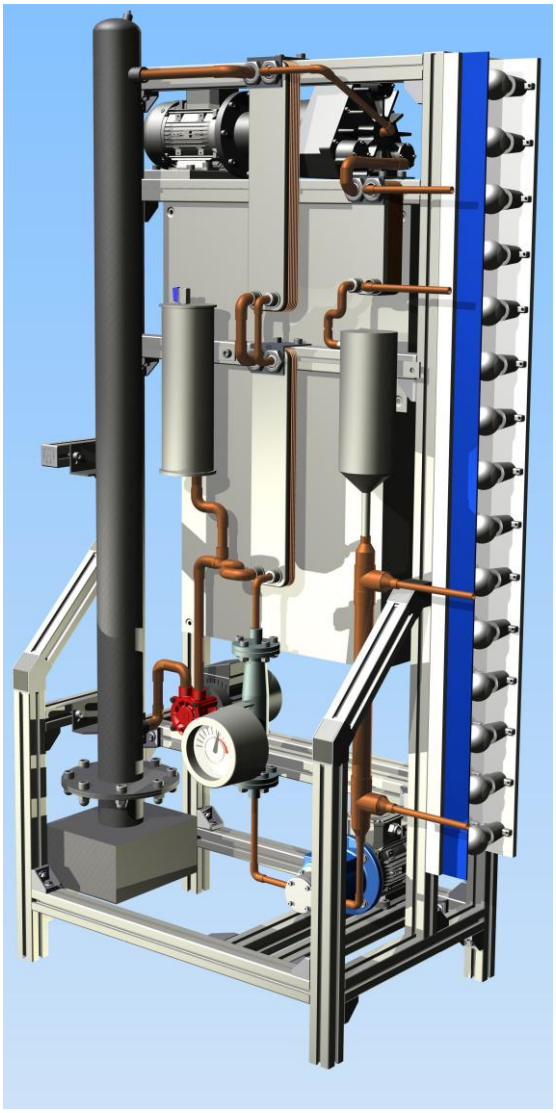

Figure 3: Design of the 1 kW ORC demonstration plant

5. LABVIEW CONTROL SYSTEM

This ORC-plant is developed to demonstrate a steam cycle and to show the function of its components. A Data Acquisition System cDAQ 9178 was used for measuring the temperature and the pressure in each condition, the electric power, the volume flow and the revolution of the scroll expander. This system is built up in a modular way and cause of the integrated signal condition the sensors are clearly arranged and direct connected. The voltage and current flow of the generator are converted by a hall effect transducer into a signal of up to 5 Volt so that the effective electric power could be calculated. The measurement equipment is shown in figure 4 and is located in a separate switchboard to reduce electric noise from inverter and motor.

To hold the required voltage and the frequency, for example 230 Volt at 50 Hz, a LabVIEW program calculates the electric load and turns on additional light bulbs or switches them off (each light bulb has nominal 100 Watt at 230 Volt). A maximum number of 15 light bulbs can show directly the produced power of the specific operating point.

The software searches for the measured temperature and pressure the values for enthalpy and entropy to the main condition points from a table. Additional to the heat power, the electrical power, the revolution and the efficiency these points are also visualized in a h-s-diagram and a T-s-diagram.

The speed of the feed pump is controlled over an inverter, shown in figure 4, to steer the mass flow of the refrigerant in the cycle to hold the evaporating temperature on one hand and to control the revolution of the scroll expander on the other hand.

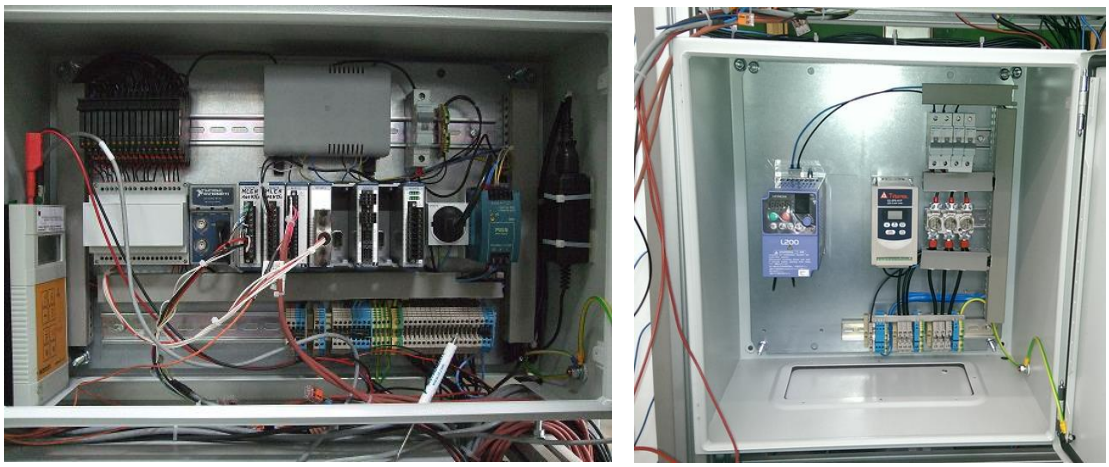

Figure 4: The measurement equipment (left) and frequency inverter to control the feed pump (right)

The electric thermal oil heater was not delivered in time, so that the scroll expander was tested with compressed air to check the control loop, the sensors and the electric load.

6. COMPRESSED AIR TEST BENCH FOR SCROLL EXPANDER TESTS

The test bench was enlarged with air pipes and an air flow meter to test the scroll expander and the generator. The supply grid for compressed air of the Laboratory for Energetics is limited to 0.95 MPa therefore it was not possible to test the expander with the maximum pressure of 1.38 MPa.
In the beginning the characteristic of the generator (voltage versus speed) was measured. The first run showed that the generator is self-excited and built up a magnetic field when the break-through-voltage of the diode is over 100 Volt the first time – like shown in figure 5. The following tests show a useful voltage of 80 Volt when the revolution per minute is higher than 1500 min^{-1}.

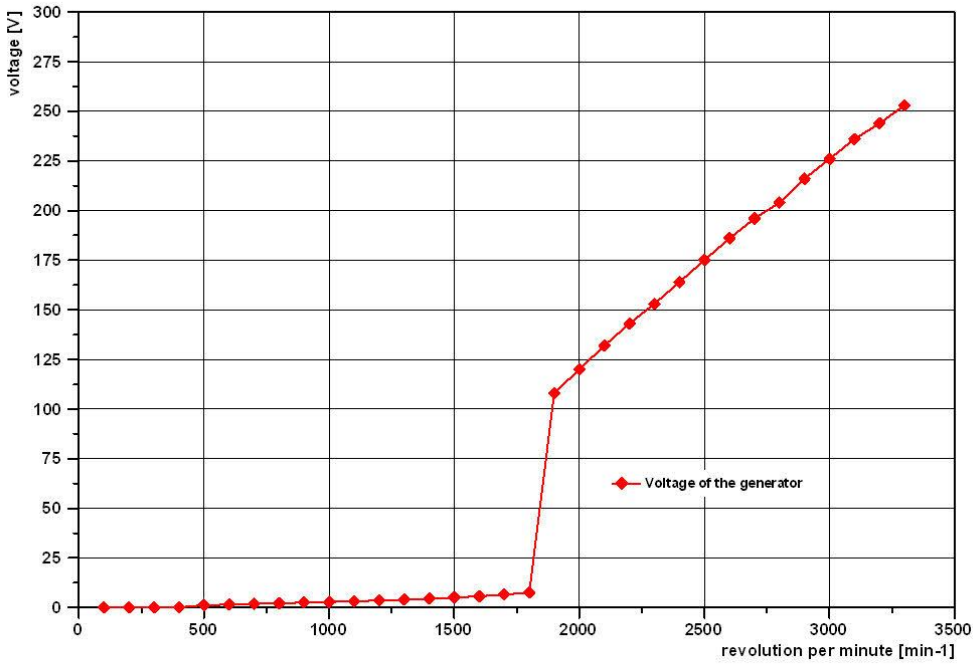

Figure 5: Characteristic of the generator Voltmaster AB30 2400 Watt - voltage vs rpm

The compressed air is expanded in the scroll expander from an inlet temperature of 19°C with a volume ratio of 3.5 to a low temperature of 10 degrees below zero at the end of the expansion that the duration of the test is limited not to risk a damage of the expander. The enthalpy and the thermal properties of the air is not comparable with the 115°C hot refrigerant of the real fluid. It is therefore necessary to increase the load of the test bench at lower revolutions per minute by external excitation of the rotor to measure the full curve of the electric power. The real refrigerant fluid with its higher energy content would cause higher speeds of the scroll engine than for air operation and is therefore in the correct speed range. Figure 6 shows the electric power versus revolution per minute for a pressure from 0.50 MPa to the maximum of 0.94 MPa. The overall efficiency is noted in numbers at every second point. The volume flow through the scroll engine increases with the increase of speed but the torque goes down to zero at maximum speed. The efficiency is higher with higher suction pressure and rise up to a maximum value a little bit higher than the half of the revolution per minute with no load. For example the efficiency for a pressure of 0.94 MPa at 3600 rpm is zero and rise up to η = 0.43 at 2200 rpm.

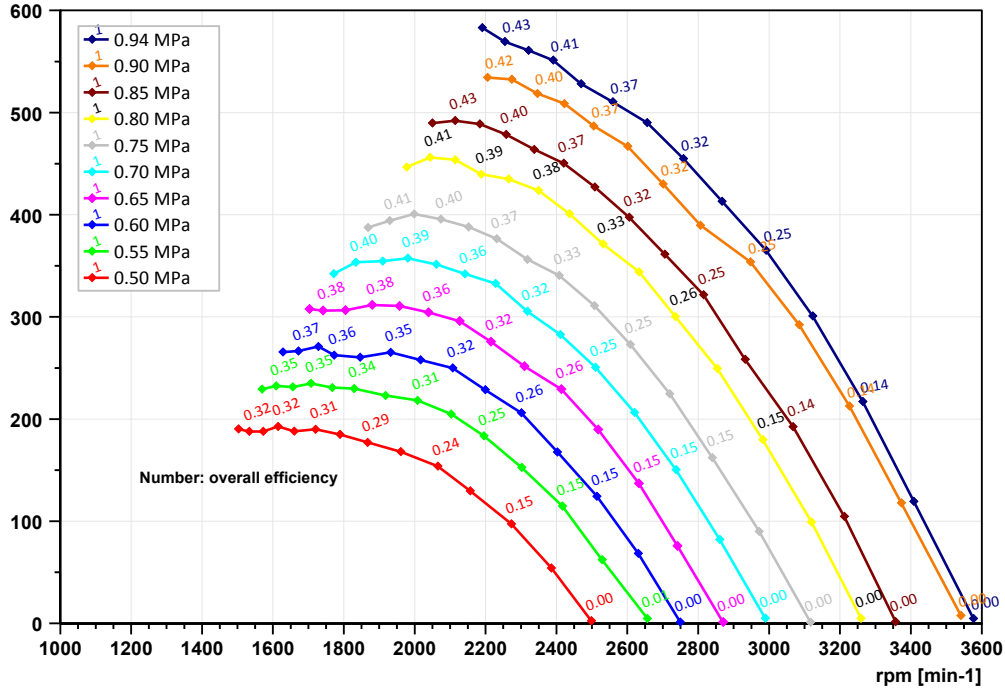

Figure 6: Electric Power versus rpm with overall efficiency

7. CONCLUSIONS AND OUTLOOK

As result of the practical orientated work, a unique 1 kW ORC installation on the base of scroll expander has been developed, designed and built, which facilitates process improvement and demonstration effects. Additionally, a test bench for scroll expander tests with pressurized air has been developed and equipped in order to investigate operational features of the expansion device as the first practical step. These preliminary tests are essential for the subsequent thermodynamic process improvement and optimization. The final presentation is going to include the first operation experiences and test results.

Related to the second stage of the ORC project a solar installation has been calculated and planed, which is going to be installed and coupled with the ORC-plant to extend it to a complex installation using a renewable energy source.

Parallel to this technical project, an additional aspect – namely economical one - has been taken into consideration by investigating the practical applicability. One concrete application possibility of the 1 kW plant for waste heat use from an industrial process was evaluated from economical point of view, in fact with a negative result. (The economic efficiency calculations have been conducted for German

energy prices and economical boundary conditions and the calculation's details would be beyond the scope of this paper). The main reason for the economic ineffectiveness is of course the costs of the unique installation, which cannot justify profitable operation under the terms of conventional economy.

REFERENCES

Angelino, G., Di Palliano, P.-C., Multicomponent working fluids for organic Rankine cycles (ORCs), *Energy*, vol. 23, No. 6, 1998, pp. 449-463.

Borsukiewicz-Gozdur, A., Nowak, W., Comparative analysis of natural and synthetic refrigerants in application to low temperature Clausius-Rankine cycle, *Energy*, vol. 32, 2007, pp. 344-352.

Eicke, A., Smolen, S., Screw Engine as Expansion Machine Applied in an ORC-Test-Installation – the First Operating Experiences – Lubrication System for a Screw Machine in Reverse Rotation, *VDI-Berichte (Energy and Environment)*, International Conference on Screw Machines, TU Dortmund University - 2014, ISSN 0083-5560, ISBN 978-3-18-092228-7.

Haberkorn, P., Herrmann, L., Sax, M., Speckmann, B., Zoche, D., KAI-ORC, Technical Project Documentation, University of Applied Sciences Bremen (Hochschule Bremen, Advisor: Smolen, S., Eicke, A.), Februar 2015, not published.

Hung, T.-C., Shai, T.-Y., Wang, S.-K., A review of organic Rankine cycles (ORCs) for the recovery of low-grade waste heat, Energy, Vol. 22, No. 7, 1997, pp. 661 – 667.

Hung, T.-C., Waste heat recovery of organic Rankine cycle using dry fluids, *Energy conversion and management*, vol. 42, 2001, pp. 539-553.

Invernizzi, C., Iora, P., Silva, P., Bottoming micro-Rankine cycles for micro-gas turbines, *Applied Thermal Engineering*, vol. 27, 2007, pp. 100-110.

Liu, B.-T., Chien, K.-H., Wang, C.-C., Effect of working fluids on organic Rankine cycle for waste heat recovery, *Energy*, vol. 29, 2004, pp. 1207-1217.

Saleh, B., Koglbauer, G., Wendland, M., Fischer J., Working fluids for low-temperature Organic Rankine Cycles, *Energy (2006), doi:10.1016/j.energy.2006.07.001*., Elsevier Ltd.

Smolen, S., Boertz, H., Calculation and optimization of heat transfer between the low enthalpy heat source and Organic Rankine Cycle applied to heat recovery systems, *Key Engineering Materials*, Vol. 597 (2014), © (2014) Trans Tech Publications, Switzerland doi:10.4028/www.scientific.net/KEM.597.45

Smolen, S., Bandean, D., Working Fluid Selection for Organic Rankine Cycle Applied to Heat Recovery Systems, *WREC, World Renewable Energy Congress 2011*, Sweden, Linköping, May 2011, www.wrec2011.com

Smolen, S., Simulation and Thermodynamic Analysis of a Two-Stage Organic Rankine Cycle for Utilization of Waste Heat at Medium and Low Temperature Levels, *Energy Science and Technology (Peer Reviewed Journal)*, Volume 1, Number 1, 28 February 2011, Canadian Research & and Development Center of Science and Cultures, www.ascanada.net, ISSN 1923-8460 [Print], ISSN 1923-8479 [Online]

Srinophakum, T., Laowithayangkul, S., Ishida, M., Simulation of power cycle with energy utilization diagram, *Energy Conversion and Management*, vol. 42, 2001, p. 1437-1456.

DIESEL ENGINE WASTE HEAT HARNESSING ORC

Jovana Radulovic[1]*, Simon Taylor[1]

[1]University of Portsmouth, School of Engineering,
Portsmouth, PO1 3DJ, United Kingdom
jovana.radulovic@port.ac.uk

ABSTRACT

Use of ORCs in waste heat recovery is widely seen as a viable and promising solution for increasing energy efficiency and emission reduction efforts, with "on-board" vehicular concepts becoming increasingly popular. In this study, the potential of an ORC harnessing exhaust energy from a diesel generator is considered. Preliminary fluid selection was based on satisfactory thermodynamic performance, and expander size requirement as the limiting parameter.

Both simple and recuperative ORC systems were considered. The effect of the exhaust temperature and the high operational pressure of the ORC model were evaluated in terms of energetic and exergetic performance. For the toluene ORC, moderate pressure values were dictated by the expander size limitation, yet this can be alleviated by high exhaust temperatures. Simple ORCs required a larger heat input and had lower exergetic efficiency. Recuperative ORCs showed better thermal efficiency and lower overall exergy destruction. The expander efficiency was identified as a vital parameter for cycle design and thermodynamic performance.

1. INTRODUCTION

With ever increasing global energy consumption and climate change concerns, reducing greenhouse gases emissions and improving energy efficiency of power systems are immediate priorities. Organic Rankine Cycle (ORC) has been long recognised as a promising technology to support the shift from conventional fossil fuels towards renewable energy sources. A number of published studies evaluated ORC potential in conjunction with biomass, solar and geothermal energy sources (Tchanche *et al*., 2011). Additionally, ORC is a powerful tool for harnessing waste heat (Quoilin *et al*., 2013) (Kolsch and Radulovic, 2015).

Basic ORC is founded on well-known transformations found in the conventional steam Rankine systems. However, the use of a volatile organic liquid as the working fluid allows for low-grade heat sources to be used. ORC is considered to be flexible in terms of the type and temperature of the heat source, and requires low maintenance. The versatility of the heat source and its modular design make ORC an attractive option, especially when waste heat is used for power generation.

Conversion of waste heat into electricity through so-called bottoming ORC improves the overall efficiency of the system whilst reducing heat pollution. The efficiency of the waste heat recovery through an ORC depends on a number of parameters: the state and quantity of the stream matter, its availability and especially its temperature. In fact, waste heat sources are categorized according to their temperature range as: low heat (< 230°C); medium heat (230°C - 650°C); and high heat (> 650°C) (Tchanche *et al*., 2011). In particular, harnessing of diesel engine exhaust heat has been the focus of recent research. Larsen *et al*. (2013) studied a plethora of potential ORC fluids for waste heat recovery in marine applications. Yu *et al*. (2013) concluded that the thermal efficiency of a diesel engine can be improved up to 6.1% through bottoming ORC implementation. Wang *et al*. (2014) proposed a dual-loop ORC system. Katsanos *et al*. (2012) evaluated the possibility of ORC installation on a diesel truck engine. Feasibility of several on-board vehicular ORC recovery systems has also been performed (Capata and Toro, 2014).

Selection of the working fluid in an ORC is a much debated issue (Tchanche *et al*., 2011). Fluid properties dictate thermodynamic performance, but also have overreaching influence on cycle design. Fluid stability and flammability have to be taken into account in order to ensure the safe operation of the device. Fluid toxicity and environmental impact must also be considered. Thus far, the scientific community agrees an ideal ORC working fluid cannot be selected, and that 'optimal' fluid choice depends on the particular application, nature and temperature of the heat source, cycle operational parameters, etc.

In this paper, an ORC implementation harnessing waste heat from a diesel generator is considered. The analysis was based on a Rolls Royce Field Electrical Power Supply (FEPS) 40 kW unit. This features a Deutz 912, air-cooled, 6 cylinder inline, direct injection diesel engine. According to the manufacturer's specification, the maximum exhaust temperature is 500°C. In this paper a small-size compact ORC, powered by the above described exhaust waste heat, for additional power generation is considered. Comprehensive fluid selection and evaluation of the cycle energetic and exergetic performance was carried out, with size limitation being the primary factor.

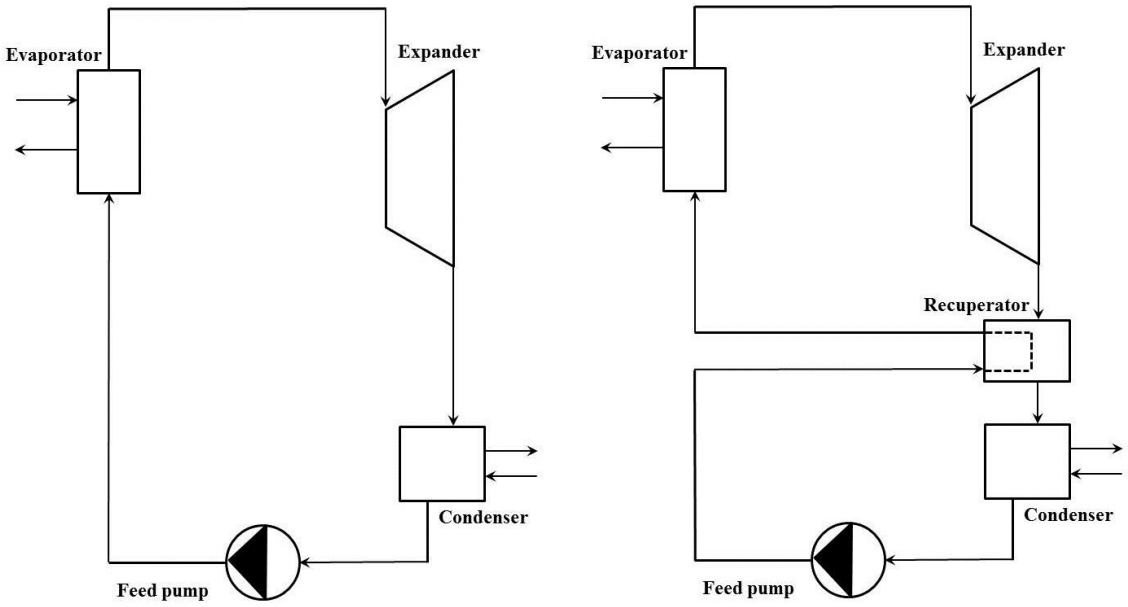

Figure 1: Schematics of simple and recuperative ORC.

2. METHODOLOGY

2.1 ORC model

Two ORC designs were considered: a simple cycle and a recuperative cycle, as shown in Figure 1. The basic processes of the ORC, and the assumptions made in our model, are as follows: pump pressure increase; isobaric heating in the evaporator by the exhaust stream; expansion; isobaric cooling of the working fluid until saturation and condensation. If the working fluid is in the superheated state at the expander outlet, it is possible to use a recuperator (Yang *et al*., 2014). The recuperator element allows for internal heat transfer between 'hot' low pressure stream from the expander outlet and 'cold' high pressure stream leaving the pump; thus, working fluid is being preheated before entering the evaporator. The pressure drop through the recuperator heat exchanger was assumed to be negligible and the low pressure stream at the outlet of the heat exchanger was assumed to be in a saturated vapour state. Further assumptions which were made included a steady-state steady-flow system, negligible kinetic and potential energy losses as well as negligible heat losses in all components and pipes.

The condenser outlet was assumed to be a saturated liquid at 298K; this assumption was used to set the operational pressure of the condenser. High cycle pressure and temperature were varied in a selected range in order to evaluate ORC performance and size requirements at different operational parameters. In the initial assessment, isentropic efficiency of the pump and the expander were fixed at 80% and 75%, respectively, although these parameters are analysed afterwards in more detail. All fluid properties were evaluated using REFPROP 9.1. Work and heat exchanges were calculated from the enthalpy gradient at specified points of the cycle. A detailed set of equations can be found in (Radulovic and Castaneda, 2014). Energy and exergy balance was carried out for individual cycle components as well as the whole system:

$$w_P + q_{in} = w_E + q_{out} \tag{1}$$

$$ex_{in} + q\left(1 - \frac{T_0}{T}\right) = ex_{out} + w + i \tag{2}$$

in order to evaluate thermal and exergy efficiency:

$$\eta_{th} = \frac{w_{net}}{q_{in}} \tag{3}$$

$$\eta_{ex} = 1 - \frac{i_{total}}{ex_{in}} \tag{4}$$

where overall exergy destruction was calculated as

$$i_{total} = i_P + i_B + i_E + i_C\left(+ i_R\right) \tag{5}$$

Table 1: Preliminary assessment of suitable working fluids

Fluid/ Performance	Benzene	Toluene	Cyclohexane	Propyl cyclohexane	Undecane	MDM
w_{net} *(kJ/kg)*	186.3	199.7	177.7	200.4	207.7	110.3
q_B *(kJ/kg)*	936.5	934.5	1029.3	1027.7	1059.2	761.1
η_{th} *(%)*	19.9	21.4	17.3	19.5	19.6	14.5
***VR** (-)*	69.8	238.8	72.4	1840.9	20552.7	2270.2
i_{total} *(kJ/kg)*	496.4	481.7	572.8	548.9	564.6	444.6
η_{ex} *(%)*	27.3	29.3	23.7	26.8	26.9	19.9

2.2 Fluid selection

The maximum exhaust temperature of the diesel generator is stated by the manufacturers to be 773K, indicated the need for a working fluid appropriate for high temperature application. Suitable candidates have been much debated in the literature. A number of fluids shortlisted in Tchanche *et al.* (2011) for high-temperature ORC systems were considered. Assuming a high cycle temperature of 616K and a moderate operational pressure of 1MPa, preliminary assessment of fluid behavior in a simple ORC was performed. Results are summarised in Table 1. The toluene cycle yielded the highest thermal and exergy efficiency. The MDM fluid family had the lowest exergetic and thermal efficiency, and the worst work output. The largest net work was calculated for the undecane cycle. However, undecane, and similarly-performing propyl cyclohexane, had unacceptably high volume

ratios. Heptane and octane, hydrocarbons with a lower molecular weight, were also evaluated, but were subsequently excluded due to the high exhaust temperatures considered here. Aromatics generally require lower heat input than cycloalkanes. Low volume ratios were found for benzene and cyclohexane expanders. Nonetheless, overall exergy destruction was found to be lower in the toluene ORC. Taking everything into consideration, toluene was selected as a fitting and manageable working fluid. Given the critical temperature and pressure of toluene, 591.75K and 4.1263 MPa respectively, only subcritical cycles were considered. Being a dry fluid, as shown on the *T-s* diagram in Figure 2, there is no risk of toluene condensation occurring at the expander outlet, which allows for the use of the recuperating element in the cycle. Notwithstanding the superior thermodynamic performance of toluene, there are other aspects that have to be considered. According to ASHRAE Standard 34 – Refrigerant safety group classification, toluene is in the A3 group (A – lower toxicity; 3 – higher flammability). Despite this feature, highly flammable fluids are commonly considered in ORC studies (Song *et al.*, 2015). Use of toluene in an 'on-board' ORC device would therefore pose a safety risk. Nonetheless, toluene-based ORC systems are already in use.

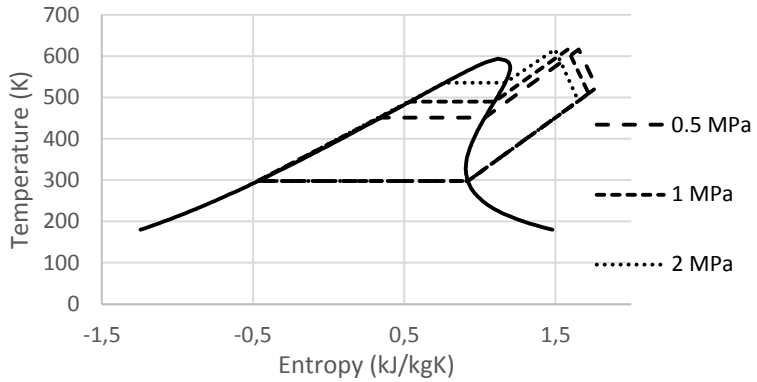

Figure 2: High pressure variation in simple toluene ORC with expander inlet temperature of 616K.

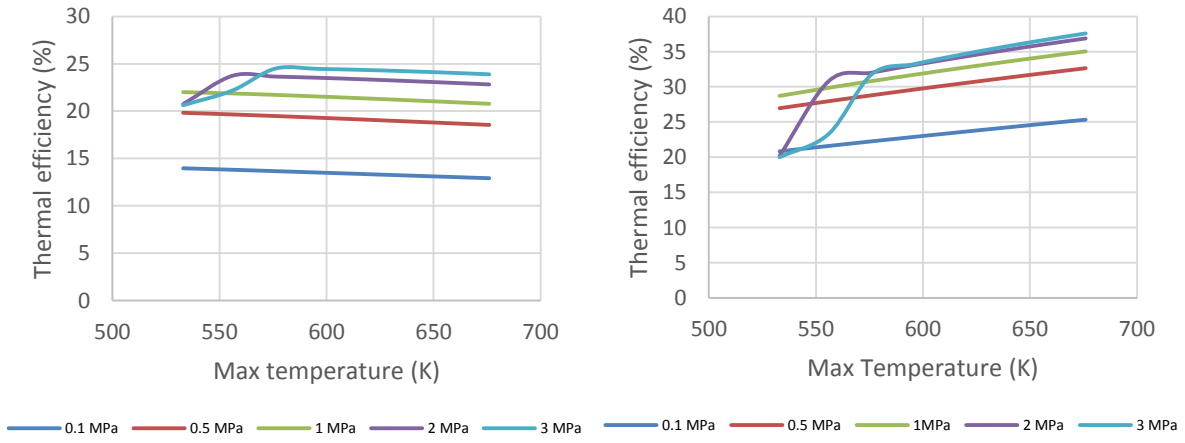

Figure 3: Thermal efficiency of simple ORC (left) and recuperative ORC (right).

2.3 Cycle Operational Parameters

The performance of a bottoming ORC is directly affected by the state of the exhaust from the diesel generator. Based on the maximum exhaust temperature specified above, the expander inlet temperature was varied between 530K and 670K. Our ORC is to operate on a subcritical cycle; therefore a high pressure limit of 3 MPa was applied. The range of high cycle temperatures and pressures is generous, mostly to allow for comprehensive thermodynamic analysis. Medium temperatures of around 616K, as assumed above, are of practical significance. A reasonably high

cycle pressure of 2 MPa is commonly mentioned in literature (Larsen *et al*., 2013) as the expected high pressure limit. High pressures are often favoured, especially for dry fluids like toluene, as they improve the cycle performance. However, apart from boosting the efficiency, high pressure levels also increase the expander volume ratio, which requires a large-sized turbine. In our case, space limitation and manageable volume ratios were prerogatives. The high pressure of our ORC is dictated by the expansion ratio it necessitates, rather than being a compromise between the desired cycle performance and the element size. Thus, pressures well below 2 MPa are desirable.

3. RESULTS AND DISCUSSION

3.1 Energetic analysis

The performance of the simple and recuperative ORC was evaluated. The effect of high cycle temperature and pressure on thermal efficiency is presented in Figure 3. As expected, the toluene cycles benefit from high evaporator pressures. The simple cycle is energetically somewhat insensitive to high cycle temperatures; in fact, efficiency decreases with high degree of superheat at the expander inlet. The exception being the combination of high pressure and low temperature, when the fluid is roughly at the saturated vapour state and the efficiency is low. In the whole range of expander inlet temperatures considered with the pressure of 1 MPa, a simple cycle efficiency above 20% is reached. Selecting a high pressure of 2 MPa leads to a 2.0% increase on average, while selecting 0.5 MPa as the operational pressure decreased the efficiency by approximately 2.2%. Naturally, recuperative ORC showed an improved energetic performance. Conversely to the simple cycle, the recuperative cycle efficiency increases with the degree of superheat at the expander inlet, making the high operational pressure a secondary parameter. Minor enhancement of the thermal performance was observed at pressures above 1 MPa (1.5%), and above 2 MPa any enhancement is practically undistinguishable. Decreasing the operational pressure of the recuperative ORC to 0.5 MPa reduces the thermal efficiency by 2.1%, like for the simple ORC.

While the recuperator increases energy efficiency, it does not alter the work output. As shown in Figure 4, net work of the cycle increases with both temperature and pressure. Similarly to the thermal efficiency, the effect of pressure is lessened above 1 MPa. While the increase in high cycle pressure improves thermal performance and work output, it also requires a larger expander. Progression of the volume ratio with high cycle pressure is presented in Figure 4, assuming a high temperature of 616K. The volume ratio grows almost linearly with pressure for the set high temperature. Hence, a compromise between acceptable values of the volume ratio and the high cycle pressure which dictates the overall system performance is necessary. Based on the calculated VR values, and having in mind the size limitation, our optimal high pressure is likely to be in 0.5-1 MPa range. Nevertheless, increase in expander inlet temperature can greatly influence the net work output and therefore act as a high pressure ‘substitute’. In a simple ORC this leads to a slightly reduced thermal performance, but not in a recuperative one. Due to the internal heat transfer between expander and pump outlet streams, overall heat input in the system is significantly reduced, as shown in Figure 5. Higher operational pressures generally require larger heat inputs, yet the effect of pressure is minor. Increase of expander inlet temperature entails a greater heat supply. Again, this is largely reduced in a recuperative ORC case.

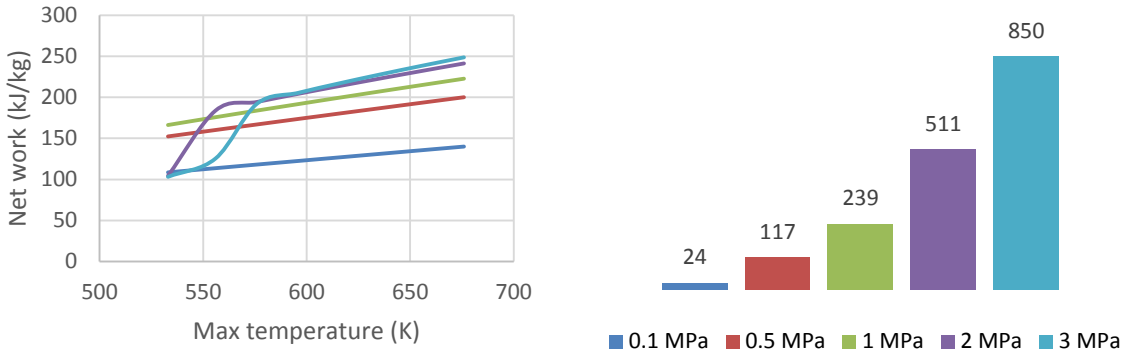

Figure 4: Effect of the high cycle pressure on net work and expander volume ratio.

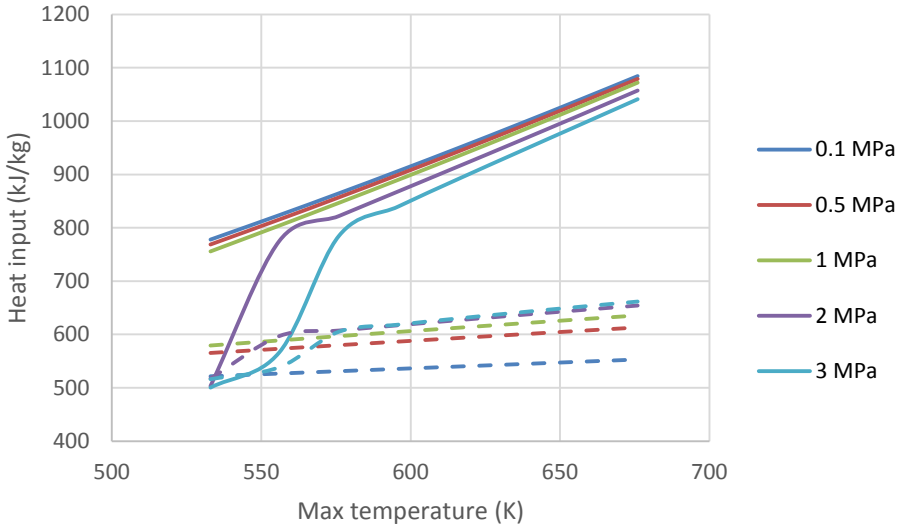

Figure 5: Required heat input in simple ORC (solid line); recuperative ORC (dashed line).

3.2 Exergetic analysis

Second law efficiency and specific exergy destruction in individual cycle components was evaluated for both simple and recuperative toluene cycles. Internal heat transfer improves the thermal performance of the ORC, but does not necessarily lead to higher exergy efficiency. Hence, use of the recuperator appears to be somewhat controversial, and a much debated issue in scientific community (Maraver *et al*., 2014). Comparison of exergetic performances as a function of high cycle temperature and pressure is given in Figure 6. The recuperative ORC achieved higher exergetic efficiencies than the simple one. Notwithstanding the peculiarity of low temperature - high pressure combination, an increase in evaporator pressure in the recuperative cycle raises the exergy efficiency. For the simple ORC, even at high operational pressures, exergetic efficiency did not reach 35%, whereas higher exergetic efficiencies were achieved at 0.5 MPa pressure in the recuperative case. Exergetic performance also improves with an increase in the expander inlet temperature for a recuperative ORC. The opposite trend is observed for the simple ORC system, in which case exergy efficiency slightly decreases with increasing high temperature.

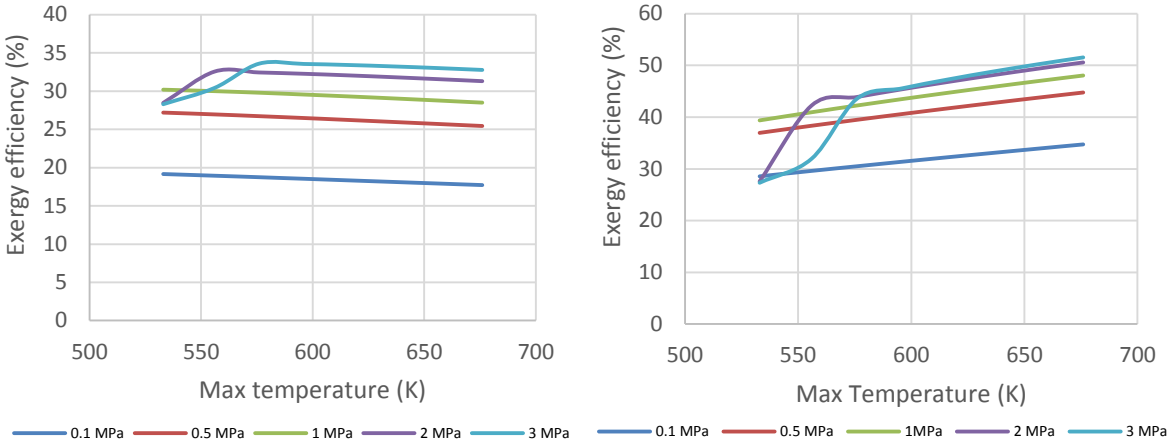

Figure 6: Exergetic efficiency of simple ORC (left) and recuperative ORC (right).

The extent and distribution of the exergy destruction in individual cycle elements is of interest. While exergy efficiency is lower for the recuperative cycle, the overall exergy destruction is greatly reduced, as shown in Figure 7. Irreversibilities decrease with increasing pressure, marginally so for the recuperative ORC. Naturally, the greatest exergy destruction rate is observed for the evaporator, which decreases with increasing pressure, for both the simple and the recuperative ORC. Approximately 10% of total irreversibilities in the simple ORC occurred in the condenser. Given that the condenser inlet state in the recuperative cycle was fixed at the saturated vapour point, the exergy destruction during the heat removal process was the same in all inspected cases, comparable to minor irreversibilities commonly evaluated for the pump. In a recuperative ORC, the heat exchanger is a more significant source of irreversibilities. The turbine destruction rate remains the same regardless of the use of the recuperating element, and it increases with the pressure. However, in the recuperative ORC exergy destruction during the heat addition process is lower, as less of heat is needed to power the cycle. Hence, the expander exergy destruction becomes more significant.

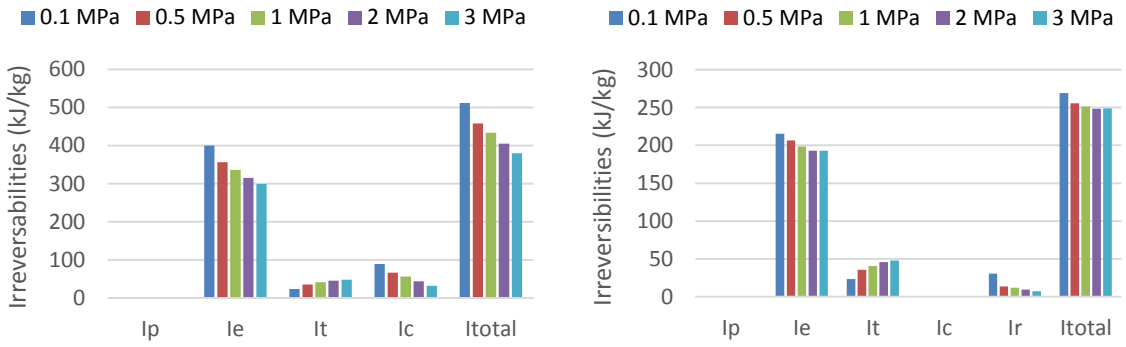

Figure 7: Exergy destruction in simple ORC (left) and recuperative ORC (right).

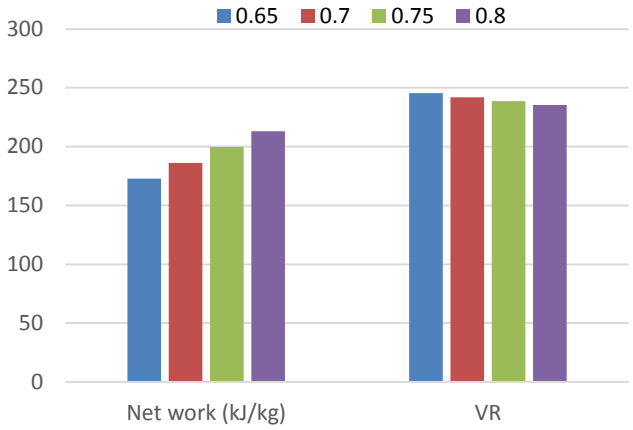

Figure 8: Net work and volume ratio of simple and recuperative ORC for variable expander efficiency at operating parameters of 1MPa and 616K.

3.3 Effect of expander efficiency

The expander, as a core component of the ORC system, has received significant scientific attention (Gao *et al*., 2015, and references within). In order to better assess the effect of the expander behavior, energetic and exergetic cycle performance was evaluated by modifying the expander isentropic efficiency to 65%, 70% and 80%. For brevity, only the results for 616K and 1MPa, as a representative temperature and pressure, are presented in Figures 8 and 9. Naturally, power output increases with improved expander efficiencies, namely ~7% higher net work is achieved per 5% expander efficiency increase, as shown in Figure 8. An equivalent rise in the cycle efficiency is found for the simple ORC. The volume ratio decreases by 1.4% on average, across all examined pressures. In the recuperative cycle, a higher expander efficiency results in less heat being available for preheating the fluid in the heat exchanger. Hence, the heat input increases by 2%, which reduces the overall improvement in the recuperative cycle efficiency to ~5%. Exergetic efficiency in a simple ORC increases due to a reduction in expander irreversibilities. In the case of the recuperative cycle, the total exergy input is higher, yet exergy destruction in the heat exchanger is lower for higher expander efficiency, and the overall exergetic efficiency improves. Still, exergetic efficiency increase is reduced compared to the simple ORC.

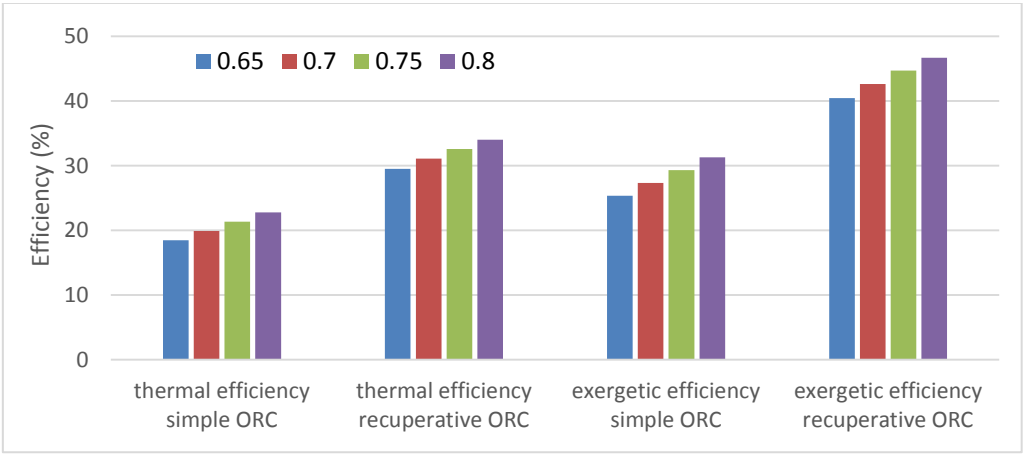

Figure 9: Thermal and exergetic efficiency of simple and recuperative ORC for variable expander efficiency at operating parameters of 1MPa and 616K.

6. CONCLUSIONS

The high temperature toluene ORC is a promising solution for diesel exhaust waste heat recovery. As a dry fluid, toluene achieves better thermodynamic performance at high pressures. However, for 'on-board' applications, size of the device is critical, and high pressures may result in an unacceptably large expander volume ratio. Hence, a compromise has been made between maximization of desired power and required expander size, indicating intermediate pressures, around 1MPa, may be the best solution. Additionally, the high temperature of the available exhaust stream may compensate for lower selected pressures.

Both simple and recuperative ORC systems were considered. The recuperative ORC reached a higher thermal efficiency, which was further augmented by the temperature increase, and required a lower heat input. Total exergy destruction was significantly reduced for the recuperative ORC, which resulted in better exergetic efficiency. Considerable effect of expander efficiency was evaluated: better thermal and exergetic performance, higher power output and a reduction in the volume ratio.

NOMENCLATURE

ex	specific exergy	(kJ/kg)
i	irreversability	(kJ/kg)
q	specific heat	(kJ/kg)
T	temperature	(K)
VR	volume ratio	(–)
w	specific work	(kJ/kg)
η	efficiency	(–)

Subscript

0	dead state
B	boiler
C	condenser
E	expander
ex	exergetic
in	input
out	output
P	pump
R	recuperator
th	thermal

REFERENCES

Capata, R., Toro, C., 2014, Feasibility analysis of a small-scale ORC energy recovery system for vehicular application, *Energ Convers Manage*, vol. 86: p. 1078-1090.

Gao, P., Jiang, L., Wang, L. W., Wang, R. Z., Song, F. P., 2015, Simulation and experiments on an ORC system with different scroll expanders based on energy and exergy analysis, *Appl Therm Eng*, vol. 75: p. 880-888.

Katsanos, C. O., Hountalas, D. T., Pariotis, E. G., 2012, Thermodynamic analysis of a Rankine cycle applied on a diesel truck engine using steam and organic medium. *Energ Convers Manage*, vol. 60: p. 68-76.

Kölsch, B., Radulovic, J., 2015, Utilisation of diesel engine waste heat by Organic Rankine Cycle. *Appl Therm Eng*, vol. 78: p. 437-448.

Larsen, U., Pierobon, L., Haglind, F., Gabrielii, C., 2013, Design and optimisation of organic Rankine cycles for waste heat recovery in marine applications using the principles of natural selection. *Energy*, vol. 55: p. 803-812.

Maraver, D., Royo, J., Lemort, V., Quoilin, S., 2014, Systematic optimization of subcritical and transcritical organic Rankine cycles (ORCs) constrained by technical parameters in multiple applications. *Appl Energ*, vol. 117: p. 11-29.

Quoilin, S., Broek, M. V. D., Declaye, S., Dewallef, P., Lemort, V., 2013, Techno-economic survey of Organic Rankine Cycle (ORC) systems. *Renew Sust Energ Rev*, vol. 22: p. 168-186.

Radulovic, J., Beleno Castaneda, N. I., 2014, On the potential of zeotropic mixtures in supercritical ORC powered by geothermal energy source. *Energ Convers Manage*, vol. 88: p. 365-371.

Song, J., Song, Y., Gu, C., 2015, Thermodynamic analysis and performance optimization of an Organic Rankine Cycle (ORC) waste heat recovery system for marine diesel engines. *Energy*, vol. 82: p. 976–985.

Tchanche, B. F., Lambrinos, G., Frangoudakis, A., Papadakis, G., 2011, Low-grade heat conversion into power using organic Rankine cycles – A review of various applications. *Renew Sust Energ Rev*, vol. 15, no. 8: p. 3963-3979.

Wang, E. H., Zhang, H. G., Fan, B. Y., Ouyang, M. G., Yang, F. Y., Yang, K., Wang, Z., Zhang, J., Yang, F. B., 2014, Parametric analysis of a dual-loop ORC system for waste heat recovery of a diesel engine. *Appl Therm Eng*, vol. 67, no 1–2: p. 168-178.

Yang, F., Dong, X., Zhang, H., Wang, Z., Yang, K., Zhang, J., Wang, E., Liu, H., Zhao, G., 2014, Performance analysis of waste heat recovery with a dual loop organic Rankine cycle (ORC) system for diesel engine under various operating conditions. *Energ Convers Manage*, vol. 80: p. 243-255.

Yu, G., Shu, G., Tian, H., Wei, H., Liu, L., 2013, Simulation and thermodynamic analysis of a bottoming Organic Rankine Cycle (ORC) of diesel engine (DE). *Energy*, vol. 51: p. 281-290.

SMALL SCALE ORC DESIGN FOR A COGENERATION SOLAR BIOMASS SUPORTED APPLICATION

J. Navarro-Esbrí[1,2,]*, F. Molés[1], B. Peris[1], A. Mota-Babiloni[1]

[1]ISTENER Research Group, Jaume I University,
Campus de Riu Sec s/n, E12071, Castellón
Spain
e-mail: navarroj@uji.es

[2]EXPANDER TECH,
Campus de Riu Sec s/n, E12071, Castellón
Spain

* Corresponding Author

ABSTRACT

Combined Heat and Power (CHP) systems and bottoming power cycles for waste heat recovery have received considerable attention over the past decades. Among the several proposed power cycles, the Organic Rankine Cycle (ORC) has been attracting increasing attention. ORCs have been proved as a feasible technology for low temperature (< 250 ºC) and small scale (< 1 MW) applications, converting renewable energy into heat and power.

The aim of this work is to present the design process of a micro scale ORC (< 100 kW), suitable for a Combined Cold, Heat and Power (CCHP) application, through an adsorption chiller, that uses solar biomass supported renewable energy as heat source. The ORC module has to be designed in order to work in cogeneration mode and generation mode (power only).

Therefore, this work deals with the preliminary design of the ORC module, including working fluid and configuration selection, from the technical requirements of the equipment imposed by the application. The optimization of the operating conditions is also addressed in order to maximize the efficiency of the system. Finally, an expander has been proposed and characterized. The experimental results from the expander have been used in order to predict the expected behavior of the ORC module in cogeneration mode, producing hot water up to 70ºC.

1. INTRODUCTION

Due to environmental constrains, Combined Heat and Power (CHP) systems and bottoming power cycles for waste heat recovery have received considerable attention. Several power cycles have been proposed for low temperature heat recovery. Among them, the Organic Rankine Cycle (ORC) has been attracting considerable attention (Vélez, 2012). Several ORC systems have been installed for recovering waste heat from power plants (Dolz *et al.*, 2012), industrial processes (Peris *et al.*, 2015a) or from internal combustion engines (Peris *et al.*, 2013). ORC systems have also been widely used for converting renewable energy, such as solar (Wang *et al.*, 2013), biomass (Huang *et al.*, 2013) and geothermal (El-Emam and Dincer, 2013) energy into power. ORCs have been studied by various authors, commonly classifying heat sources with temperatures ranging between 100ºC and 250ºC as "low temperature" heat sources and above 250ºC as "high temperature" heat sources. Brasz *et al.* (2005) considered low temperature applications and Zabek *et al.* (2013) studied waste heat recovery at high temperatures, demonstrating ORC feasibility in both cases. Focusing on residential and commercial applications, the ORC has been proposed as a suitable energy conversion technology,

since it can achieve great efficiencies from low grade heat sources and can result cost-effective for small scale and micro-scale applications, often referred to an electrical power lower than 1 MW and 15 kW, respectively (Peris *et al.*, 2015b).

The choice of the ORC working fluid has an important influence on the system efficiency, and numerous works on this subject can be found in the literature. Lai *et al.* (2011) investigated potential single-component working fluids for high temperature ORC processes and found that siloxanes and selected hydrocarbons are promising. Shale *et al.* (2007), Shengjun *et al.* (2011) and Quoilin *et al.* (2011) evaluated various working fluids for low to medium temperature applications, highlighting that hydrofluorocarbons with low critical temperatures, such as HFC-134a and HFC-245fa, are suitable. Molés *et al.* (2014) predicted attractive thermodynamic performance of ORC systems for low temperature heat sources using HCFO-1233zd-E and HFO-1336mzz-Z as low Global Warming Potential (GWP) alternatives to HFC-245fa.

About cycle configuration, different suitable configurations for low grade heat sources recovery using ORCs can be found in the literature. One of the most commonly used is the regenerative ORC, which can be performed in three ways: with an internal heat exchanger (Wang *et al.*, 2013), with open and closed feed fluid heaters using turbine bleeding (Gang *et al.*, 2010) or using a vapor injector as a regenerator (Xu and He, 2011). Another configuration proposed for low grade heat sources is based on superheating the fluid in a single stage (Roy *et al.*, 2011) or through various reheat stages (DiGenova *et al.*, 2013). Two pressure levels and the use of an ejector have been also studied by Li *et al.* (2012), increasing the output capacity compared to the basic ORC. Finally, transcritical configurations have been also proposed to allow a better temperature matching with low irreversibilities (Ho *et al.*, 2012), generally requiring higher operating pressures.

Regarding expander technology, Peris *et al.* (2015c) indicated that the volumetric expander type is most appropriate for low grade heat sources and micro-scale application. The reason is that volumetric expanders results more appropriate than turbomachines, as they are characterized by lower flow rates, higher pressure ratios, much lower rotational speeds, besides to exhibit good effectiveness and tolerate liquid phase during expansion (Quoilin, *et al.*, 2013). In this way, recent works continues improving volumetric expanders, such as rotary volumetric expanders based on the Wankel concept (Antonelli *et al.*, 2014), scroll (Song *et al.*, 2014) or screw expanders (Zhu *et al.*, 2014). Furthermore, an appropriate operating pressure ratio for the expander, a suitable working fluid and an efficient configuration are also recommendations to increase the electrical gain (Peris *et al.*, 2013).

The aim of this work is to present the design process of a small scale ORC, suitable for a Combined Cold, Heat and Power (CCHP) application that uses solar biomass supported renewable energy as heat source. So, the work presents the technical requirements of the equipment imposed by the application, discusses the working fluid selected, reports the thermodynamic cycle, presents the experimental characterization of an expander prototype and, finally, summarizes the main conclusions.

2. TECHNICAL REQUIREMENTS

The technical requirements of the equipment imposed by the application are the boundary conditions that constrain the design process of the ORC system. The overall scheme of the system is presented in Figure 1. The cogeneration unit is planned to work on two different operating modes: generation mode and cogeneration mode.

Attending to the renewable heat source activation, it consists on a solar biomass supported heat source. The heat transfer fluid will be thermal oil. The solar collectors will work at temperatures up to 270ºC, but the thermal oil inlet temperature into the ORC is expected to be, due to buffers/collectors and thermal losses, up to 245ºC. In order to maintain fixed the inlet temperature on the ORC, a buffer tank is required to avoid the solar field disturbances.

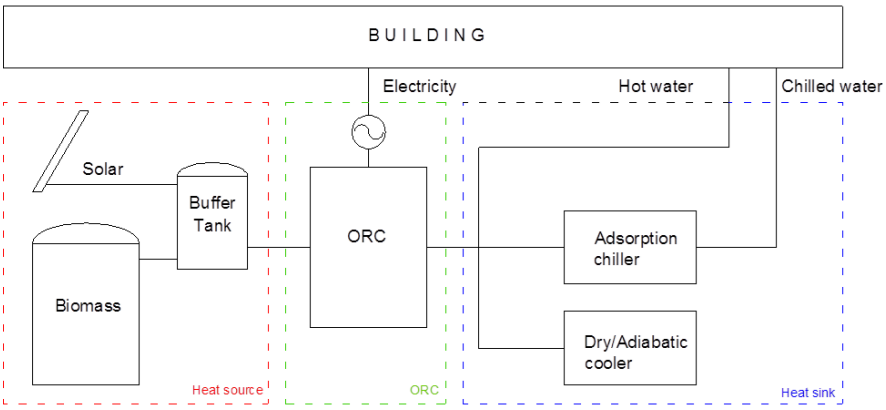

Figure 1: Overall scheme of the system

Regarding the heat sink, the different modes of the cogeneration unit result in two different condensation temperatures, fixed by the heat sink transfer fluid temperatures, in the ORC: 30ºC for generation mode and 70ºC for cogeneration mode. In generation mode the condensation heat is rejected to the ambient through a dry/adiabatic cooler. In cogeneration mode the heat sink is used to produce hot water for heating or hot water to activate an adsorption chiller. Water has been selected as the heat transfer fluid for the heat sink loop.

3. WORKING FLUID

The working fluid is a key parameter that determines the operating pressures, maximum allowable temperature, system efficiency, optimal configuration and components technology. So, it has a great influence on achieving the target. Furthermore, there are other criteria to be considered in the working fluid selection, such as security characteristics (toxicity and flammability) and environmental issues (ODP and GWP). In ORC systems with high temperature heat sources, working fluids as toluene, hydrocarbons or silicone oils are used. However, looking for security and environmental characteristics with high efficiencies at low temperatures, the following fluid families have been considered: hydrofluorocarbons (HFC), hydrofluroether (HFE), and hydrofluoroolefins (HFO).

Table 1: working fluid candidates properties

Fluid	Toxicity PEL (ppm) / Flammability	GWP	ODP	T_{crit} (ºC)	P_{crit} (bar)	T_{max} (ºC)
HFC-134a	1000/Non-flammable	1300	0	101	40.59	<200
HFC-245fa	300/Non-flammable	950	0	154	36.51	<250
SES36	1000/Non-flammable(*)	3710	0	177.55	28.49	190
HFO-1234yf	500/Low-flammability	4	0	94.7	33.82	<200
HFO-1234ze(Z)	500/Non-flammable	1	0	150	35.30	<200
HCFO-1233zd-E	300/Non-flammable	5	0	165.6	35.71	200
HFO-1336mzz-Z	500/Non-flammable	9	0	171.3	29	<250

Different working fluid options have been analyzed and evaluated for their application in the current application based on the suitable fluids found in the literature. Special attention has been taken in security properties, as toxicity and flammability, thermal stability and environmental properties, like Global Warming Potential (GWP) and Ozone Depletion Potential (ODP). Relevant thermo-physical properties of the working fluid candidates are summarized in Table 1.

Maximum allowable temperature supposes another constrain in order to avoid degradation in the working fluid. So, HFC-134a, SES36, HFO-1234yf and HCFO-1233zd-E have been discarded. HFO-1336mzz-Z is not commercially available nowadays, despite its desirable properties, as low GWP, among others. Finally, HFC-245fa has been selected as the best available working fluid candidate, with low toxicity, no flammable, maximum allowable temperature below 250ºC (240ºC) and good

expected efficiencies. HFC-245fa is commonly selected as working fluid for similar heat sources when safety levels and environmental impacts are considered (Wang *et al.*, 2011).

4. THERMODYNAMIC CYCLE

In the framework of a systematic investigation approach, various possible modifications to the simple ORC plant layout are analyzed and compared, in order to improve the ORC recovery performance; arrangements such as recuperation, superheated cycle, transcritical conditions, regenerative cycle and their combinations are taken into account.

From the analysis of the different options for the configuration of the ORC cycle, the most suitable of them, for the range of operating conditions of the targeted application, have been investigated. The adoption of a recuperative heat exchanger has been considered, due to the high temperature of the heat source compared with the critical temperature of the working fluid selected, having to work with high superheat degree. The possibility of working in transcritical conditions has been studied to allow a better temperature matching with low irreversibilities, although generally requiring higher operating pressures and more pump consumptions. Therefore, various cycles are proposed, showing their schemes in Figure 2.

After the analysis of the configurations proposed, the possibility of working in transcritical conditions has been rejected due to the increase on the pump consumption that reduces the net efficiency of the cycle. The increase on the pump consumption due to the transcritical operation can suppose, depending on the operating conditions, a 10% of the gross power produced by the expander, higher in comparison with the 5% of the pump consumption in subcritical operation. The adoption of a recuperative heat exchanger has been selected, due to the improvement on the efficiency by reducing the thermal power required. The adoption of a recuperative heat exchanger improves the efficiency between 12.5% and 31.5%, depending on the operating conditions. Finally, the best configuration is the use of a recuperative heat exchanger in subcritical conditions. This configuration has been previously selected as optimal for HFC-245fa as working fluid with similar heat source conditions for Branchini *et al.* (2013).

5. EXPERIMENTAL APPROACH

With the working fluid, configuration and operating conditions selected, the next step has been the selection of the components of the ORC module and their design. Knowing that the expander is a key parameter on the ORC efficiency, its design has been addressed constructing and testing various prototypes.

The expander technology selected to meet the prototype requirements has been analyzed and a volumetric expander is proposed. As previously introduced, the volumetric technology shows better results for low grade heat sources and small scale applications. So, the volumetric technology has been adopted for the expander design.

The main challenge in the expander design is the different operating conditions presented in generation and cogeneration mode, taking into account the maximum temperature allowable at the expander inlet of 240ºC. In this way, different designs are analysed looking for optimizing the efficiency of the system in all the range of expected operating conditions, not only the electrical efficiency but also cost, size, weight, flexibility… Therefore, two different designs are considered, one specially designed for optimizing generation mode and the other looking for optimal energy profit in cogeneration mode.

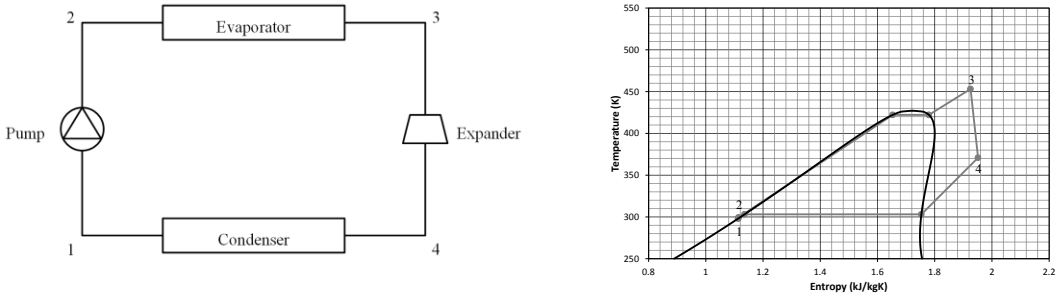

(a) Basic cycle - subcritical

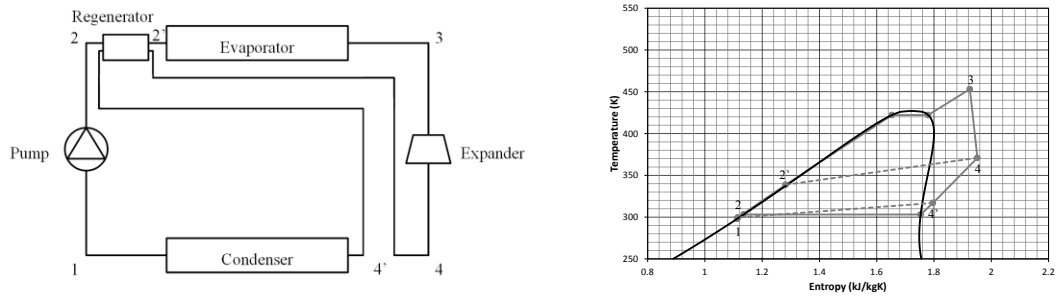

(b) Regenerative cycle - subcritical

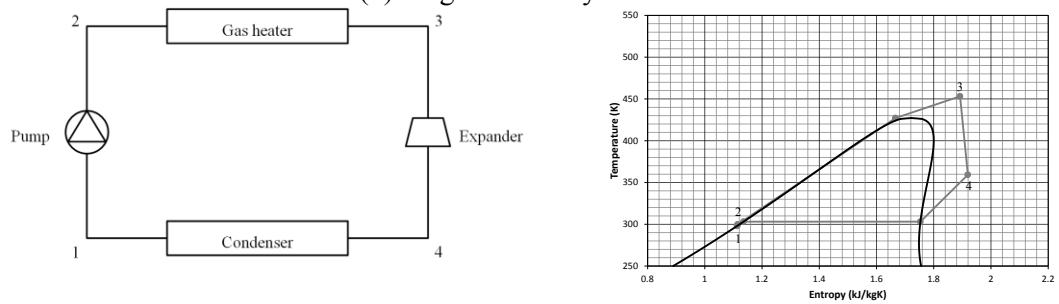

(c) Basic cycle - transcritical

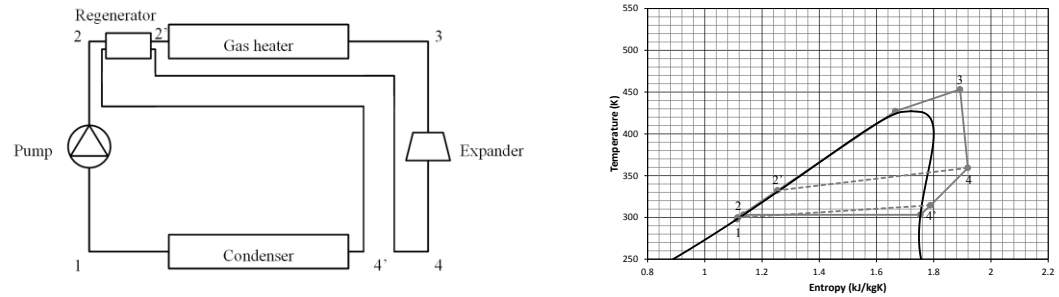

(d) Regenerative cycle - transcritical

Figure 2: Configurations proposed

The design optimized for generation mode achieves a good efficiency condensing below 30ºC but it is highly penalized above 40ºC of condensing temperature and, besides, has serious disadvantages as high cost, control handicaps, high size and weight, making the future product non feasible. On the other hand, the expander design optimized for cogeneration mode presents the best efficiency in cogeneration mode and, although it is slightly penalized in generation mode, it shows a good performance in the operating range (for the expected range of condensing temperatures) and being a cost-effective solution with the advantage of reducing considerably size and weight and simplifying ORC control.

Figure 3: Simulated and constructed prototype and the ORC test bench

Finally, the expander prototype has been designed according to the second proposal, optimizing the cogeneration mode, since the overall efficiency in this mode is much higher than in generation mode and due to the advantages exposed before. The expected performance of this expander prototype has been experimental tested in the test bench constructed ad-hoc for the expander tests. Thermal and electrical power haven been scaled down to meet the disposal thermal power on the test bench, with a 1:3 scale.

In the following, the main parameters measured of the test bench are presented. Firstly, the thermal power input is monitored in the hot side through inlet and outlet thermal oil temperatures, using surface thermocouples, and the thermal oil volumetric flow rate, that is measured using a vortex flow meter. The working mass flow rate is obtained through a Corioliss mass flow meter. The pressure and temperature at the inlet and outlet port of the expander are measured for monitoring its performance. Furthermore, its electrical power output is measured using a wattmeter located at the electric generator, while the pump electrical consumption is measured in the electric motor through another wattmeter.

The measuring devices uncertainties, extracted from manufacturer's data sheets, and the calculated parameters uncertainties, obtained as a function of the uncertainty on each measured variable by using the RSS method (Taylor, 1997), are collected in Table 2.

Table 2: uncertainties of measured and calculated parameters

Parameter	**Uncertainty**
Temperature (ºC)	1
Pressure (%)	0.5
Mass flow rate (%)	0.3
Thermal oil volumetric flow rate (%)	0.75
Electrical power (%)	1.2
Electrical isentropic effectiveness (%)	4.89
Pressure ratio (%)	0.71

For the analysis of the experimental data obtained during tests, the performance of the expander is defined as the electrical expander effectiveness by Eq. 1, often also named expander overall efficiency. This equation expresses the relationship between the electrical power measured in the electric generator and the maximum that could be ideally obtained. The pressure ratio in the expander is calculated through Eq. 2.

$$\varepsilon_{x,is} = \frac{\dot{W}_x}{\dot{m}\left(h_{x,in} - h_{x,out,is}\right)} \tag{1}$$

$$P_r = \frac{P_{x,in}}{P_{x,out}} \tag{2}$$

The electrical expander effectiveness achieved by the expander prototype in the test bench is represented in Figure 4.

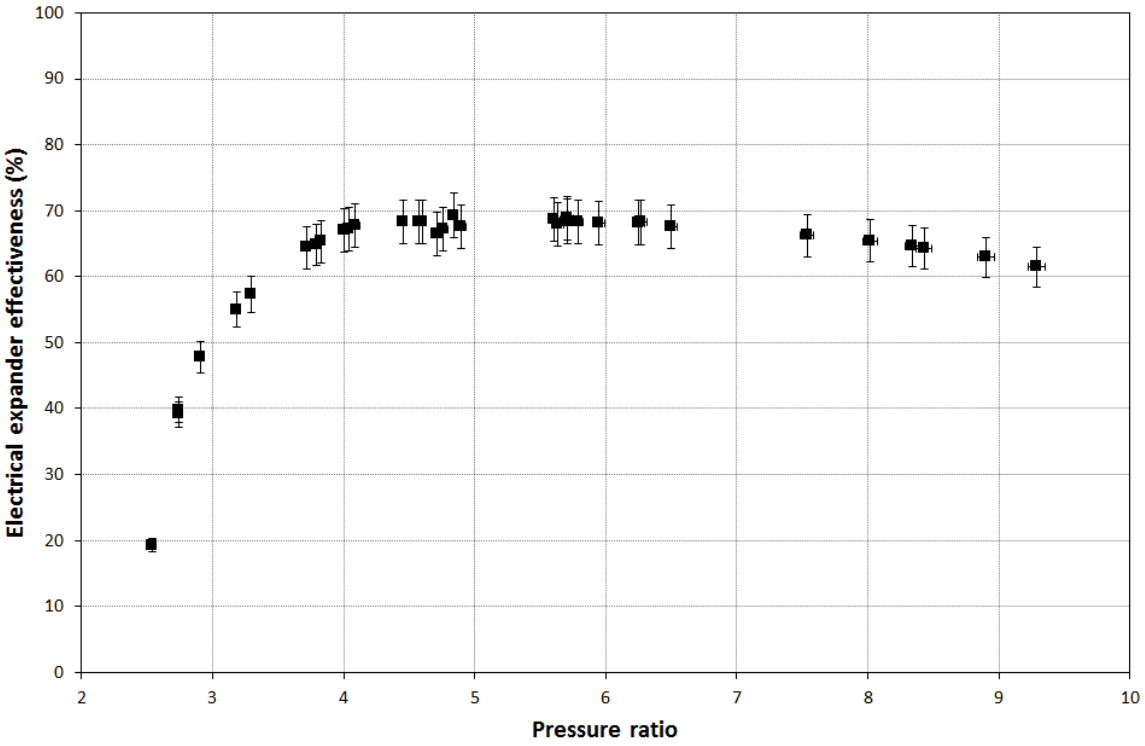

Figure 4: Electrical expander effectiveness achieved

The experimental results from the expander have been used in order to predict the expected behavior of the ORC module. The performance of the cogeneration system, producing hot water at 70ºC, is summarized in Table 3, with an uncertainty of ±15%.

Table 3: cogeneration mode performance

Heat source transfer fluid	Thermal oil
Heat source inlet temperature (ºC)	245
Heat source outlet temperature (ºC)	173.3
Heat source flow rate (m^3/h)	11.8
Heat source thermal power (kW)	480
Heat sink transfer fluid	Water
Heat sink inlet temperature (ºC)	60
Heat sink outlet temperature (ºC)	70
Heat sink flow rate (m^3/h)	34.1
Heat sink thermal power (kW)	390
Gross electrical power (kW)	70

6. CONCLUSIONS

This work presents the design process of a micro scale ORC, suitable for a Combined Cold, Heat and Power (CCHP) application that uses solar biomass supported renewable energy as heat source. The technical requirements of the equipment, working fluid selection, thermodynamic cycle configuration, design and expected performance are presented.

The technical requirements of the equipment imposed by the application are the boundary conditions that constrain the design process of the ORC system. Attending to the renewable heat source activation, it consists on a solar biomass supported heat source. The heat sink is used to produce hot water for heating or hot water to activate an adsorption chiller.

Different working fluid options have been analyzed and evaluated for their application in the current application based on the suitable fluids found in the literature. Special attention has been taken in security properties, as toxicity and flammability, thermal stability and environmental properties. HFC-245fa has been selected as the best available working fluid candidate, with low toxicity, no flammable, maximum allowable temperature below 250ºC and good expected efficiencies.

Various possible modifications to the simple ORC plant layout are analyzed and compared, in order to improve the ORC recovery performance. The possibility of working in transcritical conditions has been rejected due to the increase on the pump consumption that reduces the net efficiency of the cycle. The adoption of a recuperative heat exchanger has been selected, due to the improvement on the efficiency by reducing the thermal power required.

With the working fluid, configuration and operating conditions selected, the next step has been the selection of the components of the ORC module and their design. The expander design has been addressed and an expander prototype has been obtained. The performance of this expander prototype has been experimental characterized in the test bench constructed ad-hoc for the expander tests. Finally, the experimental results from the expander prototype have been used to obtain the expected performance of the ORC module working in cogeneration mode and producing hot water at 70ºC to activate the adsorption chiller.

NOMENCLATURE

ε	efficiency	(%)
h	specific enthalpy	(kJ/kg)
m	mass flow rate	(kg/s)
P	pressure	(bar)
T	temperature	(ºC)
W	electrical power	(kW)

Subscripts

crit	critical
in	inlet
is	isentropic
max	maximum
out	outlet
r	ratio
x	expander

REFERENCES

Antonelli, M., Baccioli, A., Francesconi, M., Desideri, U., Martorano, L., 2014, Operating maps of a rotary engine used as an expander for micro-generation with various working fluids, *Appl. Energy*, vol. 113, no. 1: p. 742-750.

Branchini, L., Pascale, A., Peretto, A., Systematic comparison of ORC configurations by means of comprehensive performance indexes, *Appl. Therm. Eng.*, vol. 61, no. 1: p. 129-140.

Brasz, J.J., Biederman, B.P., Holdmann, G., 2005, Power production from a moderate temperature geothermal resource, *GRC Annual Meeting*.

DiGenova, K.J., Botros, B.B., Brisson, J.G., 2013, Method for customizing and organic Rankine cycle to a complex heat source for efficient energy conversion, demonstrated on a Fischer Tropsch plant, *Appl. Energy*, vol. 102, no. 1: p. 746-754.

Dolz, V., Novella, R., García, A., Sanchez, J., 2012, HD diesel engine equipped with a bottoming Rankine cycle as a waste heat recovery system. Part 1: study and analysis of the waste heat energy, *Appl. Therm. Eng.*, vol. 36, no. 1: p. 269-278.

El-Emam, R.S., Dincer, I., 2013, Exergy and exergoeconomic analyses and optimization of geothermal organic Rankine cycle, *Appl. Therm. Eng.*, vol. 59, no. 1: p. 435-444.

Gang, P., Jing, L., Jie, J., 2010, Analysis of low temperature solar thermal electric generation using regenerative organic Rankine cycle, *Appl. Therm. Eng.*, vol. 30, no. 8: p. 998-1004.

Ho, T., Mao, S.S., Greif, R., 2012, Comparison of the organic flash cycle (OFC) to other advanced vapor cycles for intermediate and high temperature waste heat reclamation and solar thermal energy, *Energy*, vol. 42, no. 1: p. 213-223.

Huang, Y., Wang, Y.D., Rezvani, S., McIlveen-Wright, D.R., Anderson, M., Mondol, J., Zacharopolous, A., Hewitt, N.J., 2013, A techno-economic assessment of biomass fuelled trigeneration system integrated with organic Rankine cycle, *Appl. Therm. Eng.*, vol. 53, no. 2: p. 325-331.

Lai, N.A., Wendland, M., Fischer, J., 2011, Working fluids for high-temperature organic Rankine cycles, *Energy*, vol. 36, no. 1: p. 199-211.

Li, X., Zhao, C., Hu, X., 2012, Thermodynamic analysis of organic Rankine cycle with ejector, *Energy*, vol. 42, no. 1: p. 342-349.

Molés, F., Navarro-Esbrí, J., Peris, B., Mota-Babiloni, A., Barragán-Cervera, A., Kontomaris, K., 2014, Low GWP alternatives to HFC-245fa in Organic Rankine Cycles for low temperature heat recovery: HCFO-1233zd-E and HFO-1336mzz-Z, *Appl. Therm. Eng.*, vol. 71, no. 1: p. 204-212.

Peris, P., Navarro-Esbrí, J., Molés, F., 2013, Bottoming organic Rankine cycle configurations to increase Internal Combustion Engines power output from cooling water waste heat recovery, *Appl. Therm. Eng.*, vol. 61, no. 2: p. 364-371.

Peris, P., Navarro-Esbrí, J., Molés, F., Collado, R., Mota-Babiloni, A., 2015a, Performance evaluation of an Organic Rankine Cycle (ORC) for power applications from low grade heat sources, *Appl. Therm. Eng.*, vol. 75, no. 1: p. 763-769.

Peris, P., Navarro-Esbrí, J., Molés, F., Martí, J.P., Mota-Babiloni, A., 2015b, Experimental characterization of an Organic Rankine Cycle (ORC) for micro-scale applications, *Appl. Therm. Eng.*, vol. 79, no. 1: p. 1-8.

Peris, P., Navarro-Esbrí, J., Molés, F., González, M., Mota-Babiloni, A., 2015c, Experimental characterization of an ORC (organic Rankine cycle) for power and CHP (combined heat and power) applications from low grade heat sources, *Energy*, vol. 82, no. 1: p. 269-276.

Quoilin, S., Declaye, S., Tchanche, B.F., Lemort, V., 2011, Thermo-economic optimization of waste heat recovery organic Rankine cycles, *Appl. Therm. Eng.*, vol. 31, no. 14: p. 2885-2893.

Quoilin, S., Van Den Broek, M., Declaye, S., Dewallef, P., Lemort, V., 2013, Techno-economic survey of organic Rankine cycle (ORC) systems, *Renew. Sustain. Energy Rev.*, vol. 22, no. 1: p. 168-186.

Taylor, J.R., 1997, An introduction to error analysis; The study of uncertainties in physical measurements, *University Science Books,* Sausalito, USA.

Roy, J.P., Mihsra, M.K., Misra, A., 2011, Performance analysis of an organic Rankine cycle with superheating under different heat source temperature conditions, *Appl. Energy*, vol. 88, no. 9: p. 2995-3004.

Saleh, R., Koglbauer, G., Wendland, M., Fischer, J., 2007, Working fluids for low-temperature organic Rankine cycles, *Energy*, vol. 32, no. 7: p. 1210-1221.

Shengjun Z., Huaixin W., Tao, G., 2011, Performance comparison and parametric optimization of subcritical Organic Rankine Cycle (ORC) and transcritical power cycle system for low-temperature geothermal power generation, *Appl. Energy*, vol. 88, no. 8: p. 2740-2754.

Song, P., Wei, M., Shi, L., Danish, S.N., Ma, C., 2014, A review of scroll expanders for organic Rankine cycle systems, *Appl. Therm. Eng.*, vol. 75, no. 1: p. 54-64.

Vélez, F., Segovia, J.J., Martín, M.C., Antolín, G., Chejne, F., Quijano, A., 2012, A technical, economical and market review of organic Rankine cycles for the conversion of low-grade heat for power generation, *Renew. Sustain. Energy Rev.*, vol. 16, no. 6: p. 4175-4189.

Wang, E., Zhang, H., Fan, B., Ouyang, M., Zhao, Y., Mu, Q., 2011, Study of working fluid selection of organic Rankine cycle (ORC) for engine waste heat recovery, *Energy*, vol. 36, no. 1: p. 3406-3418.

Wang, M., Wang, J., Zhao, Y., Zhao, P., Dai, Y., 2013, Thermodynamic analysis and optimization of a solar-driven regenerative organic Rankine cycle (ORC) based on flat-plate solar collectors, *Appl. Therm. Eng.*, vol. 50, no. 1: p. 816-825.

Xu, R.J., He, Y.L., 2011, A vapor injector-based novel regenerative organic Rankine cycle, *Appl. Therm. Eng.*, vol. 31, no. 6: p. 1238-1243.

Zabek, D., Penton, J., Reay, D., 2013, Optimization of waste heat utilization in oil field development employing a transcritical Organic Rankine Cycle (ORC) for electricity generation, *Appl. Therm. Eng.*, vol. 59, no. 1: p. 363-369.

Zhu, Y., Jiang, L., Jin, V., Yu, L., 2014, Impact of built-in and actual expansion ratio difference of expander on ORC system performance, *Appl. Therm. Eng.*, vol. 71, no. 1: p. 548-558.

ACKNOWLEDGEMENT

The result presented in this paper is part of the BRICKER project (www.bricker-project.com). This project has received funding from the European Union's Seventh Framework Programme for research, technological development and demonstration under grant agreement No 609071.

CONSTRUCTION AND PRELIMINARY TEST OF AN ORGANIC RANKINE CYCLE (ORC) USING R245FA AND SINGLE SCREW EXPANDER

Biao Lei *, Yuting Wu, Wei Wang and Chongfang Ma

* Beijing University of Technology,
Ping Le Yuan 100, Chaoyang District, Beijing,
China
e-mail: leibiao@emails.bjut.edu.cn

ABSTRACT

Organic Ranking Cycle (ORC) is one of the most promising methods for converting low-grade heat into power. In this paper, an experimental ORC system, which includes a single screw expander, a shell and tube evaporator, an air-cooled fin-and-tube condenser and a metering pump, has been built. R245fa was adopted as the working fluid considering of its good performance and environmentally-friendly characteristics. The heat source of the experimental system is the conduction oil which was heated by electricity. In the evaporator of the system, R245fa was evaporated into vapor by the high-temperature conduction oil. Experiments were conducted to analyze the operational characteristics and performance of the developed ORC. The key parameters of the ORC, such as the efficiency of the cycle and the expander, were obtained. In addition, the factors which influence the performances of the developed ORC were analyzed and discussed.

REFERENCES

[1] Tchanche BF, Lambrinos G, Frangoudakis A, Papadakis G. Low-grade heat conversion into power using organic Rankine cycles – A review of various applications. Renewable and Sustainable Energy Reviews. 2011;15:3963-79.

[2] Vélez F, Segovia JJ, Martín MC, Antolín G, Chejne F, Quijano A. A technical, economical and market review of organic Rankine cycles for the conversion of low-grade heat for power generation. Renewable and Sustainable Energy Reviews. 2012;16:4175-89.

[3] Quoilin S, Aumann R, Grill A, Schuster A, Lemort V, Spliethoff H. Dynamic modeling and optimal control strategy of waste heat recovery Organic Rankine Cycles. Applied Energy. 2011;88:2183-90.

[4] Quoilin, S.; Broek, M.V.D.; Declaye, S.; Dewallef, P.; Lemort, V. Techno-economic survey of Organic Rankine Cycle (ORC) systems. Renewable and Sustainable Energy Reviews 2013, 22, 168-186

ORGANIC RANKINE CYCLE WITH ZEOTROPIC MIXTURES OF ALKANES AS WORKING FLUIDS FOR COGENERATION

Peter Collings[1], Zhibin Yu[2]*

[1]University of Glasgow, University Avenue
Glasgow, United Kingdom
(E-mail: p.collings.1@research.gla.ac.uk)

[2]University of Glasgow, University Avenue
Glasgow, United Kingdom
(E-mail: Zhibin.Yu@glasgow.ac.uk)

* Corresponding Author

ABSTRACT

Organic Rankine Cycles for the utilisation of low-temperature heat sources suffer from inherently low efficiency due to Carnot limitations, with first law efficiencies of 10-15% for heat source temperatures below 200°C. The large amount of heat rejection in the condenser that this entails means that they are potentially ideal candidates for combined heat and power schemes. This paper analyses the performance of a cycle with a recirculating heat source, using a zeotropic mixture of alkanes as the working fluid. Changing the mixture composition changes the bubble and dew points of the cycle, and introduces a temperature change during phase change, known as "glide". As the condenser outlet temperature is determined by the pinch point at the condensation temperature, the introduction of glide can increase the condenser and evaporator loading for a given condenser outlet temperature for cogeneration supply. This can work against any added benefit gained by creating a working fluid blend tailored to a specific heat source and sink. When the temperature glide is small, there is a smooth drop in condenser pressure and associated smooth increase in efficiency, When the glide is larger, the change in efficiency happens more abruptly at either end of the transition from one fluid to another, with a period of more gentle change in efficiency in between. The effect these changes have on the performance of the cycle and possible applications in cycle optimisation are an exciting area for future research.

1. INTRODUCTION

Much current research focuses on the development of systems to generate electricity from lower-quality heat sources, with temperatures of less than 250°C. However, the actual proportion of energy demand accounted for by electricity is relatively small. Figure 1, adapted from (UK DECC, 2014a), shows that only 22.8% of non-transport energy usage in the UK is accounted for by electricity.

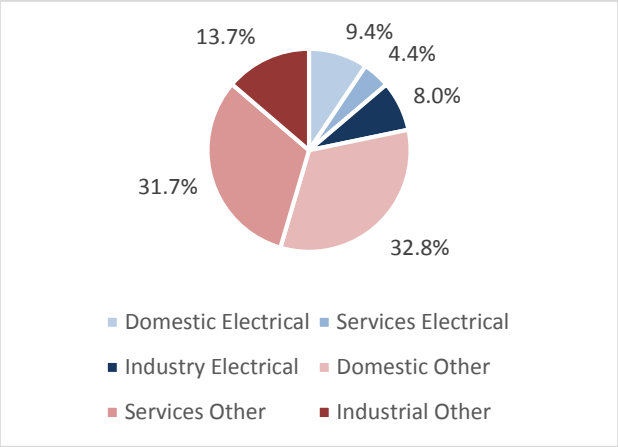

Figure 1: 2013 UK Energy Usage by Fuel and Sector (UK DECC, 2014a)

Table 1: 2013 UK Energy Usage divided into Heating and Other (UK DECC, 2014a)

Space and Water Heating	Domestic	41.9%	
	Service	13.9%	
	Industry	2.8%	58.7%
Other	Domestic	8.8%	
	Service	9.3%	
	Industry	23.2%	41.3%

Table 1, also adapted from (UK DECC, 2014a), shows the breakdown of 2013 UK non-transport energy usage into space and water heating, and other. Although this data does not account for "crossover" usage of energy, such as electric space and water heaters, or heat used for things other than space heating, for example, preheating feedstock in the chemical industry, its implications are clear; there is a large potential market for waste heat, such as that developed by power generation. This is borne out by the UK Department of Energy and Climate Change who, in their report on waste heat utilisation, estimate that there is a demand for 18.7 TWh/yr of low-grade heat (<250°C) for industrial processes (UK DECC, 2014b).

Previous research indicates that small-scale Organic Rankine Cycle systems are capable of efficiencies of the order of 10% (Fu, et al., 2005), (Shu, et al., 2014), (Kang, May 2012). The remaining ~90% of the heat that enters the system is rejected to the environment in the condenser. If this heat can be recovered and used for space and water heating, ORC systems could be ideal for CHP purposes.

This is contingent on the water outflow from the condenser being of sufficient temperature for space or water heating applications. Water heating for washing, for example, requires a temperature of 40°C (UK DECC, n.d.). Underfloor heating requires a temperature of 35-50°C (UK DECC, May 2012) (UK DECC, 2012b) (UK DECC, 2012a). Radiators may require a temperature of 60°C (Insitution of Civil Engineers, 2012). To achieve this, district heating schemes usually provide heat at 90-100°C (UK DECC, 2012c) (Poyry Energy Consulting, 2009).

The application of Organic Rankine Cycle for cogeneration has attracted considerable attentions. Twomey et al (Twomey, et al., 2013) considered a solar-powered ORC system providing water heated by the condenser at 65°C, and using a scroll device as their expander. They showed electrical efficiency of 3.47%. Stoppato (Stoppato, 2012) performed an energetic and economic investigation of an existing ORC cogeneration plant in Italy, providing district heating water at 80°C from a 310°C heat source. This cycle aims to increase exergy efficiency by splitting the flow between a regenerative heat exchanger and a fluid preheater using the primary heat source, and achieves an electrical efficiency of 18.6%, modelling the cycle components as black boxes with performance varying based

on empirical data. Uris et al (Uris, et al., 2014) performed an analysis of a biomass cogeneration plant with a 300°C heat source providing heat from 65-90°C, using various sub-and supercritical working fluids. This showed a maximum first law thermal efficiency of 22.62% for a subcritical recuperative cycle.

Typical sources of heat for ORC systems include solar thermal, geothermal, and waste heat from industry. The UK contains several potential geothermal resources with temperatures of up to 180°C (UK DECC, 2013a). Unlike geothermal resources, solar thermal resources vary in temperature depending on the incident radiation and the degree of concentration. Temperatures in excess of 700°C have been generated in practice (Deutsches Zentrum fur Luft- un Raumfahrt, n.d.). For industrial waste heat, most high-temperature sources are in the solid phase (steel billets, etc.) which is hard to effectively recover energy from. If these are excluded, 88.9% of easily-utilised waste heat, i.e. that which is available in sources in the liquid or gaseous phase, are at low temperatures, less than 250°C (UK DECC, 2014b).

So far, most research and development of ORC systems has considered single-component organic working fluids. This has several shortcomings: (i) There is always a mismatch of temperature profiles between heat transfer fluid and the working fluid because the single working fluid evaporates and condenses at fixed temperatures while the heat transfer fluid changes temperature during heat transfer. This mismatch leads to irreversibility and reduces the cycle efficiency (Chys, et al., 2012) . (ii) An ORC power plant is currently designed by selecting a working fluid to match the heat source and sink temperatures. Considering that these temperatures differ from one customer to another, and the design options are limited by the availability of suitable organic fluids, installation costs are high. A wider choice of working fluids is desirable to reduce installation and operating costs (Chys, et al., 2012).

It is proposed here that these challenges can all be addressed by using zeotropic mixtures, which have the following advantages: (i) A zeotropic mixture has a variable temperature during phase change. ***Figure 2*** shows the bubble and dew lines of a zeotropic mixture formed by Butane and Heptane. For example, for a mixture with 20% of the high-boiling-point component Heptane, the evaporation starts at the temperature T_{bubble} and ends at T_{dew}. The differential (T_{bubble}-T_{dew}) is the temperature 'glide' of this mixture, which can be used to match the temperature change of heat transfer fluid in counter flow heat exchangers, so that the irreversibility can be reduced (Rajapaksha, n.d.). The use of suitable zeotropic mixtures as working fluids can increase cycle efficiency and power production of ORC systems, especially for lower temperature applications (<250 °C) [22]. (ii) Zeotropic mixtures display bubble- and dew-point temperatures between those of the two member components, and this varies predictably with mixture percentage. This allows the formation of a mixture with a particular composition to match heat sink temperatures so that more options of working fluids are available.

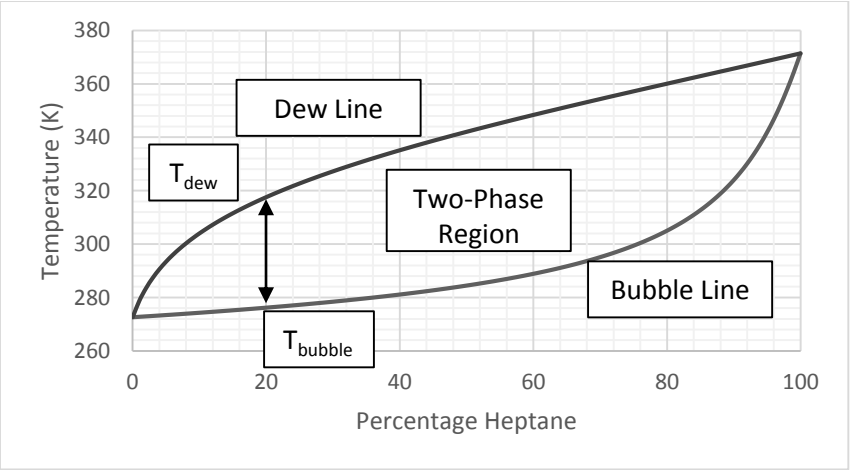

Figure 2: Glide curve of a mixture of Heptane and Butane at 1 bar

In this research, the working fluids selected for the cycle were zeotropic mixtures of alkanes. Specifically pentane, hexane and heptane, and their mixtures with butane. These substances are thermodynamically and chemically quite similar, being non-polar, dry fluids, minimising the number of independent variables to be considered when comparing results.

2. THEORY

The coolant outlet temperature from the condenser is primarily determined by the dew point of the working fluid at condenser pressure. If the dew point is at a lower temperature, or a higher enthalpy, the flow rate of coolant required to maintain the pinch point temperature difference will be greater.

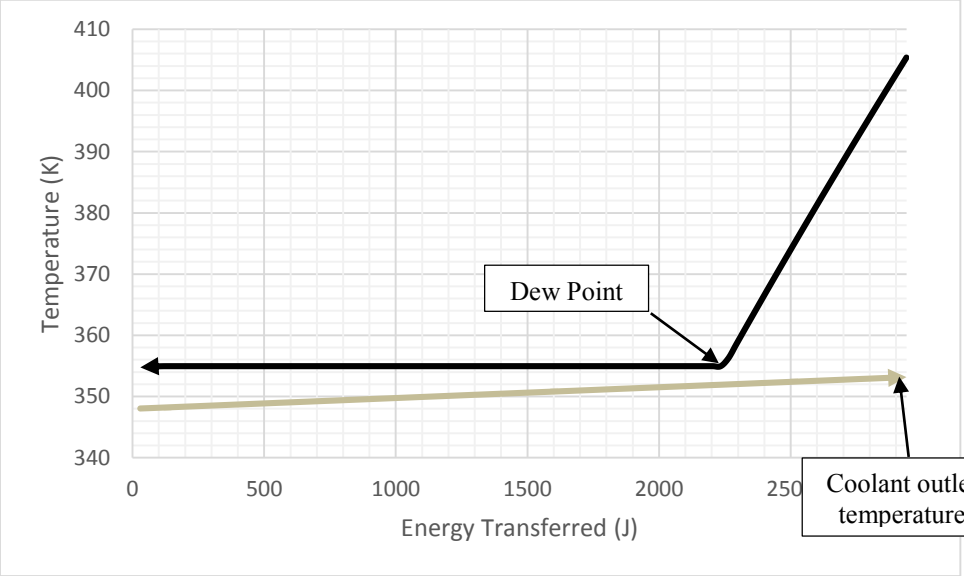

Figure 3: Condenser Temperature Profile for Heptane

Figure 3 demonstrates this principle. The pinch point in the condenser occurs at the dew point. If the dew point moves downwards (lower temperature) or to the right (higher enthalpy), the slope of the lower line must decrease in order for it to maintain the temperature gap at the pinch point. Decreasing the slope results in a lower coolant outlet temperature. In physical terms, this can be achieved by increasing the flow rate of coolant through the condenser.

When a fluid with a lower boiling point is added to one with a higher boiling point, two primary effects occur. One is that the bubble and dew points of the fluid are decreased, the other is that a degree of glide, or temperature change during phase change, is introduced. This means that the dew point increases more quickly than the bubble point. The aim of this paper is to investigate the effects these changes in bubble and dew points have on the required condenser pressures and efficiency of an Organic Rankine Cycle used for cogeneration.

3. NUMERICAL SIMULATION

There was assumed to be no pressure or heat loss from piping or heat exchangers, and no significant effects from velocity, momentum, change in elevation, or compressibility in the flow. A numerical simulation in MATLAB using REFPROP 9.1 (Lemmon, et al., 2013) was developed to analyse a cogeneration system using zeotropic working fluids. The naming convention for points in the cycle was as shown in figure 4:

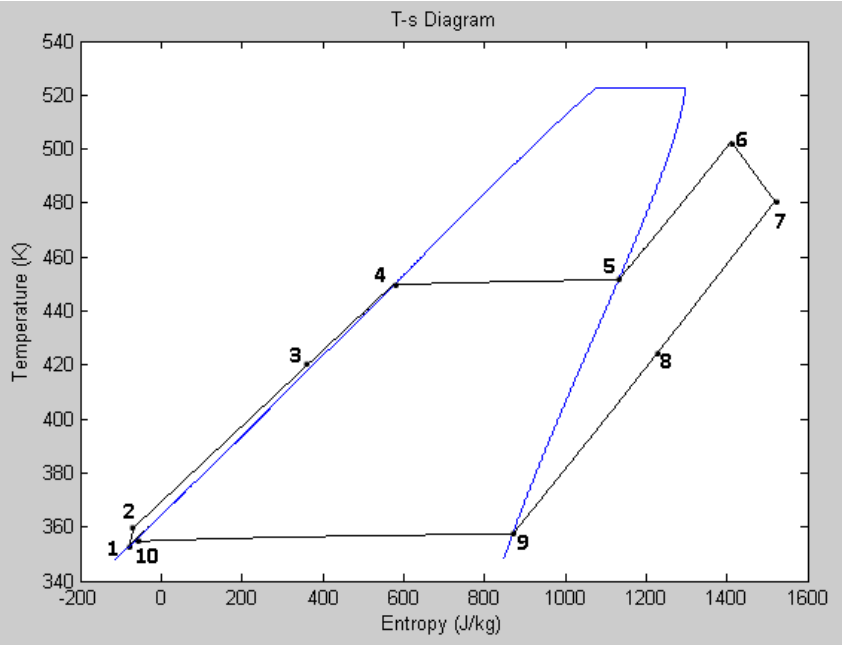

Figure 4: Cycle Diagram, with numbered points.

The pinch point temperature difference in the condenser was taken to be 5°C, which is consistent with previous research (Liu, et al., 2014), (Stefano Clemente, 2012). The coolant inlet temperature was taken to be 80°C, to represent mains water, and the outlet temperature to be 90°C, to represent a district heating scheme. The condenser pressure was then increased from an initial value of 10kPa until the pinch point opened up to the desired 5°C.

REFPROP allows for the calculation of each of the fluid properties on its extensive list given any two other properties, so temperature and pressure information is sufficient to also calculate the enthalpy and entropy of the fluid at this point.

The heat source temperature was taken to be 250°C, and the condenser pressure set to 1600kPa, which was low enough to ensure that the highest boiling point fluid, heptane, would fully vaporise at this temperature.

$$T_6 = 250°C \tag{4}$$

$$P_{evap} = 1600kPa \tag{5}$$

The isentropic efficiency of the pump and the expander were taken to be 90% and 70% respectively. Assuming isentropic pumping and expansion, $h_{2,isentropic}$ and $h_{7,isentropic}$ can then be obtained from REFPROP, and used to calculate the actual values, using the equations:

$$h_2 = h_1 + \eta_{pump} * (h_{2,isentropic} - h_1) \tag{6}$$

$$h_7 = h_6 - \eta_{expander} * (h_6 - h_{7,isentropic}) \tag{7}$$

Once this has been done, two properties are known for each of the four key points in the cycle; pump outlet, evaporator outlet, expander outlet and condenser outlet, and so equation 8 can be used to calculate the efficiency of the cycle.

$$\eta_{cycle} = \left(\frac{(h_6 - h_7) - (h_2 - h_1)}{h_6 - h_2}\right) \quad (8)$$

This allowed for the efficiency of the cycle to be calculated.

Keeping the evaporator pressure the same for comparability, the process was then repeated as the second fluid was added to the base fluid of butane in 10% increments of mass fraction. Limiting the evaporator pressure reflects the design considerations in real-world ORC plants, where higher pressures increase the cost and suffer from diminishing returns in efficiency.

This whole process was repeated using pentane, hexane and heptane as the second fluid, and the effects on the performance of the cycle observed.

The model was validated against experimental results obtained by Kang (Kang, May 2012) by using the same initial parameters, and produced results that were within 2% of his values for all points of the cycle as shown previously by the authors (Collings & Yu, 2014). This was considered reasonable in light of the assumptions that had been made in the production of the model, which offered us the confidence to apply this model to cogeneration application as presented in this paper.

4. RESULTS

As described in section 3, the heat source temperature was set to 250°C and the evaporator pressure to 1600kPa. The coolant inlet and outlet temperatures were set to 80 and 90°C respectively.

For all of the fluids under consideration, their addition to butane increased the bubble and dew points of the mixture, and allowed the condenser pressure to be dropped while maintaining the same temperature of water for cogeneration purposes at the condenser outlet, increasing the pressure ratio and therefore the efficiency of the cycle.

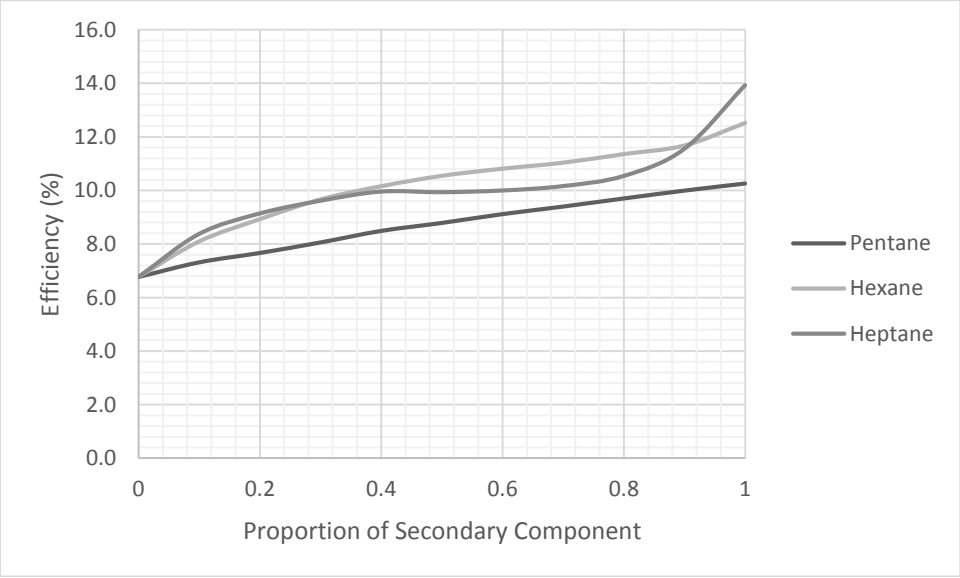

Figure 4: Performance of the system against the proportion of different secondary fluids

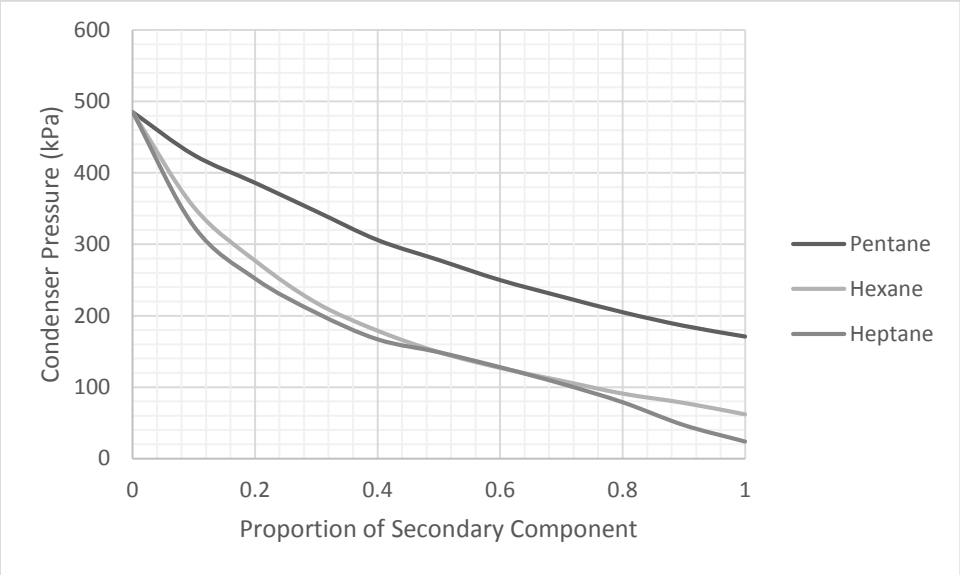

Figure 5: Performance of the system with changing condenser pressure for different secondary fluids

As shown in figures 4 and 5, the addition of pentane to butane smoothly decreases the condenser pressure and increases the efficiency, with a slightly more rapid rate of increase for lower mass fractions of butane.

A similar effect can be seen for the addition of hexane and heptane. The addition of hexane reduces the condenser pressure and increases the efficiency of the cycle. However, this change is less smooth, and the increase in the slope of the efficiency-composition line is more pronounced at very high and very low mass fractions of butane. For heptane, the increased slope at either end of the plot is far more obvious in, although the general trend of decreasing condenser pressure and increased efficiency remains.

A possible explanation for the observed shape of plot is that adding a higher-boiling-point component to the working fluid, such as heptane to butane, will tend to increase the dew point of the cycle, while leaving the bubble point largely unchanged. This allows for the condenser pressure to be dropped without closing the pinch point located at the fluid's dew point to unacceptable levels.

The rate of increase moderates between 20% and 70% heptane, due to the fact that in this region, the glide changes far more slowly, and the condenser pressure is able to decrease smoothly. Above 70% hexane, the bubble point begins to increase rapidly, which results in a sharp decrease in evaporator loading while maintaining roughly the same work output in the expander.

For pentane and hexane, these effects are also present, but the lower overall amount of glide means that the slopes of the bubble and dew lines are more similar at all compositions and results in a smoother profile as the composition changes. This is shown in **Figure 6.** The curve for butane-pentane features less glide, and so the bubble and dew curves have more similar slopes, meaning that the initial changes in bubble and dew points at each and of the scale are less drastic. The overall result of this is that the efficiency of the cycle will vary smoothly as the composition is changed, as shown in the earlier figures.

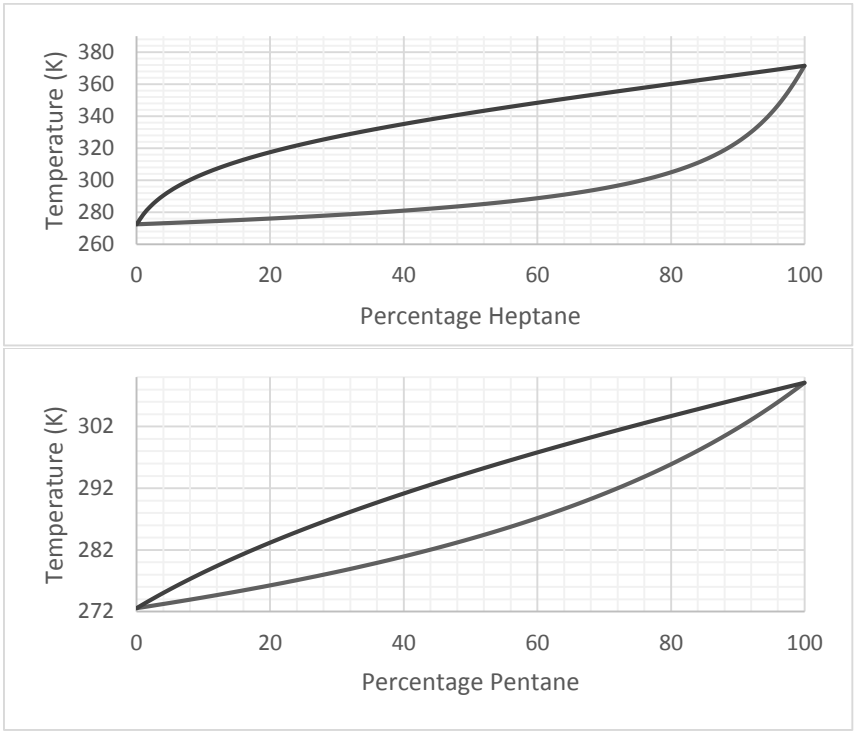

Figure 6: Comparison of glide curves for Butane-Heptane and Butane-Pentane

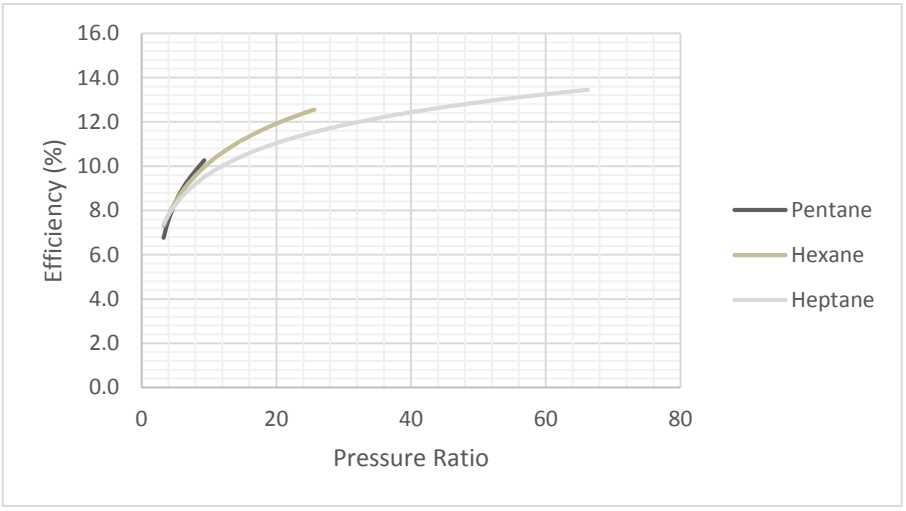

Figure 7: Relationship between pressure ratio and efficiency for different secondary fluids

For all secondary fluids, the efficiency increased as the pressure ratio increased, as shown in **Figure** *7*, with the increase tapering off, as even an infinitely large pressure ratio will never be able to overcome the Carnot limitation on the cycle.
Figure *7* also shows that the efficiency is higher at lower pressure ratios for lower boiling point secondary components, perhaps because butane-heptane mixtures exhibit higher glide for the same condenser pressure, increasing the condenser and evaporator loading without increasing expander work.

The practical implication of this for the implementation of Organic Rankine Cycles limited by condenser water outlet temperature is that working fluids can be tailored to match heat source and

sink temperatures by mixing them together, but ideally the components of the mixture must be selected to have relatively similar boiling points, otherwise sharp drops in efficiency will be observed as the composition is changed. For situations in which the pressure ratio is limited by any reason, such as the pressure rating of the evaporator and condenser, lower boiling-point secondary components, such as Pentane or Hexane, can be more efficient, however, the use of a higher boiling-point secondary component fluids in a system with a limited evaporator pressure is capable of achieving a higher pressure ratio, as the permitted condenser temperature is lower. In practice, the optimal solution will be determined by the exact configuration and limitations of the system. The higher the achievable pressure ratio, the more likely that Heptane will be the better option.

5. CONCLUSION

It has been shown that zeotropic mixtures can cause changes in the condensing temperature and pressure of a cycle, and that these changes can affect the efficiency of the cycle for a fixed coolant outlet temperature. For zeotropic mixtures consisting of components with relatively similar boiling points, this change in efficiency and condenser pressure is relatively smooth. However, if the temperature glide is too great, the larger changes in bubble and dew point at either end of the scale cause correspondingly abrupt changes in efficiency at these points.

For all mixtures, the benefit in efficiency from tailoring the working fluid to the heat source and sink outweighs the negative effect caused by the increased condenser and expander loading. This benefit is greater for a given pressure ratio when the two components of the working fluid have similar boiling points, as this results in a lower temperature glide, minimizing evaporator and condenser loading.

Potential utilisation of these effects to improve the efficiency of ORCs for cogeneration is a fertile area for future research.

NOMENCLATURE

h	Enthalpy	J/kg
P	Pressure	kPa
s	Entropy	J/kg K
T	Temperature	K
η	Efficiency	%

Subscript

1	Pump Inlet
2	Pump Outlet
3	Regenerator Outlet, cold (unused)
4	Bubble point, evaporator
5	Dew Point, evaporator
6	Expander Inlet
7	Expander Outlet
8	Regenerator Outlet, hot (unused)
9	Dew Point, condenser
10	Bubble Point, condenser
Critical	Property at critical point of the fluid

REFERENCES

Chys, M., Broek, M. v. d., Vanslambrouck, B. & Paepe, M. d., 2012. Potential of zeotropic mixtures as working fluids in Organic Rankine Cycles. *Energy,* Volume 44, pp. 623-632.
Collings, P. & Yu, Z., 2014. *Modelling and Analysis of a Small-Scale Organic Rankine Cycle System with a Scroll Expander.* s.l., s.n.
Deutsches Zentrum fur Luft- un Raumfahrt, n.d. *The Julich Solar Power Tower,* s.l.: s.n.
Fu, B.-R., Lee, Y.-R. & Hsieh, J.-C., 2005. Design, construction, and preliminary results of a 250-kW organic Rankine cycle system. *Applied Thermal Engineering,* April, Volume 80, pp. 339-346.
Insitution of Civil Engineers, 2012. *Energy Briefing: Heat,* s.l.: s.n.
Kang, S. H., May 2012. Design and experimental study of ORC (organic Rankine cycle) and radial turbine using R245fa working fluid. *Energy,* 41(1), pp. 514-524.
Lemmon, E., Huber, M. & McLinden, M., 2013. *NIST Standard Reference Database 23: Reference Fluid Thermodynamic and Transport Properties-REFPROP, Version 9.1,* Gaithersburg: s.n.
Liu, Q., Duan, Y. & Yang, Z., 2014. Effect of condensation temperature glide on the performance of organic Rankine cycles with zeotropic mixture working fluids. *Applied Energy,* pp. 394-404.
Oudkerk, J., Quoilin, S. & Lemort, V., 2011. *Evaluation of an ORC-Based micro-CHP system involving a hermetic scroll expander.* s.l., s.n.
Poyry Energy Consulting, 2009. *The Potential and Costs of District Heating Networks,* s.l.: s.n.
Rajapaksha, L., n.d. Influence of special attributes of zeotropic refrigerant mixtures on design and operation of vapour compression refrigeration and heat pump systems. *Energy Conversion and Management,* Volume 48, pp. 539-545.
Shu, G. et al., 2014. Study of mixtures based on hydrocarbons used in ORC (Organic Rankine Cycle) for engine waste heat recovery. *Energy,* September, Volume 74, pp. 428-438.
Stefano Clemente, D. M. M. R. R. T., 2012. Energy efficiency analysis of Organic Rankine Cycles with scroll expanders for Cogenerative Applications. *Applied Energy,* Volume 97.
Stoppato, A., 2012. Energetic and Economic Investigation of the Operation Management of an Organic Rankine Cycle cogeneration Plant. *Energy,* May, 41(1), pp. 3-9.
Twomey, B., Jacobs, P. & H.Gurgenci, 2013. Dynamic Performance Estimation of Small-Scale Solar Cogeneration with an Organic Rankine Cycle using a Scroll Expander. *Applied Thermal Engineering,* March, 51(1-2), pp. 1307-1316.
UK DECC, 2012a. *Detailed analysis from the first phase of the energy-saving trust's heat pump field trial,* s.l.: s.n.
UK DECC, 2012b. *First Year of Monitoring of Exhaust Air Heat Pumps with Underfloor Heating,* s.l.: s.n.
UK DECC, 2012c. *The Future of Heating: A Strategic Framework for Low-Carbon heat in the UK,* s.l.: s.n.
UK DECC, 2013a. *Deep Geothermal Review Study - Final Report,* s.l.: s.n.
UK DECC, 2014a. *Energy Consumption in the UK, 2014 Update,* s.l.: s.n.
UK DECC, 2014b. *The Potential for Recovering and Using Surplus Heat from Industry,* s.l.: s.n.
UK DECC, May 2012. *Report on Under-Floor Heating Design,* s.l.: s.n.
UK DECC, n.d. *A consultation on proposed changes to the Government's Standard Assessment Procedure,* s.l.: s.n.
Uris, M., Linares, J. I. & Arenas, E., 2014. Techno-economic feasibility assessment of a biomass cogeneration plant based on an Organic Rankine cycle. *Renewable Energy,* June, Volume 66, pp. 707-713.

ACKNOWLEDGEMENT

This research is funded by Royal Society (RG130051)

ON THE OPTIMUM AXIAL FLOW TURBINE DESIGN IN ORGANIC RANKINE CYCLES

Luca Da Lio[1], Giovanni Manente[2*], Andrea Lazzaretto[3]

[1,2,3]University of Padova, Department or Industrial Engineering,
Via Venezia 1, 35131 Padova, Italy
([1]luca.dalio@studenti.unipd.it, [2]giovanni.manente@unipd.it, [3]andrea.lazzaretto@unipd.it)

* Corresponding Author

ABSTRACT

Organic Rankine Cycles (ORCs) can effectively recover low grade heat for electricity production from industrial wastes and renewable energy. The general design problem of an ORC system is not trivial due to the choice of several design variables related to the thermodynamic cycle and equipment. Most of the optimization studies in the literature search for the optimum cycle configuration, design parameters and working fluid, disregarding the influence of these choices on expander design and efficiency. Indeed, the latter is often fixed to a constant value implicitly assuming that it will be achieved by a proper expander design in a subsequent design phase. This approach may be weak especially for the working fluids operating in ORCs having a high molecular weight and a low speed of sound. In these applications the high volumetric expansion ratios which may occur even at small temperature differences between turbine inlet and outlet markedly decrease the expander efficiency. Moreover, this efficiency is strongly affected by expander size that may vary from only few kWs up to several MWs. The aim of this study consists in searching for the optimum axial flow turbine design parameters (so called duty parameters) in a wide range of ORC operating conditions. Flow coefficient, loading coefficient and degree of reaction are selected as input values in a mean line design procedure that generates the main turbine geometrical characteristics and evaluates the turbine efficiency according to recent loss correlations. The variation of turbine efficiency with duty parameters is then shown in efficiency charts (like the Smith's one) to highlight suboptimal design options. This procedure is repeated for a range of ORC duty specifications (mass flow rate and expansion ratio) to detect their influence on turbine efficiency. So, any penalty associated with the selection of non-optimum duty parameters is clearly separated from the efficiency decay deriving from more severe operating conditions (e.g., high expansion ratios and small sizes).
keywords: Organic Rankine Cycles, axial turbine design, optimization, efficiency prediction.

1. INTRODUCTION

Organic Rankine Cycles are a viable option for the efficient use of low to medium temperature heat sources by simple cycle layouts. ORC systems are applied in the 50 to 500 kW sizes to recover heat from the exhaust gases of gas turbines or internal combustion engines, to exploit the heat content of biomass combustion gases, solar radiation or geothermal sources (Toffolo et al., 2014). Many studies in the literature compare the effects of the working fluid on plant performance for a fixed expander efficiency (Heberle and Brüggemann, 2006), whereas little focus is given to the peculiar design and characteristics of the expander. However, the specific thermodynamic properties of organic fluids necessarily affect the design of the expander, suggesting turbine configurations that differ from those operating with steam or other gases. In particular, the enthalpy drop in the expansion processes of Organic Rankine Cycles is lower than the steam enthalpy drop over the same temperature interval because of the higher molecular weight of organic fluids. The relatively small specific work can be disposed in a low number of stages with benefits in terms of turbine cost and size. On the other hand, the high expansion ratio per stage and the low speed of sound of organic fluids may result in transonic and supersonic flow conditions with

additional loss phenomena such as shock waves, which reduce turbine efficiency and ask for a specific turbine design.

Regardless of the turbine type, the consequence of all mentioned aspects is that the use of traditional tools for preliminary design and efficiency estimate (e.g., Smith chart, Balje diagram) becomes questionable when dealing with organic fluids. Hence new charts are required for organic fluids to have a reliable assessment of the expander efficiency as a function of turbomachinery design parameters. The importance of predicting real efficiency values becomes evident when the designer has to choose the thermodynamic cycle parameters (mass flow rate, evaporation and condensation temperature, kind of fluid, etc., for a given thermal source) which maximize (or minimize) a specified objective function.

In the search for the optimum cycle parameters many studies in the literature (Tchanche et al., 2009), (Khennich and Galanis, 2012) simply assume turbine efficiency values, disregarding the real possibility for the turbine to achieve these efficiencies in practice. Other studies (Sauret and Rowlands, 2011) check the assumed efficiency values only after evaluating optimum cycle parameters. A relevant contribution to the development of new preliminary design tools and efficiency charts for axial turbines operating with fluids having a low speed of sound is given by Macchi (1977), Macchi and Perdichizzi (1981). The authors warn about using efficiency charts (Balje, 1981) that depend on specific speed (n_s) and specific diameter (d_s) only, because i) they are obtained for a given range of Mach numbers and fixed ratio of specific heats and ii) do not account for the effect of reduced turbine dimensions on performance. They develop new charts based on Craig and Cox loss correlations (Craig and Cox, 1971) that link turbine efficiency and optimum specific speed to the volumetric expansion ratio (*VR*) and size parameter (*SP*). Recently, Lazzaretto and Manente (2014) have used these charts at each step of an automatic optimization procedure of the ORC system to calculate the turbine efficiency on the basis of the current thermodynamic variables. This approach eliminates the need of an arbitrary assumption about turbine efficiency at the beginning of the thermodynamic optimization procedure and supplies reliable optimum turbine efficiencies in conjunction with optimum values of other thermodynamic parameters.

In this study the axial flow turbine efficiency charts are updated by taking advantage of the current availability of real gas properties calculation programs Lemmon et al. (2010) and recent loss correlations (Aungier, 2006), which improve the classical models by (Ainley and Mathieson, 1957), (Kacker and Okapuu, 1982) and (Craig and Cox, 1971). A one dimensional meanline model of an axial flow turbine operating with *R245fa* is built in *Matlab*® environment to evaluate efficiency and main geometrical parameters. The predicted efficiencies are collected into two groups of maps: in the first one they are correlated to the parameters traditionally selected by the turbine designer (i.e, the so called "duty parameters"); in the second one to the volumetric expansion ratio and size parameter to highlight the influence of working fluid properties, thermodynamic cycle parameters and turbine size on the achievable turbine efficiency (see also (Angelino et al., 1984)).

These maps are similar to those recently obtained by the authors in (DaLio et al., 2014), the main differences being due to a more accurate evaluation of profile losses and a different evaluation of radial clearance. Moreover some preliminary results obtained for isobutane are shown. The main goal of the work is to extract all possible information from these efficiency maps in order to improve the design of turbines operating with a wide set of high molecular weight fluids and having various dimensions, and to increase the power output of the associated ORC systems.

2. THEORETICAL BACKGROUND

According to the dimensional analysis the efficiency of geometrically similar turbomachinery can be predicted in terms of dimensionless variables. In the formulation proposed by Shepherd (1956) the efficiency is a function of five independent variables: specific speed, specific diameter, Reynolds number, Mach number and specific heat ratio (Eq. 1):

$$\eta = f\left(n_s, d_s, Re, Ma, \gamma\right) \tag{1}$$

where specific speed and specific diameter are defined as:

$$n_s = \omega \frac{\dot{V}_3^{0.5}}{\Delta h_{0s}^{0.75}} \tag{2}$$

$$d_s = d \frac{\Delta h_{0s}^{0.25}}{\dot{V}_3^{0.5}} \tag{3}$$

When dealing with a turbomachinery operating with a specific fluid in a fully developed turbulent flow regime the effects of γ and Re can be neglected. So, the independent variables of Eq. (1) reduce to three. If the fluid is incompressible and Mach is below 0.5 (Csanady, 1964) the effect of Ma can be ignored, as well. The Balje diagrams (Balje, 1981) show the relationship between n_s, d_s and η under these assumptions for different types of turbomachinery.

The Balje diagram is particularly useful to calculate the turbine diameter, but it does not provide other information on turbine geometry. Other dimensionless parameters such as the loading and flow coefficients (ψ and ϕ), in the form

$$\psi = \frac{h_{01} - h_{03}}{u^2} \tag{4}$$

$$\phi = \frac{V_x}{u} \tag{5}$$

may give additional insights on turbine geometry. These dimensionless parameters are used as design parameters in this work. The well known Smith chart (Smith, 1965) clearly shows that the choice of these parameters affects axial flow turbine efficiency: the highest efficiencies generally occur at low ϕ and ψ values. Both Balje diagrams and Smith charts assign the same efficiency to turbomachinery having the same $n_s - d_s$ or $\psi - \phi$ values. Accordingly, the efficiency penalties associated with i) the high expansion ratios (high Mach number) typical of organic fluids, ii) the small turbine dimensions, iii) the different degrees of reaction, cannot be directly detected through these charts.

These effects can be explicitly taken into account by i) the volumetric expansion ratio VR ii) the size parameter SP (introduced by (Macchi and Perdichizzi, 1981)), and the degree of reaction R:

$$VR = \frac{\dot{V}_3}{\dot{V}_1} \tag{6}$$

$$SP = \frac{\dot{V}_3^{0.5}}{(h_{01} - h_{03})^{0.25}} \tag{7}$$

$$R = \frac{h_2 - h_3}{h_1 - h_3} \tag{8}$$

In this paper turbine efficiency is directly predicted from the classical ψ-ϕ complemented with the information on VR, SP and R, keeping the advantages of the traditional design tools (Smith charts) but enlarging the application to a wider spectrum of working fluids and operating conditions.

VR was preferred to the pressure ratio as an indicator of compressibility, as suggested by Macchi (1977), because it makes the correlation of the efficiency decay with expansion ratio less dependent on the working fluid being considered. On the other hand, SP accounts for the efficiency decay due to the different

ratio between viscous and inertia forces for turbomachinery of different size (Lozza, 2006) and for manufacturing limits which impose that some elements of the machine (e.g., trailing edge thickness, radial clearance, surface finish) cannot be scaled proportionally to the absolute dimension (see Table 2).

According to the suggested approach a turbine design based on given values of ψ, ϕ and R can be transferred to other turbines having the same values of these parameters only if they have the same *VR* and *SP*.

3. THE TURBINE DESIGN MODEL AND OPTIMIZATION PROCEDURE

The meanline design model described in this section aims at defining an optimum design and providing a simple procedure to predict the efficiency of a single stage axial flow turbine. The choice of non-dimensional parameters (ψ, ϕ and R) along with a first guess estimate of the turbine efficiency are used in the turbine model to define the main turbine design parameters under a given set of design specifications (T_{evap}, $\dot{m}$) properly selected to span a wide range of *SP* and *VR* (see the flowchart in Fig. 1).

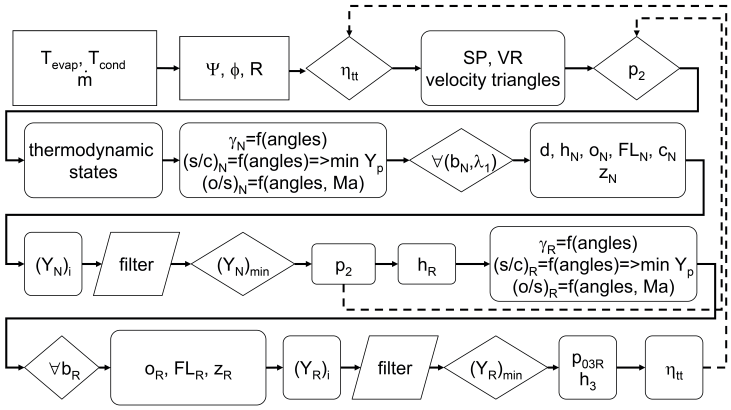

Figure 1: Model's flowchart: dotted arrows indicate updates for guess values.

The resulting geometry is then used to predict turbine design efficiency by means of an iterative procedure which embeds adequate loss models that properly take into account the effects of the high Mach numbers typical of heavy fluids working in ORCs. These models are presented in detail in Appendix A. While traditional loss models either disregard (Ainley and Mathieson, 1957) or overestimate shock and post expansion losses (Dunham and Came, 1970), the more recent Aungier's model that is applied here supplies a better estimate of the magnitude of these losses. This choice has a direct impact on turbine efficiency, and provides the performance gap and associated variation in the design parameters compared to previous literature that generally relies on the Craig and Cox (e.g. Macchi and Perdichizzi (1981)). An accurate analysis of all the loss sources occurring in the blade rows is performed to form a reliable estimate of the overall total pressure losses within the stator and rotor (Y_N and Y_R, respectively, in Fig. 1). Real fluid properties taken from *NIST Refprop* (Lemmon et al., 2010) are considered to accurately evaluate the thermodynamic behavior, particularly at high pressure and close to the vapor saturation curve. Unlike Macchi and Perdichizzi (1981) this model assumes the three requirements of a "normal" stage (named also "repeating" stage):

$$V_x = constant \quad d = constant \quad \alpha_1 = \alpha_3 \tag{9}$$

where V_x is the axial velocity, d is the root mean square diameter, α_1 and α_3 are the absolute flow angles at stations 1 and 3.

A schematic of the circumferential and meridional section of the blade row is drawn in Figures 2(a) and 2(b) to highlight the main geometrical parameters calculated by the design optimization procedure.

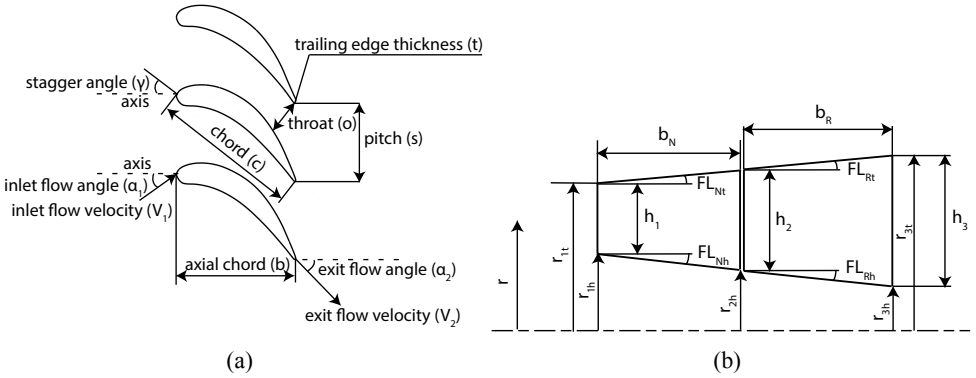

Figure 2: (a) Main geometrical blade parameters, and (b) Schematic representation of turbine stage meridional channel.

Table 1: Upper and lower bounds of the free variables in the optimization procedure.

	min value	max value
λ_1	0.30	0.95
λ_3	0.30	1
FL_N (°)	-20	20
FL_R (°)	-25	25
$(h/d)_3$	0	0.25
$\arcsin(o/s)_N$ (°)	13	60
$\arcsin(o/s)_R$ (°)	13	60
$(b/d)_N$	0	0.25
$(b/d)_R$	0	0.25
b_N (mm)	3	100
b_R (mm)	3	100
z_N	10	100
z_R	10	100

A detailed explanation of all steps required to optimize the design of the axial turbine stage, as shown in the flow chart of Fig. 1, is given in Appendix B.

4. RESULTS

The main outcomes of the design procedure presented in Section 3 are the geometry and efficiency of an axial flow turbine fulfilling given design specifications (i.e., mass flow rate and specific work). For each design specifications different turbine designs are generated assuming different values of the design parameters ψ, ϕ and R. Accordingly new Smith charts are generated showing the maximum efficiency achievable by *R245fa* at different ψ-ϕ-R values. Only Smith charts referring to optimum degree of reaction are shown for brevity (see Fig. 3). Starting from each design specification the optimum design parameters (ψ-ϕ) and efficiency are drawn from the associated Smith charts and used to build a general efficiency map in the *SP*-*VR* plane (see Fig. 4(a)).

To cover a wide spectrum of *SP* and *VR* conditions, the whole analysis is carried out by considering the following set of design specifications: evaporation temperatures (T_{evap}) in the range 50 to 110 °C at steps of 10 °C, and mass flow rates ($\dot{m}$) equal to 10, 30, 50 and 100 100 kg/s. The turbine outlet pressure

Table 2: Geometric parameters in (m) the rigorous similarity of which cannot be maintained at low actual turbine dimensions.

e	2×10^{-6}
δ	max(0.0005 *or* $0.015h_3$)
t	max(0.001 *or* 0.05 o)

is fixed in all cases at 1.97 bar, being determined by the assumed condensation temperature (33 °C). The range and step of variation of the design parameters are:

$\Psi \in (0.8 : 0.01 : 2.80)$

$\phi \in (0.40 : 0.01 : 0.90)$

$R \in (0.00 : 0.01 : 0.60)$

where the first and third terms are the upper and lower bounds and the step of variation is shown in the middle.

All possible combinations of design specifications and design parameters are simulated to generate the new charts shown in the following.

4.1 New Smith charts

Assuming that half of the axial kinetic energy in the discharge section is recovered (Macchi and Perdichizzi, 1981) the turbine efficiency becomes:

$$\eta = \frac{h_{01} - h_{03}}{h_{01} - h_{3ss} - 0.5\frac{V_x^2}{2}}. \tag{10}$$

Efficiency values calculated at optimum R through Eq. (10) are shown in ψ-ϕ plane in Figs. 3 for two extreme values of *VR* (Fig. 3(a) and 3(b)) and *SP* (Fig. 3(c) and 3(d)).

It clearly appears that the highest efficiencies are obtained at low flow coefficients and low loading coefficients, as in the original Smith chart. High ψ values imply larger deflections which require a larger blade surface area in contact with the fluid and in turn higher friction losses. As the flow coefficient ϕ increases, the deflection decreases but the axial velocity increases, resulting in additional losses (Moustapha et al., 2003).

The volumetric expansion ratio has a strong influence on turbine efficiency. The chart in Fig. 3(a) refers to $VR \approx 2.3$ ($T_{evap} = 60$ °C) and shows a maximum efficiency equal to 88.4% obtained at $\phi = 0.4$ and $\psi = 1.01$. The chart in Fig. 3(b) refers to a much higher *VR* ($T_{evap} = 100$ °C), and shows a maximum efficiency equal to 86.1% which is obtained at $\phi = 0.4$ and $\psi = 1.11$. These results demonstrate that the efficiency markedly decreases (-2.3%-points) and the optimum ψ slightly increases (+0.10) with *VR*. Similarly the effect of size parameter on turbine efficiency is shown in Figs. 3(c) and 3(d) where the efficiency penalties become 2.2%-points moving from *SP*=0.27 m to 0.09 m, decreasing the turbine diameter from 0.50 m to 0.16 m.

Table 3 compares the geometrical features and losses for two turbines having different volumetric expansion ratios in the optimum points of Figures 3(a) and 3(b). All loss sources are shown in Table 3 to explain the efficiency gap between the two cases. It clearly appears that the efficiency penalties for the higher pressure ratio is due to the high post expansion losses (in the stator they account for more than half of the total losses) which are absent for the lower pressure ratio. Indeed, the flow is supersonic both at stator and rotor outlet. Moreover, the higher secondary losses and the occurrence shock losses further reduce the efficiency.

Table 4 referring to the two optimum designs in Figs. 3(c) and 3(d) shows a significant increase of secondary, profile and clearance losses when reducing the size.

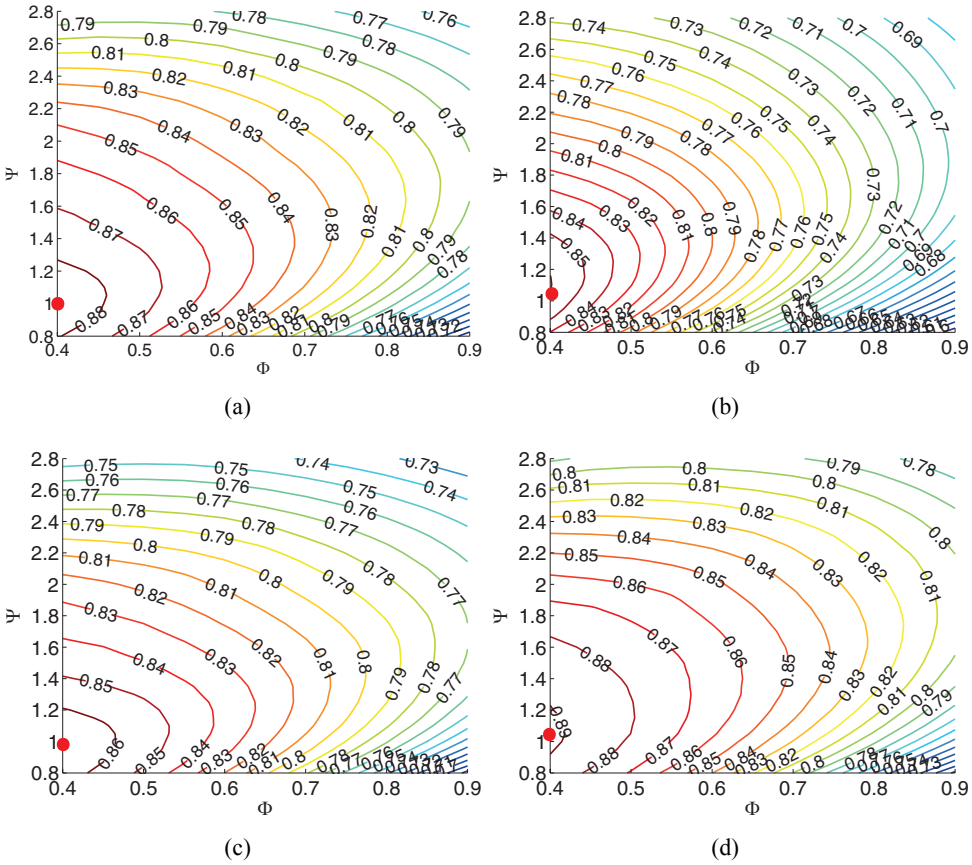

Figure 3: Smith charts showing lines at constant η for: (a) $\dot{m}$ =50 kg/s, T_{evap} =60 °C (*SP*≈0.16 m, *VR*≈2.3); (b) $\dot{m}$ =50 kg/s, T_{evap} =100 °C (*SP*≈0.16 m, *VR*≈7); (c) $\dot{m}$ =10 kg/s, T_{evap} =60 °C (*SP*≈0.09 m, *VR*≈2.3); (d) $\dot{m}$ =100 kg/s, T_{evap} =60 °C (*SP*≈0.27 m, *VR*≈2.3). Red dots indicate the best efficiency points.

Table 3: Main performance parameters and losses in the optimum points of Figs. 3(a) and 3(b).

	VR	2.3			6.9	
	ϕ	0.4			0.4	
	Ψ	1.01			1.11	
	n_s	1.02			0.93	
	R	0.47			0.45	
	η	0.884			0.861	
	V_x (m/s)	47.4			66.6	
	d (m)	0.36			0.31	
	ω (rad/s)	663			1081	
	u (m/s)	118			166	
	stator	rotor		stator	rotor	
Mach inlet	0.36	0.35		0.54	0.50	
Mach exit	0.97	0.91		1.42	1.28	
deflection	65	69		71	83	
h/c	0.93	1.73		0.51	1.10	
t/o (%)	7.74	8.11		7.69	7.91	
δ/h_3 (%)		1.5			1.5	
flaring tip (°)	11	17		12	18	
flaring hub (°)	14	25		14	25	
b (m)	0.046	0.041		0.045	0.057	
	stator	rotor	total	stator	rotor	total
profile	0.022 (32.4%)	0.020 (13.7%)	0.042 (19.6%)	0.019 (10.5%)	0.021 (8.9%)	0.040 (9.6%)
secondary	0.039 (57.3%)	0.029 (19.9%)	0.068 (31.8%)	0.050 (27.6%)	0.039 (16.6%)	0.089 (21.4%)
trailing edge	0.008 (11.8%)	0.008 (5.5%)	0.016 (7.5%)	0.008 (4.4%)	0.008 (3.4%)	0.016 (3.9%)
shock	0 (0%)	0 (0%)	0 (0%)	0.015 (8.29%)	0.008 (3.4%)	0.023 (5.5%)
postexpansion	0 (0%)	0 (0%)	0 (0%)	0.089 (49.2%)	0.049 (20.9%)	0.138 (33.2%)
clearance		0.089 (60.9%)	0.089 (41.6%)		0.110 (46.8%)	0.110 (26.4%)
total	0.068 (100%)	0.146 (100%)	0.214 (100%)	0.181 (100%)	0.235 (100%)	0.416 (100%)

4.2 SP-VR maps

In this section the effects of the design specifications on the optimum turbine design parameters and efficiency are analyzed. To this end the simulation model is run at different mass flow rates and evaporating temperatures to find the optimum designs in the range *SP* 0.05 ÷ 0.30 m and *VR* 2 ÷ 9. Each Smith chart contributes in the following *SP*-*VR* maps with its maximum efficiency point.

Figure 4(a) clearly shows that the highest turbine efficiencies are located in the region of low *VRs* and high *SPs*. At fixed *SP*, large volume variations cause relevant losses mainly due to high Mach flow regimes (i.e., high velocities). At fixed *VR*, small turbines are disadvantaged because of larger ratios between viscous and inertia forces and manufacturing limits which lead to higher clearance losses.

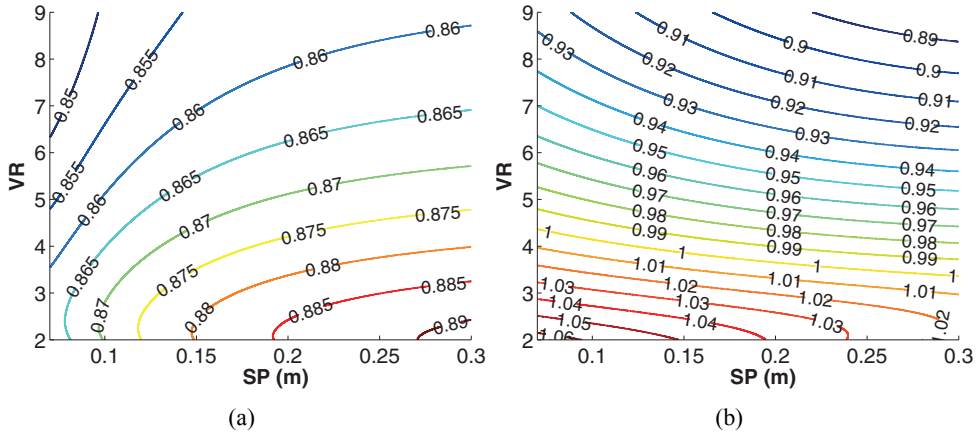

(a) (b)

Figure 4: (a) Optimum turbine efficiency, and (b) optimum specific speeds versus *SP* and *VR* for *R245fa*

Figure 4(b) shows the specific speed trend in the SP-VR plane. In agreement with the literature the

Table 4: Main performance parameters and losses in the optimum points of Figs. 3(c) and 3(d)

	SP	0.086			0.27	
	ϕ	0.4			0.4	
	Ψ	0.97			1.01	
	n_s	1.04			1.03	
	R	0.48			0.47	
	η	0.866			0.888	
	V_x (m/s)	48			47	
	d (m)	0.16			0.50	
	ω (rad/s)	1506			471	
	u (m/s)	120			119	
	stator	rotor		stator	rotor	
Mach inlet	0.36	0.35		0.36	0.35	
Mach exit	0.95	0.91		0.97	0.91	
deflection	73	68		72	73	
h/c	0.50	0.92		1.22	1.72	
t/o (%)	7.7	8.0		7.8	8.1	
δ/h_3		1.56			1.5	
flaring tip (°)	6	10		15	17	
flaring hub (°)	6	15		19	25	
b (m)	0.038	0.033		0.050	0.057	
	stator	rotor	total	stator	rotor	total
profile	0.024 (27.0%)	0.023 (13.4%)	0.047 (18.1%)	0.021 (35.0%)	0.016 (11.4%)	0.037 (18.5%)
secondary	0.058 (65.2%)	0.043 (25.1%)	0.101 (38.8%)	0.032 (53.3%)	0.028 (20.0%)	0.060 (30.0%)
trailing edge	0.008 (9.0%)	0.008 (4.7%)	0.016 (6.2%)	0.008 (13.3%)	0.008 (5.7%)	0.016 (8.0%)
shock	0 (0%)	0 (0%)	0 (0%)	0 (0%)	0 (0%)	0 (0%)
postexpansion	0 (0%)	0 (0%)	0 (0%)	0 (0%)	0 (0%)	0 (0%)
clearance		0.098 (57.3%)	0.098 (38%)		0.089 (63.6%)	0.089 (44.5%)
total	0.089 (100%)	0.171 (100%)	0.260 (100%)	0.060 (100%)	0.14 (100%)	0.20 (100%)

optimum values of n_s increase as the turbine dimensions and *VR* decrease. At constant *SP* (i.e., for constant *d*) the increase of n_s towards low *VR* is a consequence of lower enthalpy drops, which oppose to the effect of the progressive decrease of the angular speed ω due to the decrease in turbine peripheral speed (*u*).

These maps can be compared with those originally obtained by Macchi and Perdichizzi (1981) reported here in Fig. 5, where the *SP*-*VR* domain considered in this work is highlighted in red. The range of turbine efficiency is narrower in the present work varying between 0.85 and 0.89. The rising trend of turbine efficiency with *SP* up to 0.30 m at fixed *VR* is confirmed in this analysis, as well as the decreasing trend at increasing *VR*.

The decrease of optimum specific speed with *VR* is observed in this paper too. Specific speeds are higher than the optimum ones calculated by Macchi and Perdichizzi (1981) especially in the high *VR* and *SP* region and show a weaker dependence from *SP* (note that angular speeds are expressed in rpm instead of rad/s).

Fig.6 shows the *SP*-*VR*-efficiency map for *isobutane*. At given values of the couple *SP*-*VR* higher efficiencies are achieved by *iusobutane* compared to *R245fa*. However the general trend is maintained.

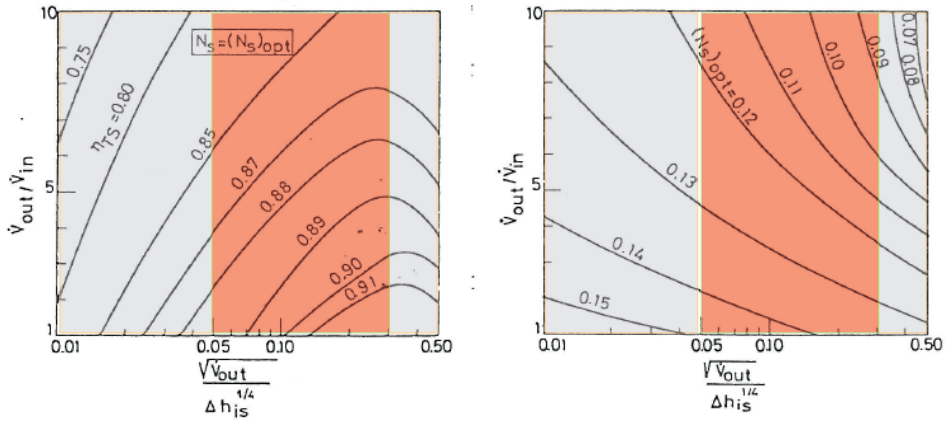

Figure 5: Efficiency prediction and optimum values of specific speed for a turbine stage (reproduced from Macchi and Perdichizzi (1981))

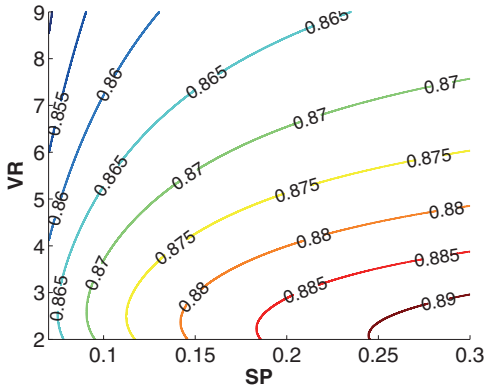

Figure 6: Optimum turbine efficiency versus *SP* and *VR* for *isobutane*.

5. CONCLUSIONS

The paper shows that new design procedures are needed for a reliable design of ORC expanders operating with high molecular weight fluids due to the wider range of operating conditions (e.g., size, pressure ratios) compared to traditional applications using conventional fluids (e.g., air or flue gases). The model of the single stage axial flow turbine developed in this work explicitly accounts for the influence of the volumetric expansion ratio (*VR*) and size (*SP*) parameters in addition to the flow and loading coefficients and degree of reaction. Expansion ratio and size parameters are found to significantly affect the achievable efficiency and cannot be disregarded even in a preliminary ORC expander design. For *R245fa*, the increase of VR from 2.3 to 7 causes a decrease of the optimum efficiency of 2.3%-points (from 88.4% to 86.1% at *SP* ≈≈0.16 m). Similarly, the penalty in the optimum efficiency reaches 2.2%-points when the size is reduced from *SP* 0.27 m to ≈0.16 m (i.e., from 88.8% to 86.6% at *VR* ≈ 2.3). The analysis has also highlighted the effects of *VR* and *SP* on the optimum design parameters ψ, ϕ and n_s. When *VR* increases from 2.3 to 7 at fixed *SP* (≈0.16 m), the optimum loading coefficient ψ increases from 1.01 to 1.11, the optimum flow coefficient ϕ remains unchanged (0.4) and the specific speed n_s reduces from 1.02 to 0.93. The comparison *R245fa-isobutane* demonstrate that the efficiency map is not strictly general but is affected by the peculiar properties of the working fluid. The developed maps improve the prediction of ORC expander performance, but they could certainly be improved by a proper tuning with new experimental data specifically retrieved from tests on real ORC systems. Nonetheless a good agreement is found with results of theoretical analyses reported in the literature.

The resulting charts could be a useful tool in a general optimization procedure of the ORC systems

design that takes into account the real turbine behavior in the search for the best thermodynamic cycle parameters.

A. LOSS MODEL

The general structure of the loss model used here is derived from Aungier's work (Aungier, 2006). The total pressure loss coefficient through the blade rows is expressed as the sum of several terms representing specific loss sources: profile, secondary, trailing edge, post expansion, shock and clearance losses.

$$Y = Y_p + Y_s + Y_{te} + Y_{ex} + Y_{sh} + Y_{cl} \tag{A.1}$$

In this section the formulation of all these loss sources is presented. Although these equations are written for a fixed row (i.e., stator) they are still valid for a rotor provided that relative flow angles (β) are substituted for absolute ones (α). When using the following equations flow angles must be expressed consistently with the blade angle convention, so that:

$$\alpha_1 = 90 + \arctan(V_{t1}/V_x) \tag{A.2}$$

$$\alpha_2 = 90 - \arctan(V_{t2}/V_x) \tag{A.3}$$

$$\beta_2 = 90 - \arctan(W_{t2}/V_x) \tag{A.4}$$

$$\beta_3 = 90 + \arctan(W_{t3}/V_x) \tag{A.5}$$

The output of the loss model is the total pressure loss coefficient of the stator (Y_N) and rotor (Y_R), respectively defined by:

$$Y_N = \frac{p_{01} - p_{02}}{p_{02} - p_2} \tag{A.6}$$

$$Y_R = \frac{p_{02R} - p_{03R}}{p_{03R} - p_3} \tag{A.7}$$

A.1 Profile losses

The profile loss is due to skin friction on the blade surface and depends on the blade area that is in contact with the fluid, the surface roughness, and Reynolds and Mach numbers. The profile loss coefficient Y_p is evaluated using a modified form of the Ainley-Mathieson model:

$$Y_p = k_{mod}\, k_{inc}\, k_p\, k_{Re}\, k_M \left((Y_{p1} + \xi^2 (Y_{p2} - Y_{p1})) \left(\frac{5 t_{max}}{c} \right)^{\xi} - \Delta Y_{te} \right) \tag{A.8}$$

where:

- Y_{p1} and Y_{p2} represent the profile losses in nozzle blades and impulse blades, respectively, and ξ is the ratio between the inlet and outlet flow angles and governs the amount of profile losses for blade configurations that are intermediate between nozzle and impulse ones. Both Y_{p1} and Y_{p2} show a minimum at an optimum pitch to chord ratio, which varies depending on the discharge flow angle.
- k_{mod}, k_{inc}, k_p, k_{Re} and k_M are correction factors accounting for:
  - i) Superior performance of modern designs due to improved design technology (k_{mod}). A value equal to 0.67 is used as suggested by Kacker-Okapuu;
  - ii) Off-design incidence flow angles (k_{inc}). k_{inc} is set to 1 because only design conditions are considered;

  - iii) Beneficial influence of high Mach numbers (k_p) (thin boundary layers and flow separations avoided) compared to flow conditions in cascade tests;
  - iv) Effects of Reynolds number and surface roughness on the friction coefficient (k_{Re});
  - v) discharge Mach number in subsonic flow regimes (k_M).
- ΔY_{te} is the trailing edge loss term that is evaluated separately from the profile losses in the Aungier's model.

A.2 Secondary losses

Secondary flows are vortices that occur as a result of the boundary layers and curvature of the blade passage causing fluid deviations from the main flow direction. Secondary losses are calculated using an updated version of the AMDC model originally proposed by Dunham and Came (Dunham and Came, 1970) and subsequently refined by Kacker and Okapuu (Kacker and Okapuu, 1982) and Aungier (Aungier, 2006). According to this model the total pressure loss Y_s is calculated starting from the loading factor Z:

$$Z = \left(C_L \frac{c}{s}\right)^2 \frac{\sin^2 \alpha_2}{\sin^3 \alpha_m} \tag{A.9}$$

where C_L is the lift coefficient defined by:

$$C_L = 2(\cot \alpha_1 + \cot \alpha_2)\frac{s}{c} \sin \alpha_m \tag{A.10}$$

A preliminary estimate of the secondary flow loss coefficient can be calculated as:

$$\widetilde{Y_s} = 0.0334 F_{AR} Z \frac{\cos \alpha_2}{\cos \alpha_{1b}} \tag{A.11}$$

where F_{AR} is a correction factor based on blade span and chord.

Aungier further refines Eq. (A.11) by imposing an asymptotic upper limit of about 0.365 to the secondary losses. Moreover, correction factors accounting for Reynolds and Mach number (k_{Re}, k_s) are also included to get:

$$Y_s = k_{Re} k_s \sqrt{\frac{\widetilde{Y_s}^2}{1 + 7.5\widetilde{Y_s}^2}} \tag{A.12}$$

A.3 Trailing edge losses

Trailing edge losses account for pressure losses due to trailing edge blockage. The trailing edge loss coefficient is expressed as a function of the ratio between trailing edge thickness and blade throat according to the following expression:

$$Y_{te} = \frac{\Delta p_0}{0.5 \rho V_2^2} = \left(\frac{t_2}{o_2 - t_2}\right)^2 \tag{A.13}$$

A.4 Shock losses

Shock losses account for the formation of shock waves also at moderate average inlet Mach numbers due to the local acceleration at blade leading edges. Although these shock waves take place next to the blading hub endwall they can be evaluated as a contribution to the mean line losses through $\widetilde{Y_{sh}}$ that enters in the definition of Y_{sh} in Eq. (A.1):

$$\widetilde{Y_{sh}} = 0.8 X_1^2 + X_2^2 \tag{A.14}$$

$$Y_{sh} = \sqrt{\frac{\widetilde{Y_{sh}}^2}{1 + \widetilde{Y_{sh}}^2}} \tag{A.15}$$

X_1 and X_2 both depend on inlet and outlet Mach numbers.

A.5 Supersonic expansion losses

Due to the low speed of sound of heavy fluids and high pressure ratios it is quite usual to deal with supersonic velocities which generate additional pressure losses as result of shock waves in the trailing edge wake. The phenomena underlying these losses are difficult to be described in an easy but reliable way using a meanline analysis approach. We observed that the models proposed by (Dunham and Came, 1970), (Li et al., 2004) give non meaningful results (that are either overestimated or underestimated, respectively) when dealing with high Mach numbers. More reliable results are instead provided by the following Aungier's correlation:

$$Y_{ex} = \left(\frac{Ma_2 - 1}{Ma_2} \right)^2 \tag{A.16}$$

A.6 Blade clearance losses

The loss coefficient is computed for the rotor only using the following expression:

$$Y_{cl} = 0.47 Z \frac{c}{h} \left(\frac{\delta}{c} \right)^{0.78} \tag{A.17}$$

B. DETAILED DESIGN PROCEDURE

1. The values of the mass flow rate ($\dot{m}$) and evaporation and condensation temperatures (T_{evap}, T_{cond}) are known from the thermodynamic cycle analysis, and represent design specifications. A saturated vapor condition is assumed at turbine inlet so that states 1 and 3_{ss} are completely defined;
2. Proper ranges of variation of ψ, ϕ and R are selected (see Section 4) to get all absolute and relative flow angles by means of Eqs. (B.1) and (B.2):

$$\begin{cases} \tan\alpha_3 = \frac{1-R-\Psi/2}{\phi} \\ \tan\alpha_2 = \frac{1-R+\Psi/2}{\phi} \end{cases} \tag{B.1}$$

$$\begin{cases} \tan\beta_3 = -\frac{R+\Psi/2}{\phi} \\ \tan\beta_2 = -\frac{R-\Psi/2}{\phi} \end{cases} \tag{B.2}$$

3. h_3 is calculated by assuming a guess value of the total-to-total efficiency η_{tt}. So, the rotor outlet state is known and *VR*, *SP* can be calculated; h_2, u and V_x are calculated from R, ψ and ϕ, respectively;
4. All the velocity triangles can be obtained by means of trivial trigonometric calculations. So, the total states 01, 03, 03_{ss} can be calculated;
5. Assuming a guess value for the pressure p_2, state 2 is located in the enthalpy-entropy plane;
6. The passage area A_1 at the inlet of the stator is calculated from the mass flow rate definition. A set of couples ``stator inlet hub-to-tip radius ratios ($\lambda_1 = r_{1h}/r_{1t}$ - see Fig. 2(b)) - nozzle axial chord (b_N)" is considered to calculate a wide spectrum of the following geometrical parameters: chord (c_N), root mean square diameter ($d = 2A_1/\pi\sqrt{(1-\lambda_1^2)/(1+\lambda_1^2)}$), blade span ($h_N$) (from continuity equation), blade pitch (s_N), number of blades (z_N) and throat opening (o_N). The set of

generated stator geometries are compared on the basis of the associated losses (Eq. (A.1)) to select the best performing one. Unfeasible solutions in the set ($\lambda_1 - b_N$) are eliminated according to the constraints summarized in Table 1, among which the most binding are those associated with the flaring angle ($FL_N < 20°$) and the hub-to-tip radius ratio at rotor outlet ($\lambda_3 \geq 0.30$). Among all feasible solutions, the couple ($\lambda_1 - b_N$) yielding the lowest total nozzle pressure loss coefficient (Y_N) is chosen. The blade spans (h) along the stator and rotor blade channels are then found from the continuity equation (see Fig. 2(b));

7. At this point the stator outlet pressure (previously assumed as a guess value at point 5) can be calculated from the definition of total pressure loss coefficient, being Y_N known:

$$Y_N = \frac{p_{01} - p_{02}}{p_{02} - p_2} = \frac{p_{01} - f(h_{02}, s_2)}{f(h_{02}, s_2) - p_2} \tag{B.3}$$

So, state 2 can be located in the enthalpy-entropy diagram. Note that the total pressure at stator outlet (p_{02}) is calculated from the known values of h_{02} and s_2 to properly take compressibility into account (i.e., the dynamic pressure in the denominator of Eq. (B.3) is not calculated as $0.5\rho_2 V_2^2$, as commonly suggested in the literature);

8. The calculation procedure of the rotor geometry and losses is similar but simpler than the stator one. In fact, the only free variable is b_R, being λ_3 ($\lambda_3 = r_{3h}/r_{3t}$ in Figure 2(b)) evaluated from λ_1 (that is known from the calculations in the stator, see step 6). Indeed, it can be demonstrated from the continuity equation that the hub-to-tip radius ratios of two consecutive sections *i* and *j* in a normal axial turbine stage can be linked to each other by means of the volumetric expansion ratio *VR*:

$$\lambda_j = \sqrt{\frac{1 + \lambda_i^2 - VR(1 - \lambda_i^2)}{1 + \lambda_i^2 + VR(1 - \lambda_i^2)}} \tag{B.4}$$

For each value of b_R the rotor geometrical parameters (s_R, z_R, o_R, etc.) and total rotor pressure loss (Y_R) are calculated (see the flowchart in Fig. 1), from good engineering practice (see (Moustapha et al., 2003)). The rotor design yielding the lowest Y_R and fulfilling all the constraints is selected. Starting from the definition of Y_R, p_{03R} is then calculated and used to find a new value of h_3, which updates the h_3 calculated from the η_{tt} guess at step 3;

9. A new estimate of the total-to-total efficiency is calculated from:

$$\eta_{tt} = \frac{h_{01} - h_{03}}{h_{01} - h_{03ss}} \tag{B.5}$$

This estimate is used as input for the next iteration until convergence.

NOMENCLATURE

α	absolute flow angle	(°)
β	relative flow angle	(°)
δ	rotor radial clearance	(m)
$\dot{m}$	mass flow rate	(kg/s)
$\dot{V}$	volumetric flow rate	(m^3/s)
η	efficiency	()
γ	sweep angle	(°)
λ	hub to tip radius ratio	()
ω	angular velocity	(rad/s)

ϕ	flow coefficient	()
ψ	loading coefficient	()
ρ	density	(kg/m^3)
A	area	(m^2)
b	blade axial chord	(m)
c	blade chord	(m)
d	root mean square diameter	(m)
e	blade surface roughness	(m)
FL	flaring angle	(°)
h	blade span	(m)
h	specific enthalpy	(J/kg)
Ma	Mach number	()
n_s	specific speed	()
o	blade throat	(m)
p	pressure	(Pa)
R	degree of reaction	()
Re	Reynolds number	()
s	blade pitch	(m)
SP	size parameter	(m)
T	temperature	(°C)
t	trailing edge thickness	(m)
u	peripheral velocity	(m/s)
V	absolute velocity	(m/s)
V_x	meridional velocity	(m/s)
VR	volumetric flow ratio	()
w	relative velocity	(m/s)
Y	total pressure loss coefficient	()
Z	loading factor	()
z	blade number	()

Subscript

0	total state
1	stator inlet
2	stator exit and rotor inlet
3	rotor exit
cond	condensing
evap	evaporating
h	hub
m	mean direction
N	stator
R	rotor
s	isentropic
t	tip
tt	total to total

REFERENCES

Ainley, D. G. and Mathieson, G. C. R. (1957). A method for performance estimation for axial-flow turbines. *ARC Technical Report , R. and M. No.2974, Great Britain*.

Angelino, G., Gaia, M., and Macchi, E. (1984). A review of italian activity in the field of Organic Rankine Cycles. *Proceedings of International VDI-Seminar, Zurich*.

Aungier, R. H. (2006). *Turbine Aerodynamics: Axial-Flow and Radial-Flow turbines Design and Analysis*. ASME, New York.

Balje, O. E. (1981). *Turbomachines: A Guide to Design, Selection and Theory*. Wiley, New York.

Craig, H. R. M. and Cox, H. J. A. (1971). Performance estimation of axial flow turbines. *Proceedings of the Institution of Mechanical Engineers 185, No.32: 407-423*.

Csanady, G. T. (1964). *Theory of Turbomachinery*. McGraw-Hill, Waterloo.

DaLio, L., Manente, G., and Lazzaretto, A. (2014). New efficiency charts for the optimum design of axial flow turbines for organic rankine cycles. *Energy 77: 447-459*.

Dunham, J. and Came, P. (1970). Improvements to the Ainley-Mathieson method of turbine performance prediction. *Trans. ASME Journal of Engineering for Power 92: 252-256*.

Heberle, F. and Brüggemann, D. (2006). Exergy based fluid selection for a geothermal organic Rankine cycle for combined heat and power generation. *Applied Thermal Engineering 30, 1326-1332*.

Kacker, S. C. and Okapuu, U. (1982). A mean line prediction method for axial flow turbine efficiency. *Trans. ASME Journal of Engineering for Power 104: 111-119*.

Khennich, M. and Galanis, N. (2012). Optimal design of ORC systems with a low-temperature heat source. *Entropy 14, 370-389*.

Lazzaretto, A. and Manente, G. (2014). A new criterion to optimize ORC design performance using efficiency correlations for axial and radial turbines. *International Journal of Thermodynamics Accepted for publication*.

Lemmon, E. W., Huber, M. L., and McLinden, M. O. (2010). NIST standard reference database 23: reference fluid thermodynamic and transport properties-RERPROP, version 9.0. *National Institute of Standards and Technology, Standard Reference Data Program, Gaithersburg*.

Li, S. M., Chu, T. L., Yoo, Y. S., and Ng, W. F. (2004). Transonic and low supersonic flow losses of two steam turbine blades at large incidences. *Trans. ASME Journal of Fluids Engineering 126: 966-975*.

Lozza, G. (2006). *Turbine a gas e cicli combinati*. (In Italian). Progetto Leonardo, Bologna, Italy.

Macchi, E. (1977). Design criteria for turbines operating with fluids having a low speed of sound. *Lecture Series n.100, Closed Gas Turbines, Von Karman Institute*.

Macchi, E. and Perdichizzi, A. (1981). Efficiency prediction for axial flow turbines operating with nonconventional fluids. *Trans. ASME Journal of Engineering for Power 103: 718-724*.

Moustapha, H., Zalesky, M. F., Baines, N. C., and Japikse, D. (2003). *Axial and Radial Turbines*. Concepts ETI.

Sauret, E. and Rowlands, A. S. (2011). Candidate radial-inflow turbines and high-density working fluids for geothermal power systems. *Energy 36, 4460-4467*.

Shepherd, D. (1956). *Principles of Turbomachinery*. The Macmillan Company, New York.

Smith, S. F. (1965). A simple correlation of turbine efficiency. *Journal of Aeronautical Society 69: 467-470*.

Tchanche, B. F., Papadakis, G., Lambrinos, G., and Frangoudakis, A. (2009). Fluid selection for a low-temperature solar organic Rankine cycle. *Applied Thermal Engineering 29, 2468-2476*.

Toffolo, A., Lazzaretto, A., Manente, G., and Paci, M. (2014). A multi-criteria approach for the optimal selection of working fluid and design parameters in Organic Rankine Cycle systems. *Applied Energy 121: 219-232*.

ORC APPLICATIONS FROM LOW GRADE HEAT SOURCES

Bernardo Peris[1]*, Joaquín Navarro-Esbrí[1,2], Francisco Molés[1], Adrián Mota-Babiloni[1, 3]

[1]ISTENER Research Group. Jaume I University
Castellón de la Plana, Castellón, Spain
bperis@uji.es

[2]EXPANDER TECH,Campus de RiuSec s/n, E12071, Castellón, Spain

[3]Institute for Industrial, Radiophysical and Environmental Safety. Polytechnic University
Valencia, Spain

* Corresponding Author

ABSTRACT

The Organic Rankine Cycle (ORC) has been proven as an efficient way to benefit from low grade heat sources, with a great interest in waste heat recovery and use of renewable heat sources. In this way, this work deals about three different applications implemented in Spain. The first application consists of a power only system for industrial waste heat recovery, taking advantage from the exhaust air of a ceramic furnace to produce a rated electrical power of 20 kW. The second application is a Combined Heat and Power (CHP) system integrated as a bottoming power cycle of an Internal Combustion Engine (ICE), with the purpose to recover waste heat from exhaust gases. This system is installed in a hospital to increase the ICE electrical production and generate hot water up to 90 ºC. The third application can operate producing power only or heat and power. In this last case, the ORC module is used to profit thermal energy from a biomass supported solar thermal system and producing a maximum electrical power about 6 kW and hot water above 80 ºC.

Moreover, focusing on the ORC modules performance, experimental data obtained from tests developed under different operating conditions in the three application cases are analyzed and discussed.

1. INTRODUCTION

The ORC (organic Rankine cycle) has been proven as an efficient way for power generation from low grade heat sources (Yamada *et al.*, 2014). It is a similar power cycle to the steam Rankine cycle, but uses more volatile fluids instead of water to improve the efficiency in low temperature applications (Li *et al.*, 2012). Its operating principle consists of recovering the thermal energy from the heat source through the evaporation of the working fluid and reducing the enthalpy in an expander to produce mechanical work, which is turned into electricity by an electric generator. This is a closed system, which condenses the vapor from the expander outlet and pressurizes the liquid to restart the cycle again. So, it is considered a simple cycle that requires little maintenance, compared to other power cycles like Kalina (Bombarda *et al.*, 2010), Goswami, transcritical cycle or trilateral-flash cycle (Chen *et al.*, 2010); in addition to its mature and proven technology against direct conversion techniques (thermo-electric, thermionic or piezoelectric) (Tchanche *et al.*, 2011).

The application of ORC systems are mainly focused on renewable and waste heat sources, with several examples like: solar thermal (M. Wang *et al.*, 2013), geothermal (Franco, 2011), oceanic (Tchanche *et al.*, 2011), biomass (Algieri & Morrone, 2012), waste heat from power plants (Dolz *et al.*, 2012), waste heat from industrial processes (D. Wang *et al.*, 2012) or others (H. Wang*et al.*, 2011).

Moreover, the ORC systems can be used for combined heat and power applications. Thus, the ORC can be used as a power only generation system (Yamada *et al.*, 2014), recovering the thermal energy from the heat source to produce electricity with the maximum efficiency achievable and rejecting the thermal energy from the condenser to the cold side. On the other hand, the thermal energy from the condenser also could be produced with a profitable temperature for users, reducing the electrical efficiency of the system, but increasing its global efficiency (Dentice d'Accadia *et al.*, 2003). Thereby, the ORC operates as a combined heat and power (CHP) system, requiring lower primary energy consumptions compared to a separate heat and power production, besides reducing global energy costs and pollutant emissions to the atmosphere.

Regarding to the ORC use for power applications, various studies can be found in the literature. So, Zhou *et al.*(2013) tested an ORC for waste heat recovery from flue gases. The authors used a liquefied petroleum gas stove to simulate the heat source and to control the temperature in the range of 90 to 220 ºC. The working fluid selected was R123 and a scroll expander, obtaining a maximum power output of 0.645 kW and a cycle efficiency of 8.5 %. Bracco *et al.* (2013) tested a small-size ORC, that used R245fa as working fluid and a scroll expander, for waste heat recovery. The heat source was simulated using an electric boiler, achieving a cycle efficiency between 8 and 9 %. Casci *et al.*(1981) used an ORC, with a rated electrical power of 40 kW, in a ceramic kiln to profit from flue gas waste heat. Forni *et al.*(2012) summarized various analysis of an ORC manufacturer in cement, glass, steel and oil&gas industries. The net electrical production went from 7.6 to 39.2 GWh/y, allowing payback periods from 7.2 to 9.2 years.

With respect to the ORC use for CHP applications, a great interest has received for residential and commercial applications. In this way, Dong *et al.* (2009) reviewed small and micro-scale biomass-fuelled CHP systems, comparing the ORC to other conversion technologies. The researchers pointed that the ORC encounters technical and economical obstacles, in comparison to medium and large-scale systems, requiring to reduce the specific investment cost and increment the electrical and CHP efficiencies. Experimental results obtained in a preliminary investigation were presented by Farrokhi *et al.* (2014) about a gas-fired ORC-based micro-CHP system for residential buildings. Thereby, using isopentane as working fluid and a vane type of expander, a maximum electrical power output of 0.774 kW and a net cycle electrical efficiency of 1.66% were achieved. Similarly, Qiu *et al* .(2012) experimented with a biomass-pellet boiler and an ORC for micro-CHP applications, by heating to 46 ºC the cooling water of the condenser outlet. The main working fluid used was HFE7000 and, again, a vane type of expander. So, 0.861 kW were generated with a gross electrical efficiency of 1.41% and a CHP efficiency of 78.69%. Declaye *et al.* (2013) characterized an oil-free scroll expander using R245fa as working fluid, showing that the cycle could produce up to 50 ºC of useful heat, a maximum shaft power of 2.1 kW and mechanical efficiency of 8.5%.

From the reviewed information, different applications and uses for the ORC can be observed. However, few works address the final application of the ORC and its experimental performance when a commercial module is used. In this way, this work deals about three different ORC applications implemented in Spain. The first application consists of using an ORC as a power only system, the second one uses the ORC as a CHP system and the last application was designed to operate with the ORC in both modes, power only and CHP. Thereby, these applications are addressed in this paper. Moreover, experimental data obtained from the tests developed in each ORC module are exposed and discussed.

For this purpose, the rest of the paper is organized as follows. Section 2 presents the three application cases. Section 3 describes the main characteristics of the ORC modules. Section 4 exposes the main results of the experimental characterization. Finally, Section 5 summarizes the main conclusions of the work.

2. APPLICATIONS DESCRIPTION

This section describes the three applications addressed in this work.

2.1 Power only application

This application consists of profiting waste heat from exhaust gases of a ceramic furnace. Specifically, recovering the waste heat available in the indirect cooling air, which are clean gases with high temperature, due to its proximity to the furnace burners the furnace. The recovery facility is mainly composed by a recuperator heat exchanger, located in a bypass of the cooling air duct, and a heat transfer loop with thermal oil that transports the thermal energy from the heat source to the ORC module, as Fig. 1.a to Fig. 1c show. Moreover, Fig. 1.d shows the scheme of the facility.

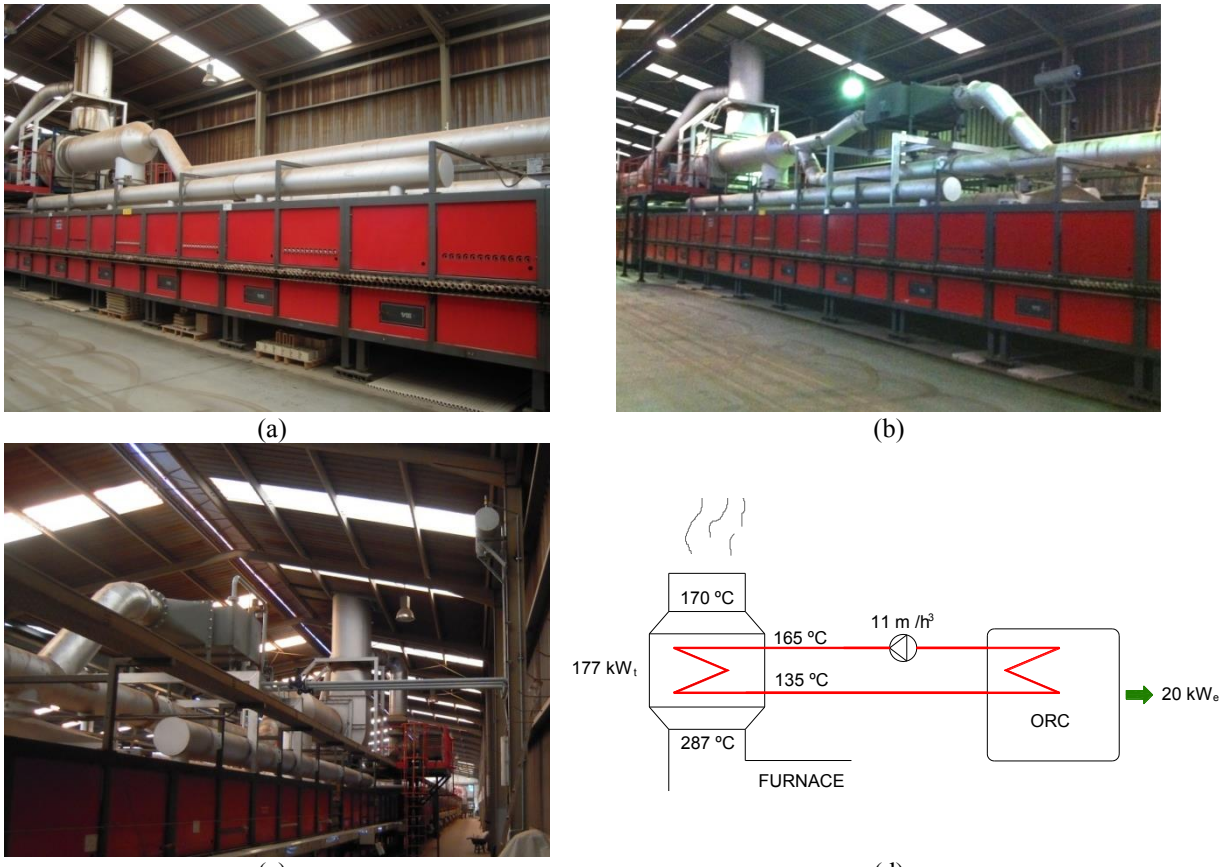

Figure 1: Industrial furnace of Keros Ceramica and heat recovery facility: (a) original facility, (b) modified facility, (c) heat transfer loop, (d) facility scheme.

The main features of the recuperator heat exchanger are listed in Table 1. This heat exchanger was designed to recover a thermal power of 177 kW from the heat source and provide thermal oil at 165 ºC to the ORC module.

Table 1: Recuperator heat exchanger features.

Thermal capacity (kW)	177
Air volumetric flow rate ($Nm^3 \cdot s^{-1}$)	1.15
Air temperatures (ºC)	287/170
Oil temperatures (ºC)	135/165
Air pressure drop (mbar)	1.90
Thermal oil pressure drop (bar)	0.8
Surface (m^2)	65.6

2.2Combined heat and power application

The original facility consisted of an Internal Combustion Engine (ICE) for a CHP application in a hospital located in Ourense (Spain). This ICE was designed to provide a rated electrical power of 1,200 kW and up to 400 kW of useful heat from the exhaust gases, as Fig. 2.a represents. Then, the aim of the project was to replace the heat exchanger by an ORC system, producing a similar useful heat, at the same temperature of 90 ºC, and more electricity, as Fig. 2.b represents.

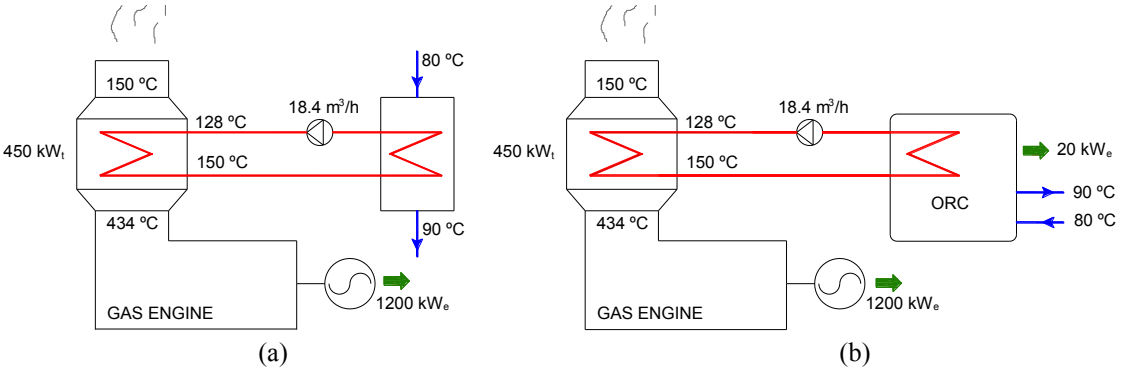

Figure 2: Heat source of the ORC system: (a) scheme of the original facility with heat exchanger, (b) scheme of the improved facility through ORC.

The main features of the recuperator heat exchanger, integrated in the chimney, are listed in Table 2. This heat exchanger was designed to recover a thermal power of 450 kW from the heat source and provide pressurized water at 150 ºC to the ORC module.

Table 2: Recuperator heat exchanger features.

Thermal capacity (kW)	450
Exhaust gas flow rate (kg/h)	5,191
Exhaust gas temperatures (ºC)	434/150
Pressurized water temperatures (ºC)	128/150
Exhaust gas pressure drop (mbar)	17
Pressurized water pressure drop (mbar)	50
Surface (m^2)	76

2.3 Power and CHP application

This system was designed to operate with renewable heat sources, specifically a biomass supported solar thermal system. Thus, the ORC should operate efficiently in both modes, power only generation and CHP production.

A typical architecture of the facility in which the ORC is integrated is illustrated in Fig. 3.a. Fig. 3.b shows the scheme of the facility. Furthermore, the design specifications from customers of this module are listed in Table 3.

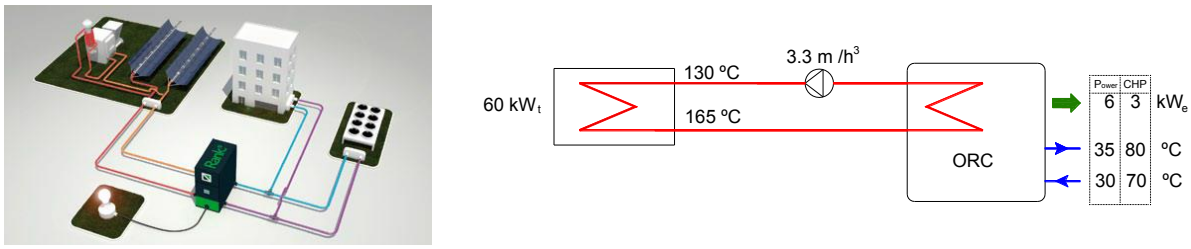

Figure 3: Power and CHP applications: (a) typical architecture, (b) facility scheme.

Table 3: Design specifications.

Thermal power input (kW)	60
Thermal fluid	Oil or Water-glycol (10%)
Inlet temperature of the thermal fluid (ºC)	165
Inlet temperature of cooling water in generation mode (ºC)	30
Inlet temperature of cooling water in CHP mode (ºC)	70

3. ORC MODULES DESCRIPTION

This section describes the main characteristics of the ORC modules, shown in Fig. 4, addressing the cycle configuration, working fluid, expander and dissipation system.

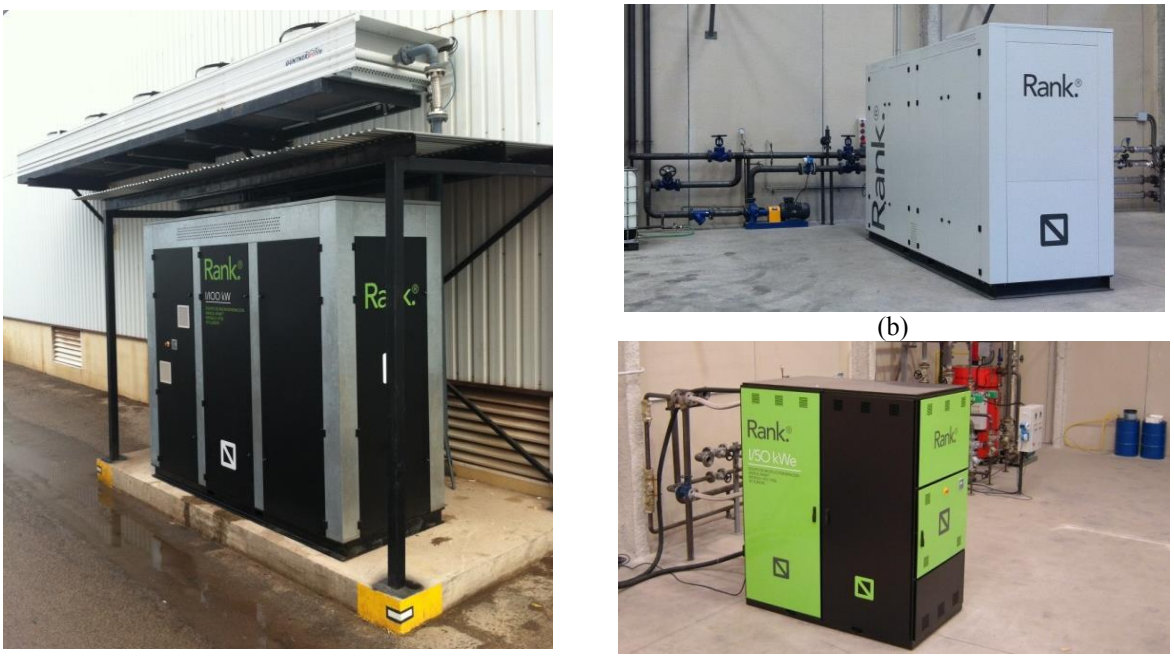

(a) (b) (c)

Figure 4: ORC modules: (a) Power generation system integrated in the industrial application, (b) CHP system during tests, (c) Power only and CHP system during tests.

3.1 Cycle configuration and working fluid

All the ORC systems used in these applications are commercial modules from Rank®, whose main characteristics are summarized in Table 4. In these studied cases, the modules employ the same architecture and use the same working fluid. Regarding to the architecture, the regenerative configuration is used. This configuration allows recovering the thermal energy from the heat source, besides the waste heat from the expander outlet to preheat the liquid, improving the cycle electrical efficiency. The working fluid used is R245fa, commonly used among ORC manufacturers (Vélez *et al.*, 2012) and the researches reviewed. This is a non flammable fluid with low toxicity and moderate environmental properties, which also has been proven as an efficient fluid for low grade waste heat recovery (Peris *et al.*, 2013). However, the characteristics of the expander differ in function of each application.

Table 4: Main characteristics of the ORC modules used.

Cycle configuration	subcritical, regenerative with superheating
Working fluid	R245fa
Expander technology	volumetric
Heat exchangers type	brazed plate
Maximum operating temperature (ºC)	170
Maximum dissipating temperature (ºC)	90

3.2 Expander

The ORC modules use rotary volumetric expanders, whose sizes, speeds and volume ratios (Vi) have been optimized to achieve the maximum efficiency during the operating point, established as design conditions. In this way, Table 5 collects the maximum efficiency ($\varepsilon_{el,\ ise}$) of the expanders and the pressure ratio (r_p) in which it was achieved. As it can be seen, the ORC designed for the power application operates efficiently at a high pressure ratio (Peris *et al.*, 2015a). In contrast, the ORC designed for the CHP application only operates efficiently at low pressure ratios. On the other hand, the third application can operate with an intermediate efficiency in both modes, being a suitable solution for a flexible system.

Table 5: Experimental expander efficiencies and its associated pressure ratios.

	$\varepsilon_{el,ise}$ (%)	r_p	References
Power application	64.89	7.93	(Peris *et al.*, 2015b)
CHP application	68.54	2.61	(Peris*et al.*, 2015c)
Power and CHP	63.77	4.10	(Peris*et al.*, 2015d)

3.3 Dissipation system

The dissipation system varies in function of the type of application. So, in a power application the thermal energy from the condenser is rejected to the ambient. For this, the dissipation system was directly implemented through an air condenser, previously shown in Fig. 4.a. This system allows reducing exergetic losses compared to a dry cooler with cooling water, besides simplifying the scheme, since there is not required another pump nor its associated safety and control devices.

On the other hand, in a CHP application the thermal energy from the condenser is considered as useful heat for users. So, the hot water from the outlet of the condenser could directly feed consumers. In order to simulate this consumption, a dry cooler with cooling water was used during tests. Thereby, reducing the dry coolers fans velocity, the condensing temperature was controlled. So, both modes, power, with fans at full velocity, and CHP, with fans at reduced velocity, were simulated during tests. The dissipation systems used in the tests are shown in Fig. 5.

(a) (b)

Figure 5: Dissipation systems: (a) CHP system, (b) power and CHP system.

4. RESULTS

In this section, the gross electrical efficiency of the cycle (η_g) and the expander electrical isentropic effectiveness ($\varepsilon_{el,\ ise}$) obtained during tests are presented and discussed.

Regarding to the ORC for power applications, Fig. 6.a shows that a maximum gross electrical efficiency of 12.47% is obtained. This efficiency is reached with a pressure ratio about 8, being a system optimized for its operating conditions. Moreover, Fig. 6.b shows that the expander operates with a stable effectiveness for high pressure ratios.

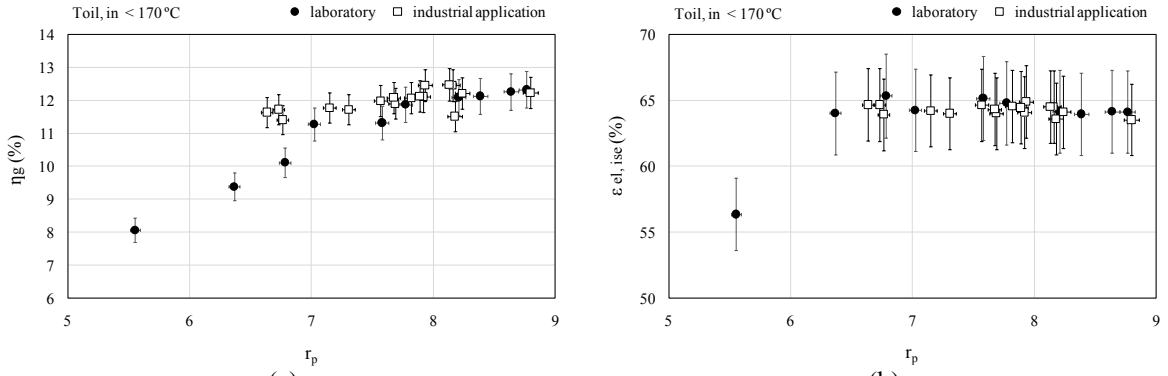

Figure 6: ORC for power applications: (a) gross electrical efficiency, (b) expander electrical isentropic effectiveness.

Regarding to the ORC for CHP applications, Fig. 7.a shows that a maximum gross electrical efficiency of 9.40% is obtained. This low value, compared to the latter, is mainly due to the different expander used. So, Fig. 7.b shows that the expander is optimized for a pressure ratio between 2-3, which is a suitable value to operate in CHP applications, but a poor value for power only generation.

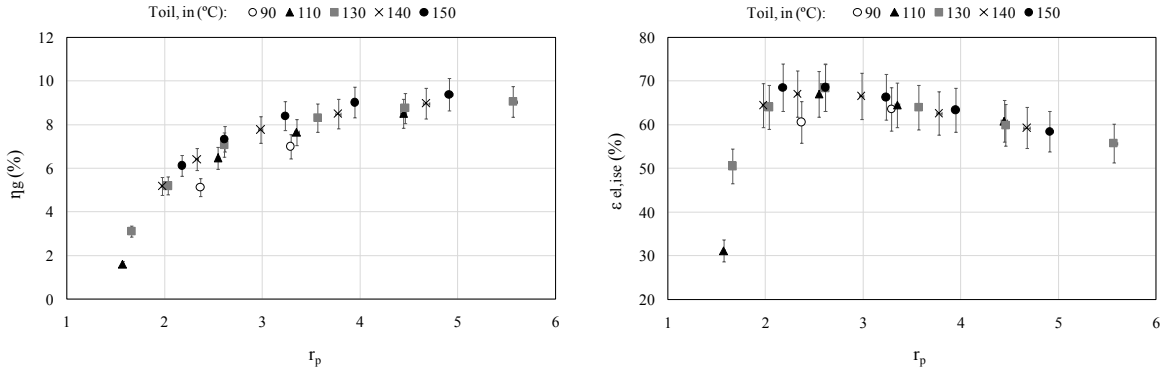

Figure 7: ORC for CHP applications: (a) gross electrical efficiency, (b) expander electrical isentropic effectiveness.

As it has been said above, the third application was designed using an expander with an intermediate Vi, that allows the operation in both modes, power only and CHP. Thereby, Fig. 8.a shows that the maximum value of electrical efficiency remains between the two previous ORC systems, with a maximum of 10.64%. The electrical effectiveness of the expander was maximized for a pressure ratio above 4, as Fig. 8.b shows, being a module suitable to operate with a moderate efficiency in both modes, but not optimized in comparison with the previous two modules.

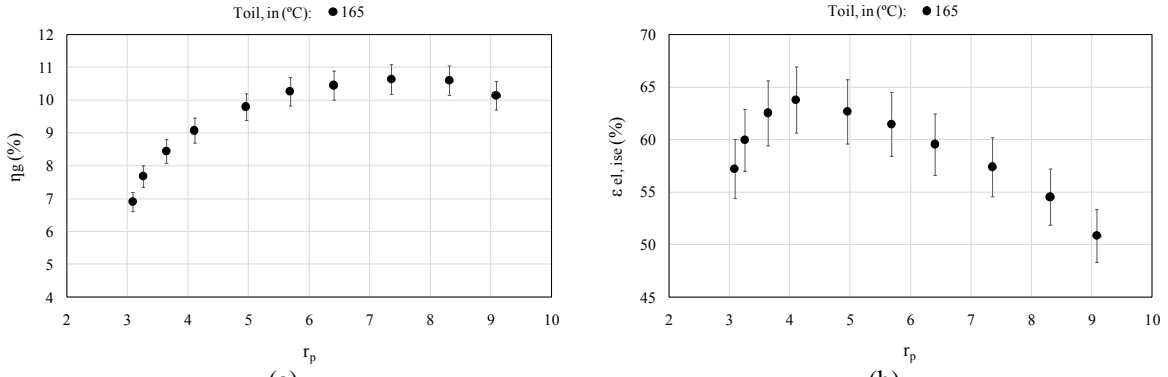

Figure 8: ORC for power and CHP applications: (a) gross electrical efficiency, (b) expander electrical isentropic effectiveness.

5. CONCLUSIONS

This work deals about three different applications developed using ORC systems in Spain. For this, the heat source, dissipation system and the main characteristics of the ORC are addressed. Moreover, the main results of the experimental characterization of each module are presented and analyzed.

In this way, the results show that the expander plays a key role in the optimization of a system for a specific application. So, a large Vi is recommended to operate in power applications, demonstrating a gross electrical efficiency of 12.47% with activation temperatures about 165ºC. A small Vi is preferable for CHP applications, being able to provide hot water up to 90 ºC with an acceptable gross electrical efficiency of 9.40%, with activation temperatures about 150ºC. However, if the system requires operating in both modes, power and CHP, an intermediate Vi results a suitable solution. So, the experimental data show a maximum gross electrical efficiency of 10.64% with activation temperature about 165ºC.

NOMENCLATURE

ε	effectiveness	(%)
η	efficiency	(%)
r_p	pressure ratio	
Vi	built-in volume ratio	

Subscripts

el	electrical
g	gross
ise	isentropic

REFERENCES

Algieri, A., & Morrone, P., 2012, Comparative energetic analysis of high-temperature subcritical and transcritical Organic Rankine Cycle (ORC). A biomass application in the Sibari district,*Applied Thermal Engineering*, *36*, 236–244.

Bombarda, P., Invernizzi, C. M., & Pietra, C., 2010, Heat recovery from Diesel engines: A thermodynamic comparison between Kalina and ORC cycles,*Applied Thermal Engineering*, *30*(2-3), 212–219.

Bracco, R., Clemente, S., Micheli, D., & Reini, M., 2013, Experimental tests and modelization of a domestic-scale ORC (Organic Rankine Cycle),*Energy*, *58*, 107–116.

Casci, C., Angelino, G., Ferrari, P., Gaia, M., Giglioli, G., & Macchi, E., 1981, Heat recovery in a ceramic kiln with an organic rankine cycle engine,*Journal of Heat Recovery Systems*, *1*, 125–131.

Chen, H., Goswami, D. Y., & Stefanakos, E. K., 2010, A review of thermodynamic cycles and working fluids for the conversion of low-grade heat, *Renewable and Sustainable Energy Reviews*, *14*(9), 3059–3067.

Declaye, S., Quoilin, S., Guillaume, L., & Lemort, V., 2013, Experimental study on an open-drive scroll expander integrated into an ORC (Organic Rankine Cycle) system with R245fa as working fluid,*Energy*, *55*, 173–183.

Dentice d'Accadia, M., Sasso, M., Sibilio, S., & Vanoli, L., 2003, Micro-combined heat and power in residential and light commercial applications,*Applied Thermal Engineering*, *23*, 1247–1259.

Dolz, V., Novella, R., García, a., & Sánchez, J., 2012, HD Diesel engine equipped with a bottoming Rankine cycle as a waste heat recovery system. Part 1: Study and analysis of the waste heat energy,*Applied Thermal Engineering*, *36*, 269–278.

Dong, L., Liu, H., & Riffat, S., 2009, Development of small-scale and micro-scale biomass-fuelled CHP systems - A literature review,*Applied Thermal Engineering*, *29*(11-12), 2119–2126.

Farrokhi, M., Noie, S. H., & Akbarzadeh, a. a., 2014, Preliminary experimental investigation of a natural gas-fired ORC-based micro-CHP system for residential buildings,*Applied Thermal Engineering*, *69*(1-2), 221–229.

Forni, D., Vaccari, V., Santo, D. Di, & Baresi, M., 2012, Heat recovery for electricity generation in industry, ECEE 2012 Summer Study on Energy Efficiency in Industry, 523–534.

Franco, A., 2011, Power production from a moderate temperature geothermal resource with regenerative Organic Rankine Cycles,*Energy for Sustainable Development*, *15*(4), 411–419.

Li, J., Pei, G., Li, Y., Wang, D., & Ji, J., 2012, Energetic and exergetic investigation of an organic Rankine cycle at different heat source temperatures,*Energy*, *38*(1), 85–95.

Peris, B., Navarro-Esbrí, J., & Molés, F., 2013, Bottoming organic Rankine cycle configurations to increase Internal Combustion Engines power output from cooling water waste heat recovery,*Applied Thermal Engineering*, *61*(2), 364–371.

Peris, B., Navarro-Esbrí, J., Molés, F., Mota-Babiloni, A., 2015,Experimental study of an ORC (organic Rankine cycle) for low grade waste heat recovery in a ceramic industry,*Energy,* doi:10.1016/j.energy.2015.03.065.

Peris, B., Navarro-Esbrí, J., Molés, F., Collado, R., & Mota-Babiloni, A., 2015, Performance evaluation of an Organic Rankine Cycle (ORC) for power applications from low grade heat sources,*Applied Thermal Engineering*, *75*, 763–769.

Peris, B., Navarro-Esbrí, J., Molés, F., González, M., & Mota-Babiloni, A., 2015, Experimental characterization of an ORC (organic Rankine cycle) for power and CHP (combined heat and power) applications from low grade heat sources,*Energy*, *82*, 269–276.

Peris, B., Navarro-Esbrí, J., Molés, F., Martí, J. P., & Mota-Babiloni, A., 2015, Experimental characterization of an Organic Rankine Cycle (ORC) for micro-scale CHP applications,*Applied Thermal Engineering*, *79*, 1–8.

Qiu, G., Shao, Y., Li, J., Liu, H., & Riffat, S. B., 2012, Experimental investigation of a biomass-fired ORC-based micro-CHP for domestic applications,*Fuel*, *96*, 374–382.

Tchanche, B. F., Lambrinos, G., Frangoudakis, a., & Papadakis, G. (2011), Low-grade heat conversion into power using organic Rankine cycles - A review of various applications,*Renewable and Sustainable Energy Reviews*, *15*, 3963–3979.

Vélez, F., Segovia, J. J., Martín, M. C., Antolín, G., Chejne, F., & Quijano, A., 2012, A technical, economical and market review of organic Rankine cycles for the conversion of low-grade heat for power generation,*Renewable and Sustainable Energy Reviews*, *16*(6), 4175–4189.

Wang, D., Ling, X., & Peng, H., 2012, Performance analysis of double organic Rankine cycle for discontinuous low temperature waste heat recovery,*Applied Thermal Engineering*, *48*, 63–71.

Wang, H., Peterson, R., & Herron, T., 2011, Design study of configurations on system COP for a combined ORC (organic Rankine cycle) and VCC (vapor compression cycle),*Energy*, *36*(8), 4809–4820.

Wang, M., Wang, J., Zhao, Y., Zhao, P., & Dai, Y., 2013, Thermodynamic analysis and optimization of a solar-driven regenerative organic Rankine cycle (ORC) based on flat-plate solar collectors,*Applied Thermal Engineering*, *50*(1), 816–825.

Yamada, N., Tominaga, Y., & Yoshida, T., 2014, Demonstration of 10- W p micro organic Rankine cycle generator for low-grade heat recovery,*Energy*, *78*, 806–813.

Zhou, N., Wang, X., Chen, Z., & Wang, Z., 2013, Experimental study on Organic Rankine Cycle for waste heat recovery from low-temperature flue gas,*Energy*, *55*, 216–225.

ACKNOWLEDGEMENT

The authors are indebted to the Minister of industry of ‘GeneralitatValenciana’ (Spain) for its financial assistance under project INIDIV2010022 and Rank®, the ORC manufacturer, for its support in this project. Also to thank greatly the Jaume I University for its financial support under the PhD grant PREDOC/2013/28 of ‘Convocatòriad'ajudespredoctorals per a la formació de personal investigadordelPla de promoció de la investigació de la UniversitatJaume I de Castelló (Spain)’.

TESTING AND MODELING A VANE EXPANDER USED IN AN ORC WORKING WITH HEXAMETHYLDISILOXANE (MM)

Vaclav Vodicka[1]*, Ludovic Guillaume[2], Jakub Mascuch[3] and Vincent Lemort[4]

[1, 3] University Centre for Energy Efficient Buildings
Czech Technical University in Prague
Trinecka 1024, 273 43 Bustehrad
Czech Republic
[1] e-mail: vaclav.vodicka@uceeb.cz
[3] e-mail: jakub.mascuch@uceeb.cz

[2, 4] Thermodynamics Laboratory
University of Liège
Campus du Sart Tilman, B49, 4000 Liège
Belgium
[2] e-mail: ludovic.guillaume@ulg.ac.be
[4] e-mail: vincent.lemort@ulg.ac.be

* Corresponding Author

ABSTRACT

Waste heat from industrial production carries considerable potential for further use. Organic Rankine Cycle (ORC) brings a possibility to produce electrical energy from heat, originally intended to be released to the surroundings. For ORC systems with power output up to 10 kW, small-scale turbines are still expensive to manufacture and their use can be problematic in terms of high shaft speed or quality of inlet vapor. It is therefore preferable to use positive displacement expanders. The first part of this paper presents and analyses the measurements conducted on a prototype of vane expander. This vane expander characterized by a 1 kW power output operates in an ORC heat engine that uses hexamethyldisiloxane as a working fluid. The expander inlet temperature varies approximately from 135 °C to 150 °C, inlet pressure varies approximately from 200 to 300 kPa abs, isentropic efficiency from 0.4 to 0.58. The second part of the paper proposes a grey-box model, which is calibrated on the base of the measured data. This lumped-parameter model takes into consideration major losses of the expander: supply and discharge pressure losses, under and over-expansion, internal leakages and mechanical losses. The model is finally used to assess the impact of each source of losses on the overall performance of the expander.

1. INTRODUCTION

ORC technology seems to be a promising solution for waste heat recovery (WHR) and combined heat and power (CHP) generation especially in a small scale (up to 10 kW_{el}). Waste heat can be recovered from many industrial processes or combustion engines; small scale CHP units for households and small businesses fit into the concept of smart grids. Rising amount of publications focused on devices with low power output shows strong importance of this topic. According to Qiu et al. (2011) the use of positive displacement expanders especially scroll or vane type is a good choice for low power ORC applications because of their low cost and good efficiency over a wide range of operating conditions. One of the most noticeable advantages of positive displacement expanders is insensitivity on a quality of admission vapor compared to turbine technology. This allows a simplification of design of a cycle and its controlling algorithms. Only a few recently published papers (e.g. Cipollone, 2014, Xia, 2013,

Yang, 2008) present experimental measurement and evaluation of sliding vane expanders. This paper presents an experimental characteristics of a sliding vane expander used in an ORC operating with hexamethyldisiloxane (MM) as a working fluid. This ORC was built and is operated at University Centre for Energy Efficient Buildings (UCEEB) at Czech Technical University (CTU) in Prague. Ongoing project at UCEEB are focused on market favorable technology especially in terms of specific cost. Various topics related to decentralized power generation were in focus at Faculty of Mechanical Engineerging (FME) at CTU in Prague. Both technical and economic issues were investigated. Current experimental work at UCEEB is based on nearly 6 years experiences from ORC construction and its operation at FME. According to economic analysis presented by Mascuch and Dlouhy (2011) a new approach to low power ORC design was developed at FME. Small CHP unit with a biomass boiler was built and operated. Boiler was separated from ORC by thermal oil circuit. Isopropylbenzene was used as a working fluid. Many engineering challenges had to be solved during this work. In general, this type of design was not successful. It was found out that the ORC has to be redesigned to be as simple as possible for the future commercial success. Total gross electrical efficiency was about 5.7% and a vane expander reached 38% of thermodynamic efficiency. Numbers were more than 50% lower than design estimations.

2. DESCRIPTION OF EXPERIMENTAL ORC TEST RIG

The experimental test rig with organic Rankine cycle at UCEEB is used for testing not only single components but also the whole cycle. Its scheme is shown in figure 1. ORC is designed as single-circuit. In the working fluid (MM) is dissolved about 5% of lubricating oil. Heat input to the cycle is approximately 20-23 kW. Main components are the evaporator, the expander, the condenser, the condensate receiver and the feed pump. Evaporator is a spiral tube exchanger. Flue gas from diesel burner is used as a source of heat. Flue gas inlet temperature ranges between 370 °C and 410 °C, outlet temperature is between 100°C and 130°C.

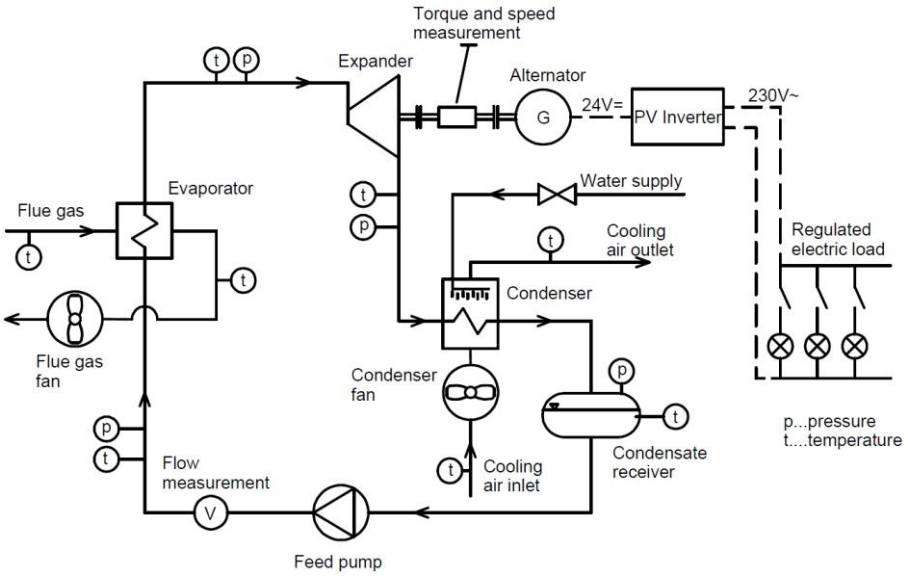

Figure 1: Scheme of the test rig

Generated vapor comes into a vane expander of own design. The expander is connected directly with the evaporator without any control valve. The expander drives a 24 VDC automotive alternator, which is connected with a common photovoltaic inverter. Bulbs with a total power consumption of 635 W are used as an electric load. Regulation step is 5 W. It is possible to connect additional load with constant power consumption as well. Condenser is similar to evaporator. It is a spiral tube exchanger designed with focus on low pressure drop. Condensation occurs inside the tubes. Condenser is air-cooled; fan speed is regulated by frequency inverter. Cooling air temperature at the inlet was about

30 – 35 °C. Water sprinkler that improves the cooling performance of the condenser was mounted above the condenser to decrease the condensing pressure even more. Condenser is followed by condensate receiver under which is placed a gear pump. The pump is connected with an asynchronous motor with nominal speed of 1500 RPM. Speed can be regulated with frequency inverter. Maximum flow is 8.5 l/min at nominal speed.
Position of all sensors can be seen in figure 1. The test rig allows measurement of temperatures at important points of the cycle, pressures, volumetric flow at the pump outlet, shaft speed of the expander and torque. Temperature of the flue gas at evaporator inlet and outlet and cooling air temperature at condenser inlet and outlet is also measured. Unfortunately it is not possible to measure the flow of flue gas and cooling air reliably. All the temperatures are measured with Pt100 sensors. Pressures are measured with common industrial piezoresistive pressure transducers. Turbine flow meter with pulse output is used for measurement of volumetric flow. Torque and speed is measured within one sensor – speed with pulse output, torque with bridge strain gauge with transducer. The data from the sensors are collected with common industrial PLC. Table 1 summarizes accuracy of used sensors.

Sensor	Range	Accuracy
Pressure - low pressure side	(0-400) kPa abs.	±0.5% f.s.
Pressure - high pressure side	(0-1000) kPa abs.	±0.5% f.s.
Temperature	(-196 - +600) °C	±(0.30°C+0.005|t|)
Volumetric flow	(1-10) l/min	±3% of reading
Torque	(0-30) Nm	±0.2% f.s.
Speed	(0-15000) RPM	±0.2% f.s.

Table 1: Range and accuracy of used sensors

Different working conditions can be reached in several ways. The shaft speed of expander can be regulated by switching the electric bulbs on and off. Decrease in the electric load results in torque reduction of alternator and shaft speed increase. Superheating of vapor can be influenced by changing the speed of pump. Lower speed leads to lower flow rate through the evaporator and larger superheating. Pressure in condenser and isentropic enthalpy gradient of expander can be influenced by changing the speed of the condenser fan and by use of the additional cooling with the water sprinkler. Performance of diesel burner slightly varied during the experiments due to decreasing of the level of fuel in a tank. Unfortunately this phenomenon cannot be controlled.

3. PROTOTYPE OF VANE EXPANDER

Expander is one of the most important components of the ORC. Its performance has significant impact on the efficiency of the whole cycle. As already written, expansion is ensured by the vane expander. This prototype was designed and built because there is no commercially available and cheap expander with a low power output of several kW. Vane expander was selected because of simple design, low manufacturing costs, reliability and possibility of reaching good thermodynamic efficiency in case of optimal design (Aoun, 2008). Design of tested expander is shown in figure 2. Expander is semi-hermetical; torque transmission is ensured by a magnetic coupling with permanent magnets. Stator is designed as a monoblock, in which a cylindrical working space, space for bearings and inlet and outlet chamber are milled. Supply and exhaust of the working fluid is radial. Rotor faces with bearings are mounted to the rotor with bolts. The bearings are placed in the stator with radial clearance, the axial movement of rotor is allowed. Rotor faces have grooves which serve for guiding the vanes during rotation. Rotor faces also create boundary of the working chambers. All the parts of the expander are made of stainless steel except the vanes, which are made of graphite. Expander has 8 working chambers with displacement of 7.66 cm^3 per one chamber. Nominal built-in volumetric expansion ratio is 3. Expander is designed to produce 1 kW of mechanical power with overall efficiency of 0.41 at the nominal conditions of the cycle. Nominal shaft speed is 3020 RPM.

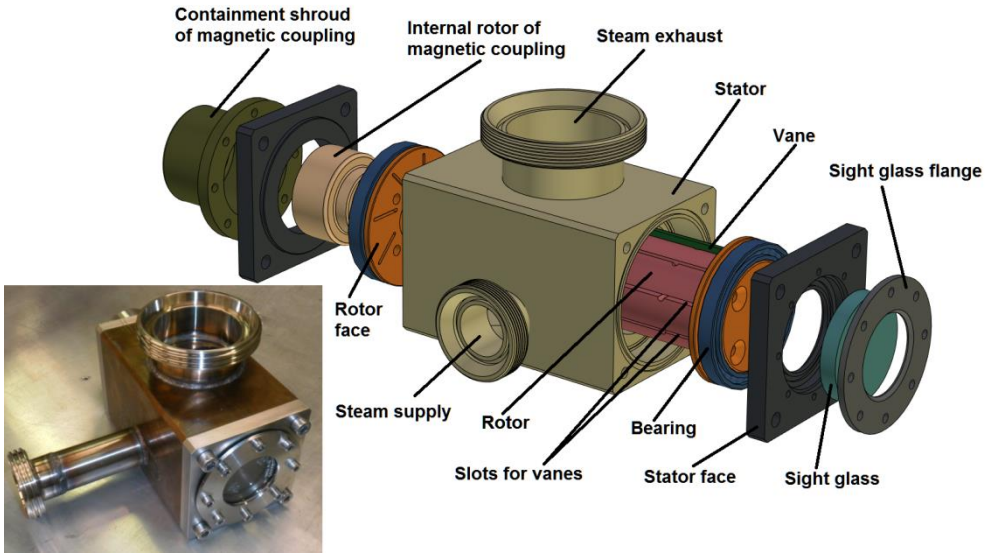

Figure 2: Design of the vane expander

It is necessary to ensure permanent contact of vanes with the inner stator surface for a proper function of the expander so that the working chambers are separated and there is no flow between adjacent chambers. Vanes are drawn out due to centrifugal force but only in case that this force is greater than a force resulting from the pressure difference above and below the vanes. Force resulting from pressure difference can be much higher than the centrifugal force especially during the initial phase of expansion. Therefore each slot for the vane in the stator has two milled grooves which connect working chamber with the space below the vane to balance the pressures. Similar solution is described by Peterson and McGahan (1972) for a vane compressor with the difference that the grooves are milled in the vanes. Another solution is to use the springs below the vanes as described e.g. by Yang *et al.* (2008).

4. EXPERIMENTAL CAMPAIGN

The measured data were recorded every second during the experiments. They were evaluated always in steady states. All the recorded values were averaged at each stable state with a period of 3 to 7 minutes. 60 steady states were captured and evaluated.

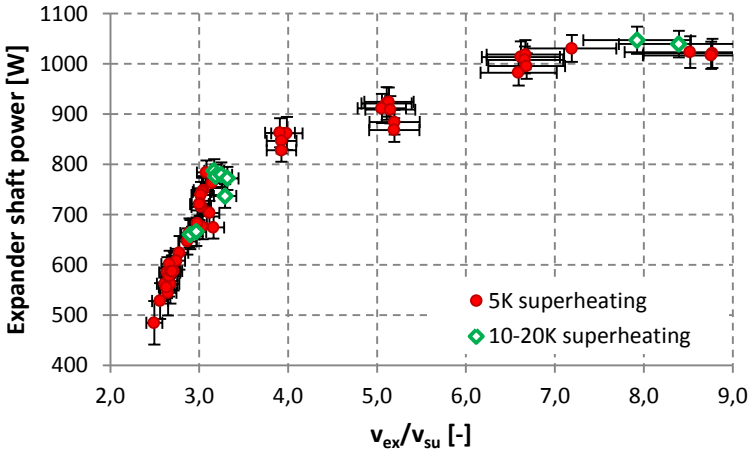

Figure 3: Measured values of expander shaft power

Admission temperature ranged from 135 to 157°C, admission pressure from 221 to 296 kPa abs., discharge pressure from 27 to 117 kPa abs. Superheating of admission vapor was maintained

at 5 K (±0.5K) during most of measurements. Several states were measured with the superheating of 10-20 K. Figure 3 shows dependence between expander shaft power and a ratio of specific volume of vapor at expander outlet and inlet (v_{ex}/v_{su}). It can be seen that the performance rises rapidly in the area where v_{ex}/v_{su} = 2.5-3.2.

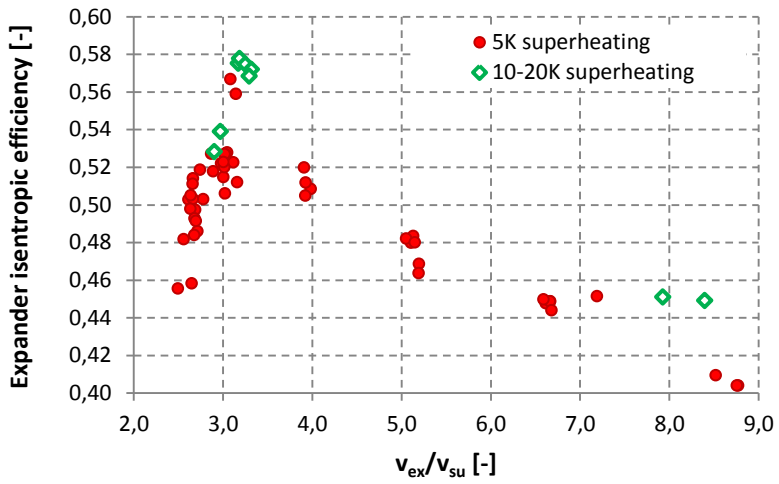

Figure 4: Expander isentropic efficiency vs. v_{ex}/v_{su}

The expander isentropic efficiency defined in equation 1 is shown in figure 4.

$$\eta_s = \frac{\dot{W}_{shaft}}{\dot{M}_{wf} \cdot (h_{su} - h_{ex,s})} \tag{1}$$

Rapid increase of efficiency can be seen in the same range of values v_{ex}/v_{su}. The highest values of expander efficiency are at v_{ex}/v_{su} = 3.2. This value approximately corresponds to the built-in volumetric expansion ratio of the expander ($r_{v,in}$=3). The efficiency falls in case that the value v_{ex}/v_{su} is higher than approximately 3.5. Performance of the expander ranged from 480 to 1050 W. Expander efficiency ranged from 0.4 to 0.58. Efficiency curve corresponds to the theoretical model. Fluctuation of values of efficiency is caused mainly because of a fluctuation of speed and, to a lesser extent, probably due to other effects. The points with superheating of 10-20 K are also highlighted in the graph in fig. 4. Only 10 stable states were measured in these conditions. It can be seen that the higher superheating mean higher efficiency in all cases. However, this fact is needed to be confirmed by further measurements. The dependence between expander efficiency and admission vapor superheating should be also measured in the future.

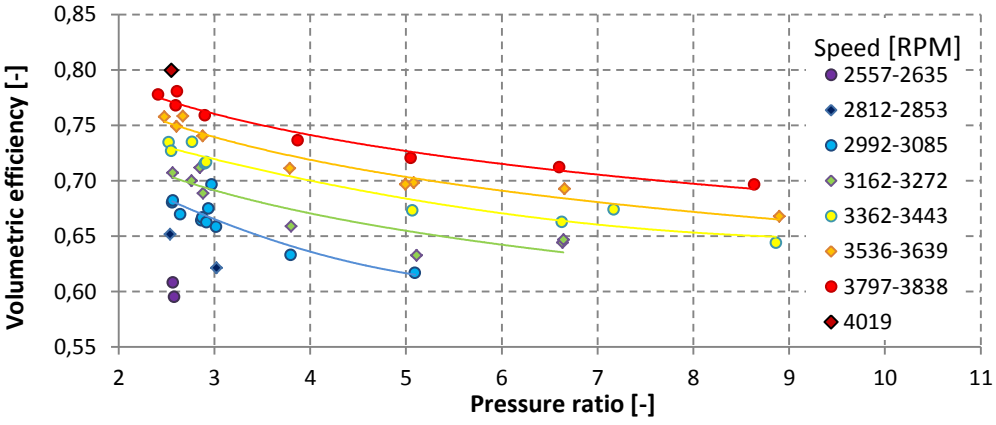

Figure 5: Volumetric efficiency vs. pressure ratio and speed, 5K superheating

Figure 5 shows the dependency of volumetric efficiency (which is defined by the equation 2) on pressure ratio and expander shaft speed. Shaft speed ranged from approximately 2550 to 4000 RPM.

$$\eta_{vol} = \frac{N_{rot,\exp} \cdot c \cdot V_c}{60 \cdot \dot{M}_{wf} \cdot v_{su}} \tag{2}$$

It was difficult to maintain precise speed of expander due to characteristics of built-in regulator in alternator. For this reason the speed and the volumetric efficiency fluctuate a bit. Nevertheless it can be seen that the value of volumetric efficiency rises with the increase of speed. This is caused by rising of the overall flow through the expander when the total leakage within the expander remains almost the same. There is also declining trend of volumetric efficiency with increasing of pressure ratio within the expander. Higher pressure ratio leads to greater leakage of working fluid from the working chambers of the expander.

5. MODELING

A semi-empirical model was calibrated on the base of the measured data. This lumped-parameter model takes into consideration major losses of the expander such as supply and discharge pressure losses, under and over-expansion, internal leakages and mechanical losses (figure 6). The model parameters were identified for the expander under investigation, integrated into a Rankine cycle and fed with hexamethyldisiloxane.

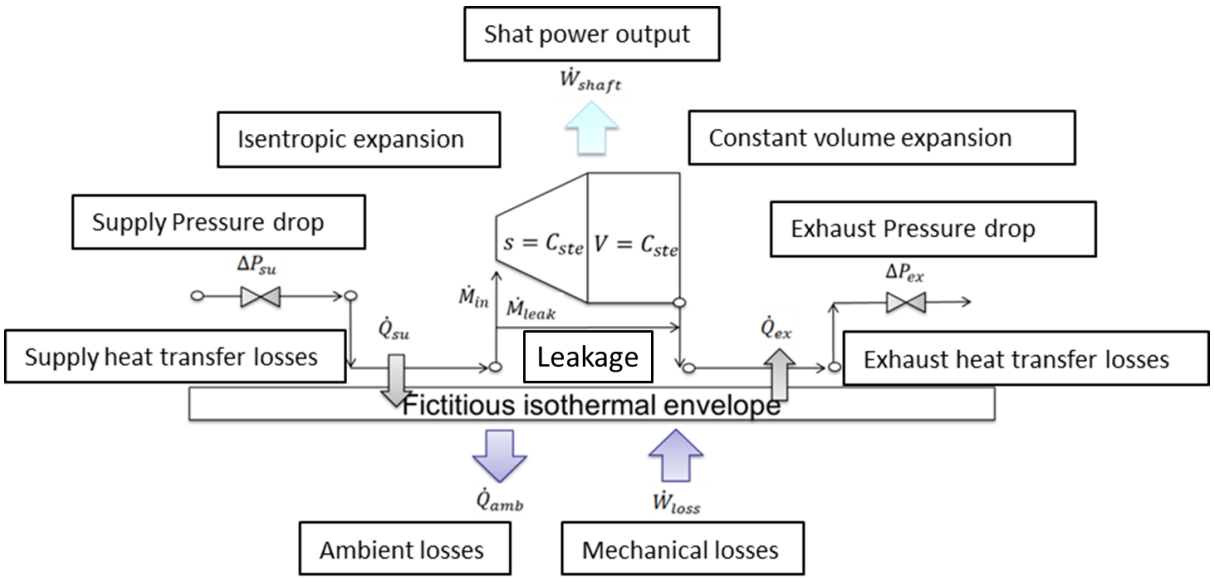

Figure 6: Schematic of the semi-empirical model

The parameter identification process was illustrated by Lemort (2009). The input variables of the model are the supply pressure, the supply temperature, the exhaust pressure and the rotational speed of the expander. The model then calculates the mass flow rate displaced by the expander, the delivered mechanical power and the exhaust temperature. A particular attention was dedicated to the identification of the leakage area parameter. Indeed, as it can be seen, this parameter almost evolves as the inverse of the rotational speed (figure 7). But it could also be shown that it depends on the pressure difference over the expansion machine and of the fluid inlet temperature.

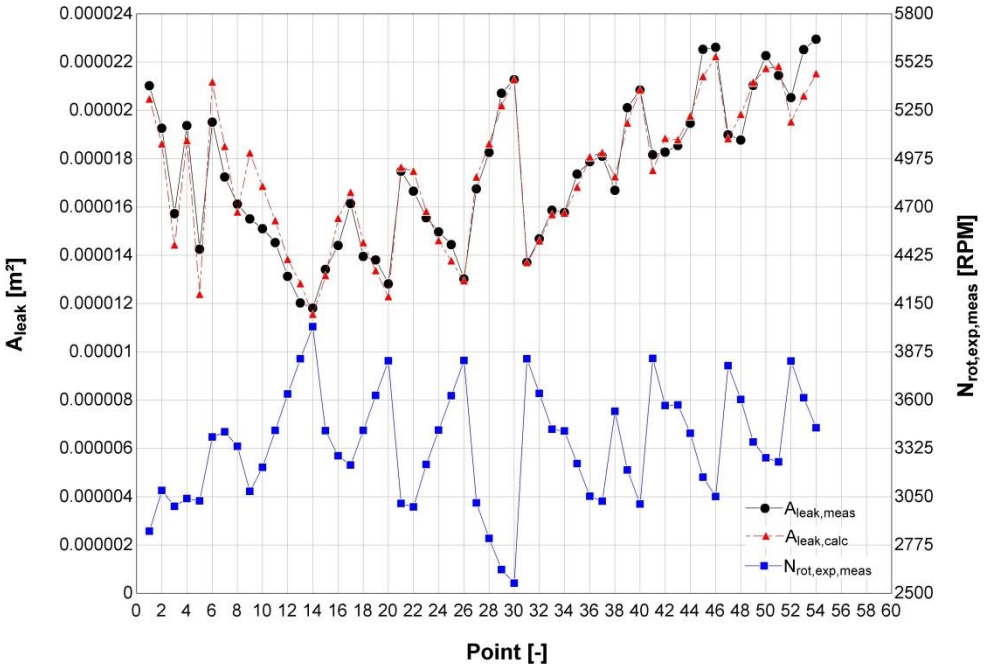

Figure 7: Identification of the fictive flow rate area

The validation of the model was realized comparing the predicted and measured values for the mass flow rate, mechanical power and the exhaust temperature of the expander. Figure 8 compares the evolutions of the mass flow rate measured and predicted by the model. It can be observed that the agreement between the measurement and the prediction by the model is very good. The maximum deviation is 3%.

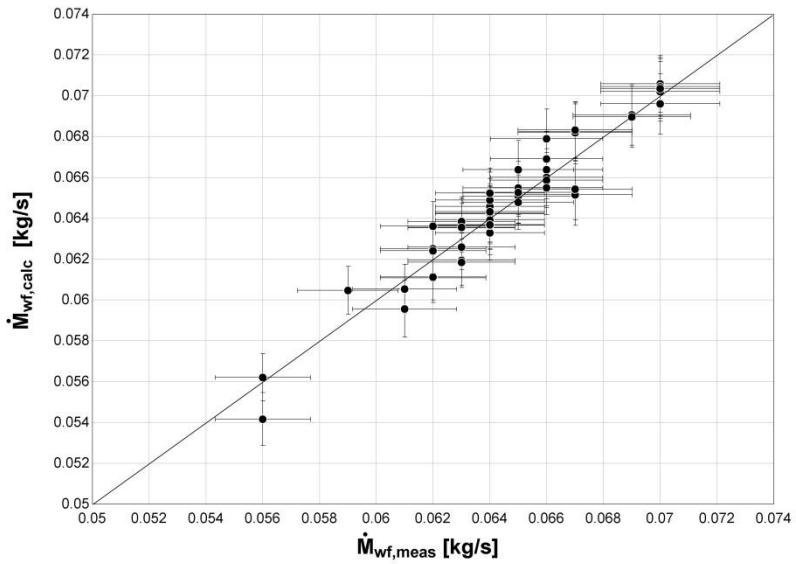

Figure 8: Validation of the expander model - comparison between predicted and measured mass flow rate

The evolutions of the shaft power, measured and predicted by the model are compared in Figure 9. It can be observed that the agreement is good. The maximum deviation between the model predictions and the measurements is 8%.

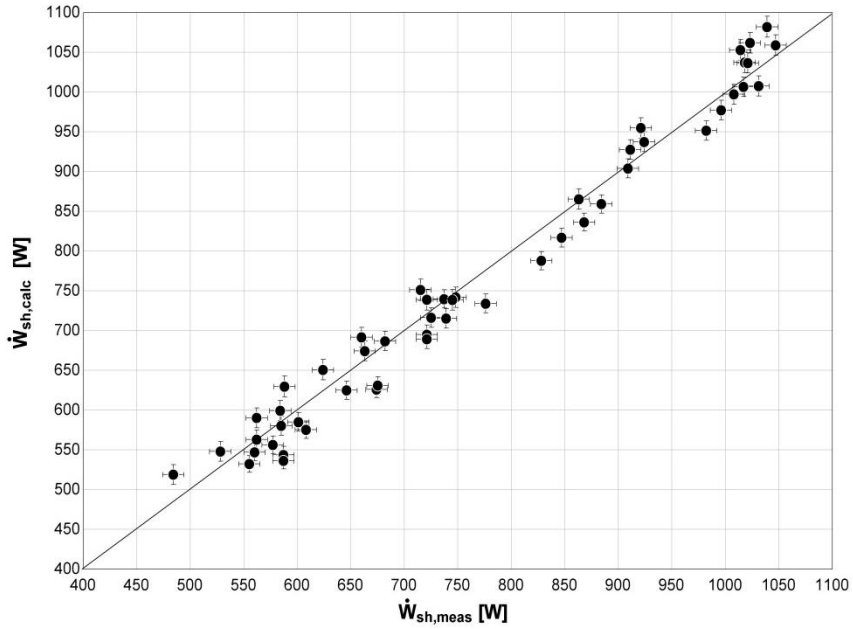

Figure 9: Validation of the expander model - comparison between predicted and measured shaft power

The model predicts the exhaust temperature within 4 K and seems to slightly underestimate it. This could be – among other things – the result of an error in the temperatures measurements during the experimental campaign. Indeed, the energy balance over the expander revealed to be incorrect and led to negative ambient losses (see equation 3). However, the balance is very sensitive to precise temperature measurement and small errors have a great influence on the difference ($h_{su} - h_{ex}$).

$$\dot{Q}_{amb} = \dot{M}_{wf}(h_{su} - h_{ex}) - \dot{W}_{shaft} < 0 \tag{3}$$

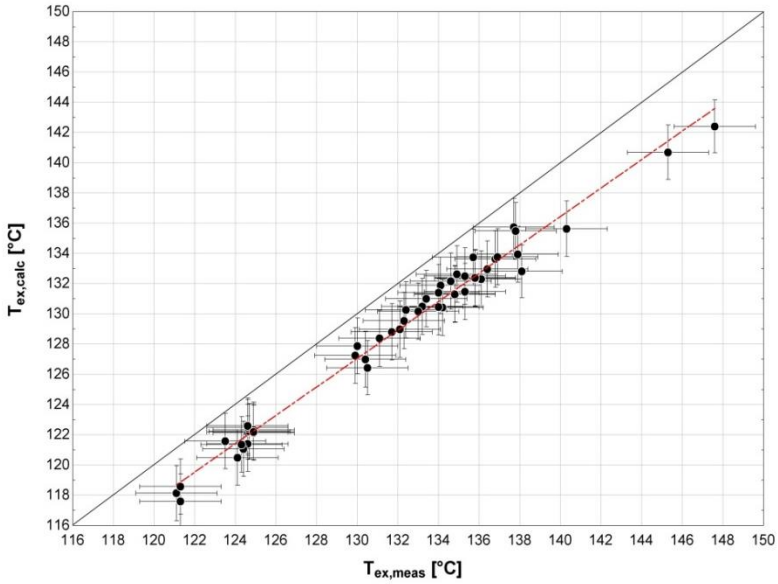

Figure 10: Validation of the expander model - comparison between predicted and measured exhaust temperature

The validated model of the expander can then be used to quantify the different losses. Figure 11 shows the evolution of the overall isentropic efficiency with the pressure ratio imposed to the expander for a particular rotational speed of 3000 RPM. The evolution at the top of the figure is

predicted by a model that only accounts for under- and over-expansion losses. The efficiency equals 1.0 at a pressure ratio adapted to the built-in volume ratio ($r_{v,\,in}$ = 3) of the expander (top curve). For smaller and larger pressure ratios, the fluid is over-expanded and under-expanded respectively. The isentropic efficiency then decreases when accounting for the heat transfers (green curve) mainly because of the supply cooling down of the fluid. It also decreases when taking into account the mechanical losses (purple curve) mainly caused by the friction of the vanes on the stator. Introducing the supply pressure drop in the modeling largely reduces the isentropic effectiveness (blue curve). A more detailed investigation should answer the question of how to reduce this pressure drop by modifying the expander geometry. The internal leakage is responsible for the major part of the performance loss (red curve). Further work should investigate the possibility of reducing this leakage without increasing the mechanical losses of the expander.

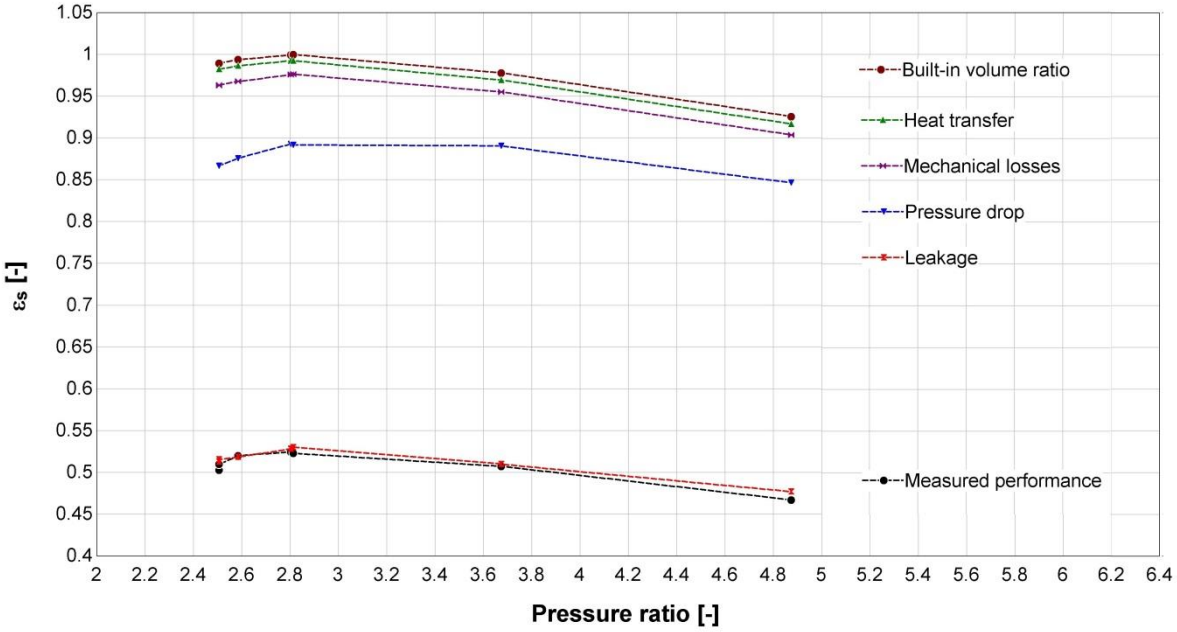

Figure 11: Model analysis - evolution of the calculated overall isentropic effectiveness with the imposed pressure ratio for a rotational speed of 3000 RPM.

6. CONCLUSION

The paper describes experimental measurements and modeling of the vane expander prototype used in an experimental ORC which uses hexamethyldisiloxane as a working fluid. The ORC is cooled by air and uses flue gas as a source of heat. The vane expander reached the maximum shaft power of 1.05 kW with the isentropic efficiency 0.45. The maximum reached isentropic efficiency was 0.58 at 800 W of shaft power. It is obvious that highest efficiencies were obtained when the ratio v_{ex}/v_{su} roughly corresponds to the internal built-in volume ratio of the expander. Further attention should be paid to the optimal superheating which apparently affects the expander efficiency. Presented results of a semi-empirical model show good agreement between calculated and measured mass flow rate and shaft power respectively. The model shows that the internal leakage is responsible for the major part of performance loss. The supply pressure drop has also significant influence on the overall performance. Therefore, further work should be focused on investigation how to reduce these major losses.

NOMENCLATURE

c	number of working chambers	(–)
ΔP	pressure drop	(Pa)

h	specific enthalpy	(J/kg)
$\dot{M}$	mass flow rate	(kg/s)
N_{rot}	rotational speed	(RPM)
$\dot{Q}$	heat transfer rate	(W)
$r_{v,\,in}$	internal built-in volumetric ratio	(–)
s	specific entropy	(J/kg.K)
v	specific volume	(m^3/kg)
V	volume	(m^3)
V_c	initial volume of working chamber	(m^3)
$\dot{W}$	mechanical power	(W)
η, ε	efficiency	(–)

Subscript

amb	ambient
calc	calculated
ex	exhaust
exp	expander
in	internal
leak	leakage
loss	losses
meas	measured
s	isentropic
shaft	shaft
su	supply
vol	volumetric
wf	working fluid

REFERENCES

Aoun, B., 2008, *Micro Combined Heat and Power Operating on Renewable Energy for Residential Building*, PhD thesis, École Nationale Supérieure des Mines de Paris, Paris, 151 p.

Cipollone, R., Contaldi, G., Bianchi, G., Murgia, S., 2014, Energy recovery using sliding vane rotary expanders, *8th International Conference on Compressors and their Systems*, p.183-194.

Lemort, V., Quoilin, S., Cuevas, C., Lebrun, J., 2009, Testing and modeling a scroll expander integrated into an Organic Rankine Cycle , *Applied Thermal Engineering*, 29, p. 3094–3102.

Mascuch, J., Dlouhy, T., 2011, Natural Gas Decentralized Micro CHP: The Czech Republic Case, *5th Annual International Travelling Conference for Young Researchers and PhD Students ERIN 2011*, p. 81-86.

Peterson, C. R., McGahan, W. A., 1972, Thermodynamic and Aerodynamic Analysis Method for Oil Flooded Sliding Vane Compressor, *International Compressor Engineering Conference*, Purdue University, p. 1-8.

Xia, C., Zhang, W., Bu, G., Wang, Z., Shu, P., 2013, Experimental study on a sliding vane expander in the HFC410A refrigeration system for energy recovery, *Applied Thermal Engineering*, 59, p. 559–567.

Yang, B., Peng, X., He, Z., Guo, B., Xing, Z., 2008, Experimental investigation on the internal working process of a CO_2 rotary vane expander, *Applied Thermal Engineering*, 29, p. 2289–2296.

ACKNOWLEDGEMENT

This work has been supported by the European Union, OP RDI project No. CZ.1.05/2.1.00/03.0091 – University Centre for Energy Efficient Buildings and OP RDI project No. CZ.1.05/3.1.00/13.0283 – Intelligent Buildings.

EFFECT OF WORKING FLUID MIXTURE COMPOSITION ON THE PERFORMANCE OF AN ORGANIC RANKINE CYCLE

Peter Collings, Zhibin Yu*

University of Glasgow,
University Avenue
Glasgow
United Kingdom
p.collings.1@research.gla.ac.uk, zhibin.yu@glasgow.ac.uk

ABSTRACT

Whereas single-component working fluids exhibit phase changes at a constant temperature, working fluid mixtures containing two or more components can exhibit a change in temperature across a phase change, known as "glide". These fluid mixtures are termed "zeotropic". Zeotropic mixtures can possess several advantages when used as working fluids in ORC systems. Similarly to supercritical cycles, they can match the temperature profiles on the hot and cold sides of the evaporator, resulting in less of a need for superheating, and increasing second law efficiency. The major advantage of a zeotropic fluid over a supercritical one is that this effect can also be felt in the condenser, which can greatly reduce the need for coolant for a given cycle efficiency. This is of particular benefit in desert areas, where cooling water is not readily available. In general, zeotropic cycles can be made to exhibit significant temperature glide at far lower pressures than an equivalent supercritical cycle.

A temperature glide can also result in a greater amount of energy being transferred in a recuperator, should one be included in the system, by increasing the difference in temperature between the cold fluid leaving the pump, and the hot fluid leaving the expander, which results in a greater transfer of energy for a given cycle configuration, especially when this enables a certain amount of phase change to occur in the recuperator.

This paper uses a numerical simulation in MATLAB to analyse the effects of varying the composition of a zeotropic mixture of R245fa and R134a on the overall performance of a cycle, both with and without a recuperator installed.

Evaluation of ORC using Low GWP Working Fluids for Waste Heats

Katsuya Yamashita[1*], Osamu Furuya[1*], Eiichi Sakaue[1*]

[1]Toshiba Corporation Power Systems Company, Power and Industrial Systems R&D Center,
New Energy and Generator Group
Yokohama, Kanagawa, Japan
Katsuya2.yamashita@toshiba.co.jp

ABSTRACT

In this study, to evaluate Organic Rankine cycle (ORC) system using low GWP working for waste heat of lower temperature (180C waste gas), R1233zd and R1234ze(E) as low GWP working have been selected comparing with the used R245fa, and evaluated ORC system efficiency. As a result, R1233zd and R1234ze(E) are more useful than R245. R1233zd is particularly found out effective and easily.

INTRODUCTION

Ironworks have various furnaces and have been exhausting waste heats of various temperatures. Though waste heats of more than 250℃ have already been utilized for electricity, heating, drying and all that. But, those of lower than 200℃ have not been effectively utilized yet. For 40 years, electric power generation system using organic working fluid has been commercialized for the geothermal hot water of lower than 200℃ in geothermal power plants. But due to environmental problems of organic working fluids, electric power generation system using organic working fluid has not been applied in the lower waste heats. Organic working fluid's problems for commercial application are toxicity, flammability, ozone depletion (ODP) and global warming potential (GWP). Recently, in respect of climate change, low GWP working fluids have been paid attention and developed. Some are being released into market. The low GWP working fluids are more degradable in high atmosphere and have much shorter lifetime than existing organic working fluid such as R134a and R245fa and less flammability than flammable working fluid such as pentane, butane, propane due to its molecule structure.

In this study, to design ORC system using low GWP working for 180C waste gas, various kinds of thermal properties of those low GWP have been evaluated using publicized reliable database like NIST, for the first step. Also other properties such as stability, productivity are evaluated to find out effective low GWP working fluids. As the second step, power generation efficiency for waste gas of lower than 200℃ using low GWP working fluids such as R1233zd and R1234ze(E) was evaluated compared with conventional one, R245fa. Various power generation system types are evaluated such as subcritical Rankine cycle, supercritical Rankine cycle and recuperated Rankine cycle, based on depending on critical temperature of working fluids and turbine outlet gas superheated temperature. Evaluations also take into accounts following factors, such as turbine efficiency, working fluid pump efficiency, generator efficiency, pinch-point temperature difference and pressure loss of heat recovery heat exchanger, condenser, recuperator, and pipe pressure loss. Since, expected power generation output is more than 1MW, and turbine inlet pressure is more than 1MPa, multi-stage axial turbine is picked up.

As the result, power generation gross efficiency and the modified efficiency are estimated and heat exchangers scales are determined by basic designation.

1. Low-GWP Working Fluids

Table.1 shows Low GWP working fluids and used R245fa. R1233zd and R1234ze(E) are 5-6 GWP, about 1/200 to R245fa. R1234ze(E) is lower than R245fa at the boiling point, the critical point, and then ORC Plant is higher pressure. And also there is flammable range. On the other hand, R1233zd has similar thermal characteristics. But the critical temperature is about 10C higher than R245fa, and is capable to generate the higher temperature vapor to the turbine.

Table.1.Comparisons of Low GWP Working Fluids

	R245fa	R1233zd	R1234ze(E)
Boiling Point Tb	15.3	16.0	-19.0
Critical Temp Tc	154.0	165.6	109.0
Critical Pressure Pc	3.65	3.57	3.97
Molecular Mass	134	130.5	114
GWP	1030	5.0	6.0
Flammability	None	None	7.0-9.5
ODP	0.0	0.0	0.0

2. Organic Rankine Cycle of Waste Heat

2.1 Power Plant System

Fig1 shows the schematic Rankine cycle including recuperator. Rankine cycle is generally used the steam power plant using fossil fuels and the turbine inlet temperature attained to over 600C. For the turbine inlet temperature more than 230C, steam power plants using water as working fluid were generally more effective than organic working fluids like hydrocarbon as Propane, Butane, and Pentane.

Organic Rankine cycles have been applied for example geothermal power plant, solar power plant, biomass power plant, heat recovery power plant. Cycle applications of low temperature source about less than 200C have been used practically and been commercialized. Schematic figure of Rankine cycle (including the recuperation) is shown in Fig1. Rankine cycle without recuperator is less advantageous, because the hot temperature level (potential) of heating fluids is made good use of. And also the outlet temperature of heating fluids is lower; the utilizing rate of heating fluids' inlet temperature is more decreasing. The recuperated Rankine cycle is more effective, because the inlet temperature of feed liquid to heat exchanger being heated by heating source, is close to the outlet temperature of heating fluids. In other word, on condition of same heating rate from the heating source, the circulating working fluid rate of cycle is increased and turbine output is higher than that without recuperator.

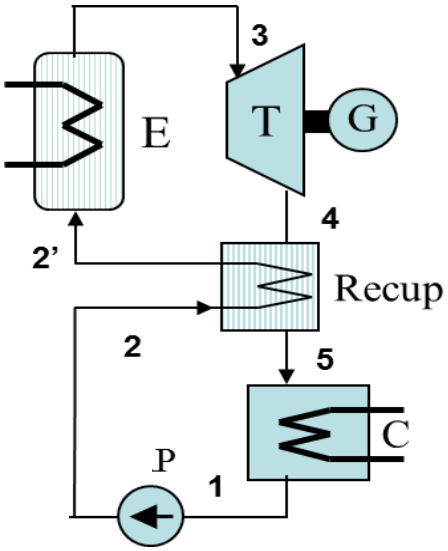

E : Evaporator
T : Turbine
G : Generator
C : Condenser
P : Pump
Recup: Recuperator

1→2 : Isentropic Compression
2→3 : Isobaric Heating
3→4 : Isentropic Expansion
4→1 : Isobaric Cooling

Fig1. Schematic Rankine Cycle System

2.2 ORC Type of Investigating

Alternate low GWP working fluids are R1233zd, R1234ze (E). The critical temperature of R1233zd is 165.6C close to waste heat gas inlet temperature 180C. And then the subcritical Rankine cycle have been investigated like used working fluid R245faas Fig2. And also super heating of evaporator is not necessary because those studied organic working fluids have the tendency of superheating by isentropic expansion in subcritical condition. Above mentioned, in subcritical Rankine cycle condition, the lower the outlet temperature of heating fluids is, the more effective power plant output is. That cycle characteristics, which the power output is unmatched the subcritical Rankine cycle efficiency is weak point of ORC.

One of heat cyclic way of improving the weak point of simple Rankine cycle is super critical Rankine cycle in fig.2. In the super critical Rankine cycle, the isobaric heating' process has not temperature limit, and then the evaporator outlet temperature can be getting close to the inlet temperature of heating fluid. The important point of super critical Rankine cycle is to been selecting the turbine inlet pressure according to working fluid, in view point of the critical condition that critical temperature, pressure, (volume). The other R1234ze(E)' critical temperature is 109C, far from waste heat gas temperature, and then the supercritical Rankine cycle have been investigated for R1234ze(E) as Fig2.

Another of heat cyclic way is the recuperated Rankine cycle in Fig.3, which is different than regenerated Rankine cycle like the steam power plant. The regenerated Rankine cycle which have been used large power plant using high pressure steam Rankine cycle, is the cycle of heating feed water using various pressure extraction steam from Steam turbine. Organic working fluids have less amount of latent heat than water, and the tendency of superheating gas by isentropic expansion. And turbine exhausted gas is higher than the feed liquid temperature of the organic fluid pump. In Fig3 the feed liquid temperature can increased by recuperator and the flow rate of the isobaric heating of evaporator (1-2) can be increased and then turbine output can be augment. The recuperated cycles have been studied for each working fluid.

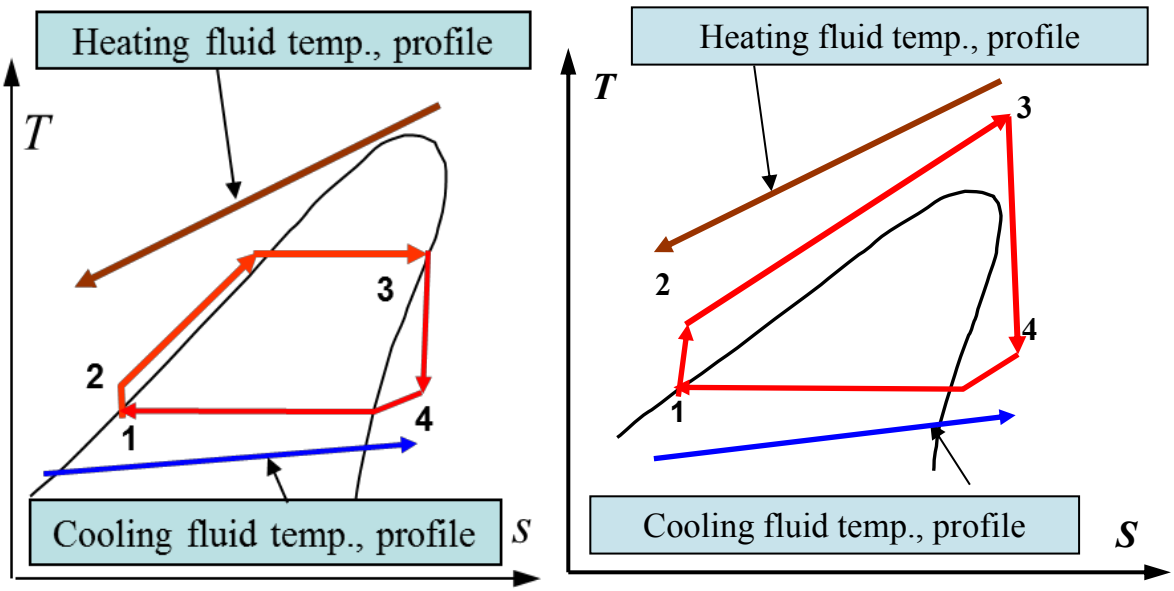

Fig.2. Subcritical & Supercritical Rankine Cycle T-S Diagram

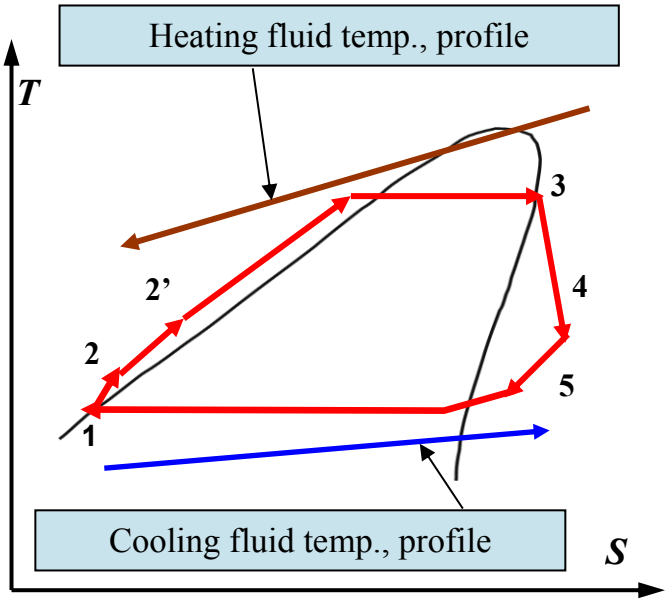

Fig.3. Recuperated Rankine Cycle T-S Diagram

2.2 Components of ORC

The above-mentioned schematic cycles are shown in Fig4-Fig5. The waste heat gas temperature is fixed at 180C. The heat recovery evaporator (HREVA) and the heat recovery preheater (HRPRE) are shown separately on the subcritical condition in Fig4 because of existing header of saturated vapor, on the other hand, the supercritical condition has one heat exchanger, the supercritical evaporator (HR-SUP EVA), because of not-restricting without turbine inlet condition, temperature, pressure. In Fig5, the recuperator (RECUP) is connecting from the organic turbine to the condenser and the recuperator heat load is determined to the pinch-point temperature difference from the condenser inlet to the high pressure feeding liquid. The cooling source is the cooling water by the cooling tower.

The main components are as followers

.

● Heat Recovery Evaporator

There are two kind of heating fluids, liquid state and gas state in ORC. As mentioned above, the lower waste heats of the ironworks are almost gas state. The waste gases have low density and then became large volume flow rate. Utilizing the existing gas duct, the heat transfer portions are packed inside, the preheater and the evaporator needs to be low pressure loss of waste gas side.

In general, like the natural circulating boiler, there is liquid-vapor separating header and the evaporating tube bundles in the upper waste gas stream, the preheating tube bundle in the downstream. In under-mentioned supercritical evaporator, the header is not necessary because of not existing phase-boundary, the heat-exchanged portion is composed of the one-through tubes. The heat transfer rate of waste gas is lower than that of inner tube heat transfer, and the high fin tube is practical used. The heat transfer rates of the supercritical fluids are practically used for inner tube. And then application of supercritical cycle to waste heats gas is reasonable.

●Turbine

The aim of ORC development using the low temperature waste heat of ironworks is to investigate high efficiency and more than MW class power plant. Because low power plant like 50～200kW is less applicability of heavy electrical duty like ironworks. In general the axial turbine is effective and practically used for more than MW electrical generation. And then the axial turbine is applied to the ORC system.

●Condenser

Organic working fluids are lower than water in thermal conductivity. The condensation heat transfer is lower, and then shell tube type condenser utilizing the enhanced tube like low-fin horizontal tube is used practically.

● Recuperator

Recuperator is heat exchanging between the high pressure working fluids' liquid and low pressure turbine exhaust vapor. The low pressure exhaust vapor is much larger volume than the working fluids' liquid and has low heat transfer rate. And then the tube bundle configuration like the above heat recovery evaporator is installed into the shell because the turbine exhaust vapor is more than atmospheric pressure

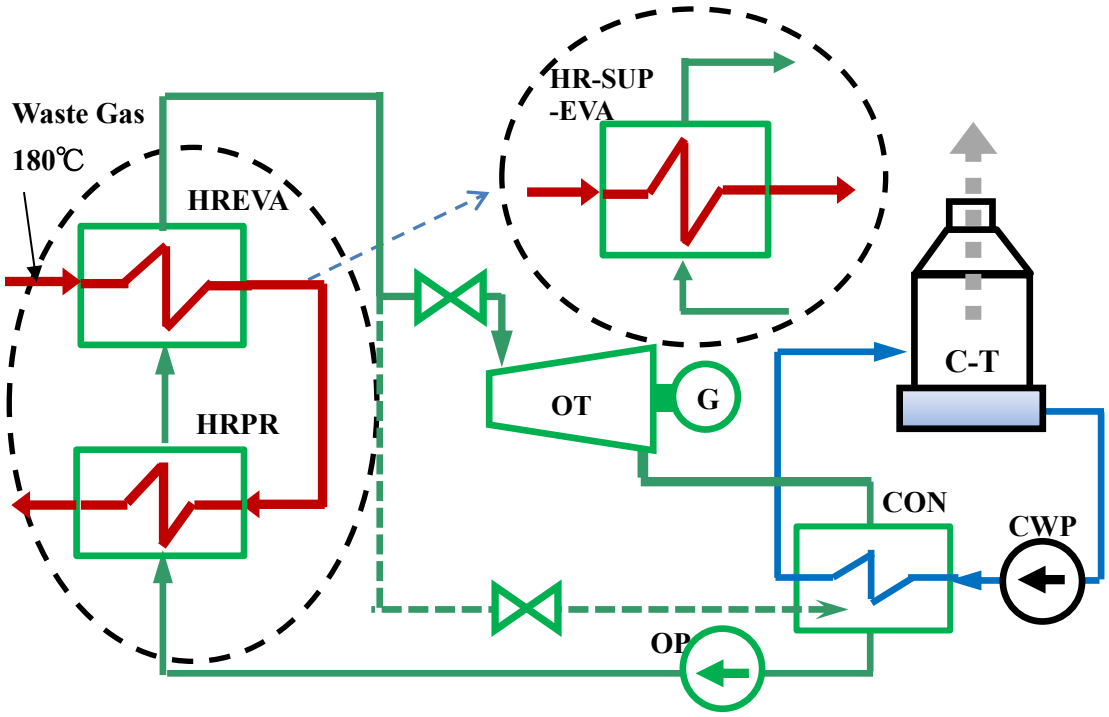

Fig.4. Schematic Subcritical & Supercritical Rankine System

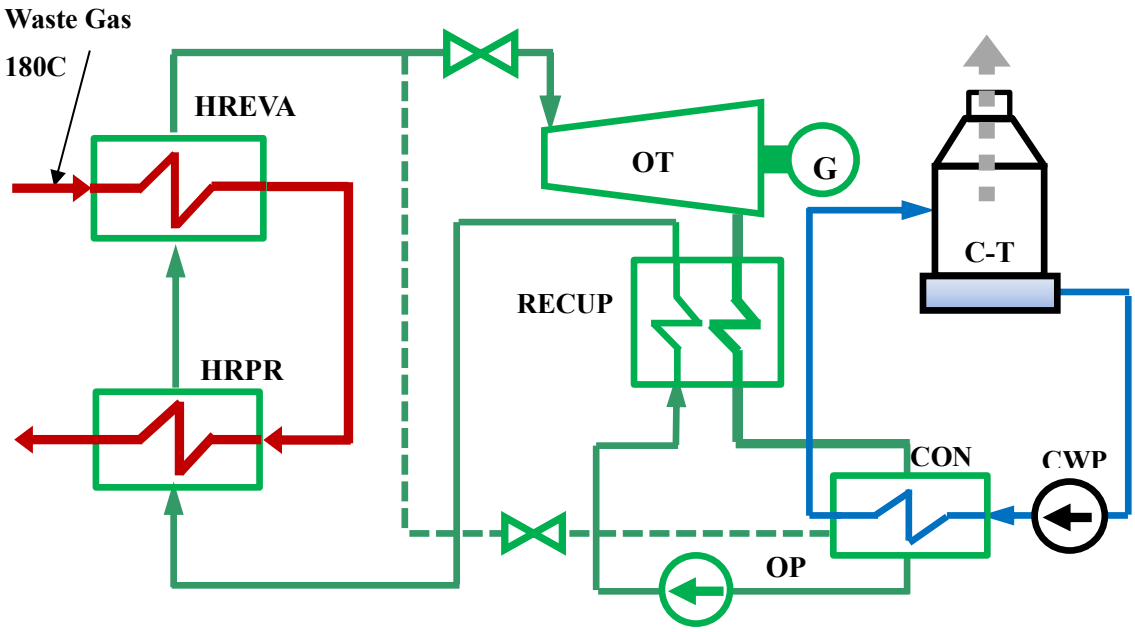

Fig.5. Schematic Recuperated Rankine System

HREVA	Heat Recovery Evaporator	HRPRE:	Heat Recovery Preheater
HR-SUP EVA:	Supercritical Evaporator	OT：	Organic Turbine
G：	Generator	CON：	Condenser
OP：	Organic Fluid Pump	CWP：	Cooling Water Pump
RECUP:	Recuperator	C-T:	Cooling Tower

3. Organic Rankine Cycle Evaluation

3.1. Rankine Cycle (Supercritical Rankine Cycle) Evaluation

The using working fluids, R245fa has the high GWP shown in Table.1. As Low GWP Organic working fluids, R1234ze(E) and R1233zd has been promising in air-conditioning, foaming agents. Inlet temperature of the waste heat gas is lower than 180℃, and the range of outlet temperature are 110－140℃, on grounds of exhausting condition and gas's contamination. Comparing the critical temperatures of working fluids with waste gas inlet temperature, R245fa and R1233zd have been analyzing as subcritical Rankine cycle, and R1234ze(E) has been analyzing as supercritical Rankine cycle as shown in Fig2. The composing difference of subcritical and supercritical cycle is evaporator and preheater which are generating the working fluids steam (gas). In subcritical cycle, there are preheater which is heating the feed liquid to the temperature close to saturation temperature (evaporating steam temperature) and evaporator which is generating steam (gas) at a certain pressure. But in supercritical cycle, there is no phase change at the heating and gas generating process, there is one heat exchanger. There is one more characteristic in supercritical cycle that is selecting temperature profile changeable by setting pressure. The comparing results of Gross Output Efficiencies of working fluids are shown in Fig.3.

The analyzing conditions are followers.

i. The heating gas is dry air and inlet temperature is 180C.
ii. The pinch point temperature difference is more than 10C of heating and evaporating heat exchangers
iii. The line of the isentropic expansion of turbine is outside of the saturated gas line in working fluid.
iv. Turbine isentropic efficiency is due to the working volume flow
v. The Generating output takes account of gear, generator, and turbine efficiency.
vi. The turbine outlet pressure loss is 4%
vii. The Condensing temperature is 32C, and the cooling water outlet temperature is 25C.
viii. The pressure loss from evaporator to turbine is 4 % including main-stop valve loss
ix. The working fluids side pressure loss is calculating at base of the pressure loss of waste heating gas is 20kPa.

As shown in Fig2 the gross output of each (every) working fluids are decreasing in proportion to the output temperature of waste heats. It means that each thermal efficiencies of their output temperature of waste heats is almost equal. It is due to that the turbine inlet temperatures have hardly any changed according to the outlet temperatures of waste heats. Fig3 shows the tendencies clearly. The gross efficiency of supercritical Rankine cycle using Low GWP working fluid R1234ze(E) is lower than that of R245fa. But varying the turbine inlet pressure and setting the pinch point temperature of the evaporator 10C, the gross efficiency is a bit more than that of r245fa. On the other hand, That of R1233zd is more than R245fa about 1.0% because of the turbine temperature of R1233zd is more than that of R245fa.

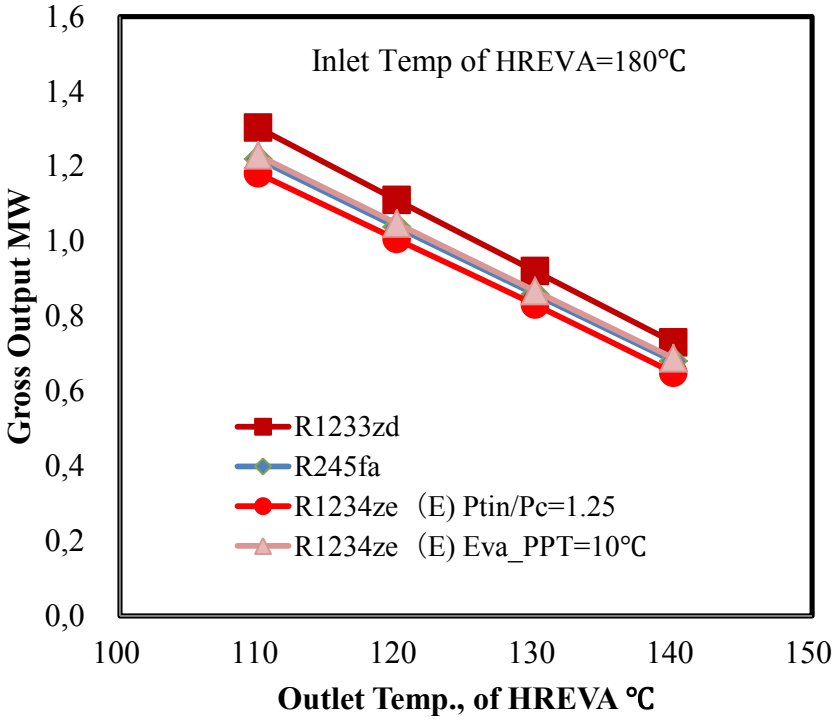

Fig.6. Gross Output of Working Fluids

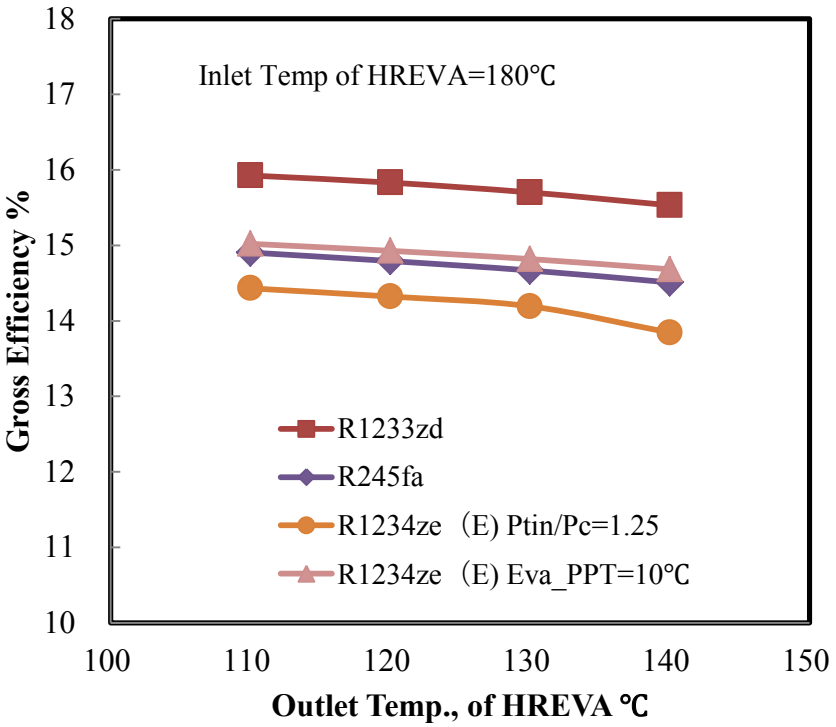

Fig.7. Gross Efficiency of Working Fluids

3.2. Recuperated Rankine Cycle (Supercritical Rankine Cycle) Evaluation

Generally Organic working fluids have the tendency which the line of the isentropic expansion is off from the saturated gas line. Turbine isentropic efficiency is about 80%, the outlet steam (gas) is more off and became superheated steam (gas). And then heating the feed liquid using the superheated temperature is recuperator (Fig5)

Superheated rate of turbine outlet is different among the investigating working fluids, supercritical cycle of R1234ze(E) has most superheated ratio, R245fa, R1233zd in order. The gross efficiency by recuperating has been shown in Fig8-Fig9. The Gross efficiency of Recuperated cycle of R245fa & R1233zd in Fig6-8, have been little increased about 1%. Their two working fluids are about same critical temperature and about same superheated rate. And then the recuperated capability is low and the recuperating ratio (= Recuperator heat load/Condenser heat load) are 6-7%.

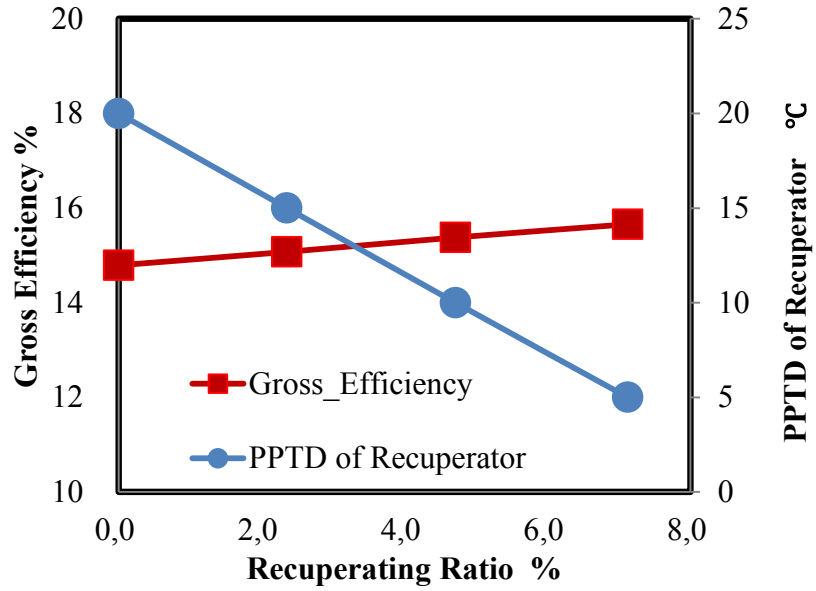

Fig.8. Gross Efficiency of R245fa by Recuperating

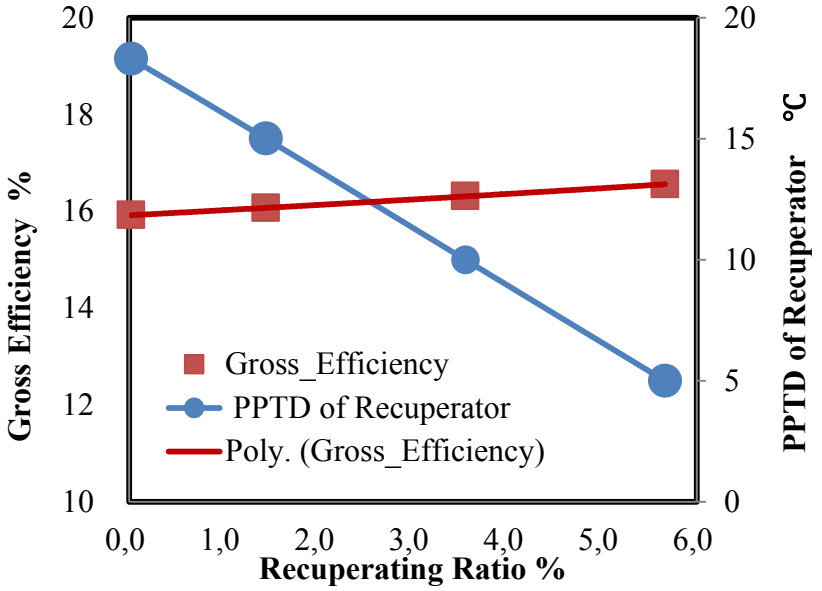

Fig.9. Gross Efficiency of R1233zd by Recuperating

Another working fluid, R1234ze(E) which is supercritical Rankine Cycle, has high recuperating ratio to 30%. And then the gross efficiency has been to 19%, as to about 30% recuperating ratio. The R1234ze(E) supercritical cycle's turbine inlet temperature attains to 168C, that is 55C superheated at the turbine outlet vapor. The superheated temperature became to more than 30℃, the condenser performance is lower than that of saturate vapor. The recuperator is indispensable to the R1234ze(E) supercritical cycle. But it is not necessary for R245fa and R1233zd subcritical cycle.

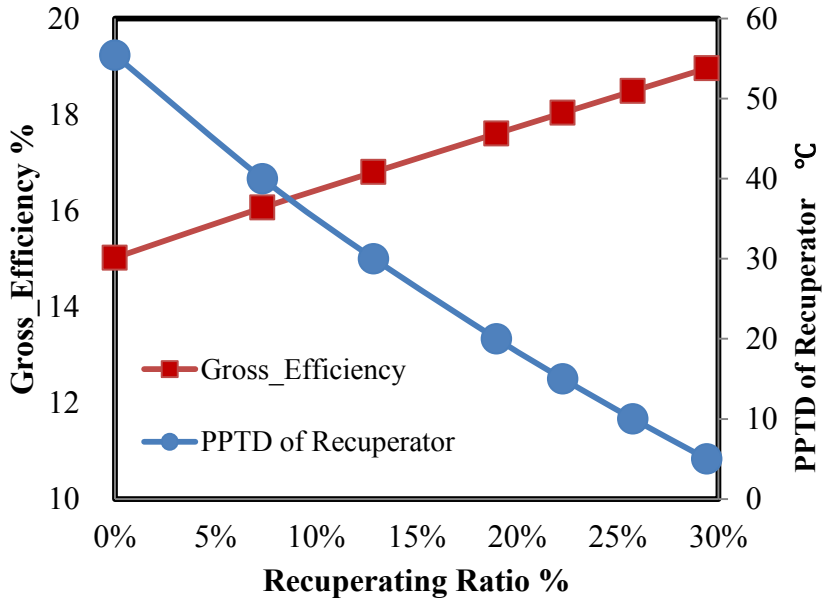

Fig.9. Gross Efficiency of R1234ze (E) Supercritical Cycle by Recuperating

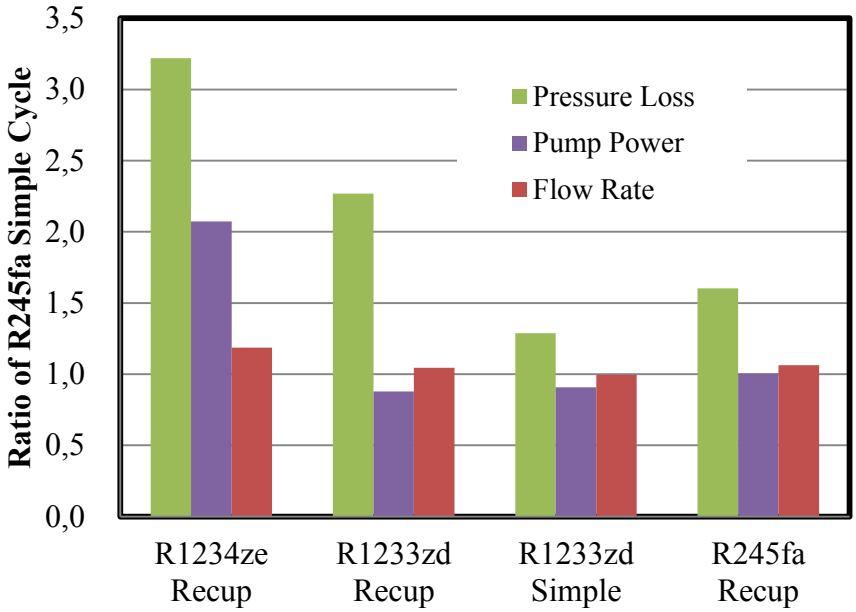

Fig.10. Comparison of Flow Rate Pump-power pressure loss Ratio

4. Comparison of R1233zd and R1234ze(E)

R1234ze (E)' supercritical recuperated Rankine cycle is highest Gross efficiency. On the investigation of Low GWP ORC, Comparison of components has been carried out. Because R1233zd is not suitable for the supercritical recuperated Rankine cycle due to the critical temperature and isentropic expansion line closed to the saturated gas line. But it is possible of R1233zd cycle that components are smaller than the R1234ze(E) cycle. Fig.10 shows the concerned value of components' size. The values of Fig.10 are the ratio of the working fluid flow rate, pump-power and pressure loss ratio heat recovery evaporator and recuperator at R245fa cycle. R1233zd is lower than R245fa both the flow rate and pump power. But all values of R1234(E) supercritical recuperated cycle is more than that of R245fa, In particular the pump power is more than twice because of supercritical cycle.

Table.2 shows the modified output which draws the pump power from the gross power. The table shows the value comparing the R245fa recuperated cycle. The recuperated Rankine cycle of R1233zd is highest output augmentation, the second is R1234ze(E) supercritical recuperated cycle which is highest gross efficiency. but if the organic pump efficiency is improved, R1234ze(E) supercritical recuperated cycle can have best performance.

R1233zd simple Rankine cycle is 8.0% higher than R245fa, replacing R245fa in used ORC power plant with R1233zd can be effective.

Table.2.Modified Output Augmentation Based on R245fa

Working fluid & Cycle	R1234ze(E)	R1233zd	R1233zd	R24fa
Evaporation Pressure	Supercritical	Subcritical	Subcritical	Subcritical
Recuperated Rate	29%	5.6%	None	6.4%
Modified Output Augmentation	11.5%	12.6%	8.0%	5.9%

5. Conclusion

The investigation of organic Rankine cycle has been carried out using Low GWP working fluids, instead of used High GWP working fluid R245fa, this paper has shown the results for 180C waste heat gas as follows

- Alternate low GWP working fluids, R1233zd, R1234ze(E) have higher gross efficiency than the used working fluid, R245fa.
- Without recuperating, R1233zd' cycle is highest gross efficiency.
- In recuperated Rankine of working fluids, R1234ze(E) is most recuperating ratio and then is highest gross efficiency of about 30% recuperating.
- On the modified output augmentation distracting the organic pump consumption, R1233zd is highest output.

6. Acknowledgement

This work was supported by the Japan Science and Technology Agency (JST) under the Strategic International Collaborative Research Program (SICORP).

7. References

1. Bala V.DATLA, Joost J.BRASZ "*Organic Rankine Cycle System, Analysis for Low GWP Working Fluids*" IRACC at Purdue, July 16-19,2012
2. Sotirios Karellas, Andreas Schuster, "*Supercritical Fluid Parameters in Organic Rankine Cycle Applications*" Int.J.of Thermodynamics,Vol.11(No.3) pp.101-108, September,2008
3. Bala V.DATTA, Joost J.BRASZ "Comparing R1233zd and R245fa for Low Temperature ORC Application" IRACC at Purdue, July 14-79,2014
4. Enrico Saverio Barbieri, Mirko Morini, Michele Pinelli "*Development of A Model for The Simulation of Organic Rankine Cycles Based Contribution Techniques* " ASME Turbo Expo GT2011,June 6-10,2011